University of Southampton

Faculty of Physical Sciences and Engineering

Department of Physics and Astronomy

The multi-wavelength properties of nearby low-luminosity Active Galactic Nuclei (LLAGN) with the Legacy e-MERLIN Multi-band Imaging of Nearby Galaxies survey (LeMMINGs)

Author

David Richard Alexander Williams

ORCID ID: 0000-0001-7361-0246

Thesis for the degree of

Doctor of Philosophy

September 2018

University of Southampton

ABSTRACT

Faculty of Physical Sciences and Engineering

Department of Physics and Astronomy

DOCTOR OF PHILOSOPHY

The multi-wavelength properties of nearby low-luminosity Active Galactic Nuclei (LLAGN) with the Legacy e-MERLIN Multi-band Imaging of Nearby Galaxies survey (LeMMINGs)

by David Richard Alexander Williams

The radio and multi-wavelength properties of active galactic nuclei (AGN) have been well documented in the literature, contributing to the unified picture of AGN as a super-massive black hole surrounded by various sub-structures. The study of low-luminosity AGN (LLAGN) is less well documented or understood, due largely to their intrinsic faintness. In this thesis, I study the radio emission of a statistically-complete sample of 280 nearby LLAGN using the Legacy e-MERLIN Multi-band Imaging of Nearby Galaxies survey (LeMMINGs), to detect the presence of kpc-scale radio jets. I compare the radio emission to the multi-wavelength properties of the host galaxy and LLAGN to understand the physical accretion mechanism in different types of LLAGN system. First, I present two in-depth multi-wavelength case studies of nearby LLAGN, observed with the LeMMINGs 'deep' survey: NGC 4151 and NGC 6217, studying long-term variability and the nuclear structures in these sources. I then present the LeMMINGs 'shallow' survey radio data for a statistically-complete sample of 280 nearby LLAGN based off the Palomar survey. I compare these observations with other available data in the literature, including X-ray observations from the *Chandra* X-ray Observatory to assess the multi-wavelength correlations of different types of LLAGN. Furthermore, I denote a type of star-forming galaxy, namely the 'jetted H II galaxies', that show similar multi-wavelength properties to that of other LLAGN, indicating that they may be hiding a LLAGN. Finally, the Fundamental Plane of Black Hole Activity (FPBHA) is correlation between the X-ray luminosity, radio luminosity and mass for black holes, spanning over eight orders of mass from Black hole X-ray binaries (BHXRBs) upto super-massive black holes in AGN. I construct the FPBHA for the LeMMINGs 'shallow' sample objects, including a sub-sample of BHXRBs, to investigate the correlation coefficients of the plane and test its validity with LLAGN sources. The results are consistent with previous formulations of the FPBHA but suggest that choice of LLAGN sub-sample is important for regressing the FPBHA parameters.

Contents

List of Figures

List of Tables

Declaration of Authorship

I, David Richard Alexander Williams, declare that this thesis entitled *The multi-wavelength properties of nearby low-luminosity Active Galactic Nuclei (LLAGN) with the LeMMINGs survey* and the work presented herein are my own and has been generated by me as the result of my own original research. I confirm that:

- This work was done wholly or mainly while in candidature for a research degree at this University;
- Where any part of this thesis has previously been submitted for a degree or any other qualification at this University or any other institution, this has been clearly stated;
- Where I have consulted the published work of others, this is always clearly attributed;
- Where I have quoted from the work of others, the source is always given. With the exception of such quotations, this thesis is entirely my own work;
- I have acknowledged all main sources of help;
- Where the thesis is based on work done by myself jointly with others, I have made clear exactly what was done by others and what I have contributed myself;
- Parts of this work have been published as:
  - Chapter 3: *Radio jets in NGC 4151: where eMERLIN meets HST*:, 2017 MNRAS 472 3842-3853
  - Chapter 4: *Unveiling the 100 pc scale nuclear radio structure of NGC 6217 with e-MERLIN and the VLA*, has been submitted for publication with MNRAS
  - Chapter 5: *LeMMINGs - I. The eMERLIN legacy survey of nearby galaxies. 1.5-GHz parsec-scale radio structures and cores*:, 2018 MNRAS 476 3478-3522

Signed: .....

Date: .....

Acknowledgements

The completion of a Ph.D. thesis is a long and often stressful process. This thesis is no exception and hence, I would like to thank some of the people who have been invaluable to the science outcomes and also supported me when I ran into problems with work and study. First, I could not have completed this work without the guidance of my supervisor Ian McHardy. In the final year of my studies, I was also aided greatly by Matt Middleton who offered to help read my work and engaged me in new areas of astrophysics. I would not have been able to complete the data reduction without the guidance of the staff at the Jodrell Bank Centre for Astrophysics at the University of Manchester. The Co-PI of the LeMMINGs sample, Rob Beswick, was always willing to lend a hand and a helpful hint or two, as well as Megan Argo and Javier Moldon, who showed me how to get the most out of AIPS and CASA! I will never forget the best piece of advice on radio astronomy given to me by Megan: "If in doubt, flag it out!".

To all my collaborators, of which there are many, thank you for your insightful comments throughout my Ph.D. research. I have also had the opportunity to make several acquaintances with other Ph.D. students and post docs around the world. Specifically, Jonathan Westcott, Jack Radcliffe, Chris Skipper and Hayden Rampadarath were always helpful. I have made some friends and colleagues throughout the world and I have enjoyed the scientific discussion with all of them.

I would like to extend my warmest thanks to several colleagues in the astronomy department in Southampton, specifically those who I shared an office with who through their knowledge and willingness to extend a helping hand, made it easier to complete this work on time. During the beginning of my Ph.D. research, Sam Connolly was there always pushing me to explore the science behind all the data reduction that at that time seemed to be endless. Dimitrios Emmanolopoulos expanded my knowledge of statistics. After Sam and Dimitrios left, I was joined in my office by Lorenzo Zanisi and Daniel Asmus, who were always willing to lend a hand. Lorenzo, Daniel and I immediately got on well and despite working on different aspects of astronomy, have always discussed our work and helped one another.

Outside of my own office, there have been several others who have made the completion of this thesis much easier. I must thank my undergraduate friends Jamie Court and Rory Brown, who continued with me in academia at Southampton; Adam Hill for his expert Python knowledge; Bella Boulderstone, John Coxon, Stephen Browett, the original

inhabitants of 4081/4083; my fellow Mayflowers, specifically Miika Pursiainen, Andy Smith and Alex Constantino and my brilliant demonstrators throughout my Ph.D.; the Ph.Ds that left before me: Chris Boon , Rob Firth, Juan Hernandez and James Matthews; the Ph.D.s and post docs that joined after me Victoria Lepingwell, Triana Almeyda, Charlotte Angus, Phil Wiseman, Peter Boorman and also to those who I knew from undergraduate, Sadie Jones and Judith Ineson. Last, and certainly not least amongst my colleagues at the University of Southampton, I have to thank Ranieri Baldi for his guidance and help throughout the time that we worked together on the LeMMINGs sample. Ranieri and I have worked closely for three years and I can honestly say that without him I would not be the scientist I am today. He has helped me with my papers and the data reduction as well as supporting me through difficulties. I couldn't have asked for anything more from a colleague and I'm proud to call him a friend.

My closest friends have heard most of difficulties of the last few years and I have to thank them for standing by me. Nick Chalk and Bethany Dexter have been two of my closest friends in the past 4 years and have no doubt gotten bored of hearing about blobs! In no particular order, I must also thank Rhys Chalk, Hamid Khan, Sara Rubio, Nick Wilson, James Strudwick, John Martin, Gary Carr, Georgios Pnevmatikakis, Kieran Dexter, Tim Deehan and Paul Edwards. I also need to thank the Southampton University Archery Club and AC Delco Bowmen for allowing me to shoot arrows to help relieve stress over the last 4 years!

From a young age, my parents instilled the value of education in me, and I will be eternally grateful to them for the opportunities they have provided me with throughout my life. From celebrating with me in my finest moments, be they academic, sport-based or other, to supporting me when I was having difficulties and problems, I cannot thank them enough. My dad, Glyndwr, has supported my Ph.D. studies right from the start, reading my papers and taking a keen interest in all the work I was producing. My mum, Christine, while claiming she didn't know what I was talking about most of the time has never stopped offering to help with everything I have done. My sister, Alexandra, and I are like chalk and cheese, but we have always supported each other through difficulties in the last four years. In addition, my sister's dog Luna, who provided much needed fluffy cuddles when I needed them most!

Finally, on a personal note, my partner Sam has stood by me throughout the duration of the writing of this thesis, despite the long hours, working at weekends and having to listen to all the problems I've faced at different points in the last four years.

Abbreviations

ADAF **A**dvection **D**ominated **A**ccretion **F**low
AIPS **A**stronomical **I**mage **P**rocessing **S**ystem
ALG **A**bsorption **L**ine **G**alaxy
AGN **A**ctive **G**alactic **N**uclei
ATCA **A**ustralian **T**elescope **C**ompact **A**rray
BH **B**lack **Hole**
BHXRB **B**lack **H**ole **X**-**r**ay **B**inary
BPT diagram **B**aldwin, **P**hillips, **T**erlevich diagram
CASA **C**ommon **A**stronomy **S**oftware **A**pplications
CXO ***C**handra* **X**-ray **O**bservatory
e-MERLIN **e**nhanced **M**ulti **E**lement **R**adio-**L**inked **I**nterferometer **N**etwork
ELR **E**mission **L**ine **R**egion
FPBHA **F**undamental **P**lane of **B**lack **H**ole **A**ctivity
FRI **F**anaroff **R**iley Type I
FRII **F**anaroff **R**iley Type II
HLA ***H**ubble* **L**egacy **A**rchive
HMXB **H**igh **M**ass **X**-ray **B**inary
HST ***H**ubble* **S**pace **T**elescope
IF **I**ntermediate **F**requency
IFU **I**ntegrated **F**ield **U**nit
IMBH **I**ntermediate **M**ass **B**lack **H**ole
IR **I**nfra-**r**ed
IRAF **I**mage **R**eduction and **A**nalysis **F**acility
IRSA **I**nfra-**r**ed **S**cience **A**rchive
ISCO **I**nner-most **S**table **C**ircular **O**rbit
ISM **I**nter**s**tellar **M**edium
JDAF **J**et **D**ominated **Accretion F**low
JIVE **J**oint **I**nstitute for **V**LBI in **E**urope
LeMMINGs **L**egacy **e**-**M**ERLIN **M**ulti-band **I**maging of **N**earby **G**alaxies **s**urvey
LF **L**uminosity **F**unction
LINER **L**ow-**I**onisation **N**uclear **E**mission-line **R**egion
LLAGN **L**ow-**L**uminosity **A**ctive **G**alactic **N**uclei

LMXB **L**ow **M**ass **X**-ray **B**inary
LRI **L**ine **R**atios **I**ndex
MCMC **M**arkov **C**hain **M**onte **C**arlo
MeerKAT **Meer** **K**aroo **A**rray **T**elescope
MERLIN **M**ulti **E**lement **R**adio-**L**inked **I**nterferometer **N**etwork
MLA **M**achine **L**earning **A**lgorithm
MTLRI **M**ulti-**T**elescope **R**adio **L**inked **I**nterferometer
NED **N**ASA **E**xtragalactic **D**atabase
NRAO **N**ational **R**adio **A**stronomy **O**bservatory
NVSS **N**RAO **V**LA **S**ky **S**urvey
OSP **O**ld **S**tellar **P**opulation
PC *HST* **P**lanetary **C**amera
RA **R**ight **A**scension
RFI **R**adio **F**requency **I**nterference
RIAF **R**adiatively **I**nefficient **A**ccretion **F**low
RLF **R**adio **L**uminosity **F**unction
ROSAT **RÃűntgen****sat**ellit
SDSS **S**loane **D**igital **S**ky **S**urvey
SED **S**pectral **E**nergy **D**istribution
SKA **S**quare **K**ilometre **A**rray
SMBH **S**uper-**M**assive **B**lack **Hole**
SPW **Sp**ectral **W**indow
ULX **U**ltra-**L**uminous **X**-ray source
UV **U**ltra-**v**iolet
VLA Karl Jansky **V**ery **L**arge **A**rray
VLBA **V**ery **L**arge **B**aseline **A**rray
VLBI **V**ery **L**arge **B**aseline **I**nterferometry
WFPC2 *HST* **W**ide **F**ield **P**lanetary **C**amera **2**
WISE **W**ide-field **I**nfrared **S**urvey **E**xplorer
XMM-Newton ***X**-ray **M**ulti **M**irror Mission*
XLF **X**-ray **L**uminosity **F**unction
XRB **X**-**r**ay **B**inary
YSO **Y**oung **S**tellar **P**opulation

Chapter 1

Introduction

As some of the most powerful and fascinating phenomena in the Universe, the study of super massive black holes (SMBHs) at the centres of galaxies has inspired and endured throughout the 20th Century. While they are regarded in science fiction as monsters that eat everything in their path, the truth is that they are responsible for some of the most extreme physics in the Universe. When a SMBH accretes matter, powerful broadband emission across the electromagnetic spectrum is observed. These bright, compact regions at the centres of galaxies are known as 'Active Galactic Nuclei' (AGN). However, AGN are not equal in their bolometric output and the weakest AGN are known as low-luminosity AGN (LLAGN).

The study of LLAGN is interesting as they probe the lowes accretion rates and BH masses observed for AGN. To first order, the accretion theory is thought to be a scale-invariant process and so it should be possible to find an empirical relationship between the most luminous AGN and LLAGN. Therefore, LLAGN allow accretion theory to be studied at the lowest luminosities and therefore identify changes in observed properties of AGN. In addition, such a relation must also scale down to the lowest black hole masses that are observed in X-ray binaries (XRBs). This thesis aims to understand how the multi-wavelength properties of LLAGN differ in the nearby Universe and relate to powerful AGN and black holes XRBs with a statistically-complete sample of nearby LLAGN.

In this chapter I discuss the the discovery of AGN from a historical perspective and how AGN differ from LLAGN and XRBs. I will describe black hole accretion theory in the context of SMBHs, detail the different mechanisms that are applied to understand accretion onto black holes as well as outline the broadband properties of AGN. I will present the orientation-based AGN unification scheme and provide an overview of the fundamentals of radio astronomy that are necessary for understanding this Ph.D. thesis. Finally I will discuss the data sources that are used in this thesis, namely the observatories, interferometers and surveys that are of most importance.

1.1 Active Galactic Nuclei

Many galaxies exhibit broadband (radio through to X-ray) emission from their nuclei. For some galaxies, this emission can be explained simply by stellar processes and thus they are considered "normal" star-forming galaxies. However, many galaxies have a bright central nuclear region that cannot be explained by star formation processes alone. For these nuclei, an additional component is required to explain the high luminosities in the nuclear region. The only process efficient enough to explain the high broadband luminosities in the galactic nucleus is the release of gravitational potential energy from the accretion of matter onto a SMBH (Rees, 1984). The excess radiation observed in the nucleus of these galaxies led to them being named 'Active Galactic Nuclei' and as such the galaxies that host an AGN are called 'active' galaxies.

The earliest observations of active galaxies can be traced back to the early 20th Century (Fath, 1913; Slipher, 1917), although the classification and the true nature of these exotic objects would not be revealed until much later. In the 1940s, (Seyfert, 1941) showed that some galaxies (laterly known as 'Seyfert' galaxies) have broad nuclear Balmer emission lines in their spectra. The broad lines were associated with brighter nuclei. But, it was not clear what process was causing the broadened Balmer lines. (Baade and Minkowski, 1954) found that several radio galaxies showed similar emission lines to Seyfert galaxies and subsequently (Schmidt, 1963) argued that the emission lines observed in the quasar[1] 3C 273 were red-shifted Balmer lines similar to those seen in Seyferts. This discovery showed that Seyfert galaxies and quasars were likely powered by the same process but with vastly contrasting luminosities. Such luminosities are much greater than what can be powered by nuclear fusion processes. Therefore, when accretion theory of matter onto compact objects was modelled in the 1970s and 80s (e.g. Shakura and Sunyaev, 1973; Begelman et al., 1984; Rees, 1984), it became clear that these objects were extragalactic sources with a central active SMBH.

It is now thought that every galaxy harbours a SMBH at its centre because the nuclear properties of galaxies have been shown to scale with the global observational galaxy properties (e.g., the BH mass − stellar velocity dispersion, or $M_{\rm BH} - \sigma$ relationship, Magorrian et al. 1998; Ferrarese and Merritt 2000; Gebhardt et al. 2000; Tremaine et al. 2002; Di Matteo et al. 2005, 2008; Shankar et al. 2016). While the presence of a SMBH in every galaxy is assumed, observationally SMBHs can be difficult to detect: the indicators of AGN activity are not observed in all galactic nuclei due to obscuration and absorption. LLAGN in particular are hard to detect due to to their low broadband emission and confusion with other processes such as circum-nuclear star formation.

[1] A quasar/quasi-stellar object (QSO) is a high redshift AGN with a very high bolometric luminosity. Quasars are often associated with radio galaxies.

1.1.1 Low-Luminosity AGN

While the characteristics of bright AGN (e.g. the presence of nuclear emission lines, luminous radio cores with M pc-scale jets or more recently compact X-ray emission from the nucleus) are well known, the characteristics of LLAGN are less well understood. It is thought that LLAGN differ from luminous AGN due to a different accretion mode. LLAGN are usually powered by radiatively inefficient accretion flows onto the SMBH, due to low BH masses or accretion rates (Ho, 1999b; Maoz, 2007; Panessa et al., 2007), resulting in low optical to X-ray luminosities. Hence, the nuclear emission lines that are observed in Seyfert galaxies may be contaminated with star formation in the host galaxy, the radio jets may have long since faded or be too small to observe, or the X-rays in the nucleus may be absorbed by intervening material. LLAGN are defined by their emission-line luminosities of $L_{H\alpha} < 10^{40}$ ergs s^{-1} (Ho et al., 1997a) or by their X-ray luminosities $L_{X-ray} < 1{\times}10^{42}$ ergs s^{-1} (Ptak, 2001). They are often radio-quiet, defined as the ratio between the radio emission (usually at 6 cm), and the optical emission (at 4400Å), is < 10 (Kellermann et al., 1989). In addition, they have low bolometric Eddington ratios (see equation 1.20) of $\lesssim 10^{-2}$ (Ho, 2008). These are broad definitions and some objects do not meet all of these requirements, but generally LLAGN are characterised by one of these three measures.

Despite their low broadband emission, LLAGN are important objects to study for several reasons. Numerically, they are the most dominant accretion source in the nearby Universe, outnumbering the more powerful QSOs, and they represent the most common mode of SMBH accretion e.g. inefficient accretion/low accretion rates. LLAGN can be used to study the transition from the radiatively efficient to the radiatively inefficient accretion state. However, they are similar to quiescent galaxies, as the central SMBH may not necessarily be active. Therefore this allows for the study of triggering emission in SMBHs. LLAGN are often associated with lower mass SMBHs, but also with lower accretion rates, which allow a wider parameter space of accretion theory to be investigated. They are important for constraining scaling relations and the evolutionary models for SMBHs and galaxies (Barausse et al., 2017). Finally, they sample the low end of the luminosity function, important for a complete census of local SMBH activity.

Since the first discovery of Seyfert galaxies, more types of LLAGN were discovered. Heckman (1980) found a new class called ‘Low-Ionisation Nuclear Emission-line regions’ (LINERs) which showed similar optical emission lines to Seyfert galaxies but at reduced ionisation levels and weak radio emission. LINERs were observed mostly in what were thought to be normal ‘quiescent’ galaxies. Further spectroscopic follow-up of a complete sample of local galaxies with the Palomar bright spectroscopic sample of nearby galaxies (hereafter "The Palomar Sample" Filippenko and Sargent, 1985; Ho et al., 1995, 1997a,d,b,c,e, 2003, 2009) showed that LINERs were actually the most dominant LLAGN population in the local Universe. The Palomar survey also defined other galaxies by their optical emission-line ratios, namely the ‘Absorption Line Galaxies’ (ALGs), nuclei with no detectable optical emission lines or lines seen in absorption, ‘H II Regions’, which showed

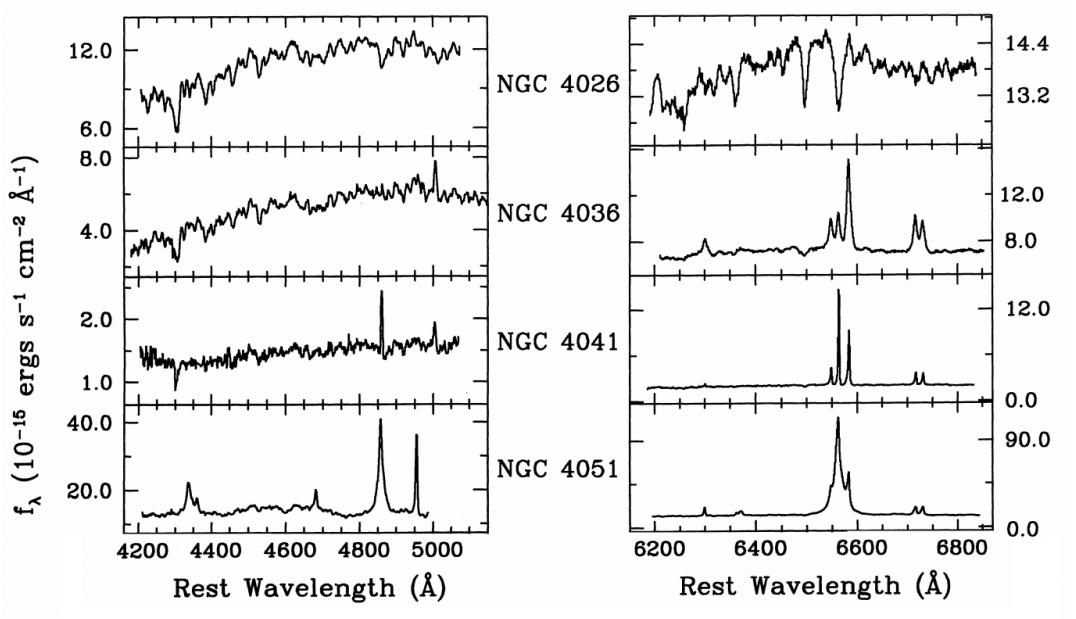

Figure 1.1: Examples of the spectra obtained in the Palomar sample (Ho et al., 1997a). NGC 4026 is an example of an Absorption Line Galaxy (ALG), where the emission lines are significantly absorbed where emission lines are expected. NGC 4036 is classified as a LINER type galaxy, as it shows significant line emission. While NGC 4041 also shows significant line emission, the [S II] doublet is weak at 6717 and 6731Åand relatively strong H_β line at 4862Å, and is therefore classified as a H II region. Finally, NGC 4051 is a clear Seyfert type galaxy as the emission lines are very large compared to any of the other types of galaxy presented in this plot.

very weak emission lines, and 'Transition' Galaxies, an intermediate class between H II Regions and ALGs.

Kilo-parsec radio jets are observed in LLAGN (Condon, 1987; Ulvestad, 2003; Ghisellini et al., 2004) but most studies thus far have concentrated on Seyferts and LINERs. As the radio waveband is not significantly absorbed by intervening gas and dust or by the atmosphere, it offers the best diagnostic of SMBH activity so long as the radio emission can be disentangled from other radio emitting processes like star formation. However, it is only responsible for $\sim 10^{-3}$ of the bolometric output of an AGN, necessitating sensitive radio observations. In local LLAGN, the spatial scales ($\sim$100 pc per arcsecond at 20 Mpc) allow for the separation of the jets from the AGN emission and background star formation. A large sample of LLAGN unbiased towards of all the optical classifications of LLAGN at high sensitivity and angular resolution is therefore needed to disentangle the LLAGN activity from the SF processes.

Radio variability has been detected in the nuclei of some LLAGN, e.g. (e.g. Wrobel, 2000; Mundell et al., 2009) though not in others, e.g. (e.g. Jones et al., 2011, 2017). However temporal studies of jets in radio-quiet AGN are rare due to their intrinsic radio weakness. Most of the studies have focussed on Seyfert galaxies with known radio jets, and have found variability over time-scales of a few months to a few years (Mundell et al., 2009). In some cases, a sudden re-brightening of an AGN has been observed (e.g. Argo et al., 2015), or a

tidal disruption event (TDE) has been discovered in other wavebands (Mattila et al., 2018) but such cases are rare.

1.1.2 X-ray binaries

Thus far I have considered only SMBHs in the centres of galaxies. However, black holes of masses $\lesssim 20 M_\odot$ are also observed in the Milky Way in binary systems where a compact object (a black hole or neutron star) is orbited by a companion star, releasing mainly X-ray emission (see equation 1.28). These objects are known as X-ray binaries (XRBs). The compact object can accrete matter from the companion via Roche lobe overflow or by stellar winds ejected from the companion. XRBs are broadly split into two arbitrary categories of low-mass XRBs (LMXBs) and high-mass XRBs (HMXBs), where the discriminating factor is the companion star's mass. LMXBs typically have a companion star mass of $\lesssim 10\ M_\odot$ and are associated with the Roche Lobe overflow method of accretion, while the HMXBs have a companion mass of $\gtrsim 10\ M_\odot$ and are typically thought to accrete via stellar winds (for example see Casares et al., 2017, for a review).

While I do not go into detail about XRBs in this thesis, a few important characteristics of these objects must be considered. First, when I compare SMBHs with XRBs, I only refer to black hole XRBs (BHXRBs). This is an important distinction as neutron stars have a surface whereas black holes have an event horizon from which electromagnetic radiation cannot escape. In addition, this thesis only considers BHXRBs in the 'low/hard' state. In the 'low/hard' state, BHXRBs have X-ray spectra dominated by a power-law and have compact radio cores (Fender, 2001; Merloni et al., 2003), similar to AGN.

1.2 Black Hole Accretion Theory

Accretion is the term used in astronomy to describe the amassing of particles into a small region due to gravitational attraction of other matter. In the context of this thesis, accretion refers to the flow of matter onto a black hole. The total energy of a test mass, m, at a distance r from a compact object of mass M is simply the sum of its kinetic energy, T, and the gravitational potential energy, U:

$$E = T + U \tag{1.1}$$

where,

$$T = \frac{1}{2}mv^2; U = -\frac{GMm}{r} \tag{1.2}$$

where v is the velocity of the particle and G is the Gravitational constant. If we assume that the particle will orbit in a circular motion, we get:

$$v^2 = \frac{GM}{r} \tag{1.3}$$

Substituting (1.3) into the expression for T in (1.2), we find:

$$T = \frac{1}{2}\frac{GMm}{r} = \frac{GMm}{2r} \tag{1.4}$$

Therefore, the total energy at a radius r is given by:

$$E = T + U = \frac{GMm}{2r} - \frac{GMm}{r} = -\frac{GMm}{2r} \tag{1.5}$$

If one considers the change of the kinetic energy and gravitational potential energy as a function of the radius, r, by differentiation:

$$\frac{\mathrm{d}T}{\mathrm{d}r} = -\frac{GMm}{2r^2}; \frac{\mathrm{d}U}{\mathrm{d}r} = \frac{GMm}{r^2} \tag{1.6}$$

hence,

$$\frac{\mathrm{d}T}{\mathrm{d}r} = -\frac{1}{2}\frac{\mathrm{d}U}{\mathrm{d}r} \tag{1.7}$$

Therefore, as material falls deeper into the gravitational potential well of the black hole, half of the potential energy is converted to kinetic energy, e.g. it gets virialised, to maintain the same orbit and conserve angular momentum, whereas the rest of the energy must be lost by radiation or mechanical processes. The energy released by the accretion process is usually expressed in terms of the rest mass energy, m, and the efficiency of the accretion, η,:

$$E_{rad} = \eta mc^2 \tag{1.8}$$

In order to estimate the amount of energy radiated by the accretion of matter onto a black hole, it is insightful to consider the innermost stable circular orbit (ISCO) of the black hole. The radius of the ISCO can be used in a simplistic approximation to estimate the energy radiated by a particle moving from infinity to the ISCO. Inside the ISCO, no stable circular orbit is possible, hence any small perturbation towards the black hole at the ISCO will cause a particle to fall into the black hole. While particles will still radiate inside the ISCO, the energy can be considered lost to fall inside the event horizon of the black hole. By considering the change in potential of moving a particle from infinity to the ISCO, the change in potential energy is:

$$\Delta V = \int_{R_{ISCO}}^{\infty} \frac{GMm}{r^2} dr = \frac{GMm}{R_{ISCO}} \tag{1.9}$$

By using general relativity and solving the Schwarzschild metric for a non-rotating static black hole, one can show that the ISCO has a radius defined by:

$$R_{ISCO} = \frac{6GM}{c^2} \tag{1.10}$$

By substituting this equation into the previous one, the change in potential is found to be:

$$\Delta V = \frac{mc^2}{6} \tag{1.11}$$

Hence, one sixth of the rest mass energy of the particle is liberated as kinetic energy. Therefore, given equation (1.7), one twelfth of the energy is radiated away, requiring an efficiency factor of $\eta = 0.083$. For context, the nuclear fusion of atoms ($\eta = 0.003$) releases only a fraction of the energy that accretion can. For example, the efficiencies are so different that powerful quasars (L$\sim 10^{46}$ erg s^{-1}) would require an accretion rate $\gtrsim$60 M$_\odot$ per year to be explained by nuclear fusion alone ($\eta = 0.003$), but only $\sim$3 M$_\odot$ per year by accretion, assuming $\eta = 0.083$ (see Peterson, 1997). Therefore only accretion onto a central compact object plausibly explains the luminosities we observe in AGN and not, for example, nuclear fusion in stars. The ISCO is closer to the black hole in the case of a rotating Kerr black hole. Efficiencies of up to 0.4 are possible for maximally spinning Kerr black holes(Shakura and Sunyaev, 1973) and as such these systems can radiate even more energy away.

1.2.1 The Eddington Luminosity

The in-falling material must also radiate and so escape the system. The outward radiation pressure that is produced can therefore regulate the accretion mechanism and hence yields a theoretical upper limit for spherical accretion. The momentum, p_γ, that can be carried by a single photon of energy E_γ is:

$$p_\gamma = \frac{E_\gamma}{c} \tag{1.12}$$

We can calculate the force, F_{tot}, exerted on the in-falling material by this radiation pressure by summing over the contribution of all the photons and differentiating with respect to time:

$$F_{tot} = \frac{\mathrm{d}}{\mathrm{d}t}\sum_\gamma p_\gamma = \frac{1}{c}\frac{\mathrm{d}}{\mathrm{d}t}\sum_\gamma E_\gamma = \frac{L_{bol}}{c} \tag{1.13}$$

L$_{bol}$ is the bolometric luminosity of the black hole. Assuming that the radiation is emitted isotropically, one can calculate the radiation pressure, P_{rad}, at a distance d:

$$P_{rad} = \frac{L_{bol}}{4\pi d^2 c} \tag{1.14}$$

This radiation pressure only applies to electrons, and is given by the Thomson cross-section, σ_T. However, I note that more generally the radiation pressure can be modified by the

opacity of the gas, which can change due to different mechanisms, for example electron scattering, bound-bound transitions, free-free transitions. The Thomson cross section is proportional to the charge of the particle to the fourth power and inversely proportional to the particle mass squared. As the mass of a proton is $\sim 2{\times}10^3$ larger than the electron but the magnitude of charges are the same, the Thomson cross-section of electrons will dominate over that of the protons. If we assume that the accreting matter is made up of hydrogen gas (1 proton, 1 electron), the force on an atom will be:

$$F_{rad} = \frac{L_{bol}\sigma_T}{4\pi d^2 c} \tag{1.15}$$

We can now compare this equation to the gravitational force on a hydrogen atom, which is dominated by the mass of the proton, m_p:

$$F_{grav} = \frac{GMm_p}{d^2} \tag{1.16}$$

Solving for the bolometric luminosity, we arrive naturally at the Eddington limit:

$$L_{Edd} = \frac{4\pi GMm_p c}{\sigma_T} \tag{1.17}$$

This can be conveniently re-written in terms of the black hole mass alone:

$$L_{Edd} = 1.26 \times 10^{38} \left(\frac{M}{M_\odot}\right) \mathrm{ergs/s} = 3.2 \times 10^4 \left(\frac{\mathrm{M}}{\mathrm{M}_\odot}\right) \mathrm{L}_\odot \tag{1.18}$$

The Eddington limit, L_{Edd}, provides an upper theoretical limit for the amount of power radiated by the spherical accretion process, under the assumption of isotropic radiation. This luminosity can easily be exceeded as in practice accretion occurs in the equatorial plane, not spherically (Shakura and Sunyaev, 1973) and changes in the opacity can increase the local Eddington limit. Although it has many simplifications, it provides a simple diagnostic to analyse and compare accretion mechanisms in different AGN systems. We can also obtain a theoretical accretion rate, $\dot{M}_{Edd}$, by considering the efficiency, η, of the gravitational potential energy that can be radiated away by this process:

$$\dot{M}_{Edd} = \frac{L_{Edd}}{\eta c^2} \tag{1.19}$$

In addition to the Eddington limit and accretion rate, the Eddington ratio, λ, is often defined as the ratio between the bolometric luminosity and the Eddington luminosity:

$$\lambda = \frac{L_{bol}}{L_{Edd}} \tag{1.20}$$

The Eddington ratio allows for comparison between AGN of different masses and accretion rates, which is very useful when comparing between vastly different BHs.

1.2.2 Bondi Accretion

It is intuitive to first consider accretion onto a black hole as a spherically symmetric process. For a gas cloud at rest at an infinite distance from a compact object, also at rest, only the radial in-fall of matter need be considered as the system has zero angular momentum. This situation was first described by Bondi (1952). For Bondi accretion, a gas cloud accreting onto a compact object does not need to conserve angular momentum or radiate away energy to accrete onto the compact object. However, while it is attractive to consider accretion as a spherically symmetric process, it isn't physical when considering accretion onto black holes as the efficiency is not high enough to explain the observed quasar luminosities. Finally, the likelihood of this type of accretion is extremely low due to the assumptions used (e.g. the angular momentum for a particle being zero), and hence a different accretion mode must be considered.

1.2.3 Efficient Accretion Disks

As spherically symmetric accretion mechanisms cannot produce the radiative efficiencies needed to explain the large bolometric luminosities observed in quasars and Seyfert galaxies, a different mechanism must be operating to transport matter to the black hole. In 1973, Shakura and Sunyaev (1973) proposed a thin disc accretion model for binary systems, whereby matter from a companion star flows onto a compact object via stellar winds or Roche lobe overflow. The authors said that the accreting matter has large angular momentum. Therefore, to accrete the matter, a mechanism must exist to allow for the efficient loss of angular momentum of the matter as it falls towards to the compact object. Shakura and Sunyaev (1973) argued that a geometrically-thin and optically-thick disk is formed and the viscosity of the disk allows for radiation to remove some of the potential energy of the system, where the viscosity is defined as:

$$v = \alpha c_s H \tag{1.21}$$

where α is the viscosity parameter and c_s is the sound speed in the disk. Shakura-Sunyaev disks are approximated as Keplerian thin disks with a scale height, H, much less than the the radius, R, and highly radiatively efficient. This allows for the efficiency required to explain the observed bolometric luminosities of quasars and Seyferts.

To achieve this result, one can consider the amount of potential energy liberated from the system by a mass dM falling in towards a black hole on an annulus at distance r and width dr:

$$dU = \frac{GM}{r^2} dM\, dr \tag{1.22}$$

It has already been shown that only half of this energy can be radiated away in equation 1.7, with the rest maintaining the circular orbit via conversion to kinetic energy. Calculating the

luminosity is therefore straight forward:

$$dL = \frac{1}{2}\frac{\mathrm{d}U}{\mathrm{d}t} = \frac{GM}{2r^2}\dot{M}dr \tag{1.23}$$

The Stefan-Boltzmann law relates the luminosity and temperature given black body radiation, for an annulus at radius r, and considering that the disk has two surfaces from which to radiate:

$$dL = 2\epsilon\sigma_{SB}T^4 \times 2\pi r dr \tag{1.24}$$

where ϵ is the emissivity, σ_{SB} is the Boltzmann constant and T is the temperature at a given radius. From this result we can equate it to equation 1.23 and see how the temperature of the accretion disk varies with radius:

$$T(r) = \left(\frac{GM\dot{M}}{4\pi r^3\epsilon\sigma_{SB}}\right)^{0.25} \tag{1.25}$$

A more general picture can be obtained by considering the viscosity of the disk and how viscous torques dissipate energy through the disk:

$$T(r) = \left(\frac{3GM\dot{M}}{8\pi r^3\epsilon\sigma_{SB}}\left\{1 - \left(\frac{R_{in}}{r}\right)^{0.5}\right\}\right)^{0.25} \tag{1.26}$$

Where R_{in} defines the radius of the inner disk If we consider a region much further away from the inner edge of the disk (e.g. $r >> R_{in}$) then:

$$T(r) \approx \left(\frac{3GM\dot{M}}{8\pi r^3\epsilon\sigma_{SB}}\right)^{0.25} \tag{1.27}$$

which can be parameterised in terms of the Schwarzschild radius $R_S = \frac{2GM}{c^2}$ and the Eddington accretion rate (equation 1.19) to show how the temperature depends on the mass, accretion rate and radius:

$$T(r) \approx 6.3 \times 10^5 M_8^{-0.25}\left(\frac{\dot{M}}{\dot{M_{Edd}}}\right)^{0.25}\left(\frac{r}{R_S}\right)^{-0.75} K \tag{1.28}$$

where I have defined additionally, M_8 as the mass of the black hole in units of $10^8 M_\odot$. From this description, we expect super-massive black holes of mass $\sim 10^8 M_\odot$ to have temperatures which peak in the UV and optical band, whereas a typical black hole XRB will have temperatures which peak in the X-rays as they have a much smaller mass $\sim 10 M_\odot$.

For this thesis, the main relevant timescale is the dynamical timescale of a particle falling through an accretion disk rotating at Keplerian velocity, from equation (1.3):

$$t_{dynamical} = 2\pi\sqrt{\frac{r^3}{GM}} \tag{1.29}$$

For a 10^8 $M_\odot$ black hole, and a typical size of an accretion disk of 0.01 pc, we find that the dynamical time of a particle falling through the accretion disk of order 10^8 years.

1.2.4 Radiatively Inefficient Accretion Flows

Below a critical accretion rate, usually $\lesssim 0.01\dot{M_{Edd}}$ (Esin et al., 1997), the mode of accretion changes from an efficient mode to a radiatively inefficient mode. At such low accretion rates, the geometry of thin Shakura Sunyaev disks is thought to break down as the accreting material becomes optically-thin. Optically-thin material is inefficient at radiating, and hence these are known as radiatively inefficient accretion flows (RIAFs). These were first discussed in Shapiro et al. (1976) and Ichimaru (1977) as a two-temperature plasma, known as an 'ion torus' applied to the BHXRB Cygnus X-1. In this two-temperature RIAF, the ions and electrons are no longer in thermal equilibrium and thus the electrons and ions are decoupled. As the ions are poor radiators, they become hotter than the electrons, so the accretion flow becomes hot and hence 'puffs up' e.g. it becomes geometrically-thick Narayan et al. (1997); Yuan and Narayan (2014). The most well-known type of RIAF, is an advection dominated accretion flow (ADAF) which advects matter directly to the event horizon of the black hole before it can radiate. Therefore this energy heats the flow but is lost to the black hole in the process.

To derive the ADAF critical accretion rate, Narayan et al. (1998) start by defining the advective transport of energy, q^{adv}, with the radiative cooling per unit volume, q^-, and the energy generated by viscosity per unit volume q^+, as:

$$q^{adv} = q^+ - q^- \tag{1.30}$$

where q^{adv} is related to the conservation of energy as follows:

$$q^{adv} = \rho v T \frac{\mathrm{d}s}{\mathrm{d}R} \tag{1.31}$$

where ρ is the density of the gas, v is the radial velocity, R is the radius, s is the specific entropy of the gas and T is the temperature of the gas. In the case of a two temperature gas, T represents the mean temperature.

It should be noted that for $q^+ \simeq q^- >> q^{adv}$ corresponds to a cooling flow where energy is radiated and represents a Shakura Sunyaev optically-thick geometrically-thin accretion disk solution. For $q^{adv} \simeq q^+ >> q^-$, cooling is much less than heating and this corresponds to an ADAF solution. Finally, for $-q^{adv} \simeq q^- >> q^{adv}$, we produce an accretion flow where energy generation is negligible, for example in Bondi accretion (Bondi, 1952; Narayan et al., 1998).

Narayan et al. (1998) considered an optically thin single temperature gas cooling only by free-free emission to derive the critical accretion rate for an ADAF. The authors showed that

the viscous heating, q^+, varied as:

$$q^+ \propto \frac{\dot{m}}{m^2 r^4} \tag{1.32}$$

while the radiative cooling scales as:

$$q^- \propto \frac{\dot{m}^2 T^{0.5}}{\alpha^2 m^2 r^3} \tag{1.33}$$

where T here only applies to the electrons, and α is the viscosity parameter defined in equation 1.21. By comparing q^+ to $q^-$and noting that for a single temperature ADAF, the electron temperature is roughly $10^{12} r^{-0.5}$ K, we arrive at:

$$\dot{M}_{crit} \propto \alpha^2 r^{-0.5} \tag{1.34}$$

This equation shows that for an ADAF to exist, $\dot{M} < \dot{M}_{crit}$ at radii near to the compact object, as $\dot{M}_{crit}$ decreases with increasing r. In this picture, there is an outer thin disc which becomes a truncated hot ADAF in the inner regions. In terms of Eddington units, the critical accretion rate can be re-written as follows:

$$\dot{M}_{crit} \approx 0.4 \alpha^2 \dot{M}_{Edd} \tag{1.35}$$

I have considered only a single temperature so far, but the ions and electrons in the flow are typically at different temperatures so a two-temperature model is more physical. All of the different types of ADAF that occure due to changing temperatures of the ions and electrons are discussed fully by Yuan and Narayan (2014).

The advantage of an ADAF model is that it easily forms outflows and by extension, radio jets (Narayan and Yi, 1995; Sądowski et al., 2013; Yuan and Narayan, 2014). Observationally, LLAGNs have been seen to be radio-loud and thus support this hypothesis (Nagar et al., 2000, 2001; Ho, 2002). At the same time, BHXRBs were shown to have radio emission in the low/hard state (e.g. Fender, 2001; Fender et al., 2004). Furthermore, it has been suggested that AGN also show a symbiosis between the disks and jets (Falcke and Biermann, 1995). Yuan and Narayan (2014) showed that this type of ADAF seemed to explain both XRB and LLAGN observations in some sources (e.g. Fender et al., 2004), indicating that the ADAFs may be a scale-invariant process responsible for the observed X-ray and radio emission in many accreting objects. Furthermore, Yuan and Narayan (2014) suggest that the difference between the radio-loud ADAF-dominated sources and the objects with geometrically-thin disks and weak radio emission may be due to three different effects: , the thicker disks that advect more of their flow onto the black hole in an ADAF flow (e.g. Livio et al., 1999), the Bernoulli parameter being larger in hot gas ADAFs thus causing stronger winds (e.g. Narayan and Yi, 1994), and the stronger winds from the ADAF collimating the jet (e.g. Appl and Camenzind, 1992).

For completeness, I also note that at high accretion rates, e.g. super-Eddington rates, an

ADAF is also possible, if the gas radiates inefficiently (Narayan et al., 1998; Yuan and Narayan, 2014). These are distinctly different from the low accretion rate flows mentioned previously, as the radiation pressure dominates, but the radiation is cannot escape the optically thick flow and therefore is dragged into the BH also.

1.3 Emission mechanisms

The radio emission observed in LLAGN is produced by two main mechanisms: Brehmsstrahlung (otherwise known as free-free) and synchrotron (sometimes known as magnetobrehmsstrahlung). In addition, spectral lines can also be observed with radio data. There are also other emission mechanism such as bound-free and bound-bound, but I do not go into them here.

1.3.1 Synchrotron radiation

When a charged particle is accelerated in a magnetic field to relativistic velocities, it emits synchrotron radiation. Such particles in magnetic fields are thought to exist in the radio jet bases of AGN as the electrons spiral around the magnetic fields. As electrons are so light, they are accelerated more by a magnetic field than heavier ions and protons, hence, electrons are likely responsible for the vast majority of radiations observed in AGN jets. This emission mechanism dominates at the lowest frequencies ($\nu < 30$ GHz, e.g. see Condon, 1992, , their Fig. 1).

The power of an electron emitting synchrotron radiation at a relativistic velocity is:

$$P = \frac{2e^2 a_\perp^2 \gamma^4}{3c^3} \tag{1.36}$$

where e is the charge of the electron, $a_\perp$ is the acceleration perpendicular to the radial vector and γ is the particle Lorentz factor. The Lorentz factor is defined as:

$$gamma = \frac{1}{\sqrt{1 - \frac{v^2}{c^2}}} = \frac{1}{\sqrt{1 - \beta^2}} \tag{1.37}$$

and the perpendicular acceleration is given by:

$$a_\perp = \frac{eBvsin\,(\theta)}{\gamma m_e c} \tag{1.38}$$

where B is the magnetic field strength. v is the velocity of the electron, m_e is the electron mass and θ is the pitch angle. The pitch angle is defined as the angle between the velocity vector and the magnetic field lines. These equations yield the following formula for power

radiated by a relativistic electron in a magnetic field:

$$P = 2\sigma_T \beta^2 \gamma^2 c U_{mag} sin^2\theta \tag{1.39}$$

where I have substituted in for $\beta = \frac{v}{c}$. The Thomson scattering cross section, σ_T , for an electron is defined as

$$\sigma_T \equiv \frac{8\pi}{3}\left(\frac{e^2}{m_e c^2}\right)^2 \approx 6.65 \times 10^{-25}\text{cm}^2 \tag{1.40}$$

and the magnetic energy density U_{mag} is defined as:

$$U_{mag} = \frac{B^2}{8\pi} \tag{1.41}$$

By averaging over the power of synchrotron emitting particles for all pitch angles:

$$\langle P \rangle = \frac{4}{3}\sigma_T \beta^2 \gamma^2 c U_{mag} \tag{1.42}$$

Hence, the power radiated by a an electron emitting synchrotron radiation depends only on a set of physical constants, the magnetic field and the kinetic energy of the electron. The amount of time that it takes for a synchrotron emitting electron to lose its energy is also possible to calculate. The energy of a relativistic electron of mass m_e is given by

$$E = \gamma m_e c^2 \tag{1.43}$$

and the power, e.g. change in energy over time is given by equation 1.41. By dividing equations 1.42 and 1.41 we can get an estimate for the timescale it would take for an electron to decay via synchrotron radiation alone:

$$\tau = \frac{E}{\frac{\text{dE}}{\text{d}t}} = \frac{3 m_e c^2}{4\sigma_T \beta^2 \gamma c U_{mag}} \tag{1.44}$$

For astrophysical synchrotron sources, the magnetic field is of order 10^{-9} T and hence τ can range between 10^5 to 10^8 years, depending on γ, which itself depends on the acceleration mechanism.

The synchrotron spectrum is flat at low frequencies. The flux density is related to the spectral index by

$$S_\nu \propto \nu^\alpha \tag{1.45}$$

where α is the spectral index. For the bases of radio jets, it is expected that $\alpha \gtrsim -0.3$, whereas optically thin emission further down a jet has a steeper spectrum $\alpha \lesssim -0.7$. Jet bases have flat spectra because electrons at different energies become optically thin at different critical frequencies, whereas down the jet the highest energy electrons become

optically thin first and hence steepens the spectrum.

1.3.2 Brehmsstrahlung (free-free) radiation

Brehmsstrahlung, meaning 'breaking radiation', is produced by accelerating or decelerating a charged particle in an electric field. An electron that passes an ion in a cloud of ionised gas experiences a force due to Coulomb's law. This interaction between an electron and ion causes a photon to be produced and is known as 'free-free' radiation as the electron is free both before and after the interaction. The interactions between electron-electron or ion-ion pairs are typically ignored as both particles in the interaction accelerate with the same magnitude in opposite directions, and thus their radiated electric fields cancel in symmetry. Additionally, the electron in electron-ion collisions radiates more than the ion due to the ratio of the rest masses of the two particles, hence we ignore the ions too.

This type of radiation is often observed in ionised clouds of Hydrogen, otherwise known as H II regions. In H II regions at low frequencies ($\lesssim 1$ GHz), the Brehmsstrahlung spectrum is similar to a blackbody. At much higher frequencies however, the H II region is transparent and flattens to $\alpha \approx$ -0.1. As there is a gradual change between these two regimes, it is expected that H II regions will have steeper spectra than synchrotron emitting sources, allowing for the two processes to be identified from one another when considering only the core of the AGN.

The brightness temperature is a quantity often used in radio astronomy to measure the received intensity of a radio emitting source. It corresponds to the temperature a black body would need to be to reproduce the observed intensity at a given frequency. In H II regions emitting by Brehmstrahlung radiation, the brightness temperature can be of order $\sim 10^4$K (Condon et al., 1991; Westcott et al., 2017). However for synchrotron emitting sources, such as those seen in radio jets from AGN, the brightness temperatures can be higher than 10^6K (Falcke et al., 2000).

In the low-frequency regime, we have the Rayleigh-Jeans law, which is defined as:

$$I_\nu \approx \frac{2k_B T \nu^2}{c^2} \tag{1.46}$$

where B_ν is the spectral radiance, k_B is the Boltzmann constant and T is the temperature. Radio astronomers often expressed as the brightness temperature, T_b:

$$T_b = \frac{I_\nu c^2}{2k_B \nu^2} K \tag{1.47}$$

which can be converted into units of the measured flux density of the source, S_ν and solid angle of the source, Ω as

$$T_b \approx \frac{S_\nu c^2}{2k_B \nu^2 \Omega} K \tag{1.48}$$

The brightness temperature clearly depends on the frequency and size of the source. With e-MERLIN observations, brightness temperatures should be considered lower limits, due to the lack of short baselines which resolve out the larger scale structure of sources and hence underestimate the true brightness temperature.

1.3.3 Spectral Lines

While this thesis focuses on continuum radio data, spectral line emission can also be observed in the radio waveband. Some examples include recombination lines, rotational lines of molecules and hyperfine lines. With regards to the 1.5 GHz radio waveband that I use in this thesis, the neutral Hydrogen 21 cm line is present in the band. This corresponds to 1420 MHz in frequency space. The 21 cm line is caused by a hyperfine transition between two energy levels due to the changing of the spins of an electron and proton in a Hydrogen atom from parallel to anti-parallel. Neutral Hydrogen is abundant in the interstellar medium (ISM) and hence it can be used to probe the mass distribution of galaxies (see the THINGs survey, e.g. Walter et al., 2008).

1.4 Unified Theories of AGN

As mentioned previously, the nuclear regions of nearby galaxies were found to have broad optical Balmer emission lines in Seyfert galaxies. Seyfert galaxies, were originally categorised into two types depending on the presence of broad or narrow emission lines (Khachikian and Weedman, 1974). Type 1 Seyferts contain broad and narrow lines, whereas type 2 Seyferts only have narrow emission lines. Additional quiescent galaxies were found to house LINER-type nuclei, which seemed to follow a similar dichotomy to that of Seyfert types (Ho, 1999a). As such it was necessary to try to explain the different line ratios observed with a unified model that could explain both the radio-loud and radio-quiet AGN, as well as the different accretion rates and luminosities seen between Seyferts and LINERs.

The origin of the two types of emission lines observed can be explained in the orientation-based scheme first presented in Antonucci and Miller (1985) and subsequently improved by several other authors (Bicknell et al., 1990; Antonucci, 1993; Urry and Padovani, 1995; Marin, 2016; Ramos Almeida and Ricci, 2017, see Figure. 1.2). The orientation-based scheme was first applied to radio-loud objects (e.g. quasars) with the addition of Seyferts. A central SMBH is required with an efficiently accreting disk. The observed broad lines come from gas clouds rotating at the Keplerian velocity very close to the SMBH, whereas the narrow lines come from the narrow line region (NLR): a lower density region further away from the central engine where both forbidden state transitions and permitted transitions occur. The broad emission line region (BLR) is thought to only be of order 1 pc (Ramos Almeida and Ricci, 2017) and is shrouded by a cool dusty structure commonly referred to as the 'torus'. While it is no longer thought to be torus-shaped (Hönig

et al., 2013; Asmus et al., 2016), the torus prevents the BLR from being seen at certain angles and hence leads to the observed difference between type 1 and type 2 nuclei. The existence of an obscuring medium like the torus also explains why so many heavily-obscured 'Compton-Thick' AGN, with an absorbing column density of $N_H > 10^{24}cm^{-2}$ are observed in the local Universe. In addition, the observed radio jets from AGN are thought to originate near the central BH as collimated flows, possibly due to the Blandford-Znajek process (Blandford and Znajek, 1977) for a rotating BH: as the BH rotates, it causes the magnetosphere to rotate also, so that the angular momentum of the spinning black hole is tapped and thus the energy from the black hole can be extracted, leading to collimated radio jets. Additionally, the Blandford-Payne mechanism (Blandford and Payne, 1982), which uses the energy from the angular momentum of the accretion flow, may alse be responsible for the radio jet production in some cases. Both processes may exist, but it is thought that the former mechanism is responsible for the relativistic jets, while the latter is likely responsible for slower outflows (Yuan and Narayan, 2014).

This broad, orientation picture explains a large number of the multi-wavelength properties seen in radio-loud AGN (see Section 1.5). The orientation-based unification scheme has a lot of strengths including the explanation of the line emission, the obscuration in the X-rays and presence of accretion disks. But, despite decades of study, several properties of AGN are not understood; primarily why are some objects radio-loud and others radio-quiet? In addition, the exact accretion geometry, effects of accretion rate, torus structure, shape and size, as well as the production of the radio jets is not known and is still the subject of current research.

1.4.1 LLAGN in the unified scheme

The radio-loud nuclei seem to follow this orientation based scheme, but what about the radio-quiet nuclei? If an ADAF is present in radio-quiet or low-luminosity AGN as suggested by both theory and observations (e.g. Section 1.2.4), then can we still use this orientation based scheme to understand the nature of the nuclear emission? What effect does the torus have on the observed emission and does it obscure genuinely weak LLAGN? In addition, are the line emitting regions that are commonly found in AGN present in LLAGN and if so how are they ionised? Hence, the low-luminosity end of the luminosity function and the changing accretion mode in these systems are incredibly important for understanding the accretion phenomenon at the weakest scales.

The nature of the accretion process in different types of LLAGN, specifically LINERs, is important for understanding how they fit into the global picture of radio-loud AGN and quasars. While the emission lines found in the nuclei of quiescent galaxies are thought to be ionised only by O and B stars, and Seyferts by the central accretion flow, it is not certain what is ionising the LINERs and 'Transition' regions. Different authors have explained the optical line properties of LINERs by post-AGB stars, old stellar populations, obscured

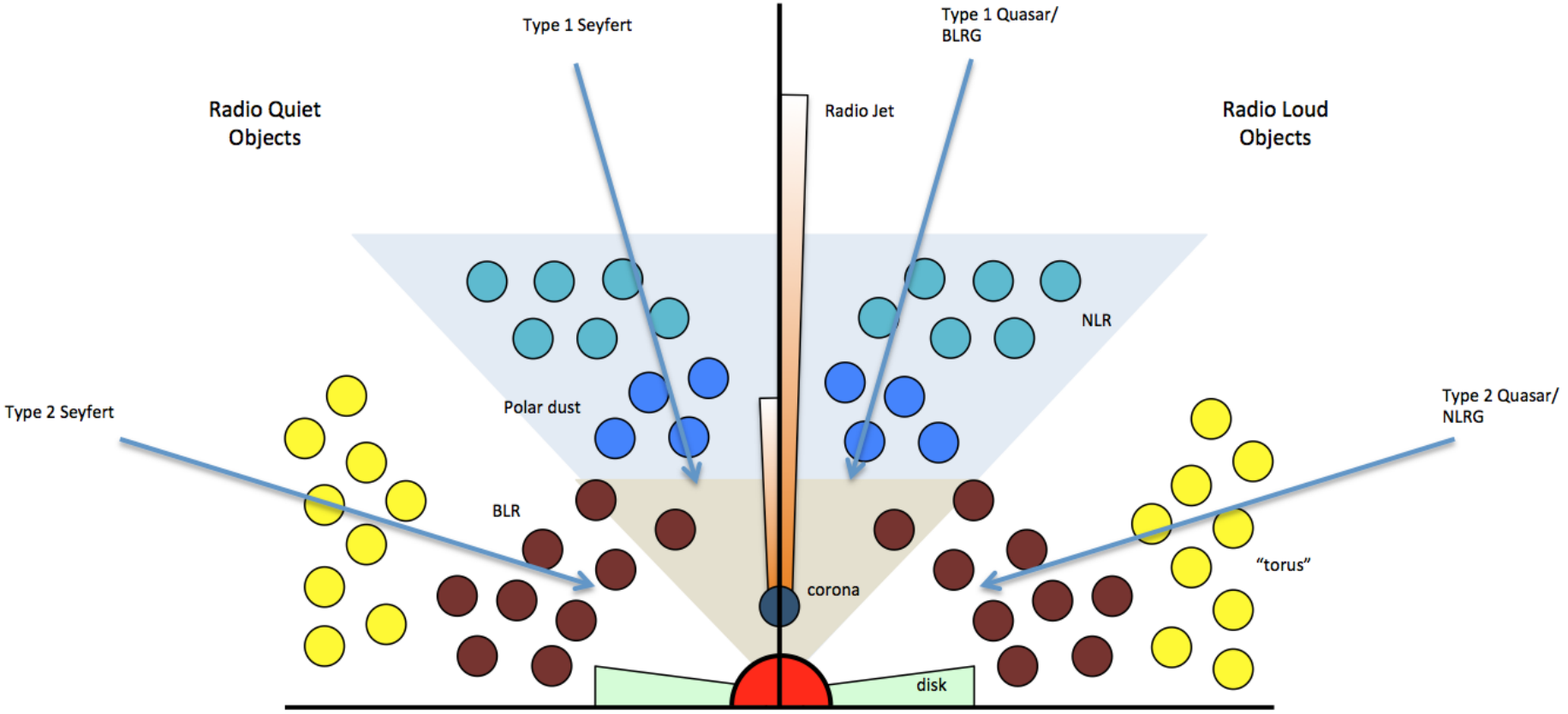

Figure 1.2: The AGN Unification diagram adapted from Ramos Almeida and Ricci (2017) with additions from Urry and Padovani (1995); Marin (2016). The diagram is not to scale, but shows the main components of an AGN. The left hand side shows radio-quiet objects, while the right hand side shows radio-loud objects. While the accretion disk is depicted as extending down to the black hole for both radio-loud and radio-quiet objects, it is not necessarily true in the case of radio-quiet objects where ADAFs are found. The colours for all of the regions represent the lines on the SED in Fig. 1.5.

AGN, LLAGN or shocks, (Heckman, 1980; Halpern and Steiner, 1983; Ferland and Netzer, 1983; Terlevich and Melnick, 1985; Taniguchi et al., 2000; Younes et al., 2011; Cid Fernandes et al., 2009; González-Martín et al., 2009; Capetti and Baldi, 2011; Singh et al., 2013). In addition, the morphological galaxy host type of these galaxies is observed to differ for different AGN classes: Seyferts are usually found in spiral galaxies, whereas LINERs are usually found in ellipticals. While most of the literature has moved towards considering LLAGN as SMBHs, the differences in the populations of LLAGN and galaxy morphological types are fundamental to understanding how black holes evolve and accrete, as well as how they effect their host galaxy.

1.4.2 BPT Diagrams

Baldwin, Phillips and Terlevich pioneered the "BPT diagram", which compares the emission line ratios of different pairs of optical emission lines, usually [O III]/Hβ with [N II]/Hα, [O I]/Hα or [S II]/Hα, to discriminate true AGN activity from that which they attributed to star formation alone[2]. In BPT diagrams, H II galaxies tend to reside in the bottom left region of the plot as the ionising radiation field is not strong enough to cause emission from the narrow lines such as [O I], [S II] and [N II]. Those above and to the right of the maximum starburst line (Kewley et al., 2001) require additional ionisation from a harder ionisation field, such as an AGN, or from shocks in the interstellar medium. These diagnostic plots were further iterated upon by Osterbrock and Pogge (1985), Veilleux and Osterbrock (1987), Kewley et al. (2001), Kewley et al. (2006) and Buttiglione et al. (2010). BPT diagrams give a good idea of the ionising source of radiation in general, but can be contaminated by off-nuclear emission if the spectroscopy is not performed with high resolution slits. Moreover, integrated field units[3] like the MaNGA survey have shown that there are many galaxies with a LINER type nucleus surrounded by star formation in the spiral arms, which could bias positions of the galaxy on a BPT diagram (Belfiore et al., 2016). A characteristic BPT diagram for the LeMMINGs sample is shown in Figure 1.3.

1.4.3 The Fundamental Plane of Black Hole Activity

To first order, accretion is believed to be a scale-invariant process, allowing the comparison of BHs with vastly different BH masses and accretion rates. It is expected that there must be a relationship between the black hole mass and the fundamental properties of compact

[2]Baldwin et al. (1981) described a line separating AGN dominated emission from what they called star forming 'H II regions'. The 'H II regions' that they described were thought to be ionised by O or B class stars and hence their emission line ratios are similar to that seen in H II regions found in the Milky Way. For clarity, I will refer to nuclear regions classified as H II regions by BPT diagrams as H II galaxies throughout this thesis to avoid confusion with H II regions which are ionised clumps of gas in a galaxy, and should not be confused for a nuclear process.

[3]integrated field units (IFUs) are a bunch of optical fibres that point at a galaxy allowing for many spectra to be obtained quickly and simultaneously across the galaxy. IFUs have the advantage that they can isolate optical emission lines in different parts of the galaxy and hence give a better representation of nuclear/SF activity.

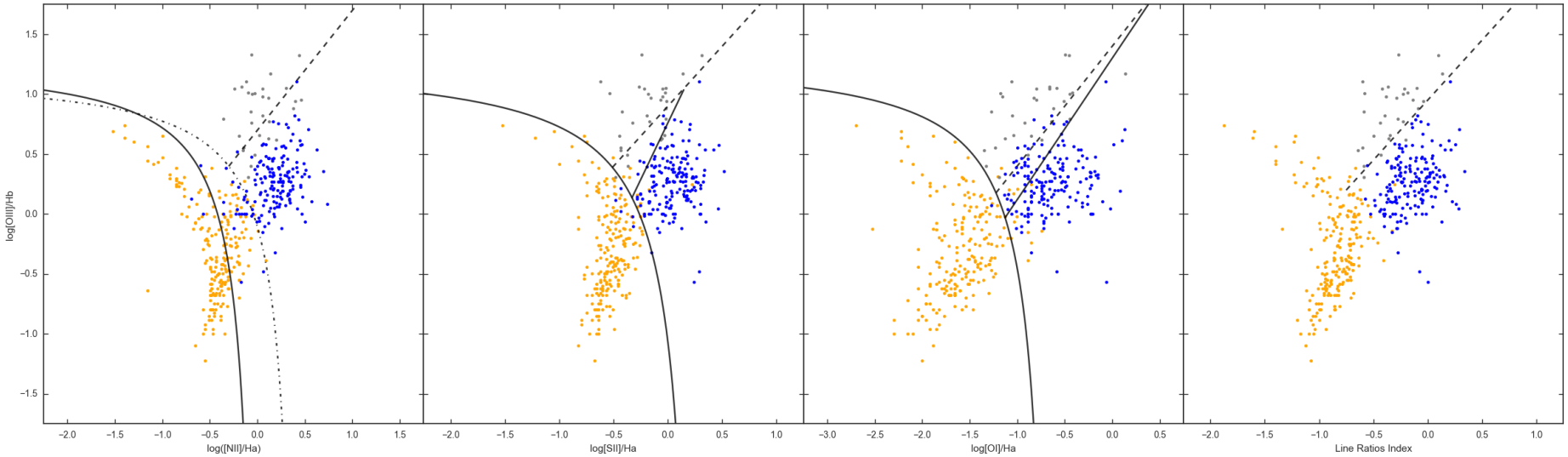

Figure 1.3: BPT emission line diagnostic diagrams for the entire Palomar sample of 486 objects. Going from left to right, the panels show the log[O III]/Hβ ratio against (panel 1) log[N II]/Hα, (2) log[S II]/Hα, (3) log[O I]/Hα and (4) Line Ratios Index. The black lines are the Kewley et al. (2001) diagnostic lines, the dot-dashed line in the first panel shows the Kewley et al. (2006) maximum starburst line and the dashed lines show the Buttiglione et al. (2010) classification between LINERs and Seyferts. HII galaxies are in orange, LINERs in blue and Seyferts in grey. Absorption Line Galaxies are not shown due to their lack of measured emission line ratios.

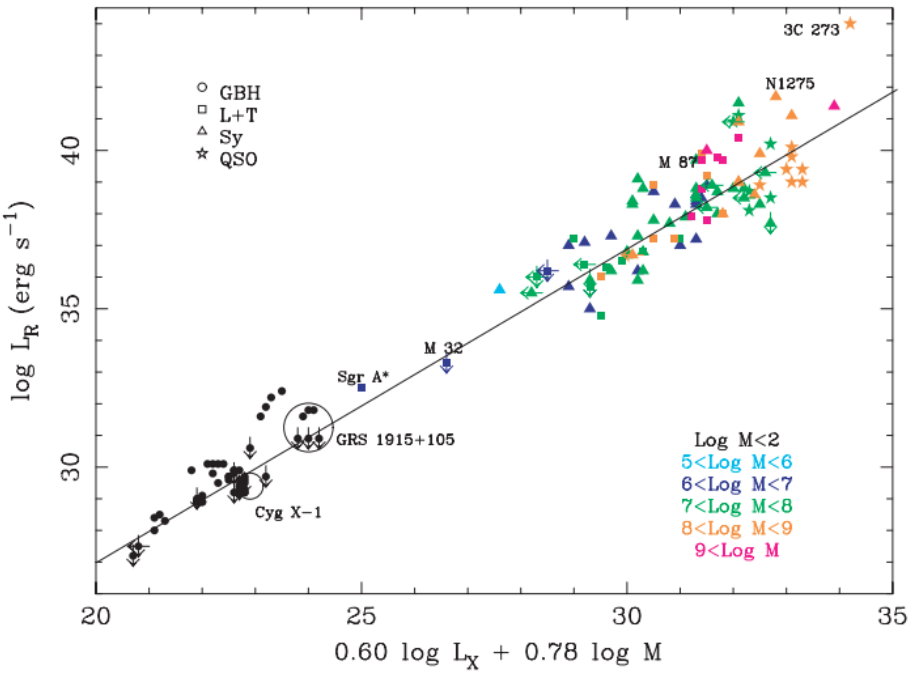

Figure 1.4: The Fundamental Plane of Black Hole Activity as shown in (Merloni et al., 2003). The plane is characterised by a best fit line of $\log(L_{Radio}) = (0.60^{+0.11}_{-0.11})\log(L_{X-ray}) + (0.78^{+0.11}_{-0.09})\log(L_{M_{BH}}) + 7.33^{+4.05}_{-4.07}$.

objects for BHXRBs, LLAGN and AGN. At all black hole masses in accreting compact objects, both synchrotron emitting radio jets and power-law X-ray emission are observed. Both the radio and X-ray emission are observed to be correlated in accreting black holes (Begelman et al., 1984; Falcke and Biermann, 1995; Fender, 2001; Fender et al., 2004). The X-ray luminosity is used as a proxy of the accretion flow, while the radio luminosity is assumed to trace the population of electrons in the jet.

By considering the radio luminosity, X-ray luminosity and black hole masses of BHXRBs in the hard state and SMBHs in quasars, Merloni et al. (2003) showed that a Fundamental Plane of Black Hole Activity (FPBHA) exists linking black holes over different mass scales - from galactic BHXRBs ($\sim 10 M_\odot$) to quasars ($\gtrsim 10^6 M_\odot$) - but with a significant scatter ($\sigma_{Radio} = 0.88$). However, subsequent publications have shown that the accretion mode (e.g efficient or inefficient) and the objects chosen, the radio spectral index of the sources and the accretion rate, as well as statistical effects caused by correlated errors have a significant effect on this result (Falcke et al., 2004; Yuan and Cui, 2005; Körding et al., 2006; Plotkin et al., 2012). Furthermore, currently unobservable parameters such as the BH spin have been proposed to change the position of an object on the FPBHA (Garofalo et al., 2010; Mościbrodzka et al., 2016). Therefore, the choice of sample and its subsequent analysis may play an important role in the observed FPBHA properties. Hence, using LLAGN as a bridge between BHXRBs and quasars may help reduce the scatter in the relation and show a real coupling between the three axes of the FPBHA.

There has been significant work in the literature to understand the biases in the FPBHA and

to extend the plane to other wavebands. The FPBHA was shown to not be a distance driven artefact (Merloni et al., 2006) but more recent work has suggested that it is biased towards the more luminous sources (Bonchi et al., 2013). Panessa and Giroletti (2013) detected VLBI cores of a sample of seventeen AGN but could not find a significant correlation between the nuclear X-ray luminosity and the VLBI radio luminosity. In addition, Saikia et al. (2015) showed that the [O III] line luminosity, e.g. the optical FPBHA, can be used in lieu of the X-ray luminosity as a proxy of the accretion flow, provided that the BHXRBs are scaled correctly to the optical using empirical relations from Heckman et al. (2005). Furthermore, with a sample of ∼10000 AGN, the optical FPBHA correlates with the fluxes obtained from the NVSS at 1.4 GHz (Saikia et al., 2018).

The FPBHA is therefore an intriguing and exciting prospect for unifying accretion onto black holes across different masses and accretion rates. However, the problems listed above in reducing the scatter in the relationship demonstrate the need for a large sample of black holes across the mass spectrum that incorporates a study of LLAGN. To perform such a study, high sensitivity radio observations are required as well as a statistically-complete sample of LLAGN of different optical classifications. In addition, the nucleus needs to be resolved in the radio, optical and X-ray bands at the same angular scale to ensure there is little contamination from other processes.

This thesis aims to extend the FPBHA relation in the low-luminosity regime with a statistically-complete sample of nearby galaxies. Consequently, the radio and X-ray data presented in this thesis aims to conclude with a broader understanding of the validity of the FPBHA and reduce the scatter in the relationship to provide answers to the problems posed above.

1.5 The Multi-wavelength properties of AGN

Given the unified scheme presented in the previous section, I will now describe the multi-wavelength data obtained for AGN, and explain how this fits into the orientation-based picture of unification, starting with the highest energies. The spectral energy distribution (SED) of a galactic nucleus can provide clues as to the existence of an AGN in the galaxy and if so, what type of AGN it is e.g. Seyfert, LINER. In Figure. 1.5, the broadband SED shows several components attributed to the AGN. I will conclude this section with the radio waveband and why it is so useful for isolating emission from SMBHs.

X-rays are produced in AGN by the Compton up-scattering of photons from the accretion disk. The X-ray emission extends from 0.1−300 keV. The X-ray spectra are normally modelled as a power law of $\Gamma \sim 1.5 - 2.1$ (Nandra and Pounds, 1994; Reeves and Turner, 2000; Piconcelli et al., 2005; Page et al., 2005; Ishibashi and Courvoisier, 2010), across the soft (0.2 − 10.0 keV) X-ray energy range. The power-law is thought to originate from scattering in the hot corona. This power-law is observed in the harder end of the spectrum,

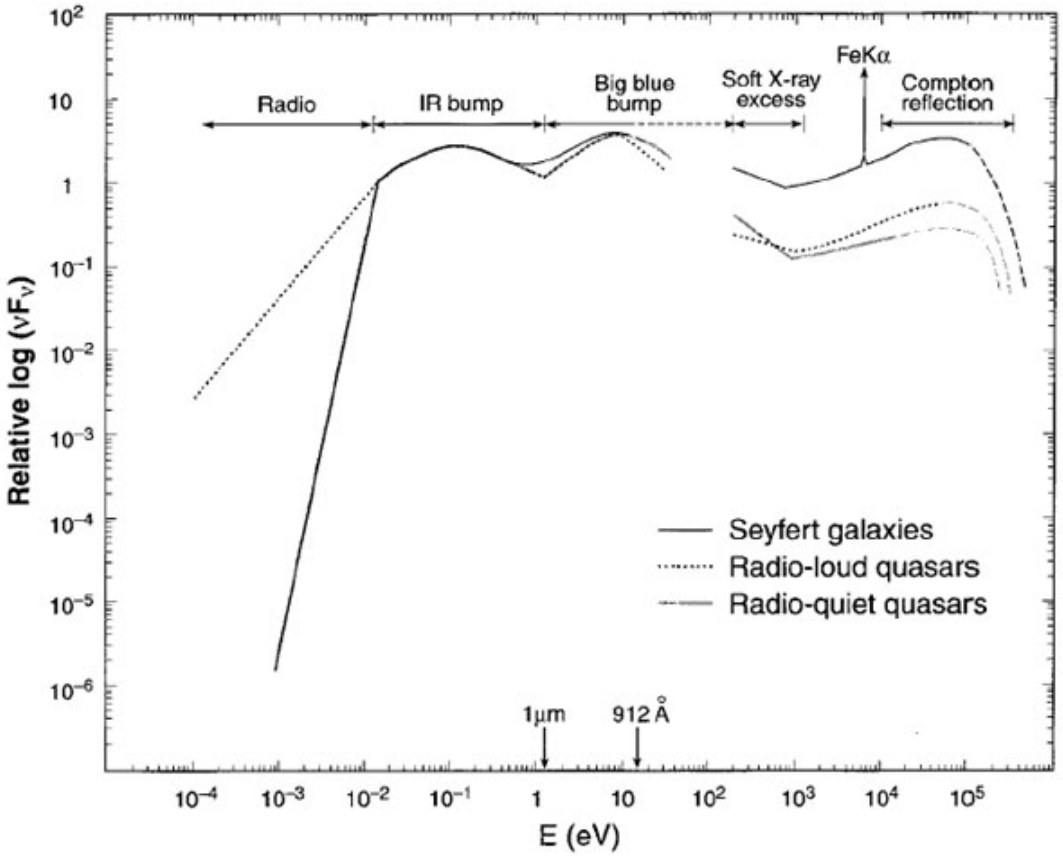

Figure 1.5: An example AGN Spectral Energy Distribution (SED) for Seyferts, radio-loud and radio-quiet quasars from Koratkar and Blaes (1999). The main regions responsible for the various emission processes are identified: An infra-red bump from the torus, the big blue bump from the accretion disk, a soft X-ray excess, Iron Fluorescence line and Compton reflection of the X-ray from the optically-thick disk. The radio is the least significant part of the SED, contributing only a small fraction to the overall bolometric luminosity.

e.g. above 2 keV. At the softer end (lower energy) of this power-law, it is often obscured by clouds of gas around the SMBH, leading to a reduction of photons in the spectra below ~0.5 keV. For objects with high column densities ($\gtrsim 10^{24} \mathrm{cm}^{-2}$), the power-law spectrum can be significantly reduced and these are known as 'Compton thick' nuclei. A "Compton hump" in the $20 - 40$ keV energy range is observed due to reflection from the X-ray corona back onto the accretion disk, while above 100 keV, the spectrum rolls over due to photons losing energy because of Compton scattering events. An Iron fluorescence line[4] is commonly seen in X-ray spectra, although not in all, at 6.4 keV. In addition, a soft excess (around $0.2 - 1$ keV) is observed, but is still the topic of active research.

The optical/UV spectra of AGN in the wavelength range of 300 to 9000 show broad and narrow lines, which I have already discussed in the previous section. However, the bulk of emission in AGN comes from the "big blue bump" in the optical/UV wavelength range. The big blue bump is thought to arise from the accretion flow and can be shown by substituting standard values into equation 1.28 for a $10^8 \mathrm{M}_\odot$ black hole. Unfortunately, the UV band where the AGN spectrum is expected to peak is largely not observable from Earth due to the atmosphere and due to Hydrogen in the ISM.

The infra-red emission observed in AGN can be explained by the presence of an optically and geometrically obscuring structure, usually referred to as the 'torus'. It is now thought to be a clumpy structure and likely not toroidal in shape, with polar outflows (Hönig et al., 2013; Asmus et al., 2016). The dust in this structure absorbs photons and re-emits at infra-red wavelengths. At longer wavelengths (sub-mm), dust heated by star formation leads to thermal emission which can dominate over the AGN emission.

Radio data have shown compact unresolved (e.g. smaller than the size of the restoring beam) components that align with the optical/IR nucleus of a galaxy. The radio emission observed is thought to be due to the base of a relativistic jet, from synchrotron radiation. The radio jets can extend upto Mpc from the galaxy nucleus in quasars (e.g. Bagchi et al., 2007; Hocuk and Barthel, 2010), but for LLAGN, the radio jet may be confined to kpc-scales (Elmouttie et al., 1995; Irwin and Saikia, 2003; Hota and Saikia, 2006; Kharb et al., 2006, 2010; Nyland et al., 2017; Baldi et al., 2018b). Broadly, the radio jet structures observed are split into two categories: Fanaroff Riley I (FR-I) and Fanaroff Riley II (FR-II), based on the classification from Fanaroff and Riley (1974). FR 1 type galaxies show twin jets emanating from a central nucleus which resemble plumes the further away from the core they get, FR II galaxies show a bright nucleus, and terminate in large lobes at 'hot-spots'. In addition, we sometimes observe blazars, where the radio emission is directed towards Earth.

The largest difference in AGN SEDs is observed in the radio band, where a dichotomy is seen between the radio brightness of sources. This is sometimes referred to as the 'radio-loudness' dichotomy. Radio-loudness, R is a measure of the relative radiative contribution of an AGN's output by comparing the radio luminosity (usually at 5 GHz, L_{5GHz}), with that of the accretion disk, either the UV/optical B band luminosity (L_B) or the

[4]Lines of other elements are sometimes observed, but the Iron fluorescence line is the most common.

X-ray luminosity in the 2−10 keV band ($L_{2-10keV}$). Radio-loud objects are those which have a L_{5GHz}/L_B ratio ≥10 (Kellermann et al., 1989) or $\log(\nu L_{5GHz}/L_{2-10keV})$ ≥-4.5 Terashima and Wilson (2003).

While all wavebands of electromagnetic radiation are needed to fully understand the origin of the emission from LLAGN, the one waveband that can offer a direct and unobscured view of the nuclear accretion properties is the radio waveband. Both star formation and AGN emit in the cm-mm band, and can be detected in the low luminosity regime, since the galaxy contributes negligibly. In addition, long-baseline interferometers such as the VLA and e-MERLIN provide a unique combination of high sensitivity and angular resolution, which is necessary to detect and isolate the low surface brightness emission from the nucleus. X-ray (e.g *Chandra*) and optical (e.g. *HST*) telescopes can also help isolate nuclear emission. However, due to the cost and resolution limitation of X-ray and optical satellites, deep radio observations of local galaxies are ideal for probing small spatial scales of often $\lesssim$500 pc in the innermost central regions and identifying the emission from AGN. As such, radio interferometers can offer the best single diagnostic of SF and nuclear accretion.

1.5.1 LLAGN in the radio waveband

Radio interferometers provide high-resolution measurements of radio emission, including the flux density and its variability, the compactness of the source, the radio spectral index, brightness temperatures and in some cases the polarisation. They are unique tools for determining the nature of the radio emission. In LLAGN, synchrotron radiation is typically the source of the radio emission, but free-free emission is also observed in some LLAGN. In addition, LLAGN are efficient at generating radio jets (e.g. Körding et al., 2008), as they are thought to be powered by ADAFs. Hence, the detection of jets or high brightness temperature radio cores in the nuclear regions of galaxies represents a valid method of the identification of an active SMBH at the galaxy centre. This is especially important in the absence of other AGN signatures such as high ionization emission lines or an X-ray nucleus, which can be obscured by the galaxy or star formation.

Many interferometric surveys have been conducted in the last half century, probing angular scales down to ∼1″ for nearby LLAGN (e.g. Ekers and Ekers 1973; Wrobel 1991; Sadler 1984; Sadler et al. 1989; Slee et al. 1994; Ulvestad and Wilson 1989; Vila et al. 1990a; Sadler et al. 1995; Ulvestad and Ho 2001a; Gallimore et al. 2006). These studies have revealed the presence of a large number of radio cores in all types of galaxies, from ellipticals, to spiral galaxies with bulges. The common problem that all radio surveys face is contamination from other radio emitting mechanisms. While a flat-spectrum radio core is usually interpreted as the jet base, it can also be attributed to thermal emission from H II regions or from free-free emission in nuclear star-bursts (Condon et al., 1991). LLAGN can also show a variety of morphologies: single core, core–jet, double lobes and complex structures. These structures are not easy to distinguish from circum-nuclear star formation

processes.

LLAGN are often radio louder than luminous AGN, due to their higher likeihood of radio emission from jets (Körding et al., 2008). Historically, there has been a lot of debate about whether radio-loudness is dichotomous, bimodal or continuous in AGN (White et al., 2000; Ho and Peng, 2001; Laor, 2003; Cirasuolo et al., 2003; Terashima and Wilson, 2003; Sikora et al., 2007). It is unknown whether a radio-loud AGN with collimated pc-to-Mpc radio jets is intrinsically different to a weak radio-quiet AGN, confined to kpc-scales. The few studies with high resolution and deep imaging of both radio-quiet and radio-loud LLAGN yield different results (Nagar et al., 2002; Anderson and Ulvestad, 2005; Wrobel and Ho, 2006; Giroletti and Panessa, 2009; Panessa and Giroletti, 2013).

1.6 Fundamentals of Radio Astronomy

The study of radio astronomy started in the 1930s, when Karl Jansky detected cosmic radio waves in the direction of the Galactic centre. Post WW2, interest in radio astronomy increased as many old radars were converted into radio astronomy dishes, e.g. the original Jodrell Bank observatory (e.g. Lovell, 1968). During the late 1960s, as computational power increased, the first radio interferometric arrays like the 'One-Mile' array in Cambridge were being built to obtain high resolution images of the radio sky.

As this Ph.D. thesis centres on a radio sample of nearby galaxies, in this section, I will describe the core tenets of radio astronomy and how it can be used as a window on the nearby Universe. I will also introduce how it is possible to calculate the magnetic field, spectral index and brightness temperatures from radio data to help discern which mechanism is responsible for the radio emission.

1.6.1 Basics of radio interferometry

The diffraction limited angular resolution in radians is

$$\theta \approx \frac{\lambda}{D} \tag{1.49}$$

where the λ is the wavelength of light and D is the diameter of the dish/reflector. The largest steerable dish is 102m in diameter, making it impossible to achieve resolutions better than a tenth of a degree in the radio band. The largest single dish radio telescope is the Five-hundred-meter Aperture Spherical radio Telescope (FAST), in China, but this still doesn't offer arcsecond resolution. However, interferometers with multiple antennas spread over large distances can overcome this and for the longest baselines, e.g. VLBI, where the diameter of the Earth is the longest baseline, can probe sub milli-arcsecond scales. The basics of radio interferometry are considered in the far-field limit of Fraunhofer diffraction.

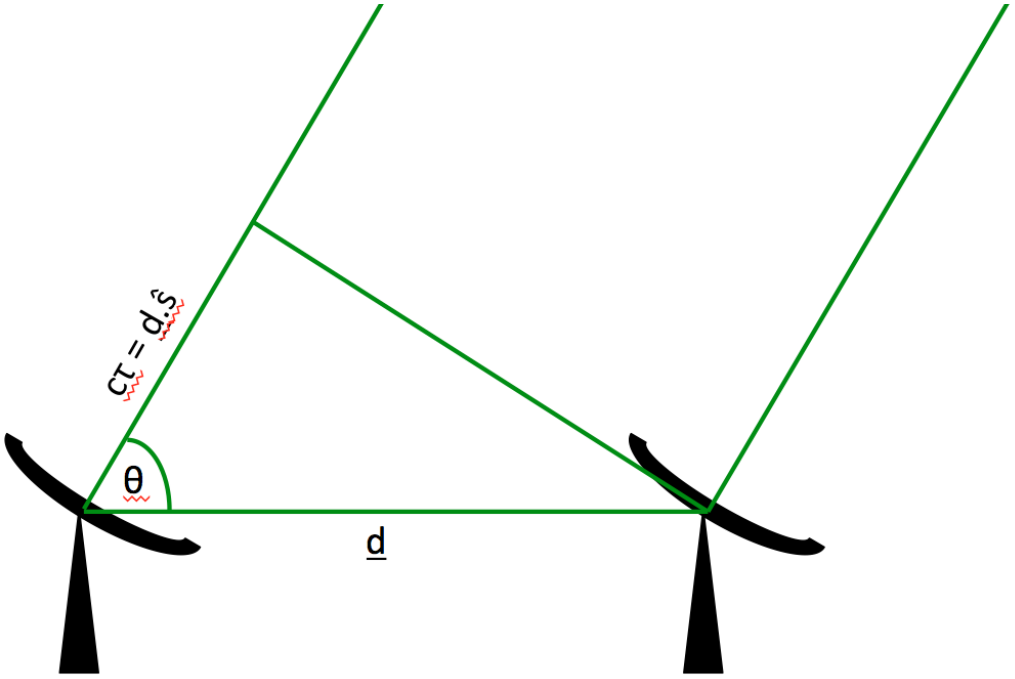

Figure 1.6: A basic two-recevier interferometer diagram showing antenna 1 on the left and antenna 2 on the right. The received signal in each antenna is described in equations 1.50 and 1.51.

In the simplest approximation, I will start with two antennas receiving a signal from the same plane wave emitted from a astrophysical source. The geometric delay, τ (see Figure 1.6), between the signal being received between the two antennas is:

$$\tau = \frac{\vec{d} \cdot \hat{s}}{c} \tag{1.50}$$

where the vector $\vec{d}$ is the distance between the two dishes, $\hat{s}$ is the source direction vector and c is the speed of light. The signal (voltage) received by the two dishes is simply:

$$V_1 = V \cos(\omega t) \tag{1.51}$$

$$V_2 = V \cos(\omega [t - \tau]) \tag{1.52}$$

Here, I have assumed that the frequency of the wave is in a narrow frequency range centred on

$$\nu = \frac{\omega}{2\pi} \tag{1.53}$$

In practice, the two signals V_1 and V_2 are correlated (combined) together by multiplication:

$$V_1 \times V_2 = \frac{V^2}{2} [\cos(\omega\tau) + \cos(2\omega t - \omega\tau)] \tag{1.54}$$

When the time t of observation is long enough, e.g. $\Delta t \gg \frac{1}{2\omega}$, the high-frequency

$\cos(2\omega t - \omega\tau)$ term disappears and the above equation reduces to:

$$V_1 V_2 = \frac{V^2}{2}\left[\cos(\omega\tau)\right] \tag{1.55}$$

This equation varies sinusoidally depending on the direction of the source, so I now define the fringe phase, ϕ, as:

$$\phi = \omega\tau = \frac{\omega}{c} d \cos(\theta) \tag{1.56}$$

The fringe phase varies sinusoidally across the sky. Atmospheric effects in the troposphere can alter the path delay to different antennas in an interferometric array so in practice, this fringe phase must be fit and removed from the delay signal. For arrays with shorter baselines than the VLA, for example, this is not an issue. However, for longer baseline interferometers, like e-MERLIN and VLBI, this can be a problem, especially if there are differing weather conditions or atmospheric effects in different parts of the world. By correcting for these fringes, it is possible to achieve milliarcsecond precision absolute positions for radio sources. Fringe fitting is an important step in e-MERLIN data reduction, which I will discuss further in Chapter 2.

The *uv* plane

A two-element interferometer as described above measures the interference pattern caused by a signal being received at slightly different times on Earth. It is directly related to the source brightness, but it is dependent on the relative positions of the two-elements. I now extend to two dimensions whereby the image plane is described by a source in the $I(x, y)$ direction on the image (or sky) plane and the telescopes are separated on Earth in the $V(u, v, w)$ directions, where u is the east-west coordinate of the two-element interferometer, v is the north-south co-ordinate, and w is the coordinate towards the source[5]. This is known as the *uv*-plane.

The *uv*-plane is recovered from measuring the complex phase of a wave at one antenna, given a reference antenna. Therefore, the image plane can be recovered by using a Fourier transform, whereby the image plane is the Fourier transform of the *uv*-plane:

$$I(x, y) = \iint V(u, v) e^{(2\pi i(ux+vy))} \mathrm{dudv} \tag{1.57}$$

By increasing the number of baselines, which by necessity must vary in *uv* co-ordinates, different scales in the *uv*-plane are observed, and consequently probe radio sources at different spatial scales. Examples of the *uv*-planes for LeMMINGs data are shown in Fig. 1.7.

[5]The w coordinate is usually ignored as it gives a negligible component to the image plane. For wide-field imaging however, it must be considered as it will vary over large fields of view.

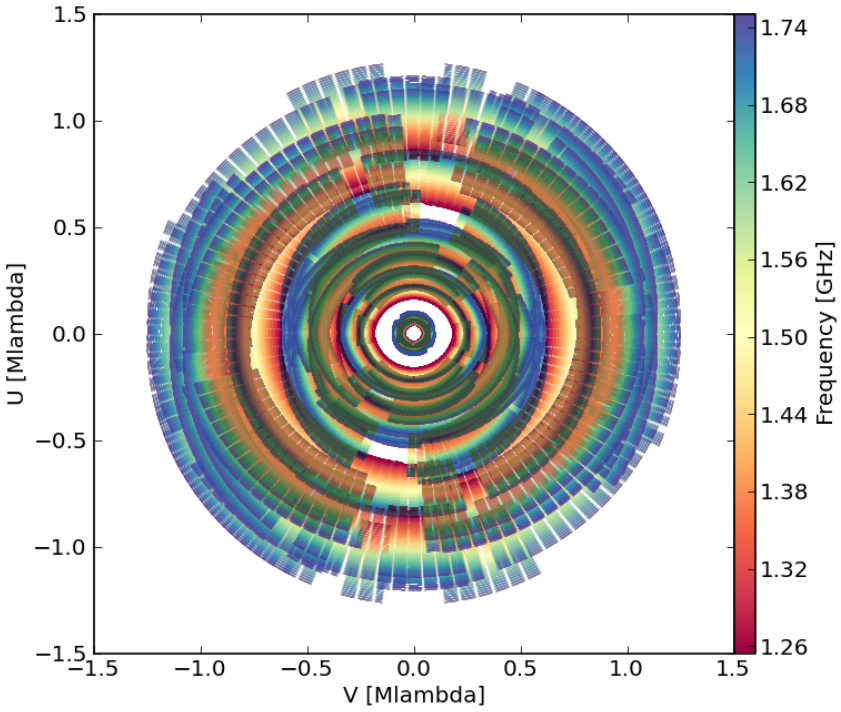

(a)

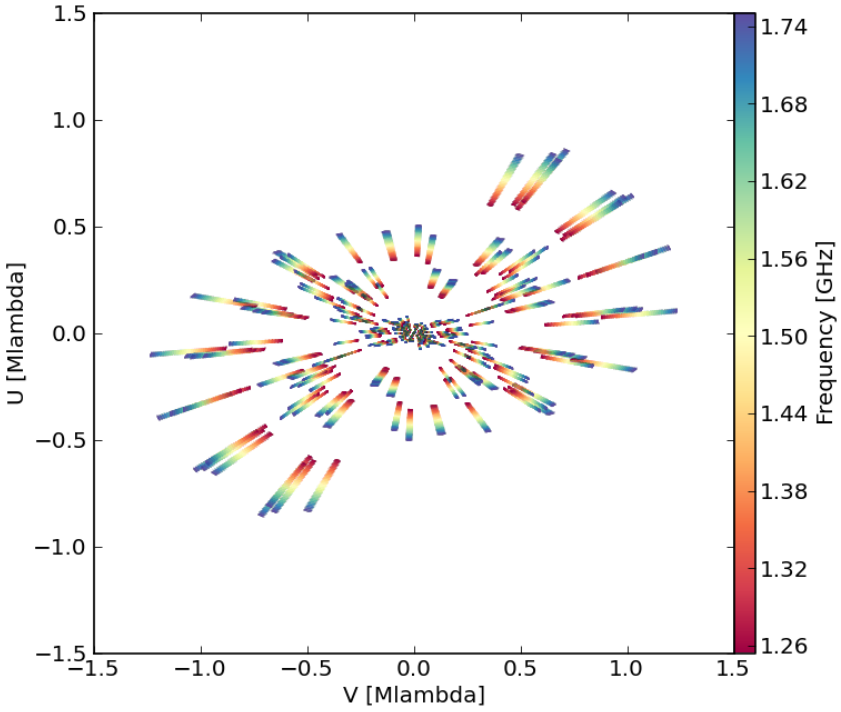

(b)

Figure 1.7: Full observed *uv*-plane of two sources from the two LeMMINGs samples: a) NGC 6217 at 1.51 GHz using the new LeMMINGs (e-MERLIN) deep data with all 7 antennas included b) a typical *uv*-plane of an example galaxy (NGC 3003), with 'snap-shot' imaging. These plots were made using the CASA e-MERLIN pipeline which can be found at https://github.com/e-merlin/CASA$_e MERLIN_p ipeline/wiki$.

Aperture Synthesis

So far, I have generalised radio interferometry to one baseline with a pair of antennas and a small frequency window of the received radiation. In reality, interferometers have many antennas and multiple baselines. For each antenn added to an array, the number of baselines scales according to the number of antennas, N, by:

$$Number\ of\ baselines = \frac{N\,(N-1)}{2} \tag{1.58}$$

Therefore, by increasing the number of antennas, the number of baselines used to sample a source increases greatly, allowing for multiple angular size scales to be observed simultaneously. However, by allowing the Earth to rotate, a radio source will see different baselines projected on the Earth's surface. This principle is known as Earth-rotation aperture synthesis, as it allows different baseline lengths (and therefore angular scales) to be probed by the same interferometer and hence increase the *uv*-plane coverage which is necessary for the best sensitivity. The example *uv*-planes in Fig. 1.7 exemplify the good *uv*-coverage; the 'deep' observation of NGC 6217 (top panel) shows a full *uv*-plane for e-MERLIN and is therefore similar to a dish with diameter 217 km.

1.7 Arrays and Telescopes

In this section, I will discuss some of the main telescopes and arrays that will be used in this thesis, from radio (e-MERLIN/JVLA), to optical (*HST*) and X-rays (*Chandra/XMM-Newton*). I have demonstrated the complementary angular resolutions of these instruments in Fig. 1.8.

1.7.1 The e-MERLIN Interferometric Array

The primary source of radio data in this thesis comes from the **e**nhanced **M**ulti-**E**lement **R**adio **L**inked **I**nterferometer **N**etwork (eMERLIN) based in Cheshire, UK. It is an asymmetric array consisting of 7 antennae of different sizes. The largest, the Lovell telescope, is 76m in diameter. All of the other telescopes[6] (bar the Mk2 antenna which is 38m in diamater and also on the Jodrell Bank site) are ∼25m in diameter. The maximum baseline of e-MERLIN (Lovell telescope to Cambridge) is 217 km, which achieves an angular resolution of 150 mas at 1.5 GHz. This angular resolution is comparable with that of the *Hubble Space Telescope*, allowing for sub-kpc identification of radio sources with optical emission, e.g. active black holes out to distances of upto 100Ṁpc. At higher frequencies (5 and 22 GHz) the angular resolution improves to 40 and 12 mas respectively, better than that of *HST*.

[6]Throughout this thesis I will refer to the antennas as follows: Lovell: Lo, Mark 2: Mk2, Knockin: Kn, Defford: De, Pickmere: Pi, Darnhall: Da, Cambridge: Cm, see Fig. 1.9

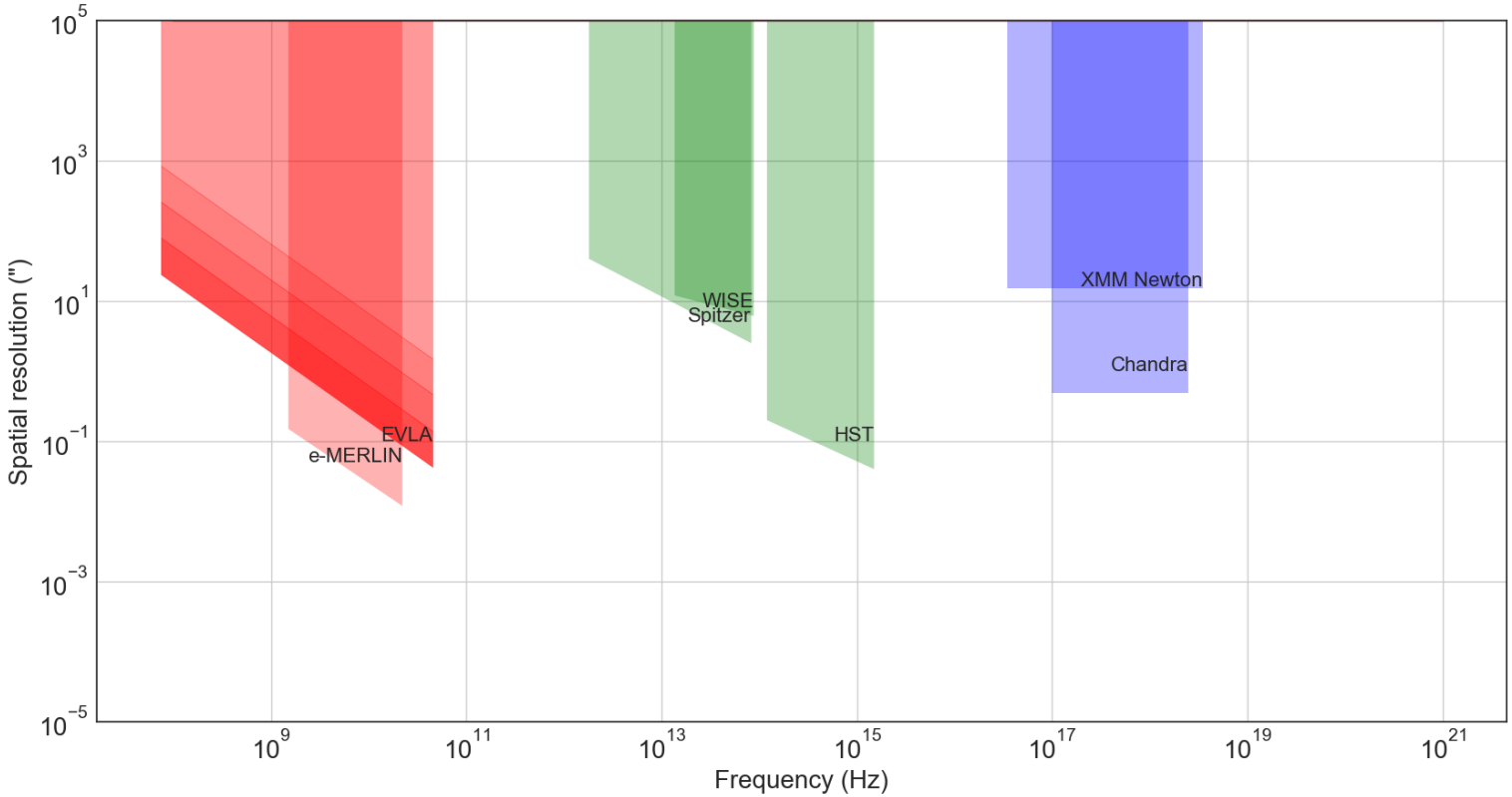

Figure 1.8: The resolution of some of the arrays and telescopes used in this thesis as a function of frequency. e-MERLIN and *HST* have similar resolutions, while *Chandra* yields the best possible resolution for an X-ray telescope currently in orbit. X-ray satellites are shown in blue, optical and infra-red missions are shown in green and the radio arrays in this thesis are shown in red. The different shadings on the VLA wedge correspond to the different configurations, with A array being the most sensitive and D array the least.

The e-MERLIN array has a long history of radio observations in the last half century. The precursos to e-MERLIN were the MTLRI and MERLIN arrays. With the exception of the decommissioning of the Wardle (Mk3) antenna, the configuration of e-MERLIN is identical to that of MERLIN. With the new correlator added to the array, the bandwidth of e-MERLIN is wider that that of MERLIN, leading to improved *uv*-coverage. The increase in bandwidth from the MERLIN array to e-MERLIN has increased the sensitivity of radio observations at 1.5 GHz from 80 μJy to 5 μJy rmsrms is the 'root-mean-square' noise is the systematic noise in the interferometer divided by the square root of the product between the bandwidth and the integration time of the observation..

The Lovell telescope has been used for over half a century to observe the radio Universe. It is one of the three largest steerable radio telescopes in the world behind Green Bank in the USA (102m) and Effelsberg (100m) in Germany. However, due to its age and original construction, it is also the slowest at slewing of the three and therefore only partakes in alternate target observations with the rest of the e-MERLIN array. However, the increase in sensitivity that the Lovell provides e-MERLIN makes it invaluable for deep observations, rincreasing the sensitivity level between 2 and 3 times compared to that which the rest of the array can otherwise obtain. The size of the antenna also reduces the field of view to $20/(\nu/1.4\,\mathrm{GHz})$ arcmin. Therefore, the decision to include it in an observing run depends on the type of observation. Hence, deep full *uv*-coverage observations include the Lovell, whereas the LeMMINGs shallow statistical survey does not use it, to allow for snap-shot imaging of a large number of galaxies in a short observing block.

The combination of the new correlator, the Lovell telescope and wider bandwidth, in addition to the size of the array, means the e-MERLIN array is unrivalled in terms of the complimentary sensitivity and angular resolution achieved. Therefore, e-MERLIN has the perfect balance between sensitivity and angular resolution for observing the local Universe and identifying and discriminating regions of star-formation and AGN activity from each other.

1.7.2 The Karl Jansky Very Large Array

The Karl Jansky Very Large Array (hereafter VLA) is a radio interferometer based in New Mexico that observes in the 58 MHz-50 GHz (4 m-7 mm) range. Originally built in the 1970s, it comprises 27 antennae in a Y-shaped array. All antennae are 25m in diameter and can be moved into different configurations (~1km to ~36 km maximum baselines) to observe radio emission at different spatial scales. The highest resolution configuration, with the longest baselines is called the 'A-Array', while the lowest resolution configuration is called 'D-array'. There are also two further intermediate configurations called 'B-array' and 'C-array'. In 2011, the Very Large Array (VLA) array was upgraded by replacing the electronics and correlator and was hence renamed the Karl Jansky Very Large Array. The VLA increased the continuum sensitivity of the VLA by a factor of 5-20 depending on

Figure 1.9: A geographical representation of the e-MERLIN array, showing that the antennas are spread across the UK and that e-MERLIN is an asymmetric array. This image is from the e-MERLIN website, www.e−merlin.ac.uk. For scale, the longest baseline is 217 km long which is between the Lovell and Cambridge antennas.

frequency band and array configuration.

The VLA is complementary to e-MERLIN, as at A-array it covers a region of the *uv*-plane that e-MERLIN doesn't currently have access to. For example, see Fig. 1.7 to see the hole in the e-MERLIN *uv*-coverage at ~0.3Mλ. This region of the *uv*-plane is surveyed by the VLA in A-array and the corresponding VLA *uv*-plane is shown in Fig. 4.1, lower panel. Hence, combining the radio data from the two arrays is essential for fully mapping milli-arcsecond spatial scales. In addition, there is a wealth of archival data available in the VLA archive[7] which can be combined with the LeMMINGs data in this thesis to fully map the diffuse radio emission of radio jets from LLAGN.

1.7.3 The Chandra X-ray Observatory

Launched in July 1999, the *Chandra* X-ray telescope (hereafter *Chandra* has provided unparalleled spectral and spatial resolution of the X-ray sky. It carries four instruments, two for imaging and two for spectroscopy: the Advanced CCD Imaging Spectrometer (ACIS), the High Resolution Camera (HRC) and the High-Energy and Low-Energy Grating Spectrometers (HETGS and LETGS respectively).

In this thesis I have used data from ACIS chips to make X-ray images of the LeMMINGs sample in the 0.2−10 keV range and extract X-ray spectra. There are two ACIS chips on *Chandra*: The I- chip and the S- chip. The only difference between the two chips is the configuration, as the four ACIS-I CCDs are in a square, sat above a line of six ACIS-S CCDs. As mentioned in Section 1.5, the presence of an X-ray power law in the 0.2−10 keV range is often used as evidence for the presence of an active nucleus. The spatial resolution of *Chandra* is ~0.5″ which far exceeds any other X-ray telescope launched prior to or since. Hence, the *Chandra* X-ray observatory is the only X-ray telescope capable of discriminating X-ray sources from one another in nearby galaxies, allowing for the study of AGN, Ultra-luminous X-ray sources (ULXs) and XRBs, depending on their separation.

1.7.4 Hubble Space Telescope

The well-known *Hubble* Space Telescope (hereafter *HST*) is an ultraviolet/optical/infra-red instrument in orbit that was launched in 1990. Over nearly 30 years of observations, it has been used to study all kinds of astrophysics, from planetary nebulae, to AGN to the origins of the Universe. It has a 2.4m mirror which yields angular resolutions of ~0.05″ at 500 nm. *HST* has six instruments currently in operation: the Advanced Camera for Surveys (ACS), the Cosmic Origins Spectrograph (COS), the Fine Guidance Sensors (FGS), the Near Infrared Camera and Multi Object Spectrometer (NICMOS), the Space Telescope Imaging Spectrograph (STIS) and the Wide Field Camera 3 (WFC3). There are several previous

[7]Data can be found at the NRAO VLA Archive Survey (NVAS) page: https://archive.nrao.edu/nvas/

instruments that have been de-commissioned over time and there have been five servicing missions to improve the optics or correct for faults in the telescope.

In this thesis, I will use some data from the Wide Field Planetary Camera 2 (WFPC2), the predecessor to the WFC3, as well as data from the WFC3 and ACS cameras. The *HST* data presented in this thesis is from both the narrow filters (e.g. centred on emission lines) and wider-band filters, described in detail in the relevant chapters. While the resolution is of the same order as the e-MERLIN/VLA interferometers, the astrometric precision for *HST* is only of order $\sim 0.3''$. Radio interferometers are required to identify AGN to better than *HST* can achieve, but *HST* data gives vital high-resolution information on the optical emission line ratios from nuclear regions, which can only be obtained in lower-resolution from ground-based observatories.

1.7.5 XMM-Newton

The *X-ray Multi-Mirror Mission* (known as *XMM-Newton*) was launched soon after *Chandra* in December 1999. It consists of three main instruments: the European Photon Imaging Cameras (EPIC), the Reflection Grating Spectrometers (RGS) and the Optical Monitor (OM). In this thesis I will use some data from the EPIC CCDs, which have an angular resolution of $\sim 5''$. While it doesn't have the same angular resolution as *Chandra*, it has observed a large number of galaxies in the Palomar sample, more so than *Chandra*. Hence, *XMM-Newton* can help provide data where *Chandra* currently cannot.

1.8 AGN Samples

To study AGN demography statistically, it is necessary to perform high-sensitivity, sub-arcsecond resolution surveys of extragalactic radio sources so that the broadband emission due to star formation and accretion activity can be discriminated and the interplay between these two phenomena assessed. In the distant Universe, the AGN in a galaxy dominates across the spectral energy distribution. However, in nearby galaxies, LLAGN are much weaker. Hence, emission from star formation can contribute equally to the SED and hence wash out the AGN emission.

1.8.1 The Palomar bright spectroscopic sample of nearby galaxies

The Palomar sample of nearby galaxies is a survey of optical spectra for all northern (Declination $\delta > 0°$) bright galaxies ($B_T \leq 12.5$ mag) (Filippenko and Sargent, 1985; Ho et al., 1995, 1997a,d,b,c,e, 2003, 2009), drawn from the Revised Shapley-Ames Catalog of Bright Galaxies Sandage and Tammann (1981) and the Second Reference Catalogue of Bright Galaxies de Vaucouleurs et al. 1976. The 486 objects in the Palomar sample were observed with the Hale 5m telescope at the Palomar Observatory with a $2\times4''^2$ slit in two

wavelength ranges, 6210−6860Å and 4230−5110Å achieving FWHM resolutions of $\sim$ 2.5Å and $\sim$ 4Å respectively. The Palomar Sample is often regarded as one of the best optically selected samples due to its good spectral line resolution, high-completeness and large signal-to-noise ratios. Due to the homogeneous nature of the sample, it consists of all morphological types of galaxy (e.g spiral, elliptical, irregular etc) and classifications of nuclear emission (e.g. LINERs, Seyferts, HII galaxies etc). These features of the sample makes it a fair representation of the emission lines in the local galaxy population. Furthermore, as the Palomar Sample has a median distance of ~20 Mpc, a good spatial resolution can be achieved for many of the objects, usually ~150-200 pc arcsec^{-1}.

The Palomar galaxies are optically classified, based on the ratios of their emission lines by using emission-line diagnostic diagrams (see Section 1.4.2). As mentioned previously, Ho et al. (1997a) separated H II galaxies, Seyfert, LINER, and 'Transition' galaxies among the objects which show prominent emission lines, with the division between LINERs and Seyferts described by Heckman (1980). This thesis uses the optical information obtained from the Palomar sample as a means to re-classify all the objects by updated classification methods presented by Kewley et al. (2006) and Buttiglione et al. (2010) (see Chapter 2). The Palomar Sample also forms the framework for the LeMMINGs survey: the radio data that forms the core of this thesis.

The vast majority of galaxies observed by the Palomar sample are H II galaxies (~42% of the Palomar sample), where the emission line ratios can be explained solely due to young massive stars. LINERs are the next most common type identified in the Palomar sample (~19% of the sample) and Seyferts make up ~11% of the sample. The Seyferts and LINERs represent the two active classes in the Palomar sample, where the ionisation can be explained by an active SMBH. Transition galaxies make up ~14% of the sample and show composite characteristics of LINER nuclei contaminated by H II emission regions (e.g. Ho et al. 1993). The rest of the sample (~14%) is made up of absorption line galaxies (ALGs) which are commonly found in elliptical and lenticular galaxies, and have no significant emission lines. These galaxies can be explained by an inactive SMBH, an undetected very weak active SMBH like a LINER (Ho et al., 2003; Best et al., 2005b; Baldi and Capetti, 2010), an old stellar population Buttiglione et al. 2009 or extinction due to the host galaxy (Goulding and Alexander, 2009).

While the active galaxies in the Palomar sample have been observed at low and high resolution (arcsec and mas) at different cm-band frequencies (VLA, Nagar et al. 2000, 2001, 2002; Filho et al. 2000; Nagar et al. 2005; Ho and Ulvestad 2001a; VLBA/VLBI, Falcke et al. 2000; Ulvestad and Ho 2001b; Nagar et al. 2002; Anderson et al. 2004; Filho et al. 2004; Nagar et al. 2005; Filho et al. 2004; Nagar et al. 2005; Panessa and Giroletti 2013; MERLIN, Filho et al. 2006), a large number of the H II galaxies, 'Transition' galaxies, and ALGs have not been. Hence, a sub-arcsecond sub-mJy rms radio study of the Palomar sample, including the inactive galaxies is still needed to properly assess the activity of SMBHs in the nearby Universe. This is the aim of the LeMMINGs survey.

1.8.2 The LeMMINGs Survey

The **L**egacy **e**-**M**ERLIN **M**ulti-band **I**maging of **N**earby **G**alaxies **S**urvey - LeMMINGs (Beswick et al., 2014) is the second largest of the e-MERLIN legacy surveys with 810 hours of observing time. The goal of LeMMINGs is to study the processes of accretion and star-formation in the local Universe to better understand their relative importance to the co-evolution of galaxies. There are two parts to the LeMMINGs survey: the 'shallow' survey and the 'deep' survey; data from both parts are presented in this thesis.

The shallow survey consists of 280 galaxies selected from the Palomar sample of nearby galaxies above Declination $\delta \geq 20°$. This declination cut is necessary to avoid significant elongation of the beam with e-MERLIN at lower declinations. The LeMMINGs sample encompasses all galaxy morphologies and all AGN types (see Chapters 5 and 6). The galaxies extend in distance out to 120 Mpc, but with a median distance of ~20 Mpc, similar to the original Palomar sample. Hence, the declination cut still gives a large complete sample of galaxies, while avoiding the elongated beam sizes.

All of the 280 galaxies have been observed at 1.5 GHz (data presented in this thesis) and will be also observed at 5 GHz (not presented in this work). Each object is observed for ~50 minutes total in "snap-shot imaging" mode. This mode breaks observations into blocks of 10 galaxies (see Fig. 1.10), requiring 28 observing blocks per band. Each object has an associated nearby, unresolved phase calibrator source from the VLBA calibrators list which alternates with the object. Each of the object-calibrator pairs are observed in 10 minute windows, with ~7 minutes on the target and ~3 minutes on the associated calibrator. The object-calibrator pairs are cycled through until each target has ~50 minutes on-source time. This approach spreads out observations of each target over a longer observing window which fills in more of the *uv*-plane (see Fig. 1.7).

The deep survey consists of six scientifically interesting targets observed for longer on-source times (typically >4 hours) to obtain a larger *uv*-coverage and achieve better sensitivities as the rms is inversely proportional to the square of the on-source time. The observations of these six sources include the Lovell telescope which allows for better sensitivities due to the additional 5 baselines[8] and the size of the Lovell antenna. All of the deep observations are published as separate papers: M 82 (Muxlow et al., 2010), IC 10 (Westcott et al., 2017), NGC 4151 (Williams et al., 2017), NGC 5322 (Dullo et al., 2018a), M 51b (Rampadarath et al., 2018), and NGC 6217 (Williams et al, in prep.). The work on NGC 4151 and NGC 6217 are presented in this thesis in chapters 3 and 4.

[8]The Lo-Mk2 baseline is always flagged by the correlator at Jodrell Bank first as it is usually just correlated noise from mobile phone signals, satellites and wifi.

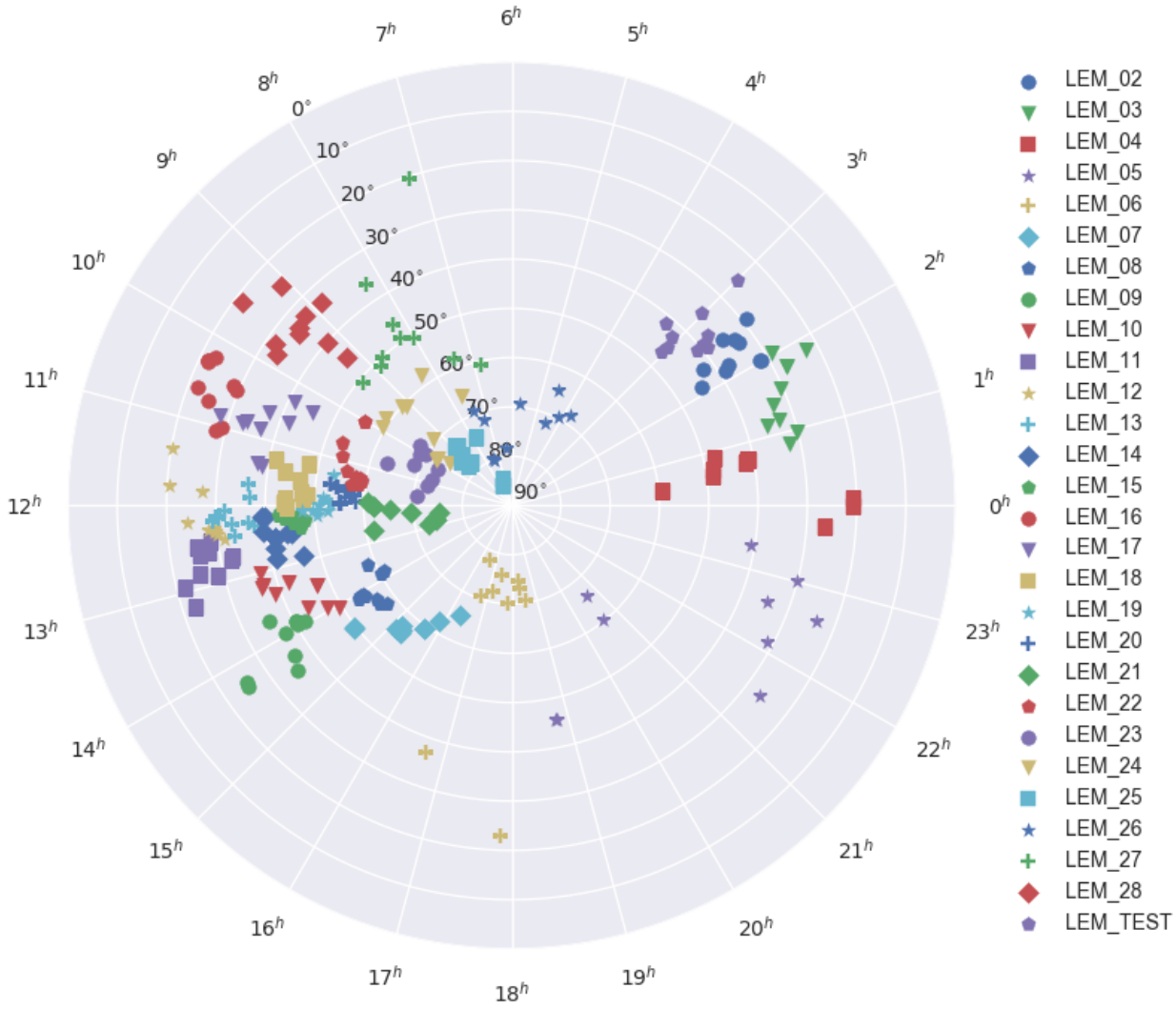

Figure 1.10: The distribution of LeMMINGs blocks across the sky. The blocks are clustered in RA to reduce slewing time between sources. All of the blocks are $\delta > 20°$.

1.9 Thesis Summary

The broad research topic of this thesis is the investigation into the radio emission of a statistically complete sample of LLAGN in the local Universe with the LeMMINGs survey and the comparison with other galaxy properties and ancillary wavelength data. In this thesis I explore a variety of relationships, starting with individual source studies (Part 1), followed by the radio analysis of the LeMMINGs shallow sample (Part 2) and concluding with the multi-wavelength analysis and correlations that are found from these data (Part 3).

In Chapter 2, I will discuss the data reduction procedures for all of the data in this thesis, focussing on the e-MERLIN data reduction procedures. I will also introduce the re-classification scheme I have used based on the BPT diagrams. The black hole masses from the M-σ relation (Tremaine et al., 2002; Graham and Scott, 2013; Kormendy and Ho, 2013) are also provided for context in later chapters. With regards to the science in this thesis, in Part 1, I will begin with the LeMMINGs 'deep' sample, focussing on NGC 4151 (Chapter 3) and NGC 6217 (Chapter 4). The multi-wavelength data that is available for these two galaxies allows for the discrimination of the nucleus and identification of the ionising mechanisms in the AGN. These two galaxies offer contrasting views of LLAGN and hence provide a counterpoint to the wider 'shallow' survey that I will introduce in Chapter 5 (Part 2). This chapter is used in Part 3 with the X-ray data presented in Chapter 6 to investigate the FPBHA in Chapter 7. Finally, in Chapter 8, I will conclude.

Chapter 2

Observations and Data Reduction

2.1 Introduction

In this chapter I will describe the calibration techniques for the data in this thesis, concentrating on the LeMMINGs radio data calibration and describe the imaging procedures for both the 'deep' and 'shallow' LeMMINGs samples. I will also introduce the other complementary multi-wavelength data that is used throughout this thesis, e.g. the Palomar survey optical data and the *Chandra* X-ray data. I will outline the X-ray data reduction procedure, and the spectral fitting process. I will describe the multi-wavelength properties of the LeMMINGs sample by using the emission line ratios obtained for the Palomar sample to re-classify all the galaxies in my survey into AGN types. Furthermore, I will explain how the black hole masses for the LeMMINGs sample are obtained and the biases involved with any black hole mass estimates that are not dynamically confirmed. Any observations and data reduction necessary for specific Chapters is not presented here and will be presented in the corresponding Chapter.

2.2 e-MERLIN Data Reduction and Imaging Technique

The e-MERLIN pipeline (Belles et al., 2015), originally written in AIPS[1] but also now available in CASA[2], provides all of the necessary inputs to import, calibrate and image e-MERLIN radio data. I will give a broad overview in this section of the data reduction technique, focussing on the AIPS pipeline procedures and noting how it differs from the newer CASA pipeline. It should be noted that the data for the first LeMMINGs data release (Baldi et al., 2018b) used the AIPS procedures, while any new data used the CASA procedures. I will then focus on the differences in the technique between the 'deep' and 'shallow' LeMMINGs samples. All of the LeMMINGs data calibration procedures

[1]the Astronomical Image Processing Software from NRAO, available at www.aips.nrao.edu
[2]https://science.nrao.edu/facilities/vla/data-processing/pipeline

presented below were performed by Ranieri Baldi (RB) and myself on all of the available datasets. RB and I flagged, calibrated and imaged about 50% of the 'shallow' datasets each, and I calibrated and imaged all of the 'deep' datasets presented in this thesis.

The data reduction for the first data release of the LeMMINGs 'shallow' survey (see Chapter 5 and Baldi et al., 2018b) was carried out using AIPS software, following the calibration steps detailed in the e-MERLIN cookbook (Belles et al., 2015; Argo, 2015). The data were obtained from Jodrell Bank after it had first been correlated, loaded into AIPS and then averaged by time and frequency into a smaller and more manageable dataset. The CASA pipeline requires raw unaveraged fits files to run through the calibration pipeline and as such the data processed with CASA were obtained unaveraged in time or frequency. The averaging procedure reduces the number of channels in the e-MERLIN band to 25% of the full capability, without the loss of sensitivity. All of the LeMMINGs data in this thesis were observed in continuum mode and centred at 1.51 GHz (L-band). The bandwidth of e-MERLIN at L band is 512 MHz. Each observation was split into 8 intermediate frequencies (IFs) of 64 MHz each. In CASA, IFs are known as spectral windows (spws). When data was uploaded to CASA or the CASA pipeline was run, the data were divided into 8 spws. I will use the term 'IF' when referring to AIPS calibrated data and 'spw' when referring to data being calibrated or imaged in CASA. Each dataset includes a flux calibrator (FX-Cal), 3C286 (a high redshift quasar), for which the flux scale is well known at e-MERLIN baseline lengths. All observations include a bright point-source calibrator (PT-Cal), OQ208 (an unresolved Seyfert galaxy), which is unresolved to calibrate the bandpass response. Although not used in this thesis, most observations included a polarisation calibrator (POL-Cal), 3C84 (another well-known Seyfert with polarisation measurements, also known as NGC 1275 in this thesis). All of these calibration sources are standard amongst LeMMINGs datasets. It should be noted that sometimes due to atmospheric disturbance, antenna drop-outs or scheduling of the observations, one or more of the FX-Cal, PT-Cal or POL-Cal were not included or observed in a given dataset. As a large number of the LeMMINGs datasets were observed together, it was possible to copy the *uv* information for these calibrators across to a dataset and continue with the calibration. Each target had an associated phase reference source (PHS-Cal). All phase reference sources were picked from the VLBA calibrators list (Beasley et al., 2002). As the VLBA has longer baselines than e-MERLIN, the VLBA calibrators[3] are all unresolved point sources at e-MERLIN baseline scales, such that the complex telescope gains, e.g. the radiated power on a particular part of the sky, were calculated as a function of time. These variations can occur on the order of minutes, and so solutions from the phase calibrators must then be passed onto the target fields to ensure the correct calibration of gains for the target. In general, a phase calibrator was observed for two minutes, and the target for 6-8 minutes.

After receiving the data from Jodrell Bank, the data were loaded onto a local disk to look at the diagnostic plots output by the AIPS e-MERLIN pipeline. The first step RB and I

[3]The VLBA calibrator list can be found at: http://www.vlba.nrao.edu/astro/calib/

performed was to flag radio frequency interference (RFI) in the 1.51 GHz band. A large amount of RFI can be found in the ~1.51 GHz waveband due to terrestrial sources, such as modems, satellites, mobile phones and radars. As the RFI appears as spikes in amplitude in the visibilities, the inverse Fourier transform of a spike in the data is a sinusoid which will be imprinted into the sky image when it comes to imaging targets at the end of the calibration process. Hence, to achieve the best sensitivity possible, RFI must be removed prior and during calibration steps. Hence, the SERPent (Peck and Fenech, 2013) flagging code, written in ParselTongue (Kettenis et al., 2006), was used to remove the worst occurences of RFI from the data. SERPent works similar to AOFlagger by calculating a limiting threshold based off the raw data Offringa et al. (2012) above which data is 'flagged' and subsequently removed from the dataset. Currently, AOFlagger is used as part of the CASA e-MERLIN pipeline as SERPent was written especially for use with e-MERLIN data and AIPS. Both SERPent and AOFlagger use similar algorithms to assess the quality of data and flag any instances of RFI, so no noticeable difference should be seen in the datasets calibrated with CASA or AIPS. The flagging threshold can be changed depending on the dataset, but I do not go into detail here and recommend Offringa et al. (2012) for further details. Figure 2.1 shows an example of about one half of a 'shallow' sample observation pre-flagging and post-flagging using SERPent/AOFlagger. Post flagging, the raw data was inspected with AIPS tasks `SPFLG` and `IBLED` to remove any low-level RFI not picked up by SERPent/AOFlagger. Due to the high-RFI environment that the e-MERLIN array resides in, it is important to manually look through the data to check for low-level RFI, as it is not temporally expensive to do. Spurious, low-level RFI can especially affect the target observations, which are expected to be intrinsically weak in the radio. In addition to these flags, the channels showing no coherent phase (e.g. where the phase variations do not vary smoothly as a function of time) at the ends of each IF were also flagged. It is estimated that approximately 10% of the on-source data were flagged during the flagging processes outlined above before calibration and imaging.

2.2.1 Data calibration

I note first that the calibration steps discussed in this section are only performed for the FX-Cal, PT-Cal, POL-Cal and PHS-Cals in the datasets. To begin the calibration procedures, we fitted the offsets in delays using the AIPS task `FRING`. As described in Chapter 1, calculating the fringe offsets are important for long baseline interferometers. In the case of e-MERLIN, it is not always necessary and the fringe phases are usually zero. It is recommended to inspect the solutions of the `FRING` task and excise any additional RFI that could cause the fringe offsets to be displaced from ~zero ns. Once the data had been inspected, the solutions were applied to the data using the task `CLCAL`. Currently, there is no fringe fitting procedure available in any version of CASA. The CASA e-MERLIN pipeline assumes that the fringe phases are all zero and hence scales the data accordingly. In the near future, the Joint Institute for VLBI in Europe (JIVE) are working on implementing a "global

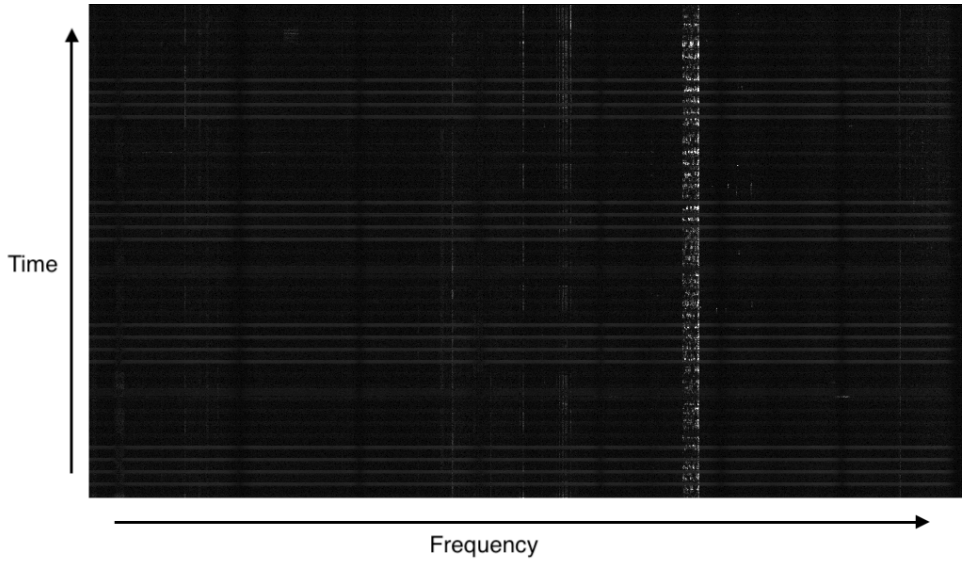

(a)

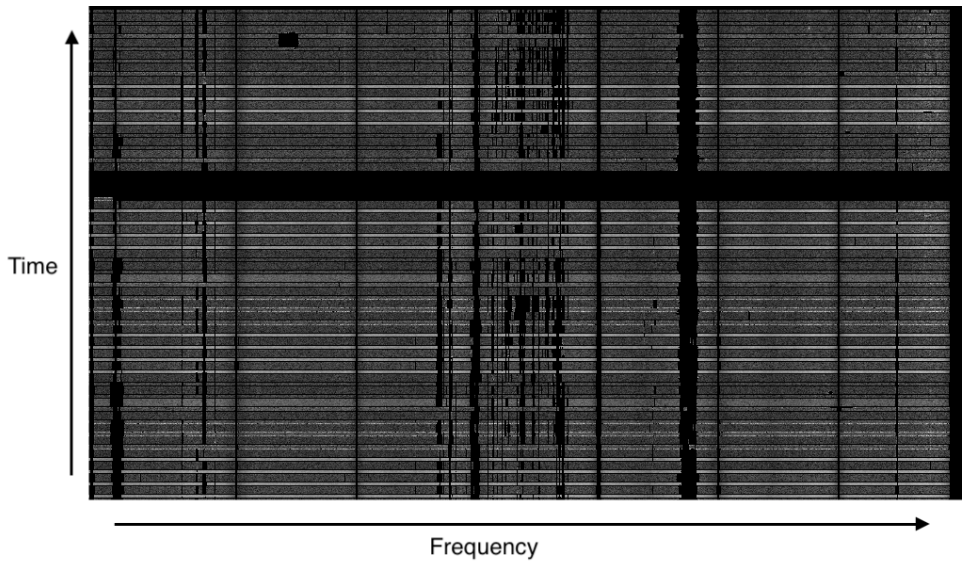

(b)

Figure 2.1: Pre-flagged (*top*) and post-flagged (*bottom*) data for one baseline of LeMMINGs 'shallow' block 23, using the AOFlagger software and shown with AIPS. The outputs shown above are produced using `SPFLG` in AIPS. The x axis represents the channel number (or frequency), while the y axis shows the time of the observation, and the intensity of the pixels represents the amplitude of the uncalibrated data. The unflagged data show several spikes of RFI (in white) in the *top* panel, which are removed completely by the AOFlagger software in the *bottom* panel. In addition, some of the low level RFI is removed by AOFlagger, but not all, as can be seen at the top of the bottom panel as a white spike in the third IF along, going from left to right. This sort of low-level interference would have to be removed by manual flagging with `SPFLG` or `IBLED` in AIPS, or using the `flagdata` command in CASA.

fringe fitter" into CASA, so that pipelines can be written in Python for long-baseline interferometers. Once this task is implemented in CASA, it will be used on all e-MERLIN datasets. For the e-MERLIN 'deep' data, fringe fitting was essential for Cambridge baselines, as the delay rate evolved by order 50 ns over a 2 hour period in the middle of the observation.

Next, the closure phases (e.g. the sum of the phase variations) were solved across at least 3 antennas with solution intervals of 2-3 minutes, so that phase variations over short time-scales were mitigated. The 2-3 minute time interval ensures that short phase-variations can be identified while the need for closure across only 3 antennas allows for plenty of solutions to be found. An initial bandpass table was made to account for the changes of sensitivity across the band with the AIPS task `BPASS`. Once the bandpass and phase solutions were calculated, assessed and subsequently applied to the data, a more robust amplitude and phase calibration was undertaken. The amplitude and phase calibration step requires phase closure across 4 antennas, but with longer time intervals as the short variations have already been accounted for in the previous phase-only calibration step. Both the phase-only and the amplitude and phase calibrations followed a two step process: the first step was to calibrate the flux calibrator with a given model[4] as it is partially resolved at e-MERLIN baselines and the second step was to calibrate with all the other calibrators. Only the central region of each IF was used for calculating the solutions as the edge channels are noisier. The AIPS pipeline recommends that only the central 70% of channels are used for calibration purposes, but the CASA pipeline uses the inner 90%.

After the calibration of the amplitude and phases for all calibrators, the flux scales are set and applied to the data. Up until this point, the solutions applied to the data have changed the relative scalings between individual visibilities, channels, IFs, antennas or baselines. The values of the IFs for the FX-Cal were scaled to the other calibrators and applied to ensure that the flux scale was correct. This was done with the task `GETJY`. It is often best to exclude the Lovell and Defford antennas for this step as the Lovell is highly sensitive, while the Defford antenna is usually less sensitive. Variance in antenna sensitivities across the array can affect the flux scale, hence the removal of the Lovell and Defford antennas. Following this step, a second bandpass table was calculated with information on the flux density and spectral index of the PT-Cal. The solutions from the amplitude and phase calibration and the bandpass table were applied to the data to assess the data quality with `POSSM`. After the steps outlined above, the main calibration had been completed, and imaging of the phase calibrators began.

2.2.2 e-MERLIN Radio Imaging

The first part of the imaging process was to flag for any outliers in the calibrated data with `UVPLT`, `CLIP` and `SPFLG`. Following this last flagging step for the phase calibrators, an

[4]Models at 1.5 and 5 GHz for 3C286 can be found on the e-MERLIN website.

imaging self calibration loop began. This involved imaging the calibrator with the standard multiscale, multi-frequency synthesis algorithm `IMAGR`, finding the positive components that describe the real sky model and finally applying these solutions to the data itself. `IMAGR` used the Hogbom clean method (Högbom, 1974), which assumes that the sky is made up of lots of small point sources in an empty sky. This method finds the brightest point source in the image, subtracts it from the dirty, non-cleaned map to build a sky model, which is then convolved with the beam to provide a clean image. The data were imaged with a cellsize of $0.05''$ and natural weighting to maximise signal-to-noise. There are three main types of weighting that I will use in this thesis: Natural, Uniform and Briggs weighting. The natural weighting scheme gives constant weights to all visibilities and therefore only the noise of a given visibility contributes to its weighting. Hence, this weighting tends to maximise the signal to noise. The uniform weighting scheme weights the data equally, therefore visibilities at greater *uv*-baselines are treated the same as those in the middle. This weighting tends to be good at detecting point source emission but increases the noise level. Finally, Briggs weighting (Briggs, 1995) is an intermediate weighting scheme between natural and uniform weighting. It usually gives a good compromise between point source detection and sensitivity.

Several rounds of phase-only self calibration on the phase calibrators were performed plus a final round of self-calibration in phase and amplitude. Self calibration is a process that uses the data itself to adjust the relative gains for each antenna, assuming that the gains vary with time. This can be observed as a cloud passing across an antenna over a short time period and changing the amplitude or phase detected by the antenna. Hence, this is a valid process to use to help improve the calibration and imaging fidelity of the data. The phase solutions are usually stable to within $\pm 20^{\circ}$ independent of baseline. The amplitude solutions show typical variations within a range of 10−20%. The solutions from self-calibration of the phase calibrators were then applied to the target field(s), however, for some scans, the calibration failed due to a lack of sufficiently long exposure times on the phase calibrator caused by antenna problems, hence the data for the affected calibrator-target scans were deleted.

A similar flagging followed by a phase self calibration cleaning routine that was used for the phase calibrators was then used for the target fields. The individual visibilities for the targets were re-weighted using `REWAY` to account for variable sensitivity as a function of antenna. As the Lovell is so much more sensitive than the rest of the antennas in the e-MERLIN array, it was up-weighted so the data from it contributed more to the final imaging procedures. Conversely, the Defford antenna was down-weighted due to a lack of sensitivity. RB and I focused only on the central region of fields within an area of at least 1024×1024 pixels with a cell size of $0.05''$ around the target position from NED (optical or infra-red images), which corresponds to an area of $0.73'^2$ (within the primary beam). Bright sources nearby in the target fields were imaged separately while imaging the targets to reduce the noise in the field. The large separation between the e-MERLIN antennas yield projected baselines in the *uv*-plane of up to $\sim$1300 kλ for the LeMMINGs sample, resulting in high-resolution maps (beam FWHM $\sim$150 mas). However, if significant data was flagged

on individual datasets, or worse, if the data from an entire antenna was flagged then this could significantly reduce the resolution of the images produced. For this reason, phase solutions on the Cambridge antenna were necessary for achieving the angular resolution that e-MERLIN is capable of. Furthermore, the Defford antenna often had poor phase solutions, but contributes greatly to keeping the beam circular and not elliptical, due to the *uv*-coverage. In addition, because of the large bandwidth, the H I absorption line was expected not to significantly contribute to the flux densities of the data and, hence, it was not considered later in the calibration and in the imaging process.

'Shallow' sample procedures

The 'shallow' sample was observed in 'snap-shot' imaging mode. This mode entails observing a target and its associated calibrator several times over an observing run, but not sequentially. Instead, for the LeMMINGs 'shallow' survey, the targets were grouped in blocks of ten, so that each phase calibrator-target pair would be revisited once every ∼90 minutes. Each target was observed at least six times (∼48 mins in total), meaning that the observing runs are ∼12 hours long, including the FX-Cal, BP-Cal and Pol-Cal, and hence fill most of the *uv*-plane. The benefits to this imaging mode are that many angles in the *uv*-plane are sampled. Other surveys take single observations of a target but have no information on other *uv*-baselines through Earth rotation aperture synthesis, whereas LeMMINGs attempts to circumvent this problem with the 'snap-shot' imaging. However, the 'snap-shot' images are incredibly sensitive to calibration errors as the loss of phase on one phase calibrator means losing one of only 6 areas in the *uv*-plane for that target. To minimise this loss, the targets are grouped together on the sky as close as they can in Right Ascension (RA), as slewing with e-MERLIN is much faster in declination than RA, so that the e-MERLIN antennas can slew quickly between each target and phase calibrator pair. Each block therefore has a range of declination values which can be seen in Figure 1.10, especially in LEM blocks 6 and 27. All of the phase calibrators are also chosen to be close to their target to minimise slewing losses.

As RB and I concentrated on the nuclear regions of the target galaxies, imaging of the entire primary-beam field was not undertaken. Images of each of the target fields were created in different resolutions to study the low-brightness diffuse emission and morphology of each source, to increase the probability of detection in case no source appears in the full-resolution map, and finally to detect any possible background sources or off-nuclear components. Lower resolution maps were obtained using different values of the `UVTAPER` parameter in the `IMAGR`, ranging between 750 kλ to 200 kλ. The `UVTAPER` parameter specifies the width of the Gaussian function in the *uv*-plane to down-weight long-baseline data points. Smaller units of this parameter correspond to a shallow angular resolution, i.e. a larger beam size, up to a factor 10 larger than ones reached in full resolution (i.e. ∼1.5 arcsec). For sources with elliptical restoring beams, e.g. those where the major-to-minor axis ratio was larger than two, usually caused by losing the Defford antenna due to no phase

information available on that antenna. RB and I made a further map using a circular beam with a radius corresponding to the area equivalent to the elliptical beam. This approach helps us to identify possible genuine radio morphological elongations of the sources in the direction of the major axis of the beam.

'Deep' sample procedures

I reduced LeMMINGs 'deep' sample data on NGC 4151 (Williams et al., 2017), NGC 6217 (Williams et al. submitted) and NGC 5322 (Dullo et al., 2018b). These three datasets were more straight-forward to calibrate than the 'shallow' data as they only included data on one target field and its associated PHS-Cal. Hence, if a single PHS-Cal scan had no phase information, then the following PHS-Cal scan could be used to calibrate the data and hence the target field. The 'deep' data had at least half a full *uv*-track on each of the sources (see Chapter 3 and 4). Therefore, I was able to flag bad data more readily than on the 'shallow' sample, where every *uv*-visibility was important, however noisy. In addition to the RFI flagging, the first two IFs of the left-left (LL) polarisation (e.g. the correlated signal from both the left-hand polarisation channels on a given baseline) were flagged on all Lovell baselines due to the inclusion of a test filter on the antenna. In general, this increased the amount of pre-calibration flagging that was made on the 'deep' sample, but overall, the inclusion of the Lovell meant the data quality was on average only slightly worse on the 'deep' data compared to the 'shallow' data. The data quality was also helped by the much larger on-source time, meaning that the additional flags did not have a significant effect on the final image rms sensitivities.

For NGC 6217, the delay rates calculated by the AIPS task `FRING` were found to vary on the Cambridge antenna approximately 4 hours into the observation, resulting in the delay changing from ~0 ns to ~50 ns over a 2 hour period. I changed the parameters in `FRING` from those in the cookbook (Belles et al., 2015) to also fit the delays and the delay rates to take account of this problem. However, at the points where the rates change most drastically, I was unable to keep the data and hence flagged it to avoid getting erroneous phase solutions in the rest of the calibration procedure. This analysis in AIPS of the changing delays on the Cambridge antenna were crucial for incorporating the long baseline information. It is not currently implemented in the CASA pipeline but will be when the JIVE global fringe fitter is released.

Self calibration improved the signal-to-noise and the final images of the 'deep' sample were created with the noise in the naturally weighted image often approaching a few 10s of μJy/beam. Due to the complex nature of the 'deep' sample sources, great care was taken to only include what are deemed to be genuine emission features in the self calibration process. The re-weighting of the individual antennas for the 'deep' data was especially important due to the inclusion of the Lovell antenna in these datasets and improved the signal-to-noise level greatly.

2.3 Chandra Data Reduction

Chandra data are publicly available from the HEASARC website[5] and the Chandra Interactive Analysis of Observations (CIAO)[6] software is commonly used to reduce the data. *Chandra* is used due to the sub-arcsecond spatial resolution and the good energy resolution in the 2−10 keV range that it provides. Of the 280 galaxies in the Palomar sample, ACIS-S or ACIS-I *Chandra* data is available for 162 (∼58%) of them in the archive, prior to 2017. Additional *Chandra* data was obtained in proposal cycle 18 to complete the LeMMINGs sample in the declination range 40-65°, to add to the archival data. This additional data includes mostly H II regions and takes the overall LeMMINGs sample available in the archive to 211 (∼75%). The lack of H II regions in the *Chandra* archive does effect the completeness of the LeMMINGs sample, and is discussed further in Chapter 7.

The standard reduction procedure used for all *Chandra* data sets in this thesis followed the same steps. I wrote a simple Python code to use the CIAO tools to re-process and to carry out the data analysis of all the *Chandra* data obtained from the archive and cycle 18 observations. The basic reduction procedure is as follows. First, the *Chandra* reprocessing script `chandra_repro` was run on all data sets to create a new bad pixel file and events file. The `fluximage` task was used to create broadband exposure-corrected image and exposure files. Next, I used a PANDAS dataframe (obtained from NED[7]) of the positions of the nuclear regions of all the galaxies and observations. It should be noted that not all of the positions in the NED database are correct, hence I searched the literature where necessary to get better position estimates. I made circular regions of radius 2″, 5″and 10″, with background annuli ranging in size from 2-5″, 5-10″and 10-20″respectively. The values of the fluxes given in Appendix D are obtained from the 2″ aperture and the 10-20″ background region. I chose these region sizes to encompass any nuclear emission from sources based off the optical *HST*/NED positions. These regions were then used to run `srcflux`, which calculates the fluxes and count rates, as well as the uncertainties in the measurements. The default model that `srcflux` fits uses an absorbed power-law, which should fit most AGN cores well, between the 0.2-10.0 keV energy band (e.g. Ishibashi and Courvoisier, 2010). However, the output spectra are best fit individually, as they may contain thermal emission from star formation at lower energies or evidence of line emission (e.g. the Iron Kα fluorescence line) or pile-up in the spectra. These spectra are shown in Appendix D.

As *Chandra* has sub-arcsecond resolution, it is possible to detect X-ray emission in other parts of the galaxy than from just the nucleus. I used the CIAO tools `mkpsfmap` and `wavdetect` to detect X-ray emission further away from the nuclear region in all the galaxies to build a complete catalogue of X-ray sources in the LeMMINGs sample. However, the data for the off-nuclear X-ray sources in the LeMMINGs survey is not presented in this thesis. `wavdetect` works by comparing emission at different scales to that specified by the

[5]https://heasarc.gsfc.nasa.gov/db-perl/W3Browse/w3browse.pl
[6]http://cxc.harvard.edu/ciao/
[7]the NASA/IPAC Extragalactic Database; https://ned.ipac.caltech.edu/

user, running a Mexican-Hat filter[8] on each of these points to see if any sources detected are significant. This allows for separation of closely spaced X-ray sources but can detect spurious results further away from the center of the point spread function (psf) generated with `mkpsfmap`. After finding all the galactic sources with `wavdetect`, I ran the tasks `roi` and `splitroi` to create background regions of all the sources, without including other sources in these background regions. This process allows the task `srcflux` to be run on all the sources in each observation of each galaxy separately, using a standard model of an absorbed power-law with Γ of 2.0, and hence extract limiting fluxes for all the sources. In future publications, I will remove any sources further away from the optical extent of each galaxy (e.g. the D_{25} diameter) to make sure that I only include sources likely to be attributed to the galaxy, as well as removing any spurious sources from the catalogue on the edges of the ACIS-S and -I chips, where the psf is worse.

2.3.1 X-ray spectral fitting

To obtain more precise measurements of the nuclear fluxes, I manually fitted the X-ray spectra of all of the sources. Spectral fitting of all X-ray data was undertaken using the XSpec software (Arnaud, 1996). Post calibration, the 0.2−10 keV X-ray spectra were uploaded into XSpec. In general the X-ray emission from LLAGN is rather weak and therefore only simple models were used to fit the X-ray spectra in most cases. The response files (rmf and arf files) as well as a background region file for the *Chandra* data were made using the procedure outlined in the previous section, allowing for the background to be removed from the spectra.

The spectra were modelled first as an absorbed power-law with PHABS × POWERLAW. The PHABS component models the galactic absorption in the direction towards a target and the values are found in Kalberla et al. (2005)[9]. For objects showing a soft excess (for example see Done et al., 2007), an additional thermal APEC component was added to the spectral fit. The APEC model assumes emission from a collisionally ionised diffuse gas[10]. If additional absorption was observed in the spectrum, then it was modelled with an extra ZPHABS model, to take into account the redshift of the sources. A handful of sources showed a bright Iron fluorescence line at ~6.4 keV, which was modelled with a Gaussian with the GAUSS model. A small minority of sources showed pileup in their spectra, which was modelled with the PILEUP model. Pileup is the increase in high energy photons in the detector due to two or more photons being received in a time interval less than the detector can read out. Hence, the detector adds them up and they appear as a single higher energy photon instead of one or more softer photons. This only tends to effect very bright X-ray sources of which there are few in the LeMMINGs sample.

[8]This is defined in the CIAO documention: http://cxc.harvard.edu/ciao/download/doc/detect$_manual/wav_theory.html wav_theory_m h$

[9]An online tool exists at: https://heasarc.gsfc.nasa.gov/cgi−bin/Tools/w3nh/w3nh.pl

[10]More information including abundances for the APEC model can be found at: https://heasarc.gsfc.nasa.gov/xanadu/xspec/manual/XSmodelApec.html

For all sources, the X-ray spectra were fit with χ^2 statistics where there were more than 200 counts in the spectrum. The data were re-binned if there were a large number of counts, so that the bin sizes and number of counts in each bin were Gaussian. For objects with less than 200 counts in the spectrum, I used Cash Cash (1979) statistics to perform the X-ray spectral fits. Cash statistics are more appropriate in the low-counts regime, as it models the data as a Poissonian distribution as opposed to a Gaussian distribution for χ^2 fitting. After finding the best fit model from the X-ray spectra, the fluxes for the objects were obtained using the FLUX command in XSPEC in the ranges 0.2-10.0 keV and 2-10.0 keV. I removed all absorbing columns and ran the FLUX command again to estimate the unabsorbed nuclear flux. Errors in the fluxes were obtained using the CFLUX command. These values for the best fit parameters, and nuclear fluxes can be found in Appendix D.

2.4 Re-classifying the LeMMINGs sample by Optical Emission Lines

In Chapter 1, I introduced the concept of BPT diagrams that delineate the low-ionisation nuclei of star-forming H II galaxies from the higher excitation nuclei of LINER and Seyfert galaxies with a suitable choice of emission line ratios. The initial Palomar sample used spectroscopic criteria of Veilleux and Osterbrock (1987) to separate 'active' nuclei from H II nuclei. Similarly, the original Palomar classifications used the Heckman (1980) scheme to delineate low-excitation LINERs from high-excitation Seyferts. The Veilleux and Osterbrock (1987) and Heckman (1980) schemes are now outdated, as several authors have made new schemes based on much larger samples (Kewley et al., 2006; Buttiglione et al., 2010). Hence, I use the state-of-the-art spectroscopic diagnostic diagrams introduced by Kewley et al. (2006) using SDSS emission-line galaxies and by Buttiglione et al. (2010) using optical spectra for the 3C radio galaxies. The newer scheme of Kewley et al. (2006) discriminates LINERs from Seyferts differently from Heckman (1980) and Buttiglione et al. (2010) introduces the 'line ratios index', defined as the average of the low ionization lines ratios of [N II], [S II] and [O I] and is more stable (e.g. the average of the three lines removes any large error that would be observed in one line on its own) than the individual emission line ratio diagrams. Hence, re-classifying the entire Palomar sample is required to ensure that the correct optical spectroscopic classifications are attributed to all of the nuclei in the LeMMINGs sample. Finally, I removed the transition galaxies from the list of optical classification types, as the transition class is not commonly used since its selection is more restrictive than the other optical classes. Therefore the 'Transition' galaxies were converted into LINERs or H II galaxies based on the different line diagnostics. Each object is classified as H II, LINER, or Seyfert based on at least two of the diagnostic diagrams, in case the third disagrees with the previous two.

The ratios I have used to disciminate between H II galaxies and LINERs/Seyferts are first

presented in Kewley et al. (2006) and Buttiglione et al. (2010) and are as follows:

$$\log(\frac{[O\ III]}{H_\beta}) = 1.19 + \frac{0.61}{\log(\frac{[N\ II]}{H_\alpha}) - 0.47} \tag{2.1}$$

$$\log(\frac{[O\ III]}{H_\beta}) = 1.30 + \frac{0.72}{\log(\frac{[S\ II]}{H_\alpha}) - 0.32} \tag{2.2}$$

$$\log(\frac{[O\ III]}{H_\beta}) = 1.33 + \frac{0.73}{\log(\frac{[O\ I]}{H_\alpha}) + 0.59} \tag{2.3}$$

To discriminate between LINERs and Seyferts I used:

$$\log(\frac{[O\ III]}{H_\beta}) = 1.89 \log(\frac{[S\ II]}{H_\alpha}) + 0.76 \tag{2.4}$$

$$\log(\frac{[O\ III]}{H_\beta}) = 1.18 \log(\frac{[O\ I]}{H_\alpha}) + 1.30 \tag{2.5}$$

and the 'line ratios index' is defined as:

$$LRI = \frac{1}{3}\log(\frac{[N\ II]}{H_\alpha}) + \frac{1}{3}\log(\frac{[S\ II]}{H_\alpha}) + \frac{1}{3}\log(\frac{[O\ I]}{H_\alpha}) \tag{2.6}$$

In the original Palomar sample, the nuclei were classified as follows: 206/486 (42%) H II galaxies, 96/486 (20%) LINERs, 69/486 (14%) ALGs, 60/486 (12%) 'Transition' galaxies and 50/486 (10%) Seyferts. The original Palomar classifications have many sub-classifications, for example, Seyferts and LINERs are classified as type 1, 1.5, 1.8, 1.9 and 2. In addition, the data has a quality flag for the strength of the classification, where ':' stands for uncertain and '::' stands for a very uncertain classification. Some of the nuclear classifications include a second classification, e.g. T2/S2, which is a 'Transition' galaxy or a Seyfert type 2. These ratios include only the first classification in the Ho et al. (1997a) and are irrespective of the confidence of the classification. As mentioned previously, I have removed the transition class from the list as it is a composite class of H II galaxies and AGN, based only on one diagnostic panel ([O III]/H_β vs [N II]/H_α in the BPT diagrams).

For the LeMMINGS data presented in this thesis, of 280 sources, 129 are detected (i.e. having line uncertainties smaller than 50 per cent in Ho et al. (1997a) with four emission lines, leading to a secure BPT diagram classification. Out of the rest of the sources, 46 are classified based on recent data in the literature (see notes in Table A.1 and Table B.1). The classification of 31 galaxies, all ALGs, remains unchanged from Ho et al. (1997a), because further spectra was not available in the literature with detectable emission lines. In addition, we reclassify the LINERs, NGC 5982 and NGC 6702 as ALGs because they do not show any significant emission lines.

Using the new classifications I arrive at the following numbers for the Palomar sample: 209/486 (43%) H II galaxies, 174/486 (36%) LINERs, 71/486 (14%) ALGs and 32/486

(7%) Seyferts. These ratios include seven galaxies (NGC 1003, NGC 1055, NGC 6482, NGC 6501, NGC 6503, NGC 6689 and NGC 7080) that did not have a clear classification, hence I have kept the original classification from the Palomar sample. A large number of the 'Transition' galaxies have been re-classified as LINERs, and some of the previously classified Seyferts are now classified as LINERs too. Whereas Ho et al. (1997a) concluded that LINERs outnumbered Seyferts 2:1, the new classification schemes suggest that LINERs are even more common than first thought, by 5:1 over Seyferts. In addition, the predominance of H II galaxies is nearly matched now by the LINER class. The additional ALGs have come from more recent data as outlined in Baldi et al. (2018b) which show that two additional galaxies (NGC 5982 and NGC 6702) are actually ALGs rather than LINERs, as thus were classified in the original Palomar scheme. From the new scheme, the LeMMINGs sample encompasses 135/280 (48%) H II galaxies, 92/280 (33%) LINERs, 33/280 (12%) ALGs and 20/280 (7%) Seyferts. The LeMMINGs data represents the same population of nuclear properties in the nearby Universe as the Palomar sample. The LeMMINGs sample does have more H II galaxies and slightly more Seyferts than its parent sample, and slightly fewer ALGs and LINERs as a percentage than the Palomar survey. However, we can still consider the LeMMINGs sample as a statistically-complete sample that accurately represents nuclear emission line properties in the nearby Universe. All of the classifications can be found in the Appendix in Table A.1. The BPT diagrams from which these classifications are based upon are presented in Appendix C for the entire LeMMINGs sample, grouped by LeMMINGs block.

2.4.1 Galaxy Morphological Types

In addition to comparing the radio sample obtained from LeMMINGs to the nuclear properties of the galaxy, I have also investigated how the radio emission varies as a function of galaxy morphological type. The galaxy morphological types are obtained from the original Revised Shapley-Ames catalogue (Sandage and Tammann, 1981) and the Second Reference Catalogue of Bright Galaxies (de Vaucouleurs et al., 1976), and compiled first by Kraan-Korteweg (1986). These morphological classifications are presented in Ho et al. (1997a) and are included in Table A.1. The LeMMINGs sample encompasses all galaxy morphologies (E, S0, Sa-b-c-d-m, I0, Pec). Most of the LeMMINGs objects are late-type galaxies (from Sa to Sd, ~75 per cent), with a smaller fraction of elliptical and lenticulars (E and S0).

The galaxies in the LeMMINGs sample extend in distance out to 120 Mpc, with a median distance of ~20 Mpc. The extent and median distance of the LeMMINGs sample is similar to the original Palomar sample. Hence, the LeMMINGs 'shallow' sample presented in this thesis is representative of the entire Palomar sample and, by extension, of the population of nearby galaxies.

2.5 Black hole masses and the M-σ relation

As mentioned in Chapter 1, there is a well-known relationship between the black hole mass at the centre of galaxies and the stellar velocity dispersion, σ, of the galaxy bulge itself. There are other correlations, e.g. M_{BH}-M_{bulge} but it is thought that M-σ relationship is the fundamental one, invoking the co-evolution of galaxies and black holes (e.g. **?**). This relationship between the black hole mass and the stellar velocity dispersion allows for an estimation of the black hole mass which is important for working out the Eddington luminosity and accretion rate (see equations 1.18 and 1.19).

Using the stellar velocity dispersions measured from the optical spectra by Ho et al. (2009) (see Tables A.1 and B.1) and the empirical relation from Tremaine et al. (2002):

$$\log\left(\frac{M_{\rm BH}}{M_\odot}\right) = 8.13 + 4.02\log\left(\frac{\sigma}{200\ {\rm km\ s^{-1}}}\right) \tag{2.7}$$

I calculated the BH masses for all the objects in the Palomar and LeMMINGs samples, the values of which range between 10^4 and 10^9 $M_\odot$. I do note that in objects of masses $10^4 M_\odot$ would be considered Intermediate Mass Black Holes (IMBHs), and therefore not necessarily SMBHs. But I also note that the M-σ relationship is very uncertain at low BH masses and the stellar velocities of these objects are also uncertain too, due to them mostly residing in irregular and dwarf galaxies. There are several different equations in the literature for the $M_{\rm BH} - \sigma$ relation, depending on selection effects and the galactic environment. Hence, I also derived the BH masses using the $M_{\rm BH} - \sigma$ relations from Graham and Scott (2013) and Kormendy and Ho (2013). The different relations lead to different $M_{\rm BH}$ measurements, but the median and standard deviations for the LeMMINGs sample are similar. The median $M_{\rm BH}$ and standard deviations of the $M_{\rm BH}$ distribution for our sample using the three $M_{\rm BH} - \sigma$ relations are (in logarithmic scale) 6.85, 6.46, and 7.09 $M_\odot$ and 1.18, 1.62, 1.29 $M_\odot$ for Tremaine et al. (2002), Graham and Scott (2013) and Kormendy and Ho (2013) respectively. The Tremaine et al. correlation produces the smallest $M_{\rm BH}$ scatter for our sample. The Graham and Scott (2013) relation is as follows:

$$\log\left(\frac{M_{\rm BH}}{M_\odot}\right) = 8.15 + 6.08\log\left(\frac{\sigma}{200\ {\rm km\ s^{-1}}}\right) \tag{2.8}$$

and the Kormendy and Ho (2013) relation is:

$$\log\left(\frac{M_{\rm BH}}{10^9 M_\odot}\right) = -0.50 + 4.42\log\left(\frac{\sigma}{200\ {\rm km\ s^{-1}}}\right) \tag{2.9}$$

The effect these relations have on the inferred black hole masses of the LeMMINGs sample is shown graphically in Fig 2.2. The different relations lead to $M_{\rm BH}$ measurements, which mostly agree for mass between $\sim 10^6$-10^7 $M_\odot$, but differ at higher BH masses within 0.5 dex and more significantly at lower BH masses within 1 dex. Direct measurements of black hole masses derived from stellar and gas dynamics, mega-masers and reverberation mapping are

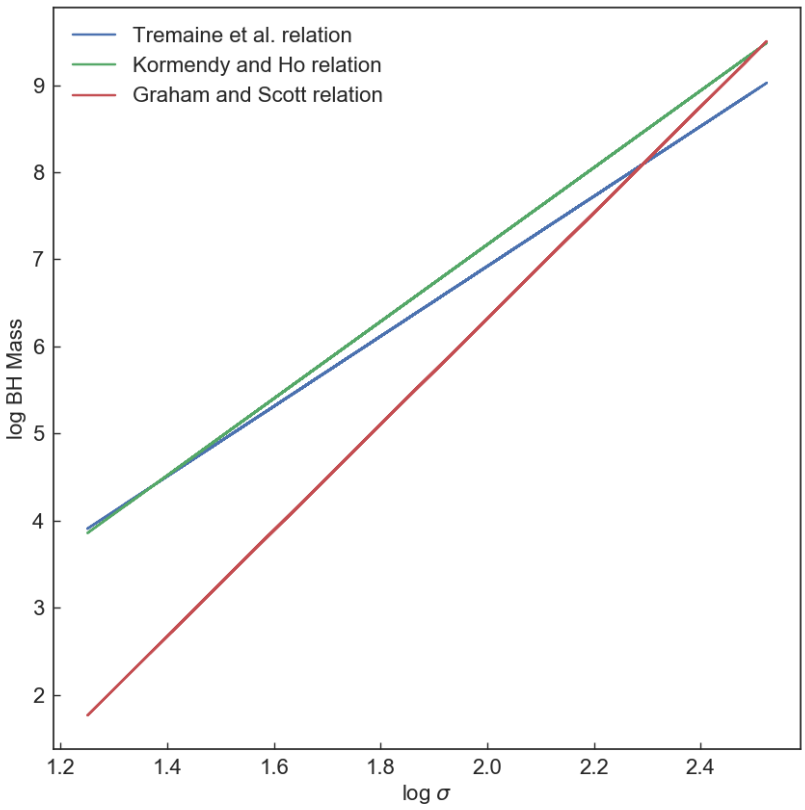

(a)

Figure 2.2: Black hole masses for the LeMMINGs sample extrapolated from the different M–σ relations presented in Tremaine et al. (2002), Graham and Scott (2013) and Kormendy and Ho (2013).

available from the BH mass compilation of van den Bosch (2016). Where possible, values from the van den Bosch (2016) compilation are used instead of values from the $M_{BH} - \sigma$ relation in the rest of this thesis. The values from the black hole mass compilation are consistent with the values obtained using the $M_{BH} - \sigma$ relation from Tremaine et al. (2002), but the choice of relation does not significantly affect the inferred black hole masses for the LeMMINGs sample or the following analysis that use those values. The most massive BHs are found in the elliptical galaxies that host LINERs and ALGs. All of the values for the black hole masses for the LeMMINGs sample can be found in the Appendix A.

Part I

The LeMMINGs 'deep' sample'

Chapter 3

Radio jets in NGC 4151: where e-MERLIN meets HST

This Chapter has been published in *Radio jets in NGC 4151: where eMERLIN meets HST*, 2017 MNRAS 472 3842-3853

3.1 Introduction

The well-known Seyfert 1.5 NGC 4151 is one of the brightest AGN in the sky in X-rays (Gursky et al., 1971; Boksenberg et al., 1995; Ogle et al., 2000; Wang et al., 2010, 2011a) and the radio-brightest of the radio-quiet AGN (Zdziarski et al., 2000). As such it is a great probe of the intermediate regime of radio-loudness, to explore the mechanisms of jet propagation through the interstellar medium (ISM). NGC 4151 is a nearly face-on ($i \approx 21°$) barred spiral galaxy. It has one of the most precise distance measurements of an AGN to date, due to dust-parallax measurements, of 19 Mpc (Hönig et al., 2014). This corresponds to an angular scale of ~91 pc per arc second.

NGC 4151 has been extensively studied in the radio waveband for several decades (Wilson and Ulvestad, 1982; Johnston et al., 1982; Booler et al., 1982; Harrison et al., 1986; Carral et al., 1990; Pedlar et al., 1993; Mundell et al., 1995; Ulvestad et al., 1998; Mundell et al., 2003; Ulvestad et al., 2005). The nuclear radio structure is characterised by a double-sided jet at PA ~77° extending from a nucleus with VLBI centre at α_{J2000}=$12^{h}10^{m}32.5758^{s}$ and δ_{J2000}=+39°24′21.060″ (Ulvestad et al., 2005). Archival VLA/MERLIN observations (Carral et al., 1990; Pedlar et al., 1993; Mundell et al., 1995) detect six radio components along this structure named C1 to C6 with the naming convention going from west to east. Further resolved components were discovered with VLBA/VLBI images of Ulvestad et al. (2005), who renamed the components A to I (Fig. 3.1). Throughout this Chapter I shall use the original C1-C6 nomenclature, unless specified otherwise. The core radio component (named C4) is co-incident with the optical nucleus in Mundell et al. (1995) (hereafter

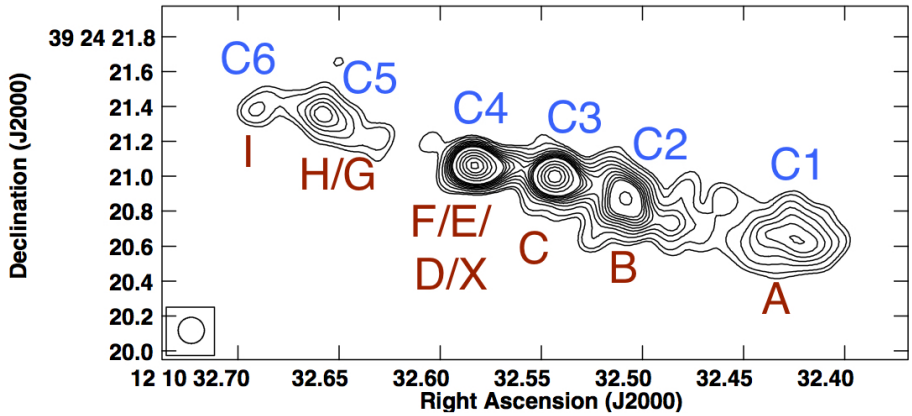

Figure 3.1: Naturally weighted archival MERLIN image of the central, $4 \times 2''$ (~360×180 pc) radio structures of NGC 4151, re-reduced with the MERLIN pipeline. The FWHM of the restoring beam was set to $0.15'' \times 0.15''$ (14×14 pc) and the entire *uv*-range with all 8 antennas in the MERLIN array was used to produce this image in AIPS. For consistency, the contours are the same as Fig. 2 in (Mundell et al., 1995): 1.5, 2, 3, 4, 5, 6, 7, 8, 9, 10, 15, 20, 25, 30 mJy/beam. The naming conventions are shown above with Carral et al. (1990) nomenclature in blue, and the Ulvestad et al. (2005) nomenclature in red.

referred to as M95) leading to its identification as the AGN. In this Chapter I present LeMMINGs 'deep' sample 1.51 GHz observations of NGC 4151 with the upgraded e-MERLIN radio interferometer allowing, by comparison with M95, study of changes in the jet morphology over a 22 year period.

A number of observers (Perez et al., 1989; Evans et al., 1993; Robinson et al., 1994; Boksenberg et al., 1995; Winge et al., 1997; Hutchings et al., 1998; Winge et al., 1999; Hutchings et al., 1999; Kaiser et al., 2000; Kraemer et al., 2008) have shown optical emission line images of the nuclear regions of NGC 4151. Whilst it is generally agreed that photoionisation from the AGN is an important contributor to the ionisation, the importance of the radio jet is not so clear. Here, by combining the e-MERLIN image with *HST* Hα, [O II], and [O III] images, I will explore the contribution of the jet in more detail.

In Section 3.2, I present the e-MERLIN observations and data reduction. In Section 3.3, I discuss morphological changes between the present image and the previous MERLIN image. In Section 3.4, I discuss the relationship between the radio jet and the optical line emission region and I summarise and conclude in Section 3.5.

3.2 Observations and Data Reduction

3.2.1 e-MERLIN Data Reduction

Observations of NGC 4151 were performed at L-band (weighted central frequency of 1.51 GHz) with the e-MERLIN array as part of the LeMMINGs 'deep' sample (see Chapters 1 and 2). All 7 antennas in the array participated in the observation on 2015 April 29, including the Lovell telescope. NGC 4151 was observed on-source for 3.81 hours with data

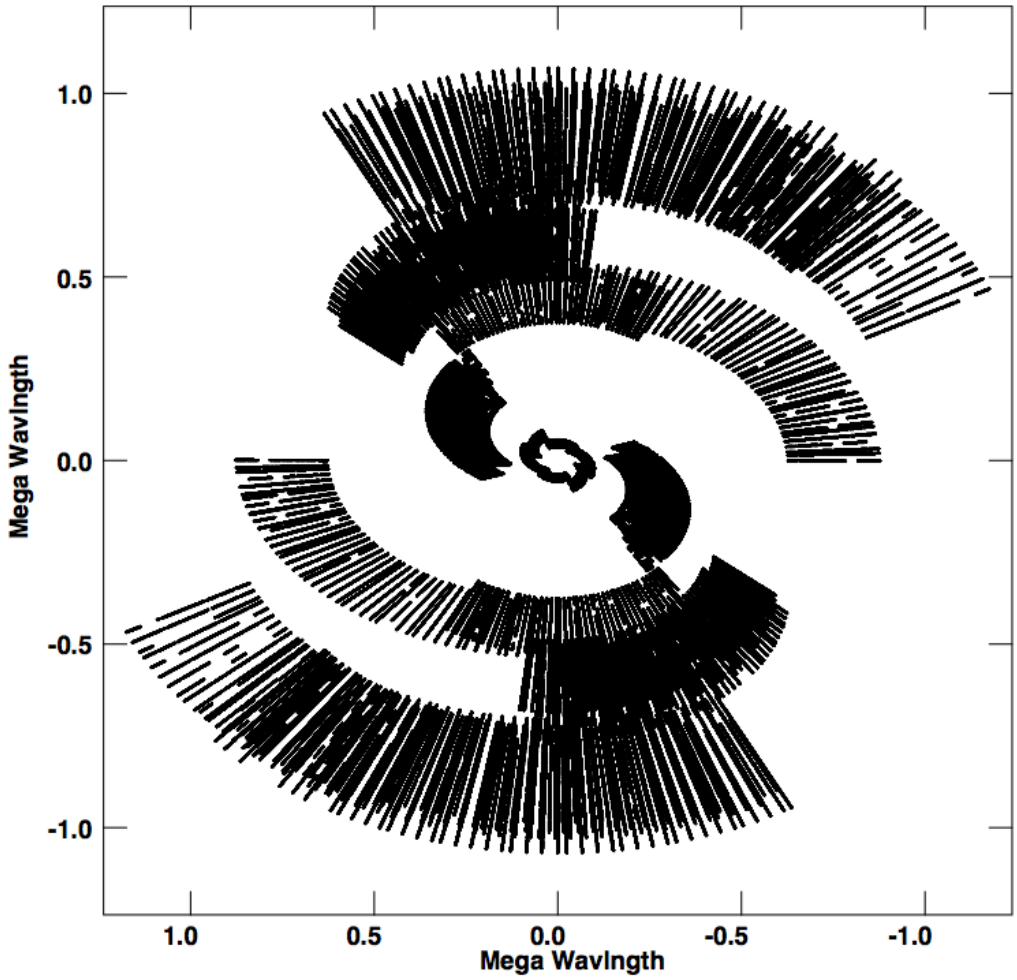

Figure 3.2: Full observed *uv*-plane of NGC 4151 at 1.5 GHz, using the LeMMINGs 'deep' data with all 7 antennas included.

reduction and imaging following the steps outlined in the e-MERLIN cookbook and pipeline (Belles et al., 2015; Argo, 2015) with AIPS (Wells, 1985, see Chapter 2). The full *uv*-plane of the e-MERLIN observations is shown in Fig. 3.2. The calibrator NVSSJ120922+411941 (J1209+4119) was used for phase referencing and OQ208 and 3C286 were used as the band pass and flux calibrators respectively. The target and phase calibrator alternated during the observing run, with blocks of approximately 2.5 mins on the phase calibrator and 7 mins on the target, with the flux and band pass calibrators observed at the end of the observing run. The final image was naturally weighted and achieved a noise of 35μJy. This image is shown in Fig. 3.3. Due to the complex nature of this source and its brightness, great care was taken to include only real features deemed to be genuine emission features in the self-calibration process. An amplitude and phase self-calibration did not produce stable phases or amplitudes, so only the final phase self-calibrated data are shown. This data set was then used to create all further images of NGC 4151.

Archival MERLIN Data Reduction and Imaging

Archival data originally published in M95 were re-reduced to compute accurate positions and flux density measurements to compare to the new e-MERLIN data set. NGC 4151 was observed in November 1993 at 1.42 GHz. The MERLIN data was calibrated with the MERLIN pipeline[1] in AIPS and re-imaged to account for RFI, alter the beam size and re-weight the data. As the data were originally taken in spectral line imaging mode to study the neutral hydrogen absorption in NGC 4151 (see M95), to create a continuum image I flagged all channels that were contaminated by this line to ensure the flux measurements on the core component C4 were not affected by this absorption feature. The amount of on-source time was 9.8 hours, achieving an rms noise of 0.25 mJy/beam. All stations in the MERLIN array took part in this observation including the Lovell telescope. All images produced were made at the same resolution as those published by M95, in order to be able to directly compare all data. The re-reduced natural image of the data is shown in Fig. 3.1 together with the contouring scheme from M95. Note that the extended low surface brightness structures seen to the south of C2 in Fig.2 of M95 is not present in the re-reduced image, probably due to improved imaging fidelity of these new e-MERLIN data due to the large bandwidth (512 MHz compared to 8 MHz) resulting in more complete sampling of spatial scales.

Comparison between the two radio epochs

When comparing the two epochs of data, some caution needs to be taken since archival MERLIN data does not completely match the new e-MERLIN data in terms of *uv*-range, number of antennas, bandwidth, central frequency and observing time.

[1] www.merlin.ac.uk/archive/

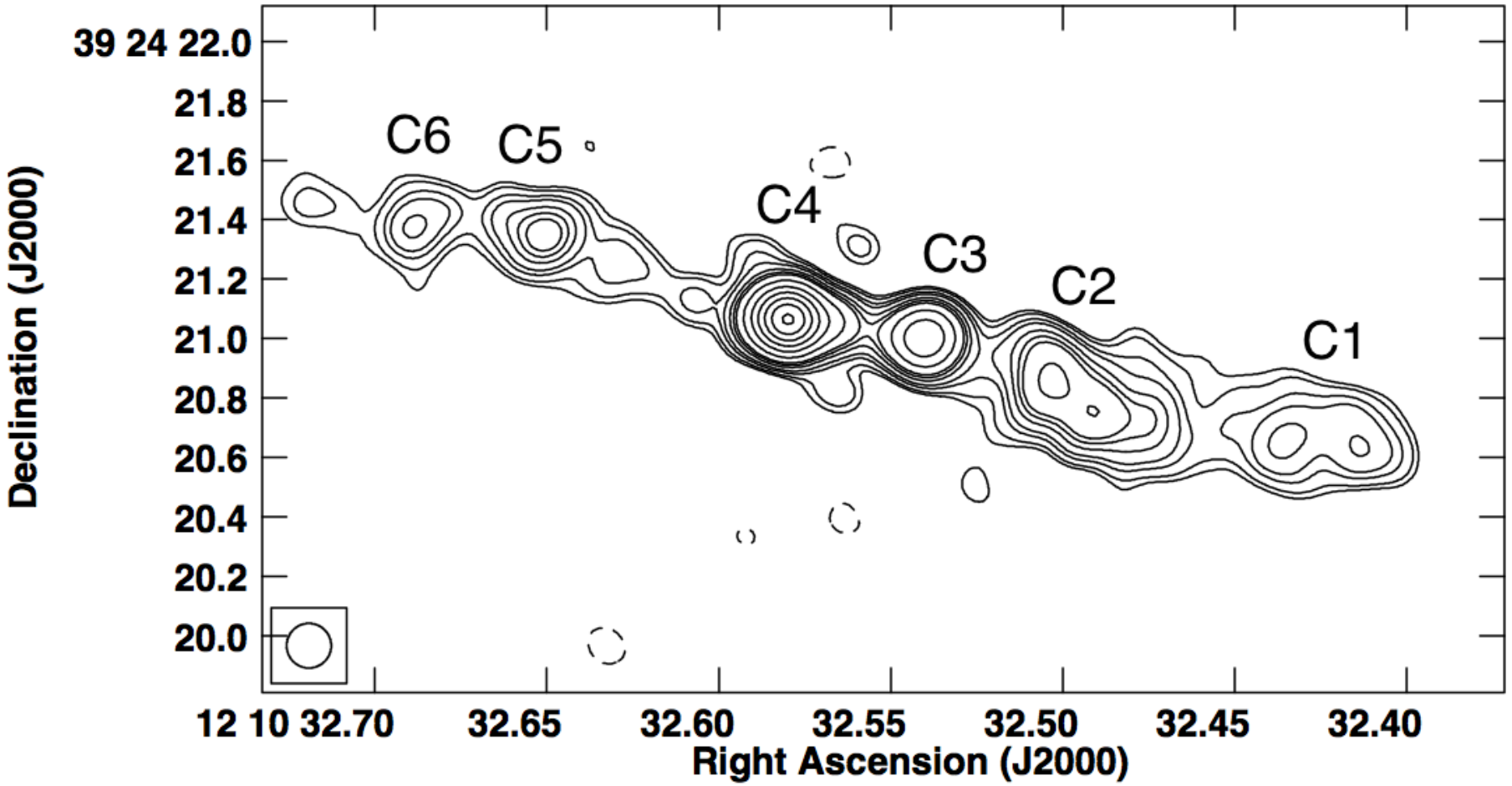

Figure 3.3: New full-resolution e-MERLIN image of the central $4 \times 2''$ (~360 × 180 pc) region of NGC 4151 using all 7 e-MERLIN antennas and a natural weighting. As in Fig. 3.1, the entire *uv*-range was used with a $0.15'' \times 0.15''$ FWHM restoring beam. Contours set are at -0.25, 0.75, 1, 1.5, 2, 3, 4, 5, 9, 16, 25, 36, 49, 64 mJy/beam.

Therefore, to make an unbiased comparison of the source structure at the two data epochs, I made two additional images with similar conditions for each dataset. The *uv*-range was limited to between 100 and 1000 kλ where the two datasets overlapped. I excluded the now defunct Mark III (Wardle) antenna from the MERLIN data. All of the images were made with the same FWHM restoring beam size of $0.15{\times}0.15''^2$, corresponding to 14×14 pc. The final images are shown in Fig. 3.4 and Fig. 3.5 based on MERLIN and e-MERLIN respectively. The emission on the same spatial scales is now directly comparable from these two images.

The e-MERLIN data were then loaded into CASA to produce an in-band spectral index image with clean and nterms set to 2. The spectral index image is shown in Fig. 3.6.

3.2.2 Optical Data

Perez et al. (1989) presented [O III] and Hα ground-based imaging of NGC 4151 and show that the ratio of [O III]/Hα defines a large ($\sim$10″, 910 pc) cone-like structure to the south-west of the nucleus of PA $\sim$50°, misaligned with respect to the radio structure. Evans et al. (1993) and Boksenberg et al. (1995) have presented *HST* Planetary Camera (PC) images in [O III] and Hα. HST Wide Field Planetary Camera 2 (WFPC2) images in [O II], [O III] and Hα have been presented by Hutchings et al. (1998, 1999); Kaiser et al. (2000) and Kraemer et al. (2008).

High-resolution *HST* Wide-Field Planetary Camera 2 (WFPC2) images of NGC 4151 were taken, from the GO-5124 program (PI: H. Ford), in the F336W, F375N ([O II]), F502N ([O III]), F547M, F658N (Hα) and F791W filters were retrieved from the public Hubble Legacy Archive (HLA[2]). The data were observed on 1995 January 22. These data were reduced by Bililign Dullo (BD), using the state-of-the-art reduction techniques described in Dullo et al. (2016), providing [O II], [O III] and Hα emission line images and produce an *HST* [O III]/Hα image which has not been previously presented. These images are considered, together with the e-MERLIN radio image, in Section 3.4.

In order to create the emission line images, BD used the WFPC2 PC1 F336W, F375N, F502N, F547M and F658N images and followed the procedures outlined in Knapen et al. (2004), Sánchez-Gallego et al. (2012) and Dullo et al. (2016). BD compared the narrow-band F375N ([O II]) image with the broad-band F336W image to create the [O II] continuum-subtracted emission line image (Fig. 3.7). BD created the [O III] and Hα emission line images by comparing the F502N ([O III]) and F658N (Hα) images with the F547M image of the galaxy. Figs. 3.7 and 3.8 show the new e-MERLIN L-band image overlaid on these three ([O II], [O III] and Hα) line images and on the [O III]/Hα emission line ratio, respectively.

The $V - H$ dust map of NGC 4151 by Martini et al. (2003, their Fig. 1) shows that the

[2]http://hla.stsci.edu

galaxy has spiral dust arms at $R \gtrsim 100$ pc. However, this dust map and the visual inspections of the *HST* images (see Fig. 3.7) show that the emission-line regions in the galaxy are only weakly obscured by dust. Therefore, BD did not attempt to correct for the spiral dust arms, although dust extinction may somewhat affect the [O II] line flux measurement since dust absorption is relatively higher at shorter wavelengths. However, when the emission line fluxes were extracted from the images (Section 3.4), the reddening using the extinction law from Calzetti et al. (2000) was taken into account.

I note that the coordinates of the radio core (component C4) in the e-MERLIN image (Fig. 3.3) differ by 0.″2 (18 pc) from those of the continuum core in the *HST* images. The radio positions are linked to the positions of VLBI phase calibrator sources. Systematic positional uncertainties are $\lesssim$ 1 mas, which can be neglected here. The *HST* positions are linked to the positions of stars in the Guide Star Catalogue (Jenkner et al., 1990) which are typically accurate to 0.″3 (27 pc at this distance). Thus the discrepancy between the radio and optical core positions is likely attributed to uncertainties in the *HST* positions. I therefore aligned the radio and optical images so that the maximum surface brightness at the core of each optical image is coincident with the radio core, C4. The images were moved in Right Ascension and Declination and not rotated. To align the radio and optical data I used astropy[3] to edit the FITS file header for the central Right Ascension and Declination values.

3.3 Radio Morphology and Spectral Index

The full-resolution naturally-weighted 1.5 GHz e-MERLIN image of NGC 4151 (Fig. 3) shows the six previously known components. C1-C6, extending over 4″ (0.4 kpc), similar to the twin-jet morphology observed in M95. The morphology shown in this image is similar to the naturally weighted MERLIN image (Fig.3.1) but the core, C4, is definitely brighter, by a factor of 1.5, in the e-MERLIN image. The jets, particularly the western jet, also appear narrower.

I now consider the morphological changes in the radio components, from C1 to C6, between the MERLIN and e-MERLIN images, as well as changes in positions and fluxes. I fitted 2D Gaussian components to each of the components C1-6 using the AIPS task JMFIT. The peak flux density, integrated flux, RA and Dec, and size of each component were extracted and are shown in Tables 3.1 and 3.2. The positions of the components stated in Table 3.2 refer to the self-calibrated data. These positions are consistent with the values from the dirty image without any self-calibration applied, to within 0.001″, much smaller than the FWHM of the restoring beam. Note that in those tables I list only the error given by JMFIT from fitting the components. The true error, including the rms noise level on the image, possible contamination by sidelobes from other components and uncertainties in the flux density calibrator, is hard to define but is likely to be at least 3 times larger.

[3]http://docs.astropy.org/

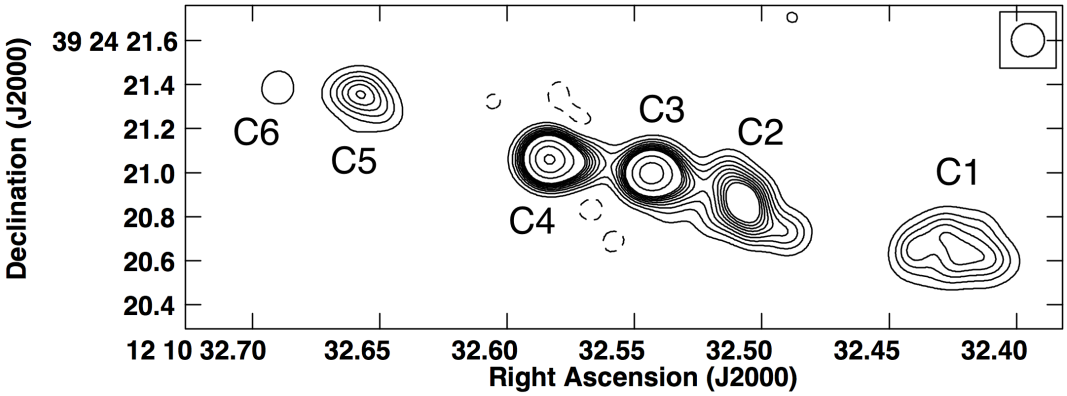

Figure 3.4: Naturally weighted archival MERLIN image of the central 3.6 × 1.2″ (~330 × 110 pc) region of NGC 4151, re-reduced with the MERLIN pipeline here. The beam was set to 0.15″ × 0.15″ and a restricted *uv*-range of 100 − 1000 kλ was used to produce this image in AIPS to overlap with the same *uv*-range in the e-MERLIN image. All antennas except the Mk III (Wardle) in the MERLIN array were used so as to include only those antennas in the current e-MERLIN array. The contours are -0.75, 1, 2, 3, 4, 5, 6, 7, 8, 9, 16, 25, 36, 49, 64 mJy/beam. The naming convention from Carral et al. (1990) are overlaid in black.

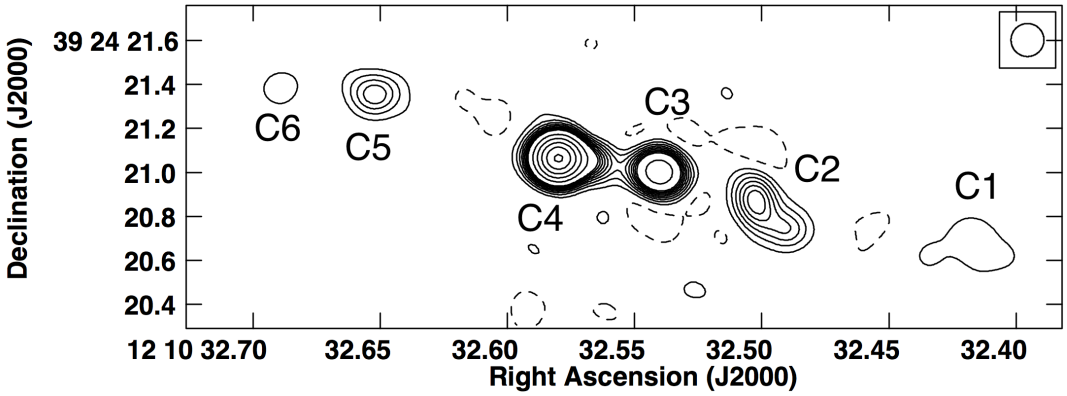

Figure 3.5: Same as Fig. 3.4 but using the new e-MERLIN data and reduced with the e-MERLIN cookbook. This included all 7 e-MERLIN antennas. As in Fig. 3.4, the *uv*-range was limited to 100 - 1000 kλ.

In the following sections I will focus on each component of the jet in turn to study their morphology, possible movement and flux density change with respect to the two epochs. In terms of the radio morphology, the full resolution images are compared, while flux density variations come from the comparison of the *uv*-range restricted images (Fig. 3.4 and Fig. 3.5). I caution, however, that small differences in *uv*-coverage can have a noticeable effect in imaging, particularly of low brightness structures. Here, although the 1D *uv*-range is restricted to be the same for the MERLIN and e-MERLIN images (Figs. 3.4 and 3.5), it is not possible to restrict the 2D *uv*-coverage of the MERLIN image to be the same as for e-MERLIN as the reduction in sensitivity is then too great to allow useful imaging of low brightness structures.

3.3.1 The Individual Components

C1 and C2

Comparing Figs. 3.4 and 3.5, the overall peak flux density of the components C1 and C2 appears to have decreased. However the different *uv*-coverage of the MERLIN and e-MERLIN datasets may affect the detection of large scale structure, giving rise to negative bowls underlying the more compact emission and hence reducing peak flux densities, in the e-MERLIN image. In this respect it is interesting to note that with the lower contour levels for the full-resolution e-MERLIN image (Fig. 3.3), the extended structures of C1 and C2 resemble those of the MERLIN image (Fig. 3.1).

C3 and C4

C3 is unresolved, even at the highest angular resolution achievable with e-MERLIN. Similar to components C1 and C2, the flux density in C3 decreased by a factor of ~1.5. I again caution that at least part of this change may be due to changes in 2D *uv*-coverage but for an unresolved component the differences in *uv*-coverage should not be so important. Higher-resolution 1.4 GHz VLBA observations (Ulvestad et al., 1998) show a faint (2.6mJy total flux density) component at the location of C3. This indicates that the emission associated with component C3 by MERLIN and e-MERLIN must be related to an extended and diffuse region, undetectable with the VLBA.

The core, where the jet base is located, corresponds to component C4. It is slightly elongated on the western side towards C3, where the 4 mJy/beam contour level connects it to C3 as it did in the previous M95 image. In addition, other weaker extensions are associated with C4 towards the north, south and east. I cannot conclude anything about their nature because of their small size and weakness.

C4 is the brightest component, with a peak flux density of ~67 mJy/beam, higher than in the MERLIN observations by nearly a factor of ~2 and corresponding to a luminosity of 3.87×10^{37} ergs s^{-1}. VLBI observations at 18 cm with an angular resolution of a few mas show several components along the jet axis located within the core C4, which are not resolved by e-MERLIN (Ulvestad et al., 1998; Mundell et al., 2003; Ulvestad et al., 2005). The flux density of one of these VLBI components (D3b) increased by ~30 per cent in 4 years between the observations of Ulvestad et al. (1998) and Ulvestad et al. (2005). The larger flux density changes seen between the MERLIN and e-MERLIN observations are quite consistent with these VLBI changes and confirm that C4 contains a currently active AGN core, injecting relativistic particles into the inner jet.

C5 and C6

Moving to the eastern side of the jet, a 0.4″ (36 pc) significant elongation bridges C4 and C5 (Fig. 3.3). C5 has a clear extension to the west, similar to that in the 1993 observations. Furthermore, this extension overlaps with a VLBA component G (Mundell et al., 2003). The peak intensity of component C5 remains mostly unchanged. C6 is the last component of the eastern jet and is consistent in flux and morphology with previous MERLIN images. This element has a PA 125°, clearly different from the other components, suggesting a possible bending of the jet spine. A further weak component appears east of C6 which is not present in the previous MERLIN data. This component requires further investigation with e-MERLIN to confirm its presence and morphology.

Summary

Component C4 has definitely increased in flux density (by factor nearly 2) in the 22 year period between the MERLIN and e-MERLIN observations. Components C5 and C6 in the eastern jet have not changed noticeably. This lack of change leads confidence to the finding of a decrease in flux density of components C3, C2 and C1 in the western jet is real.

3.3.2 Estimation of the jet speed

The intrinsic velocity, v, of a component in a jet over a given time period is related to the angle that the line of sight subtends with the angle of the jet, θ, and its measured apparent transverse velocity v_0 for relativistic jets (Kellermann et al., 1989).

$$v = \frac{v_0}{[sin(\theta) + \frac{v_0}{c} cos(\theta)]} \tag{3.1}$$

Pedlar et al. (1993), Robinson et al. (1994) and Vila-Vilaro et al. (1995) estimate that the pointing angle of the radio jet with respect to the line of sight is ~40° based on a combination of geometric arguments, velocity images of the narrow line region (Winge et al., 1997; Hutchings et al., 1998; Winge et al., 1999) and the galactic disc inclination. I take this pointing angle into account when calculating the jet speed.

To accurately estimate the jet speed, components with reliable positions are needed. Hence only the unresolved components with no significant extensions can provide a precise astrometric position by fitting them with a 2D-Gaussian provided by the JMFIT task. This is the case for C3 and C4. As the data is self calibrated, the absolute astrometric positions of the components between the two epochs of data is lost. However the relative positions between sources remain intact and so it is still possible to measure changes in separation between C3 and C4. I measured a change in separation of 2 mas but given a beam size of

Table 3.1: Flux densities obtained from Fig. 3.4 and Fig. 3.5, where the resolution of the data is matched, of each component in NGC 4151. The spectral index was obtained from the spectral index image in Fig. 3.6, the size of the components as found from the fitting process in section 3.3 and the minimum energy and magnetic field obtained from this process.

Comp.	Peak Flux Density MERLIN (mJy beam^{-1})	Integrated Flux Density MERLIN 1993 (mJy)	Peak Flux Density e-MERLIN (mJy beam^{-1})	Integrated Flux Density e-MERLIN (mJy)	Spectral Index e-MERLIN	Component Size in e-MERLIN image (mas^2)	B_{min} (mG)	log(U_{min}) (J)
C1	5.92 ±0.06	2.74 ±0.35	1.94 ±0.04	6.09 ±0.05	-0.9	346.8 × 203.4	0.39	44.02
C2	13.64 ±0.07	28.69 ±0.20	6.51 ±0.04	15.36 ±0.04	-0.9	327.0 × 162.9	0.59	44.16
C3	31.66 ±0.07	42.38 ±0.15	22.92 ±0.04	25.74 ±0.02	-0.7	172.0 × 147.0	0.76	44.01
C4	37.14 ±0.07	46.68 ±0.14	66.76 ±0.04	72.00 ±0.02	-0.4	161.2 × 150.6	0.96	44.21
C5	6.05 ±0.07	10.69 ±0.17	4.83 ±0.04	6.85 ±0.03	-0.9	202.8 × 157.3	0.54	43.85
C6	1.87 ±0.07	1.98 ±0.13	1.95 ±0.04	1.86 ±0.02	-0.9	156.5 × 137.5	0.44	43.43

Table 3.2: Astrometric measurements of radio components compared to the position of the core C4 obtained from the self-calibrated data. These positions are compared to observations first published in M95, but have been re-reduced here (see section 3.2.1). All positions given are in J2000 co-ordinates, with the difference calculated from the core C4 in that given image. The difference of these two values is shown in column 8 which is used as a measure of the relative shift of each component. The errors in the position from the fitting process are of the order half the beam size, i.e. ~0.075″ (7 pc).

Comp.	RA e-MERLIN	Dec e-MERLIN	Difference	RA MERLIN	Dec MERLIN	Difference	Relative Shift
C1	$12^h10^m32.41726^s$	+39°24′20.6601″	1.928″	$12^h10^m32.42493^s$	+39°24′20.6475″	1.877″	+0.051″
C2	$12^h10^m32.49967^s$	+39°24′20.8362″	0.959″	$12^h10^m32.50832^s$	+39°24′20.8694″	0.886″	+0.073″
C3	$12^h10^m32.54025^s$	+39°24′21.0026″	0.466″	$12^h10^m32.54319^s$	+39°24′20.9964″	0.464″	+0.002″
C4	$12^h10^m32.57989^s$	+39°24′21.0646″	-	$12^h10^m32.58279^s$	+39°24′21.0597″	-	-
C5	$12^h10^m32.65199^s$	+39°24′21.3570″	0.884″	$12^h10^m32.65756^s$	+39°24′21.3505″	0.913″	-0.029″
C6	$12^h10^m32.68911^s$	+39°24′21.3844″	1.306″	$12^h10^m32.68911^s$	+39°24′21.3885″	1.275″	+0.031″

150mas, I do not claim any detectable movement. Taking the 2mas figure at face value would give a velocity of 0.04c, consistent with the upper limits measured from VLBI observations by Ulvestad et al. (2005) but over a period of 4 years.

3.3.3 Radio Spectral Index

In this Chapter, I use the definition of radio spectral index, α, where the flux density, S at frequency ν is given by $S_\nu \sim \nu^\alpha$. A flat spectrum ($\alpha \gtrsim -0.3$) is representative of a compact synchrotron self-absorbed source. Most AGN cores have flat spectra whereas extended, optically thin, emission has a steeper spectrum ($\alpha \lesssim -0.7$).

I derived the spectral index for the full-resolution e-MERLIN image, using the full 512 MHz bandwidth. I used the CASA task clean with nterms = 2 to interpolate through all the intermediate frequencies (Rau and Cornwell, 2011). I considered only the emission above 2mJy/beam to remove unreal fluctuations due to low S/N. The spectral index image is presented in Fig. 3.6. The calculated α values range between -3 and 1.

Table 3.1 contains the radio spectral index of the components along the jet, ascertained from Fig. 3.6 at the location of the flux peak of each component. The unresolved bright components, i.e. C3 and C4, provide the most reliable spectral indices. The core C4 shows the flattest radio spectrum within the e-MERLIN bandwidth with a value of ~ -0.4. This is consistent with α obtained with wider-band spectra by (Pedlar et al., 1993, in the 5−8 GHz band) and by (Carral et al., 1990, in the 1.6−15 GHz band), both with the MERLIN array. The component C3 has a steeper index ~ -0.7, consistent with the broad-band values in the literature from MERLIN (Carral et al., 1990; Pedlar et al., 1993) and also with the assertion that most of the flux density from C3 comes from a region which is extended on VLBI scales.

The remaining components show steeper spectra still, although the lower S/N in these regions leads to large sporadic variations at the edges of components which are almost certainly not real. Broadly, I note a steepening spectrum further away from the core, consistent with the classical picture of a jet losing energy by electron ageing and expansion (Condon and Ransom, 2016).

3.3.4 Estimation of the magnetic field along the jet

One possible explanation for a reduction in radio luminosity is radiative losses. To estimate the loss time-scale it is necessary first to estimate the magnetic field strength, shown below.

Assuming the minimum energy condition applies to the target, I estimate the magnetic field B_{min} of each component along the jet. This assumption folds in information on the spectral index, size, flux density, the jet composition and the pitch angle of the magnetic field. I assume that the depth of the source is equivalent to the minor axis of the component, unity

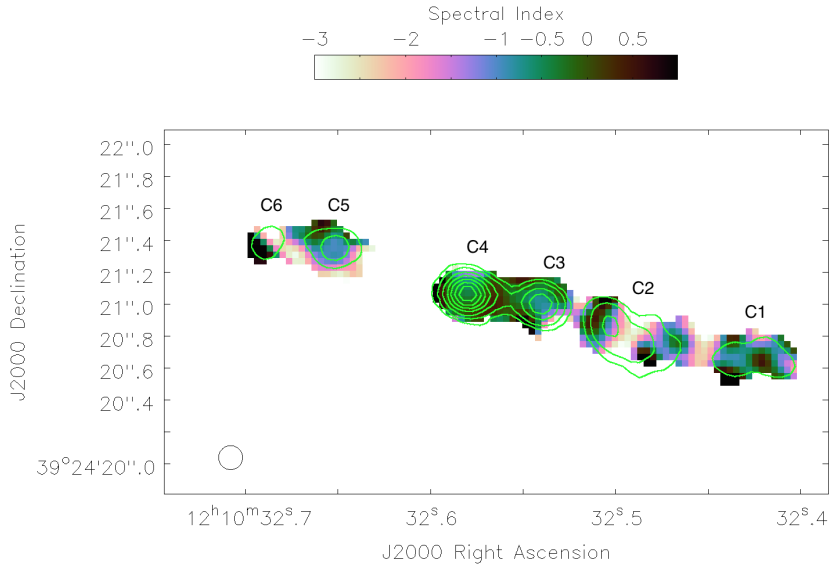

Figure 3.6: CASA e-MERLIN spectral index image of the central 3.7 × 1.8″ (~340 × 160 pc) of NGC 4151 at 1.51 GHz. The contours plotted are 2, 4, 9, 16, 25, 36, 49, 64 mJy/beam from the full resolution e-MERLIN image. Data were clipped at 2mJy in the full resolution CASA e-MERLIN image so that spurious low signal-to-noise regions were removed. All data were displayed with CASA and the range of colours reduced to −3.0 to 1.0 so as to remove any further spurious regions of non-physical spectral index from the image. The naming convention from Carral et al. (1990) are overlaid in white.

in the ratio of energy in electrons and ions, no angular dependence on the direction of the magnetic field and the line nof sight and a frequency range of 0.01−100 GHz. The observational constraints come from the integrated flux densities, the spectral indices and the deconvolved sizes of the components shown in Tab. 3.1.

I computed the magnetic field for all the components. However, as discussed above, the low signal-to-noise ratio can significantly degrade the accuracy of the fitting parameters for each component. Since C3 and C4 are bright resolved components, the estimates of their magnetic fields are likely more reliable and are of the order of 1mG. The remaining components show slightly smaller values of B_{min}, decreasing down the jet. Booler et al. (1982), performing a similar analysis for NGC 4151 using MERLIN data, estimated magnetic fields of the same order.

VLBI/VLBA observations resolve further structure in components C3 and C4, corresponding to smaller physical regions in the jet (Ulvestad et al., 1998; Mundell et al., 2003; Ulvestad et al., 2005). Therefore, I calculated B_{min} using these higher-resolution data (flux, size[4] and spectral index) for the VLBI central core, D3, located at the component C4 and the VLBA component C, located at C3. The B_{min} for D3 is 5.38×10^{-2} Gauss, while it is 1.35×10^{-2} Gauss for VLBA component C. I note that these values are larger by a factor of several tens than the e-MERLIN values due mainly to the smaller size of the component used when calculating B_{min}. Broadly, the range of B_{min} values obtained with this approach

[4]Since the VLBI/VLBA observations do not provide the deconvolved sizes of the components, I used a component size half the size of the beam: 1.6×0.9 mas^2 for VLBI and 2.9×2.4 mas^2 for VLBA.

are consistent with the values of the magnetic field of radio jets from the literature for AGN jets/cores (Marscher and Gear, 1985; Biretta et al., 1991; Jester et al., 2005; Worrall and Birkinshaw, 2006).

3.3.5 The cause of the reduction in radio flux density: synchrotron cooling or adiabatic losses?

The synchrotron decay time scale, τ, is related to the magnetic field strength and observing frequency by $\tau \propto \mathrm{B}^{-1.5}\ \nu^{-0.5}$. Although much of the emission from C3 is extended on scales larger than those probed by VLBI, I estimate the fastest decay time-scale by taking the magnetic field strength from VLBI measurements. This decay time-scale for C3 is ~700 years. Thus in 22 years, only 3% decrease is expected, compared to the observed decrease of nearly 30 per cent. For the lower surface brightness components, C1 and C2, the time-scales would be longer. Thus, assuming that the flux density decrease is real, additional energy loss processes are required, e.g. adiabatic expansion losses. Scheuer and Williams (1968) show that, for a linear expansion factor F (and for $S_\nu \propto \nu^{+\alpha}$), the flux density at a particular frequency will change by $F^{(4\alpha-2)}$. Thus for $\alpha = -0.70$ from the spectral fitting of component C3, the flux density changes by $\sim F^{-5}$. Thus only a very small expansion (F=1.06) is required to produce a decrease of 25 per cent. The source size is not known but to explain the flux seen by e-MERLIN but not detected by VLBA, will probably exceed a few VLBA beam sizes, i.e. ~1 pc.

Given this size and expansion factor, the expansion speed of the component C3 in 22 years would be ~2600 km s^{-1} but as the source size and flux decrease are not accurately known, this speed is uncertain. However velocities of order ~1000 km s^{-1} are not unexpected for shocks around expanding radio sources (Bicknell et al., 1998; Axon et al., 1998; Capetti et al., 1999) and so it is plausible that adiabatic expansion could explain the flux decrease of C3.

For the lower surface brightness components the characteristic radiation decay time-scale is ~10^5 years, which is similar to the value estimated by Pedlar et al. (1993). However given the uncertainty in measuring the flux density changes I do not speculate further about these components. Clearly, for C4, injection of new high energy particles dominates over any radiation or expansion losses.

3.4 The possible connection between the radio jet and the emission line region

In Fig. 3.7 I show the HST emission lines images from the new reduction by BD in Hα, [O III], and [O II] and in Fig. 3.8, I show an emission line ratio image, [O III]/Hα. e-MERLIN radio contours are superimposed in all cases.

In the emission line images (Fig. 3.7) there is a relatively bright region of emission of size $\sim 8 \times 3''$ (730 pc $\times$ 270 pc) broadly surrounding the radio jet, although the emission line region (major PA ~57°) and jet (PA ~ 79°) are not exactly aligned. The [O III]/Hα ratio image defines a larger cone-like structure (PA ~ 53°) extending at least 11″ (1 kpc) from the core. The emission line images show the presence of sub-structures, arches and haloes, indicating a clumpy distribution of the gas.

The range of [O III]/Hα ratio is between 0 and 5, based on values obtained for similar ELR for radio galaxies (Baldi et al., in prep). This ratio is a useful diagnostic tool for investigating the nature of the ionising source, i.e. shocks or photoionisation (Kewley et al., 2006; Allen et al., 2008; Capetti and Baldi, 2011). [O III]/Hα<1 can be reproduced by shocks or by a weak radiation field from an AGN or star-formation, while strong illumination from the AGN or a young stellar population can yield [O III]/Hα>2 (Baldi et al., in prep).

The [O III]/Hα values increase from very low values (~ 0.5) near the core and around the radio jet to > 1.5 in the more distant parts of the cone. This change in ratio suggests a change in the mechanism of ionisation from shock heating near the core to AGN photoionisation further out. Therefore, I consider in more detail whether shocks, such as might be associated with the jet, can explain the ionisation of the inner, brighter, ionisation region. The bright region 2″ (180 pc) south of the core which is visible in the [O III] and [O III]/Halpha image is a "ghost" caused by internal reflection (Hutchings et al., 1998).

3.4.1 Origin of the emission line region: jet or AGN?

The ratio of the radio luminosity to the emission line luminosities provide powerful diagnostics of the source of the ionisation, (e.g., Pakull et al., 2010). Bicknell et al. (1998) present the [O III] and radio luminosities of various samples of AGN. They state that the [O III] luminosities are consistent with the predictions of a model for ionisation based on the expansion of radio lobes (Bicknell et al., 1997). Here the emission line luminosities of the ELR are calculated.

To determine the Hα, [O III] and [O II] luminosities of the brighter extended ELR surrounding the radio jet Ranieri Baldi (RB) selected a circle of radius 2″ (180 pc), centred on C4. RB performed a standard analysis, using the task RADPROF in IRAF (Tody, 1986, 1993) for the aperture photometry of the *HST* images F658N, F502N, F375N. To estimate the emission line fluxes from the ELR it is necessary to first measure and subsequently remove the large unresolved component from the AGN nucleus. RB therefore measured the flux within a radius of 0.125″ (11 pc) centred on the core. RB subtracted this flux from the flux within the 2″ radius area. RB converted the extracted fluxes into physical units using the parameter PHOTFLAM, the flux-density normalisation value, and the image bandwidths. RB corrected the fluxes for reddening using the Calzetti dust extinction law (Calzetti et al., 2000). Furthermore, RB estimated the contamination from other emission lines falling within these bands. For F658N, to estimate the Hα it is necessary to take into account the

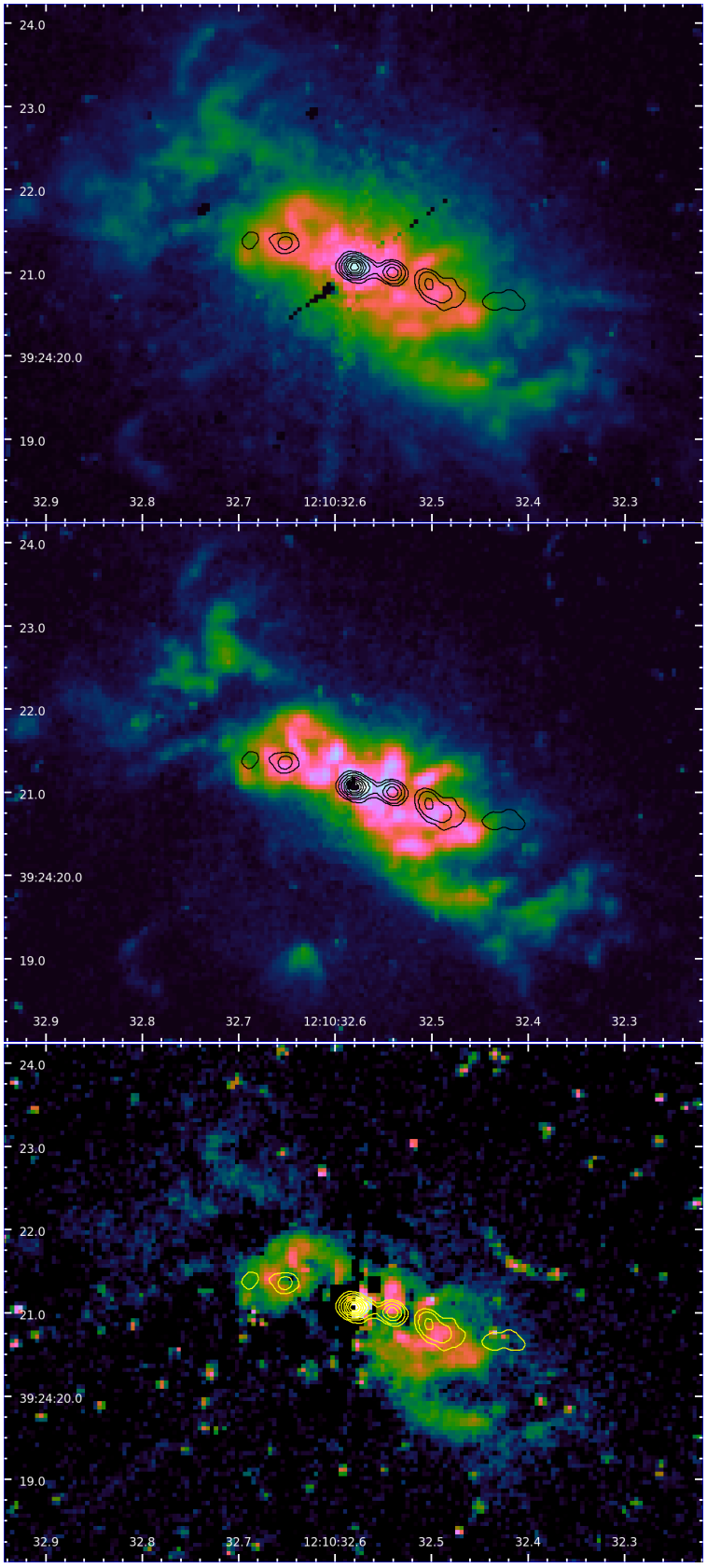

Figure 3.7: HST emission line image of NGC 4151 for Hα (*top*), O III (*middle*) and O II (*bottom*). The full resolution e-MERLIN radio contours are plotted on top of all the images and are at 2, 4, 9, 16, 25, 36, 49, 64 mJy/beam. North is up and east is to the left. The image size corresponds to the central $\sim 8 \times 6''$ of the nucleus of NGC 4151, ($\sim 740 \times 550$ pc).

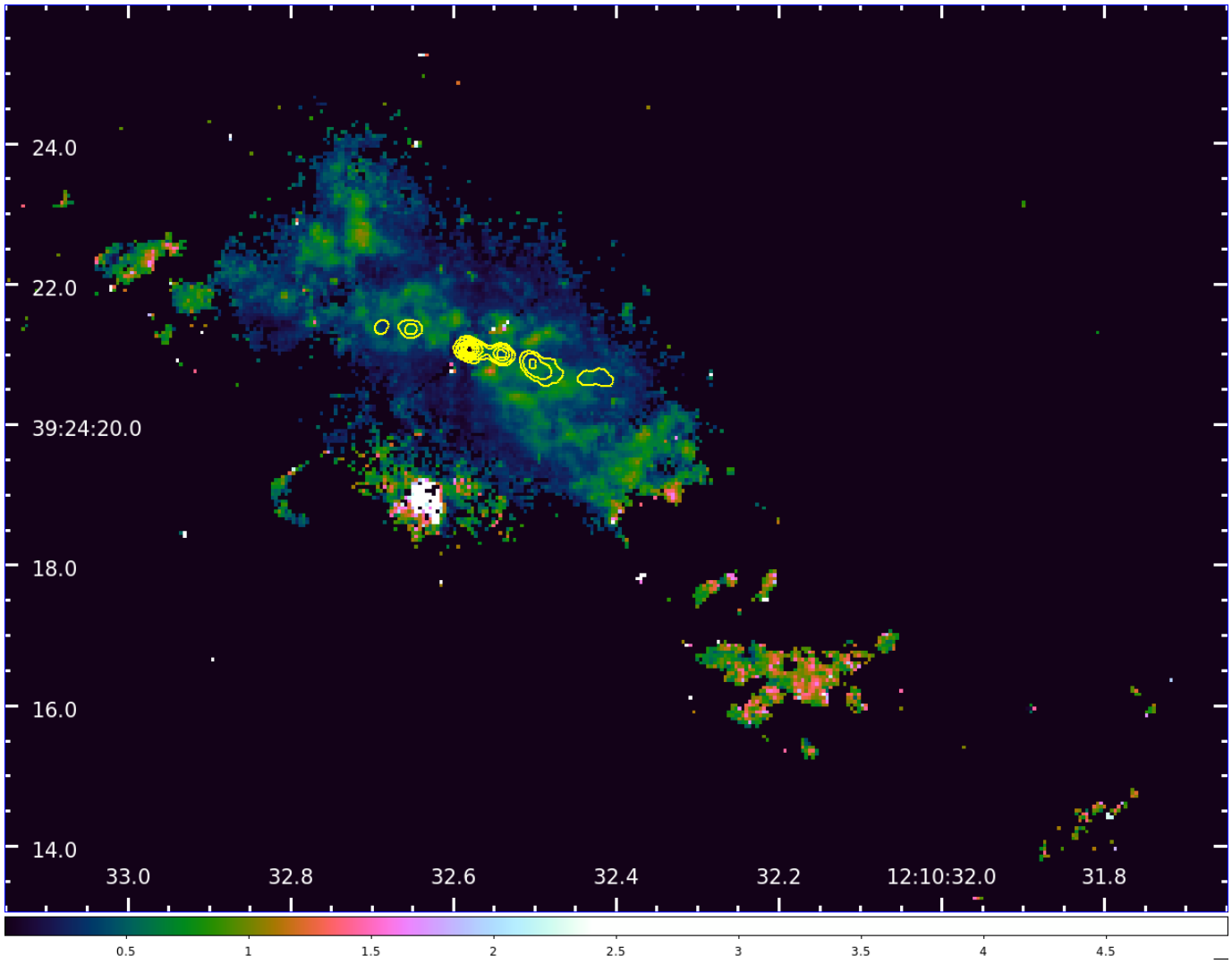

Figure 3.8: Image showing the ratio of the optical [O III] to Hα line emission from HST imaging of the central ~21 × 12″ (~1930 × 1100 pc) of NGC 4151. The full resolution e-MERLIN radio contours are plotted on top and are at 2, 4, 9, 16, 25, 36, 49, 64 mJy/beam I clipped out any pixels with S/N < 4 to remove spurious artefacts. The larger-scale structure of the ionisation region is seen south west of the core. This lines up more closely with the PA of the overall line emission ~50° but it is clear that the inner region bounded by the radio jet is at a slightly different angle at ~57°. In this image, north is up and east is to the left.

[N II] doublet, using the observed ratio of [N II]λ6583 = 0.68 Hα from the optical spectrum (Ho et al., 1997a). Only the [O III]λ5007 line of the [O III] doublet falls in the F502N band and only the [O II]$\lambda\lambda$,3726,3729 doublet falls in the F375N band. Hence, the total ELR fluxes within the 2″ radius but not including the unresolved contribution from the nucleus, are 1.54×10^{-14}, 1.10×10^{-13} and 1.43×10^{-13} erg s^{-1} cm^{-2}, respectively for Hα, [O III], and [O II]. Assuming a distance of 19 Mpc for NGC 4151, the calculated luminosities are 6.65×10^{38}, 4.74×10^{39} and 6.16×10^{39} erg s^{-1}. The ratio of the [O III] to radio luminosity here is consistent with the observations presented by Bicknell et al. (1998). Changes in the positioning and size of the subtraction region of the central core is the major source of error in measurement of line fluxes from the ELR and may be up to a factor of 3.

Shock models can be used to predict line luminosities. Nelson et al. (2000) used the MAPPINGS II code to estimate the expected Hβ luminosity from shocks in NGC 4151. Here RB and I repeated the Nelson et al. (2000) analysis using results from the MAPPINGS III code (Dopita and Sutherland, 1996; Allen et al., 2008), and similar to the analysis of e-MERLIN and *HST* observations of M 51b by Rampadarath et al. (2018). First, taking Hβ/Hα=0.29 from long-slit spectra (Ho et al., 1997a), then from the measured value of Hα luminosity (above) I find that $L_{H\beta} = 1.93 \times 10^{38}$ erg s^{-1}. The ratio of Hβ luminosity to luminosity in ionising radiation produced from shocks is $\propto v_s^{-0.59}$, where v_s is the velocity of the shock. Here, in agreement with Nelson et al. (2000), I find that a low velocity shock overpredicts $L_{H\beta}$ and shock speeds of $v_s > 2700$ km s^{-1} are required, similar to the calculated jet expansion speed, to reduce the predicted $L_{H\beta}$ to the observed level. I note that the MAPPINGS III code assumes a relatively high conversion efficiency of jet kinetic power into ionising radiation ($\sim$ 27/77, Weaver et al. 1977). A reduced efficiency could therefore make the observed $L_{H\beta}$ consistent with lower shock velocities. I also note that Weaver et al. (1977) refers to low velocity stellar winds but faster shocks with velocities > 1500 km s^{-1} are observed in narrow line regions of other nearby radio-bright Seyferts, similar to NGC 4151 (Axon et al., 1998; Capetti et al., 1999).

The emission line ratios [O III]/Hβ and [O II]/Hβ can provide another constraint on the shock velocities (Allen et al., 2008). The ratio values from the 2″ apertures are $\sim$25 for [O III]/Hβ and $\sim$30 for [O II]/Hβ. These ratios imply $v_s \gg 1000$ km s^{-1}, broadly consistent with the velocities derived from $L_{H\beta}$.

I qualitatively compare the energetics from the AGN radiation with those of the radio jets. I estimate the kinetic jet power from the radio core luminosity according to the empirical relation found by Merloni and Heinz (2007) by using 5 GHz core components from VLA data. For NGC 4151, I use the 5 GHz data obtained in Pedlar et al. (1993) and hence calculate a jet power of 1.4×10^{42} erg s^{-1}. The AGN radiative power was estimated from the X-ray nuclear emission. Wang et al. (2011b) measure the nuclear X-ray emission using Chandra as 1.13×10^{-10} erg s^{-1} cm^{-2}, corresponding to a luminosity of 4.6×10^{42} erg s^{-1}, although they do note that this is variable. Therefore the values derived for the energetics of the AGN radiation and of the radio jets are consistent assuming uncertainties in the Merloni

and Heinz (2007) relation.

Mundell et al. (2003) conclude that the AGN radiation field is the main source of ionising power in the ELR, but that the radio jet interaction with line-emitting clouds could contribute to the observed ionisiation. By fitting Chandra X-ray spectra, Wang et al. (2011a) also argue that shocks could make up to 12% of the ionised extended emission. Generally, the results are consistent with the conclusions of Mundell et al. (2003) and Wang et al. (2011a) about the jet contribution to the ionisation of the ELR. Combined with changing ionisation parameter in the [O III]/Hα image, I therefore conclude that in the ELR at greater distances from the AGN core than the radio jet e.g. further away from C4 than 360 pc, that photoionisation from the AGN is the only significant source of ionising power for the ELR. However in regions close to the radio structure ($\leq$360 pc), the jet cannot be ruled out as at least one component of the ionising power. As it is not possible to fully disentangle the contribution of the two main ionising sources, I cannot quantitatively estimate the fractional ionisation due to the radio jet relative to the AGN illumination in the ELR from the results.

3.5 Summary and Conclusions

The Seyfert galaxy NGC 4151, with twin radio jets, is the radio-brightest of the so-called 'radio-quiet' AGN and is thus one of the few such AGN for which it is possible to observe temporal changes in the structure of its jets. In this Chapter I have presented high-resolution 1.5 GHz images obtained as part of the LeMMINGs legacy survey with the e-MERLIN array. I compared these images with those made 22 years previously with the structurally very similar MERLIN array (M95). These images clearly show that the central AGN (component C4) has brightened by almost a factor 2. The components in the eastern jet (C5, C6) do not appear to have changed but components in the western jet, particularly C3, seem to have decreased in intensity. These observations show that the AGN core, C4, is still very much active in NGC 4151 and still injecting particles into the inner jet but energy loss mechanisms are dominating further out in the jet.

No significant change in the separation between the core, C4, and the only other unresolved component in the e-MERLIN image, C3, was detected. The resultant upper limit to the jet velocity $\leq$0.04c is consistent with the upper limits set by VLBI observations (Ulvestad et al., 2005) over a shorter (4 year) time period. However, given the beam size of 150mas, it is impossible to claim any detectable movement of C3 away from the core C4.

I derived a spectral index image from within the e-MERLIN bandwidth. The radio spectrum of the core, C4, is flat as expected from a jet base, and steepens down the jet, probably due to radiative losses. Further e-MERLIN observations have been made at 5 GHz which when calibrated and imaged will better constrain the spectral indices of the jet components and resolve the smaller-scale emission (Williams et al., in prep).

I have estimated the magnetic fields in all components in NGC 4151, assuming the

minimum energy condition. The values found, taking sizes from e-MERLIN observations, are ~few mG, consistent with similar MERLIN observations in the literature. Magnetic fields derived using VLBI observations are factors of 10 higher. The characteristic synchrotron decay time-scale, inferred from the magnetic field derived from VLBI observations for the unresolved bright component C3, is of the order of ~700 years, longer than that required to account for the flux decrease in 22 years. However, I find that given adiabatic losses, a very small linear expansion factor of 6% can produce the measured flux density decrease of 25 per cent.

High-resolution optical emission line images (Hα, [O III], and [O II]) from HST of the nucleus of NGC 4151, reduced by BD, have been presented. The misalignment between the radio and optical line emission regions has been discussed by previous authors, e.g. Evans et al. (1993) and Pedlar et al. (1993) and are not discussed further here. I used these data to investigate the origin of the ionisation of the ELR as a function of distance from the AGN. I note that the [O III]/Hα ratio close to the AGN, near the radio jet, is best produced by shocks whereas, far from the AGN ($\geq$360 pc), the ratio is more consistent with photoionisation. I also note that the ratio of radio to emission line luminosity shown here is similar to that found by Bicknell et al. (1998) for various samples of radio galaxies and is consistent with models for ELR ionisation based on expanding radio lobes. Although the estimate is very uncertain, the derived expansion velocity of C3 is in agreement with the higher shock velocities needed to avoid overproduction of Hβ emission. I also note that the brightest parts of the ELR are those directly surrounding the radio jet. Therefore I conclude that although the parts of the ELR further from the core than the e-MERLIN radio jet ($\geq$360 pc) are ionised largely by photons from the AGN, in the region of the ELR close to the radio jet, the jet is probably also a significant contributor to the ELR ionisation.

Chapter 4

Unveiling the nuclear region of NGC 6217 with e-MERLIN and the VLA

This Chapter has been submitted for publication and is under review as *Unveiling the nuclear region of NGC 6217 with e-MERLIN and the VLA* in MNRAS.

4.1 Introduction

NGC 6217 is a barred spiral galaxy which unlike NGC 4151, has not been observed in multi-wavelength data, expect for in some radio surveys (e.g., Hummel et al., 1985; Condon, 1987). However, it was selected for the LeMMINGs 'deep' sample as some authors had claimed a coincident X-ray jet that aligned with the radio emission from the nucleus (Pietsch and Arp, 2001; Falocco et al., 2017). Pietsch and Arp (2001, hereafter PA01) compared radio images of NGC 6217 from the NVSS (Condon, 1987) with *ROSAT* X-ray contour plots and claimed an extension south-west of the nucleus of NGC 6217 that was aligned in both wavebands. PA01 hence concluded that it was possible that the X-rays could form the base of a radio jet. However, with the resolution of the VLA (for the NVSS in D/DnC arrays) and ROSAT being 45″ (at 1.4 GHz) and ~25″ (at 1 keV) respectively, neither observation was capable of adequately resolving any jets in NGC 6217. More recently, Falocco et al. (2017, hereafter F17), analysed *XMM-Newton* images and spectra of NGC 6217, obtained in 2001, 2002 and 2007, and reported on the alignment of three X-ray 'knots' and hence a 'likely' X-ray jet emanating from the core in a south-west direction extending over 3′. They supported the original PA01 assertion from the poorer angular resolution X-ray data. However, both PA01 and F17 used the same NVSS images of NGC 6217. Higher resolution radio data from sub-arcsecond resolution radio interferometers are required to analyse the X-ray emission in the putative X-ray jet in this galaxy.

The presence of co-spatial X-ray emission has been observed in some higher luminosity systems in the literature (Schwartz et al., 2000; Chartas et al., 2000; Harris and Krawczynski, 2006; Worrall, 2009). However, there are very few objects near enough to spatially resolve these X-ray jets, so new candidates for radio/X-ray/optical follow-up are useful; for example, 3C273 (Sambruna et al., 2001; Jester et al., 2005; Harris et al., 2017), M 87 (Marshall et al., 2002; Wilson and Yang, 2002) and Centaurus A (Kraft et al., 2002; Hardcastle et al., 2003) are just three objects which can be resolved, but are all radio-loud sources. NGC 6217 is a radio-quiet source in the local neighbourhood (20.1 Mpc with an angular scale of 97 pc per arcsecond, see also Cabrera-Lavers and Garzón, 2004), making it an ideal case study for X-ray jets in radio-quiet LLAGN systems.

In the literature, NGC 6217 has not been well observed at radio frequencies other than in surveys with poor angular resolution. The 1465 MHz radio image of NGC 6217 at a resolution of $\sim 15''$ from Hummel et al. (1985) shows an elongation along a P.A. of 160°, emanating from a core, but the follow up survey at lower resolution, $\sim 0.9'$, by Condon (1987) showed only a core with a weak elongation in the south west (P.A. $\sim 225°$), and no symmetrical counter-jet or outflow. However, Vila et al. (1990b) showed a mostly unresolved source at 1.49 GHz with the VLA in A array, but with a significant extension to the south-east and north-west along a P.A. of $\sim 135°$ and clearly larger than the beam size at 20 cm of $1\farcs5 \times 1\farcs06$. Therefore the e-MERLIN interferometer was used as part of the LeMMINGs 'deep' sample to take deeper, high-resolution data to directly image the nuclear region at 150 mas scales at 1.51 GHz. In addition, new VLA-A array data were obtained to improve the definition of the arcsecond-scale structure.

NGC 6217 is of morphological type (R'L)SB(rs)b (Sandage and Tammann, 1981; de Vaucouleurs et al., 1991; Buta et al., 2015) i.e. a barred spiral galaxy with an inner and outer (pseudo-) ring structure and with a star formation rate of $\sim 2.9\,M_\odot$ per year (James et al., 2004; Knapen and James, 2009). Different authors classify the nuclear region in NGC 6217 variably as a Seyfert 2 (Cabrera-Lavers and Garzón, 2004), H II Region (Ho et al., 1997a; Véron-Cetty and Véron, 2006) or a LINER (Nicholson et al., 1997; Falocco et al., 2017). The exact nuclear classification is important for understanding the ionisation mechanisms in the nucleus: Seyferts are ionised by an AGN, whereas H II regions are ionised through SF processes. On the other hand, LINERs are thought to be ionised by post-AGB stars, LLAGN or shocks, (**?**Halpern and Steiner, 1983; Ferland and Netzer, 1983; Terlevich and Melnick, 1985; Capetti and Baldi, 2011; Singh et al., 2013). The mass of the black hole in NGC 6217 is estimated from the M-σ relation in Chapter 2 to obtain a black hole mass of $2.0 \times 10^6 M_\odot$.

The purpose of this chapter is two-fold: to investigate the nature of the nuclear emission in NGC 6217 and to check if radio emission in the galaxy spatially is coincident with the X-ray jet suggested by PA01 and F17. I will use multi-wavelength data to ascertain the nuclear emission process and investigate the nature of the X-ray jet with SED fitting and X-ray data.

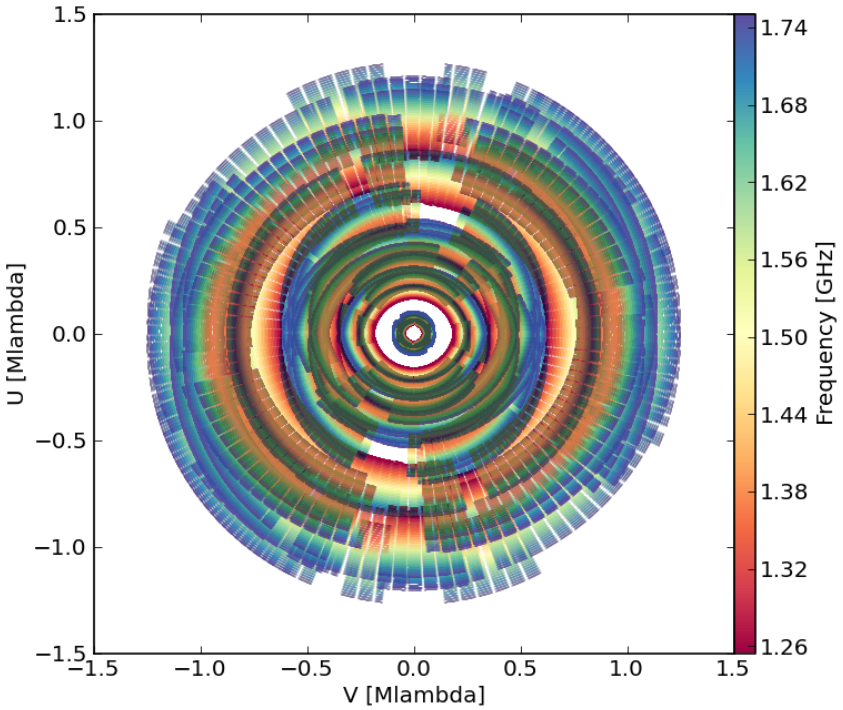

(a)

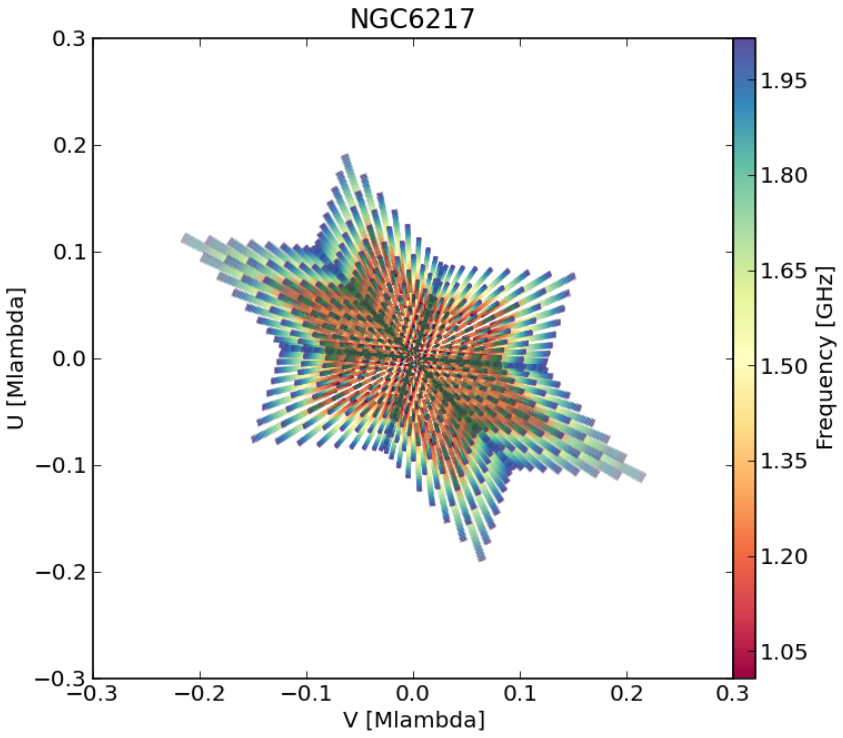

(b)

Figure 4.1: Full observed *uv*-plane of NGC 6217 at 1.51 GHz, using a) the new LeMMINGs (e-MERLIN) deep data with all 7 antennas included and b) the new VLA A-array data with all antennas.

4.2 Observations and Data Reduction

Here, I discuss the main data sources relevant to this chapter: the recently acquired full-resolution 1.51 GHz e-MERLIN and VLA data, *XMM-Newton* and other ancillary wavelength data.

4.2.1 Radio Data Reduction and Imaging

e-MERLIN

The e-MERLIN L-band (1.51 GHz) observations of NGC 6217 were obtained as part of the LeMMINGs survey (Beswick et al., 2014; Baldi et al., 2018b). The data were obtained on 7th April 2016 with all 7 antennas, including the Lovell Telescope, participating in the observing run and 21 hours on-source time. The calibrator J1723+7653 (J172359.4+765312) was used for phase referencing and OQ208 and 3C286 were used as the band pass and flux calibrators respectively. The target was observed for ∼12.5 minutes, alternating with a ∼2 minute observation of the phase calibrator. The flux and band pass calibrators were observed near the beginning of the run. The *uv*-plane coverage of e-MERLIN and VLA data made with the CASA e-MERLIN pipeline[1] is shown in Fig 4.1. The data calibration procedure presented in Chapter 2 was used to flag, calibrate and image the e-MERLIN data. The final image was created when the noise in the image reached 7μJy. While initial images were made in AIPS, further image making was processed in CASA (McMullin et al., 2007).

VLA-A Array data

NGC 6217 was observed with the VLA in A configuration on 16th December 2016 for 4.3 minutes centred at 1.51 GHz (L band) over a bandwidth of 1.024 GHz in 16 spectral windows of 64 MHz, each with 64 channels. Standard VLA flagging and calibration routines were performed using version 4.7 of the VLA pipeline in CASA 4.7[2]. The pipeline products were reviewed and additional RFI excision was made where necessary. Due to excessive RFI contamination, spectral window 8 was flagged and removed before the final image making procedures. The resulting image achieved an rms of 53μJy/beam.

The VLA data were imaged in CASA using `clean`, first with a large field to help identify the bright sources in the field and then with smaller fields to remove the effects of these contaminating sources of emission from the NGC 6217 image. The data were naturally weighted to ensure good signal to noise.

[1] https://github.com/e-merlin/CASAe-MERLINpipeline/wiki
[2] https://science.nrao.edu/facilities/vla/data-processing/pipeline

Table 4.1: Radio datasets of NGC 6217 at different frequencies with different arrays used in this paper. The e-MERLIN and VLA-A Array datasets observed in 2016 were made as part of the LeMMINGs 'deep' sample.

Data	e-MERLIN	VLA
Obs. Date (yyyy-mm-dd)	2016-04-07	2016-12-16
Central Frequency (GHz)	1.51	1.51
Bandwidth (GHz)	0.512	1.024
Time on Source	21 hours	4.3 mins
Beam size ($'' \times ''$)	0.15×0.15	1.33×0.84
Noise level (μJy/beam)	7	53

Data combination

After the data were calibrated, I exported the e-MERLIN and VLA datasets to CASA and combined them. First, both datasets were re-weighted using the CASA task `statwt` to re-weight each individual visibility by its rms value. Following this step, both datasets were combined and imaged with `tclean` in CASA with clean boxes specified around the core and all radio sources identified from the e-MERLIN and VLA images and a Briggs weighting scheme (`robust = 0`) to image both the compact and diffuse structure. I attempted cleaning with different values of the `multiscale` parameter and the robustness in the Briggs parameter and found the default values of `robust = 0` and `multiscale = [0,5,10]` to give the best compromise between diffuse structure and compact, point-like sources. To properly sample the hybrid point spread function (PSF) of the combined e-MERLIN and VLA data, I oversampled the beam by a factor of sixteen (Jack Radcliffe, priv comm). This approach means the correct hybrid PSF can be calculated, which can then be used as the `bmaj`, `bmin` and `bpa` parameters in `tclean`. I could then image with standard Nyquist sampling while correctly fitting the hybrid PSF.

4.2.2 XMM-Newton Data Reduction

The *XMM-Newton* X-ray data were originally published in F17 and I refer to that paper for details. I do not fit the data that falls on the edges of the chips, for the core and all the knots which is presented in Table 4.2. The data reduction was performed using the standard reduction procedures with version 15 of the Science Analysis System (SAS)[3]. To produce an X-ray image, I aligned and stacked the MOS1, MOS2 and PN event files from all datasets using the task `evselect` to choose the spectral windows and combined all the epochs and instruments with the FTOOLS task `XSELECT`. As other optical data are available at better than the $4''$ angular resolution of the optical monitor (OM), I did not reduce the OM data for these *XMM* observations (see Section 4.2.3). Due to low count rates on this galaxy, I did not analyse the RGS data.

[3]https://www.cosmos.esa.int/web/xmm-newton/what-is-sas

Table 4.2: *XMM-Newton* datasets on NGC 6217 from the HEASARC archive relevant to this chapter. The observation ID, observation date, instruments available in each observation, exposure time and P.I. of each observation. Notes: [a] The PN was turned off for this observation, [b] The source fell on the edge of the chip for MOS1, [c] The source fell on the edge of the chip for PN. I refer to the data observed on 2007 February 15 as 2007a, and those observed on the 2007 February 17 as 2007b throughout the rest of this work.

Obs. ID	Obs. Date	Exposure	Available Instruments			
	dd-mm-yyyy	ks	Core	Knot 1	Knot 2	Knot 3
0061940301	20-09-2001	6.1	MOS2[a,b]	MOS1+2[a]	MOS1+2[a]	MOS1+2[a]
0061940901	11-04-2002	9.7	MOS1+2/PN	MOS1+2/PN	MOS1+2[c]	MOS1+2[c]
0400920101	15-02-2007	40.4	MOS1+2/PN	MOS1+2[c]	MOS1+2/PN	MOS1+2/PN
0400920201	17-02-2007	38.9	MOS1+2/PN	MOS1+2[c]	MOS1+2/PN	MOS1+2[c]

Table 4.3: X-ray source positions in NGC 6217, updated from F17, including the 3σ uncertainty from our surface brightness profile fits (4), and the offset of the positions from those in F17 (5).

Object	RA	Dec	Err.″	Δ″
(1)	(2)	(3)	(4)	(5)
Core	$16^h32^m38.65^s$	+78°11′53.8″	1.78	2.74
Knot 1	$16^h32^m24.21^s$	+78°11′12.0″	5.47	7.28
Knot 2	$16^h32^m11.37^s$	+78°10′28.1″	4.46	6.74
Knot 3	$16^h32^m01.93^s$	+78°09′57.5″	5.53	6.35

Spectral Analysis of the core and X-ray knots

For each X-ray source reported in F17, Mayukh Pahari (MP) measured the surface brightness profile. MP used a slice 40″ in length and measured 1000 surface brightness profiles, chosen from a random position and orientation for each source to ensure a Gaussian distribution of positions and orientations. The mean of the distribution was measured for each source and the average profile was fit to estimate the source position as a function of RA and DEC. The errors quoted are the 3σ uncertainty of the fit profiles. This method is particularly useful for cases where the sources are elongated rather than circular. I note that in performing this surface brightness profile fitting, the positions given in F17 were offset by up to 7.3″ from the centre of the sources for all of the X-ray knots. Furthermore, none of the source positions in F17 agree within the 3σ uncertainty of our profile fitting. The lack of agreement between the positions calculated by MP and F17 is possibly due to MP's fitting method sampling all orientations and positions across each of the knots, and using a profile slice that is much longer than the PSF of the X-ray data. Furthermore, the X-ray knots are faint and extended - knot 3 is resolved into two sources - which makes ascertaining a precise position of the centroids difficult. MP and I extracted spectra from the regions centred on the knots from our measured RA and Dec, which are given in Table 4.3.

To have commensurate source extraction regions with F17, MP and I used a source extraction radius of 25″ around the nucleus and removed the background from a region of the same size from a nearby area void of sources and on the same chip. For the individual knots, we employed the same strategy but with a source region radius of 21″. MP and I found that spectral fits that agreed with one another, although the fits of MP are given in Table 4.3. I checked for pile-up with `epatplot` but found no significant contribution to the spectra over any epoch, chip or source. MP and I corrected the X-ray data for Galactic absorption in the direction of NGC 6217 of 3.90×10^{20}cm^{-2} (Kalberla et al., 2005).

4.2.3 Ancillary Data

As NGC 6217 is part of the Palomar sample (Filippenko and Sargent, 1985; Ho et al., 1995, 1997a,d,e,b,c, 2003, 2009), there exists a large amount of ancillary data in optical and infra-red surveys. With the intention of fitting the Spectral Energy Distributions (SEDs) of

all sources coincident with the galaxy nuclear and X-ray jet knot emission, Ranieri Baldi (RB) and I retrieved data from several missions from infra-red to optical: *Spitzer*, *WISE*, SDSS and *HST*. There are two observations of NGC 6217 in the *Spitzer* Heritage Archive[4] (AORKEY 30924544, 31025408, PI: K. Sheth). These data were observed at 3.6 and 4.5μm on 2009 October 27 and 2009 November 27. I downloaded the already reduced data from the S4G Survey (Sheth et al., 2010) on the NASA Extragalactic Database (NED) website[5]. I then used the software `SExtractor`[6] to extract all sources in the 3.6 and 4.5μm images above a 3σ threshold. I also downloaded the archival Wide-field Infra-red Survey Explorer (*WISE*) data from the IRSA [7] in the four bands (3.4, 4.6, 12, and 22 μm) (Wright et al., 2010) to help give better constraints on the SED fits for the core and knots at different wavelengths. The IRSA catalogue also provides the aperture photometry for our sources detected in *WISE* and *Spitzer*. I downloaded SDSS archival data from the DR12 Science Archive Server [8] in all the Johnson $ugriz$ filters. As NGC 6217 is on the edge of one of the SDSS fields, I downloaded data from two fields (fields 15 and 68) so that we could fit the entire extent of the galaxy, including the putative X-ray jet. I also obtained high-resolution *HST* images of NGC 6217 from the public Hubble Legacy Archive (HLA[9]). I downloaded the HST ACS F814W, F625W and F435W images (PI: Siranni) taken on the 2009 June 13 and 2009 July 8 to create a three-colour image for reference with regards to the other ancillary data. This colour image is shown with the overlaid contours of the ancillary data and radio images inset in Figure. 4.2. The Hα image was taken with the HST ACS, through its F658N filter, and reduced as part of the preparatory work for the paper of Comerón et al. (2010). For continuum subtraction an ACS F814W broad-band image was used, following procedures in Knapen et al. (2004), Sánchez-Gallego et al. (2012) and Dullo et al. (2016).

4.3 Data Analysis

Figure 4.2 shows all of the ancillary data overlaid on the three colour *HST* image (see the figure caption for an explanation of the contours and sources in different bands). Three X-ray sources appear to spatially align at a P.A. of ~225° from the X-ray source at the centre of NGC 6217. While knots 1 and 2 show more compact X-ray emission, knot 3 reveals a more diffuse two-sided X-ray brightness which makes harder the identification of multi-band counterparts.

I searched for possible radio (e-MERLIN and VLA) and IR (*Spitzer*) identification of the knots within the X-ray extraction regions (yellow dashed circles in Figure 4.2). The putative X-ray jet shows no evident radio components from the VLA A-Array and e-MERLIN images. However a single compact source is detected at a position of $16^{h}32^{m}16.99^{s}$,

[4]http://sha.ipac.caltech.edu/applications/Spitzer/SHA/
[5]https://ned.ipac.caltech.edu/
[6]https://www.astromatic.net/software/sextractor
[7]http://irsa.ipac.caltech.edu/frontpage/
[8]https://dr12.sdss.org/fields
[9]http://hla.stsci.edu

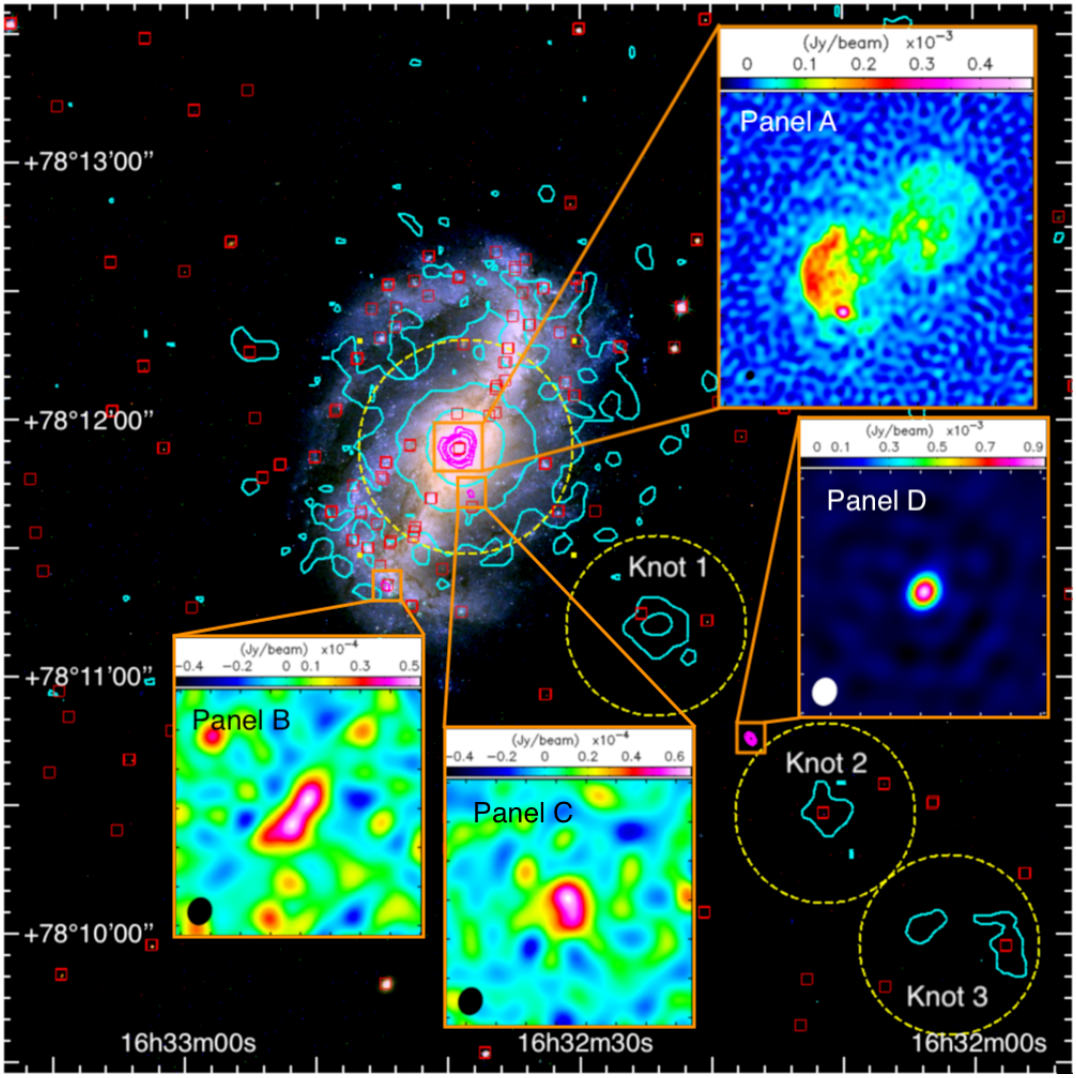

Figure 4.2: Multi-wavelength image of NGC 6217 and the putative 160 kpc X-ray jet from F17, including insets of the nuclear region and 3 other sources detected with the combined VLA A-array and e-MERLIN data. The background image utilises *HST* F814W (red), F625W (green) and F435W (blue) images to create a three-colour image of NGC 6217. All three filters are weighted evenly on a linear scale. The cyan colours represent the 7, 12 and 30 count levels of the 0.3-2.0keV *XMM-Newton* image, was smoothed with a Gaussian filter of radius 2″.The yellow dashed circles correspond to the *XMM-Newton* data spectral extraction regions for the nucleus, and all the X-ray knots from the updated values in Table 4.3, with radius the same from F17 and in this paper: 25″ for the nucleus and 21″ for each of the knots. The magenta contours show the VLA A-Array data at 0.25, 0.5, 1.0 and 5.0 mJy/beam. The red squares denote 3σ detections of sources with the archival 3.6 and 4.5 micron *Spitzer* data. The inset images show the combined e-MERLIN/VLA data of interesting regions, complete with colour bar for intensity scale. Panel A (top right) shows the nuclear region of NGC 6217, panel B (bottom left) shows a compact region in the spiral arm of NGC 6217 south-east of the core, panel C (bottom centre) is a zoom-in of a small region of radio emission in the galaxy bulge slightly south of the core and panel D shows a discrete radio source between the X-ray knots 1 and 2, south-west of the core. These panels are shown in contour plots in further detail in Figure 4.3. The main figure corresponds to a scale of $4' \times 4'$ (25 kpc × 25 kpc), while the scales of each of the inset images are shown in the Figure 4.3 (for panels A − D respectively). Note the size of the inset squares overlaid on the HST image are not to scale. In this figure and all the inset images, north is up and east is left.

+78°10′45.82″, between X-ray knots 1 and 2, specifically ∼34″ from knot 1 and ∼25″ from knot 2. Concerning the 3σ-significance *Spitzer* 3.6 and/or a 4.5μm sources, one or two IR counterparts were detected for each knot within the 21″ X-ray extraction regions. For knots 1 and 2, I only consider the nearest IR source (<5″) to the centroid of the X-ray knot as a possible identification. For knot 3, one *Spitzer* source lies on one of two distinct components of the X-ray knot (with a separation larger than *XMM-Newton* resolution, see details in Sec. 4.3.2). This IR identification is of course much weaker than the other two X-ray knots.

I also show other sources of radio emission in the inset boxes in Figure 4.2, hereafter called secondary sources, with the combined e-MERLIN and VLA data. Inset panel A shows the nuclear region, inset panel B shows a small source south-east of the nucleus on the spiral arm of NGC 6217, inset panel C shows a region of radio emission south of the core and in the bulge of the galaxy, and panel D shows the source along the same P.A. as the putative X-ray jet mentioned previously, hereafter known as component R for SED fitting purposes (see Sec. 4.3.2).

4.3.1 The new e-MERLIN and VLA Data

Radio Morphology of the nucleus

The upper left panel of Fig. 4.3 shows the $10 \times 10''^2$ nuclear region of NGC 6217 for the combined 1.51 GHz e-MERLIN and VLA A-Array data, hereafter referred to as the 'combined' data, with 'Briggs' weighting to show both the diffuse emission provided by the VLA and the compact core regions that e-MERLIN is sensitive to. The combined image shows a two-sided radio structure (P.A.∼ 135°) akin to a 'peanut', with no apparent core at the centre of this structure. Resolving structures such as this is only possible with the e-MERLIN interferometer with its unique combination of sub-arcsec and sub-mJy imaging.

The south-eastern lobe-like structure in the combined image is clearly brighter than the north-western one, with an integrated flux density of 18.74±0.24 mJy compared to 11.60±0.22 mJy. There is a hot-spot at $16^h32^m39.39^s$, +78°11′52.6″. North of this bright point of emission is a bending arc of radio emission extending ∼1.5″ north and slightly west. The hot spot in the southern lobe is clearly the brightest source of radio emission in the nuclear region, but it is offset from the nucleus and of similar size to the beam (0.″20 × 0.″14 mas, deconvolved from the beam). It has an integrated flux density of 1.16±0.12 mJy and peak flux density of 0.451±0.034mJy/beam. Therefore, it makes up only ∼5 per cent of the total flux density of this region when compared with the VLA. The north-western region of emission appears clumpy and not well defined by any one structure.

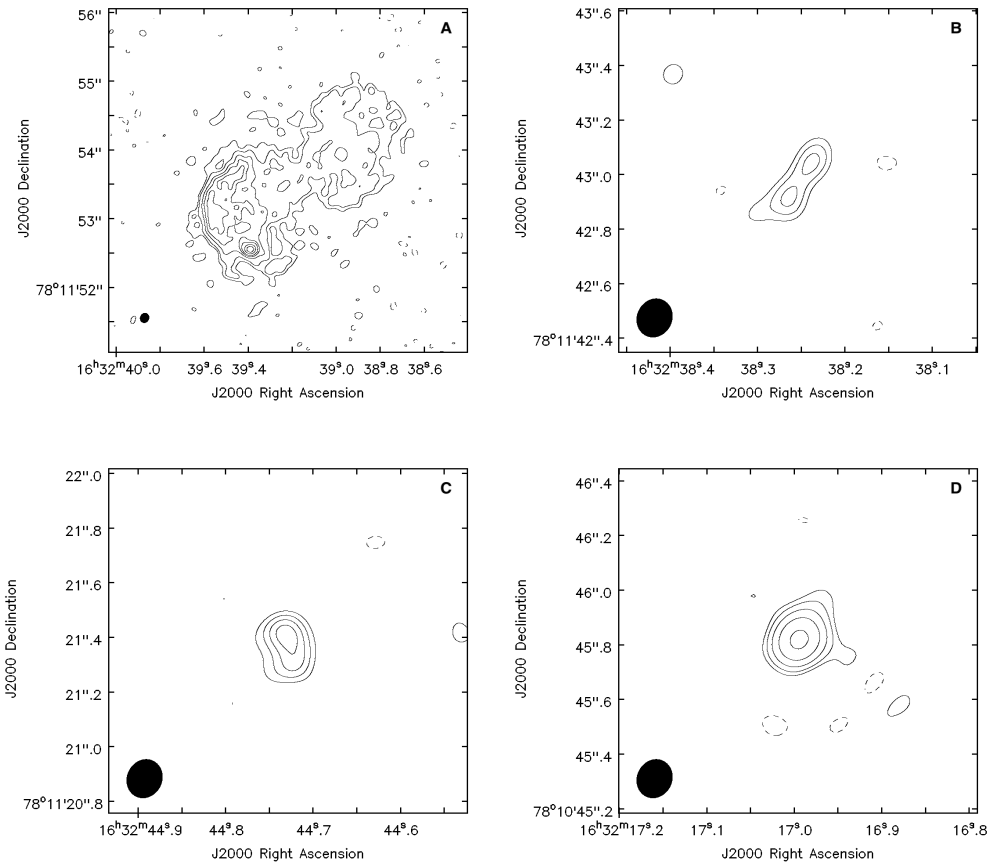

Figure 4.3: Combined e-MERLIN/VLA A-Array, Briggs-weighted contour images of the sources detected with the VLA. The letters in the top-right of each panel correspond to the panels in Fig. 4.2. The top left is the central 5 $''$ × 5 $''$, corresponding to 485 × 485 pc, nuclear region in NGC 6217, as previously shown in panel A of Fig. 4.2. The combined beam (0.$''$14 × 0.$''$12) is shown in the bottom left hand corner as a filled black circle. The contour scale is -20, 30, 50, 100, 150, 200, 300, 400, 500 × 10^{-6}Jy beam^{-1}. The top right image is the radio source south-east of the nuclear core of NGC 6217, showing a region 1.$''$2 × 1.$''$2, corresponding to 116 × 116 pc, shown previously in panel B of Fig. 4.2. The beam is 0.$''$14 × 0.$''$12 and the contour scale is -20, 30, 40, 50 × 10^{-6}Jy beam^{-1}. The bottom left image is the radio source directly south of the nuclear core of NGC 6217, shown in panel C of Fig. 4.2. The beam (0.$''$14 × 0.$''$12) and the contour scale is -20, 30, 40, 50, 60 × 10^{-6}Jy beam^{-1}. The bottom right image is the radio source south-east of the nuclear core of NGC 6217 and in between X-ray knots 1 and 2, shown in panel D of Fig. 4.2. The contour scale is -50, 50, 100, 200, 400, 800 × 10^{-6}Jy beam^{-1} and the beam size is 0.$''$14 × 0.$''$12. In all contour plots, north is up and east is to the left.

Radio Morphologies of the secondary sources

The combined e-MERLIN/VLA images show 3 radio sources in the environs of NGC 6217. First, there is radio emission in the VLA-only and combined images at $16^{h}32^{m}38.30^{s}$, $+78°11'42.9''$ in the spiral arms, seen in inset panel B of Fig. 4.2 and the top right panel in Fig. 4.3. It has a slightly resolved two-lobed structure. The VLA-only data shows a mostly unresolved source, with flux densities of 0.317±0.041 mJy/beam (peak) and 0.597±0.114 mJy (integrated). This source has a 3σ *Spitzer* counterpart.

The second source (inset panel C in Fig. 4.2 and the bottom left panel in Fig. 4.3) observed is in projection within the main galactic bulge, only ∼0.5′ south of the nucleus ($16^{h}32^{m}44.73^{s}$, $+78°11'21.4''$). It appears as a compact source in the VLA-only and combined images, with a possible small extension east, although given the beam-size and resolution, it is consistent with being an unresolved source. It also has low VLA flux densities of 0.556±0.044 mJy/beam (peak) and 0.501±0.074 mJy (integrated).

Interestingly, there is a prominent unresolved source of radio emission at $16^{h}32^{m}16.99^{s}$, $+78°10'45.82''$, along the same P.A. as the putative X-ray jet between knots 1 and 2 of the X-ray emission (see panel D of Fig. 4.2 and bottom right panel in Fig. 4.3). The VLA integrated flux density of this source is 1.34±0.16 mJy, which compares to 0.974±0.036 mJy with e-MERLIN. This source was not detected above the 3σ threshold by the SExtractor procedure, but a weak *Spitzer* counterpart is clearly visible in the image (see Section 4.3.2).

Radio Properties and Spectra

The nuclear region appears resolved in the combined data, hence it is possible that the diffuse emission is resolved out reducing the flux level, as e-MERLIN is not sensitive to those scales. Table 4.4 shows the flux densities for the core and all of the other radio sources found in the e-MERLIN-only and VLA-only data shown in Fig 4.2. I additionally compare the nuclear region to the NVSS values of NGC 6217 to fully consider any diffuse emission in the galaxy. From the NVSS and VLA data, I conclude that ∼50% of the total emission was lost moving to the longer baseline array. There is a similar drop when comparing the VLA to the e-MERLIN data. Hence, there is diffuse emission that e-MERLIN alone cannot account for in this nuclear region.

As for the three discrete sources of radio emission seen in the VLA images other than the nuclear region, the two sources in panel B and C in Fig. 4.2 seem to significantly resolve out flux when the e-MERLIN-only (or combined) data is compared to the VLA-only data. For these two sources, e-MERLIN only captures ∼40% of the total flux for these regions seen in the VLA-A array data. Hence, the diffuse elongations seen by the combined e-MERLIN/VLA data may in fact be real for these sources. For the third source in panel D in Fig. 4.2, e-MERLIN data reproduces over 80% of the total flux density of this source when compared to the VLA data, indicating it is likely a very compact source.

Table 4.4: Radio flux densities of the core region (panel A in Fig. 4.2) and all three secondary sources in the inset panels of Fig. 4.2. All values were obtained from Briggs weighted data, and were made using the CASA 2D fitter where possible, whereas the e-MERLIN integrated flux densities for the core and the individual lobes were obtained using `TVSTAT` in AIPS due to their being extended in nature. The peak flux density of the core region in the e-MERLIN data was not estimated as it is a resolved source and no radio core is observed between the two e-MERLIN radio lobes. The integrated flux for the entire nuclear region was extrapolated from all of the emission from both the lobes, as the lobes are resolved at e-MERLIN and e-MERLIN/VLA baselines. The e-MERLIN data did not detect the sources in panel B and C alone, hence they have no flux values given, but must be less than 3 times the noise in the image (0.02mJy). The columns are presented as follows: (1) is the radio source, (2) is the radio array used, (3) is the integrated flux density from the whole source in the given array, (4) is the peak flux density from the source.

Radio Source (1)	Radio Array (2)	Int. Flux (mJy) (3)	Peak Flux (mJy/beam) (4)
Total	NVSS	80.3±2.4	57.8±1.1
Northern Lobe	VLA	-	-
	e-MERLIN	11.60±0.22	0.146±0.003
Southern Lobe	VLA	-	-
	e-MERLIN	18.74±0.24	0.205±0.003
Southern Hot-spot	VLA	-	-
	e-MERLIN	1.16±0.12	0.451±0.034
Nuclear Structure	VLA	40.4±3.2	7.28±0.50
	e-MERLIN	29.84±0.16	-
Source in Panel B	VLA	0.597±0.114	0.317±0.041
	e-MERLIN	-	-
Source in Panel C	VLA	0.501±0.074	0.556±0.044
	e-MERLIN	-	-
Source in Panel D	VLA	1.34±0.16	1.297±0.088
	e-MERLIN	0.974±0.036	0.955±0.020

I checked for any variability in the core between the Vila et al. (1990b) observations and the new VLA-A array data. The flux densities of the new VLA A-array data and of Vila et al. (1990b) agree within errors, indicating that there has likely been no significant change over the period of nearly 30 years.

Due to the low signal for the nuclear region, it was not possible to make an in-band spectral index image from the 1.51 GHz e-MERLIN observations. However, using the VLA data at 1.51 GHz, I was able to get a crude in-band spectral index using CASA and by setting `nterms = 2`. I estimate a flat spectral index of -0.2 ($S_\nu \sim \nu^\alpha$), although the uncertainties in this value are likely of order ± 0.5, as NGC 6217 is not bright enough in the VLA data to properly constrain α. I note that Vila et al. (1990b) estimate a compact nuclear spectral index of -1.0 based on archival VLA data at 20 cm and 6 cm, albeit with a larger beam size.

4.3.2 Spectral Energy Distributions

RB and I carried out multi-band counterpart identification of the X-ray knots and the VLA-detected radio source, using SDSS *ugriz* bands, the 3 *HST* ACS bands (F435W, F625W, and F814W), *Spitzer* 3.6 and 4.5μm data and the 4 *WISE* bands. RB performed aperture photometry on an area which includes the FWHM of the PSF for each instrument, properly centred on the position of the detected *Spitzer* sources, isolating the genuine emission of the counterparts and subtracting the background emission. The extracted magnitudes of the detected sources are consistent with the values reported in the IRSA catalogue within the uncertainties. For the sources not detected, RB derived 3σ upper limits on the multi-band counterpart. The optical-IR magnitudes for our sources are presented in Table 4.5.

RB built up the optical-IR SEDs for the knots by collecting multi-band photometry from the SDSS *u*-band to *WISE* 22μm band, using fourteen photometric points. RB did not include the radio and X-ray data-points in the SEDs because these data would not help to constrain the photo-z. In fact, the optical/radio, optical/X-ray, radio/X-ray spectral indices are largely degenerate with the possible classifications, from being radio-quiet/loud active galaxies (Seyferts and LINERs) to inactive star forming and passive galaxies (e.g., Kellermann et al., 1989; Elvis et al., 1994; Terashima and Wilson, 2003; Ho, 2008; Kandalyan and Al-Naimiy, 2002; Blumenthal et al., 1982; Padovani et al., 2003). Conversely, the optical-IR part of the SED includes prominent features (the 4000Å break, the spectral rise in the blue band for the big blue bump or a young stellar population, the spectral cut-off in the near-IR band for old stellar population), which are unique spectral markers that are useful for ascertaining the photometric redshifts.

RB fit the SEDs with the *2SPD* code developed by Baldi et al. (2013b) and Baldi et al. (2014). This code allows for the inclusion of two different stellar populations, typically one younger and one older (YSP and OSP, respectively) which correspond to different starburst ages, a dust component with a single (or two) temperature black-body emission(s), AGN

Table 4.5: The multi-band magnitudes and fluxes of the sources found coincident with the three X-ray knots and the radio knot (Panel D of Fig. 4.2). The positions of the *Spitzer* sources are given, as well as the difference in position, Δ, which was calculated from the difference of the *Spitzer* source position to the X-ray knot centroid from our analysis in Table 4.3. The SDSS, *HST* and *WISE* values are given in AB magnitudes and the IRAC data are given in mJy. The photometric redshift and corresponding bolometric luminosities are given for all of the sources, ascertained from the *2SPD* fitting code of Baldi et al. (2013b) and Baldi et al. (2014). The Photon Index, Γ, and the corresponding fluxes and luminosities of each of the X-ray knots is also given, found from the X-ray spectral fitting process in Section 4.3.3. We show the X-ray luminosities given the distance to NGC 6217 (see Section 4.1) and the photometric redshifts ascertained from the SED fits. The errors on the X-ray luminosities include only the uncertainties in the fluxes, and not the distance.

	A	B	C	R
Associated X-ray knot	1	2	3	-
RA	$16^h32^m25.32^s$	$16^h32^m11.49^s$	$16^h31^m57.66^s$	$16^h32^m16.99^s$
DEC	+78°11′15.1″	+78°10′28.4″	+78°09′57.0″	+78°10′45.8″
Δ	4.62″	0.48″	13.15″	-
SDSS *u*	<22.15	22.27±0.37	21.93±0.24	<22.20
SDSS *g*	<22.20	20.43±0.03	22.00±0.10	<22.30
SDSS *r*	<22.40	21.91±0.14	21.65±0.11	<22.20
SDSS *i*	<21.40	21.71±0.17	21.32±0.11	<21.20
SDSS *z*	<21.45	20.55±0.25	21.35±0.42	<21.60
HST F425W	–	21.32±0.15	22.10±0.13	< 22.71
HST F625W	–	21.19±0.14	21.55±0.15	< 22.21
HST F814W	–	21.58±0.14	–	<22.42
WISE W1	16.02±0.30	17.42±0.09	17.30±0.07	18.03±0.18
WISE W2	16.01±0.20	16.18±0.10	17.13±0.22	17.73±0.48
WISE W3	<12.28	12.50±0.27	<12.96	<13.20
WISE W4	<8.19	9.02±0.29	<9.40	<9.65
IRAC 1	55.10±8.72	39.34±4.91	29.35±5.35	19.00±6.80
IRAC 2	58.45±7.25	51.57±4.23	31.11±4.40	22.56±7.34
z_{phot}	$0.48^{+0.25}_{-0.12}$	$0.70^{+0.03}_{-0.02}$	$0.46^{+0.19}_{-0.06}$	$0.19^{+0.25}_{-0.12}$
L_{bol}, erg s^{-1}	7.9×10^{43}	8.3×10^{43}	9.3×10^{43}	4.6×10^{42}
Photon Index, Γ	$1.59^{+0.27}_{-0.25}$	$1.38^{+0.45}_{-0.37}$	$1.54^{+0.54}_{-0.46}$	-
Total Flux 0.3-10 keV ($\times10^{-14}$ erg s^{-1} cm^{-2})	$6.92^{+2.20}_{-1.67}$	$4.37^{+3.58}_{-2.46}$	$4.27^{+3.32}_{-2.08}$	-
Unabs. Flux 0.3-10 keV ($\times10^{-14}$ erg s^{-1} cm^{-2})	$8.13^{+2.34}_{-1.96}$	$4.79^{+3.73}_{-2.65}$	$4.90^{+3.42}_{-2.33}$	-
$L_{X-ray,Unabs}$ at NGC 6217 ($\times10^{39}$ erg s^{-1})	$3.93^{+1.13}_{-0.95}$	$2.32^{+1.80}_{-1.29}$	$2.37^{+1.65}_{-1.13}$	-
$L_{X-ray,Unabs}$ at photo-z ($\times10^{43}$ erg s^{-1})	$7.58^{+2.18}_{-1.83}$	$17.33^{+13.51}_{-9.58}$	$4.13^{+2.88}_{-1.96}$	-

spectrum with emission lines. The code searches for the best match between the sum of the different models and the photometric points minimising the appropriate χ^2 function (see Baldi et al. 2013b for details). The main parameters which *2SPD* returns are the photometric redshift and the bolometric luminosity of the source. To estimate the uncertainties on the photo-z and mass derivations, RB measured the 99% confidence solutions for these quantities.

The synthetic stellar templates used to model the observed SEDs are from Bruzual and Charlot (2011), with single stellar populations with ages ranging from 1 Myr to 12.5 Gyr. RB adopted a dust-screen model for the extinction normalised with the free parameter A_V, and the (Calzetti et al., 2000) extinction law. The emission lines are taken from the AGN atlas covering the ultraviolet to near-infrared spectral range from Seyfert/QSO templates[10] (Francis et al., 1991).

RB ran the *2SPD* fitting code for different sources: X-ray knot 1 associated with *Spitzer* source A, X-ray knot 2 associated with *Spitzer* source B, X-ray knot 3 associated with *Spitzer* source C, and then the VLA radio component with *Spitzer* source R. The results from the SED-fitting procedure are found in Table 4.5. RB did not perform SED fitting for the radio sources in panels B and C in Fig. 4.2 as the multi-band contamination from the host galaxy NGC 6217 is significant, preventing an accurate extraction of the genuine emission from those sources.

X-ray Knot 1 has two *Spitzer* components within the X-ray spectral extraction region, however RB only performed an SED fit for the source (A) at $16^{\rm h}32^{\rm m}25.32^{\rm s}$, $+78^\circ11'15.1''$, which is consistent with the the X-ray knot centroid within the position errors. It is detected only in IRAC bands 1 and 2 (3.5 and 4.5μm), and *WISE* 1 and 2 bands (3.4 and 4.6μm). In addition, there are two detected *HST* sources 1.2″ and 2.5″ away from this *Spitzer* source, but they are not detected in the SDSS. As it is not certain whether and which of the two HST sources are genuinely related to the *Spitzer* source, they were not included in the SED fit. Using the only detections from *Spitzer* and WISE W1/W2 bands, *Spitzer* source A has an SED that is consistent with an obscured 6 Gyr old stellar population. The photometric redshift derived is $0.48^{+0.25}_{-0.12}$ and its bolometric luminosity is 7.9×10^{43} erg s^{-1}. The paucity of accurate data-points in the SED of this source makes the physical parameters derived from the fit for this source doubtful. Therefore the uncertainties on the the redshift and bolometric luminosity are likely much larger than that quoted here.

X-ray Knot 2 also has two *Spitzer* counterparts falling in the X-ray extraction region but the closest to the X-ray knot matches with the *Spitzer* position (separation <0.3″) and is named as *Spitzer* source B ($16^{\rm h}32^{\rm m}11.49^{\rm s}$, $+78^\circ10'28.4''$). It is detected in all the fourteen available photometric bands. Its SED shows a rising blue part, flat IR spectrum and interestingly the *g* and *z* band counterparts are significantly brighter than the other adjacent SDSS bands by ∼1.5 magnitudes. The only physical interpretation of those broad-band peaks is the contribution from emission lines in the band-widths of *g* and *z* bands. The

[10]http://www.stsci.edu/hst/observatory/crds/cdbs_agn.html

best-fit model of the SED includes a Seyfert/QSO-like spectrum, which is able to reproduce simultaneously the blue spectral rising and emission lines, Mg II and a Hβ, which contribute to ~70 and ~66 per cent of the total flux in the g and z band, respectively. The wavelength of the emission lines within the SDSS bands constrains the photo-z at $0.70^{+0.03}_{-0.02}$. The near- and mid-IR data are modelled by a 3-Gyr old stellar population and two-temperature black bodies. The bolometric luminosity is 8.3×10^{43} erg s^{-1}.

As mentioned previously, the shape of X-ray Knot 3 is convoluted as it is made up of two distinct X-ray components which makes the centroid difficult to determine. The western part of this knot ($16^{\rm h}31^{\rm m}57.66^{\rm s}$, $+78°09'57.0''$) aligns well with *Spitzer* source C, which is detected in all bands, except the last two *WISE* bands. The blue spectral rising has been fitted with a YSO of 0.03 Gyr and the optical and near-IR region with a OSP of 4 Gyr. The contribution from an AGN is not needed to fit the optical-IR data-points. As the blue spectral curvature is the only feature to constrain the photometric redshift, this results in a mediocre photo-z determination, corresponding to $0.46^{+0.19}_{-0.06}$. The bolometric luminosity is 9.3×10^{43} erg s^{-1}. The tentative identification of the X-ray knot with the *Spitzer* source C must be taken as a reasonable attempt to infer the multi-band properties of this X-ray knot without giving any confidence in its correctness.

RB also performed an SED fit for the radio component in the inset panel D in Figure 4.3, bottom right panel, detected with the VLA and coincident with *Spitzer* source R. Its radio emission is unresolved and lies along the putative 'X-ray jet' in NGC 6217 between knot 1 and 2. Its association with one of the two X-ray knots seems to be unlikely due to its large relative distance (>25″). This source is detected at near-infrared wavelengths (two IRAC and two *WISE* bands). The resulting SED fitting returned an obscured 4 Gyr old stellar population with a photometric redshift of $0.19^{+0.25}_{-0.12}$ and a bolometric luminosity of 4.6×10^{42} erg s^{-1}. The small number of photometric data-points reflects on a poor accuracy of its photo-z determination. Therefore the values inferred for this component must be considered with caution and are meant to provide a possible interpretation of this radio component.

4.3.3 X-ray Data analysis

X-ray spectral fits

MP and I first re-binned the spectra using the `grppha` command in FTOOLS. As there were more than 200 counts in the core spectrum, it was binned with 15 counts per bin for both 2007 datasets and we used χ^2 statistics. For all the knots in all epochs, and the 2001 and 2002 data for the core region, there were too few counts to fit with χ^2 statistics. Hence, these data were binned with 1 count in each bin and used Cash statistics (Cash, 1979) to fit them, which is more appropriate in the low-counts regime. The re-binned spectra (see Section 4.2.2) were loaded into XSPEC version 12.8.2 (**?**) and we fitted each spectrum in the energy range 0.3−10.0 keV for each epoch and CCD chip separately to ascertain whether there was any variability in any of the sources across the six years of data.

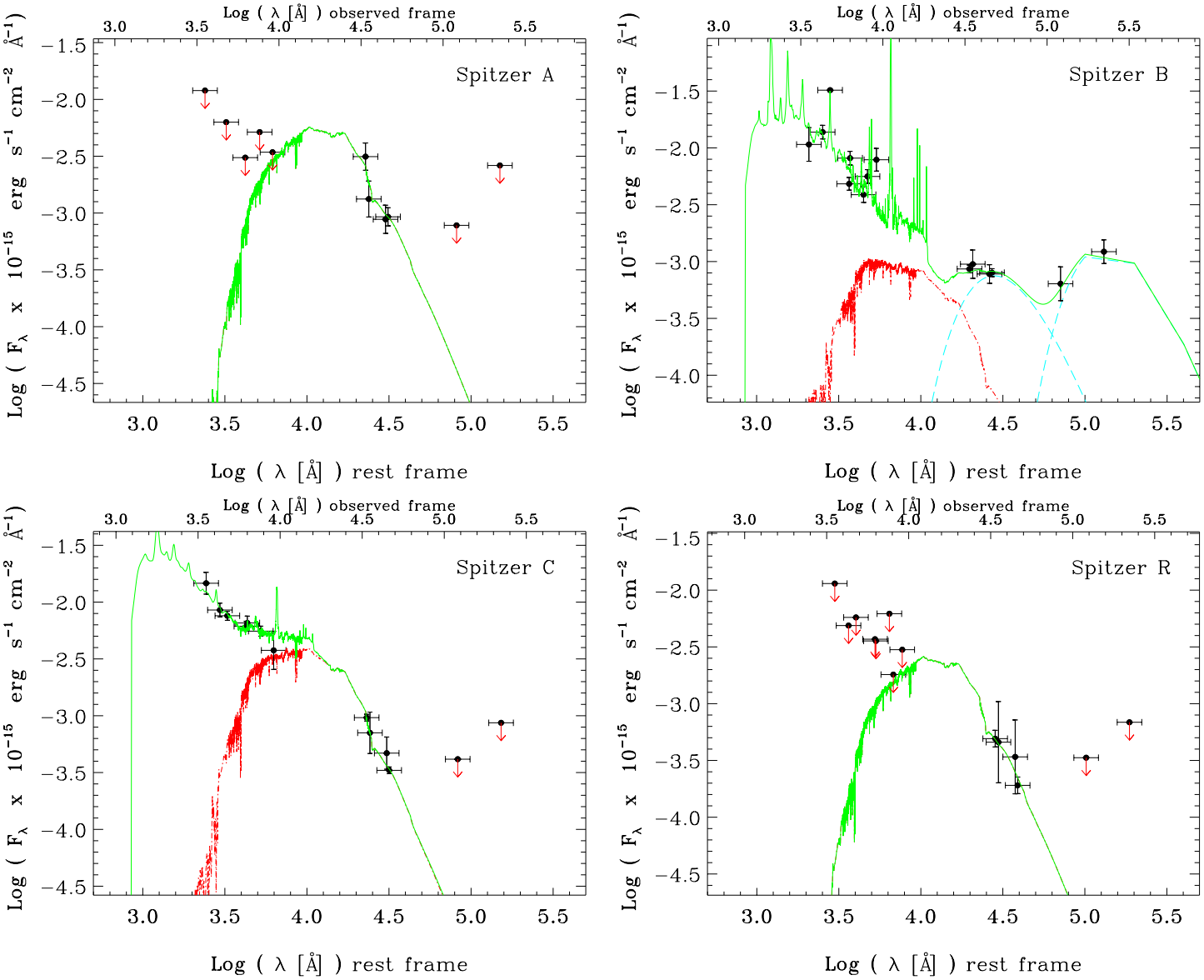

Figure 4.4: Optical-infrared SEDs of the multi-band counterparts of the sources associated with the X-ray knots (Table 4.2) and the VLA radio component. The first X-ray knot is associated with *Spitzer* source A (upper left panel), X-ray knot 2 with *Spitzer* source B (upper right panel), X-ray knot 3 with *Spitzer* source C (lower left panel), and then the radio component detected with the VLA as *Spitzer* source R (lower right panel). The photometric points are fit with the *2SPD* fitting code: the stellar population is the red (dot-dashed) line, the dust Black-body components are the light-blue (dashed) lines and the total model is the green solid line, which also can include the emission line template. For all the panels, the wavelengths on the top of the plots correspond to observed wavelengths, while those on the bottom are in the rest frame.

F17 combine their different epoch/CCD images before extracting a spectrum, creating 4 spectra: one PN spectrum from 2002, one spectrum from the merged 2001 and 2002 data from the MOS detectors, one merged PN spectrum from the two 2007 datasets and one merged spectrum from the 2007 observations. We chose to fit each of the four epochs (2001, 2002, 2007a, 2007b) separately, fitting the X-ray data for each chip simultaneously due to the different responses of the PN, MOS1 and MOS2 detectors. The spectral fitting procedure that MP and I used is preferred for different epoch/CCD data to ensure that the correct response matrices are generated for each observation[11]. MP and I used a cross-calibration weighting factor in the spectral fitting process between the PN, MOS1 and MOS2 detectors. We allowed the cross-calibration constant between the instruments to take into account differences in absolute flux calibration and as such all fluxes given are relative to the PN detector. We fit all the X-ray knots and the core with the same X-ray spectral models as F17 and compared their results with our different X-ray analysis procedure.

Nuclear region spectral fits

F17 found that the best fit model (named MEPL) was an absorbed power-law with an additional thermal component due to a collisionally ionised plasma. The best fit parameters of the MEPL model from the new X-ray spectral analysis in Table 4.6 for the 2007 datasets. The X-ray fit parameters (e.g., photon index, see Table 4.6) ascertained from the two 2007 datasets agree with one another within the uncertainties. The parameters for the 2001 and 2002 datasets also agreed with the 2007 epochs within the uncertainties, despite having much lower count rates. Therefore, the nuclear region did not vary over the four epochs. As the data for the 2001 and 2002 epochs did not have enough counts in the MOS detectors to use χ^2 statistics, we only give the values for the two 2007 datasets fit separately with the models in Table 4.6. I note that the photon index obtained in our analysis is slightly lower than that obtained in F17, although this is likely due to the wider band 0.3−10.0 keV band used for fitting.

Spectral fits for the X-ray knots

MP and I employed the same simultaneous fitting method outlined in Section 4.3.3 for all of the knots separately. We fit an absorbed powerlaw (as in F17) for the knots and we found that the parameters (photon index, Γ and power-law normalisation) agreed with one another between observations, for each knot separately. I used the redshifts obtained from Section 4.3.2 as well as the redshift for NGC 6217 (z=0.0045, d=20.1 Mpc) (Cabrera-Lavers and Garzón, 2004) for the spectral analysis of all the knots, but found no difference in the fit parameters or validity of the fits.

[11]Documentation on recommended data combination with *Chandra* can be found at http://cxc.harvard.edu/ciao/download/doc/combine.pdf

Table 4.6: Spectral fits of the nuclear region of X-ray emission in NGC 6217 for the 2007a and 2007b epochs. The models are outlined in Section 4.3.3. Γ refers to the photon index of a power law fit, with a respective normalisation of the photon index "Photon Index, norm". kT and norm refer to the temperature and normalisation of the thermal component (e.g. *apec*)The reduced χ^2 statistic (χ^2/d.o.f.) is given for the core, where there are sufficient counts to model the data. The total flux was calculated using the XSPEC `flux` command, and is given for all models and datasets in the 0.3-10.0 and 2.0-10.0 keV energy ranges, as well as those corrected for absorption. All fluxes are given in the units of erg cm^{-2} s^{-1}. All errors are to 90% confidence level.

Param.	Model 1 (2007a)	Model 1 (2007b)
(1)	(2)	(3)
Constant (MOS 1)	$1.08^{+0.41}_{-0.33}$	$1.01^{+0.12}_{-0.11}$
Constant (MOS 2)	$1.39^{+0.51}_{-0.42}$	$1.04^{+0.13}_{-0.12}$
Photon Index, Γ	$2.32^{+0.21}_{-0.21}$	$2.41^{+0.21}_{-0.20}$
Photon Index, norm.	$2.05^{+0.45}_{-0.45}\times10^{-05}$	$2.16^{+0.37}_{-0.37}\times10^{-05}$
kT, keV	$0.80^{+0.04}_{-0.04}$	$0.76^{+0.04}_{-0.04}$
norm	$3.33^{+0.33}_{-0.33}\times10^{-05}$	$4.02^{+0.40}_{-0.39}\times10^{-05}$
Reduced χ^2	1.126	0.9162
Total Flux 0.3-10 keV	2.05×10^{-13}	2.01×10^{-13}
Unabs. Flux 0.3-10 keV	2.24×10^{-13}	2.38×10^{-13}

Although the spectral fits agree with F17 to within the uncertainties, the errors on the fit parameters are large, especially in the 2001/2002 datasets, mainly due to the low number of photons. In addition, I note that for knots 1, 2 and 3, the photon index values for the 2007 data ($1.59^{+0.27}_{-0.25}$, $1.38^{+0.45}_{-0.37}$ and $1.54^{+0.54}_{-0.46}$ respectively) agree within the uncertainties to the values found in F17, but the absolute values are slightly smaller than those in F17 (1.74, 1.71 and 1.70 for each knot respectively). I attribute this discrepancy to the different spectral extraction methods and fitting with a wider spectral energy range in our procedure. However, I did not attempt to combine all of the data into one dataset for each knot, nor did I attempt a fit of all epoch data for all knots as the photon statistics for each knot is so poor that any approach might turn in similar fit results because of the large uncertainties.

If the sources are assumed to be at the same distance as NGC 6217, the unabsorbed X-ray luminosities in the 0.3-10.0 keV energy band for knots 1, 2 and 3 are $3.93^{+1.13}_{-0.95}\times10^{39}$, $2.32^{+1.80}_{-1.29}\times10^{39}$ and $2.37^{+1.65}_{-1.13}\times10^{39}$ erg s^{-1} respectively. However, if the distances found in Section 4.3.2 are considered, I arrive at values of $7.58^{+2.18}_{-1.83}\times10^{43}$, $1.73^{+1.35}_{-0.96}\times10^{44}$ and $4.13^{+2.88}_{-1.96}\times10^{43}$ erg s^{-1} for knots 1 to 3, respectively.

4.4 Discussion

4.4.1 The nuclear region of NGC 6217

As noted previously, the optical classification of the nucleus is debated in the literature (see Section 4.1) whether its optical spectrum is dominated by an AGN or SF. I investigate two main possibilities: twin-lobed radio emission caused by a LLAGN or a compact star forming region in the centre of NGC 6217. I also consider whether a combination of both LLAGN activity and SF can explain the observed multi-wavelength emission.

A LLAGN origin

As explained in Section 4.3.1, there are two radio lobe-like structures extending $\sim 3''$ north-west and south-east of the optical nucleus. Furthermore, the southern lobe-like feature is more prominent than the northern one, with complex structures and a bright hot-spot. No core has been detected in the radio images. Morphologically, the twin-lobed radio structure of NGC 6217 is similar to an expanding radio cocoon, consistent with compact steep spectrum (CSS) or gigahertz-peaked (GPS) sources (Orienti, 2016). However, CSS and GPS sources typically show two bright hotspots but only one hotspot is observed in NGC 6217.

The radio structures do not unambiguously match with the line emitting region in the Hα *Hubble* image. However, assuming an astrometric error of $0\farcs3$ of the *Hubble* image, I note there exists a small faint region of Hα emission, approximately located at the centre of the total radio structure. This optical center likely corresponds to the centre of the galaxy and the location of the AGN.

By considering the radio and X-ray properties of NGC 6217, I discuss whether a LLAGN is present at the center of the galaxy. With regard to the X-ray spectra, the photon index (Γ=2.3) is a little higher than the range reported in the literature for typical AGN ($\Gamma \sim$ 1.5–2.1, Nandra and Pounds, 1994; Reeves and Turner, 2000; Piconcelli et al., 2005; Page et al., 2005; Ishibashi and Courvoisier, 2010), although not completely inconsistent with some of the sources reported in those publications. Furthermore, soft X-rays from the inner jet or due to a second nuclear component like an ultra-luminous X-ray source (ULX) or X-ray binary (XRB) may increase the photon index (e.g. Hardcastle et al., 2007). The shallow resolution of the X-ray data, which encompasses most of the optical extent of the galaxy, supports the hypothesis of the X-ray contribution of additional nuclear component. Regarding the radio emission, similar edge-brightened radio structures have been observed with the e-MERLIN array in nearby galaxies hosting LLAGN (see Chapter 5, Baldi et al. 2018b). In addition, the orientation of the radio lobe structures along the major axis of the galaxy strengthens the AGN scenario, since starburst super-winds tend to produce radio bubbles aligned with the minor axis (Ulvestad and Wilson, 1984; Baum et al., 1993; Colbert et al., 1996a; Kinney et al., 2000; Gallimore et al., 2006; Robitaille et al., 2007; Irwin et al.,

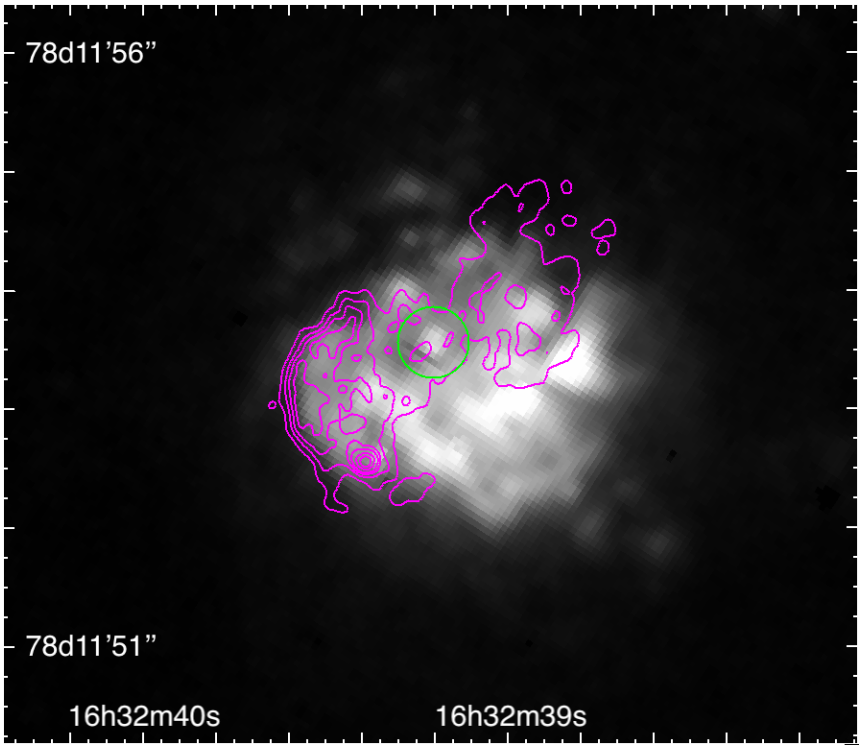

Figure 4.5: The *HST* Hα image of the central 7 $''$ × 7 $''$, corresponding to 680 × 680 pc, nuclear region in NGC 6217, overlaid with the radio contours from the combined e-MERLIN/VLA data in magenta. The radio contours are set at 50, 100, 150, 200, 300, 400, 500 × 10^{-6}Jy beam^{-1}. The green circle is centred on the hottest pixel in the Hα image and the radius corresponds to the typical *HST* offset of 0.$''$3. North is up and east is to the left.

2017). Therefore, assuming that the radio structure is powered by the central BH, two possible classes of LLAGN can be considered: LINERs and Seyferts.

LINERs typically show more core-brightened radio morphologies than NGC 6217, but several cases of parsec-scale double-lobed jetted structures associated with LINERs are present in the LeMMINGs survey. The multi-band luminosities of the nucleus lead to a LINER scenario. In fact, the comparison of [O III] line luminosity, measured from the Palomar survey, 1.78 × 10^{39} ergs s^{-1} with the 2-10 keV unabsorbed nuclear luminosity, set NGC 6217 in a region occupied mostly by LINER-like sources in the X-ray–[O III] diagram (Hardcastle et al. 2009; Torresi et al. 2018). Furthermore, the e-MERLIN radio observations yield an upper limit of the 1.51 GHz luminosity of the core of 1.91× 10^{35} ergs s^{-1}, which when compared to the L_{core} - $L_{[O\ III]}$ relation of (Baldi et al., 2018b, their Fig.6), falls in the region of the LINERs. Another argument in favour of the LINER scenario is the location of this target in fundamental plane of BH activity in the optical band (see Saikia et al., 2015, 2018) within the region covered by LINERs (Baldi et al., 2018b, their Fig.8). F17 extrapolated the NVSS flux for NGC 6217 to 151 MHz and found it consistent with a LINER based on radio, infra-red and X-ray properties (Mingo et al., 2016). In addition, F17 calculated the logarithm of the Eddington ratio for NGC 6217 as -4.09, consistent with a low-level accreting AGN such as LINERs.

Seyfert galaxies typically show large-scale AGN-driven outflows (Colbert et al., 1996a), which appear in radio as double-lobed and less diffuse than radio structures of LINERs (Baldi et al., 2018b). Similar morphologies have been observed in the Narrow Line Seyfert 1 galaxy Mrk 783 (Congiu et al., 2017), which has a similar southern edge-brightened lobe and hot spot seen in NGC 6217. There have been a number of other investigations into Seyfert nuclei showing similar pc–kpc 'bubble-like' structures, attributed either to AGN activity, SF or a combination of the two (Wilson and Ulvestad, 1983; Elmouttie et al., 1998; Kukula et al., 1999; Hota and Saikia, 2006; Kharb et al., 2006, 2010; Nyland et al., 2017; Ramírez-Olivencia et al., 2018).

Another possible scenario is a 'relic' radio source, supported by the lack of a clear core and the diffuse relaxed bubble morphology. A similar conclusion of a turned-off AGN has been drawn for Mrk 783 by Congiu et al. (2017), based on the steep-spectral index of the lobe. To explore this possibility, I calibrated archival VLBA data on NGC 6217 at 8 GHz using the AIPS VLBA pipeline `VLBARUN`. The VLBA data show no detection of NGC 6217 at the 5-sigma level (rms noise 3×10^{-4}Jy/beam). These data could either suggest that the AGN is currently inactive, or that the radio core has an inverted spectral index with a turnover frequency greater than 8 GHz, similar to that seen in NGC 7674 (Kharb et al., 2017).

A star formation origin

Fig. 4.5 shows a large amount of nuclear Hα emission but not aligned with the radio emission, possibly caused by diffuse SF. In fact, the optical *Hubble* ACS F814W image of NGC 6217 shows the presence of strong SF in the galaxy and across the spiral arms. In addition, an inner stellar ring with radius $\sim$1.3″, with a dust spiral roughly at the radius of this inner stellar ring, is present. Certainly, there is SF that is contributing to the observed multi-wavelength nuclear properties of NGC 6217. Therefore, all these features may suggest a SF related origin of the radio structure of NGC 6217 observed with e-MERLIN.

The ratios of emission lines taken from the optical spectrum provided by the Palomar survey (Ho et al., 1997a,d) ([N II], [S II], [O III] and [O I] forbidden lines and the Hα and Hβ lines) are used to diagnose the nature of gas ionisation in the so called BPT diagrams (Baldwin et al., 1981; Kewley et al., 2006; Buttiglione et al., 2010). NGC 6217 falls into the region of star forming galaxies in this diagram (see Figure C.1), consistent with Palomar survey classification (Ho et al., 1997d), despite the updated separation between AGN- and SF-dominated area in the BPT diagrams introduced by Kewley et al. (2006). However, it is worth mentioning that the Palomar optical spectra were obtained with a slit of effective aperture 2−4 ″ in size, which would include most of the SF visible in the *Hubble* image for the object. Therefore, it is also possible that a LLAGN is hidden in the very centre, but not contributing significantly to the line emission.

Parsec-scale radio bubbles have been observed in local star forming galaxies (i.e., see Chapter 5, Baldi et al. 2018b). These lobed structures can be driven by super-wind bubbles

inflated by supernovae (SNe) (Pacholczyk and Scott, 1976; Heesen et al., 2009). I computed the energy budget of the lobes assuming that they could be driven by a nuclear starburst using a similar process as described in Kharb et al. (2006) for Mrk 6, a local galaxy which a radio structure similar to NGC 6217 looks. This methodology involves computing the time for a lobe to expand to the observed physical size and comparing this to time taken for SNe to explain the observed emission, assuming adiabatic expansion. I calculated the volume of each lobe assuming the lobes are spherical with a radius (r ∼0.3 kpc). The pressure within the ISM is $\sim 10^{10}$ dynes cm^{-2} and the energy required is therefore $4PV \approx 3.2 \times 10^{53}$ ergs. Kharb et al. (2006) postulate an average SNe energy of 10^{51} ergs, which if applied here requires 3.2×10^2 SNe in this nuclear region. Assuming wind speeds of 10^3 km s^{-1}, it would take $\sim 3 \times 10^5$ years to inflate the 'bubble' to its present size, requiring a SNe rate of $\sim 1.1 \times 10^{-3}$ per year. This value for the SNe rate is similar to that calculated for M 82 for a nuclear region of a similar size to that shown here for NGC 6217 (Baldi et al., 2018b). Hence, this calculation energetically shows that the SF scenario for the radio emission of NGC 6217 is plausible.

Another argument in favour of the SF scenario is the low brightness temperature T_B observed in the NGC 6217. T_B is a metric that is often used to discriminate compact, star forming H II regions from AGN as H II regions tend to be limited to $T_B \lesssim 10^5$K (Condon, 1992). For objects above this threshold, additional emission from relativistic electrons from the AGN is required to explain the high brightness temperature. The low T_B measured for the target suggests that SF can account for the low-brightness diffuse emission detected in the eMERLIN image. However, as pointed out by Baldi et al. (2018b), since brightness temperatures depend on the flux densities and the sizes, at eMERLIN resolution and sensitivity only sources brighter than 5 mJy beam^{-1} can yield brightness temperatures greater than 10^6 K. Therefore, even considering the brightest unresolved component in NGC 6217, which is the southern hot spot with 0.45 mJy, T_B is far below the separation threshold between AGN and SF. Therefore, the low T_B cannot provide a conclusive answer to the nature of the the faint extended radio emission in NGC 6217.

A LLAGN and SF origin

Due to the large amount of contrary evidence, it is difficult to conclude with certainty whether the observed radio emission is due to SF or a LLAGN. Another possibility for the observed multi-band emission, is that both an LLAGN and SF contribute to different observed properties. This interpretation is supported by the large ongoing SF visible in the *HST* images and the radio and X-ray properties, more consistent with a phenomenon of accretion onto a supermassive BH. I conclude that the nuclear region of NGC 6217 probably contains a LINER-type LLAGN, similar to some of the H II galaxies observed in the LeMMINGs 'shallow' sample (Baldi et al., 2018b). However, the contribution from second nuclear component like X-ray binaries cannot be ruled out given the data resolution. Hence, I agree with the conclusions of F17 regarding the combined AGN and SF origin of the

nuclear emission. Higher resolution (e.g. *Chandra*) X-ray data is required to properly understand the nuclear properties of this source.

4.4.2 The putative X-ray Jet of NGC 6217

A detailed analysis of the X-ray jet in NGC 6217 is presented in F17, who consider *XMM-Newton* observations. In addition to emission from the galaxy itself, they note three X-ray emission knots in a line along a P.A. of ~225° (Fig 4.2), oriented towards the galaxy, with the most distant being ~15 kpc from the nucleus. They find no optical counterparts in the XMM-Optical Monitor (OM) images or the SDSS data for knot 1. For knot 2, F17 find one associated source, at 1.6″ away from the X-ray position in the OM *u* filter and a further source in the SDSS *r*-band at 0.9″ away, but conclude that these sources are likely unrelated stars. For knot 3, F17 found an association with an SDSS source 1.2″ away but conclude that it is likely from a passive spiral galaxy.

F17 note that radio emission from the galaxy in low resolution NVSS images shows a 2′ elongation along the line of the three X-ray components. They consider various scenarios to explain the X-ray and radio emission components, including background sources, but eventually favour a jet origin. They do however, note that higher resolution radio observations are required to confirm at least the radio extension as coming from a jet. Here, in the light of such higher resolution radio observations, I reconsider the jet origin of the radio and X-ray emission.

From the e-MERLIN and VLA observations there is clearly emission on the scale of a few arcseconds associated with the galaxy itself. In addition, three very compact (sub-arcsecond) sources are observed, one of which lies exactly along the putative radio extension shown in the NVSS images but not associated with the X-ray knots. I explore the nature of this radio component in Section 4.4.3. It is unlikely that a radio jet structure exists in the intermediate scales between the resolution of the VLA in A Array at 1.51 GHz (beam size ~1″) and the NVSS survey (beam size ~45″) as archival VLA data[12] in C configuration and at 1.51 GHz (beam size ~16″) show only an unresolved source and no extension in any direction. Moreover, van Driel and Buta (1991) show no extension towards the X-ray jet in H I images of NGC 6217 at a resolution of 20″. Thus, from this new high resolution data and archival datasets, a jet origin of the X-ray knots observed NGC 6217 is ruled out and I conclude that there is no large-scale (arcmin) jet-like radio structure associated with NGC 6217. This interpretation is supported by the global properties of NGC 6217. In fact, there are no examples in the literature of sources similar to our target, i.e. low-luminosity radio-quiet AGN with a small BH mass (2.0×10^6 $M_\odot$), which can launch radio jets that are also visible in the X-rays. This is a restrictive prerogative of powerful radio-loud AGN, which show large kpc-scale collimated jets and massive BH ($>10^8$ $M_\odot$).

Therefore, I now consider the three X-ray knots in turn and attempt to explain plausible

[12]Images obtained from the VLA Imaging Pilot https://archive.nrao.edu/nvas/

origins for these X-ray knots, given the multi-wavelength data. RB extracted optical-IR counterparts associated with the X-ray knots within the 21″ X-ray extraction region and built up their SEDs. The genuine physical relation between the X-ray and optical-IR counterparts goes beyond our reasonable attempt to investigate the nature of these knots. Therefore, caution needs to be taken when considering the physical properties derived for these sources.

The X-ray spectroscopy of knot 1 agrees with the one performed by F17 within the uncertainties. Concerning the multi-band identifications, two *Spitzer* sources fall within the 21″ X-ray extraction region. The SED fit for the source nearest the X-ray knot centroid is reported and a photometric redshift of $0.48^{+0.25}_{-0.12}$ with a bolometric luminosity of $7.9{\times}10^{43}$ erg s^{-1} is obtained. This source is interpreted as a possible background extragalactic object. However, the four IR data-points available for this SED reduces the reliability of the results derived for this source. For the sake of clarity, RB also extracted the SED of the secondary *Spitzer* source found in the extraction region of knot 1. This source is detected in SDSS *r*,*i* and *z* as well as all the IR bands and RB found a photometric redshift of $0.49^{+0.16}_{-0.13}$, consistent with the former *Spitzer* source. Given these similar redshifts and their proximity to one another, their separation can be estimated to be of order of 100 kpc. Therefore I tentatively propose that the two *Spitzer* sources may belong to a cluster of galaxies where the detected X-ray emission would correspond to the hot cluster halo.

Similar to knot 1, two *Spitzer* sources fall within the X-ray spectral extraction radius of knot 2, but unlike knot 1, one of the two *Spitzer* sources well matches the centroid of X-ray knot 2 within 0.5″. This *Spitzer* source also has SDSS and *WISE* detections, as well as a *HST* detection. This co-spatiality increases the probability that the X-ray knot and the optical-IR counterparts are physically related. It should be noted that the optical/IR detections described here are not related to the background star mentioned in F17, 1.6″ away from the knot, as this source is now outside the error bars for the centroid position of this knot in our analysis. The optical-IR SED fit requires the inclusion of the spectrum of an (Seyfert-like) AGN with strong emission lines which constrains its photo-z at $0.70^{+0.03}_{-0.02}$ with a bolometric luminosity of $8.3{\times}10^{43}$ erg s^{-1}. The X-ray spectral fits yield a photon index of $1.38^{+0.45}_{-0.37}$, which is a little low for an AGN, but agrees with the literature values within the uncertainties. Although a background AGN origin is preferred for knot 2, it is not possible to rule out the knot association with an X-ray binary within NGC 6217, despite its large distance (∼2′, 12 kpc) from the centre of NGC 6217.

Finally, X-ray knot 3 has a complicated X-ray morphology, with two distinct X-ray blobs in the X-ray extraction region. There is a *Spitzer* source coincident with the western X-ray component in this knot (see Fig. 4.2), which is also coincident with the extended SDSS source discussed by F17 and a *HST* source that F17 attributed to an unrelated galaxy. The knot as a whole has an X-ray photon index of $1.54^{+0.54}_{-0.46}$, which agrees within the uncertainties of F17. Assuming that the optical-IR counterparts are related to the emission of the knot 3, the SED is modelled with a young and old stellar population with a photo-z of

$0.46^{+0.19}_{-0.06}$ and a bolometric luminosity of 9.3×10^{43} erg s^{-1}. This tentative multi-band identification of the X-ray emission from knot 3 makes the nature of this knot as a background source questionable.

Although caution on the interpretation of these knots is needed, the multi-band counterparts found for the X-ray knots may suggest an extragalactic background origin for these components. This interpretation is supported by the large inferred X-ray and bolometric luminosities, ($\sim10^{43}$ erg s^{-1}, assuming the photo-z are correct) and X-ray photon indices consistent with an AGN origin (Nandra and Pounds, 1994; Reeves and Turner, 2000; Piconcelli et al., 2005; Page et al., 2005; Ishibashi and Courvoisier, 2010). However, in the case the sources belong to the host galaxy, NGC 6217, all of the knots would have luminosities ($\sim10^{39}$ erg s^{-1}) consistent with X-ray binaries, although they would be very far away from the nucleus. Therefore, it is not possible to put firm conclusions on the nature of any of these X-ray knots, but I conclude that they are all likely background sources. Further high resolution data with *Chandra* will greatly improve the understanding of these distinct X-ray knots, by providing higher angular and spectral resolution data.

Chance Alignment of the X-Ray knots

To ascertain whether the *Spitzer* sources are genuinely related to the X-ray knots, I computed the number of 3σ *Spitzer* detections that are expected in one of the circular $21''$ X-ray extraction regions, from the *Spitzer* catalogue (e.g. the red squares in Fig 4.2). I found 148 *Spitzer* detections in the $5.2' \times 5.2'$ *Spitzer* CCD field-of-view, corresponding to $\sim$2 sources per $21''$ radius spectral extraction region. There are two 3σ detections in the spectral extraction region of knots 1 and 2, and one detection in the spectral extraction region for knot 3, although a second object is very close to said region (see Fig 4.2). Hence the number of *Spitzer* objects in each extraction region is consistent with the number we expect and it is therefore likely that the X-ray emission and the *Spitzer* sources are correlated. Furthermore, given the $21''$ extraction regions for the X-ray data, it is not possible to conclude how much X-ray emission each *Spitzer* source contributes to the final X-ray spectra (if any).

Further to the analysis of the co-spatiality between *Spitzer* sources and the X-ray knots, I calculated the likelihood of the three X-ray knots forming a line from the centre of NGC 6217 by chance. To perform this statistical analysis I used the integral source counts for *XMM-Newton* (Ranalli et al., 2013). First, I calculated the number of sources one would expect in a given radius from the nucleus to knot 1. Then I found the number of sources in the radius from knot 1 to knot 2 and multiplied this value by the angle subtended by knot 2 on knot 1. I performed this step again, but for knots 2 and 3. The product of these three values gives us a small probability of chance alignment of 1.37×10^{-4}. However, one must also consider the sources that both the NVSS and *XMM-Newton* have observed to estimate the likelihood of seeing such an alignment present in NGC 6217. As an example, I used the NGC catalogue, which has 7840 galaxies present. Of these, 7074 sources have been

observed by the NVSS. Of these 7074 galaxies, 1455 have *XMM-Newton* data in the archive. Therefore, the likelihood of seeing such a chance alignment in the *XMM-Newton* data which is unresolved by the NVSS data is 1.37×10^{-4} multiplied by 1455, yielding a value of ~0.2. This value should be treated as an upper limit since I do not consider the probability that the spectra, fluxes and hardness ratios (see F17) are similar among the knots. Therefore, it is not implausible to observe this sort of chance alignment in the X-ray data when comparing to NVSS data.

4.4.3 Radio Emission from secondary sources in NGC 6217

For the sources that were within the optical extent of the galaxy (panels B and C in Fig 4.2), RB and I did not attempt to extract their SEDs or look for X-ray emission because emission from the galaxy would confuse the SED fits and the *XMM-Newton* data is not of sufficient resolution to identify these objects separately. Both sources have e-MERLIN flux densities of $\lesssim$5 mJy at a size of $0\farcs15 \times 0\farcs15$, and therefore have brightness temperatures too low to claim a clear AGN activity. However, these do not align with the star forming regions found by Gusev et al. (2012) and Gusev et al. (2016) in NGC 6217. The source found in the spiral arms (Panel B in Figure 4.2) shows an extended structure and is co-incident with a 3σ *Spitzer* source. Judging from the radio emission alone, these radio sources are possibly either H II regions or background AGN. Additional high-resolution X-ray data would help in to identify these sources.

The radio source located between the X-ray knots 1 and 2 (Panel D) is associated with a weak *Spitzer* source (R). Modelling the only detected IR part of its SED provides an inconclusive photo-z of $0.19^{+0.25}_{-0.12}$ with a bolometric luminosity of 4.6×10^{42} erg s^{-1}. This source appears compact and unresolved at e-MERLIN and VLA A-Array baseline scales, with similar flux density values and appears unrelated to the X-ray emission of the contiguous knots. The most simple interpretation of this source is a background galaxy associated with a low-luminosity radio AGN, with a radio structure confined in a kpc scale. This scenario is in line with the population of compact radio galaxies (named FR 0s, Baldi et al., 2015, 2018a) found in the local Universe. In addition, it also likely that this radio source contributes to the radio elongation observed in NVSS at larger beam sizes along the putative X-ray jet.

4.5 Conclusions

High resolution radio interferometric data of the barred spiral galaxy NGC 6217 have been obtained with the high angular resolution and sensitivity of e-MERLIN. For the first time, the nuclear region of NGC 6217 has been resolved, which consists of two radio lobes projected north-west to south-east, contrary to previous publications that claimed there was an asymmetric radio jet to the south-west. The nuclear morphology is similar to compact

steep spectrum (CSS) or gighertz-peaked (GPS) sources (Orienti, 2016) but shows no core component. Starburst super-winds have been observed to show similar morphologies, but usually oriented along the minor axis of the galaxy (Ulvestad and Wilson, 1984; Kinney et al., 2000; Gallimore et al., 2006). The *XMM-Newton* X-ray spectra suggest a good fit (χ^2/d.o.f. $\sim$ 1) for an absorbed power law, with an additional thermal component. The energetics, optical line ratios and radio brightness temperature of the core region cannot rule out SF as the main contributor to the emission, but are also consistent with a LLAGN emission origin. Given the radio morphology, X-ray spectra and lack of alignment with the galaxy minor axis, I conclude that the nuclear region is most likely powered by a LLAGN, probably with a LINER type nucleus, with multi-band contamination from SF or other nuclear X-ray sources. Therefore, the 400-pc twin-lobed structure of NGC 6217 constitutes one of the smallest radio structures observed in the nuclei of nearby LLAGN. Such a radio structure would not be able to have been observed without the high resolution and sensitivity of the e-MERLIN interferometer. To confirm the emission mechanism, further high resolution X-ray data (e.g. *Chandra*) and optical (photometry and spectroscopy from *HST*) data are needed.

The 'putative' X-ray jet in NGC 6217 is not coincident with any radio emission observed with e-MERLIN or the VLA at 1.51 GHz. Furthermore, the extension of the nuclear radio bubble is oriented almost perpendicular to the putative X-ray jet. The background source origin of the X-ray knots was re-considered as multi-band sources co-incident within the X-ray centroid errors of the knots were found. By extracting photometry of all these sources in the optical/IR bands, spectral energy distribution fits were performed and showed that all of the X-ray knots were plausibly consistent with higher redshift ($\gtrsim$ 0.4) sources such as background AGN and galaxy clusters and therefore likely not belonging to NGC 6217. However, the sparse multi-band coverage of the SEDs of the X-ray knots does not ensure the correctness of the physical parameters inferred for these knots and therefore I cannot come to a definite conclusion on the nature of these sources as they are intrinsically faint and could be also consistent with XRBs and ULXs. Therefore, these X-ray knots would benefit from higher resolution X-ray data to confirm their optical/IR counterparts. However, the jet origin of the X-ray knots is ruled out based on the lack of radio counterparts.

I also investigated the other radio components observed in the new high-resolution images of NGC 6217. A radio source that coincidentally aligned along the P.A. of the putative X-ray jet was found, but not associated with any of the X-ray emission. I suggest that this may be due to a background radio AGN of redshift ~0.19. The two other sources of radio emission are possibly H II regions in the galaxy or background AGN, but additional data are required to test this hypothesis.

Part II

The LeMMINGs 'shallow' sample

Chapter 5

The LeMMINGs 'shallow' Sample

Some of the data in this Chapter has been published in *LeMMINGs - I. The eMERLIN legacy survey of nearby galaxies. 1.5-GHz parsec-scale radio structures and cores*, 2018 MNRAS 476 3478-3522

5.1 Introduction

Thus far in this thesis, I have considered only the physics that can be extracted from multi-wavelength data of individual objects from the LeMMINGs 'deep' sample. The 'deep' LeMMINGs sample presented in Chapters 3 and 4 has shown that 1) radio variability on decadal timescales exist in LLAGN and may contribute to scatter in any radio-based relationship, 2) low-level radio emission consistent with an LLAGN origin exists in different optically classified nuclei and 3) multi-wavelength analysis of the LeMMINGs sample is required to investigate the dominant processes responsible for the radio emission.

However, the properties of LLAGN are best understood in a large complete sample where the accretion process can be investigated on a statistical level. With this goal in mind, in this chapter, I will present the first release of the e-MERLIN data of the 'shallow sample' at 1.51 GHz (L-band), as well as the additional LeMMINGs data made available since the first data release in (Baldi et al., 2018b). The radio data reduction procedure has already been described in detail in Chapter 2. Furthermore, all the galaxies in the LeMMINGs 'shallow' sample have already been reclassified (see Chapter 2). Some of the data analysis has already been presented in Baldi et al. (2018b), but I will extend this analysis by including double the dataset of Baldi et al. (2018b), reduced with the new e-MERLIN CASA pipeline. I will compare the two data releases to ensure that the different calibration methods between them are consistent and do not effect the completeness of the sample.

I will focus on the central galaxy region ($0.73''^2$) to explore the nuclear radio properties of the LeMMINGs 'shallow' sources. I will detail how RB and I determined whether a source had been detected or not and provide a radio luminosity function (RLF) for the LeMMINGs

'shallow' sample for the first time. Furthermore, I will describe the detections as a function of all the other physical and global parameters of the galaxies, e.g. black hole mass, optical nuclear spectroscopic classification and galaxy morphological type. In addition I will described the power of the LeMMINGs 'shallow' sample with reference to the 'deep' sample to detail the potential scientific gain from such a legacy sample.

Finally, I will explore the physical interpretations of the different optically classified galaxies, e.g. the LINERs, Seyferts, ALGs and H II galaxies, based off the radio and optical data presented here.

5.2 Observations

In this chapter, I present the data from the LeMMINGs blocks made available to RB and I prior to March 2018. This includes data on 25 blocks, of which I include data on 241 galaxies. Eleven blocks (2, 3, 4, 5, 7, 9, 10, 17, 18, 25, 27) were first presented in Baldi et al. (2018b) while a further fifteen blocks (6, 8, 11, 12, 13, 14, 15, 16, 19, 21, 22, 23, 24, 26) have since been calibrated and imaged to more than double the number of sources in this thesis. All of the blocks have been observed since 2015. Some of the blocks were re-observed due to problems with antenna 'drop-outs' or problems with imaging the data.

Some blocks were not able to be included in this thesis for various reasons: LeMMINGs block TEST has not been observed, block 20 only had 2 scans of the targets and hence the *uv*-coverage is not good enough for the sample and block 28 did not have good enough data as the Cambridge antenna and some of the short-baseline antennas had 'dropped-out'[1] to warrant calibrating and including in this thesis. Nine galaxies (NGC 783, NGC 2685, NGC 3395, NGC 4369, NGC 4485, NGC 5033, NGC 5354, NGC 5548 and NGC 7080) were not observed in their blocks due to either poor calibrators or the target itself being not observed (see Table 5.1. The data presented in Baldi et al. (2018b) was calibrated and imaged using AIPS, whereas the additional fifteen blocks in this thesis have been calibrated and imaged with CASA by RB and me. The average rms noise level in the blocks was ~0.07mJy/beam. I present the full and low-resolution maps of the detected sources in Appendix A (Figures A1 and A2) together with the *uv*-tapered images. The *uv*-tapered images are mostly obtained with *uv*-scales of $\sim$750 kλ, corresponding to a resolution of 0.4″, which is double that of the full-resolution images. The radio images have a large dynamic range which highlights their quality. For a small fraction of sources (in blocks 2, 3, 8, 9, 12, 13, 15, 22, 24, 25 and 26), the image quality is modest, usually due to an antenna 'drop-out', but still adequate for the purposes of our survey (see Table 5.2).

[1] e.g. the antennas had no phase for the targets and hence no amplitudes. All of the information for baselines with these antennas was effectively correlated noise and so these antennas needed flagging

Table 5.1: Table of LeMMINGs sources not included in this thesis due to various reasons.

Galaxy	LeMMINGs Block	Reason
NGC 783	02	Missing core baselines
NGC 2685	25	Incorrect Pointing Position
NGC 3395	17	Incorrect Pointing Position
NGC 4369	14	Incorrect Pointing Position
NGC 4485	14	No calibration possible
NGC 5033	10	Not observed
NGC 5354	09	No calibration possible due to PHS-Cal
NGC 5548	09	No calibration possible due to PHS-Cal
NGC 7080	05	No calibration possible due to PHS-Cal

Table 5.2: Data Quality of the LeMMINGs observations per block

LeMMINGs block	Data Quality
TEST, 20, 28	Unobserved
02, 03, 08, 09, 12, 13, 15, 22, 24, 25, 26	Modest
04, 05, 06, 07, 10, 11, 14, 16, 17, 18, 19, 21, 23, 27	Good

5.3 Results

5.3.1 Radio maps and source parameters

As the data presented in this Chapter focusses on the radio emission associated with the SMBH at the center of a galaxy, RB and I searched for sources in the innermost regions of the radio data, corresponding to a radius of 5 kpc at a distance of 20 Mpc. RB and I imaged the data in full resolution and at different *uv*-tapering scales to attempt to detect both compact and diffuse emission co-spatial with the optical galaxy centre.

At full resolution, the typical beam size was $0.15-0.2''$. In the detected sources, this beam size revealed single or multiple components. RB and I adopted the same source parameter extraction method to ensure that the data was self-consistent between blocks reduced separately by myself and RB. We used the AIPS task `JMFIT` to extract the position, deconvolved size, peak flux density, integrated flux density, beam size and PA for all the sources that were included in the first data release in Baldi et al. (2018b). For the new data included since that publication, the CASA e-MERLIN pipeline was used. Hence, RB and I used the in-built CASA fitting tool, `imfit` to extract the same source parameters. Both `JMFIT` and `imfit` work in the same way by fitting a Gaussian across the source to estimate the parameters, hence no bias should be induced by this approach. For extended resolved structures, RB and I used `IMEAN` for rectangular boxes or `TVSTAT` for irregularly shaped regions, to interactively measure the flux density of the sources. RB and I repeated the measurements several times and derived an average value. We used the task `IMSTAT` to estimate the rms near the nuclear region for detected sources. For sources with no detectable nuclear emission, RB and I estimated the rms value in a region around the optical

centre. In CASA, we used the interactive `viewer` to estimate the rms in the same way as the AIPS calibrated data. If source components had flux densities above 3σ of the local noise of the source, they were considered detected. The same procedure was applied to the *uv*-tapered images. Some components appeared in the *uv*-tapered images as the larger beam is more sensitive to diffuse low-brightness emission. In the few cases of diffuse low-level emission, RB and I derived a 3σ upper-limit to the flux density for the undetected counterparts at full resolution.

The final naturally-weighted full-resolution images generally achieved an rms of 70μJy beam^{-1}, irrespective of the calibration method used, with a standard deviation of 0.36. For the entire sample presented in this thesis, RB and I detected significant radio emission ($\gtrsim$0.2 mJy) coincident with the optical centre for 100/241 sources (~41%). For these sources of radio emission, RB and I also extracted their counterparts in the *uv*-tapered images. The full-resolution parameters (beam size, PA, rms) are listed in Table B.1, and the detected source parameters in all resolutions are listed in Table B.2 and Table B.3 in Appendix B. The remaining 141 sources had no radio emission above the 3σ detection limit in the core region in either the full or low-resolution images.

There is a large variety of radio morphologies in the detected sources, ranging from pc-scale unresolved single components to extended and complex shapes. The lower-resolution images typically show more extended radio structures than the full-resolution images, with notable cases being NGC 3348, NGC 3665, NGC 5005, NGC 5194 and NGC 5377 which show kpc-scale lobes in the lower resolution images. The radio structures vary in size from 150 mas at the smallest scale for unresolved sources to upto 26″ for sources like NGC 5005. The median size of the radio structures is 1.5″, corresponding to a physical linear range of ~10-1700 pc (median ~100 pc), depending on the distance to the galaxy of the sample. All of the radio sizes for the unresolved sources are listed in Table B.2 and B.3.

It is difficult to disentangle whether the radio emission in compact unresolved sources is due to an AGN or star formation without spectral information. However, RB and I performed an additional step in the analysis to identify the radio core. We defined the radio cores as the unresolved central radio source, which may represent the AGN jet base (or a central SF region). RB and I used the specific radio morphologies of each source combined with the optical centre of the galaxy obtained from the *HST* optical centroid to gauge the distance of the radio source from the optical centre. Where no *HST* data exist, the NED catalogue position was used. For sources with a double-sided jet, the central unresolved component was taken to be the radio core, but for one sided and asymmetric sources the brightest component was used. The distance between the optical galaxy centre and the closest possible radio component is the main criterion for a core identification. We further discriminated sources into 'identified' and 'unidentified' based on this criteria, discussed further in Sections 5.3.2 and 5.3.3 respectively.

There have been several previous VLA observations of the Palomar sample which have detected radio cores at a resolution of ~1″ (e.g. Nagar et al., 2002; Filho et al., 2000; Nagar

et al., 2005). These observations generally are coincident with the optical galaxy centres. As the LeMMINGs observations are five times higher in spatial resolution, it is possible to use the VLA 1″ beam to estimate the offset between the radio and optical positions expected in the sample. This offset corresponds to ~100 pc for the LeMMINGs sample. The typical radio-optical offset observed in the LeMMINGs sample is ~0.3″, e.g. inside the resolution of the VLA.

For 70 out of the 100 detected sources in the full LeMMINGs sample presented in this thesis, radio emission was detected within the 1″ of the optical centre of the galaxy. Fourteen sources were observed to have a radio core within 2.0″ of the galaxy optical centre. For all the 84 (70+14) objects detected within 2.0″ of the optical centre, I will hereafter assume that they have been correctly identified (see Section 5.3.2) and refer to them as 'identified' sources. For the remaining 16 sources (NGC 147, NGC 891, IC 342, NGC 1569, NGC 3034, NGC 3690, NGC 4013, NGC 4162, NGC 4242, NGC 4631, NGC 4736, NGC 5012, NGC 5273, NGC 5676, NGC 5907, NGC 6015), the radio emission is more than 2″ from the optical centre and hence it is not clear whether the radio emission detected is due to the core or due to other sources of radio emission[2]. In two cases, NGC 3034 and NGC 3690, radio emission was detected within 2″ from the optical centre but are known not to be associated with the AGN - in the case of NGC 3034 - or is relic emission from a tidal disruption event: NGC 3690. Some of the sources have multiple components of ambiguous nature and without the multi-spectral information, it is not possible to tell whether the sources are spectrally flat and hence indicative of an self-absorbed radio core. Furthermore, an additional 6 sources (NGC 2342, NGC 3077, NGC 3198, NGC 4111, NGC 4220 and NGC 4826), show an further radio emission other than the radio core already identified. Such sources are possibly related to a background AGN or star formation in the galaxy. These 22 (16+6) objects will be referred to as 'unidentified' sources hereafter (see Section 5.3.3).

5.3.2 Identified sources

The full and low-resolution maps are presented in Appendix B, along with the tables including source characteristics (Table B.1), radio countours and restoring beams (Table B.2) of all of the detected radio sources within 2.0″ of the galaxy optical centre.

To ensure that the 'identified' sources are genuine, RB and I calculated the probability of detecting a radio source above the survey 0.2 mJy detection limit of the LeMMINGs survey within a given area of sky. As no e-MERLIN wide-field survey exists at this frequency in the literature, we used the source count distribution obtained with 1.4 GHz VLA observations of the 13^{th} XMM-Newton/ROSAT Deep X-ray survey area (Seymour et al., 2004) over a 30-arcmin diameter region. Based on the results of Seymour et al. (2004), it is expected that one radio source out of ~ 100 galaxies within a circular radius of 3.7″ would

[2]NGC 147 was classified as 'identified' in Baldi et al. (2018b), but a more careful analysis of the HST position indicates that the object is further away from the optical nucleus than stated in that publication.

appear randomly in the sample. Hence, given this result, it is likely that the radio sources identified within 2.0″ of the optical centre are likely to be the associated target sources.

Radio emission consistent with the optical centre was detected at full resolution for all sources bar (NGC 3430, NGC 3675, NGC 5985, and NGC 6702), which only reveal radio cores in the lower resolution radio images. Most of the sample have peak core flux densities ∼1 mJy beam^{-1} at scales of ∼0.2″. The brightest source is NGC 315 which reaches a ∼500 mJy beam^{-1} peak flux density. Most of the central components can be considered unresolved as the deconvolved source sizes are smaller than the beam size. Furthermore, the peak flux densities of the radio core components are usually consistent with the integrated flux densities to within a factor of ∼2. Those which have significantly larger integrated flux densities than their peak flux densities usually include extensions or multiple components. The cores appear slightly resolved, and often show a protrusion associated with a core–jet morphology (Conway et al., 1994).

For 39 identified sources, clear extended radio structures are observed. As this thesis concerns the radio emission from AGN, I favour that the extended radio emission originates from radio jets, based on their morphologies. There are several reasons for favouring a radio jet origin: 1) the e-MERLIN LeMMINGs observations have a high spatial resolution (150 mas) and hence resolve out diffuse emission usually associated with the galaxy disc and 2) the use of 'snap-shot' imaging means that the the LeMMINGs observations are insensitive to diffuse low-brightness emission, as expected by a galaxy disc (Brown and Hazard, 1961; Kennicutt, 1983). Hence, I will consider the extended emission from the radio cores as due to radio jets, but this doesn't preclude the possibility that the radio emission arises from circum-nuclear star formation (see Section 5.6.4).

The identified sources were classified due to the observed radio structures in both the full- and low-resolution maps (see column 8 of Table B.1). The five morphologies are discussed below:

- The *core/core–jet* morphology, marked as A (45 galaxies): These sources show bright cores and sometimes have a possible elongation in one direction (e.g. a radio core with a jet). The radio components are aligned in the same direction of the possible jet. Some examples include NGC 3031 and NGC 3941.
- The *one-sided jet* morphology, marked as B (9 galaxies): The one-sided jets show a clear asymmetric extended jet structure. The presence of a one-sided jet may be due to relativistic beaming of the jet. Some examples include NGC 3077 and NGC 4041.
- The *triple-source* morphology, marked as C (18 galaxies): Triple-sources have three components that are aligned in one direction. These components are interpreted as the radio core and symmetric jets/lobes. These sources may appear as twin-symmetric jets in the lower resolution images. Some examples include UGC 4028 and NGC 4151.
- The *double-lobed* morphology, marked as D (5 galaxies): These sources have two

large radio lobes over extended scales in either the full or low resolution images. Some examples include NGC 5005 and NGC 5194.

- The *jet+complex* morphology, marked as E (7 galaxies): These sources show a complicated morphology or many radio components. They sometimes reveal a possible jet but overall the number of nuclear radio components makes it difficult to classify these sources into one of the previous four classes. It is likely that radio emission due to star formation also contributes to these objects. Some examples include NGC 2655 and NGC 4102.

To further discriminate the radio sample, the radio sources which show 'jet-like' morphologies (e.g. one-sided, two-sided, triple, double-lobed sources) are hereafter called 'jetted' and those without a clear jet, 'non-jetted'.

5.3.3 Unidentified sources

The sources that were considered as 'unidentified' in Section 5.2.1 are now assessed. 22 radio sources were classified as 'unidentified' and 16 do not show a clear, unequivocal radio core within 2″ of the optical centre. The remaining 6 are unknown sources detected in the central imaging field of the LeMMINGs sample. Figure B.2 in Appendix B shows the full and low-resolution maps for these 'unidentified' sources (for radio contours and restoring beam see Table B.4) and their radio source parameters are listed in Table B.3.

I will now investigate the 'unidentified' sources in detail. NGC 891 is not detected in the full-resolution image but three components are detected in the lower resolution image[3]. Interestingly, the galaxy optical centre lies almost equidistant between the two northern radio components, ~2.5″ from each one. It is possible that the central component of the three sources is the radio core, but it is not near enough to the optical centre to be considered 'identified'. In two galaxies (NGC 4013 and NGC 5273), radio emission is detected in a circular shape around the optical nuclear core. This circum-nuclear star formation is probably associated with a nuclear star-forming ring. In NGC 3034, many sources of radio emission are detected. NGC 3034 is a well known star forming nucleus and it has no known AGN (see Section 5.4.1) as all of the radio emission in the galaxy is due to star formation (e.g. radio supernovae) or from X-ray sources like Ultra-luminous X-ray sources (ULXs) or XRBs. In NGC 3690, the radio emission detected near the core is from a tidal disruption event (see Section 5.4.2). For all of the cases listed above, the radio core identification is not possible or ambiguous. However, it is likely that the radio emission is associated with the galaxy.

For the other 'unidentified' sources, radio emission is detected further away from the optical nucleus than 20″. This angular distance corresponds to $\gtrsim$20 kpc at the median distance of the LeMMINGs sample. Hence it is unlikely that the radio emission in these sources are

[3]SN 1986J, present in NGC 891 and detected in the radio band by VLA (Pérez-Torres et al., 2002), is located ~1 arcmin south of the optical centre, which is beyond the region considered in our analysis.

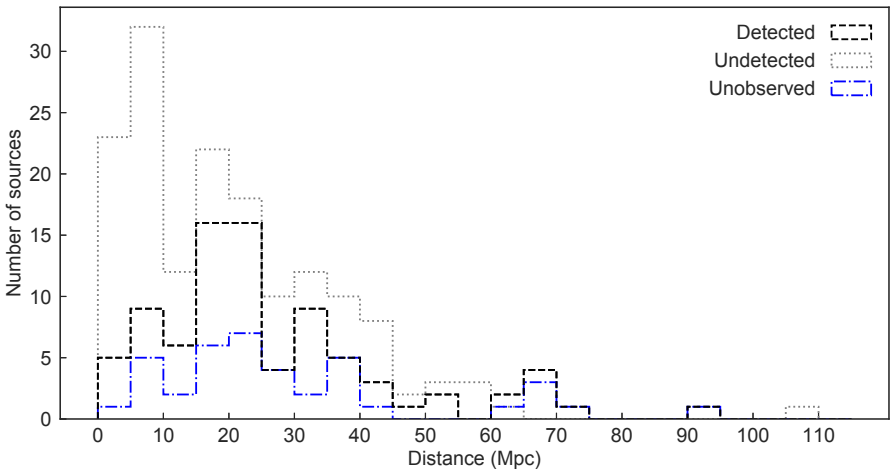

Figure 5.1: Histogram showing the number of detected, undetected and unobserved sources in the LeMMINGs sample as a function of distance. The undetected sources includes all those that are labelled as 'unidentified' and undetected.

associated with an AGN in the core and they are therefore likely SF or background sources. Seven radio sources appear in the field of the galaxies (NGC 2342, NGC 3077, NGC 3198, NGC 4013, NGC 4111, NGC 4220 and NGC 4826, note that NGC 4220 has two additional radio sources), which already have 'identified' radio cores. These off-nuclear sources are considered 'unidentified' and are likely background sources. Indeed, the sources appear two-sided and elongated, and hence these sources possibly belong to unknown background AGN.

By using the same approach as in Section 5.3.2, it is possible to estimate the likelihood of radio sources falling within radii 4 and 20″ (the offsets measured above) and hence consider whether they are likely related to the nuclear core. The obtained values are 1.2 and 39.2 respectively, suggesting that the interpretation above of the off-nuclear sources are potentially background objects.

It is important to note that while the radio core has not been detected in the 'unidentified' and the undetected sources, these galaxies may still conceal active galactic nuclei. They may be below the radio detection limit of the LeMMINGs survey or not identified in the more complex structures listed above. Future e-MERLIN 5 GHz observations of the LeMMINGs sample will have better resolution and are less affected by RFI. In addition, matching resolution *HST* data will help provide better constraints on the optical nuclei of the galaxies in the sample (e.g. NGC 147, NGC 891, IC 342 and NGC 4736 may have been detected, but given current optical positions, it is not possible to conclude this with certainty).

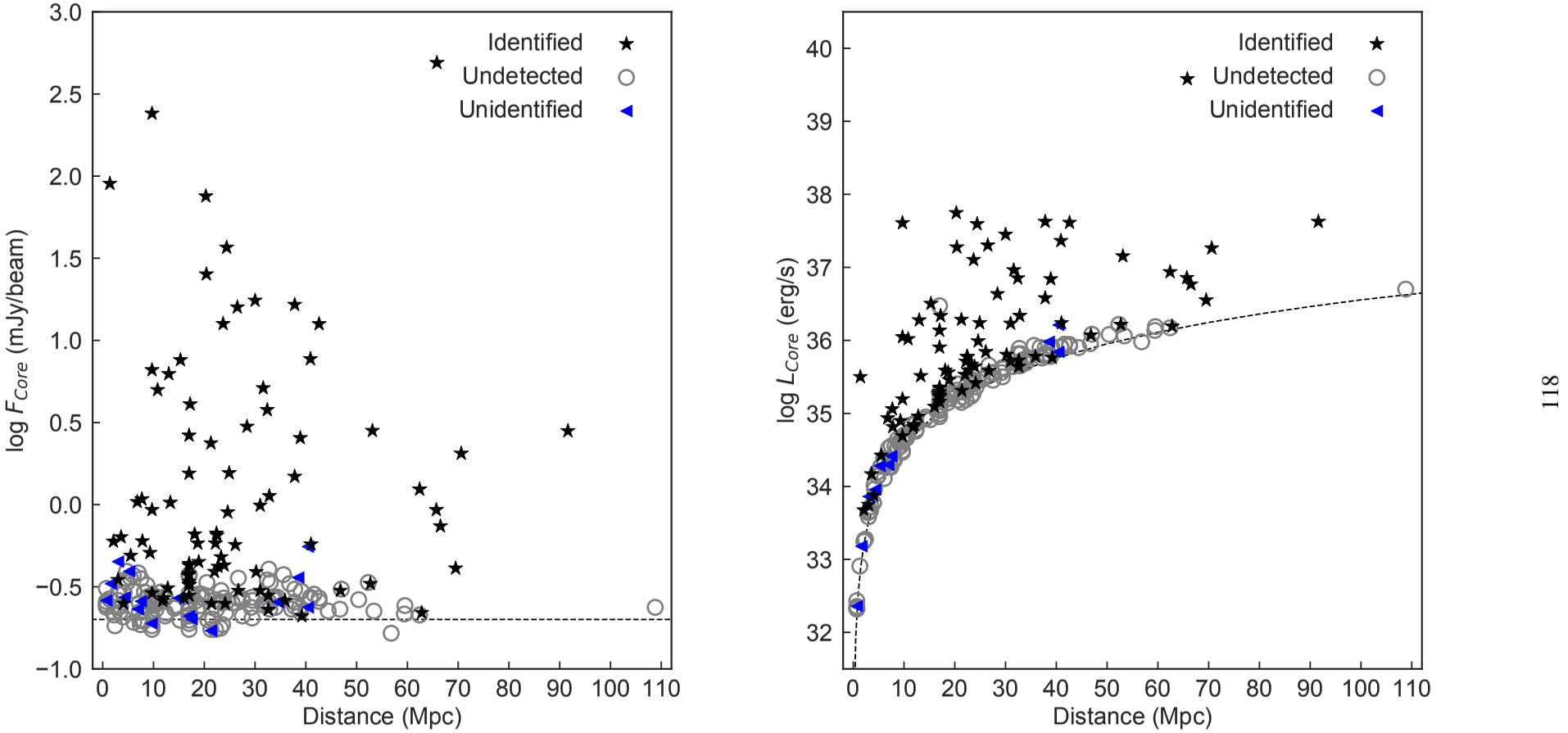

Figure 5.2: Radio core flux density (F_{core} in mJy beam^{-1}) (upper panel) and its luminosity (L_{core} in erg s^{-1}) (lower panel) as a function of the distance (Mpc) for the entire sample. The dashed lines correspond to the flux density and luminosity curves at a 3σ flux limit (0.2 mJy beam^{-1}). The different symbols correspond to identified sources, unidentified and undetected radio sources. For these last two types of sources, the values on the y-axis are meant as upper limits.

5.3.4 Radio brightness

The LeMMINGs 'shallow' survey has detected many faint radio cores (< 1mJy) at scales of 10s of parsecs. Radio sources are detected out to 100 Mpc and are shown in Figure 5.1. The detections increase at the longest distances in general, with only ∼20% of sources detected at distances closer than ∼20 Mpc. The survey has detected radio emission from both active and quiescent galaxies for the first time. The 3σ detection limit is ∼0.2mJy (Fig. 5.2, *left* panel), assuming good calibration and all antennas participating in the observation (see Chapter 2). All of the radio luminosities of the galaxies in the sample are shown in Table B.1. The luminosity-distance curve of the LeMMINGs 'shallow' sample is presented in Fig. 5.2, *right* panel. The identified sources lie above the luminosity curve, while the undetected and unidentified sources follow it.

The core luminosities range between 10^{33} to 10^{40} erg s^{-1}, with a median value of 6.0×10^{35} erg s^{-1}. When comparing to previous surveys of the Palomar survey, the LeMMINGs 'shallow' survey luminosities extend to lower luminosities by a factor of 10. For example, the Nagar et al. (2002); Filho et al. (2006) surveys reached a luminosity of 10^{35} erg s^{-1}. Our observations are within 100-1000 times higher than the luminosity of Sgr A*. The total radio powers for our sample estimated from the low-resolution radio images have a median value of 1.4×10^{36} erg s^{-1}. The total luminosities cover a similar range to the core luminosities (see Table B.1). The radio core typically contributes ∼26% of the total radio emission.

The brightness temperature was introduced in Chapter 1. It is a measure of the expected radio emission from a radio source emitting only by Brehmstrahlung radiation. Below 10^6K, the radio emission can be explained purely by Brehmstrahlung emission but above this limit synchrotron emission (e.g. from radio jets of AGN) is required to explain the brighter temperature. At the resolution of e-MERLIN at 1.5 GHz, a flux density of 5 mJy beam^{-1} is required to meet this limit (Baldi et al., 2018b). Only sixteen LeMMINGs sources[4] meet this requirement and most are significantly below this value. These sixteen sources are associated with all types of radio morphologies observed. However, the calculated values less than 10^6K do not preclude an active SMBH origin. Such sources could be very weak LLAGN and the radio brightness is not useful in discriminating radio emission from LLAGN in these sources.

5.3.5 The Radio Luminosity Function of the LeMMINGs sample

The radio luminosity function (RLF) of the LeMMINGs sample shows the number of objects in a given radio luminosity bin as a function of volume. Previous RLFs for the Palomar survey galaxies suggested a break in the luminosity function at $\sim10^{19}$ W/Hz, to explain the luminosity of the Galactic centre, Sgr A* (Nagar et al., 2005). However, the

[4]NGC 315, NGC 2639, NGC 2655, NGC 2768, NGC 2787, NGC 3031, NGC 3079, NGC 3147, NGC 3504, NGC 4151, NGC 4203, NGC 4278, NGC 4589, NGC 5322, NGC 5353, NGC 5844)

(Nagar et al., 2005) sample was biased towards known 'active' LLAGN (e.g. Seyferts and LINERs) and only probed down to a limiting 3σ flux density of ~1 mJy. However, it sampled nuclei at a similar - 0.15″ - resolution to the e-MERLIN observations presented here with the VLA. Hence, it is the best comprehensive sample of the same objects to compare to. As the detection limit of the LeMMINGs radio survey is 0.2 mJy, the region of luminosity space probed by LeMMINGs is 100-1000 times the Galactic centre Sgr A*, and can attempt to reconcile the break in the luminosity function reported by Nagar et al. (2005). More recent observations have also concluded that a break at 15 GHz is observed (Saikia et al., 2018).

To construct the RLF, I used the same method as Filho et al. (2006) and Saikia et al. (2018), that is to use the V/V_{max} method (Schmidt, 1968). I include all of the 84 detected and optically identified sources and do not consider the unidentified or non detected objects. As the LeMMINGs survey is for all northern objects at declinations $\gtrsim 20°$, the fraction of the sky is limited to 1.314π steradians. The optical Palomar survey is limited to 12.5 mag. In order to build the RLF, the identified sources were spread over bins of equal radio power. For each of the bins, the differential RLF is calculated by:

$$\Phi\left(\log L_*\right) = \frac{4\pi}{\sigma} \sum_{i=1}^{n(\log L_*)} \frac{1}{V_{max(i)}}, \tag{5.1}$$

where $\frac{4\pi}{\sigma}$ is the fraction of the sky surveyed, $n\left(\log L_*\right)$ is the number of objects in a given luminosity bin L_*, and $V_{max(i)}$ is the maximum volume in which the object would be observed to, given the limiting magnitudes/fluxes in both the parent Palomar sample and the LeMMINGs radio sample. The smaller of the two volumes is used, to ensure that the object would be detected in both samples. Due to the low number of objects in each bin and the low number of detected objects in the LeMMINGs sample, Poisson statistics are used to estimate the errors. The RLF is plotted in Figure 5.3.

The LeMMINGs RLF presented here for all of the identified objects in the LeMMINGs survey is roughly in agreement with the previous literature for the Palomar survey (Ulvestad and Ho, 2001a; Nagar et al., 2005; Filho et al., 2006). The observations of the LeMMINGs sample have probed an order of magnitude fainter than the previous Nagar sample: the minimum luminosity in the LeMMINGs sample is 17.5 W/Hz, compared to 18.62 W/Hz in Nagar et al. (2005). However, the LeMMINGs objects at 1.5 GHz do not require a break in the RLF at any luminosity to explain the observations. In fact, I searched for a simple linear regression fit for all luminosity bins and found a gradient of -0.65, which is similar to the Seyferts and LINERs in the previous literature (Ulvestad and Ho, 2001a; Nagar et al., 2005; Filho et al., 2006). In addition, this fit is in agreement with the local population, e.g. Sgr A*, extrapolated from 86 GHz to this observing band, 1.5 GHz (Krichbaum et al., 1998).

I have also plotted in Figure 5.3 - for comparison purposes to the literature - a break at

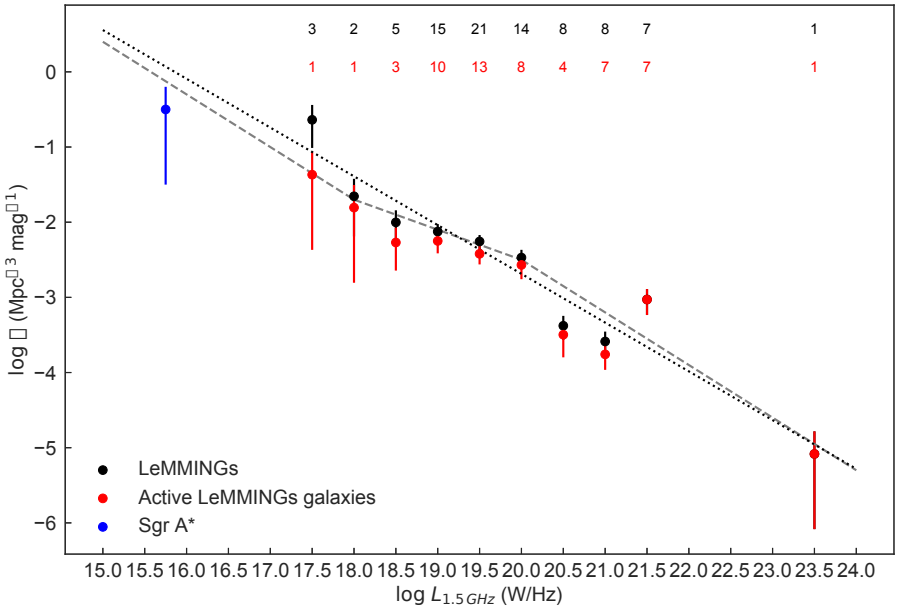

Figure 5.3: The radio luminosity function (RLF) of the LeMMINGs radio sample at 1.5 GHz. The black points show the radio detections of all identified sources in the sample. The red points indicate the 'active' galaxies based off the BPT diagnostic plots in Chapter 2, e.g. the LINERs and Seyferts. The blue point is the RLF point for Sgr A* based off VLBI observations scaled down to 1.5 GHz from Krichbaum et al. (1998). The dotted line is a formal fit to the data, with a power-law of α = -0.65. The dashed line shows three broken power laws similar to previous RLFs of the Palomar survey (e.g. Ulvestad and Ho, 2001a; Nagar et al., 2005; Filho et al., 2006; Saikia et al., 2018), with the power-laws in the range log(L_*) <18.0 and > −20.0 as a power-law with slope α = -0.7. For the central luminosity range, log(L_*) = 18.0−20.0 of α = -0.4. In addition the number of objects in each bin is written above each bin in the same colour as the sample used. The errors are drawn from a Poissonian distribution.

Table 5.3: Spectral–radio morphological classification breakdown

	optical class				
radio class	LINER	ALG	Seyfert	HII	Tot
core/core–jet (A)	27	3	5	10	45
one-sided jet (B)	3	0	0	6	9
triple (C)	11	2	2	3	18
doubled-lobed (D)	4	0	1	0	5
jet+complex (E)	1	0	1	5	7
Tot	46	5	9	24	84
unidentified	4	1	1	10	16
undetected	27	23	6	85	141
Tot	77	29	16	119	241

Notes. The sample is divided in radio and optical classes based on their radio detection, core-identification or non-detection.

10^{19}W/Hz, using a power-law of -0.7 above 10^{20}W/Hz and a power-law of -0.4 between 10^{18} and 10^{20}W/Hz (Nagar et al., 2005; Saikia et al., 2018). Below 10^{18}W/Hz I have plotted a power-law of -0.7 once more. These are not formal fits as such, but given an indication of the changes in gradient that can be observed in the region of low-number statistics. This effect seems more pronounced in only the 'active' sources, e.g. the LINERs and Seyferts as the flattening is more dramatic in the 10^{18} and 10^{20}W/Hz range. Therefore, this indicates that if one considers the radio sources detected in the H II galaxies and ALGs in this sample as LLAGN, then they can possibly explain the luminosity break at less than 10^{20}W/Hz.

5.3.6 Radio versus optical classification

Table 5.3 summarises the number of detected, unidentified, and undetected sources dividing the sample by optical class. LINERs have the highest detection rate (50/76, ~66%) in the sample. This detection rate is comparable to the first data release detection rate. The second largest detection rate belongs to the Seyferts, which are detected in the radio images in 10/17 (~59%) sources. The lack of Seyferts in the first data release - only four Seyferts were observed in total, but all were detected - limited the interpretation of the detection rate. However, now the detection rate is more robust due to the larger number of objects included in the sample. H II galaxies have a smaller detection rate 34/119 (~29%) and Absorption Line galaxies galaxies are lower still at 6/29 (~21%). For those sources that a radio core is identified, the detection fraction reduces for all classes as sixteen sources (one ALG, one Seyfert, four LINERs and ten H II galaxies) are excluded. The final identified radio core fractions are therefore: LINERs 46/76, Seyferts 9/17, ALGs 5/29 and HII galaxies 24/119.

The LeMMINGs sample encompasses all radio morphological types across all of the radio categories (see Table 5.3). Furthermore, the radio classes which suggest the presence of a radio jet (B, C and D) encompass all the optical classes. LINERs exhibit a variety of morphologies, but are most commonly observed as core/core–jet and triple structures. The

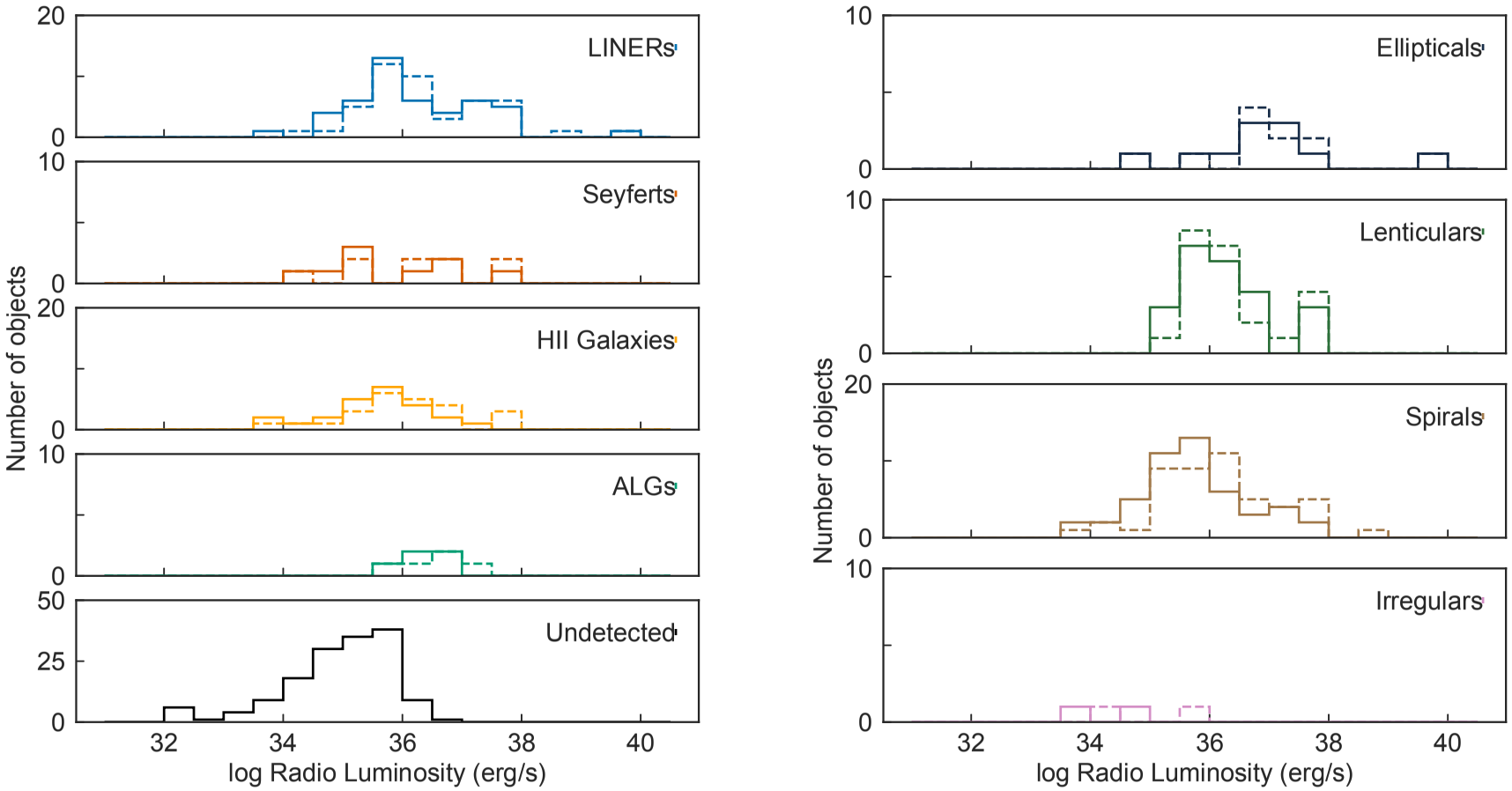

Figure 5.4: Histograms of the radio luminosity (erg s^{-1}) per optical class (upper plot) and host morphological type (lower plot). The solid-line histogram represents the radio core luminosity distribution and the dashed line corresponds to the total radio luminosity distribution. In the bottom panel of the upper plot, we also show the $3\,\sigma$ upper limit radio luminosity distribution for the undetected and unidentified sources.

ALGs are mostly core/core–jet, while the Seyferts tend to show edge-brightened morphologies. In contrast, the H II galaxies are in general not associated with double-lobed like morphologies. While H II galaxies are classified as star forming by their BPT diagrams, the presence of a jet is not precluded in these sources. Instead, the H II galaxies span all of the other four radio morphologies and nine of them show clear 'jet-like' morphologies. One of the sources is NGC 3665 which exhibits a FR I radio morphology extended over ~3 kpc at the VLA scale (Parma et al., 1986). The other fourteen H II galaxies do not show clear 'jet-like' morphologies and the radio emission may indeed be related to SF instead of a jet.

While spiral galaxies are the most abundant host type (159/241, 66%), early-type galaxies (ellipticals and lenticulars) are the most detected radio sources (34/70, ~49%). Spiral galaxies are detected in 30% of galaxies and are associated with all the types of radio morphology. The early-type galaxies are usually associated with the jetted radio morphologies. Only two irregular galaxies are detected out of the twelve in this sample.

The luminosity distribution for the LeMMINGs sample is presented in Figure 5.4, for both the peak radio core luminosities and the total integrated radio emission, split by optical class. In general, LINERs have the largest radio core luminosities with a median value of 8.4×10^{35} erg s^{-1}. ALGs have a higher median value for the radio core luminosity (1.7×10^{36} erg s^{-1}) but this value is drawn from a sample of only five objects. In contrast, the Seyferts and H II galaxies have the lowest median core powers, at 2.0×10^{35} and 3.9×10^{35} erg s^{-1}, respectively. The undetected/unidentified galaxies have radio luminosities ranging between 10^{32} to 10^{36} erg s^{-1}, with a median radio luminosity of 1.4×10^{35} erg s^{-1}.

The total integrated luminosities of the sample show a similar range of values to the core powers. The LINERs are once again the most powerful radio sources and the H II galaxies are the weakest. The core dominance, defined as the ratio of the radio core power to the total flux density changes but has a large variance with each optical class: Seyferts are the most core dominated (~75%)[5], followed by LINERs and ALGs with moderate core dominance (~65%), while the H II galaxies have the smallest core dominance (~35%).

It is also possible to compare the LeMMINGs sample by galaxy morphological type. The elliptical galaxies show the highest radio luminosities as they are mostly have LINER or ALG-type nuclei (Fig. 5.4). The spiral galaxies and lenticulars on the other hand have similar distributions and lie at slightly lower radio luminosities to the ellipticals. The irregular galaxies detected have low core and total luminosities too.

The brightness temperatures broadly reflect the flux density distribution. Of the sources that exceed the normal brightness temperature cut off for synchrotron emission from relativistic jets (e.g. 10^6K, Baldi et al., 2018b), fourteen of them are LINERs. The other two galaxies above this limit are the Seyfert NGC 4151 and the H II galaxy NGC 3504. All of the other detected sources have brightness temperatures less than 10^6K, sometimes going down to 10^3K. As such brightness temperature cannot be used as a diagnostic of the presence of an

[5]In the first data release, Seyferts were the least core dominated, but this was due to only three objects.

AGN for the vast majority of the sample.

5.3.7 Radio properties vs BH mass

BPT diagrams assign the emission line ratios for Seyferts and LINERs to the central AGN. Hence, radio cores detected co-incident with the optical emission are expected to be due to an active SMBH. However, for H II galaxies, where the ionisation may be due to SF processes, LLAGN or shocking in regions of size ~100 pc (Condon et al., 1982; Varenius et al., 2014; Salak et al., 2016). Hence, caution has to be taken to ascribe the emission line ratios to a specific ionising process. In contrast, ALGs may exhibit radio emission from SMBHs but are undetected in the optical band by their emission lines.

There are two other diagnostics to help identify genuine radio emission from active SMBHs: the BH mass and the radio luminosity, although neither are 100% indicative of AGN activity. The BH mass is often used as an indicator of activity as active nuclei are preferentially associated with massive BHs (e.g., Best et al. 2005a; Gallo et al. 2010). The radio luminosity roughly assesses the likelihood of the source being radio-jet dominated: a sign of an active SMBH. Both quantities are connected in active nuclei, as radio-emitting AGN tend to become more powerful (e.g. radio louder) with larger black hole masses (e.g. Best et al. 2005a). The radio core detection as a function of BH mass in the LeMMINGs sample is shown in Figure 5.5 and it is clear that the detection fraction increases with BH mass. For M_{BH} >10^7 $M_\odot$, this fraction is ~50% reaching 55% in the last bin, ~10^8–10^9 $M_\odot$, while it drops to less than 16% below 10^6 $M_\odot$.

The distribution of core luminosities as a function of the BH mass is presented in Figure 5.5. For the objects above 10^7 $M_\odot$, a correlation between the radio and M_{BH} is observed. This correlation includes all jetted and active galaxies. However, at lower masses, below 10^6 $M_\odot$, the correlation flattens. Despite the scatter, the LINERs and Seyferts, which tend to have higher black hole masses and are detected as having an active BH in emission line diagrams, follow the radio-M_{BH} sequence. ALGs are not detected in the emission line diagrams but also appear to follow this correlation, but H II galaxies, which are mostly at lower BH masses, tend to emerge in the flatter plateau lower than 10^6 $M_\odot$.

The linear radio-M_{BH} correlation was fit for all the detected radio sources above a black hole mass of ~10^7 $M_\odot$ and found to have the form of L_{core}~$M_{BH}{}^{1.1\pm0.2}$ with a Pearson correlation coefficient (r-value) of 0.574. This r-value shows the likelihood of the two quantities not correlating as less than 3.15×10^{-6}. Conversely, the correlation is much less significant if all detected radio sources for the entire range of BH masses is included in the fit, with an r-value of 0.642 with a probability of 4.3×10^{-4}, due to the radio-M_{BH} break at ~$10^{6.6}$ $M_\odot$ causing a much flatter correlation (L_{core}~$M_{BH}{}^{0.7\pm0.2}$).

Overall, both the LINERs and Seyferts (the 'active' galaxies), and the ALGs appear to broadly follow the correlation, indicating that the radio core emission is likely dominated with an AGN. Interestingly, the H II galaxies which have both jetted radio morphologies and

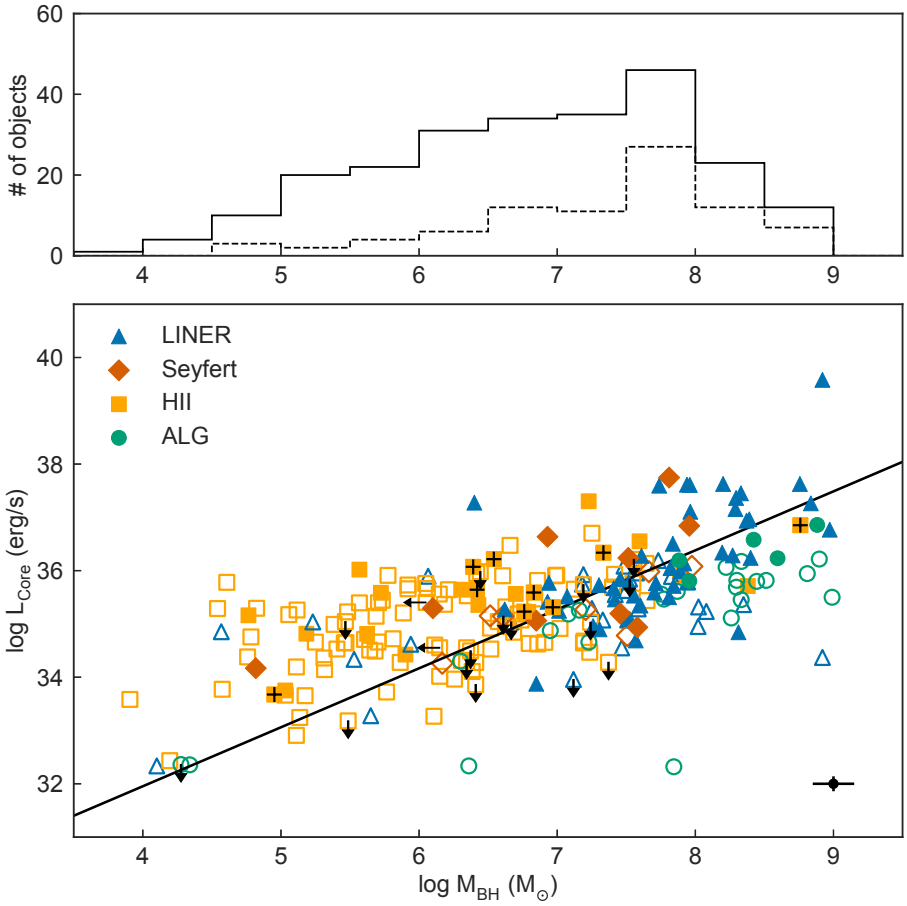

Figure 5.5: In the upper plot, I show the histograms of the entire sample (solid line) and of the detected/identified sources (dashed line) in bins of BH mass to estimate the detection fraction. In the lower panel, we show the radio core luminosities (L_{core} in erg s^{-1}) as a function of the BH masses ($M_\odot$) for the sample, divided per optical class (symbol and color coded as in the legend). The jetted HII galaxies show an additional plus symbol. The filled symbols refer to the detected radio sources, while the empty symbols refer to undetected radio sources. The unidentified sources are the empty symbols with radio upper limits. The solid line represents the linear correlation found for all the jetted or active galaxies (corresponding to $M_{BH} \gtrsim 10^7\ M_\odot$). In the bottom-right corner, we show the typical error bars associated with the points.

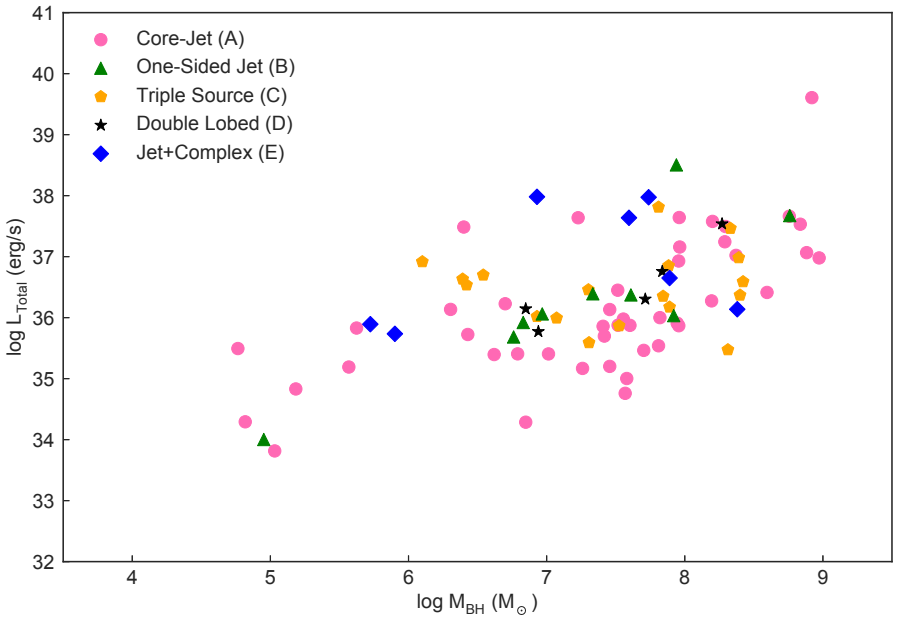

Figure 5.6: The total radio luminosity (L_{tot} in erg s^{-1}) as a function of the BH masses ($M_{\odot}$) for the sample, divided per radio morphological class A, B, C, D, and E (symbol and color coded according to the legend).

have $M_{BH}>10^6$ $M_{\odot}$, mostly follow the correlation, as well as one source at $\sim10^5$ $M_{\odot}$. In contrast, the non-jetted H II galaxies tend to fall on the plateau with $M_{BH}<10^6$ $M_{\odot}$. This difference between the radio morphologies of the nuclei in the H II galaxies suggests that the former, jetted class are possibly associated with AGN-driven radio emission while those on the plateau of the radio-M_{BH} correlation are likely due to SF processes.

All of the radio morphological classes are represented along the radio-M_{BH} correlation (Fig 5.6). Specifically, core/core–jet structures are observed across the BH mass and total radio luminosity ranges. The other morphological radio types are generally found between 10^6 and 10^8 $M_{\odot}$. However, there is no overall trend to link specific radio morphological classifications to a given range of radio luminosities.

5.3.8 Radio properties and [O III] luminosity

The [O III] emission line is a forbidden line, coming from the narrow-line region near to the BH, on scales of pc to kpc. Despite being slightly dependent on the orientation of the ELR and obscuration of the AGN (e.g. Risaliti et al. 2011; Baldi et al. 2013a; Dicken et al. 2014; Bisogni et al. 2017), [O III] line luminosity, $L_{[O\ III]}$, it is a good indicator of the bolometric AGN luminosity (L_{bol}=3500×$L_{[O\ III]}$, Heckman et al. 2004).

The radio core luminosity as a function of the [O III] luminosity is shown in Figure 5.7, top panel, for the LeMMINGs sample. The three optical classifications (H II, Seyfert, LINER)

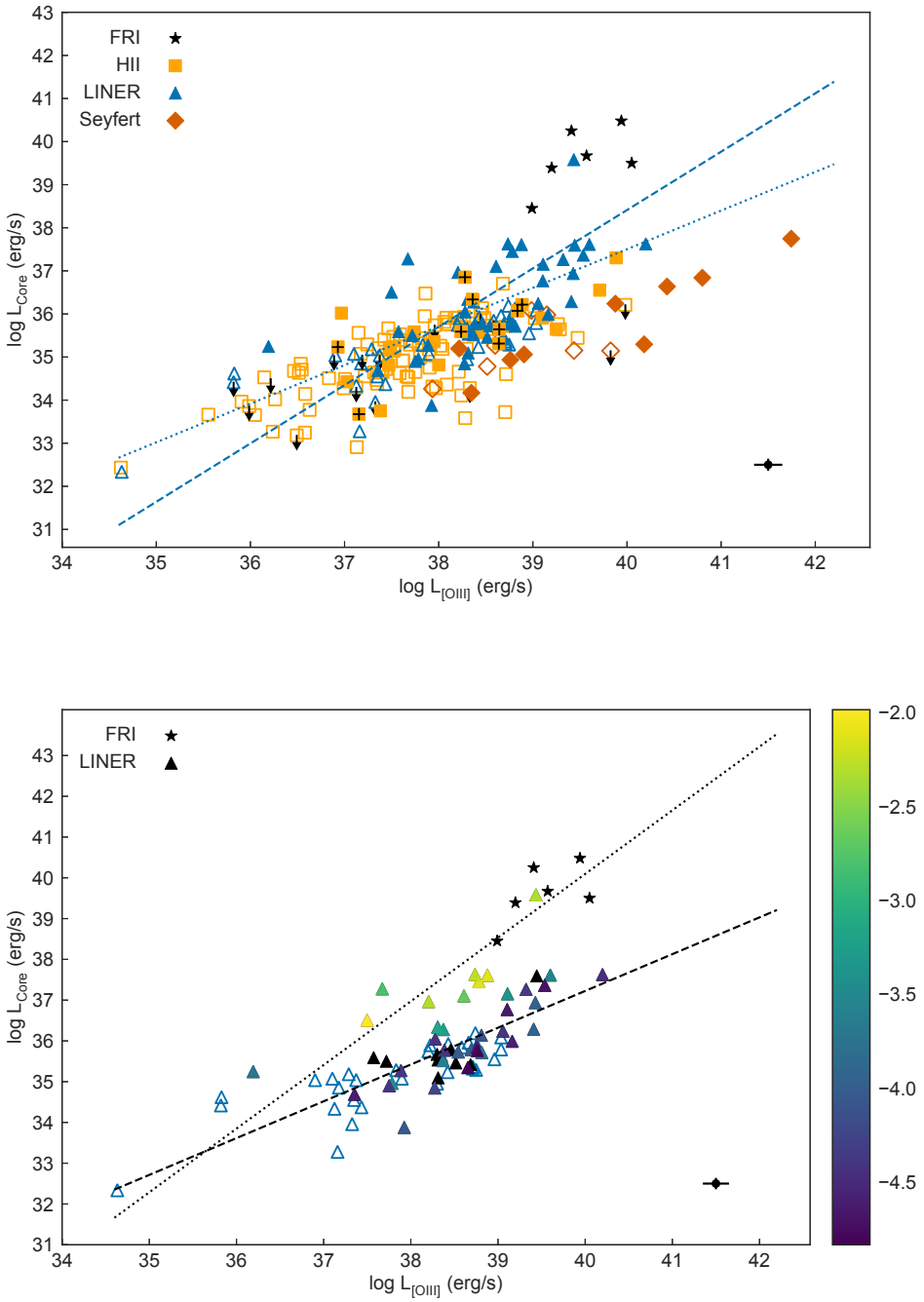

Figure 5.7: *Top panel:* [O III] luminosity ($L_{[O\ III]}$ in $ergs^{-1}$) vs radio core luminosities (L_{core} in $ergs^{-1}$) for the LeMMINGs sample. The different optical classes are coded (symbol and color) in the plot according to the legend. The jetted HII galaxies show an additional plus symbol. The filled symbols refer to the detected radio sources, while the empty symbols refer to undetected radio sources. The unidentified sources are the empty symbols with radio upper limits. The FR I radio galaxies are the filled black stars. The dotted line represents the linear correlation by fitting only the LINERs, while the dashed line represents the fit by including the FR I radio galaxies observed with MERLIN. The bars in the bottom-right corner indicate the typical errors for the data points. *Bottom panel:* Same as the top panel for the LINERs and FRIs only. The detected LINERs are coloured by their radio-loudness parameter shown as a colour bar on the right hand side of the plot (see text for definition). The dashed line corresponds to the fit for the LINERs with radio-loudness parameters <-3.0 and the dotted line corresponds to the fit for the LINERs with radio-loudness parameters >-3.0 and the FRIs from the MERLIN data.

Table 5.4: FR Is observed by MERLIN from literature.

name	z	F_{core} mJy	L_{core} erg s^{-1}	$L_{[O\ III]}$ erg s^{-1}	Ref
3C 66B	0.021258	180	39.40	40.05	FR97
3C 264	0.021718	170	39.39	39.20	BA97
3C 78	0.028653	700	40.25	39.41	UN84
3C 338	0.030354	163	39.67	39.57	GI98
3C 274	0.004283	530	38.45	38.99	GO89
3C 189	0.042836	512	40.48	39.94	BO00

Column description. (1) name; (2) redshift; (3)-(4) radio core flux density and luminosity from MERLIN observations from literature data; (5) [O III] luminosity from Buttiglione et al. (2010); (6) MERLIN radio references: FR97 Fraix-Burnet et al. (1997); BA97 Baum et al. (1997); UN84 Unger et al. (1984); GI98 Giovannini et al. (1998); GO89 Gonzalez-Serrano et al. (1989); BO00 Bondi et al. (2000).

tend to cluster in different regions of the [O III]-radio core plot: Seyferts have the highest [O III] luminosities while the H II galaxies have the lowest, with the LINERs at intermediate values. The Seyferts have a mean [O III] luminosity of 5.0×10^{39} erg s^{-1}, with a standard deviation of 1.2. In contrast, the H II galaxies have a mean [O III] luminosity of 1.5×10^{38} erg s^{-1} and a standard deviation of 0.85. Bridging the gap between the Seyferts and H II galaxies, LINERs have a mean [O III] luminosity of 3.5×10^{38} erg s^{-1} and a standard deviation of 0.72. In the first data release, RB and I reported that the LINERs appear to follow a linear trend in the [O III]-radio plot. For the original dataset, a tentative correlation of the form $\log(L_{[O\ III]}) \propto 1.35 \log(L_{core})$ was found, with an error on the gradient of 0.31. However, with the additional data in Figure 5.7, top panel, this is more difficult to assess and the fit with the additional CASA calibrated data is now $\log(L_{[O\ III]}) \propto 0.9 \log(L_{core})$ with a gradient error of 0.17.

The change in the $L_{[O\ III]} \propto L_{core}$ gradient needs investigating, therefore I have plotted in the bottom panel of Figure 5.7 the LINER-only data colour coded by the radio-loudness parameter extrapolated from the X-ray data explored in Chapter 6. The radio-loudness parameter, R_{opt} is usually defined as the radio between the radio and optical luminosities, but given that both of these parameters are plotted in Figure 5.7, it is prudent to use an independent assessment of the radio loudness. The X-ray radio-loudness parameter, R_{X-ray}, introduced by Terashima and Wilson (2003) to help identify radio-loud sources in heavily obscured AGN, but using radio observations from the VLA. Here, I define it as the logarithm of the ratio between the e-MERLIN core radio luminosity and the *Chandra* unabsorbed 0.3−10 keV luminosity (see Chapters 2 and 6). By plotting the LINERs as a function (shown in the colour bar in Figure 5.7, bottom panel), there is a bimodality in the radio-loudness parameter, split around R_{X-ray} = -3. By fitting the radio-loud LINERs, a correlation of $\log(L_{[O\ III]}) \propto 1.13 \log(L_{core})$ is observed (gradient error 0.35). The radio-quiet LINERs have a shallower slope, $\log(L_{[O\ III]}) \propto 0.90 \log(L_{core})$ with a 0.14 gradient error. The corresponding r-values for the radio-loud and radio-quiet fits are 0.636 and 0.777, indicating the two luminosities for LINERs do not correlate with a probability of

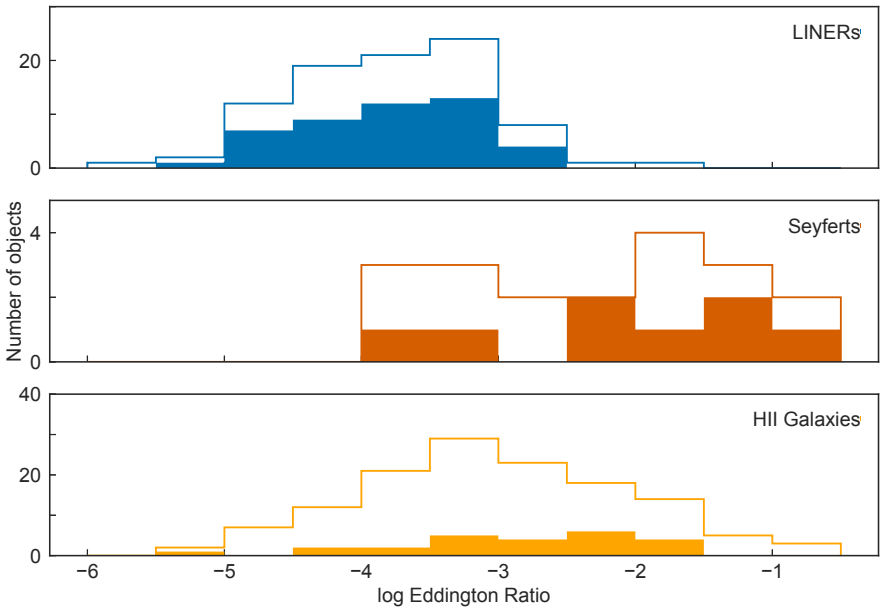

Figure 5.8: The Eddington ratio (ratio between the bolometric and Eddington luminosity) for the sources detected in [O III]: LINERs, Seyferts and HII galaxies. The distribution of the identified sources is shown as a filled histogram.

3×10^{-2} and 7×10^{-7} respectively. Furthermore, the sources with a core/core–jet or triple structure tend to follow the correlation, as they are mostly classified as LINERs. In a similar vein, most of the elliptical and lenticular galaxies also follow the correlation, and are often classed as LINERs.

LINERs and FR I galaxies are thought to have a common central engine, e.g. an ADAF disc with a coupled jet (Falcke et al., 2004; Nemmen et al., 2014). Hence, RB compiled a sample of 1.5 GHz MERLIN observations of FR I radio galaxies from the literature at z<0.05, to look for a continuation of the linear correlation found for LINERs in the LeMMINGs sample alone. There are six sources in the literature, which have similar resolution to our LeMMINGs data, which are listed in Table 5.4. These objects with the LeMMINGs data are shown in Figure 5.7, and indicated that the FR I galaxies extend the correlation to higher luminosities. The linear correlation obtained with the radio-loud LINERs and FR Is is $\log(L_{[O\ III]}) \propto 1.56\ \log(L_{core})$ and a gradient error of 0.24, with an r-value of 0.780, hence indicating a likelihood of 3×10^{-5} to be random. This correlation is also consistent within the uncertainties of the LINER-only LeMMINGs correlation. This indicates that the FR Is are the more luminous cousins of the radio-loud LINERs, extending to luminosities that are $10-10^3$ higher in the radio, but still in the low-luminosity regime. The radio-quiet LINERs on the other hand show a different correlation and may be the radio-quiet versions of FRIs.

Other than LINERs, the Seyferts tend to lie below the correlation as they are up to a factor of 100 more luminous in the [O III] emission line. On the other hand, the H II galaxies that

are detected as non-jetted radio sources (e.g. single core component or with a complex radio morphology) are above the correlation by up to a factor of 30. The jetted H II galaxies fall on the same line found for the LINERs, possibly indicating again that they are due to a central engine similar to a LINER. However, it is unclear whether the non-jetted H II galaxies are similarly powered, as they too often fall onto the correlation set by the LINERs and FRIs. Hence, the Seyferts are the only AGN type that shows a clear distinction from the others in this plot.

The Eddington ratio, as explained in Chapter 1, is a good proxy for the accretion rate onto the BH. In Table B.1, I have listed the bolometric and Eddington luminosities obtained from the radio and optical observations presented in this Chapter. The derived Eddington radios for the detected radio sources in the 'shallow' sample are presented in Fig. 5.8. If the [O III] line emission is assumed to be AGN-powered, then the Seyferts have the highest Eddington ratios, followed by the H II galaxies and then finally the LINERs. The Eddington ratios of LINERs are typically below 10^{-3}, while the values of Seyferts are above. This threshold is used to distinguish between low- and high-accretion onto the SMBHs (Best and Heckman, 2012). While the H II galaxies are less luminous, their Eddington ratios appear to be slightly higher than LINERs, but they may also include additional photo-ionisation from circum-nuclear SF processes which cannot be removed from the [O III] luminosity in the Palomar data. Higher resolution [O III] line data would be needed to disentangle the AGN and SF activity in the optical, and would likely lead to lower line luminosities in many of the sources. We do not find any correlation between the Eddington ratio and the radio core luminosity for our sample.

5.4 Comparing samples and Technical Discussion

5.4.1 Comparing the AIPS and CASA calibrated data

In Chapter 2, I discussed the different calibration pipelines used to reduce the radio data presented in this chapter. 103 objects in this thesis were reduced with AIPS and originally presented in Baldi et al. (2018b) and 138 new observations calibrated with CASA are included here. To assess any biases between these two calibration methods, I will compare the two in terms of detected and undetected sources, and note the differences in the calibration methods involved.

With regards to detections, the AIPS calibrated data recorded 40 'identified' sources and 7 'unidentified' sources, recording a detection fraction of ~46%. The CASA calibrated data had a slightly lower detection fraction, recording 44 'identified' sources and 9 'unidentified' sources, e.g. ~38%. As these two values are similar and less than 150 objects are included in both calibration methods, it is likely that the percentage difference in the two methods is purely down to low-number statistics, rather than the calibration method used. However, I explore this further below to understand this possible discrepancy.

In terms of AGN optical types, the 'active' galaxies would be expected to have more radio emission, and hence the Seyferts and LINERs could be responsible for the changes in observed detection fraction. The AIPS calibrated data included 52 H II galaxies (50%), 33 LINERs (32%), 14 ALGs (14%) and 4 Seyferts (4%), compared to the CASA data which had 67 H IIs (49%), 44 LINERs (31%), 15 ALGs (11%) and 12 Seyferts (9%). There are more Seyferts as a percentage in the CASA calibrated sample but fewer ALGs. However, the number of active galaxies differs only by 4% in the two different calibration regimes, with more 'active' objets in the CASA calibrated data, hence the AGN type is unlikely to be able to explain this difference.

In terms of galaxy morphology, more radio emission is expected from early-type (elliptical and lenticular) galaxies as the mergers would drive accretion and hence outflows in the form of radio jets. The AIPS calibrated data has 74 spirals (72%), 15 lenticulars (15%), 12 ellipticals (12%) and 2 irregulars (2%), whereas the CASA calibrated sample has 85 spirals (62%), 30 lenticulars (22%), 13 ellipticals (9%) and 10 irregulars (7%). The large number of irregular galaxies in the CASA sample compared to the AIPS sample may be a contributing factor to the non-detections, but the fraction of spirals changes by a similar amount between the two calibration groups. Hence it is unclear whether the galaxy morphologies are significantly different between the two samples to cause the difference in detection ratios.

I also looked for a difference in the two calibration methods with regards to the AGN black hole mass, as that has been shown to correlate well with likelihood of detection (see Fig 5.5). However, the mean and median black hole masses are similar for both the samples: $10^{6.85}$ $M_\odot$ and $10^{6.93}$ $M_\odot$ for the AIPS calibrated data and $10^{6.83}$ $M_\odot$ and $10^{7.01}$ $M_\odot$ for the CASA calibrated data. Furthermore, the standard deviation of the black hole masses are also similar between the two samples and there it is also unlikely that differences in black hole mass between the two samples has caused the difference in detection statistics.

Another consideration is the data quality in the two calibration methods. The median rms in the LeMMINGs CASA calibrated blocks is 87μJy/beam, compared to 82μJy/beam in the AIPS calibrated data. This difference in rms levels could potentially skew the 3σ detection limit so having more galaxies observed in the AIPS data, although it is unlikely responsible for the additional 10 galaxies that are required from the CASA calibrated data to reach the detection level of the AIPS calibrated data. However, it should also be noted that the CASA calibrated data include more modest datasets (7) compared to the AIPS calibrated data (4). This could potentially explain why the median rms is different between the two differently calibrated samples and hence why fewer objects are detected in the CASA calibrated data.

With regards to data quality, the amount of flagging could potentially make a difference to the number of detected sources. Figure 2.1 shows the output flagged raw data file using the AOFlagger software implemented in the CASA pipeline. In general, the AOFlagger software seems to make appropriate flags more often than the SERPent (AIPS) flagger, as very few manual flags are needed during the calibration process. The AIPS calibrated data often required several hours of manual flagging on each block to ensure that the data quality

was good enough for calibration. This difference in the pipeline flagging algorithms could potentially cause small noise components to be included in the AIPS data which would be flagged in the CASA calibrated data, and hence folded into the final images.

Finally, I consider the numerical statistics of these data, comparing the number of detected sources in the AIPS calibrated data to the CASA calibrated data, to show whether there is a purely statistical reason for the detection discrepancies. If one considers these detection statistics as a binomial distribution, then the variance one would expect on n detections in a sample of x is $\left[x\left(\frac{n}{x}\right)\left(1-\frac{n}{x}\right)\right]^{0.5}$. For the AIPS sample, this gives an error of detected sources of ±5, and for the CASA sample, the error is ±6. These values yield detection fractions which are consistent with one another within the uncertainties. Therefore, the two calibration methods produce consistent results statistically and possibly any differences between the calibration methods can be put down to the low number (less than 150) of sources in each of the calibration samples. However, I note that a full re-reduction of the AIPS calibrated datasets with CASA is necessary to truly understand the intrinsic differences between the two calibration methods. Such a reduction will need to be performed in future before final publication of the entire sample and before the data becomes publically available.

5.4.2 Statistics

Throughout this Chapter, I have been considering only the detected sources for performing statistical analysis and correlations. However, some sources may have been detected below the noise level of the LeMMINGs survey. The difference in noises levels may impact the detection statistics of the differently calibrated datasets discussed in the previous section. Hence, the correlations presented in this Chapter (and the next), should be considered as conservative estimates of the true population. However, I note that in all of the correlations I have presented in this Chapter, the upper limits do not sit far from the observed correlations and are therefore unlikely to have a significant effect on the results presented in this thesis. But I will comment on the possible differences below.

To correctly fit the data, it is necessary to fit the whole population, including the upper limits, e.g. the censored data. In future publications of this work with the entire radio sample observed, I will be fitting the data including all the data points, detected and undetected. In order to model and fit the undetected objects properly to any regression line, it is necessary to consider the probability distribution of each source below their detection limit. To properly account for the upper limits, a Bayesian regression routine is therefore required. Several are available in the literature, but few can take into account measurement errors in both the dependent and independent variables. In Chapter 7, I will outline a Bayesian regression routine that I have used to fit the Fundamental Plane of Black Hole Activity for the detected sources in the LeMMINGs sample. This routine will be edited in future to include fitting of upper limits in a Bayesian way and also is able to deal with

correlated uncertainties, such as the distance is the radio and [O III] line luminosities.

5.4.3 The LeMMINGs 'deep' sources as seen in the 'shallow' data

In this section I will go through a some of the sources that were either observed as part of the e-MERLIN 'deep' sample, comparing them to the newer LeMMINGs 'shallow' survey data. Other than specific sources with structures not presented in the main data release or future data releases, all of the images of the following sources in this section and the next section can be found in Appendix B.

NGC 4151

As the LeMMINGs 'deep' sample is a subset of the 'shallow' sample, it is possible to directly compare the radio emission in the two samples. NGC 4151 is the first of the two galaxies I have discussed from the 'deep' sample in this thesis. The 'shallow' sample was observed ~2 years after the 'deep' sample. As such, it is unlikely to have varied much. However, it is important to confirm the doubling of flux of the nuclear component observed in the 'deep' data in Chapter 3 to ensure that it wasn't due to a calibration error. The NGC 4151 'shallow' sample data were also calibrated with the CASA e-MERLIN pipeline whereas the 'deep' data were calibrated with the AIPS pipeline, which allows for good cross calibration of the two pipelines.

The CASA-calibrated LeMMINGs 'shallow' sample data for NGC 4151 show the same increase in flux as the AIPS-calibrated LeMMINGs 'deep' data. The two datasets also agree in the reduction of flux of the nearest component to the core, C3. It is encouraging that the two datasets agree within errors and suggests that in future, bright sources such as NGC 4151 can be observed with smaller on-source observing time to look for variability over year-long timescales.

NGC 5322

As part of my Ph.D. research, I reduced the e-MERLIN 'deep' sample data for NGC 5322, an elliptical galaxy with a double-sided jet structure (Dullo et al., 2018a) on the north/south axis of the galaxy. The southern jet is much more clearly defined in the 'deep' data than the northern jet, which is much weaker. The e-MERLIN 'shallow' survey detects a compact core with a secondary compact component immediately south of the core with a couple of additional bright radio components further south in the jet, indicating areas where the jet is interacting more with the ISM. The northern jet is not detected in the 'shallow' data, as it doesn't have as many bright knots of emission as the southern jet in the 'deep' data. It is interesting to note this difference between the two datasets as it indicates that at worse sensitivities the radio jets in nearby sources fall below the detection limit, and as such we

may be missing more jets in the objects we have detected with the 'shallow' sample. Certainly, the single sided jets in the LeMMINGs 'shallow' sample may also have a companion jet on the opposite side.

NGC 6217

The second 'deep' source I have presented in this thesis (Chapter 4) is NGC 6217. Like NGC 4151, the NGC 6217 data was calibrated using the CASA e-MERLIN pipeline, but unlike NGC 4151, it is intrinsically faint in the 'deep' data: the bright hotspot only has a peak flux density of 0.45 mJy/beam. For the best quality images, it is possible that this flux density would correspond to a 5σ detection on the hot-spot, but the low-level radio emission associated with the lobes would not be detected.

The LeMMINGs 'shallow' data have some low-level emission around the nucleus, but curiously the hot-spot is not detected. However, given the noise level in the map being poorer than most (rms = 0.102 mJy), the hot-spot would not have been detected at 3σ significance. Therefore it is unsurprising that it wasn't detected. But, a bright spot of emission is detected near to where the nucleus should be which is surprising at 0.45 mJy/beam. Hence, it is unclear whether that the 'shallow' data image is showing the LLAGN that has turned on, the 'deep' data has unflagged RFI in it which is causing bright spots to be picked up elsewhere or if the positions have not been properly extrapolated from the phase calibrator. Never-the-less, NGC 6217 is an interesting source that warrants further investigation.

IC 10, NGC 5194 (M51) and NGC 3034 (M 82)

The star forming galaxy IC 10 was investigated as part of the LeMMINGs 'deep' survey by Jonathan Westcott (see Westcott et al., 2017, , hereafter JW). JW found several compact H II regions, background sources and SNe remnants in the galaxy. Westcott et al. (2017) did not find any evidence of a central SMBH in IC 10. The brightest sources reached a peak flux density of ~1 mJy/beam, but often were diffuse across a couple of arcseconds. In addition, the LeMMINGs data required cross-matching with VLA images to help ensure identification of genuine sources, which is something not undertaken so far in the LeMMINGs 'shallow' survey. The LeMMINGs 'shallow' data did not detect any sources despite several of them being over the detection threshold of the observations for that data (3σ = 0.27mJy/beam). It is possible that some detections of the sources have therefore been missed in this case and potentially others. In addition, this source was calibrated using AIPS and therefore it would be prudent to re-calibrate the data using the CASA pipeline with the more robust flagging software to help identify real sources.

The LeMMINGs 'shallow' sample data for M 51 was included in Rampadarath et al. (2018) as the 'deep' data had several calibration problems. Hence it is not possible to make any

comparisons between the 'deep' and 'shallow' datasets. However, it does show a double-jetted structure, indicating the presence of an AGN, over 10″ scales. Further high-resolution radio data is required to compare how a 'deep' e-MERLIN image of this source would appear, as it is potentially similar in the 'shallow' maps to NGC 5322. Never-the-less, it shows the power of the 'shallow' LeMMINGs sample to help isolate for future publications of specific sources; the LeMMINGs 'shallow' survey is not just powerful in terms of its statistical completeness, but helps disentangle physical mechanisms of acrretion in individual cases.

M 82 is a well-known starburst galaxy that has a large amount of extinction in the optical and infra-red bands, making radio observations necessary for detecting and investigating supernovae in the galaxy. There are dozens of supernova remnants and these have been followed by e-MERLIN over the last few decades (e.g. Muxlow et al., 2010). The 'shallow' sample data resolves out a lot of the diffuse radio emission but is still useful for detecting the compact unresolved SNRs, SNe and H II regions in the galaxy. The new LeMMINGs 'shallow' sample data of M 82 detects more than 20 SNRs. Amongst them is the supernova 2008iz which is the brightest source in the LeMMINGs images of M 82 and still has a peak luminosity of ~60 mJy at 1.5 GHz. This bright source is likely due to the formation of dust $\gtrsim$1000 days after the explosion and has been described by (e.g., Brunthaler et al., 2010a,b; Kimani et al., 2016). There are several other interesting sources in M 82, notably the radio transient discovered by Muxlow et al. (2010) at RA $09^{h}55^{m}52.5083^{s}$, Dec. +69°40′45.410″ (J2000) which is not seen in our 'shallow' images. One of the interesting sources detected in the LeMMINGs 'shallow' data is 41.95+575, which has a double-lobed structure at VLBI resolution and has been decreasing at ~8% per year for the last 5 decades. Hence, 41.95+575 may in fact be a remnant of a Gamma Ray Burst instead of a conventional SNR (Muxlow et al., 2005).

5.4.4 Science with the LeMMINGs 'shallow' objects

In this section I will briefly discuss some of the potential scientific output from a selection of sources that have been observed as part of the 'shallow' survey that show interesting radio morphologies. As the LeMMINGs sample is a legacy dataset, it is important to identify the galaxies of interest, some of which may never have been observed before, especially at the high resolution and sensitivity of the e-MERLIN interferometer, to look for new and interesting radio emission. The list below is by no means exhaustive, but gives a glimpse of the sensitivity and power of such high-resolution observations performed with e-MERLIN in isolation.

LLAGN and jets

Several of the LeMMINGs objects show jet-like and lobe-like structures, thought to be related to AGN activity. The 'shallow' survey observations show that for some sources at

least, these structures are bright enough in nearby galaxies to study with short observations and potentially monitor to see how they evolve over long periods.

NGC 4051 is one of the objects that show a double-sided jet in the 'shallow' survey. It is a well known Seyfert with plenty of archival data at multiple radio frequencies and resolutions (for example, see Jones, 2012). In the LeMMINGs 'shallow' observations, NGC 4051 has a brighter eastern jet component than the core, which possibly indicates relativistic beaming of that side of the jet towards us. However, 8.4 GHz VLA A-configuration data show that the core and eastern component have similar flux densities (Jones, 2012). As the 1.5 GHz e-MERLIN observations and 8.4 GHz VLA A-configuration observations have similar beam-sizes, it suggests that the eastern component has a flatter spectral index than the core, possibly indicating continued injection of particles into that component. In addition, the western jet appears to separate into two components in the full resolution LeMMINGs image, which is not observed in the VLA data from Jones (2012).

Another source with double-sided jets is NGC 5005, a LINER-type nucleus. At lower resolution, the LeMMINGs images show lobes over nearly half an arcminute in size. This emission is not attributed to the radio emission in the disk observed with the VLA (Richards et al., 2015), indicating that the lobes are likely related to genuine nuclear outflows. Another similar source is NGC 3348 which is an ALG, which has not been observed much in the literature and would be a good candidate for future observsations to diagnose the nature of the lobes, e.g. either due to relic emission or a more recent injection of particles. Hence, the LeMMINGs sample provides the necessary resolution and sensitivity to detect these small radio lobes/jets in nearby galaxies, but multi-wavelength data is needed at similar resolution to diagnose the nature of the emission.

Star formation

While M 82 and IC 10 have had some deep images of the SNRs and H II regions in them, several other star-forming galaxies exist in the broader 'shallow' sample. Several of these objects have never been observed in such high-resolution and sensitivity radio observations before and merit further investigation to conclude the nature of the radio sources in these observations.

One such object is IC 342, which is a star forming galaxy with several known ULXs and XRBs, as well as some known radio sources. In the LeMMINGs 'shallow' data, four sources are observed within 4″ of the optical centre of the galaxy, but none are within 2″ of the centre. It is likely that these sources are in fact H II regions or SNRs in this star forming galaxy that have been previously undetected. This is supported by their morphologies a they are largely unresolved, even in the low resolution images, similar to the SNRs in M 82.

The e-MERLIN LeMMINGs 'shallow' sample data reveal a star-forming ring in the central nuclear region of NGC 5273. However, 15 GHz VLA data obtained in A configuration by Saikia et al. (2018) show a single unresolved core. Curiously, the unresolved core does not

line up with the brightest component in the LeMMINGs image. These two observations at different frequencies but matching resolution show that multi-frequency coverage of LLAGN is needed to remove the contribution of star-formation from the images.

Tidal disruption events

The interacting galaxy NGC 3690 is made up of two separate spiral galaxies: Arp299a and Arp299b. The new LeMMINGs 'shallow' survey data detect three sources of radio emission in NGC 3690: one source corresponds to each of the Arp interacting galaxies, and the other corresponds to a potentially undiscovered H II region/SNR. There are also two known SNe in this galaxy merger, which wider field imaging will aim to detect in future investigations. Specifically, the source in Arp299b is actually a transient source which was first observed in 2005 (Mattila et al., 2005). Subsequent radio and IR observations showed an increase in luminosity over several years, and it is now thought to be a tidal disruption event (Mattila et al., 2018, and references there-in). A tidal disruption event (TDE) is the ripping apart of a star that falls close to a SMBH, with half of the star's material falling onto the BH and the rest escaping. The subsequent accretion of matter onto the BH allows for multi-band emission as well as radio jets to be produced (e.g., van Velzen et al., 2016).

The TDE in Arp299b is one of the best studied events of this class, with the radio jets appearing to accelerate at 0.99c immediately after their production, but have since slowed down in recent years to 0.25c (Mattila et al., 2018). While the e-MERLIN observations presented here do not have the same angular resolution as the VLBI observations presented in Mattila et al. (2018), they are 2 years after the last VLBI observation, so it is worthwhile estimating how much movement there would be over the short time-scale. At the distance of NGC 3690 (44.8 Mpc), and assuming the radio jet is still expanding at 0.25c, over two years a movement of 0.15 pc would be expected, corresponding to an on-sky movement of ~0.7 mas, much smaller than the 150 mas beam of e-MERLIN at 1.5 GHz. However, this scale is encouraging for future observations with e-MERLIN of TDEs as the 5 GHz and 22 GHz bands have a resolution of 40 mas and 12 mas respectively, opening up the opportunity to study these exotic events with e-MERLIN observations in the future. This would especially exciting for observations taken immediately after the event, when the jet is expanding at velocities approaching the speed of light.

5.5 Scientific Discussion

The LeMMINGs 'shallow' survey represents the deepest radio study of the Palomar survey to date, reaching an rms sensitivity of ~70μJy. More importantly, the LeMMINGs sample probes activity in all galaxies, irrespective of known activity in the nucleus from optical emission line diagrams. This characteristic makes the LeMMINGs survey very powerful and distinct from previous observations of the Palomar survey which only observed Seyferts

and LINERs. In this chapter, I have presented the radio observations for 241/280 objects in the LeMMINGs sample as well as comparing them to the optical [O III] forbidden line emission luminosity from the Palomar survey. In total, 100/241 (42%) of the sample were detected at 1.5 GHz by LeMMINGs. This detection rate is consistent with previous radio observations of the Palomar sample with the VLA/VLBA (see Ho 2008 for a review), which focussed mostly on the active sources e.g. the Seyferts and LINERs. Furthermore, for 84/100 (~84%) of the sample, radio emission within the central 2.0″ of the optical centre of the galaxy is observed, indicative of an active SMBH.

Comparison with previous radio studies is non-trivial as the transition galaxies were reclassified by the new discriminating BPT diagrams described in Chapter 2. However, for the active sources in the BPT diagrams, e.g. LINERs and Seyferts, more than half show compact radio cores or jetted structures. Of the identified sources, ~40% show one of the clear jet-like morphologies (e.g. triple sources, twin jets, double lobed, one-sided jets, 32/84). Interestingly, ~38% of the sources identified as H II galaxies in BPT diagrams show jet-like structures in their core, a possible sign of an active SMBH. Seven sources have a complicated structure (jet+complex category) and may have a radio jet associated with an AGN with some diffuse SF. The most common radio morphology observed in the LeMMINGs sample is the core/core–jet morphology 45/84. This is unsurprising as the high-resolution of e-MERLIN can resolve out some of the diffuse emission associated with jets, unless the jet is intrinsically luminous. The nature of these unresolved radio components, whether an unresolved radio jet base or a SF nuclear region on the scale of <100 pc, can be revealed by using further diagnostics such as [O III] luminosities and BH masses in the absence of clear jet-like structures. These multi-wavelength data are discussed in the following sub-sections.

5.5.1 LINERs

The LINERs in the LeMMINGs sample have the largest number of radio detections and are hosted in elliptical, lenticular and spiral galaxies. The detection rate (50/77, 65%) of the LINERs is higher than in the previous Palomar sample (~44%, Ho 2008). In the LeMMINGs sample, LINERs tend to be associated with single radio core components (27/46), but are also detected as triple radio sources which turn into twin jets at lower resolutions (11/46), double-lobed structures (4/46), one-sided jets (3/46) and complex morphologies (1/46). Only four objects lack an identification of the core. The LINER radio luminosities are higher than Seyferts and HII galaxies by a factor 2-3 on average.

As mentioned in previous chapters, the emission line ratios of LINERs can be produced by an AGN, or shocks, or post-AGB stars, or potentially a combination of processes (Allen et al., 2008; Sarzi et al., 2010; Capetti and Baldi, 2011; Singh et al., 2013). However, there are several points that indicate an AGN origin for the radio emission in the LeMMINGs sample. First, the LINERs are often associated with symmetric radio jets on scales from

~0.05-1.7 kpc. Such morphologies cannot easily be explained by SF at the typical LINER luminosities of $\sim 10^{36}$ erg s^{-1}, as SF is dominant in the sub-mJy regime below 10^{34} erg s^{-1} (Bonzini et al., 2013; Padovani, 2016). Second, the radio jets are core-brightened, similar to FR Is, suggesting that the jets are probably collimated and launched relativistically, but slow down along the jet propagation axis. This characteristic is similar to what is seen in nearby low-luminosity radio galaxies (Parma et al., 1987; Morganti et al., 1987; Falcke et al., 2000; Giovannini et al., 2005). Third, the radio core luminosities for LINERs correlate with the BH masses, suggesting further that the SMBH has a role in the production of radio jets in LINERs. Finally, the brightest radio core flux densities and hence the highest brightness temperatures are associated with the LINERs. There are fourteen LINERs with radio cores (> 5 mJy) and hence have brightness temperatures $>10^6$ K, indicating the synchrotron emission from radio jets associated with a SMBH. This interpretation is supported by high brightness temperatures ($>10^8$ K) of radio cores detected with the VLBA for LINERs (Falcke et al., 2000).

The LINERs are associated with different types of host galaxy, but they tend to have some of the largest BH masses ($>10^7$ $M_\odot$) and some of the lowest accretion rates ($<10^{-3}$ Eddington rate). This combination of low accretion rate and large black hole mass is commonly interpreted as a radiatively inefficient disc model, usually as an advection-dominated, geometrically thick, optically thin accretion disc (ADAF, see reviews from Narayan et al. 1998; Narayan and McClintock 2008). As LINERs are usually radio louder than the other optical classes (Capetti and Balmaverde, 2006; Kharb et al., 2012), it is likely that these properties can be described by an ADAF disc which can efficiently produce radio jets. This is corroborated by multiple theoretical and analytical studies (Narayan and Yi, 1994; Meier, 2001; Nemmen et al., 2007; Begelman, 2012) as well as numerical simulations (Tchekhovskoy et al., 2011; McKinney et al., 2012; Yuan et al., 2012). The ADAF disk and jet model is similar to FR I radio galaxies (JDAF, Falcke et al. 2004). The radio-loud LINERs and a small sample of MERLIN FR I galaxies follow a similar [O III]-radio correlation but the radio-quiet LINERs seem to fall off this correlation. Therefore, it is likely that the FR Is and LINERs share the same central engine but the FR Is are scaled-up versions of the LINERs. This result is analogous to what has been found for low-luminosity radio-loud LINERs in early-type galaxies (e.g., Balmaverde and Capetti 2006a).

5.5.2 Seyferts

There are sixteen Seyferts in the LeMMINGs sample observations presented in this thesis, based on the revised BPT diagrams. The Seyferts are mostly found in spiral galaxies, but not all of them are detected at 1.5 GHz (10/16, 63%). The Seyferts with the higher BH masses are preferentially detected in the radio. One source, (NGC 5273, a lenticular galaxy) does not show a radio core at 1.5 GHz, but a ring of radio emission possibly associated with SF. However, at 15 GHz, Saikia et al. (2018) showed that only one component in NGC 5273 is detected and that it could be associated with a radio core. The radio morphologies

observed for the nine detected and identified Seyferts are: five core/core–jets, two triple sources, one double-lobed source and one with a complex morphology with a possible jet, all suggestive of a jetted structure on a scale of ~50-400 pc. The detection rate is larger than previous radio surveys of the Palomar sample for this class of sources (~47%, Ho 2008). The larger detection rate in the LeMMINGs data can possibly be attributed to the sensitivity of the e-MERLIN interferometer.

The high emission line ratios found in Seyferts necessitate photo-ionization from an AGN (Kewley et al., 2006). But, it is not clear whether the observed radio emission in Seyferts arises from active SMBHs or SF. In the LeMMINGs survey, the jets of Seyferts appear to be more edge-brightened than LINERs and similar to the radio morphologies of local Seyferts (e.g. Kukula et al. 1993, 1995; Gallimore et al. 1996; Morganti et al. 1999; Wrobel 2000; Kharb et al. 2006). For four of the Seyferts identified in the LeMMINGs sample, diffuse radio structures appear in the lower resolution images resembling radio lobes. Such structures appear to be more common in Seyfert galaxies than LINERs (Baum et al., 1993; Gallimore et al., 2006). The larger lobe structures indicate that the jets are not necessarily relativistic at the core and they eventually hit the surrounding interstellar medium causing a bow shock, hence resulting in a bubble-like outflow. AGN can explain these radio structures, either from a weak jet, a turned off radio source that expands into the ISM or in inverted spectrum sources (e.g., see Chapter 4), but it is not possible to rule out SF super winds causing the observed lobe structure (Pedlar et al., 1985; Heckman et al., 1993; Colbert et al., 1996b).

As mentioned previously, the Seyferts tend to have a [O III] line excess with respect to the [O III]-radio correlation found for LINERs (Fig. 5.7). This excess suggests that a brighter ionising nuclear source than an ADAF disk is required at the centres of these galaxies. As the [O III] line luminosity is a proxy for the AGN bolometric power, higher accretion rates ($>10^{-3}$ Eddington rate) are required to explain these properties in Seyferts. Therefore, the central engine in Seyferts is likely different to that in LINERs. For example, a geometrically thin, optically thick standard disk Shakura and Sunyaev 1973 is commonly inferred in Seyfert nuclei to account for the multi-band properties of Seyferts. Such disks are not as efficient as ADAFs at launching jets but are still able to produce less collimated and slower jets (e.g. see Yuan and Narayan, 2014, and references therein).

Many of the Seyferts in the LeMMINGs sample are associated with radio jets, similar to previous studies of local Seyferts (e.g. Ho, 2008). The presence of low-power radio jets in Seyferts suggests that they are an intermediate regime of accretion activity between the JDAF dominated LINERs and the near-Eddington luminous QSOs (Ho, 2002, 2008; Kauffmann et al., 2008; Sikora et al., 2008). It is plausible that this intermediate stage is simply an evolutionary transition between the efficiently accreting thin disks to the inefficient ADAFs, tuned by the accretion rate and/or disc radiative efficiency (Trippe, 2014). However, it is difficult to make concrete evaluations of the evolutionary track of accretion due to the paucity of radio studies of QSOs in the literature, as they are at higher

redshifts. It is difficult to ascertain whether the emission in radio-quiet AGN is due to a scaled-down version of a radio-loud jet (Barvainis et al., 1996; Gallimore et al., 2006), coronal emission from magnetic activity above the accretion disc as an outflow (Field and Rogers, 1993; Laor and Behar, 2008; Behar et al., 2015), or thermal free–free emission/absorption (Gallimore et al., 2004). The exact form of the emission in radio-quiet AGN like Seyferts therefore still remains to be fully understood.

5.5.3 Absorption line galaxies

As mentioned previously, ALGs lack evidence for BH activity but may still conceal an active BH. In the LeMMINGs sample, radio emission was detected for the nuclear region in 5/29 ALGs (~17%). In general, they are morphologically single radio cores (3/5), but are also seen as triple sources (2/5). The ALGs in the LeMMINGs survey are generally found in elliptical or lenticular galaxies, which harbour SMBHs with masses larger than 10^8 $M_\odot$ and the ALGs have similar radio luminosities to the LINERs in the LeMMINGs sample.

As the ALGs have a lack of available detected optical emission lines, it limits the analysis of AGN bolometric luminosities or SF rates. Hence, a complementary multi-band study of ALGs is needed to ascertain whether they have active SMBHs or not. A cross-matching of optical SDSS (Stoughton et al., 2002) and radio FIRST (Becker et al., 1995) data of local radio galaxies shows that for galaxies with no emission lines, the radio emission, nuclear properties and host properties associated with them is similar to that of LINERs (Baldi and Capetti, 2010), although at higher luminosities than the LeMMINGs sample (10^{39}-10^{41} erg s^{-1}). Baldi and Capetti (2010) showed that extended radio structures were found in ~27% of ALGs, slightly higher to the detection rate of ALGs in LeMMINGs. Hence, the LeMMINGs observations argue for the presence of an active SMBH in at least a fifth of ALGs, which is supported by previous studies also.

In contrast, the lack of evidence of an active SMBH in a large number of ALGs could be due to a nuclear recurrence scenario due to an intermittent accretion phenomenon (Reynolds, 1997; Czerny et al., 2009). Given the large fraction of undetected ALGs in the LeMMINGs survey and the detected sources, any AGN active phase must have a range of time-frames to explain the wide range of values with short active periods favoured over the longer ones. For NGC 6702, which has the largest extended radio jet for an ALG in the LeMMINGs sample (~700pc), and assuming a bulk jet speed of ~0.02c typical for low-power radio galaxies (Massaglia et al., 2016), the limit on the age of this source is ~1.3×10^5 years. This value is an upper limit of the length of radio activity in ALGs and is consistent with the typical duty cycles of radio AGN, i.e. 10^4-10^8 years estimated at different wavelengths (see Morganti 2017 for a review). Furthermore, this recurrent nuclear activity may explain the higher core dominance in the detected sources, indicating a younger radio structure.

5.5.4 HII galaxies

The H II galaxies are interpreted as SF-dominated nuclei, based off the emission line ratios in BPT diagrams, but this does not preclude them from having a weak AGN at the galaxy centre. H II galaxies have not been observed often in the literature except for exceptional cases like M 82 which has a large number of SNRs. Because of the lack of observations of H II galaxies, there is a lack of detections of AGN emission in the literature (~7.5%, Ulvestad and Ho 2002 and references therein). The LeMMINGs survey includes a representative sample of H II galaxies in the local Universe and have detected radio emission for 29% (34/119) of the H II galaxies. For the 24 identified H II galaxies, nine show jetted structures (one-sided and twin jets), ten show single core detections and five show complex morphologies. However for ten sources a clear core component indicating an AGN is missing from the e-MERLIN maps. The H II galaxies have, on average, lower radio luminosities than those of LINERs by a factor ~2 and radio structures of order 50-500 pc.

There are two different types of H II galaxy that appear in the LeMMINGs survey: jetted and non-jetted. The jetted H II galaxies (NGC 972, NGC 2146, UGC 3828, UGC 4028, NGC 3077, NGC 3665, NGC 4041, NGC 4217 and NGC 7798) are found to have higher black hole masses in general, larger than 10^6 $M_\odot$, possibly indicating the presence of an active AGN; the only one of these jetted H II galaxies not above this mass threshold is NGC 3077 ($10^{4.95}$ $M_\odot$). However, the emission line ratios for these jetted sources do not delineate from the non-jetted H II galaxies in a quantifiable way on the BPT diagrams. Further evidence for these nine jetted sources housing an AGN comes from them following the [O III]–radio correlation found for LINERs. Furthermore, NGC 3665, shows an FR I radio morphology at VLA resolution (Parma et al., 1986). Six sources NGC 972, NGC 2146, NGC 3077, NGC 3665, NGC 4041, NGC 4217 show one-sided jets, which might indicate the Doppler boosting effect of relativistic jets. This category of jetted H II galaxies probably do host an AGN but too weak to make a significant contribution to the optical emission line ratios in BPT diagrams and are probably dominated by nuclear SF. The LLAGN found in the jetted H II galaxies are similar to the sub-Eddington LINERs, rather than the efficiently accreting Seyferts. In addition, the jet morphologies are similar between the jetted H II galaxies and the LINERs (e.g., core-brightened) and roughly follow the LINER correlations too.

In contrast, the other H II galaxies which are non-jetted (NGC278, NGC 1560, NGC 2342, NGC 3198, NGC 3245, NGC 3310, NGC 3430, NGC 3432, NGC 3504, NGC 3938, NGC 4088, NGC 4100, NGC 4102, NGC 6217 and NGC 6946), generally have BH masses below $10^{6.5}$ $M_\odot$, show a clear deficit in the [O III] line by a factor ~30 and sometimes have a large radio excess with respect to the [O III]–radio correlation found for LINERs. These characteristics are consistent with a low-radiation field that is ionised by SF alone, accounting for both the observed radio and optical emission line properties.

At 1.5 GHz, most of the radio emission is of a non thermal nature, justifying the conclusion

that the radio emission from the non-jetted H II galaxies is like SF-related. To further emphasise the likelihood of the radio emission coming from SF, RB and I calculated nuclear supernova rates ν_{SN} assuming that the total radio emission is dominated by cosmic rays accelerated in supernova remnants (SNR), using the formula from Condon (1992), $L_{radio}/(1.4\times10^{38}$ erg s^{-1}) = 11 $\times(\nu_{SN}/\mathrm{yr}^{-1})$. The calculated SNe rate corresponds to 2×10^{-5} -6×10^{-4} yr^{-1} in the central core region of ~50 pc and compares favourably to the SNe rates expected in M 82 (15-30 yr^{-1} for the entire galaxy, Muxlow et al. 1994; Fenech et al. 2008) extrapolated to a region 100 times smaller, or 3-6$\times10^{-4}$ yr^{-1}. Furthermore, assuming that some radio emission comes from thermal stellar processes, the predicted free–free radio emission expected from the Hα luminosities ($10^{37.7-38.8}$ erg s^{-1}, Ho et al. 1997a) due to thermal stellar emission (Ulvestad et al., 1981; Filho et al., 2002) would be conservatively higher within a factor ~10 than the measured radio luminosities of AGN-dominated sources, i.e. Seyferts and LINERs. This would correspond to SF rates of 4×10^{-4}-5×10^{-3} $M_\odot$ yr^{-1} in the central radio core, derived from the Hα luminosities (assuming a Salpeter mass function for 0.1-100 $M_\odot$ and solar metallicity from Kennicutt, 1998). In conclusion all these calculations favour a SF origin of the radio emission, possibly from a pc-scale nuclear starburst, for the non-jetted HII galaxies.

Now that a large fraction of the LeMMING survey has been observed, it is clear that a small number of galaxies show intense bursts of star formation (Muxlow et al., 2010; Murphy et al., 2017; Herrero-Illana et al., 2017), e.g. M 82, based only on the radio properties. However, single radio components might hide unresolved nuclear star-bursts and complex radio morphologies might also be due to the presence of star-forming regions, possibly induced by radio jets (for example, see NGC 2273, NGC 2655 and NGC 4102). The only cases where the radio-optical results support for a possible star-forming scenario, are the non-jetted H II galaxies. In the unidentified sources, the nature of the detected radio emission is still unclear, but two objects (NGC 4013 and NGC 5273) clearly show circum-nuclear radio-emitting rings, which were not seen before at lower resolution. These two sources are the most evident cases of SF in our sample, based on their radio morphology.

For the objects further than 4 Mpc, which are the majority of the sample, the spatial frequencies covered by e-MERLIN are suited for detecting compact SNR (Westcott et al., 2017). However, the snapshot imaging technique used in this survey is not appropriate for detecting diffuse, low-brightness radio emission ($<10^5$ K), typical of old SNR. Conversely, young SNR and HII regions could be detected since they are more compact and brighter. At distances less than ~4 Mpc, VLA data are required to study old SNR (> 400–500 yrs), which would be resolved out by the e-MERLIN baselines. The addition of shorter spacing VLA data combined with the e-MERLIN data - as in Chapter 4 - to this project will enhance the ability to detect more diffuse lower surface brightness emission from SF products.

5.5.5 The host galaxies

Half of the early-type galaxies (e.g. ellipticals and lenticulars) in the LeMMINGs sample host a radio source coincident with the optical centre, that is determined to be an active SMBH. However, only ∼30% late-type galaxies (spirals and irregulars) have a radio-emitting central active SMBH, with irregulars only being detected in 2/12 objects in the sample. Quantitatively, the sample has detected radio emission in ∼50% of galaxies earlier than Sb and the detection rate drastically drops at later Hubble types, as only 21% of Sc-Sd galaxies are detected. Hence, the LeMMINGs sample agrees with the detection fractions of previous radio studies of the Palomar study (Ho and Ulvestad, 2001a; Ulvestad and Ho, 2001a; Nagar et al., 2005; Ho, 2008), which found flat-spectrum radio cores predominantly in massive early-type galaxies (Sadler et al., 1989; Wrobel and Heeschen, 1991; Capetti et al., 2009; Miller et al., 2009; Nyland et al., 2016).

This survey has detected nuclear activity for SMBHs with masses greater than 10^6 $M_\odot$, but it should be noted that the detection fraction greatly reduces below 10^7 $M_\odot$. Previous radio studies have shown that the radio brightness of AGN correlates strongly with the host/BH mass, proportional to M_{BH}^{α}, where α is usually in the range $1-2$, (Laor, 2000; Best et al., 2005a; Nagar et al., 2002; Mauch and Sadler, 2007). The LeMMINGs survey shows a similar correlation for the radio sources with jetted morphologies correlating with the BH mass. This dependence of black hole mass on radio brightness explains the detection ratios in the different galaxy morphologies, as the early-type galaxies tend to have more massive black holes than the late-types (Decarli et al., 2007; Gallo et al., 2008). The correlation between the radio detections with the BH mass or host type is an indirect consequence of a more fundamental relationship between radio luminosity and optical bulge luminosity (Ho, 2002; Nagar et al., 2002). The more massive elliptical galaxies are more efficient at producing radio emission as they have larger SMBHs, and hence, are more likely to be radio-louder than the spiral galaxies for M_{BH} $>10^8$ $M_\odot$ (Chiaberge and Marconi, 2011).

5.6 Conclusions

I have presented the LeMMINGs 1.5 GHz radio data for 241/280 galaxies, optically-selected from the Palomar sample (Ho et al., 1997a) with $\delta > 20^\circ$ at an angular resolution of 150 mas. The survey has detected significant radio emission in the central regions (0.73 arcmin^2) for 100/241 (∼42%) galaxies with flux densities $\gtrsim$0.2 mJy in all types of optically classified LLAGN, from the active Seyferts and LINERs to the quiescent (or inactive) H II and ALG type galaxies. For 84 sources, radio cores associated with the optical galaxy centre were found with a variety of radio morphologies: core/core–jet, one-sided jet, triple sources, twin jets, double lobed, and complex shapes with extents of 40–1700 pc. It should be noted that in previous studies with the VLA these sources would have been unresolved and the complex structures left undetermined, further showing the power of the unique

regime of high angular resolution (150 mas) and high sensitivity provided by e-MERLIN. The jetted radio sources in the sample (9 one-sided jets, 18 triple sources and 5 double-lobed sources) are associated with galaxies with $M_{BH} > 10^6$ $M_\odot$ (bar NGC 3077). The jetted sources are interpreted as a sign of the presence of an active SMBH. However, for those sources that show single cores or complex morphologies, (45 core/core-jet and 7 jet+complex), more caution is needed as the unresolved single components could be due to an unresolved jet base or due star-forming based cores.

As the sensitivity of the e-MERLIN observations are of order 70μJy/beam, the radio core powers of the sources (10^{32}-10^{40} erg s^{-1}) are of order 100 times lower than those measured from previous radio surveys of the Palomar sample, 10^{35} erg s^{-1} (Nagar et al., 2005; Filho et al., 2006). Considering the different optical classifications, the most common detected radio galaxies are LINERs and early-type galaxies, and typically show single cores or jetted morphologies. The Seyferts in the sample tend to be more edge brightened than the LINERs with intermediate luminosities, whereas the ALGs are mostly single cores and highly core-dominated. The detected H II galaxies in the sample show both jetted and non-jetted morphologies, but with lower radio luminosities compared to the 'active' classes of Seyferts and LINERs. The radio cores typically contribute to ~26% of the total detected emission. Concerning the host type, half of the early-type galaxies and one third of the late-type galaxies are detected in our survey. In addition, I have shown the radio luminosity function (RLF) of the LeMMINGs 1.5 GHz survey. The LeMMINGs RLF indicates that the H II galaxies and ALGs may explain the break in the RLF of previous studies of the Palomar survey, if these 'inactive' galaxies are considered LLAGN. This RLF gives credence to continued observations of LLAGN in the nearby Universe irrespective of prior knowledge of activity.

Empirical correlations between the core luminosities and BH masses and [O III] line luminosity are good diagnostics of SMBH activity and can be used to investigate the nature of the radio emission in sources of different optical type. In the LeMMINGs survey, the core power, indicative of the jet energetics, correlates with the BH mass for masses $\gtrsim 10^7$ $M_\odot$. However, at $\lesssim 10^6$ $M_\odot$, a plateau emerges in this correlation. The early-type galaxies (ellipticals and lenticulars) as well as the jetted galaxies (including the H II galaxies) tend to lie along this correlation. This results indicates a symbiosis between the SMBH activity and the jet production. For a hierarchical evolution of galaxies, the most massive (usually early-type) galaxies have mergers, grow their black holes and evolve to low-Eddington ratios (Volonteri et al., 2013). As the most massive SMBHs provide the right conditions for jet launching (Falcke et al., 2004), SMBHs with $\gtrsim 10^7$ $M_\odot$ explain the empirical radio–M_{BH} relation. However, for SMBHs with masses $\lesssim 10^6$ $M_\odot$, the radio detection rate decreases in our sample. These low-mass BHs are commonly found in the less massive late-type galaxies like spirals, where a contribution from SF in the radio band could account for the flattening of the radio-M_{BH} relation.

The luminosity of the forbidden [O III] line is a good indicator of AGN bolometric

luminosity, and is found to broadly correlate with radio core power. However, different optical classifications (Seyfert/LINER/H II) have different radio emission efficiencies i.e. the fraction of the radio emission produced with respect to the bolometric luminosity of the AGN. This result is in agreement with previous multi-band studies for different classes of LLAGN and extends to more powerful radio galaxies (e.g., Chiaberge et al. 1999; Nagar et al. 2005; Panessa et al. 2007; Balmaverde et al. 2006; Balmaverde and Capetti 2006a; Hardcastle et al. 2009; Baldi et al. 2010; de Gasperin et al. 2011; Panessa and Giroletti 2013; Asmus et al. 2015; Mingo et al. 2016).

In conclusion, the LeMMINGs survey has uncovered activity from a broad variety of radio active SMBHs in the local Universe, many of which were not detected or identified before. The resolution granted by the e-MERLIN telescope has detected the radio core morphologies of different types of LLAGN for the first time, which would have previously have been not possible to achieve with the VLA. The discovery of the previously unobserved galaxies and radio morphologies is fundamental for conducting a fair census of the local BH population and to provide robust constraints on cosmological galaxy evolution models (Shankar et al., 2009). The LeMMINGs survey is important as it will, for the first time, address the local BH demography and activity to a large survey with a multi-wavelength approach, pushing towards the low-end of the radio luminosity function. Future e-MERLIN observations at 5 GHz will extend the radio luminosity function of the local Universe down to 10 times the luminosity of Sgr A* and help to discriminate SF from genuine AGN activity. Additional VLA A array data at 1.5 and 5 GHz will be combined with the e-MERLIN data to detect the diffuse radio jet structures and improve the detection fractions of the radio sources in the survey. Furthermore, complementary data, which include optical (HST), X-ray (Chandra), and infrared (Spitzer) band, will unveil the origin of the parsec-scale radio emission and properties of the central engines of the local LLAGN population. Such work will be studied in future papers from the LeMMINGs consortium.

Part III

Multi-wavelength correlations of the LeMMINGs sample

Chapter 6

The X-ray Properties of the LeMMINGs Sample

6.1 Introduction

The X-ray emission from AGN is thought to originate in the X-ray corona above the BH (see Chapter 1). The X-rays are produced by Comptonisation of the optical/UV photons in the disk and are often observed (to first order) as a power-law over the 0.3−10 keV band. The X-rays are emitted close to the black hole and can be observed as a compact point source by X-ray telescopes and as such, a nuclear X-ray source is often used as a clear indication of an active SMBH. Such X-ray emission from powerful AGN is usually of order 10^{42-48} erg s^{-1} depending on the accretion rate. For LLAGN in the nearby Universe, which are not accreting efficiently or at high rates (e.g. LINERs), the X-ray luminosity can be of order 10^{39} to 10^{42} erg s^{-1}. This luminosity is similar to the luminosity of Ultra-luminous X-ray sources (ULXs) and X-ray binaries in nearby galaxies. Hence high angular resolution is required to resolve the nucleus from these other sources of contaminating radiation.

X-ray data also provides spectral information about the X-ray source. The power-law made by the X-ray corona is often absorbed at the lowest energies (0.2-2 keV) by a column of intervening material. With sufficient spectral resolution it is also possible to detect the presence of spectral lines, specifically at 6.4 keV for the Iron Kα fluorescence line. In some cases, a collisionally ionised plasma component is needed to model an underlying distribution at lower energies due to thermal processes. By properly fitting the observed X-ray spectra with these different components, it is possible to accurately measure the flux density of the source. However, to get enough throughput to the detectors, X-ray telescopes with good spectral resolution and low background levels are needed.

The *Chandra* X-ray observatory (hereafter *Chandra*) has good spectral resolution (∼100 eV at 1.5 keV), angular resolution (PSF ∼0.5″) and low background levels. As such, it is ideally suited for X-ray studies of LLAGN, being able to resolve the nucleus from contaminating

sources and obtain detections at the lowest flux levels. *Chandra* offers the perfect complimentary resolution to the *HST* and e-MERLIN (see Figure 1.8). In addition, large numbers of the LeMMINGs sample have already been observed previously with *Chandra*. Hence, the *Chandra* X-ray observatory is the perfect instrument for detecting nuclear X-ray emission from nearby galaxies in the LeMMINGs survey.

Previous observations of the Palomar sample of galaxies in the X-ray bands have largely been limited to low-resolution studies with *ROSAT* (e.g. Roberts and Warwick, 2000) and other X-ray observatories or have focussed primarily on the Seyferts and LINERs (Panessa et al., 2006; Akylas and Georgantopoulos, 2009; Hernández-García et al., 2014). The studies conducted with *Chandra* have either not focussed on the Palomar sample (e.g. 187 objects $\lesssim$15 Mpc, Zhang et al., 2009) or large samples but of a biased data set (for example, Liu, 2011, analysed 383 objects from the entire *Chandra* archive). Hence, the opportunity to perform a large, statistically-complete sample of X-ray nuclear emission in nearby galaxies presents itself with the LeMMINGs sample.

In this Chapter I will present the X-ray observations of the LeMMINGs sample, obtained from the *Chandra* archive and from new observations obtained in 2017 and 2018. As the black hole mass and spectroscopic classifications are available for the LeMMINGs sample, I will discuss the X-ray spectra of the LeMMINGs sample and compare them to the radio and optical properties of the sample from Chapter 5.

6.2 *Chandra* Observations

I queried the *Chandra* archive for X-ray data for the LeMMINGs objects and processed it as described in Chapter 2. Of the 280 objects in the LeMMINGs sample, ~140 had been observed by *Chandra* as of June 2015 by multiple observers. An additional 48 objects were observed as part of an observing program to complete the sample in the declination range 40−65° and galactic latitude $|b| > 20°$ as part of *Chandra* observing cycle 17 (programme ID 19708646 and 18620515, PI: McHardy). The declination cut was requested to reduce the number of objects to ensure a successful proposal, but also to ensure that the sample was not biased towards known active AGN (e.g. LINERs and Seyferts). The only additional cut on objects was the galactic latitude, which was set to $|b| > 20°$, to avoid too much extinction from the Milky Way. Unfortunately, three objects, NGC 2685, NGC 3613 and NGC 5473 were missed from the original observing list. The additional 48 objects included a handful of targets that had been previously observed by *Chandra* to increase the overall exposure on these galaxies to 10 ks. An exposure of 10 ks was proposed because it is sufficient for detecting a source at 10^{39} erg s^{-1} at the median distance of the LeMMINGs sample (~20 Mpc), even if it is obscured with an absorbing column of upto 10^{23} cm^{-2}.

Over the intervening three years, additional objects in the LeMMINGs sample have been observed as part of other observing programmes, and these have also been downloaded and

reduced. As such, as of June 2018, high-quality X-ray data now exists on 211/280 objects (~75%) in the LeMMINGs sample. The LeMMINGs *Chandra* X-ray sample has therefore increased by ~40% over the last three years due to new observations being made as part of the new proposal and additional observations in other programmes. From here on in I will refer to the 211 galaxies observed by *Chandra* as the X-ray LeMMINGs sample.

While ~75% of the LeMMINGs objects now have high-quality *Chandra* observations, the data obtained from the Chandra archive has not been observed in a homogeneous or complete way. Therefore, it is prudent to consider the ramifications of these data on the statistical-completeness of the LeMMINGs sample. Indeed, a large amount of the observed LeMMINGs objects in the *Chandra* archive are known 'active' galaxies based off their optical BPT classifications, and as such the archive is biased to Seyferts and LINER-type sources. Some objects with interesting X-ray/multi-wavelength sources have also been observed, for example M 82 which has known ULXs and SNe, but in general, the *Chandra* archival observations favour 'active' sources to 'inactive' objects.

A quantitative assessment of the data obtained from the *Chandra* archive alone, without the additional cycle 17 data, shows that of the 280 LeMMINGs galaxies, 70/135 (52%) H II galaxies and 22/33 (60%) ALGs have been observed, whereas 15/21 (71%) of Seyferts and 57/91 (64%) of LINERs have been observed. Hence, there is a very real dearth of H II galaxies that have been observed with the high quality and resolution of *Chandra*. Therefore, more observations of 'inactive' galaxies are necessary to ensure a statistically-complete LeMMINGs sample in the X-rays. Most of the objects in the newly obtained data have never been observed with *Chandra* before and most of them are H II galaxies (28/48), which greatly helps the statistical completeness of the LeMMINGs X-ray data. In fact, out of the 211 objects observed by *Chandra*, the numbers are now more reasonable: 98 H IIs, 24 ALGs, 15 Seyferts and 77 LINERs, from an original ratio of 70H:22A:14S:59L. Comparing to the overall fraction of AGN in the LEMMINGs sample (48% H II galaxies, 33% LINERs, 12% ALGs, 7% Seyferts), the X-ray LeMMINGs sample AGN corresponds to 47% H II galaxies, 35% LINERs, 11% ALGs and 7% Seyferts, which is very similar to the parent LeMMINGs sample.

While the overall sample is not yet fully complete, the sample in the 40−65° declination range and $|b| > 20°$ is statistically-complete bar the three objects mentioned previously and is a reasonably sized sub-sample (110 objects) to compare to. For ease of reading, in the rest of this thesis, I will refer to the 110 galaxies in the 40−65° declination range as the "Complete" X-ray LeMMINGs sample. However, as the 211 objects in the X-ray LeMMINGs sample are a good representation of the overall AGN population in the LeMMINGs sample, I will not go into depth in this Chapter about this sub-sample. However, I note that the AGN in this declination range also compare favourably to the percentage of each of the AGN types from the full LeMMINGs sample: 50% of sources are H II galaxies, 35% LINERs, 9% ALGs and 6% Seyferts. In future calls for proposals, it is intended to extend this declination range and to gradually complete the entire LeMMINGs

radio survey with *Chandra* data.

6.3 Results

In this Section I will perform a similar analysis to Chapter 5: I will describe the X-ray fluxes, luminosities and spectra, and compare them to the ancillary information, e.g. BH mass, as well as complementary optical data and the LeMMINGs radio data. I will compute an X-ray Luminosity Function (XLF) and compare the X-ray luminosity to the accretion rates in the X-ray LeMMINGs sample. I note here that the *Chandra* data reduction is described in Chapter 2.

6.3.1 Properties of the X-ray sources

Overall, out of the 211 galaxies that have been observed with *Chandra*, 149 show X-ray emission co-incident with the optical core of the galaxy, e.g. the circular aperture at the *HST* optical position for the core identifies a nuclear X-ray source above the detection limit of the dataset. These sources are therefore considered to have been "detected". The other 62 sources are considered "undetected". This yields a detection fraction of 149/211 (71%). Of the 149 detected sources, 120 had enough counts in their spectra for fitting in the 0.3−10 keV energy band and hence provide a more accurate determination of the flux. In addition to these 120 sources, a further six sources (NGC 598, NGC 3031, NGC 4151, NGC 5194, NGC 5273 and NGC 5548) had very complicated spectra and therefore their flux values are taken from the literature where possible[1]. There were 23 sources that were detected but did not have sufficient counts, due to low exposure times, to fit a spectrum to. Hence, for these 23 detected low-count sources, the flux values in the 0.3−10 keV band, both absorbed and unabsorbed, were obtained from the *Chandra* X-ray pipeline I wrote and described in Chapter 2.

For the detected sources that I fit X-ray spectra for, the 0.3−10.0 keV X-ray fluxes range from 2.9×10^{-15} to 2.7×10^{-11} erg cm^{-2} s^{-1}, while the luminosities span from 9.2×10^{35} to 1.6×10^{43} erg s^{-1}. For the unabsorbed 0.3−10.0 keV X-ray fluxes and luminosities, the range is broadly similar, as very few sources had significant additional absorption (see Section 6.3.2). I note that while I did not fit the data for NGC 5548, it has the highest unabsorbed flux and luminosity of all the sources, of 4.9×10^{11} erg cm^{-2} s^{-1} and 2.7×10^{43} erg s^{-1}. These flux and luminosity ranges are similar to previous studies of nearby galaxies made with Chandra observations (Liu, 2011).

[1]The references to the relevant publications are Shu et al. (2010); Liu (2011) and are included in Table D2. Where the relevant flux values were not available in the same bands used in this thesis, I converted the fluxes from the observed data into the relvant band by using the online Web PIMMS tool: https://heasarc.gsfc.nasa.gov/cgi-bin/Tools/w3pimms/w3pimms.pl . As a consequence of not fitting these data myself, I will not use them in statistical fitting or correlations in the rest of this Chapter, but will plot them for comparison.

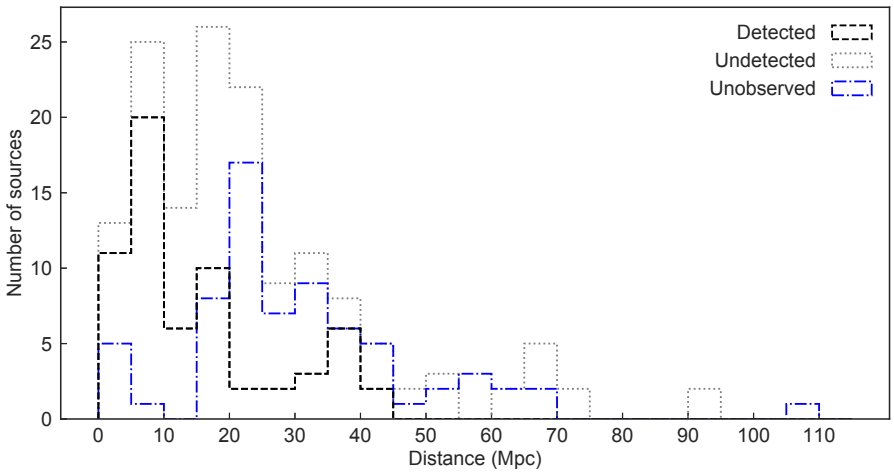

Figure 6.1: Histogram showing the number of detected, undetected and unobserved sources in the X-ray *Chandra* LeMMINGs sample as a function of distance, in 5 Mpc bins. The black dashed line shows the detected sources, the undetected sources are shown by the dotted gray line, and the blue dot dash line represents the unobserved sources.

However, I note that sources with nuclear luminosities $<10^{39}$ erg s^{-1} could be ULXs near the optical nucleus and not necessarily X-ray emission related to the black hole. This is especially true for star forming objects like the H II galaxies, as the number of ULXs has been shown to correlate with increased star formation (King, 2004; Gilfanov et al., 2004; Swartz et al., 2009). In addition, transient objects (such as the tidal disruption event NGC 3690) will have large changes in flux over year to decadal time scales, and as the X-ray observations were performed at different dates, it is possible that some of the X-ray fluxes may have changed. Changes in X-ray flux over short time periods is unlikely to effect the majority of the sample and the X-ray emission should remain constant over long periods of time (> 100s of years). However, given these observational properties, I remove any sources that are known not to be AGN (e.g. NGC 3690) or have lots of circum-nuclear X-ray emission not associated with the AGN (e.g. NGC 3034) or as in the cases of NGC 4150 and IC 342, the nuclear sources are ULXs and hence it is considered undetected (Liu, 2011).

Another important consideration that could bias the X-ray data is the distance of the sources in the X-ray sample compared to the unobserved sample: nearer sources are more likely to be detected, even at lower fluxes, e.g. a Malmquist bias (Malmquist, 1922). Figure 6.1 shows the number of detected, undetected and unobserved sources in the X-ray LeMMINGs sample as a function of distance. This figure indicates that while the distributions for the detected/undetected sources are similar, they are not the same as the unobserved distribution. However, there does not appear to be a bias in favour of the more distant objects compared to the the nearer ones and so it is unlikely that the distance of the source has an effect on the likelihood of detection. But future studies to complete the entire LeMMING sample with *Chandra* will help to eliminate this potential bias.

Figure 6.2 shows the flux and luminosity values obtained for the entire sample as a function of distance. I also plot in orange the new 48 observations which all had 10 ks exposures as a comparison. Again, this plot shows no distance dependence of the sources, with a wide range of fluxes and luminosities observed at all distances. Above 40 Mpc, all objects are above the limiting detection luminosity threshold set at a flux level of $3{\times}10^{-15}$ erg cm^{-2} s^{-1}. But, objects are detected below the threshold for sources $\lesssim$40 Mpc. Therefore I checked to see if there was an exposure length difference as a function of distance. Indeed this effect is observed, as objects at distances greater than 40 Mpc have a mean exposure of 35 ks, whereas less distant objects have a 30 ks exposure on average. It is therefore possible that exposure times may play a role in the likelihood of detection.

For the entire X-ray LeMMINGs sample, the median exposure time of detected sources is 20 ks, whereas the median exposure for undetected sources is 10 ks. For the objects that had a spectral fit, the median exposure climbs to 29 ks, and out of these spectrally fit data, those fit with χ^2 statistics were observed for a median time of 43 ks compared to the median for those fit with Cash statistics was 10 ks. Hence, there is a clear increase in the likelihood of detection of sources for exposures greater than 10 ks. However, the 10 ks limit seems like a reasonable exposure time for at least a simple fit to the data, and strengthens the case for observing the rest of the LeMMINGs sample with at least 10 ks exposures in the future. In the rest of this Chapter, I will use a flux value of the $3{\times}10^{-15}$ erg cm^{-2} s^{-1} as a limiting flux for the X-ray LeMMINGs sample as that is representative of the flux limit of the Complete X-ray LeMMINGs sample data and future 10 ks observations to complete the rest of the sample. It should be noted however, the biases in the exposure length will still be a problem for future studies, unless all objects are observed for the same exposure time or a restricted exposure for all the observations is used.

6.3.2 Spectral Properties of the X-ray sources

The 0.3−10 keV spectra were fit to get a better estimate of the flux in each source, as the automated pipeline described in Chapter 2 assumes a spectral model which cannot be true for all sources. Of the 120 sources that I fit spectra for, 60 had enough counts (>200) to be fit with simple multi-component models using χ^2 statistics, while the other 60 had fewer counts and hence a Poissonian distribution is assumed for the counts and therefore Cash statistics was used (See Section 4.3.3 for a discussion on the use of Cash statistics in the low-counts regime). As such, all of the fits performed with Cash statistics used a simple absorbed power-law, as it is not possible to make additional reliable inferences on a spectrum with few counts. For those fitted with χ^2 statistics extra components such as additional absorption, an Iron fluorescence line or a soft collisionally ionised plasma were used to fully fit the spectrum.

When fitting the spectral data in XSPEC, the extinction along the line of sight was measured

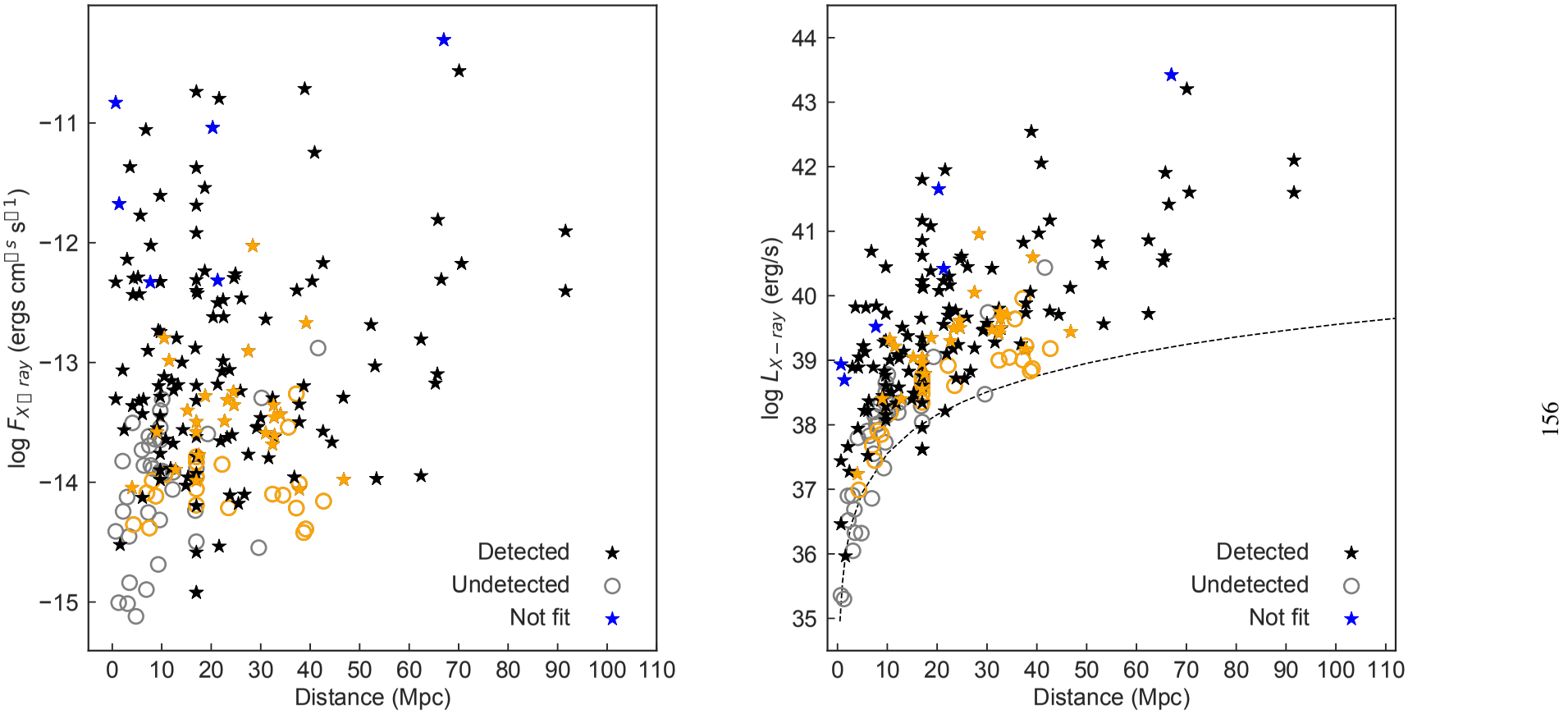

Figure 6.2: Unabsorbed X-ray flux density (F_{X-ray} in erg cm^{-2} s^{-1} in the 0.3−10 keV band) (left panel) and its luminosity (L_{X-ray} in erg s^{-1}) (right panel) as a function of the distance (Mpc) for the entire sample. The dashed line corresponds to the limiting flux density of the X-ray LeMMINGs Complete sample, corresponding to a flux limit of 3×10^{15} erg cm^{-2} s^{-1}. The different symbols correspond to detected (stars) sources and undetected (open circles) radio sources. For the undetected sources, the values on the y-axis are meant as upper limits. The blue stars represent the six objects where spectral fits were not possible and as such the unabsorbed fluxes are obtained from the literature. The orange data points represent the 48 new *Chandra* observations obtained in proposals 19708646 and 18620515. As a more complete sample, these new observations show a similar distribution to the archival data, but with a higher limiting flux/luminosity.

from Kalberla et al. (2005) using the HEASARC web interface[2] and varies between 10^{19} to 10^{21} cm^{-2}. The photon indices are related to the AGN power-law by $\Gamma = \alpha + 1$ (e.g. Ishibashi and Courvoisier, 2010) and range from ~ -2 to 5, but most of the photon indices are in the range 1.5−2.5, which is mostly expected for AGN. The extremal photon indices are usually found in sources with very few counts or those with highly complex spectra. In seventeen cases, an additional absorption component was required to properly model the spectrum, usually $>10^{21}$ cm^{-2}. Seventeen sources had an additional collisionally ionised plasma model (APEC in XSPEC) to help fit the lower energy spectra. Most of these seventeen sources with the collisionally ionised plasma had a temperature of ∼0.8 keV. Only six objects had enough counts and a visible Iron fluorescence line for modelling, mostly centred around 6.4 keV.

Of the 60 objects that had sufficient counts to be fitted with χ^2 statistics, 40 were fit with only an absorbed powerlaw, 12 of which were fit with an additional absorption component, 13 required an absorbed powerlaw with an additional APEC component, and 7 objects required a gaussian to model the Iron fluorescence line at ∼6.4 keV line, with additional parameters such as an APEC thermal collisionally ionised plasma or additional absorption. The X-ray sources and associated spectra are presented in Appendix D. The tables including X-ray flux values are presented in Table D1, and the spectral information is shown in Table D2.

While it is not my intention to explore the specific spectral properties in great detail in this part of my thesis, I note that a full analysis of the spectra is necessary to understand all of the nuclear properties of the central engines in different AGNs. I note that some sources show interesting characteristics below:

- NGC 315 has a well known X-ray jet and may explain some of the additional soft X-ray emission in the spectrum.
- NGC 507 could only be fit with a Gaussian component at ∼0.9 keV, as additional absorbers and plasmas could not account for the shape of the spectrum.
- NGC 1275, NGC 3516, NGC 4051, NGC 4258 and NGC 5033 all require additional pile-up models to fit the spectra
- NGC 2273 has a very prominent Iron line at 6.4 keV, but an unusually flat spectrum.
- NGC 2683 has a highly inverted spectrum, as does NGC 3190, NGC 4013 and NGC 4036.
- NGC 2782 and NGC 3690 are similar to NGC 2273 in that it has a prominent Iron line with an unusually flat spectrum, but with an additional soft component from a hot plasma.
- NGC 4102 is odd in that it needs a very broad Iron line.

[2]https://heasarc.gsfc.nasa.gov/cgi−bin/Tools/w3nh/w3nh.pl

Table 6.1: X-ray detected sources by morphological classification breakdown

	optical class				
X-ray	LINER	ALG	Seyfert	HII	Tot
detected (Chi)	35	5	8	12	60
detected (Cstat)	23	13	1	23	60
detected (no fit)	6	3	5	15	29
Tot	64	21	14	50	149
undetected	10	3	1	48	62
Tot	74	24	15	98	211

Notes. The sample is divided in optical classes and X-ray statistically fitting regime based on their X-ray detection non-detection.

- NGC 4258 is heavily absorbed, as is NGC 4395.

Future publications with this dataset will look more in detail at the nuclear spectral properties of these sources, but for the purposes of this thesis, I will not go into any deep analysis of the spectral properties.

6.3.3 X-ray luminosity function

In section 5.3.5, I computed the radio luminosity function (RLF) of the LeMMINGs sample. Here, I use the same methodology to compute the X-ray luminosity function (XLF) of the observed X-ray LeMMINGS sample. As mentioned previously, the exact distribution of luminosity functions is important for modelling galaxy evolution across cosmic time. For the X-ray flux limit, I use the flux limit of the statistical X-ray LeMMINGs sample, e.g. $3{\times}10^{15}$ erg cm^{-2} s^{-1}.

Figure 6.3 shows the X-ray Luminosity Function of the LeMMINGs X-ray sample. It shows a similar distribution to that of the RLF presented in Chapter 5, in that it is fit fairly well by a single power-law of slope α = -0.59. There are some deviations along the XLF notably at $10^{16.5}$ W/Hz and $10^{14.0}$ W/Hz, where the XLF appears as nearly flat in both the black (all sources) and red (only 'active' sources) points. Certainly, it appears that three power laws may fit better to the local population of LLAGN or a steeper single power law (e.g. more similar to the RLF of ∼-0.7), as Sgr A* would fit better. As in the RLF presented in Chapter 5, the changes in the overall appearance of the luminosity functions are more apparent in the 'active' sources, indicating that the H II galaxies, which are often unobserved in X-ray and radio surveys - are pre-selected out of previous XLFs in the literature.

6.3.4 X-ray luminosity versus optical properties

It is useful to compare the X-ray emission to the optical properties, similar to that performed for the radio data in Section 5.5, as it reveals the interplay between the AGN and the emission mechanism. Table 6.1 shows the number of detected and undetected sources

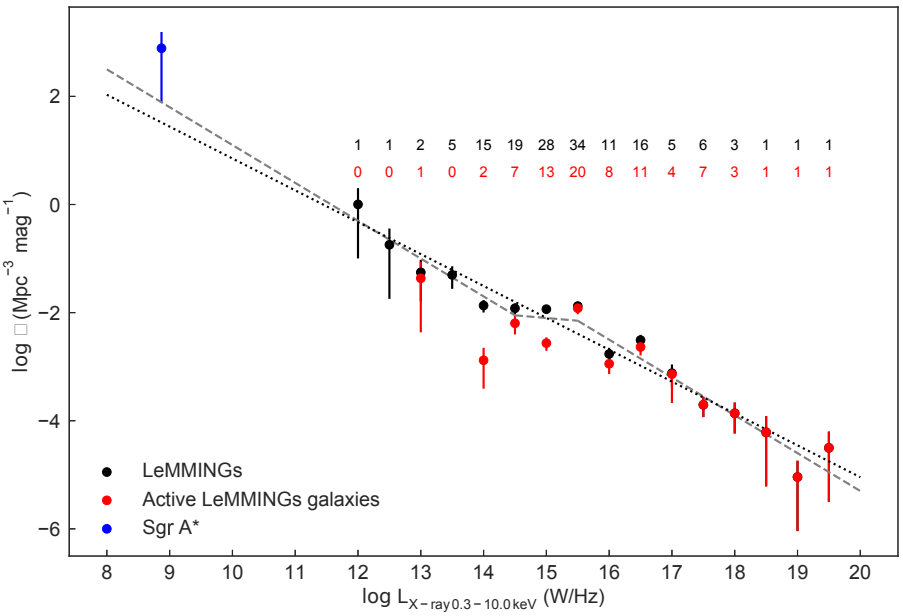

Figure 6.3: The X-ray luminosity function (XLF) of the LeMMINGs X-ray sample. The black points show the X-ray detections in the sample. The red points indicate the 'active' galaxies based off the BPT diagnostic plots in Chapter 2, e.g. the LINERs and Seyferts. The blue point is the XLF point for Sgr A* based off *Chandra* observations scaled to the 0.3−10 keV band from Baganoff et al. (2003). The dotted line is a formal fit to the data, with a power-law of α = -0.59. The dashed line shows three broken power laws, with the power-laws in the range log(L_*) <14.5 and > −15.5 as a power-law with slope α = -0.7. For the central luminosity range, log(L_*) = 14.5−15.5 of α = -0.1. In addition the number of objects in each bin is written above each bin in the same colour as the sample used. The errors are drawn from a Poissonian distribution.

divided by optical class. Seyferts are the most detected optical AGN type (14/15, 93%), followed by the ALGs (21/24, 88%) and LINERs (64/74, 86%), with H II galaxies being much less detected (50/98, 51%).

As the dataset is inhomogeneous - some objects have longer observations than others - and the previous data in the archive was statistically incomplete, I compared the exposure times of the different optical AGN types over the observed X-ray sample. In general, Seyferts have been observed with longer exposures, with a mean exposure of 63 ks, compared to 29 ks for LINERs, 28 ks for H II galaxies and 24 ks for ALGs. A similar trait is seen in the median exposure times per class: Seyferts (29 ks), LINERs (15 ks), H II galaxies (10 ks) and ALGs (12 ks). The same disparity is observed in the 'complete' sample. However, the distribution of exposure times is broadly similar between the optical classes. An effect of these different exposure times leads to differences in the statistical fitting routine used. The Seyferts, which have longer exposure times in general are usually fit with a χ^2 treatment, whereas the H II galaxies which tend to have lower exposure times are most commonly fit with Cash statistics. As a consequence, not only are Seyfert galaxies more likely to be detected than H II galaxies, but they also have better sampled spectra and are therefore more likely to be able to be fit with a more complicated spectrum than an absorbed power-law.

The X-ray luminosity as a function of AGN optical class is presented in the left panel of Figure 6.4. The four AGN types appear to reside in different areas of this plot. First, the LINERs are the most common type observed and detected with a median luminosity of 5.7×10^{39} erg s^{-1}, with X-ray luminosities usually above $\sim10^{39}$ erg s^{-1}. The Seyferts occupy a similar region in this plot to the LINERs and have a higher median luminosity of 3.6×10^{40} erg s^{-1}. The H II galaxies by-and-large reside at lower X-ray luminosities, between $\sim10^{37}$ and 10^{40} erg s^{-1}, with a median luminosity of 6.7×10^{38} erg s^{-1}. The ALGs have a median luminosity of 2.9×10^{39} erg s^{-1} but show a similar distribution to H II galaxies at lower luminosities. As for the upper limits (dashed lines in Figure 6.4), the upper limits of the H II galaxies broadly follow the same distribution of the detected galaxies. This effect may be due to exposure time, as the H II galaxies that were detected had a median exposure of 30 ks, whereas the undetected objects has a median exposure of 10 ks. For the other three optical classes, the difference between these two values is much less, and hence the upper limit distributions are generally at lower flux densities than the detected distributions.

The right panel of Figure 6.4 shows the X-ray luminosity as a function of galaxy morphological type. The median values of all of the different detected galaxies by morphological type are of order 10^{39} erg s^{-1}. Specifically, the median values for the sample are as follows: 4.25×10^{39} erg s^{-1} for ellipticals, 3.18×10^{39} erg s^{-1} for lenticulars, 1.95×10^{39} erg s^{-1} for irregulars and 1.17×10^{39} erg s^{-1} for spirals. Most of the elliptical galaxies are detected, and they appear to show a bimodal distribution of X-ray luminosities, with one peak at $\sim10^{39}$ and another peak at $\sim10^{42}$. However, due to the low number of ellipticals (19) in the X-ray sample, it is possible that this is not a real effect. As for the spiral galaxies, which are the most common type in the LeMMINGs sample, about two thirds (80) of them

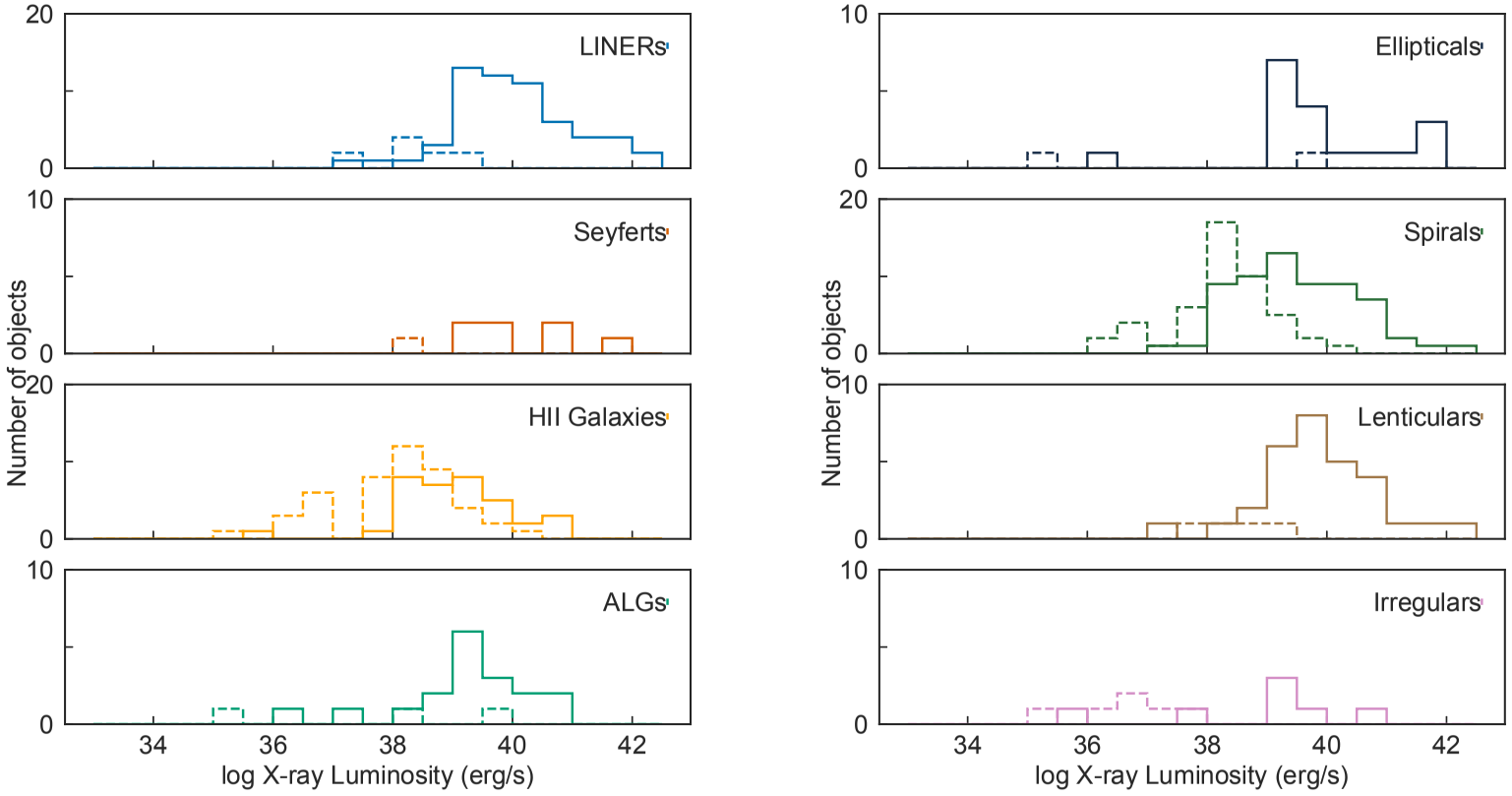

Figure 6.4: Histograms of the X-ray luminosity (erg s^{-1}) per optical class (left plot) and host morphological type (right plot). The solid-line histogram represents the X-ray core luminosity distribution of the detected sources and the dashed line corresponds to the upper limits obtained from the non-detected objects.

are detected and the other third (50) are undetected. Those which are detected tend to be observed at $\gtrsim 10^{38}$ erg s^{-1}, peaking at $\sim 10^{42}$ erg s^{-1}. The non detected spirals have upper limits that peak at $\sim 10^{38}$ erg s^{-1}, suggesting there may be a lower luminosity tail to the spirals that has not been observed. The lenticular galaxies peak at $\sim 10^{40}$ erg s^{-1}, but show a broad distribution (though narrower than that of spirals) between $\sim 10^{39}$ erg s^{-1} and $\sim 10^{41}$ erg s^{-1}. The irregulars do not show any common distribution, likely due to the inhomogeneous nature of these galaxies, but they do include a couple of very low luminosity ($\lesssim 10^{37}$ erg s^{-1}) sources.

6.3.5 X-ray properties vs black hole mass

X-ray emission from a point source co-incident with an optical nucleus is expected to be due to an accreting SMBH. As mentioned in Section 5.5.1, larger black hole masses tend to be correlated with increased activity in AGN. But in some cases, the X-rays can be produced by ULXs, which can have similar X-ray luminosities to LLAGN $\sim 10^{39}$erg s^{-1}, and are most common in star forming galaxies (King, 2004; Gilfanov et al., 2004; Swartz et al., 2009). Therefore, using the black hole masses from the stellar velocity dispersions it is possible to separate these two phenomena apart.

Figure 6.5 shows the X-ray luminosity as a function of the black hole mass obtained from the stellar velocity dispersions in the M$-\sigma$ relation discussed in Chapter 2. The detection of X-ray sources increases with BH mass, similar to the radio vs BH mass plot (Figure 5.5), but the detection fraction difference is less dramatic across the different mass bins. The detection fraction for objects with BH masses $\gtrsim 10^{8}$M$_{\odot}$ is 100% (39/39), but below 10^{6}M$_{\odot}$, the detection fraction falls to 38% (20/52).

While the black hole masses range over ∼5 orders of magnitude, clear distinctions in the different types of nuclei are apparent from Figure 6.5, lower plot. First, the detected Seyfert galaxies tend to have the highest X-ray luminosities for each mass bin. However, there are several Seyfert galaxies that fall within the middle of the X-ray luminosity range for the whole population of X-ray detected sources. Never-the-less, the Seyferts generally cluster 1−2 decades above the other AGN types in X-ray luminosity. The LINER population of X-ray detected sources tend to fall in the higher mass bins with high X-ray luminosities. There is a significant scatter in the LINER X-ray luminosity of order 2−3 decades in each mass bin. The detected ALGs tend to lie in the same mass bins as the LINERs, but usually at lower X-ray luminosities. The low mass H II galaxies are not often detected, but they appear to follow the same overall trend as the rest of the detected X-ray population, but with more scatter towards the lowest black hole masses.

A tentative correlation for all the detected sources is plotted in Figure 6.5, lower panel. The correlation is defined as $L_{X-ray} \sim M_{\odot}{}^{0.65\pm0.07}$ with a Pearson correlation coefficient (r-value) of 0.596, suggesting that the two quantities do not correlate with a probability less than 10^{-15}. The dashed line shows a similar albeit steeper correlation for only the sources

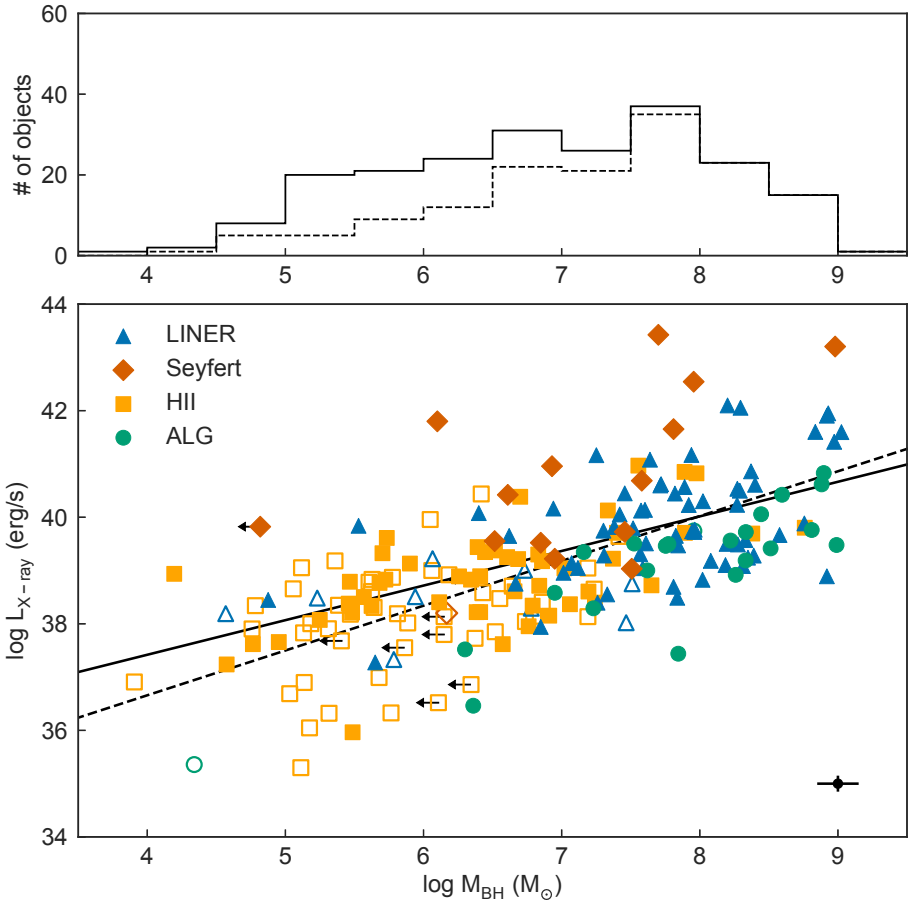

Figure 6.5: In the upper plot, I show the histograms of the entire sample (solid line) and of the detected sources (dashed line) in bins of BH mass to estimate the detection fraction. In the lower panel, I show the unabsorbed X-ray 0.3−10.0 keV luminosities (L_{X-ray} in erg s^{-1}) as a function of the BH masses ($M_\odot$) for the sample, divided per optical class (symbol and color coded as in the legend). The filled symbols refer to the detected radio sources, while the empty symbols refer to undetected radio sources. The solid line represents the linear correlation found for all the detected galaxies. The dashed line is a fit to all of the sources with a mass $\gtrsim 10^7 M_\odot$. In the bottom-right corner, I show the typical error bars associated with the points.

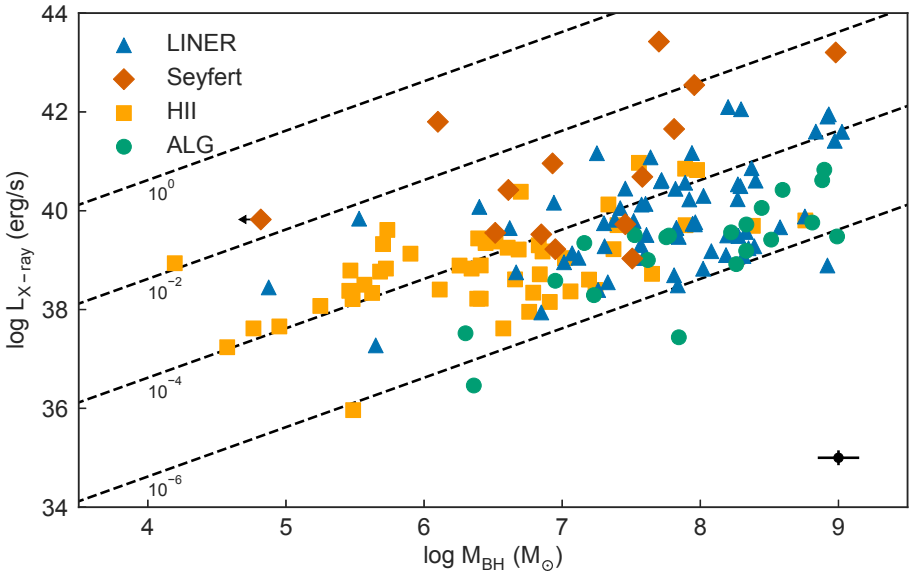

Figure 6.6: The unabsorbed X-ray 0.3−10.0 keV luminosities (L_{X-ray} in erg s^{-1}) as a function of the BH masses ($M_{\odot}$) for the detected sources in the sample, divided per optical class (symbol and color coded as in the legend). The dashed lines represent the Eddington ratios λ to compare to the X-ray luminosity and BH masses. The exact Eddington ratio is labelled next to each line. In the bottom-right corner, I show the typical error bars associated with the points.

above $10^{7}M_{\odot}$. However, given the scatter, it is not possible to consider this a concrete relation between the sources. Furthermore, it is clear there are differences in the AGN types that cause a large amount of scatter in this correlation. For example, the Seyfert are on average 2-4 orders of magnitude above the correlation in all mass bins. In the literature, several authors have not found significant correlations between the X-ray luminosity and the BH masses for Seyferts (Pellegrini, 2005; Panessa et al., 2006) although some have found correlations (Koratkar and Gaskell, 1991; Kaspi et al., 2000). Given the scatter in the Seyferts presented here, it is not possible to find any strong correlation between the X-ray luminosity and BH mass. This is reinforced by the correlation for just the Seyferts which is of the form $L_{X-ray} \sim M_{BH}^{0.93\pm0.32}$ with a Pearson correlation coefficient (r-value) of 0.638. With the low number of Seyferts, the probability of the two quantities not correlating is 0.014, much higher than that obtained for the entire sample.

I performed the same analysis for the LINERs, ALGs and H II galaxies and found them to all be correlated between the X-ray luminosity and BH mass. The LINERs correlate as $L_{X-ray} \sim M_{BH}^{0.71\pm0.13}$ with a r-value of 0.568 and a p-value of 9.80×10^{-7}. For the ALGs, the correlation is $L_{X-ray} \sim M_{BH}^{0.92\pm0.17}$ with a r-value of 0.782 and a p-value of 2.85×10^{-5}. The H II galaxies follow a correlation of $L_{X-ray} \sim M_{BH}^{0.57\pm0.11}$ with a r-value of 0.606 and a p-value of 3.13×10^{-6}. I do note that all of these correlations are fit with only the detected sources, and therefore if the undetected sources are also considered, then the fits may change. Certainly, this could be the case for the H II galaxies, where only half of them are

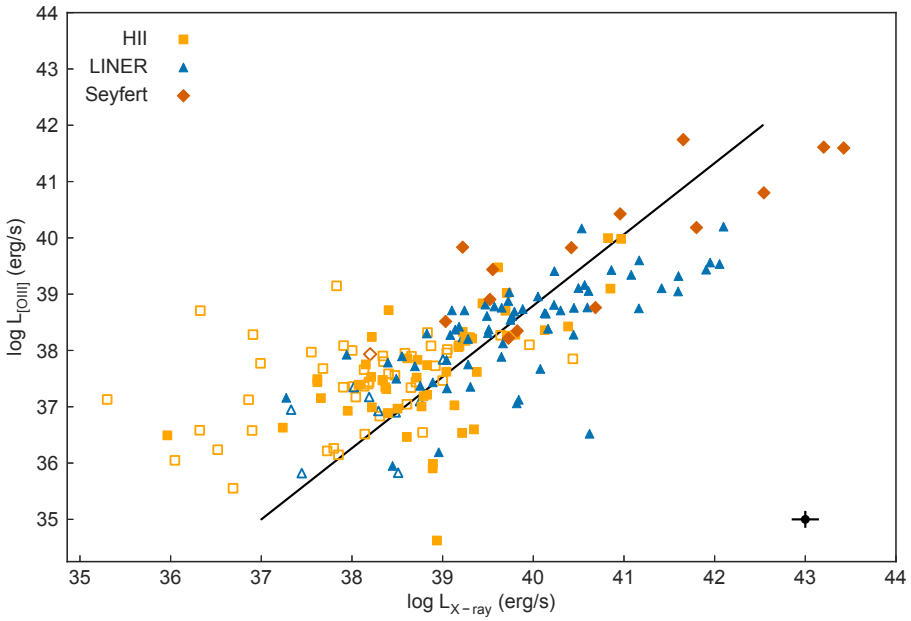

Figure 6.7: The [O III] luminosity ($L_{[O\ III]}$ in erg^{-1}) vs unabsorbed 0.3−10.0 keV luminosities (L_{X-ray} in erg^{-1}) for the X-ray LeMMINGs sample. The different optical classes are coded (symbol and colour) in the plot according to the legend. The filled symbols refer to the detected X-ray sources, while the empty symbols refer to undetected X-ray sources. The dotted line represents the linear correlation by fitting all of the detected LeMMINGs sources, The bars in the bottom-right corner indicate the typical errors for the data points.

detected. However, these fits are encouraging and may indicate a genuine correlation between the X-ray luminosity and the BH mass for these AGN types.

In addition to the simplistic fits presented above, I followed the procedure of Panessa et al. (2006), comparing the X-ray luminosity and BH mass plot to the Eddington ratio, λ, for the detected sources in the sample (Figure 6.6). To produce this plot, I assumed that the bolometric luminosity = 30×X-ray luminosity in the 0.3−10.0 keV band. As stated in Panessa et al. (2006), this is a very simplistic assumption to make, as the bolometric luminosity relies on the shape of the spectral energy distribution for the AGN, which could differ amongst LLAGN types. Furthermore, the value of 30 is valid for more powerful AGN, but observationally, this value ranges from 3 to 16 (Ho, 1999b). Hence, for a lower scaling value of L_{bol} to L_{X-ray},for example 10, the lines on Figure 6.6 would drop by a factor of 3. However, even with these approximations, the plot shows that the Seyferts are generally associated with the higher L_{bol}/L_{Edd} values, indicative of a higher accretion rate, while the other classes have Eddington ratios of $\lesssim 10^{-3}$, consistent with a radiatively inefficient AGN.

6.3.6 X-ray compared to [O III] line luminosity

Both the X-ray luminosity and forbidden [O III] emission line luminosity are used as proxies of the accretion flow onto AGN (see Section 5.5.2). While the X-ray emission is generally better at estimating the accretion rate, reliable X-ray observations of the nuclear emission of galaxies can be hard to obtain. The [O III] line can be observed from ground-based optical observatories and the emission line region extends much further away from the obscuring torus than the X-rays will (see (Saikia et al., 2015) and references there-in). Hence it is useful to compare these two tracers of accretion rate so that additional optical information can be used in lieu of high quality X-ray data.

Figure 6.7 shows the [O III] line luminosity obtained from the Palomar survey of all the detected and undetected X-ray sources plotted against the unobscured X-ray luminosity in the 0.3−10 keV band. A clear linear correlation exists between these two indicators but with some scatter ∼2−3 decades in $L_{[O\ III]}$ per X-ray luminosity. The scatter in the correlation is larger in the X-rays at the lower luminosities, spanning 4−5 decades of X-rays per [O III] luminosity. The Seyferts have the highest [O III] and X-ray luminosities of the sample and appear at the top of the correlation. The LINERs occupy the central region of this plot whereas the H II galaxies are at the lowest X-ray and [O III] luminosities. However, there is a lot of mixing between the lower luminosity Seyferts and the higher luminosity LINERs, and similarly between the LINERs and H II galaxies, so no clear region for each optical AGN class emerges. I note that many of the undetected objects have upper limits on the X-ray and [O III] emission in this plot. Many of these objects that are detected in neither the X-rays nor the [O III] line have more stringent X-ray upper limits than [O III] ones, e.g. they fall to the left of the X-ray/[O III] correlation. Therefore the statistical correlation would definitely benefit from including censored data (see Section 5.4.2). However, the H II galaxies that are detected broadly follow the relation but with larger scatter at the lower luminosities. Hence the H II galaxies occupying similar regions to the LINERs and Seyferts could be AGN powered, but those at the lowest X-ray and [O III] luminosities may not be, and more care must be given for the treatment of these low luminosity H II objects.

Given the correlation in Figure 6.7, I searched for a simple linear correlation between the X-ray detected objects and their optical emission and found a correlation of the form $L_{X-ray} \sim L_{[O\ III]}^{0.79\pm0.06}$, with an r-value of 0.760, indicating that the probability of these two quantities not correlating as 2.3×10^{-25} and therefore the correlation is strong. However, there is a clear difference between the correlations of the three optical classes if you fit them separately. For Seyferts, there is a 1:1 trend across all X-ray and [O III] detected sources, as the correlation is $L_{X-ray}\sim{L_{[O\ III]}}^{1.00\pm0.19}$ (r-value = 0.835, p-value = 0.0002), but with so few objects and significant scatter, is difficult to come to a firm conclusion. The LINER correlation is shallower, $L_{X-ray}\sim{L_{[O\ III]}}^{0.81\pm0.11}$ (r-value = 0.697, p-value = 4.64×10^{-10}) and is much more statistically significant. The H II galaxies show an even shallower slope: $L_{X-ray}\sim{L_{[O\ III]}}^{0.54\pm0.11}$ (r-value = 0.589, p-value = 6.49×10^{-6}). These different correlations show that the AGN type is important when considering the X-ray and [O III] line

luminosities in this sample, an effect which may become more apparent when fitting with censored data too.

Comparing the data to the literature, the X-ray and [O III] correlations tend to show a 1:1 ratio, similar to that found here for the Seyferts (Panessa et al., 2006; Hardcastle et al., 2009). The X-ray LeMMINGs data corroborates the findings in the literature, indicating that the X-ray and [O III] ionising radiation are coupled down to very low luminosities. However, many of the observations do not probe much below 10^{39} erg s^{-1} in either X-ray or [O III] line luminosity. Furthermore, the previous work in the literature has focused on radio-loud galaxies like the 3C sample, and these objects may therefore harbour more powerful AGNs in general. Hence, the X-ray LeMMINGs sample presents the first opportunity to study the relationship between the X-ray properties of nearby LLAGN and the optical line luminosities in both a statistically-complete way and at high enough resolutions and sensitivities to make remove contaminating radiation from non-AGN processes.

It should also be noted that comparable resolution is required to be certain of the correlations between the X-ray luminosity and [O III] line luminosity, for example by comparing to *HST* data for the line emission (e.g. see Balmaverde and Capetti, 2006b). The data presented here are obtained from the Palomar survey and as such have much larger errors on the [O III] line emission, and may be contaminated with other circum-nuclear star formation and thermal processes not due to the AGN.

6.3.7 X-ray vs Radio Correlation

As the X-ray and radio emission are thought to trace the input and output of the accretion process respectively, it is important to consider, at what level, the two parameters are correlated. However, previous studies of the Palomar sample with the VLA and available X-ray data have not shown any strong correlation between the two parameters (e.g. Saikia et al., 2018). But, other authors have shown that a weak correlation may exist (e.g. Merloni et al., 2003). Indeed, if AGN are the scaled up versions of the XRBs, then one may expect a coupling between the disk and jet through the X-ray and radio emission (Falcke and Biermann, 1995). I will discuss this further in the next Chapter. Numerically, only 63 objects have both a radio and X-ray detection, 68 are detected in the X-rays and not in the radio, 3 are detected in the radio but not in the X-rays, and 48 are detected in neither. The reduced sample size (182 objects) is due to the 39 objects that haven't been observed with e-MERLIN as of yet and the 69 that have not been observed with *Chandra*. Fig 6.8 appears to show a general trend of the X-ray correlating with the radio for the detected sources, however even these sources have a large amount of scatter: the X-ray and radio detections cover at least 3 decades per bin. In addition the most powerful radio sources lie at least 2 decades off the best fit line, suggesting that the correlation may not hold for all types of LLAGN. Furthermore, the fit for the detected data does not align well with those that have at least one non-detection in the radio or X-ray. This may have an effect on this particular

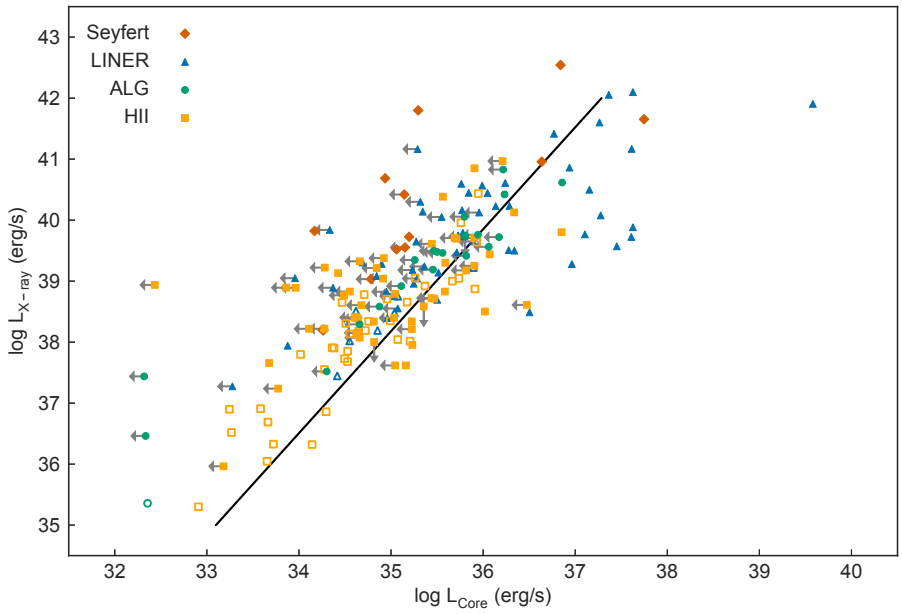

Figure 6.8: The unabsorbed X-ray luminosity in the 0.3−10 keV band vs the radio core luminosity obtained from Chapter 5. The different optical classes are coded (symbol and colour) in the plot according to the legend. The filled symbols refer to the detected X-ray sources, while the empty symbols refer to undetected X-ray sources. The solid black line represents a fit to the objects which have been detected in the X-rays and radio but extrapolated down several orders of magnitude.

correlation as more objects have an upper limit in at least one of the axes (119) compared to those detected in both the X-ray and radio (68). With this in mind, I do not claim any correlation between the radio and X-ray from Fig 6.8.

6.4 Discussion

The LeMMINGs X-ray *Chandra* sample presented in this Chapter represents the largest X-ray survey of nearby LLAGN, detecting X-ray emission in all optical AGN types down to a limiting luminosity of $\sim 3\times10^{35}$ erg s^{-1}. It is an excellent complementary dataset to the main LeMMINGs sample presented in Chapter 5 for studying nuclear accretion properties in nearby LLAGN. I have presented the 211 LeMMINGs objects that as of June 2018 have been observed with *Chandra*. I have compared the X-ray data to the other optical and radio data available, similar to Chapter 5, and altogether, 150/211 (71%) objects were detected by *Chandra*. This detection rate is higher than previous studies of a subset of the Palomar sample using poorer resolution/quality data from *ROSAT* (54% Roberts and Warwick, 2000) and *Chandra* (62% Ho and Ulvestad, 2001b).

By comparing to the optical classifications described in Chapter 2, I find that almost all Seyferts, ALGs and LINERs have a nuclear X-ray core, co-incident with the optical nucleus

of the galaxy. In addition, around half of the H II galaxies in the sample are detected in the X-rays at the optical nucleus. As to nature of these X-ray sources, the LINERs and Seyferts appear to be associated with luminosities $\gtrsim 10^{39}$erg s^{-1} in most cases, but the H II galaxies and ALGs represent a less-luminous population of nuclear X-ray emission that may be due to LLAGN, or potentially other X-ray sources in the galaxy. To ascertain the nature of the nuclear emission, I used the other multi-wavelength data available, which I discuss below in the case of each of the AGN types.

6.4.1 Seyferts

There are 15 Seyferts in the X-ray LeMMINGs sample presented in this Chapter, of which 14 are detected (93%). The Seyferts have the highest X-ray luminosities, all above 10^{39} erg s^{-1}, occupying regions of higher X-ray luminosity per black hole mass bin and [O III] emission line luminosity. There is no observed correlation between the X-ray luminosity and the black hole mass for Seyferts, which is probably due to the wide range of Eddington values that they can take. Also, the Seyferts tend to have the most complicated spectra, due largely in part to longer exposures and more observations: four of the detected Seyferts (NGC 4151, NGC 5194, NGC 5273 and NGC 5548) have complex spectra which cannot be easily fit with a combination of an absorbed power-law with an Iron fluorescence line, additional absorption and/or a collisionally ionised plasma model.

The observed X-ray properties of Seyferts can be reconciled with an efficient slim-disk model (Shakura and Sunyaev, 1973). The higher Eddington rates obtained from the X-ray data and the radio data in the previous Chapter indicate that Seyferts are efficient accretors and therefore are likely to have their X-ray emission dominated by the up-scattered photons from the disk. However, the Seyferts that have lower Eddington rates ($\lesssim 10^{-3}$ (Merloni et al., 2003)) are possibly powered by radiatively inefficient inflows, similar to those of LINERs. Several individual studies have looked at modelling Seyferts as efficient and inefficient flows and found that they could be described equally well by either (Lasota et al., 1996; Quataert et al., 1999; Fiore et al., 2001; Yuan et al., 2002; Ptak et al., 2004). However, the prevailing wisdom is that from the X-ray properties and the scaling with the [O III] line luminosity, the local Seyfert population are likely scaled down versions of the more powerful AGN in quasars, accreting at lower rates (Panessa et al., 2006) in a geometrically-thin, optically-thick disk..

6.4.2 LINERs

Of the 74 LINERs in the X-ray LeMMINGs sample, 64 of them are detected (86%). They are mostly detected with luminosities $\gtrsim 10^{39}$ erg s^{-1}, with a handful detected below this limit. The LINERs are associated with the highest black hole masses in general and follow a similar X-ray-[O III] gradient to the Seyferts, but at a level around two decades lower. They appear to bridge the gap between the highly X-ray luminous Seyfert galaxies and the H II

galaxies at lower luminosities. LINERs also show a large scatter in the X-ray-radio plot, likely due to the LINERs being radio-louder than the other classes.

As mentioned in the previous chapter, the LINERs are usually described as some form of RIAF. The X-ray observations in this Chapter support this interpretation as the inferred Eddington ratios in Figure 6.6 indicate that most LINERs have $\lambda \lesssim 10^{-4}$ and much weaker X-ray luminosities than those of Seyferts. Below $\lambda = 10^{-3}$, it is thought that an advection-dominated geometrically thick, optically thing accretion disk is responsible for the multi-wavelength emission. The X-ray emission could be from the inner-accretion flow or possibly from the base of the jet (e.g. Balmaverde et al., 2006). Never-the-less, the X-ray emission in the LINERs in the LeMMINGs sample are indicative of LLAGN as opposed to shocks or post-AGB stars, which would not be able to explain such high nuclear X-ray luminosities (Allen et al., 2008; Sarzi et al., 2010; Capetti and Baldi, 2011; Singh et al., 2013). Given the radio properties of the LINERs presented in Chapter 5, and the X-ray luminosities for most of the LINERs being $\gtrsim 10^{39}$ erg s^{-1}, it is very likely that most of the LINERs are powered by some form of LLAGN, likely an ADAF.

6.4.3 ALGs

The ALGs are detected in 21/24 cases (88%) in the X-ray LeMMINGs sample. They are associated with X-ray luminosities similar to the LINERs and Seyferts, around 10^{39} erg s^{-1}. ALGs tend to be detected in the higher mass bins, but generally fall below the X-ray-M_{BH} correlation of the whole sample. As ALGs lack optical line data, it is not possible to determine the ionisation method from the [O III] line, but instead must be compared to the other AGN types using the other diagnostic plots. Given their proximity to LINERs in many of the diagnostic plots and similarity to LINERs in X-ray luminosities, it is possible that they have a central engine similar to LINERs. Very few publications have focused on the nuclear properties of ALGs, but Baldi and Capetti (2010) showed that for the galaxies where optical emission lines could not be detected, their multi-wavelength data were similar to that of the low-excitation objects, e.g. LINERs in the LeMMINGs sample. While it remains to be seen whether ALGs can be truly considered as LINERs or recurrent emission (see 5.5.3) from a more powerful AGN, they do show similar X-ray properties to the LINERs and possibly can possibly be interpreted as having the same central engine as LINERs too.

6.4.4 H II galaxies

Of the 98 H II galaxies observed by *Chandra*, only 50 were detected (51%). Of the detected objects, only 21 are at similar X-ray luminosities to that of LINERs and Seyferts e.g. $\gtrsim 10^{39}$ erg s^{-1}. The H II galaxies with the highest black hole masses tend to have the higher X-ray luminosities. However, for the [O III]-X-ray correlation, H II galaxies appear at the lower end of the plot and are often X-ray weaker than the correlation found for all objects, especially if they are not detected. The objects with X-ray luminosities $\gtrsim 10^{40}$ erg s^{-1} tend

to follow the [O III]-X-ray correlation closely, there are a number of objects in the 10^{38} -10^{40} erg s^{-1} range that deviate from the correlation, with higher than expected X-ray luminosities. One source in particular, NGC 598, has a very high X-ray luminosity (8.66×10^{38} erg s^{-1}) compared to the [O III] line luminosity (4.21×10^{34} erg s^{-1}). However, I note that NGC 598 is one of the few galaxies that I used X-ray measurements from the literature due to the complicated spectrum presented by the source, and hence the error on it may be large.

In terms of the central engine powering H II galaxies, it very much depends on individual galaxy properties. For the H II galaxies with a detected radio core and X-ray core, with X-ray luminosities $\gtrsim 10^{39}$ erg s^{-1} and higher BH masses $\gtrsim 10^{7}$M$_{\odot}$, it is likely that they are powered by some form of radiatively inefficient nucleus similar to that of LINERs. Alas, only four H II galaxies (NGC 2146, NGC 3245, NGC 3665, NGC 4102) meet all of these requirements. All of these sources show some sort of 'jetted' or 'complex' radio structure. Therefore, H II galaxies are possibly powered by LINER-like nuclei, but putting an exact number on these is difficult due to the lack of detections of these sources and high BH masses; only 15 H II galaxies have a radio and X-ray detection, not including objects like NGC 3690 and NGC 3034. However, it is reasonable to assume that the H II galaxies that have a combination of a X-ray core and a 'jetted' radio morphology should be sufficient to classify the object with reasonable confidence as an LLAGN. For the other objects, further investigation is required to classify them as genuine LLAGN or imposters in the form of XRBs and ULXs.

6.4.5 The importance of long exposure times for X-ray detections

This X-ray analysis has made substantial efforts to attempt to complete the LeMMINGs (and Palomar) samples with high resolution *Chandra* X-ray data. However, a clear issue with the current data set is the inhomogeneous nature of the exposure lengths across the sample. In general, the detected sources have had the longest exposures (median 20 ks) compared to the undetected sources (median 10 ks). This effect has unreasonably biased the sample in favour of the most well-known or interesting objects, e.g. Seyfert galaxies like NGC 4151, star-burst galaxies like NGC 3034, X-ray jets (see image of NGC 315) or transient events (NGC 3690). As mentioned previously, Seyferts have the longest median exposure length of all the AGN types: 10−15 ks for LINERs, ALGs and H II galaxies compared to 29 ks for Seyferts. Hence, the LLAGN in H II galaxies, LINERs and ALGs are less likely to be detected than Seyferts. In addition, due to the longer exposures and higher count rates of Seyferts, they are also more likely to have a robust spectral fit and therefore include additional components in their spectra. Being able to reliably fit the spectrum of the different sources allows for a more accurate determination of the flux in the observed X-ray band, as well as additional information on the nuclear properties of the X-ray source.

This Chapter has presented an additional 48 observations of nearby LLAGN which had not

been previously observed with *Chandra*. A large number of these objects (28/48) were of H II galaxies, which has considerably helped in giving a more representative sample of X-ray emission in LLAGN. However, only 26 of the 48 objects were detected (55%). As the number of detections with exposure times $\gtrsim$10 ks was 97/114 (85%), future investigations should have increased exposure lengths to ensure nuclear detections. Therefore, a ∼10 ks exposure time is a good minimum requirement for a simple detection and spectral fitting of an 'active' nuclear source, but ideally more exposure time is required to allow for more complex spectral fits to be undertaken. In an ideal world, all objects would be observed in a large *Chandra* programme, for example, observing all 280 LeMMINGs objects for 20 ks. However, such a proposal would require ∼2 months of *Chandra* observing time and as such is unlikely to be approved. Therefore the best way of completing the LeMMINGs sample to continue with small samples of the currently unobserved sources as was performed for proposals 19708646 and 18620515.

6.4.6 Any contamination from XRBs and ULXs?

The advantage of using *Chandra* observations over other observatories is the 0.5″ resolution that it provides, allowing for the discrimination of different contaminating X-ray sources from the nuclear AGN component. However, *Chandra* observations do not completely negate the X-ray emission near to the nucleus from other sources, which may still contribute to the nuclear emission in some objects (for example, see NGC 4150). If one uses a discriminating luminosity of 10^{38} erg s^{-1}, then all of the detected Seyferts and 97% of LINERs meet this threshold, but only 85% of ALGs and 84% of H II galaxies reach this limit. If a higher limit of 10^{39} erg s^{-1} is used, consistent with some ULXs, then these percentages drop to 94%, 84%, 65% and 40% for Seyferts, LINERs, ALGs and H II galaxies respectively. In terms of the Hubble types, this effect is most pronounced in the spirals and irregular galaxies: 92% of spirals and 75% of irregulars are above a 10^{38} erg s^{-1} threshold, but falls to 62% and 75% respectively for a 10^{39} erg s^{-1} threshold. On the other hand, the ellipticals and lenticulars are mostly all detected above both thresholds: 96% for both types combined above 10^{38} erg s^{-1} and 88% above 10^{39} erg s^{-1}. As the link between star formation and prevalence of off-nuclear X-ray sources is known (King, 2004; Gilfanov et al., 2004; Swartz et al., 2009), it is therefore very likely that some of the X-ray LeMMINGs sample, especially the spiral and the H II galaxies are contaminated with emission from non-LLAGN related sources. This shows the necessity of using high-resolution *Chandra* data to try and separate out the X-ray emission from these other sources. In future publications of this work, I will be aiming to look at all of the off-nuclear objects in the sample and also try to classify any additional nuclear objects which may not be AGN (Pahari et al., in prep). Such a project will give an unbiased view of off-nuclear X-ray emission in LLAGN and allow for further discussion on the nature and prevalence of ULXs in nearby galaxies.

6.5 Conclusions

I have presented the *Chandra* X-ray observatory data for 211/280 (75%) objects in the LeMMINGs sample, reaching limiting flux levels of $\sim 3\times10^{-15}$ erg cm^{-2} s^{-1}. The X-ray LeMMINGs sample has detected X-ray emission co-incident with the optical centre of 149/211 (71%) of the observed galaxies across all optical AGN types and galaxy morphologies. This study has exemplified the need for high resolution and sensitive X-ray observations of nearby LLAGN, as nuclear X-ray emission is often detected with *Chandra*. Of the 149 X-ray detected galaxy centres, 60 of them had enough counts to be spectrally fit with robust χ^2 fitting and 60 with Cash statistics. Of the other 29 objects, 23 did not have enough counts to fit a spectrum to, so their fluxes were obtained from an automated code assuming a given spectrum. The other 6 objects had very complicated spectra that could not be fit with simple models and as such their flux values were obtained from the literature. The detection rate of the *Chandra* data of nuclear X-ray emission compares favourably to previous X-ray studies of the Palomar sample: 71% detections compared to 54% in Roberts and Warwick (2000) and 62% in Ho and Ulvestad (2001b). X-ray emission associated with the AGN is observed about 80% of the time in Seyferts, LINERs and ALGs, but also in H II galaxies in 50% of objects.

In terms of the empirical correlations between the X-ray luminosity and other diagnostics of SMBH activity, e.g. BH mass, [O III] line luminosity, radio luminosity, correlations were obtained for different optical classes. No strong correlation was observed for Seyferts for X-ray luminosity and BH mass, but the H II galaxies, ALGs and LINERs appeared to follow a similar correlation in the X-ray-BH mass plane. The most revealing conclusion from comparing to the BH mass is that the LINERs, ALGs and H II galaxies all have very low Eddington ratios and hence low accretion rates. A reasonably strong correlation is observed for all sources when considering the X-ray and [O III] line luminosities. This argues for a scaling between the X-ray emission and ionising source which still holds also at low luminosities. Finally, the X-ray and radio correlation shows no consistent correlation between these two quantities for all the sources, likely due to LINERs being radio-louder than the rest of the sources and the Seyferts being radio-quieter.

Care must be taken in ensuring that the objects co-incident with the nuclear optical core position is actually due to the LLAGN, and not circum-nuclear X-ray emission from ULXs and XRBs, which may be the case in star-forming galaxies. The *Chandra* observations have improved the spatial resolution of the X-ray data compared to previous samples, but, as can be seen in NGC 4150, nuclear X-ray emission not attributed to the LLAGN is still observed. Hence, a fully comprehensive study of the X-ray source population with *Chandra* in all of the LeMMINGs galaxies is needed to remove contaminating sources of X-ray emission from the true LLAGN. Another problem is the large range of exposure lengths in the LeMMINGs X-ray sample, contributing to a wide range of limiting fluxes. However, owing in large part to the high resolution and sensitivity granted by the *Chandra* X-ray Observatory (0.5″), the

luminosities in the detected objects range from 10^{35} to 10^{43} erg s^{-1}, improving on previous surveys by up to three orders of magnitude (e.g. Roberts and Warwick, 2000).

This Chapter has only touched the surface of the amount of science that can be performed with the X-ray LeMMINGs sample. Not only is it useful for testing multi-wavelength correlations, the X-ray data provide the spectral precision needed to investigate Compton thickness in different AGNs, the properties of the Iron line in LLAGN and probe the ULX and XRB population in nearby galaxies. My future work with this project is to continue examining the X-ray data further to investigate the spectral properties of the LeMMINGs sample in greater detail and publish a complete source catalogue of ULXs and XRBs.

Chapter 7

The Fundamental Plane of Black Hole Activity

7.1 Introduction

In the previous two chapters, I described the radio and X-ray properties of the LeMMINGs sample of nearby LLAGN at high-resolution, using e-MERLIN and *Chandra*. However, the accretion process is not limited to the most massive objects in the Universe as BHXRBs are observed in our own galaxy. The only fundamental difference between AGN and BHXRBS are the masses of the BHs involved in the accretion process: SMBHs in AGN have masses $\sim 10^8 M_\odot$ whereas BHXRBs are of order $\sim 10 M_\odot$. By observing both BHXRBs and SMBHs, it is possible to build up a holistic view of accretion in the Universe. The large number Richards et al. more than a million, see 2009 of catalogued AGN allows for statistical studies, while the BHXRBs show variability that can be observed on 'human' time-scales (Plotkin et al., 2012, hereafter P12). Furthermore, it has been suggested that there is some form of disk-jet symbiosis (Begelman et al., 1984; Falcke and Biermann, 1995) in both BHXRBs and SMBHs. Hence, a great deal of observational and theoretical work has been undertaken to correlate the accretion properties in these two types of system and explain how the accretion process in BHXRBs analogous to that observed in SMBHs.

BHXRBs are thought to be the low-mass analogues of SMBHs for several reasons. BHXRBs are observed in a variety of states which can show either rapid variability in the X-ray emission or jet launching: in the high/soft state, the radio jet emission in BHXRBs is quenched, but in the low/hard state, persistent jets are observed (e.g. Stirling et al., 2001). The radio and X-ray emission of BHXRBs in the low/hard state is observed to be correlated, and scales as $L_{radio} \propto L_{X-ray}^{0.7}$ (Corbel et al., 2003; Gallo et al., 2003). In this state, the jets are thought to be similar to those observed in LLAGN and presented in Chapter 5 of this thesis, but radio vs X-ray correlations have also been observed in some AGN samples but not in all (Hardcastle and Worrall, 2000; Panessa et al., 2006; Hardcastle et al., 2009). In the

high/soft state, it has been shown that BHXRBs fall off this radio vs X-ray relationship (e.g. Gallo et al., 2003). Furthermore, it has been suggested that AGN may show a similar set of states, with quenched radio emission in the high/soft state (Maccarone et al., 2003). In the low/hard state, it is thought that the X-rays in BHXRBs arise from a partially self-absorbed jet (Fender, 2001; Fender et al., 2004). But in SMBHs, various authors have attributed the X-ray emission in the AGN to either an optically thin jet (labelled 'jet' here-after and in Körding et al., 2006, , hereafter K06) or as due to the accretion flow (labelled 'ADAF/jet' in K06) but have often come to difference conclusions based on different sub-samples (Merloni et al., 2003; Falcke et al., 2004; Körding et al., 2006; Wang et al., 2006; Gültekin et al., 2009; Yuan et al., 2009). However, it is likely that the X-rays come from a mixture of both mechanisms in most objects and discerning the dominant process is therefore challenging.

Observational attempts at explaining the similarities between the X-ray and radio properties of SMBHs and BHXRBs eventually culminated in the discovery of the 'Fundamental Plane of Black Hole Activity' (hereafter 'FPBHA' Merloni et al., 2003; Heinz and Sunyaev, 2003; Falcke et al., 2004). The FPBHA is a 3-dimensional hyperplane that correlates the radio luminosity with the X-ray luminosity, scaled by the mass of the BH. While there is significant scatter in the radio luminosity axis (0.88 dex, Merloni et al., 2003, hereafter M03), the correlation does seem to hold for all BHXRBs and SMBHs. In essence, it is similar to the low/hard state radio/X-ray correlation found for BHXRBs, only modified by a mass term (P12). Hence, the FPBHA is one of the major pieces of evidence that strengthen the arguments for a scale-invariant accretion mechanism.

By using a similar approach to M03, Saikia et al. (2015, hereafter, S15) introduced a new version of the FPBHA using the [O III] luminosity as a tracer of the accretion, instead of the X-ray luminosity and found an analogous correlation for active BHs. Saikia et al. (2015) used a modified scaling of the Heckman et al. (2005) relation to obtain the Optical FPBHA, showing that the optical [O III] line luminosity can be used in lieu of available X-ray observations for larger samples of AGN. Using the [O III] line luminosity instead of the X-ray luminosity has its advantages, as the [O III] line emission often extends further away from the nucleus than the X-ray emission and can be measured from the ground with reasonable resolution (e.g. the Palomar survey, Ho et al., 1997a), unlike the X-rays. Furthermore, with regards to the LeMMINGs sample, the optical [O III] line luminosity is available for all the galaxies from the Palomar survey, hence increasing the number of detected objects that can be used for the FPBHA.

However, there is a large amount of debate in the literature about the exact correlation coefficients of the FPBHA, the effects of statistical bias and coupled uncertainties in the data, the size and the quality of the BHXRB and SMBH samples and the source of the data used to construct the samples. For example, much of the early literature focused on removing statistical biases from the samples, such as the correlated distance uncertainties in the radio and X-ray luminosity axes. It was thought that the FPBHA correlation could be a "distance-driven artefact" of the detected objects, leading to a linear correlation even if

drawn from a random distribution of fluxes (Merloni et al., 2006). To test the validity of this problem, partial correlation analysis performed by Merloni et al. (2003, 2006) showed that the correlated distances were not causing the relationship between the luminosities of the AGNs and XRBs. An additional issue comes from plotting the FPBHA as a 3D logarithmic plot, as the correlation appears linear and potentially hides a great deal of variation in the underlying sample. If plotted on a linear scale, the correlation may not look so convincing, so it is important to keep this factor in mind when performing such a regression. While a great deal of work has been performed to alleviate potential statistical problems with the FPBHA relation, there is still much to do to test the significance of the FPBHA and its physical interpretation.

Creating an unbiased sample has proven difficult over the years due to a number of reasons. The state changes and rapid variability observed in BHXRBs necessitates simultaneous observations in different wavebands to ensure that the object is in the low/hard state. As such, much of the simultaneous data in the literature focusses on a handful of well-known sources (for example GX 339-4, Corbel et al., 2013). Conversely, for AGN, a large number of observations have been made for many sources, but rarely simultaneously, so one must assume that the X-ray and radio emission observed years apart is still related. It is expected that over timescales of decades, the radio luminosity of AGNs should not significantly change, but as I showed in Chapter 3, some LLAGN sources have been shown to vary over timescales of two decades (Mundell et al., 2009; Panessa et al., 2007; Williams et al., 2017) and the X-ray emission in AGN is known to vary on short timescales (e.g. Mushotzky et al., 1993; González-Martín and Vaughan, 2012; Connolly et al., 2016). Furthermore, most of the SMBHs used in FPBHA investigations have sampled the most powerful AGN, as they are often detected in both the radio and X-ray wavebands. Such sources may not be in the analogous low/hard state (e.g. they may be efficiently accreting) to fit on the FPBHA correlation.

A further problem with the FPBHA is the lack of known BHXRBs that help constrain the low-mass end of the relation: of ~60 candidate or confirmed BHXRBs (Corral-Santana et al., 2016), only a small number (of order 10s) have reliable mass estimates. A similar problem exists for SMBHs as estimates of the black hole masses in AGN systems are reliant on the M-σ relation used (see Chapter 2), as dynamical BH measurements only exist for a small number of sources (e.g., see van den Bosch, 2016). The BH mass is important for probing the accretion flow. As shown in equation 1.28, the accretion disk temperature is proportional to $M^{-0.25}$, and therefore the AGN accretion flow peaks in the UV/Optical while the XRBs peak in the X-rays, complicating direct comparison between the two groups of object.

Finally, the inhomogeneity in the datasets used makes systematic errors inevitable in most previous studies of the FPBHA. Due to the paucity of simultaneous data with the same telescopes, multiple different radio arrays (e.g. VLA, ATCA, VLBA) and X-ray instruments (e.g. *Swift*, *Chandra*, *XMM-Newton*) have been used to obtain the flux measurements for

both the BHXRBs and SMBHs. The use of different radio arrays at different frequencies, especially those with low sensitivity/resolution causes problems with comparing the data directly. While it is possible to scale between different frequency bands assuming a flat radio spectral index ($\alpha \sim -0.4$), it is not straight forward to scale between different array configurations with different beam sizes. The use of different interferometers is especially problematic for the AGN as they are more distant and hence the linear scales probed by radio observations changes greatly as a function of distance.

With the LeMMINGs sample I presented in Chapters 5 and 6, there is now a reasonably sized (280 total objects with 241 radio and 211 X-ray observations) statistically-complete sample of LLAGN with good sensitivity in both the radio (0.2 mJy at 3σ confidence) and the X-rays (limiting flux of $3{\times}10^{-15}$ergs s^{-1} cm^{-2}), which has been observed with only one instrument in both bands at high resolution to isolate the nuclear activity, which can now be used to investigate the FPBHA at the lowest radio and X-ray luminosities. Thererfore, in this Chapter I will investigate the FPBHA with the data outlined in the previous chapters of this thesis for the LeMMINGs sample. I will briefly explore the statistical techniques I employ to study the FPBHA and overview the theoretical study of the FPBHA. I will present the FPBHA in the X-rays and Optical for the LeMMINGs sample, including a complementary sample of BHXRBs from M03 and K06.

7.2 Statistical Techniques

Previous work investigating the FPBHA has utilised different fitting methods and explored the statistical problems with each. The original M03 FPBHA was described as follows:

$$\log L_R = \alpha \log L_X + \beta \log M_{BH} + \gamma \tag{7.1}$$

where L_R is the radio luminosity at 5 GHz, L_X is the X-ray luminosity in the 2−10 keV band, M_{BH} is the black hole mass, α is the correlation coefficient for the X-rays, β is the correlation coefficient for the black hole mass and γ is the intercept of the plane. In this formulation, the radio luminosity is the dependent variable. However, subsequent studies (K06, P12) recast the X-ray luminosity as the dependent variable to investigate the origin of the X-rays (see Section 7.4), and reformulated the plane thus:

$$\log X = \xi_R \log L_R + \xi_M \log M_{BH} + B \tag{7.2}$$

where the ξs are the correlation coefficients for the radio and mass respectively, and B is the intercept. It should be noted that both formulae for the FPBHA presented above are the same and therefore the coefficients can be found for one by inverting the equation for the other. However, P12 notes that due to the intrinsic scatter about the plane, one cannot directly convert from one set of coefficients to the other and hence a new regression must be performed. In this Chapter, unless otherwise stated, I will use the formalism set out by M03,

that is that the radio luminosity is the dependent variable, so that I can compare directly to the M03 paper without having to perform an additional regression. I will cast the correlation coefficients are b_{X-ray} and b_{Mass} for the X-ray and mass axes respectively, to avoid confusion with the previous literature.

7.2.1 A Frequentist Approach

As the FPBHA is a 3-dimensional plane with dependent variables and measurement uncertainties on all three axes, traditional multi-variate fitting techniques do not apply. Standard regression techniques do not treat the dependent and independent variables symmetrically and normal Chi-squared regression only considers the error in the y axis. Therefore, to overcome the problems of traditional regression formalism and estimate the coefficients of the FPBHA, many authors use the Merit Function: a modified Chi-squared estimator that allows for uncertainties in all variables. The Merit Function has been used in various estimations of the FPBHA (M03, Merloni et al., 2006; Saikia et al., 2018, K06, S15) and is described in Fasano and Vio (1988) and Press et al. (2002), often written in the form:

$$\chi^2(a,b) = \sum_i \frac{\left(y_i - a - \sum_j b_j x_{ij}\right)^2}{\sigma_{y_i}^2 + \sum_j b_j^2 \sigma_{x_{ij}}^2} \tag{7.3}$$

where y_i is the independent variable, in this case the radio Luminosity, a is the intercept of the line, b_j are the parameters attributed to the gradient of the line, e.g. for the X-ray Luminosity and Mass, the $\sigma_{x_{ij}}$ and $\sigma_{y_{ij}}$ are the standard deviations on x and y for the ith point respectively. However, a subtlety emerges in the treatment of the FPBHA using the Merit function, in that the χ^2 function now includes the b_js in the denominator, which means that the slopes $\frac{\partial \chi^2}{\partial b_j} = 0$ are non linear. As the condition for the intercept is linear, it is possible to minimise with respect to the slopes, e.g. the b_js, using:

$$a_{min}(b) = \frac{\sum_i \left[\frac{(y_i - \sum_j b_j x_{ij})}{\sigma_{y_i}^2 + \sum_j b_j^2 \sigma_{x_{ij}}^2}\right]}{\sum_i \frac{1}{\sigma_{y_i}^2 + \sum_j b_j^2 \sigma_{x_{ij}}^2}} \tag{7.4}$$

while using equation 7.3 simultaneously to ensure that the minimum with respect to the b_js is minimized with respect to a. However, it is not possible to consider censored data (e.g. upper limits) or correlated errors (e.g. the distance estimates in both the luminosities) in such an approach. A further discussion by K06 attempted to refine the FPBHA by selecting a representative sample of the objects expected to be in the same physical hardness state and by considering the variances on the data points. The authors found that the variances in the mass, X-ray and radio luminosities were highly correlated, and hence cannot be considered to be isotropic, as was performed in the M03 work. K06 found that anisotropies in the uncertainties of the different axes increased the fitted errors greatly, and therefore it is necessary to take care when considering such uncertainties and errors in future fits.

7.2.2 A Bayesian Approach

Given the limitations of the Merit function described above, I chose to explore other options, including a Bayesian approach, which has been used before in regressions of the FPBHA by P12. The fundamental difference between the frequentist approach outlined above and a Bayesian approach is that the latter samples the posterior probability distribution of the coefficients of the FPBHA, given the measured data. The Bayesian method implemented here (and in P12) assumes that the measurement errors are Gaussian, as is the intrinsic scatter in the FPBHA and that all the variables can be approximated as a set of Gaussian functions. These assumptions allow a Markov Chain Monte Carlo (MCMC) simulation that builds the posterior probability distribution by randomly sampling the set of possible FPBHA coefficients, given the data. Formally, the MCMC Bayesian approach presented here is marginalizing over the parameter space to solve the maximum likelihood function for the given problem and output the posterior probability distribution for the FPBHA.

The benefit of a Bayesian approach means that it can overcome the problems with correlated errors and potentially also handle upper limits properly, by building them into the priors of the model. The other benefit is that the intrinsic error, σ_{int} does not have to be varied to reduce the χ^2 value to unity, as in M03 and K06; the intrinsic scatter comes immediately from the data and the Bayesian regression. By properly solving for the maximum liklihood of the plane, it is possible to reduce the errors in the values of the correlation coefficients (see K06, P12). I refer the reader to P12 for an in depth discussion of the benefits of such a method. Furthermore, I will not explicitly derive the maths for this method here, but I refer the reader to the work of Hogg et al. (2010) and VanderPlas (2014) which give excellent examples of the method[1] using the MCMC algorithm developed by Dan Foreman-Mackey EMCEE (Foreman-Mackey et al., 2013).

In writing the code to fit the FPBHA, I used the detections of the original M03 publication to compare to, ensuring that the Bayesian method I have used is consistent with the literature coefficients of the FPBHA. The coefficients published by M03 remove the upper limits and includes both the BHXRBs and AGN. Furthermore, the M03 sample did not include measurement errors and estimated the intrinsic scatter in the plane by varying the parameter until the reduced χ^2 was unity. The computed values[2] from the Bayesian code gave b_{X-ray}=$0.60^{+0.05}_{-0.05}$, b_{Mass}=$0.75^{+0.05}_{-0.04}$ and a=$7.33^{+1.64}_{-1.66}$. This compares to the M03 coefficients of b_{X-ray}=$0.60^{+0.11}_{-0.11}$, b_{Mass}=$0.78^{+0.11}_{-0.09}$ and a=$7.33^{+4.05}_{-4.07}$. These computed values show that the basic premise of the Bayesian sampling method that I have employed reproduces the literature values of the FPBHA within the uncertainties, and in fact improves upon those found by M03.

[1] A fully 3-dimensional example of EMCEE including errors can be found at https://dfm.io/posts/fitting-a-plane/ and further examples can be found at http://jakevdp.github.io/blog/2014/03/11/frequentism-and-bayesianism-a-practical-intro/

[2] I used the version of the FPBHA outlined in M03 and equation 7.1 in computing these coefficients to ensure that the intrinsic error was not biasing the results.

Upper limits

A large number of the LeMMINGs sample are not detected in the radio or X-ray bands. However, I have obtained upper limits for these sources based on the noise levels in the radio and X-ray images (see Chapters 5 and 6 respectively). These data give important information on the gradient of the FPBHA at the lowest luminosities and can be used to help constrain the parameter space between BHXRBs and LLAGN. While some packages that include censored data are available, like ASURV (Lavalley et al., 1992) and LINMIX (Kelly, 2007), it is difficult to properly treat censored data in three dimensions with frequentist statistics. However, using the Bayesian approach outlined above, it is possible. I have not currently implemented the upper limits into the code, but it is planned for future publication of the dataset.

7.3 Theoretical Predictions of the FPBHA

The theoretical framework for the FPBHA was first discussed and mathematically derived in M03 and Heinz and Sunyaev (2003), assuming synchroton radio emission from a scale-invariant jet. The radio emission from such a jet depends on the accretion rate and black hole mass. On the other hand, the X-ray emission can be due to Compton up-scattering from a corona in an ADAF type flow (the 'ADAF/coronal' model), or due to optically thin jet synchrotron emission (the 'jet' model). Both of these processes may equally contribute to the observed X-rays and it is thought that the different contributions of these sources of X-ray emission may explain some of the intrinsic scatter in the FPBHA (P12). Therefore, previous FPBHA studies have concentrated on understanding the dominant sources of X-ray emission to diagnose the type of accretion flow. In addition to the 'coronal' and 'jet' models, M03 also computed the theoretical coefficients for the FPBHA for a standard optically-thick, geometrically-thin disk. It is not my intention to repeat this work here, and I refer the reader to M03, Heinz and Sunyaev (2003), F04 and P12 for complete discussions on the derivation of the coefficients and the different nomenclature used in the literature. However, I will summarise the findings for comparison in later sections.

7.3.1 The 'ADAF/coronal' model

M03 explained the X-ray emission as due to the accretion flow in the form of a hot X-ray corona of Compton up-scattered electrons. In this model, the X-rays probe the inflow towards the BH, whilst the radio emission is a mechanical outflow in the form of jets. It should be noted that the X-ray emission in the coronal model is due to an inefficient flow, and not necessarily due to a standard disk. The mathematical expression for the correlation coefficients in this model are obtained from M03:

Table 7.1: The different correlation coefficient model parameters of the FPBHA

Model	q	$\partial \ln \Phi_B / \partial \ln M$	$\partial \ln \Phi_B / \partial \ln \dot{m}$
ADAF/coronal	2.3	-0.5	0.5
Brehmsstrahlung	2	-0.5	0.5
Disc/corona, gas	1	-0.5	0.5
Disc/corona, rad	0.5	-0.5	0.25

$$(\xi_M)_{cor} = \frac{2p+13+2\alpha_R}{p+4} + \frac{\partial \ln \Phi_B}{\partial \ln M}\left(\frac{2p+13+\alpha_R p+6\alpha_R}{p+4}\right) - \frac{\partial \ln \Phi_B}{\partial \ln \dot{m}}\left(\frac{2p+13+\alpha_R p+6\alpha_R}{q\,(p+4)}\right);$$
$$(\xi_X)_{cor} = \frac{\partial \ln \Phi_B}{\partial \ln \dot{m}}\left(\frac{2p+13+\alpha_R p+6\alpha_R}{q\,(p+4)}\right) \tag{7.5}$$

where α_R is the radio spectral index[3] and p is the power-law index of the electrons, usually between 2 and 3, Φ_B is the magnetic field at the jet base which depends on the accretion rate $\dot{m}$ and M and q is the radiative efficiency of the accretion flow. The values for q and both the partial differentials of the magnetic field are given for different models in M03 and are reproduced in Table 7.1 for completeness here. In addition, M03 also calculate the expected values for when the X-ray spectrum is dominated by Brehmsstrahlung emission (shown in Table 7.1), thought to occur when the ADAF flow is modified by outflows and/or convection. The correlation coefficients for the optically-thick, geometrically-thin disk model are given in Table 7.1, for direct comparison with M03 for a slim disk where gas pressure dominates ('gas') and where the radiation pressure dominates ('rad').

7.3.2 The 'jet' model

The 'jet' model assumes that the X-rays come from the base of the radio jet, rather than from the accretion flow from the corona. In this case, the X-ray emission comes from optically thin synchrotron radiation and the correlation coefficients can be explained by the radio spectral index, α of the radio emission, assuming a given power-law index of the particles, p. It is expected that the intrinsic scatter about the plane should be less for optically thin synchrotron X-ray emission, as the radio and X-ray wavebands both trace the same part of the accretion flow. Mathematically, this translates to:

[3]Here the radio spectral index is defined in the more classical way, unlike in previous chapters where I have used the CASA convention of S$\propto \nu^{\alpha}$. From here in I will use the notation S$\propto \nu^{-\alpha}$ so that an inverted spectrum has a negative α_R value, e.g. an inverted spectral index is one where S increases with frequency.

$$
\begin{aligned}
(\xi_X)_{jet} &= \frac{2\,(2p + 13 + \alpha_R p + 6\alpha_R)}{(p + 4)\,(p + 5)}; \\
(\xi_M)_{jet} &= \frac{2p + 13 + 2\alpha_R}{p + 4} - \frac{6\,(2p + 13 + \alpha_R p + 6\alpha_R)}{(p + 4)\,(p + 5)}
\end{aligned}
\tag{7.6}
$$

where α_R and p are defined as before in the 'coronal/ADAF' model. As the correlation coefficients in this model are a function of the radio spectral index and make up of the electrons, hence it is simple to compare any fit values of the FPBHA with this model by varying these two parameters. Such a comparison is given in P12, who show the 'jet' and 'ADAF/coronal' models graphically by varying the parameters.

7.4 The Black Hole sample

7.4.1 The LeMMINGs LLAGN

The radio data for the LLAGN in the sample are obtained from the LeMMINGs sample presented in Chapter 5 and 6. I obtained 84 radio detections and 149 X-ray detections of LLAGN in the entire LeMMINGs sample presented in this thesis. Of these, 62 sources were detected in both the radio and X-ray and have a reliable mass measurement. Previous studies have split up the samples to minimise the scatter in the fit results (e.g. K06), which I also perform as follows:

- First, I define the 'Complete' sample, which includes all of the LeMMINGs sources with radio and X-ray detections with reliable black hole mass measurements. This sample includes 62 sources.
- Second, I define the 'AGN-only' sample which includes all LeMMINGs objects that are optically classified as LINERs or Seyferts. This cut is made to ensure less contamination from star-formation. This sample includes 45 sources. I also make a cut of these sources which includes only those with accretion rates below $10^{-3}\dot{M}_{\odot}$, which includes 38 sources and is called the 'Low $\dot{m}$ AGN' sub-sample.
- Third, I define the 'ADAF-only' sample, which includes all of the LINERs, H II galaxies and ALGs, but crucially not the Seyferts. As discussed in Chapters 5 and 6, Seyferts are thought to be powered by a geometrically thin, optically-thick accretion disk, unlike that of the low/hard state BHXRBs. All of the other AGN classifications have shown similar properties that lead to the conclusion that they may be powered by an ADAF-type flow. This sub-sample includes 55 sources.
- Fourth, I define the 'jetted' sample, which includes all the AGN types which have jet-like morphologies, including the jetted H II galaxies shown in Chapter 5. As the jetted H II galaxies appear to follow the radio/X-ray/Mass/[O III] relations in Chapters

5 and 6, it is useful to compare them with other similar sources to investigate the central engines in this specific source type. This sub-sample includes 25 objects.

- Fifth and finally, I define the 'LINER-only' sample which includes all 38 LINERs with radio and X-ray detections from the LeMMINGs sample. The LINERs are all thought to be powered by ADAF-type flows and hence are worthy of investigating on there own, especially considering the number of them in the LeMMINGs sample.

I will also use these sub-samples when discussing the [O III] line luminosity in the Optical FPBHA. The X-ray data for all of the LeMMINGs sources comes from the *Chandra* data presented in Chapter 6. I will use the 0.3-10.0 keV luminosities for all of the LeMMINGs sources. The radio data used in this analysis includes all of the core luminosities of the detected sources. The [O III] line luminosity comes from the Palomar sample (Ho et al., 1997a). The black hole masses used for this sample are obtained from the M-σ relation of Tremaine et al. (2002) although where possible, dynamical black hole masses are obtained from van den Bosch (2016).

7.4.2 A sample of BHXRBs

Obtaining a homogeneous sample of radio data for BHXRBs is difficult, as the data need to be simultaneous with X-ray observations and using the same radio telescope. Unfortunately, no sample exists, but there have been several independent campaigns in the literature to intensively monitor a small number of BHXRB sources with simultaneous X-ray and radio data. Where simultaneous X-ray/radio data exists for BHXRBs, I have used the flux values in the literature to form my BHXRB sample. M03 used all different types of BHXRB including upper limits on the black hole mass, X-ray and radio luminosities. However, K06 removed some of these BHXRBs due to their known properties that were unlikely to correlate on the FPBHA. As such I remove the same sources: Cyg X-1 was excluded from K06 as it changes state frequently (Gallo et al., 2003), GRS 1915+105 was excluded as it does not go into the "canonical" low/hard state (van Oers et al., 2010) and LS 5039 was excluded as it was not known whether it was a neutron star or black hole (e.g. see Moldón et al., 2012). In addition, I remove observations that have upper limits in any of the measured X-ray, radio or mass observations. In total, I have 5 sources, with 24 data points of BHXRBs in the low/hard state, but I stress this should not be considered a complete or representative sample of BHXRBs, but a conservative one from the observations in the literature. In addition to the BHXRBs outlined above, I will also use the Sgr A* observation outlined in M03 as the only example of an extremely radio-quiet LLAGN. In the rest of this thesis I will refer to FPBHA regressions that include the modified M03 BHXRB outlined above by writing '+ BHXRB' with the LLAGN sample. I note in future publication of this work, a larger BHXRB sample will be used.

While the BHXRB sample is useful for constraining the FPBHA correlation coefficients, I note that the previous studies of the FPBHA have often used variations of the same BHXRB

sub-sample derived from the sample of Gallo et al. (2003) e.g. M03, K06, P12. The BHXRB sub-sample of Gallo et al. (2003) is an inhomogeneous set of different BHXRBs, observed with a variety of X-ray instruments and radio arrays. In a large number of these studies, the assumed flux, distance and BH mass uncertainties vary and are not always available in the literature for the required X-ray flux band. For this reason, previous FPBHA publications have assumed an error budget for the BHXRBs, and assumed that all of the sources will have the same uncertainties for the flux, distance and BH mass estimates. I use the same error budget used for fitting the Optical FPBHA for the BHXRBs as Saikia et al. (2015). The assumed errors on the fluxes (O III, radio or X-ray), distance and BH mass are therefore 0.05 dex, 0.15 dex and 0.34 dex respectively. However, I note that these values are mostly arbitrary and some objects may be constrained better (or worse) than these uncertainties.

7.5 The Fundamental Plane of Black Hole Activity

In this section I will describe the best fit parameters for all of the different samples explained in the previous section. In Table 7.2, I give all of the best fit parameters for all of the different samples. In Figure 7.1 I show the best fit FPBHA of the LeMMINGs sample for all of the detected sources, e.g. the 'Complete' sample with the modified BHXRB sample of M03 outlined in Section 7.4. I also show the marginalised posterior probability distributions of the fit parameters, b_{X-ray}, b_{Mass}, intercept and intrinsic scatter, for the 'Complete' and 'Complete + BHXRB' samples. Furthermore, the marginalised posterior probability distributions for b_{X-ray} and b_{Mass} are plot against the theoretical values for the 'ADAF' and 'jet' models outlined in Section 7.3. The additional plots for all of the other sub-samples are included in Appendix E.

From Figure 7.1, the detected radio and X-ray sources of the LeMMINGs sample clearly align with the BHXRBs of M03, K06. There is some scatter around the FPBHA, but the LINERs appear to closely follow the line, as do the jetted H II galaxies. The non-jetted H II galaxies fall to the left of the regression, by up to a factor of ~100 because of their smaller BH masses and lower X-ray luminosities. Finally, the ALGs appear to mostly lie on the correlation as do the Seyferts, although the Seyferts are usually radio-quieter than the fit regressions of all the sub-samples. Comparing the different sub-samples, the selection of the LLAGN used changes the correlation coefficients of the FPBHA. I note that for all correlations, regardless of the objects included, the inclusion of the BHXRBs almost always improves the fit parameters, although not always the intrinsic scatter, and therefore I will only consider the sub-samples that include the BHXRBs in the following discussion. Without the BHXRBs to help constrain the relation, the regressions are very poor in the sub-samples with very few objects (e.g. the 'Low Accretion Rate' sub-sample) causing the correlation coefficients to be highly uncertain.

The 'Complete + BHXRB' sample includes all of the X-ray and radio detected sources with

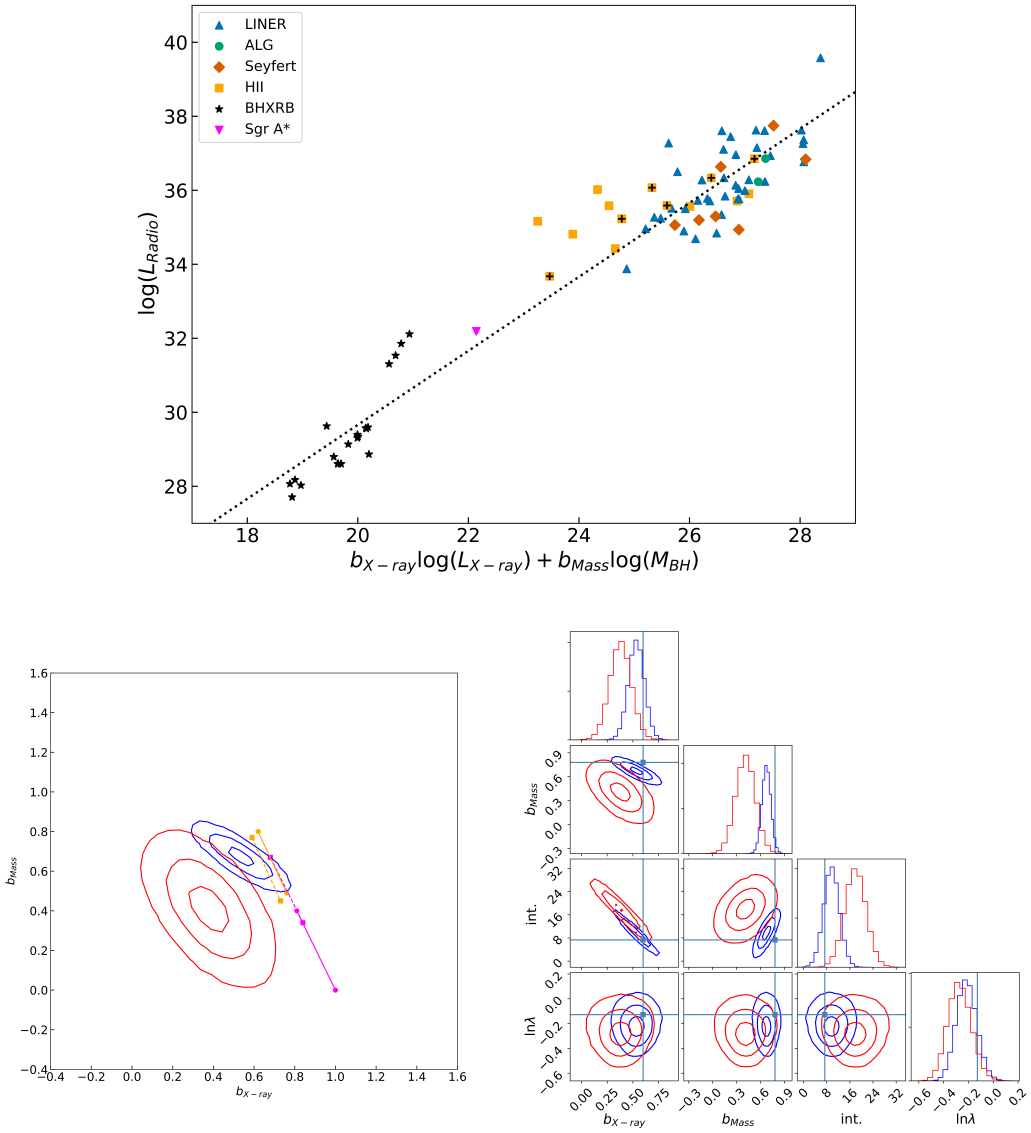

Figure 7.1: *Top panel:* The FPBHA for the 'Complete + BHXRB' sample, with the luminosities in erg s^{-1} and BH masses in $M_\odot$. The different classes are coded (colour and symbol) according to the legend. The jetted HII galaxies show an additional plus symbol. *Bottom panel, left:* The posterior probability distribution of the marginalised slopes for the 'Complete' (red) and 'Complete + BHXRB' (blue) samples, as detailed in Section 7.4 and Table 7.2. The contours show the 1, 2 and 3 σ levels of the 2d Gaussians for the slopes b_{X-ray} and b_{Mass}. The orange lines correspond to the 'ADAF' model and the magenta lines correspond to the 'jet' model. The radio spectral index increases from 0.0 to 0.5 as you go down and to the right along the lines, with each end corresponding to these values respectively. The filled lines correspond to a particle distribution of p = 2, and the dashed lines correspond to p = 3. *Bottom panel, right:* The corner plot of the marginalised posterior probability distribution for the entire parameter space, including b_{X-ray}, b_{Mass}, intercept and intrinsic scatter, for both the 'Complete' (red) and 'Complete + BHXRB' (blue) samples, as detailed in Section 7.4 and Table 7.2. The green lines correspond to the values of those parameters as published in M03.

Table 7.2: Best fit parameters of the FPBHA with the various samples described in Section 7.4, including the errors which are denoted by the 16th and 84th percentiles, e.g. the 1σ uncertainties. The values shown are the median values of the posterior probability distribution of the fit parameters.

Sample Selection	b_{X-ray}	b_{Mass}	intercept	σ_{int}
'Complete'	$0.38^{+0.10}_{-0.10}$	$0.41^{+0.13}_{-0.13}$	$17.96^{+3.64}_{-3.70}$	0.54
'Complete' + 'BHXRB sample'	$0.53^{+0.08}_{-0.08}$	$0.67^{+0.06}_{-0.06}$	$9.68^{+2.72}_{-2.72}$	0.61
'Low $\dot{m}$ Complete'	$0.26^{+0.34}_{-0.35}$	$1.06^{+0.53}_{-0.53}$	$17.42^{+10.69}_{-10.61}$	0.74
'Low $\dot{m}$ Complete' + 'BHXRB sample'	$0.66^{+0.10}_{-0.10}$	$0.62^{+0.06}_{-0.06}$	$5.24^{+3.42}_{-3.42}$	0.54
'AGN'	$0.43^{+0.12}_{-0.11}$	$0.72^{+0.19}_{-0.19}$	$13.28^{+4.40}_{-4.42}$	0.58
'AGN' + 'BHXRB sample'	$0.57^{+0.09}_{-0.09}$	$0.65^{+0.05}_{-0.05}$	$8.15^{+2.65}_{-2.69}$	0.52
'Low $\dot{m}$ AGN'	$0.40^{+0.18}_{-0.18}$	$0.72^{+0.25}_{-0.25}$	$14.55^{+6.22}_{-6.33}$	0.64
'Low $\dot{m}$ AGN' + 'BHXRB sample'	$0.61^{+0.08}_{-0.09}$	$0.63^{+0.06}_{-0.06}$	$6.84^{+3.15}_{-3.13}$	0.55
'ADAF'	$0.49^{+0.13}_{-0.13}$	$0.29^{+0.14}_{-0.14}$	$14.26^{+4.49}_{-4.55}$	0.50
'ADAF' + 'BHXRB sample'	$0.59^{+0.09}_{-0.09}$	$0.64^{+0.06}_{-0.06}$	$7.54^{+2.98}_{-3.00}$	0.59
'LINER-only'	$0.52^{+0.16}_{-0.16}$	$0.58^{+0.25}_{-0.24}$	$10.88^{+5.50}_{-5.51}$	0.58
'LINER-only' + 'BHXRB sample'	$0.64^{+0.08}_{-0.08}$	$0.63^{+0.06}_{-0.06}$	$5.96^{+2.89}_{-2.88}$	0.50
'Jetted'	$0.31^{+0.14}_{-0.14}$	$0.57^{+0.18}_{-0.18}$	$19.37^{+5.45}_{-5.38}$	0.38
'Jetted' + 'BHXRB sample'	$0.59^{+0.08}_{-0.08}$	$0.65^{+0.06}_{-0.06}$	$7.39^{+2.80}_{-2.80}$	0.43

reliable mass estimates from the LeMMINGs sample plus all of the BHXRBs and Sgr A*. It includes objects accreting at very different rates (ranging from $\dot{m} = 10^{-6}$ $M_{\odot}$ to 0.3 $M_{\odot}$) and therefore potentially includes objects that accrete with physically different mechanisms, which may not be applicable to the formulation of the FPBHA. By comparing the objects that are reliably designated as AGN, e.g. the LINERs and Seyferts combined with the BHXRBs and Sgr A*, the size of the posterior probability distribution and correlation coefficient uncertainties in the sample was slightly reduced. The intrinsic scatter was reduced in the 'AGN + BHXRB' sample compared to the 'Complete + BHXRB' sample, largely due to the removal of the non-jetted H II galaxies at the low end of the SMBH part of the relation. Furthermore, the low accretion rate AGN sample showed a larger intrinsic scatter but with parameters that are closer to the values obtained from M03. This sample removed a large number of the Seyfert galaxies, but there is still scatter induced by the LINERs. On their own, the LINERs show similar correlation coefficient values and scatters to the low accretion rate AGN sample. The 'ADAF-only + BHXRB' sub-sample included all non-Seyfert galaxies, owing to their multi-wavelength similarities. There was a larger amount of intrinsic scatter in this regression than the AGN sample, probably due the non-jetted H II galaxies once more. The 'low accretion rate' sample had the smallest intrinsic scatter and had good reasonable uncertainties on the fit parameters, as well as values closest to the M03 sample, but this sample is mostly constrained by the inclusion of the BHXRBs, as the fit is very poor without them.

The regressions shown in Table 7.2 show that the slopes of the Black Hole Mass and X-ray Luminosity are both shallower than that found by M03, the most directly comparable previous piece of literature. M03 used the Merit function in their estimation of the FPBHA, and P12 claim that the differences in the slopes between the Bayesian and Frequentist methods can largely be attributed to the correct handling of correlated measurement errors (e.g. due to the distance) between the radio and X-ray. The intrinsic scatter in the LeMMINGs fit data with and without the BHXRB samples are always smaller than that observed by the regression of M03 (0.88 reported with the Merit function, 0.79 using my Bayesian analysis), but I stress that the two samples are not directly comparable: M03 had a much larger dynamic range in all three parameter spaces and included AGN objects that are unlikely to follow the relationship well like radio-loud AGN. The refined full K06 sample of BHs yields a similar intrinsic scatter (0.58) to that found in this work, but over a larger BH mass range as it includes some FR I and BL Lacs. Therefore, future investigations will likely be improved by including an e-MERLIN sub-sample of similar AGN objects, like the FR Is presented in Chapter 5, for example.

7.5.1 The Fundamental Plane of Black Hole Activity in the Optical Band

Saikia et al. (2015) introduced the Optical FPBHA using the [O III] luminosity as a tracer of the accretion, instead of the X-ray luminosity and found an analogous correlation for active BHs. Therefore, using the optical [O III] line emission values from the Palomar sample, I

Table 7.3: Best fit parameters of the FPBHA with the various samples described in Section7.4

Sample Selection	b_{X-ray}	b_{Mass}	intercept	σ_{int}
'Complete'	$0.45^{+0.10}_{-0.10}$	$0.47^{+0.09}_{-0.09}$	$14.52^{+3.80}_{-3.78}$	0.47
'Complete' + 'BHXRB sample'	$0.60^{+0.06}_{-0.06}$	$0.60^{+0.05}_{-0.05}$	$7.49^{+2.38}_{-2.36}$	0.48
'Low $\dot{m}$ Complete'	$0.13^{+0.57}_{-0.56}$	$1.24^{+0.69}_{-0.72}$	$21.04^{+17.33}_{-17.62}$	0.64
'Low $\dot{m}$ Complete' + 'BHXRB sample'	$0.67^{+0.09}_{-0.09}$	$0.58^{+0.07}_{-0.07}$	$4.85^{+3.43}_{-3.40}$	0.50
'AGN'	$0.46^{+0.12}_{-0.11}$	$0.81^{+0.17}_{-0.17}$	$11.09^{+4.64}_{-4.61}$	0.52
'AGN' + 'BHXRB sample'	$0.57^{+0.07}_{-0.07}$	$0.62^{+0.06}_{-0.06}$	$8.37^{+2.58}_{-2.56}$	0.50
'Low $\dot{m}$ AGN'	$0.34^{+0.24}_{-0.24}$	$0.85^{+0.25}_{-0.25}$	$15.77^{+8.55}_{-8.50}$	0.58
'Low $\dot{m}$ AGN' + 'BHXRB sample'	$0.61^{+0.09}_{-0.09}$	$0.59^{+0.07}_{-0.07}$	$6.84^{+3.17}_{-3.18}$	0.52
'ADAF'	$0.57^{+0.15}_{-0.14}$	$0.40^{+0.10}_{-0.10}$	$10.0^{+5.15}_{-5.13}$	0.46
'ADAF' + 'BHXRB sample'	$0.67^{+0.08}_{-0.08}$	$0.56^{+0.06}_{-0.06}$	$4.77^{+2.67}_{-2.66}$	0.47
'LINER-only'	$0.57^{+0.21}_{-0.21}$	$0.68^{+0.24}_{-0.24}$	$7.93^{+7.31}_{-7.36}$	0.57
'LINER-only' + 'BHXRB sample'	$0.65^{+0.09}_{-0.08}$	$0.58^{+0.06}_{-0.06}$	$5.59^{+3.04}_{-3.05}$	0.51
'Jetted'	$0.41^{+0.14}_{-0.14}$	$0.54^{+0.15}_{-0.15}$	$15.27^{+5.45}_{-5.49}$	0.33
'Jetted' + 'BHXRB sample'	$0.60^{+0.07}_{-0.07}$	$0.59^{+0.06}_{-0.06}$	$7.34^{+2.47}_{-2.47}$	0.37

computed the Optical FPBHA for the LeMMINGs sample too. In this section I will describe the best fit parameters for the same sub-samples outlined for the Optical FPBHA. In Table 7.3, I give all of the best fit parameters for all of the different optical samples. In Figure 7.2 I show the best fit Optical FPBHA of the LeMMINGs sample for all of the detected sources, the marginalised posterior probability distributions of the fit parameters, and the marginalised posterior probability distributions for $b_{X-ray,opt}$ and b_{Mass} are plot against the theoretical values for the 'ADAF' and 'jet' models outlined in Section 7.3. The additional plots for all of the other sub-samples are included in Appendix E.

When considering our sample in the optical FPBHA, LINERs and Seyferts appear to follow the same trends as the X-ray FPBHA. As with the X-ray FPBHA, the jetted and non-jetted H II galaxies appear in two different areas of the plot: the former sources cluster where LINERs lie, while the latter are offset by a factor ~100 because of their smaller BH masses and lower [O III] luminosities. Overall, the Optical FPBHA best fit parameters are similar to that found in the X-ray FPBHA fits, but usually with smaller scatter when directly comparing sub-samples, as the increased number of objects detected in the [O III] reduces the scatter slightly. The overall findings between the sub-samples is identical to that of the X-ray FPBHA plots.

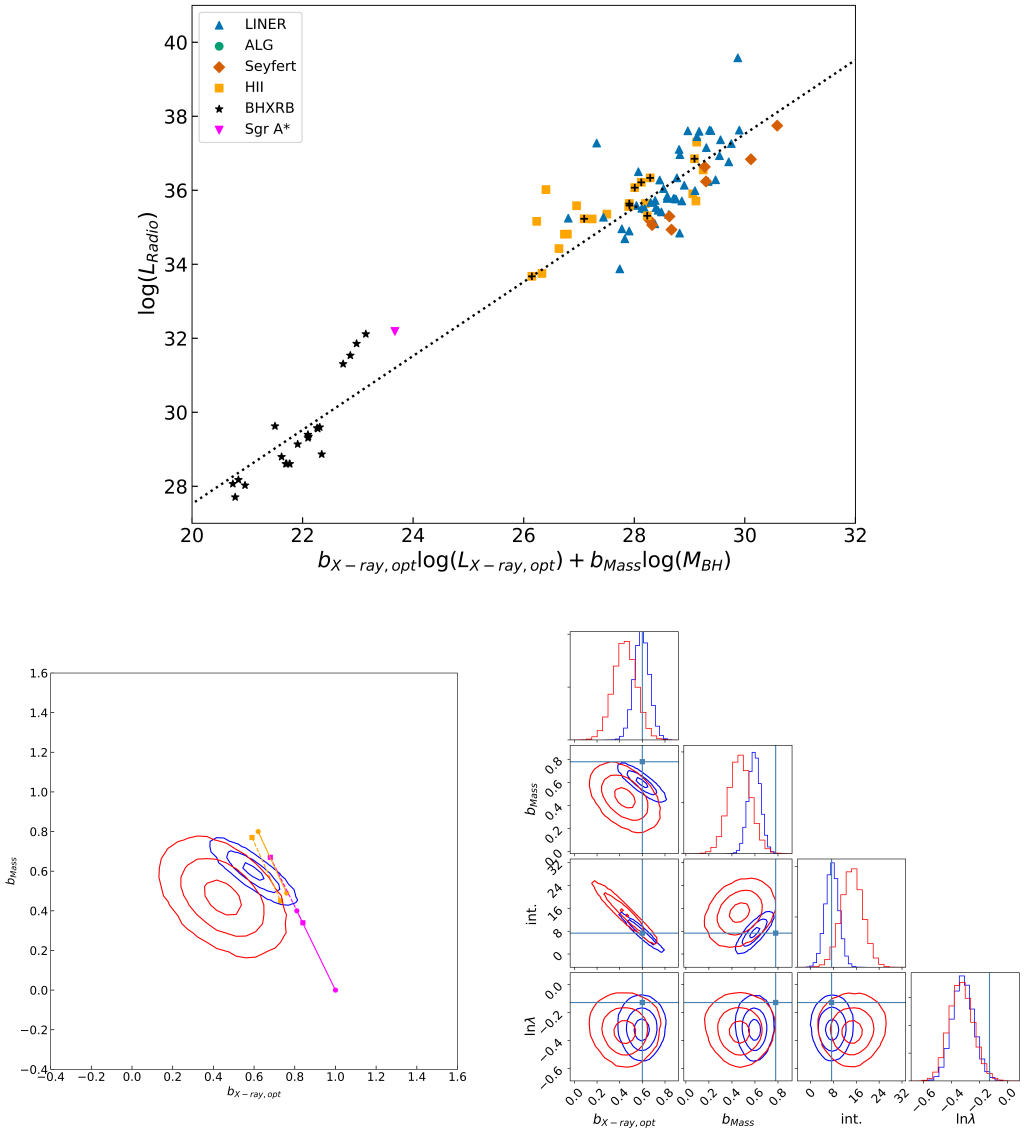

Figure 7.2: *Top panel:* The FPBHA for the 'Opt Complete + BHXRB' sample, with the luminosities in erg s^{-1} and BH masses in $M_\odot$. The different classes are coded (colour and symbol) according to the legend. The jetted HII galaxies show an additional plus symbol. *Bottom panel, left:* The posterior probability distribution of the marginalised slopes for the 'Opt Complete' (red) and 'Opt Complete + BHXRB' (blue) samples, as detailed in Section 7.4 and Table 7.2. The contours show the 1, 2 and 3 σ levels of the 2d Gaussians for the slopes b_{X-ray} and b_{Mass}. The orange lines correspond to the 'ADAF' model and the magenta lines correspond to the 'jet' model. The radio spectral index increases from 0.0 to 0.5 as you go down and to the right along the lines, with each end corresponding to these values respectively. The filled lines correspond to a particle distribution of p = 2, and the dashed lines correspond to p = 3. *Bottom panel, right:* The corner plot of the marginalised posterior probability distribution for the entire parameter space, including b_{X-ray}, b_{Mass}, intercept and intrinsic scatter, for both the 'Opt Complete' (red) and 'Opt Complete + BHXRB' (blue) samples, as detailed in Section 7.4 and Table 7.2. The green lines correspond to the values of those parameters as published in M03.

7.6 Discussion of the FPBHA

7.6.1 The physical interpretation of the FPBHA

Given the regression analysis, the correlation coefficients for both the X-ray and Optical sub-samples are similar: all of the sub-samples are consistent with an 'ADAF/jet' or 'jet' model. None of the samples presented are consistent with a slim disk model thought to power efficient accretors. This observation is unsurprising as a large number of the objects in the LeMMINGs sample are LLAGN and very few accrete above $0.01\dot{m}$ and therefore efficiently. In all of the sub-samples that include the BHXRB sample, the 'ADAF/jet' model is slightly preferred to the 'jet' only models. However, it is likely that there is some mixing between the two models that contribute to the X-ray emission in most sources, hence it is not possible to say one model is more likely than the other with great confidence.

In calculating the theoretical models, I have used a relativistic election coefficient, p, of 2 and 3, e.g. the filled and dashed lines in the FPBHA corner plots respectively. The magenta lines represent the 'jet' model, which are consistent with the regressed correlation coefficients in most of the sub-samples which include the BHXRB sample when p equals three. However, when considering an 'ADAF/jet' model, a value of p equals two suffices to explain the observed correlation coefficients and when p is increased to three, then all models pass closer to the 1σ boundary region on the plots. Hence, using a value of p=3 is more likely in several of the sub-samples regardless of whether the 'ADAF/jet' or 'jet-only' models are used. However, most of the literature assumes a value of p=2 as it implies that for the region where the X-rays are produced, radiative cooling is negligible (M03). The steeper p=3 spectrum would require a continuous injection of electrons with some radiative cooling, which is not necessarily physical in such low luminosity systems and values of $p \sim$ 2.0-2.4 are more likely in AGN (Ishibashi and Courvoisier, 2010, and references there-in). Hence, assuming that p should be ~2.0, the 'ADAF/jet' model is marginally more likely than the 'jet-only' model for the LeMMINGs LLAGN. But, I stress once more that the constraints on the posterior probability distributions do not indicate one specific model for any sub-sample and it is likely that a combination of the two models explain the X-ray emission in a large number of the LeMMINGs sample.

It is also worth investigating the average radio spectral index that the objects in the samples may have, judging by the regressed correlation coefficients. For a value of p=2, the radio spectral index in the 'ADAF/jet' model lies somewhere between 0.0 and 0.5, with the centre of the posterior probability distribution usually consistent with a value ~0.25. This is unsurprising, given the values of the spectral index found in Chapter 3 of this thesis for the core of NGC 4151 is 0.4. In contrast, using an electron coefficient of p=2 in the 'jet-only' model implies an inverted spectral index for the posterior probability distributions shown in this thesis, or a flat spectral index but with a p coefficient closer to three. Hence, I favour the interpretation that the data are more consistent with a radio spectral index of ~0.25 for a p value of 2.0 in the 'ADAF/jet' model.

7.6.2 What role do H II galaxies play in the FPBHA?

One of the main findings of the previous two Chapters was that some, although not all, H II galaxies can be interpreted as having a similar central engine to that of LINERs, motivated by the similar radio and multiwavelength properties. The H II objects which seem to follow most closely to that of the LINERs are those which show 'jetted' morphologies, thought to arise naturally from an ADAF-like flow that is observed in many LINERs. As only 6 'jetted' H II objects exist in the LeMMINGs sample that are detected in both the X-rays and radio, with a reliable mass estimate, it is not possible to construct a sub-sample with only these objects to compare to. However, I did create a 'jetted' only sub-sample with all types of AGN with jetted radio morphologies, which increases the sample to 24 objects. It is therefore worthwhile to investigate how these objects compare to the LINER-type objects in the regressions of the FPBHA described above.

The H II galaxies often sit on, or above the FPBHA correlations obtained for the various sub-samples. This effect is best exemplified by the 'ADAF' and 'jetted' sub-samples. The 'jetted' sub-sample with the BHXRBs yields the lowest intrinsic scatter of all the sub-samples, and has some of the lowest correlation coefficient uncertainties of all the sample. Furthermore, the regression coefficients for the 'jetted' sub-sample are similar to the original M03 coefficients and provide one of the closest fits of all of the sub-samples to the theoretical predictions of the 'ADAF/jet' model. The 'jet-only' model is not consistent within the 3σ bound of the posterior probability distribution with a p value of 2.0, whereas the 'ADAF/jet' model is consistent for almost all values of the radio spectral index from 0.0 to 0.5. Given there are six jetted H II galaxies in this sub-sample, which all seem to fit well to the correlation, including one object, NGC 3077, which is only within 2 orders of magnitude of the radio luminosity of Sgr A*, it suggests that the jetted H II galaxies are likely similar to the other 'jetted' sources. Given that most of the other 'jetted' sources are LINERs or low accretion rate Seyferts, the central engine in these sources is very likely to be an ADAF of some form. The presence of these jetted H II galaxies following the same correlation as other ADAF-powered sources suggests previous radio studies may have missed an important number of objects due to only their position on BPT diagrams. Such objects warrant further investigation in future studies to understand the full nature of these nuclei and understand why they fall into different regions of BPT diagrams, given that their radio and X-ray properties would suggest that they are indeed genuine LLAGN.

For the non-jetted HII galaxies, which induce the break in both the X-ray and Optical FPBHAs at low radio luminosities, Baldi et al. (2018b) verified that assigning a core luminosity via the radio–M_{BH} relation found at larger BH masses, these sources nicely line up on the fundamental plane. Using the larger number of objects in this thesis, this effect is still found to be true and corroborates the suggestion that SF powers the radio emission in the non-jetted HII galaxies because otherwise they would not be radio louder than the FPBHA. However, it should be noted that of the 88 H II galaxies so far observed with both e-MERLIN and *Chandra*, only fifteen of these have been detected in both wavebands and

only six of these have 'jetted' radio structures consistent with the LINERs in the LeMMINGs sample. Hence, while there are accreting objects that have certainly been missed in previous samples of LLAGN due to selection criteria based off BPT diagrams, the numbers of missed objects make up a small (∼10%) percentage of those correctly identified by the BPT diagrams as LINERs or Seyferts. In terms of the other AGN classes, e.g. ALGs and Seyferts, the dearth of these objects in the LeMMINGs sample means that there are too few of both types of these object to make meaningful sub-samples for them.

7.6.3 How does accretion rate affect the FPBHA?

The accretion rate of the LLAGNs defines what type of central engine is responsible for the observed parameters. Objects with accretion rates less than $10^{-2}M_{\odot}$ are thought to be powered by ADAF-type accretion flows, whereas those above $10^{-2}M_{\odot}$ are thought to be powered by slim disk central engines (Esin et al., 1997). However, to ensure I chose only ADAF-type flows in my objects I used a sample of LeMMINGs LINERs and Seyferts with accretion rates less than $10^{-3}M_{\odot}$ and a sample of all the detected objects with accretion rates less than $10^{-4}M_{\odot}$. The former sample includes 38 objects that are thought to be AGN, although the Seyferts may still be powered by a thin disk, whereas the latter sample includes only 18 objects, but with all types of LLAGN allowed.

Never-the-less, accretion rate does have a strong effect on the correlation coefficients and the intrinsic scatter of the FPBHA. The 'Low Accretion Rate' sample showed some of the best fit parameters coupled with the lowest intrinsic scatter of any of the different sub-samples. Furthermore, the AGN 'Low Accretion Rate' sample compared more favourably to the M03 sample, although with worse intrinsic scatter and correlation uncertainties than the 'AGN-only' sample. These findings indicate that the objects with the lowest accretion rates are very likely powered by the same types of flows. Furthermore, the literature values of $\sim 10^{-2}M_{\odot}$ may include some objects which deviate slightly from the FPBHA. In fact, lower accretion rates may be required to ensure that the objects are genuinely in the radiatively inefficient state. Furthermore, some Seyferts may also be in the same radiatively inefficient state as they follow the 'jetted' and low accretion rate sub-sample correlations well. But, care should be taken in including such objects in samples as they are generally radio-quieter than the LINERs and may be inducing additional scatter in correlations.

Yuan and Cui (2005) claimed that below a critical X-ray luminosity, $L_{X-ray,crit}$, usually $\lesssim 10^{-5}$ to 10^{-6} L_{Edd}, the generation of the X-rays no longer comes from the inefficient accretion flow but instead is dominated by emission from the jet. As such the relation between L_{radio} and L_{X-ray} steepens, which should be visible in the FPBHA. This steepening of the correlation has been shown for a small number of sources but not with a complete sample of LLAGNs (Yuan et al., 2009; Xie and Yuan, 2017). However, most of the detected LeMMINGs objects have X-ray luminosities lower than 10^{-6} L_{Edd} and no steepening of the FPBHA is observed in any of the sub-samples. P12 suggested that such a

steepening may be an observational effect caused by high mass BHs, above a BH mass of $10^8 M_\odot$. Such BHs may be dominated by synchrotron cooled X-ray emission rather than from the Compton up-scattered X-rays from the corona, purely because their BH masses cause their L_{X-ray}/L_{Edd} to be lower. The LeMMINGs objects includes 52 objects with $L_{X-ray}/L_{Edd} < 10^{-5}$ and 27 objects with $L_{X-ray}/L_{Edd} < 10^{-6}$, but the effect of Yuan and Cui (2005) is not observed as the BH masses probed by these objects are usually less than $10^8 M_\odot$. Hence, while I agree with P12 that it is possible for some objects to follow the steeper X-ray luminosity track suggested by Yuan and Cui (2005), it is likely that the mass term may be important in defining a sample for investigating such an effect.

7.6.4 How do the X-ray and optical FPBHAs compare?

In this Chapter I was able to fit the Optical FPBHA using the Bayesian regression method outlined in Section 7.2. The Optical FPBHA identified by Saikia et al. (2015) used VLA radio core detections at 15 GHz by Nagar et al. (2005) at a resolution (~0.13 arcsec). This resolution is comparable to the LeMMINGs observations presented in Chapter 5. The difference in frequency yields a difference in radio powers (in νL_ν) and hence the LeMMINGs sample have core luminosities lower than the VLA counterparts by a factor ~4, on average, corresponding to a spectral index between 1.5 and 15 GHz of $\alpha \sim 0.4$ ($F_\nu \sim \nu^{-\alpha}$). As the correlation coefficients for the X-ray and Optical FPBHAs both indicate that the 'ADAF/jet' model is marginally preferred for the LeMMINGs sample, and the values between $\alpha = 0.0$ and 0.5 agree best with the observed data, these changes in flux density between the 15 GHz VLA and 1.5 GHz e-MERLIN observations are not surprising. In fact, the spectral index further indicates that if the radio spectral index of the LLAGN in the LeMMINGs sample is generally between $\alpha = 0.0$ and 0.5 then the 'ADAF/jet' model is more likely, with a reasonable value of the electron distribution $p = 2$.

The power of the Optical FPBHA lies in the availability of high-quality ground-based [O III] line measurements. Given the similarity between the FPBHA and the Optical FPBHA, it may be possible in future to supplement a large radio sample of LLAGN with [O III] observations in lieu of available X-ray data. The underlying assumption of the Optical FPBHA is that the [O III] line luminosity can trace the genuine X-ray luminosity of a LLAGN. However, it is not clear how uniform this relationship is across different AGN classifications and types, as I reported different X-ray-[O III] correlations in Chapter 6. There have also been some suggestions that the environment of the AGN sample of the Optical FPBHA may alter the fit coefficients of the plane (Shabala, 2018). In this work, I have not assessed the environmental dependence of the Optical FPBHA, but will do so in future publications. However, the Optical FPBHA is a promising idea that could greatly help support the FPBHA and the scaling relationship between BHXRBs and SMBHs.

7.7 Conclusions

In this Chapter, I have presented the Fundamental Plane of Black Hole Activity (FPBHA) for the LeMMINGs sample. I have outlined the Bayesian method used to fit the FPBHA, which provides better regressions to the FPBHA than a standard Frequentist fit using the Merit function. By combining the high resolution e-MERLIN and *Chandra* observations from Chapters 5 and 6, the FPBHA of the LeMMINGs sample agrees with the previous publications, e.g. M03, K06, P12, S15. The high resolution and sensitivity of these observations therefore adds further weight to the argument that accretion is a scale-invariant process from solar mass BHXRBs up to the $10^8 M_{\odot}$ SMBHS found in AGN. Furthermore, future work will allow me to modify the Bayesian model to include upper limits from the entire sample in all 3 dimensions and analyse the effect the upper limits have on the correlation coefficients.

The physical interpretation of the LeMMINGs FPBHA is marginally more consistent with an 'ADAF/jet' origin than a 'jet' origin. This physical interpretation supports the idea that the X-rays are more likely due to inverse Compton scattered electrons than due to X-rays from optically thin synchrotron jet emission. However, like previous authors (e.g. P12), I note that it is likely that both processes likely contribute to the overall X-ray emission. Hence, without a large and robust sample of BHXRBs, LLAGN and AGN, it is not possible to favour one physical emission process over the other. Furthermore, the LeMMINGs FPBHA in the Optical waveband shows similar correlations to the FPBHA in the X-ray waveband. Therefore, the scaling between the [O III] and X-ray is likely valid for low-luminosity objects and suggests that the [O III] may be useful in future studies for adding to samples and further regressing the FPBHA. A slight separation of the different optical classes is evident across the FPBHA (with the Seyferts at lower radio luminosities than LINERs), which was not observed in previous works at lower VLA resolution. The e-MERLIN interferometer has resolved the parsec-scale jet base and has helped bring this effect in the FPBHA to light. The origin of this stratification in the optical FPBHA might be still reminiscent of the different accretion modes for each optical class.

Future work with the FPBHA will require large surveys of both BHXRBs and AGN to build up a more complete picture of how the FPBHA varies as a function of other observable parameters, such as AGN type and radio spectral index. The upcoming MeerKAT and SKA arrays will help to build up a large number of radio observations of AGN and BHXRBs, but without coordinated X-ray (and [O III]) follow up, it will not be possible to see vast improvements in the correlation coefficients of the FPBHA. While *Chandra* and *HST* can provide high-quality high-resolution X-ray and [O III] data respectively, they are over-subscribed which makes future improved FPBHA surveys difficult. Never-the-less, VLA observations of the entire LeMMINGs sample are currently being completed, as are *Chandra* observations of the rest of the LeMMINGs sample, which will help with reducing the scatter in the fit parameters in this Chapter.

Chapter 8

Conclusions

8.1 Summary of Findings

In this thesis I have presented the results from the LeMMINGs (**L**egacy **e-M**ERLIN **M**uti-band **I**maging of **N**earby **G**alaxies **s**urvey) survey, for both the 'deep' and 'shallow' samples. Using data from the 'deep' sample I analysed the multi-wavelength properties of two objects in isolation, investigating the nuclear regions of the galaxies NGC 4151 and NGC 6217. I expanded my findings in light of the data from the LeMMINGs 'shallow' sample, where I investigated the radio properties of nearby LLAGN, detecting radio emission coincident with the optical nucleus in ~40% of objects. Finally, I used the LeMMINGs data in conjunction with X-ray data from the *Chandra* X-ray observatory to investigate the Fundamental Plane of Black Hole Activity (FPBHA). In this final chapter, I will summarise the conclusions of all the preceding work and discuss the future perspectives of the LeMMINGs sample and its legacy value.

In summary, the main conclusions of this thesis are:

- State-of-the-art diagnostic emission line diagrams are required to properly ascertain nuclear AGN classifications (see Chapter 2).
- Radio variability exists in Seyfert nuclei over long time periods, e.g. two decades, which can be due to adiabatic expansion in jet components or new periods of activity in the core (see Chapter 3).
- Multi-wavelength datasets of high angular resolution are required to properly ascertain the nuclear emission mechanisms of nearby AGN (see Chapter 4).
- Radio emission coincident with the optical nucleus is observed in ~40% of galaxies, mostly in early-type galaxies and those with known activity, such as LINERs and Seyferts (see Chapter 5).
- 'Jetted' H II galaxies show similar multi-band properties to LINERs, and are therefore possibly powered by the same central engine (see Chapters 5 and 6).

- Nuclear X-ray emission is observed in ~70% of galaxies, indicating a likely LLAGN, but care must be taken to remove ULXs and XRBs. The X-ray dataset also needs improving as it is not currently complete (See Chapter 6).
- A FPBHA is observed for the LeMMINGs galaxies that show similar multi-wavelength properties analogous with the low/hard state BHXRBs, e.g. LINERs, 'jetted' H II galaxies and low accretion rate galaxies (see Chapter 7).

8.1.1 The LeMMINGs 'deep' sample

The LeMMINGs 'deep' sample was originally intended for full *uv*-coverage observations of a small sub-set of galaxies to investigate interesting aspects of astrophysics in specific sources. Nearly all the data for the 'deep' survey are published in separate papers: M 82 (Muxlow et al., 2010), IC 10 (Westcott et al., 2017), NGC 4151 (Williams et al., 2017), NGC 5322 (Dullo et al., 2018a), M 51b (Rampadarath et al., 2018), and NGC 6217 (Williams et al, in prep.). My contribution to this work has been in the radio data reduction for half of these papers, specifically NGC 4151, NGC 6217 and NGC 5322, and the scientific analysis of NGC 4151 and NGC 6217. In this thesis I have presented the multi-wavelength observations of NGC 4151 (Chapter 3) and NGC 6217 (Chapter 4), highlighting the need for 'deep' radio imaging. Broadly, the LeMMINGs 'deep' survey has observed star formation processes in nearby galaxies (Muxlow et al., 2010; Westcott et al., 2017), LLAGN-only processes (Williams et al., 2017; Dullo et al., 2018a) and a mixture of the two, whereby the radio and multi-wavelength emission must be used to understand aspects of galaxy scale feedback (Rampadarath et al., 2018) or probing nuclear regions of star forming galaxies with no optically identified AGN (Williams et al., submitted.).

NGC 4151

Regarding the first of the two main sources I investigated in this thesis, NGC 4151 is a fascinating object with remarkable radio jets (Mundell et al., 2003). The e-MERLIN observations showed that the central unresolved component C4 had brightened over a 20 year period. This increase in flux density showed that LLAGN can vary over decadal timescales. Seyferts have been observed to vary over time-scales of five to seven years (Mundell et al., 2009) and some LLAGN have brightened suddenly leading to suggestions of new periods of activity in AGN (Argo et al., 2015). Hence, it is important to carry out long term monitoring campaigns on Seyfert galaxies, and possibly LINERs and H II galaxies to measure the duty cycles of AGN. Differing duty cycles naturally have an impact on models of AGN feedback and galaxy evolution. Therefore, for this reason alone, long-term monitoring campaigns at high resolution are essential for understanding fuelling mechanisms in LLAGN. Furthermore, the nearest component to the nucleus, C3, was observed to decrease in flux density, owing to a likely adiabatic expansion over twenty years. This observation adds further weight to the need for long term monitoring campaigns

of LLAGN to measure their spatio-temporal properties. Furthermore, the e-MERLIN images obtained for NGC 4151 were unable to ascertain a jet velocity, largely due to the size of the beam, 150mas, at 1.5 GHz. However, higher frequency observations at 5 GHz or 22 GHz in the future with e-MERLIN will probe scales of up to 10s of milli-arcseconds due to the smaller beam sizes, which for NGC 4151 corresponds to a scale of a few parsecs. Previous observations of jet velocities in LLAGN have used longer baseline interferometers like the VLBA (Ulvestad et al., 2005) or VLBI (Ulvestad, 2003). But at higher frequencies, it will be possible for long-term e-MERLIN campaigns to monitor bright objects with discrete ejecta to probe the jet physics in LLAGN, and investigate the interactions between the emission-line region and the jet.

NGC 6217

The study of NGC 6217 revealed some of the smallest radio-lobes (~0.4 kpc) previously observed for a LLAGN. Radio emission such as the lobes in NGC 6217 would not have been observed with any other radio array than e-MERLIN, as they do not have the same unique combination of angular resolution and sensitivity. The lobes may be small due to projection effects whereby the jets are oriented towards us. Never-the-less, the radio morphology of the nucleus in NGC 6217 is fascinating as it is not clear whether the radio emission is from a LLAGN, star formation, or from a combination of the two processes. In Chapter 4 I concluded it was likely a combination of the two processes, due to the radio morphology, X-ray spectra, optical Hα emission and multi-wavelength correlations from the literature. Assuming that the radio emission in NGC 6217 is possibly representative of nearby LLAGN that are optically classified as H II galaxies, then it is likely that other systems such as NGC 6217 exist at the lowest luminosities. One of the main reasons for observing NGC 6217 was to investigate the presence of an X-ray jet extending 15 kpc away from the nucleus, as reported in two publications in the literature (Pietsch and Arp, 2001; Falocco et al., 2017). The LeMMINGs 'deep' observations of NGC 6217 have cast serious doubt on the existence of an X-ray jet in this system. Moreover, multi-wavelength data showed that several of the X-ray 'knots' identified by Falocco et al. (2017) are possibly consistent with being background sources from SED fitting procedures. Therefore the X-ray jet in NGC 6217 does not exist, although that is not to say that such jets are not observed in nearby AGN, as NGC 315 has a known X-ray jet. Therefore future attempts to find LLAGN X-ray jets in nearby sources are still worthwhile, but must be carried out at the highest resolution.

8.1.2 The multi-wavelength properties of the LeMMINGs 'shallow' sample

In Chapter 5, I presented the radio and optical data for the LeMMINGs 'shallow' sample, aimed at studying a statistically-complete sample of nearby (active and quiescent) galaxies, based off the Palomar sample with $\delta > 20°$. In this thesis I have presented the new e-MERLIN radio data for 86% (241/280 galaxies) in the LeMMINGs sample. For 84

objects, radio emission coincident with the optical core of the galaxy was observed, consistent with emission from a nuclear radio source, e.g. an LLAGN. The e-MERLIN observations reached a sensitivity of ~70μJy and an angular resolution of ~150 mas, which corresponds to limiting luminosities (~10^{32}erg s^{-1}), which are up to 100 times lower than previous radio observations of the Palomar survey. Sources where radio emission was observed, but further than 2″ from the optical nucleus, were considered background sources, or radio emission coincident with other non-LLAGN-related processes, e.g. star formation. The sample is not finished, but can still be considered both a success and statistically-complete in its current format, as all optical AGN classes, galaxy morphologies and black hole masses are probed equally given the inherent distribution from the parent sample, the Palomar survey.

In Chapter 6, I presented the currently available X-ray data for the LeMMINGs survey with the *Chandra* X-ray Observatory. *Chandra* has the most comparable angular resolution of an X-ray telescope to the e-MERLIN observations presented in Chapter 5, allowing for the nuclear regions to be disentangled from circum-nuclear X-ray emission from XRBs. Of the 211 objects in the LeMMINGs sample that have been observed by *Chandra*, the nuclear source in 149 of them were detected, to a limiting flux of 3×10^{-15} ergs cm^{-2} s^{-1}. Of these 149, 120 had enough counts for spectral fitting in the 0.3−10.0 keV regime to be performed. The *Chandra* observations therefore detected X-ray emission in LLAGN from ~71% of objects, which compares favourably to the previous *ROSAT* detection rate of the same sample (54%, Roberts and Warwick, 2000). The *Chandra* sample is still in the process of being completed, as only 75% of the LeMMINGs have so far been observed, but the detection of so many sources is encouraging for future studies, and builds the legacy of the LeMMINGs project further.

The main conclusion of the LeMMINGs 'shallow' sample was the detection of nuclear radio and X-ray emission irrespective of optical spectroscopic class, galaxy morphological classification or black hole mass. Nuclear radio emission was detected in ~40% of objects, while X-ray emission attributed to the central object was detected in ~70% of objects. The LeMMINGs sample has shown that AGN with different BH masses and hosted in different galaxies, can produce jets with similar power, size, and morphology (Gendre et al., 2013; Baldi et al., 2018a). This result indicates that (currently) directly unobservable quantities, such as BH spin, magnetic field strength, and accretion rotation, might play an important role in the jet launching mechanism (Garofalo et al., 2010; Tchekhovskoy and McKinney, 2012; Garofalo, 2013), regardless of the AGN and host properties.

Furthermore, independent of optical class, the 'active' galaxies and the 'jetted' H II galaxies appear to broadly follow similar correlations in the radio-M_{BH} plane. The 'jetted' H II galaxies could represent a missing group of objects from the literature, ignored previously due to their optical emission line ratios. However, it is likely that such objects only represent a small fraction (~10%) of the overall population of LLAGN. In addition, I showed the RLF and XLF of the LeMMINGs sample, which showed similar distributions when all AGN

types were considered and showed that the H II galaxies and ALGs could be responsible for the break in the LFs at lower luminosities. Furthermore, the X-ray properties of the detected LINERs, ALGs and H II galaxies suggested common X-ray-M_{BH} and X-ray-[O III] scalings. Therefore, in the low-luminosity regime, the physical process which regulates the conversion of the accretion flow into radiative and kinetic jet energy could be universal across the entire SMBH mass scale and for different optical classes.

8.1.3 The Fundamental Plane of Black Hole Activity

In Chapter 7 I investigated the FPBHA, using the e-MERLIN data presented in Chapter 5 and the *Chandra* data shown in Chapter 6. The FPBHA obtained with the LeMMINGs sample compared favourably with previous investigations into the plane (e.g., Merloni et al., 2003; Körding et al., 2006; Plotkin et al., 2012; Saikia et al., 2015). The various sub-samples used to fit the FPBHA in Chapter 7 generally agree with an 'ADAF/jet' origin for the X-rays, suggesting that the LLAGN in the LeMMINGs sample are broadly powered by the same central engines. However, it is not possible to rule out the 'jet-only' model categorically and it is highly probable that the observed X-ray emission comes from a mixture of both proposed models for LLAGN. Furthermore, the regressions in all the sub-samples were better when including the BHXRB sample, indicating that a reliable BHXRB sample is needed in order to produce the best marginalised posterior probability distributions for the correlation coefficients.

The different sub-samples highlighted interesting properties and mostly yielded better regressions with tighter posterior probability distributions than previously shown in the literature. In terms of the different AGN types, the LINERs appear to follow the FPBHA closely while the radio-quietness of the Seyferts usually mean they reside below the line. The 'jetted' H II galaxies follow the same correlations as the LINERs, and in fact all the sources showing 'jetted' morphologies follow the FPBHA. This observation adds further weight to the discussions in Chapter 5 and 6 that 'jetted' H II galaxies are powered by the same engine as that of the other LLAGN, like LINERs. In addition, the low accretion rate sub-samples appear to follow the correlation well, but care must be taken to ensure that only sources in similar accretion modes are used.

In conclusion, it is likely that the majority of low accretion rate sources that show jetted features in high resolution radio images, including LINERs, 'jetted' H II galaxies and some low accretion rate Seyferts and ALGs, are likely powered by the same ADAF-type central engine. Therefore, in the LLAGN regime, the physical process which regulates the conversion of the accretion flow into radiative and kinetic jet energy could be universal across the entire SMBH mass scale and for different optical classes. Such a process does not necessarily require the same disc–jet coupling since the classes are differently powered. However, it suggests a common scaling relationship with regards to BH properties (mass, spin, disc-BH alignment and co-rotation), accretion, and jet production, which are distinct

for each AGN class, but appear similar when all are combined in the FPBHA, as validated by magnetic-hydrodynamic simulations (Heinz and Sunyaev, 2003). Without the high resolution of e-MERLIN, such an effect would not have been observed.

8.1.4 The central engines of different LLAGN

Given the radio, optical and X-ray properties outlined in Chapters 5 and 6, and the FPBHA discussed in Chapter 7, the type of accretion can be investigated to give an idea of the different central engines and their radio jet launching mechanisms:

- **LINERs**. The LeMMINGs sample shows that LINERs have a propensity towards jetted radio structures and align well on the FPBHA with an 'ADAF/jet' model. Furthermore, there is evidence of an affinity between the LINERs and FR I radio galaxies, as they follow similar correlations in the [O III]–radio plane and in the FPBHA (Baldi et al., 2018b). The similarity between these two types of galaxy indicate a common nuclear emission origin: the non-thermal synchrotron emission from a jet, dominating the spectral output of the AGN at different wavelengths (Körding et al., 2008). Furthermore, the low Eddington rate of LINERs/FR Is suggest a radiatively inefficient accretion flow (e.g. an ADAF) which is responsible for the jet production due to its funnel-like structure and poloidal magnetic field. These results agree with previous multi-band studies for LINER-like LLAGN using a 'ADAF/jet' model (Falcke et al., 2004; Balmaverde and Capetti, 2006a; Balmaverde et al., 2006; Panessa et al., 2007; Baldi and Capetti, 2009). It also accounts for the inverse correlation between their Eddington rate and radio-loudness (Ho, 2002, 2008).

- **Seyferts**. The Seyferts are often associated with radio jets, but not always (usually at lower BH masses), and appear more edge-brightened than those observed in LINERs. This type of morphology indicates lower jet bulk speeds than those in LINERs. When coupled with the high emission line ratios, large [O III] luminosities and the large [O III] excess compared to LINERs, and the higher X-ray luminosities, the radio morphologies and multi-wavelength characteristics suggest a different central engine for Seyferts: a radiatively efficient disc accreting at higher rates than in LINERs. The Seyferts are in an intermediate position between the jetted LINERs/FR Is and the radio-quiet near-Eddington QSOs (Balick and Heckman, 1982; Ho, 2002, 2008; Busch et al., 2014). This separation of classes suggests a continuum of radio properties of LLAGN (Kharb et al., 2014) and is probably a consequence of a luminosity/accretion dependence on the jet efficiency (Trippe, 2014) from a thick to a thin accretion disc (Donea and Biermann, 1996, 2002; Markoff et al., 2005; King et al., 2011).

- **H II galaxies** are a mixed bag of galaxies which either host weakly active or silent SMBHs, and have SF which may be dominant over the AGN activity. The lack of H II galaxy detections is unsurprising given the optical emission line ratios, but is higher

than previous radio studies of nearby H II galaxies. The X-ray emission is usually weak in H II galaxies, which is further complicated by the prevalence of BHXRBs and ULXs in the circum-nuclear regions of H II galaxies. The observed dichotomy of 'jetted' and 'non-jetted' H II galaxies can be explained by the 'jetted' sources having a weakly active SMBH, similar to LINERs, whereas the 'non-jetted' sources are better explained with SF-dominated radio emission. The 'jetted' H II galaxies also follow the same correlations as LINERs, including the FPBHA, therefore these sources are likely explained with a similar engine to those of LINERs.

- **Absorption line galaxies** are detected in the LeMMINGs sample, but a conclusion as to the nuclear engine is difficult due to the lack of optical emission lines. Several ALGs are detected in the X-rays and appear to follow similar relations to that of the LINERs and jetted H II galaxies, but at lower X-ray luminosities. Nevertheless, ALGs are mostly associated with core–jet/triple radio morphologies and are commonly hosted in massive ellipticals, similar to LINERs. Furthermore, the radio emission of the ALGs may be due to a nuclear recurrence scenario whereby the AGN turns on and off periodically causing the observed radio morphologies. This may reconcile with the occasional lack of activity observed in massive early-type galaxies, due to general duty cycles of nuclear activity (Morganti, 2017).

8.2 Future Perspectives

The LeMMINGs sample provides a single perspective of accretion in the nearby Universe. However, it is a rich sample with plenty of complementary data across the electromagnetic spectrum. This thesis has demonstrated that it is only possible to understand the full accretion process from inflow to outflow by considering the full multi-wavelength data available. Hence, I have considered several possible future investigations that could be undertaken based off the LeMMINGs sample.

8.2.1 Extending the LeMMINGs sample

With regards to the 'deep' sample and specifically NGC 4151, future European VLBI Network campaigns have been proposed and 5 GHz data has been acquired with e-MERLIN. The new 5 GHz data have been reduced and are in the process of being imaged. For NGC 6217, the source of the nuclear emission remains unclear. If nothing else, the case studies of NGC 4151 and NGC 6217 have exemplified the need for high-resolution, good-sensitivity and multi-wavelength coverage of the nuclear regions of nearby galaxies.

The LeMMINGs sample is selected to be statistically-complete. While this is the case for the LeMMINGs radio data, the archival complementary data is not. I have described the data available for the *Chandra* X-ray telescope which can isolate X-ray emission from nuclear regions to within $\sim 0.5''$. However, the data currently available is only 75%

complete, which limits the conclusions of this work somewhat as a holistic picture of accretion in nearby galaxies cannot be finished. Hence, future proposals will be undertaken to complete the sample in the X-rays with *Chandra*.

The LeMMINGs survey only encompasses 280 galaxies, but it would be improved by including all of the Palomar sample galaxies. However, the LeMMINGs survey is limited by declination and hence would benefit from the proposed inclusion of another antenna for e-MERLIN based at Goonhilly in Cornwall. This additional antenna would open up the other 200+ galaxies in the Palomar sample to be imaged at sub-arcsecond and subμJy levels with the e-MERLIN interferometer. It would also increase the maximum baseline length of e-MERLIN to over 400 km and hence provide even better angular resolution and identification of the nuclear radio emission in nearby galaxies.

Finally, in terms of the statistical interpretation of the work presented in this thesis, a large number of objects are not detected in either the radio or X-ray wavebands. Using only the detected objects, or those with reliable mass estimates limits the analysis as many objects would be detected below the detection limits of the observations described here. Therefore, to fully understand the nature of the regressions presented throughout Chapters 5, 6 and 7, upper limits should really be included in the fits. For both the X-ray and radio correlations, the upper limits lie above and below the detected correlations. Therefore, they should not significantly change the fits, but should still be considered regardless. Furthermore, it is not possible to properly handle such censored data with frequentist statistics, and so I will be improving my Bayesian regression code to investigate the effect of upper limits in future.

8.2.2 Additional complementary radio data and analysis

While angular resolution and sensitivity is important for radio interferometers, it is also prudent to consider using interferometers sensitive to different spatial scales. In Chapter 4 I showed the power of the e-MERLIN array when combined with VLA A-array data to help image the diffuse emission in the nuclear region of NGC 6217. The inclusion of the VLA can help fill the gap in the *uv*-plane of e-MERLIN, and therefore examine the more diffuse spatial scales of nearby LLAGN and their radio jets. This technique is especially important for looking at how radio jets expand or age over time, which I discussed first in Chapter 3 for NGC 4151.

In addition to helping image the diffuse emission with interferometers like the EVLA, it is also important to observe objects at different frequencies to ascertain the spectral index of jets. The spectral index is important when calculating the ages of jets when considering equipartition (see Chapter 3 e.g. NGC 4151) and for discerning genuine emission from an AGN to that of the decaying jets or circum-nuclear star formation. This effect has been observed in some of the galaxies in the LeMMINGs sample when compared to a 15 GHz survey undertaken by Saikia et al. (2018). For example, NGC 5273 shows a single core in the 15 GHz image from the VLA at the same resolution to the LeMMINGs data, which

show a complicated circular structure in the nucleus.

Finally, the current 1.5 GHz e-MERLIN data still has more information in it that has not been presented here. For example, the 1.5ĠHz data of the LeMMINGs sample offer an opportunity to study the abundance of nuclear neutral hydrogen, as the HI line falls into the band (1420 MHz). The HI line can be used to measure rotation in galaxies and trace out the spiral arms in them. In addition, all of the LeMMINGs data blocks include a POL-Cal in 3C84 and in principle, could be used to investigate the polarisation of the LeMMINGs sources. The degree of polarisation would measure how ordered the magnetic fields are and their strengths in the nuclei of different LLAGNs.

8.2.3 Optical spectroscopy

The Palomar bright spectroscopic survey has been one of the best measures of optical emission lines in nearby galaxies for two decades. While the slit spectroscopy obtained by (Ho et al., 1997a) was state-of-the-art at the time, it is important to use matching spatial resolution so that emission at the same scales can be compared. Unfortunately with the slit size of the Palomar sample ($4''\times2''$), it is not possible to directly compare the radio emission in the nucleus with the optical emission. Given the proximity of the galaxies in the Palomar sample, it is possible that the optical line measurements are contaminated by star formation, shocks or post-AGB stars. As a first attempt, better quality spectra would be ideal so that only the nuclear region is observed. *HST* data have a similar resolution to that of e-MERLIN at 1.5 GHz (see Chapter 2) and can be used to compare the [O III] line - and other lines - of the LeMMINGs sources with the radio data presented in this thesis.

However, using a single slit is not ideal given the technological advances of the last 20 years. The inception of integrated field spectrographs (IFUs) onto several large optical telescopes (for example MaNGA and MUSE) has brought many scientific discoveries to light (e.g. Belfiore et al., 2016). With regards to the nuclear regions of the LeMMINGs sample, the spectra obtained from MaNGA and MUSE in particular have shown several star forming galaxies with LINER-type nuclei that would have been misclassified previously in BPT diagrams. In addition, IFUs can give a better understanding of the galaxy wide properties like the stellar velocity dispersions which are necessary for the M-σ relations. The emission lines and their ratios that IFUs can yield allow for the investigation of galaxy-scale AGN feedback processes and for the discrimination of star formation from AGN activity in a waveband other than the radio.

8.2.4 Machine Learning

One of my personal projects has been to pursue the use of machine learning techniques in my day-to-day work. Machine learning algorithms (MLAs) are able to classify large numbers of sources by their different properties, but require a 'training' set from which the

MLA can sort the objects. One of the strengths of the LeMMINGs survey is that is has a built-in 'training' set in the form of the other 206 galaxies in the Palomar survey not observed in LeMMINGs. Multi-wavelength data are available for most of the Palomar sample, and hence I have been looking into using the freely available data from the NASA Extragalactic Database (NED) as a starting point for a multi-wavelength classification and SED fitting programme, with MLAs at the heart of it. The NED database has 28000 measurements of the LeMMINGs sources in it, and so with some careful selection of the best datasets to use, can be a good start for such a programme.

8.3 Final Remarks

The radio observations presented in this thesis have discovered radio emission associated with all types of LLAGN and highlight the need for statistical-completeness, high-resolution and sensitivity when conducting radio surveys. Combined with suitable matching complementary multi-wavelength data, radio surveys such as LeMMINGs provide the backbone for interpreting the physical engines of LLAGN. The future for radio astronomy is bright with the advent of the SKA, and the e-MERLIN observations in this thesis are only the tip of the iceberg for investigating the central engines of SMBHs. It is therefore exceedingly likely that further advancements of our knowledge of LLAGN will continue over the next few decades, completing a unified model of AGN and their multi-wavelength characteristics.

Appendix A

LeMMINGs Basic Data

A.1 LeMMINGs Dataset

Galaxy name	Right Asc.	Declination	LEM Block	Calibrator	Distance [Mpc]	Hubble Type	Ho. AGN Class	New AGN Class
NGC 7817	00 03 58.90	+20 45 08.4	LEM04	J0004+2019	31.5	SAbc: spin	TRANS	HII
IC 10	00 20 17.34	+59 18 13.6	LEM04	J0027+5958	1.3	IBm?	HII	HII
NGC 147	00 33 12.12	+48 30 31.5	LEM04	J0039+4900	0.7	dE5 pec	ALG	ALG
NGC 185	00 38 57.97	+48 20 14.6	LEM04	J0039+4900	0.7	dE3 pec	LINER	LINER
NGC 205	00 40 22.05	+41 41 07.5	LEM04	J0038+4137	0.7	dE5 pec	ALG	ALG
NGC 221	00 42 41.83	+40 51 54.6	LEM04	J0038+4137	0.7	E2	ALG	ALG
NGC 224	00 42 44.35	+41 16 08.6	LEM04	J0038+413	0.7	SA(s)b	ALG	ALG
NGC 266	00 49 47.80	+32 16 39.8	LEM03	J0048+3157	62.4	SB(rs)ab	LINER	LINER
NGC 278	00 52 04.31	+47 33 01.8	LEM04	J0039+4900	11.8	SAB(rs)b	HII	HII
NGC 315	00 57 48.88	+30 21 08.8	LEM03	J0048+3157	65.8	E+:	LINER	LINER
NGC 404	01 09 27.02	+35 43 05.3	LEM03	J0112+3522	2.4	SA(s)0-:	TRANS	LINER
NGC 410	01 10 58.90	+33 09 06.9	LEM03	J0112+3522	70.6	E+:	LINER	LINER
NGC 507	01 23 39.92	+33 15 21.8	LEM03	J0112+3522	65.7	SA(r)0	ALG	ALG
NGC 598	01 33 50.89	+30 39 36.5	LEM03	J0137+3122	0.7	SA(s)cd	HII	HII
IC 1727	01 47 29.89	+27 20 00.1	LEM03	J0151+2744	8.2	SB(s)m	LINER	LINER
NGC 672	01 47 54.47	+27 25 58.0	LEM03	J0151+2744	7.5	SB(s)cd	HII	HII
NGC 697	01 51 17.57	+22 21 28.7	LEM03	J0152+2207	41.6	SAB(rs)c:	TRANS	HII
NGC 777	02 00 14.93	+31 25 45.8	LEM02	J0205+3219	66.5	E1	LINER	LINER
NGC 783	02 01 06.61	+31 52 56.8	LEM02	J0205+3219	68.1	SAc	HII	HII
NGC 784	02 01 16.93	+28 50 14.1	LEM03	J0151+2744	4.7	SBdm: spin	HII	HII
NGC 812	02 06 51.50	+44 34 22.5	LEM02	J0204+4403	108.8	SAB(r)0/a: pec	HII	HII
NGC 818	02 08 44.51	+38 46 38.1	LEM02	J0204+3649	59.4	SABc:	TRANS	HII
NGC 841	02 11 17.39	+37 29 49.6	LEM02	J0204+3649	59.5	(R')SAB(s)ab	LINER	LINER
NGC 890	02 22 01.01	+33 15 57.8	LEM02	J0226+3421	53.4	SAB(r)0-	ALG	ALG
NGC 891	02 22 32.91	+42 20 54.0	LEM02	J0222+4302	9.6	SA(s)b? spin	HII	HII
NGC 925	02 27 16.91	+33 34 44.0	LEM02	J0226+3421	9.4	SAB(s)d	HII	HII

Table A.1 : *cont.*

Galaxy name	Right Asc.	Declination	LEM Block	Calibrator	Distance [Mpc]	Hubble Type	Ho. AGN Class	New AGN Class
NGC 959	02 32 23.95	+35 29 40.8	LEM02	J0226+3421	10.1	SAdm:	HII	HII
NGC 972	02 34 13.39	+29 18 40.5	LEM02	J0237+2848	21.4	SAab	HII	HII
IC 239	02 36 27.82	+38 58 09.1	LEMTEST	J0230+4032	16.8	SAB(rs)cd	TRANS	LINER
NGC 1003	02 39 17.03	+40 52 21.3	LEMTEST	J0230+4032	10.7	SA(s)cd	ALG	ALG
NGC 1023	02 40 24.01	+39 03 47.7	LEMTEST	J0230+4032	10.5	SB(rs)0-	ALG	ALG
NGC 1058	02 43 30.01	+37 20 28.7	LEMTEST	J0253+3835	9.1	SA(rs)c	SEYFERT	LINER
NGC 1156	02 59 42.85	+25 14 28.4	LEMTEST	J0301+3512	6.4	IB(s)m	HII	HII
NGC 1161	03 01 14.17	+44 53 50.7	LEMTEST	J0257+4338	25.9	SA0	LINER	LINER
NGC 1167	03 01 42.34	+35 12 19.9	LEMTEST	J0301+3512	65.3	SA0-	LINER	LINER
NGC 1169	03 03 34.76	+46 23 10.7	LEMTEST	J0303+4716	33.7	SAB(r)b	LINER	LINER
NGC 1186	03 05 30.85	+42 50 07.7	LEMTEST	J0257+4338	35.4	SB(r)bc:	TRANS	HII
NGC 1275	03 19 48.16	+41 30 42.1	LEMTEST	J0313+4120	70.1	Pec	LINER	SEYFERT
IC 342	03 46 48.51	+68 05 46.0	LEM26	J0426+6825	3.0	SAB(rs)cd	HII	HII
IC 356	04 07 46.88	+69 48 44.7	LEM26	J0426+6825	18.1	SA(s)ab pec	LINER	LINER
NGC 1569	04 30 49.19	+64 50 52.5	LEM26	J0426+6825	1.6	IBm	HII	HII
NGC 1560	04 32 49.09	+71 52 59.2	LEM26	J0501+7128	3.0	SA(s)d spin	HII	HII
NGC 1961	05 42 04.61	+69 22 42.3	LEM26	J0501+7128	53.1	SAB(rs)c	LINER	LINER
NGC 2146	06 18 37.71	+78 21 25.3	LEM26	J0632+8020	17.2	SB(s)ab pec	HII	HII
NGC 2273	06 50 08.62	+60 50 44.7	LEM27	J0707+6110	28.4	SB(r)a:	SEYFERT	SEYFERT
NGC 2342	07 09 18.09	+20 38 09.9	LEM27	J0700+1709	69.5	S pec	TRANS	HII
UGC 3714	07 12 32.68	+71 45 01.9	LEM26	J0721+7120	40.9	S? pec	HII	HII
NGC 2268	07 14 17.44	+84 22 56.2	LEM25	J0702+8549	34.4	SAB(r)bc	TRANS	HII
UGC 3828	07 24 35.74	+57 58 03.5	LEM27	J0707+6110	46.8	SAB(rs)b	HII	HII
NGC 2336	07 27 03.66	+80 10 42.0	LEM26	J0721+7120	33.9	SAB(r)bc	LINER	LINER
NGC 2276	07 27 14.26	+85 45 16.3	LEM25	J0702+8549	36.8	SAB(rs)c	HII	HII

Table A.1 : *cont.*

Galaxy name	Right Asc.	Declination	LEM Block	Calibrator	Distance [Mpc]	Hubble Type	Ho. AGN Class	New AGN Class
NGC 2366	07 28 51.85	+69 12 31.1	LEM26	J0632+8020	2.9	IB(s)m	ALG	ALG
IC 467	07 30 18.40	+79 52 21.1	LEM26	J0632+8020	27.4	SAB(s)c:	HII	HII
NGC 2300	07 32 20.05	+85 42 32.6	LEM25	J0702+8549	31.0	SA0	ALG	ALG
NGC 2403	07 36 51.40	+65 36 09.2	LEM24	J0737+6430	4.2	SAB(s)cd	HII	HII
UGC 4028	07 50 49.94	+74 21 27.3	LEM25	J0749+7420	52.7	SAB(s)c?	TRANS	HII
NGC 2500	08 01 53.16	+50 44 13.6	LEM27	J0808+4950	10.1	SB(rs)d	TRANS	HII
NGC 2543	08 12 57.96	+36 15 16.2	LEM27	J0815+3635	32.9	SB(s)b	HII	HII
NGC 2537	08 13 14.64	+45 59 23.3	LEM27	J0806+4504	9.0	SB(s)m pec	HII	HII
NGC 2541	08 14 40.11	+49 03 42.1	LEM27	J0808+4950	10.6	SA(s)cd	HII	HII
NGC 2549	08 18 58.35	+57 48 10.9	LEM24	J0837+5825	18.8	SA(r)0 spin	ALG	ALG
NGC 2639	08 43 38.09	+50 12 19.9	LEM27	J0849+5108	42.6	(R)SA(r)a?	LINER	LINER
NGC 2634	08 48 25.43	+73 58 01.6	LEM25	J0930+7420	30.2	E1:	ALG	ALG
NGC 2683	08 52 41.35	+33 25 18.5	LEM28	J0857+3313*	5.7	SA(rs)b	LINER	LINER
NGC 2681	08 53 32.74	+51 18 49.4	LEM27	J0849+5108	13.3	(R')SAB(rs)0/a	LINER	LINER
IC 520	08 53 42.33	+73 29 27.5	LEM25	J0930+7420	47.0	SAB(rs)ab?	SEYFERT	LINER
NGC 2685	08 55 34.75	+58 44 03.9	LEM25	J0930+7420	16.2	(R)SB0+pec	SEYFERT	SEYFERT
NGC 2655	08 55 37.97	+78 13 23.2	LEM25	J0919+7825	24.4	SAB(s)0/a	LINER	LINER
NGC 2750	09 05 47.89	+25 26 14.5	LEM28	J0905+2849	38.4	SABc	HII	HII
NGC 2742	09 07 33.58	+60 28 45.8	LEM24	J0921+6215	22.2	SA(s)c:	HII	HII
NGC 2715	09 08 06.21	+78 05 07.2	LEM25	J0919+7825	20.4	SAB(rs)c	TRANS	HII
NGC 2770	09 09 33.62	+33 07 24.3	LEM28	J0919+3324	29.6	SA(s)c:	HII	HII
NGC 2768	09 11 37.50	+60 02 14.8	LEM24	J0921+6215	23.7	E6:	LINER	LINER
NGC 2776	09 12 14.53	+44 57 17.6	LEM28	J0909+4253	38.7	SAB(rs)c	TRANS	HII
NGC 2748	09 13 43.04	+76 28 31.2	LEM25	J0930+7420	23.8	SAbc	HII	HII
NGC 2782	09 14 05.12	+40 06 49.1	LEM28	J0909+4253	37.3	SAB(rs)a pec	TRANS	HII

Table A.1 : *cont.*

Galaxy name	Right Asc.	Declination	LEM Block	Calibrator	Distance [Mpc]	Hubble Type	Ho. AGN Class	New AGN Class
NGC 2787	09 19 18.54	+69 12 11.6	LEM24	J0921+7136	13.0	SB(r)0+	LINER	LINER
NGC 2832	09 19 46.88	+33 44 59.4	LEM28	J0919+3324	91.6	E+2:	ALG	LINER
NGC 2841	09 22 02.66	+50 58 35.3	LEM27	J0929+5013	12.0	SA(r)b:	LINER	LINER
NGC 2859	09 24 18.53	+34 30 47.5	LEM28	J0919+3324	25.4	(R)SB(r)0+	SEYFERT	LINER
NGC 2903	09 32 10.11	+21 30 03.0	LEM28	J0935+1929	6.3	SAB(rs)bc	HII	HII
NGC 2950	09 42 35.12	+58 51 04.4	LEM24	J0947+5907	23.3	(R)SB(r)0	ALG	ALG
NGC 2964	09 42 54.23	+31 50 50.2	LEM28	J0958+3224	21.9	SAB(r)bc:	HII	HII
NGC 2977	09 43 46.80	+74 51 34.9	LEM24	J0921+7136	40.9	SAb:	HII	HII
NGC 2976	09 47 15.46	+67 54 59.0	LEM23	J0958+6533	2.1	SAc pec	HII	HII
NGC 3003	09 48 36.05	+33 25 17.4	LEM28	J0958+3224	24.4	SAbc?	HII	HII
NGC 2985	09 50 22.23	+72 16 4.0	LEM24	J0921+7136	22.4	(R')SA(rs)ab	TRANS	LINER
NGC 3031	09 55 33.17	+69 03 55.1	LEM23	J0958+6533	1.4	SA(s)ab	LINER	LINER
NGC 3027	09 55 40.63	+72 12 12.8	LEM24	J0921+7136	19.5	SB(rs)d:	HII	HII
NGC 3034	09 55 52.43	+69 40 46.9	LEM23	J0958+6533	5.2	IAO spin	TRANS	HII
NGC 3043	09 56 14.85	+59 18 25.6	LEM24	J0947+5907	39.1	SAb: spin	HII	HII
NGC 3073	10 00 52.20	+55 37 07.9	LEM22	J0957+5522	19.3	SAB0-	ALG	HII
NGC 3077	10 03 19.10	+68 44 1.6	LEM23	J0958+6533	2.1	IAO pec	HII	HII
NGC 3079	10 01 57.80	+55 40 47.2	LEM22	J0957+5522	20.4	SB(s)c spin	LINER	LINER
NGC 3162	10 13 31.59	+22 44 15.2	LEM16	J1014+2301	22.2	SAB(rs)bc	HII	HII
NGC 3147	10 16 53.62	+73 24 02.3	LEM23	J1031+7441	40.9	SA(rs)bc	SEYFERT	LINER
NGC 3185	10 17 38.56	+21 41 17.8	LEM16	J1014+2301	21.3	(R)SB(r)0/a	SEYFERT	SEYFERT
NGC 3190	10 18 05.63	+21 49 55.6	LEM16	J1014+2301	22.4	SA(s)a pec spin	LINER	LINER
NGC 3184	10 18 16.91	+41 25 27.6	LEM17	J1020+4320	8.7	SAB(rs)cd	HII	HII
NGC 3193	10 18 24.88	+21 53 38.3	LEM16	J1014+2301	23.2	E2	LINER	LINER
NGC 3198	10 19 54.99	+45 32 58.9	LEM17	J1020+4320	10.8	SB(rs)c	HII	HII

Table A.1 : *cont.*

Galaxy name	Right Asc.	Declination	LEM Block	Calibrator	Distance [Mpc]	Hubble Type	Ho. AGN Class	New AGN Class
NGC 3245	10 27 18.39	+28 30 26.8	LEM16	J1037+2834	22.2	SA(r)0?	TRANS	HII
IC 2574	10 28 23.62	+68 24 43.4	LEM23	J1034+6832	3.4	SAB(s)m	HII	HII
NGC 3254	10 29 19.92	+29 29 39.2	LEM16	J1037+2834	23.6	SA(s)bc	SEYFERT	SEYFERT
NGC 3294	10 36 16.25	+37 19 28.9	LEM17	J1033+3935	26.7	SA(s)c	TRANS	HII
NGC 3301	10 36 56.03	+21 52 55.8	LEM16	J1036+2203	23.3	(R')SB(rs)0/a	LINER	LINER
NGC 3310	10 38 45.86	+53 30 11.9	LEM22	J1046+5354	18.7	SAB(r)bc pec	TRANS	HII
NGC 3319	10 39 09.46	+41 41 12.0	LEM17	J1033+3935	11.5	SB(rs)cd	HII	HII
NGC 3344	10 43 31.15	+24 55 20.0	LEM16	J1043+2408	6.1	(R)SAB(r)bc	TRANS	HII
NGC 3359	10 46 36.86	+63 13 27.3	LEM23	J1101+6241	19.2	SB(rs)c	HII	HII
NGC 3348	10 47 10.00	+72 50 22.8	LEM23	J1031+7441	37.8	E0	ALG	ALG
NGC 3395	10 49 50.11	+32 58 58.3	LEM17	J1050+3430	27.4	SAB(rs)cd: pec	HII	HII
NGC 3414	10 51 16.21	+27 58 30.4	LEM17	J1102+2757	23.9	SA0 pec	LINER	LINER
NGC 3430	10 52 11.40	+32 57 01.6	LEM17	J1050+3430	26.7	SAB(rs)c	HII	HII
NGC 3432	10 52 31.13	+36 37 07.6	LEM17	J1050+3430	7.8	SB(s)m spin	HII	HII
NGC 3448	10 54 39.20	+54 18 17.5	LEM22	J1046+5354	24.5	IAO	HII	HII
NGC 3486	11 00 23.87	+28 58 30.5	LEM16	J1102+2757	7.4	SAB(r)c	SEYFERT	SEYFERT
NGC 3504	11 03 11.21	+27 58 21.0	LEM16	J1102+2757	26.5	(R)SAB(s)ab	TRANS	HII
NGC 3516	11 06 47.49	+72 34 06.9	LEM23	J1134+7249	38.9	(R)SB(s)0:	SEYFERT	SEYFERT
NGC 3556	11 11 30.97	+55 40 26.8	LEM22	J1127+5650	14.1	SB(s)cd spin	HII	HII
NGC 3583	11 14 10.89	+48 19 06.7	LEM18	J1110+4817	34.0	SB(s)b	TRANS	HII
NGC 3600	11 15 52.01	+41 35 27.7	LEM18	J1110+4403	10.5	SAa?	HII	HII
NGC 3610	11 18 25.27	+58 47 10.6	LEM22	J1128+5925	29.2	E5:	ALG	ALG
NGC 3613	11 18 36.11	+58 00 00.0	LEM22	J1128+5925	32.9	E6	ALG	ALG
NGC 3631	11 21 02.87	+53 10 10.5	LEM19	J1107+5219	21.6	SA(s)c	HII	HII
NGC 3646	11 21 43.08	+20 10 10.4	LEM12	J1125+2005	56.8	Ring	SEYFERT	SEYFERT

Table A.1 : *cont.*

Galaxy name	Right Asc.	Declination	LEM Block	Calibrator	Distance [Mpc]	Hubble Type	Ho. AGN Class	New AGN Class
NGC 3642	11 22 17.89	+59 04 28.3	LEM22	J1128+5925	27.5	SA(r)bc:	TRANS	LINER
NGC 3652	11 22 39.03	+37 45 54.4	LEM17	J1130+3815	33.5	SAcd?	HII	HII
NGC 3665	11 24 43.67	+38 45 46.3	LEM17	J1130+3815	32.4	SA(s)0	TRANS	SEYFERT
NGC 3675	11 26 08.58	+43 35 09.3	LEM18	J1110+4403	12.8	SA(s)b	LINER	LINER
NGC 3690	11 28 32.30	+58 33 43.0	LEM22	J1128+5925	40.4	IBm pec	TRANS	HII
UGC 6484	11 29 11.76	+57 07 55.4	LEM22	J1127+5650	32.4	SB(rs)c	ALG	HII
NGC 3718	11 32 34.85	+53 04 04.5	LEM20	J1146+5356	17.0	SB(s)a pec	LINER	LINER
NGC 3726	11 33 21.12	+47 01 45.1	LEM18	J1138+4745	17.0	SAB(r)c	HII	HII
NGC 3729	11 33 49.32	+53 07 32.0	LEM20	J1146+5356	17.0	SB(r)a pec	TRANS	HII
NGC 3738	11 35 48.79	+54 31 26.0	LEM20	J1146+5356	4.3	IAm	HII	HII
NGC 3735	11 35 57.30	+70 32 08.1	LEM23	J1134+7249	41.0	SAc: spin	SEYFERT	SEYFERT
NGC 3756	11 36 48.02	+54 17 36.8	LEM20	J1146+5356	23.5	SAB(rs)bc	HII	HII
NGC 3780	11 39 22.36	+56 16 14.4	LEM20	J1146+5356	37.2	SA(s)c:	LINER	LINER
NGC 3813	11 41 18.66	+36 32 48.5	LEM13	J1149+3559	26.4	SA(rs)b:	HII	HII
NGC 3838	11 44 13.76	+57 56 53.6	LEM20	J1146+5848	24.6	SA0/a?	ALG	ALG
NGC 3877	11 46 07.70	+47 29 39.6	LEM18	J1138+4745	91.6	SA(s)c:	HII	HII
NGC 3884	11 46 12.18	+20 23 29.9	LEM12	J1145+1936	91.6	SA(r)0/a	LINER	LINER
NGC 3893	11 48 38.19	+48 42 39.0	LEM18	J1153+4931	17.0	SAB(rs)c:	HII	HII
NGC 3900	11 49 09.46	+27 01 19.3	LEM12	J1147+2635	29.4	SA(r)0+	LINER	LINER
NGC 3898	11 49 15.37	+56 05 03.7	LEM20	J1146+5356	21.9	SA(s)ab	LINER	LINER
NGC 3917	11 50 45.43	+51 49 28.8	LEM19	J1200+5300	17.0	SAcd:	TRANS	LINER
NGC 3938	11 52 49.45	+44 07 14.6	LEM18	J1155+4555	17.0	SA(s)c	TRANS	HII
NGC 3941	11 52 55.36	+36 59 10.8	LEM13	J1149+3559	18.9	SB(s)0	SEYFERT	LINER
NGC 3945	11 53 13.73	+60 40 32.0	LEM21	J1203+6031	22.5	(R)SB(rs)0+	LINER	LINER
NGC 3949	11 53 41.72	+47 51 31.3	LEM18	J1153+4931	17.0	SA(s)bc:	HII	HII

Table A.1 : *cont.*

Galaxy name	Right Asc.	Declination	LEM Block	Calibrator	Distance [Mpc]	Hubble Type	Ho. AGN Class	New AGN Class
NGC 3953	11 53 48.92	+52 19 36.4	LEM19	J1200+5300	17.0	SB(r)bc	LINER	LINER
NGC 3963	11 54 58.71	+58 29 37.1	LEM20	J1146+5848	42.7	SAB(rs)bc	HII	HII
NGC 3982	11 56 28.13	+55 07 30.9	LEM20	J1146+5356	17.0	SAB(r)b:	SEYFERT	SEYFERT
NGC 3992	11 57 35.98	+53 22 28.3	LEM19	J1200+5300	17.0	SB(rs)bc	LINER	LINER
NGC 3998	11 57 56.13	+55 27 12.9	LEM20	J1146+5356	21.6	SA(r)0?	LINER	LINER
NGC 4013	11 58 31.38	+43 56 47.7	LEM18	J1155+4555	17.0	SAb spin	LINER	LINER
NGC 4026	11 59 25.19	+50 57 42.1	LEM19	J1158+4825	17.0	SA0 spin	ALG	ALG
NGC 4036	12 01 26.75	+61 53 44.8	LEM21	J1203+6031	24.6	SA0-	LINER	LINER
NGC 4041	12 02 12.20	+62 08 14.0	LEM21	J1203+6031	22.7	SA(rs)bc:	TRANS	HII
NGC 4051	12 03 09.61	+44 31 52.8	LEM18	J1155+4555‘	17.0	SAB(rs)bc	SEYFERT	SEYFERT
NGC 4062	12 04 03.83	+31 53 44.9	LEM13	J1214+3309	9.7	SA(s)c	HII	HII
NGC 4088	12 05 34.19	+50 32 20.5	LEM19	J1158+4825	17.0	SAB(rs)bc	HII	HII
NGC 4096	12 06 01.13	+47 28 42.4	LEM19	J1158+4825	8.8	SAB(rs)c	HII	HII
NGC 4100	12 06 08.45	+49 34 57.7	LEM19	J1158+4825	17.0	(R’)SA(rs)bc	HII	HII
NGC 4102	12 06 22.99	+52 42 39.9	LEM19	J1200+5300	17.0	SAB(s)b?	TRANS	HII
NGC 4111	12 07 03.13	+43 03 56.6	LEM15	J1221+4411	17.0	SA(r)0+: spin	LINER	LINER
NGC 4125	12 08 06.02	+65 10 26.9	LEM21	J1219+6600	24.2	E6 pec	LINER	LINER
NGC 4136	12 09 17.69	+29 55 39.4	LEM13	J1217+3007	9.7	SAB(r)c	HII	HII
NGC 4138	12 09 29.78	+43 41 07.1	LEM15	J1221+4411	17.0	SA(r)0+	LINER	LINER
NGC 4143	12 09 36.06	+42 32 03.0	LEM15	J1221+4411	17.0	SAB(s)0	LINER	LINER
NGC 4144	12 09 58.60	+46 27 25.8	LEM15	J1223+4611	4.1	SAB(s)cd? spin	HII	HII
NGC 4145	12 10 01.52	+39 53 01.9	LEM14	J1206+3941	20.7	SAB(rs)d	TRANS	LINER
NGC 4151	12 10 32.58	+39 24 20.6	LEM14	J1206+3941	20.3	(R’)SAB(rs)ab:	SEYFERT	SEYFERT
NGC 4150	12 10 33.65	+30 24 05.5	LEM13	J1217+3007	9.7	SA(r)0?	LINER	LINER
NGC 4157	12 11 04.37	+50 29 04.8	LEM19	J1158+4825	17.0	SAB(s)b? spin	HII	HII

Table A.1 : *cont.*

Galaxy name	Right Asc.	Declination	LEM Block	Calibrator	Distance [Mpc]	Hubble Type	Ho. AGN Class	New AGN Class
NGC 4162	12 11 52.47	+24 07 25.2	LEM12	J1209+2547	38.5	(R)SA(rs)bc	TRANS	HII
NGC 4169	12 12 18.78	+29 10 45.9	LEM13	J1217+3007	50.4	SA0	SEYFERT	SEYFERT
NGC 4183	12 13 16.88	+43 41 54.9	LEM15	J1221+4411	17.0	SA(s)cd? spin	HII	HII
NGC 4203	12 15 05.06	+33 11 50.4	LEM13	J1214+3309	9.7	SAB0-:	LINER	LINER
NGC 4214	12 15 39.17	+36 19 36.8	LEM13	J1228+3706	3.5	IAB(s)m	HII	HII
NGC 4217	12 15 50.90	+47 05 30.4	LEM15	J1223+4611	17.0	SAb spin	HII	HII
NGC 4220	12 16 11.71	+47 52 59.7	LEM15	J1223+4611	17.0	SA(r)0+	SEYFERT	LINER
NGC 4236	12 16 42.12	+69 27 45.3	LEM21	J1240+6958	2.2	SB(s)dm	HII	HII
NGC 4244	12 17 29.66	+37 48 25.6	LEM13	J1228+3706	3.1	SA(s)cd: spin	HII	HII
NGC 4242	12 17 30.18	+45 37 09.5	LEM15	J1223+4611	7.5	SAB(s)dm	HII	LINER
NGC 4245	12 17 36.77	+29 36 28.8	LEM12	J1217+3007	9.7	SB(r)0/a:	TRANS	HII
NGC 4251	12 18 08.25	+28 10 31.4	LEM12	J1217+3007	9.7	SB0? spin	ALG	ALG
NGC 4258	12 18 57.50	+47 18 14.3	LEM15	J1223+4611	6.8	SAB(s)bc	SEYFERT	SEYFERT
NGC 4274	12 19 50.59	+29 36 52.1	LEM12	J1217+3007	9.7	(R)SB(r)ab	TRANS	HII
NGC 4278	12 20 06.82	+29 16 50.7	LEM12	J1217+3007	9.7	E1+	LINER	LINER
NGC 4291	12 20 18.20	+75 22 15.0	LEM21	J1243+7442	29.4	E	ALG	ALG
NGC 4314	12 22 31.82	+29 53 45.2	LEM12	J1217+3007	9.7	SB(rs)a	TRANS	HII
NGC 4346	12 23 27.94	+46 59 37.8	LEM15	J1223+4611	17.0	SA0 spin	LINER	LINER
NGC 4369	12 24 36.20	+39 22 58.8	LEM14	J1225+3914	21.6	(R)SA(rs)a	HII	HII
NGC 4395	12 25 48.86	+33 32 48.9	LEM13	J1214+3309	3.6	SA(s)m:	SEYFERT	SEYFERT
NGC 4414	12 26 27.10	+31 13 24.7	LEM12	J1228+3128	9.7	SA(rs)c?	TRANS	HII
NGC 4449	12 28 11.10	+44 05 37.1	LEM14	J1221+4411	3.0	IBm	HII	HII
NGC 4448	12 28 15.43	+28 37 13.1	LEM11	J1230+2518	9.7	SB(r)ab	HII	HII
NGC 4460	12 28 45.56	+44 51 51.2	LEM14	J1221+4411	8.1	SB(s)0+? spin	HII	HII
NGC 4485	12 30 31.13	+41 42 04.2	LEM14	J1225+3914	9.3	IB(s)m pec	HII	LINER

Table A.1 : *cont.*

Galaxy name	Right Asc.	Declination	LEM Block	Calibrator	Distance [Mpc]	Hubble Type	Ho. AGN Class	New AGN Class
NGC 4490	12 30 36.24	+41 38 38.0	LEM14	J1225+3914	7.8	SB(s)d pec	HII	LINER
NGC 4494	12 31 24.10	+25 46 30.9	LEM11	J1230+2518	9.7	E1+	LINER	LINER
NGC 4559	12 35 57.65	+27 57 36.0	LEM11	J1230+2518	9.7	SAB(rs)cd	HII	HII
NGC 4565	12 36 20.78	+25 59 15.6	LEM11	J1230+2518	9.7	SA(s)b? spin	SEYFERT	SEYFERT
NGC 4589	12 37 25.00	+74 11 30.9	LEM21	J1243+7442	30.0	E2	LINER	LINER
NGC 4605	12 39 59.38	+61 36 33.1	LEM21	J1241+6020	4.0	SB(s)c pec	HII	HII
NGC 4618	12 41 32.85	+41 09 02.8	LEM14	J1244+4048	7.3	SB(rs)m	HII	HII
NGC 4648	12 41 44.39	+74 25 15.4	LEM21	J1243+7442	27.5	E3	ALG	ALG
NGC 4631	12 42 08.01	+32 32 29.4	LEM11	J1257+3229	6.9	SB(s)d spin	HII	HII
NGC 4656	12 43 57.73	+32 10 05.3	LEM11	J1257+3229	7.2	SB(s)m pec	HII	HII
NGC 4750	12 50 07.27	+72 52 28.7	LEM21	J1243+7442	26.1	(R)SA(rs)ab	LINER	LINER
NGC 4725	12 50 26.58	+25 30 02.9	LEM11	J1249+2817	12.4	SAB(r)ab pec	SEYFERT	SEYFERT
NGC 4736	12 50 53.06	+41 07 13.7	LEM14	J1244+4048	4.3	(R)SA(r)ab	LINER	LINER
NGC 4800	12 54 37.80	+46 31 52.2	LEM14	J1254+4536	15.2	SA(rs)b	TRANS	HII
NGC 4793	12 54 40.62	+28 56 19.2	LEM11	J1249+2817	38.9	SAB(rs)c	HII	HII
NGC 4826	12 56 43.64	+21 40 58.7	LEM11	J1255+1817	4.1	(R)SA(rs)ab	LINER	LINER
NGC 4914	13 00 42.95	+37 18 55.0	LEM10	J1308+3546	62.4	E+	ALG	ALG
NGC 5005	13 10 56.23	+37 03 33.1	LEM10	J1308+3546	21.3	SAB(rs)bc	LINER	LINER
NGC 5012	13 11 37.04	+22 54 55.8	LEM11	J1321+2216	40.4	SAB(rs)c	SEYFERT	LINER
NGC 5033	13 13 27.47	+36 35 38.2	LEM10	J1308+3546	18.7	SA(s)c	LINER	LINER
NGC 5055	13 15 49.33	+42 01 45.4	LEM10	J1324+4048	7.2	SA(rs)bc	LINER	LINER
NGC 5112	13 21 56.40	+38 44 04.9	LEM10	J1324+4048	20.5	SB(rs)cd	HII	HII
NGC 5204	13 29 36.51	+58 25 07.4	LEM08	J1335+5844	4.8	SA(s)m	HII	HII
NGC 5194	13 29 52.71	+47 11 42.6	LEM10	J1335+4542	7.7	SA(s)bc pec	SEYFERT	SEYFERT
NGC 5195	13 29 59.59	+47 15 58.1	LEM10	J1335+4542	9.3	IA0 pec	LINER	LINER

Table A.1 : *cont.*

Galaxy name	Right Asc.	Declination	LEM Block	Calibrator	Distance [Mpc]	Hubble Type	Ho. AGN Class	New AGN Class
NGC 5273	13 42 08.34	+35 39 15.2	LEM09	J1340+3754	21.3	SA(s)0	SEYFERT	SEYFERT
NGC 5297	13 46 23.68	+43 52 20.5	LEM10	J1335+4542	37.8	SAB(s)c: spin	LINER	LINER
NGC 5308	13 47 00.43	+60 58 23.4	LEM08	J1335+5844	32.4	SA0- spin	ALG	ALG
NGC 5322	13 49 15.27	+60 11 25.9	LEM08	J1335+5844	31.6	E3+	LINER	LINER
NGC 5353	13 53 26.69	+40 16 58.9	LEM09	J1405+4056	37.8	SA0 spin	LINER	LINER
NGC 5354	13 53 26.70	+40 18 09.9	LEM09	J1405+4056	32.8	SA0 spin	LINER	LINER
NGC 5371	13 55 39.94	+40 27 42.3	LEM09	J1405+4056	37.8	SAB(rs)bc	LINER	LINER
NGC 5377	13 56 16.67	+47 14 08.5	LEM10	J1358+4737	31.0	(R)SB(s)a	LINER	LINER
NGC 5383	13 57 04.97	+41 50 46.5	LEM09	J1405+4056	37.8	(R')SB(rs)b:pec	HII	HII
NGC 5395	13 58 37.98	+37 25 28.1	LEM09	J1340+3754	46.7	SA(s)b pec	LINER	LINER
NGC 5448	14 02 50.03	+49 10 21.7	LEM10	J1358+4737	32.6	(R)SAB(r)a	LINER	LINER
NGC 5457	14 03 12.54	+54 20 56.2	LEM08	J1408+5613	5.4	SAB(rs)cd	HII	HII
NGC 5473	14 04 43.23	+54 53 33.5	LEM08	J1408+5613	33.0	SAB(s)0-:	ALG	ALG
NGC 5474	14 05 01.61	+53 39 44.0	LEM08	J1408+5613	6.0	SA(s)cd pec	HII	HII
NGC 5485	14 07 11.35	+55 00 06.1	LEM08	J1408+5613	32.8	SA0 pec	LINER	LINER
NGC 5523	14 14 52.32	+25 19 03.4	LEM09	J1419+2706	21.5	SA(s)cd:	HII	HII
NGC 5548	14 17 59.53	+25 08 12.4	LEM09	J1419+2706	67.0	(R')SA(s)0/a	SEYFERT	SEYFERT
NGC 5557	14 18 25.72	+36 29 36.8	LEM09	J1426+3625	42.6	E1	ALG	ALG
NGC 5585	14 19 48.20	+56 43 44.6	LEM08	J1408+5613	7.0	SAB(s)d	HII	HII
NGC 5631	14 26 33.30	+56 34 57.5	LEM08	J1408+5613	32.7	SA(s)0	LINER	LINER
NGC 5660	14 29 49.81	+49 37 21.6	LEM07	J1439+4958	37.2	SAB(rs)c	HII	HII
NGC 5656	14 30 25.51	+35 19 15.7	LEM09	J1426+3625	42.6	SAab	LINER	LINER
NGC 5678	14 32 05.61	+57 55 17.2	LEM08	J1408+5613	35.6	SAB(rs)b	TRANS	HII
NGC 5676	14 32 46.85	+49 27 28.5	LEM07	J1439+4958	34.5	SA(rs)bc	HII	HII
NGC 5866	15 06 29.50	+55 45 47.6	LEM07	J1510+5702	15.3	SA0 + spin	LINER	LINER

Table A.1 : *cont.*

Galaxy name	Right Asc.	Declination	LEM Block	Calibrator	Distance [Mpc]	Hubble Type	Ho. AGN Class	New AGN Class
NGC 5879	15 09 46.73	+57 00 00.7	LEM07	J1510+5702	16.8	SA(rs)bc?	LINER	LINER
NGC 5905	15 15 23.32	+55 31 02.5	LEM07	J1510+5702	44.4	SB(r)b	HII	HII
NGC 5907	15 15 53.77	+56 19 43.6	LEM07	J1510+5702	14.9	SA(s)c: spin	TRANS	HII
NGC 5982	15 38 39.83	+59 21 21.0	LEM07	J1559+5924	38.7	E3	LINER	ALG
NGC 5985	15 39 37.09	+59 19 55.0	LEM07	J1559+5924	39.2	SAB(r)b	LINER	LINER
NGC 6015	15 51 25.23	+62 18 36.1	LEM07	J1559+5924	17.5	SA(s)cd	HII	HII
NGC 6140	16 20 58.16	+65 23 26.0	LEM07	J1623+6624	18.6	SB(s)cd pec	HII	HII
NGC 6217	16 32 39.20	+78 11 53.4	LEM06	J1723+7653	23.9	(R)SB(rs)bc	TRANS	HII
NGC 6207	16 43 03.75	+36 49 56.7	LEM06	J1635+3808	17.4	SA(s)c	HII	HII
NGC 6236	16 44 34.65	+70 46 48.8	LEM06	J1642+6856	23.3	SAB(s)cd	HII	HII
NGC 6340	17 10 24.85	+72 18 16.0	LEM06	J1752+7311	22.0	SA(s)0/a	LINER	LINER
NGC 6412	17 29 37.51	+75 42 15.9	LEM06	J1723+7653	23.5	SA(s)c	HII	HII
NGC 6503	17 49 26.43	+70 08 39.7	LEM06	J1806+6949	6.1	SA(s)cd	ALG	ALG
NGC 6482	17 51 48.81	+23 04 19.0	LEM06	J1745+2252	52.3	E:	ALG	ALG
NGC 6643	18 19 46.41	+74 34 06.1	LEM06	J1752+7311	25.5	SA(rs)c	HII	HII
NGC 6654	18 24 07.57	+73 10 59.6	LEM06	J1752+7311	29.5	(R')SB(s)0/a	ALG	ALG
NGC 6689	18 34 50.25	+70 31 26.1	LEM06	J1806+6949	12.2	SAd? spin	TRANS	LINER
NGC 6702	18 46 57.58	+45 42 20.4	LEM05	J1852+4855	62.8	E:	ALG	ALG
NGC 6703	18 47 18.83	+45 33 02.3	LEM05	J1852+4855	35.9	SA0-	LINER	LINER
NGC 6946	20 34 52.32	+60 09 14.1	LEM05	J2010+6116	5.5	SAB(rs)cd	TRANS	HII
NGC 6951	20 37 14.09	+66 06 20.3	LEM05	J2015+6554	24.1	SAB(rs)bc	SEYFERT	LINER
NGC 7080	21 30 01.95	+26 43 04.1	LEM05	J2125+2442	64.1	SB(r)b	ALG	ALG
NGC 7217	22 07 52.39	+31 21 33.6	LEM05	J2217+3156	16.0	(R)SA(r)ab	LINER	LINER
NGC 7331	22 37 04.01	+34 24 55.9	LEM05	J2253+3236	14.3	SA(s)b	SEYFERT	LINER
NGC 7332	22 37 24.54	+23 47 54.0	LEM05	J2238+2749	18.2	SA0 pec spin	ALG	ALG

Table A.1 : *cont.*

Galaxy name	Right Asc.	Declination	LEM Block	Calibrator	Distance [Mpc]	Hubble Type	Ho. AGN Class	New AGN Class
NGC 7457	23 00 59.93	+30 08 41.8	LEM05	J2253+3236	12.3	SA(rs)0-?	ALG	ALG
NGC 7640	23 22 06.58	+40 50 43.5	LEM05	J2312+3847	8.6	SB(s)c	HII	HII
NGC 7741	23 43 54.37	+26 04 32.2	LEM04	J2343+2339	12.3	SB(s)cd	HII	HII
NGC 7798	23 59 25.50	+20 44 59.5	LEM04	J0004+2019	32.6	S	TRANS	HII

Table A.1: Column Description: (1) Galaxy Name; (2) Right Ascension as in NED; (3) Declination as in NED; (4) LeMMINGs Observation Block Number; (5) LeMMINGs calibrator Source; (6) Distance in Mpc; (7) Hubble Type; (8) Optical Spectroscopic Classification based on Ho et al. (1997a); (9) New Optical Spectroscopic Classification

Appendix B

eMERLIN LeMMINGs Shallow Survey L Band Maps

B.1 e-MERLIN LeMMINGs Shallow Survey 1.5 GHz Maps of identified sources

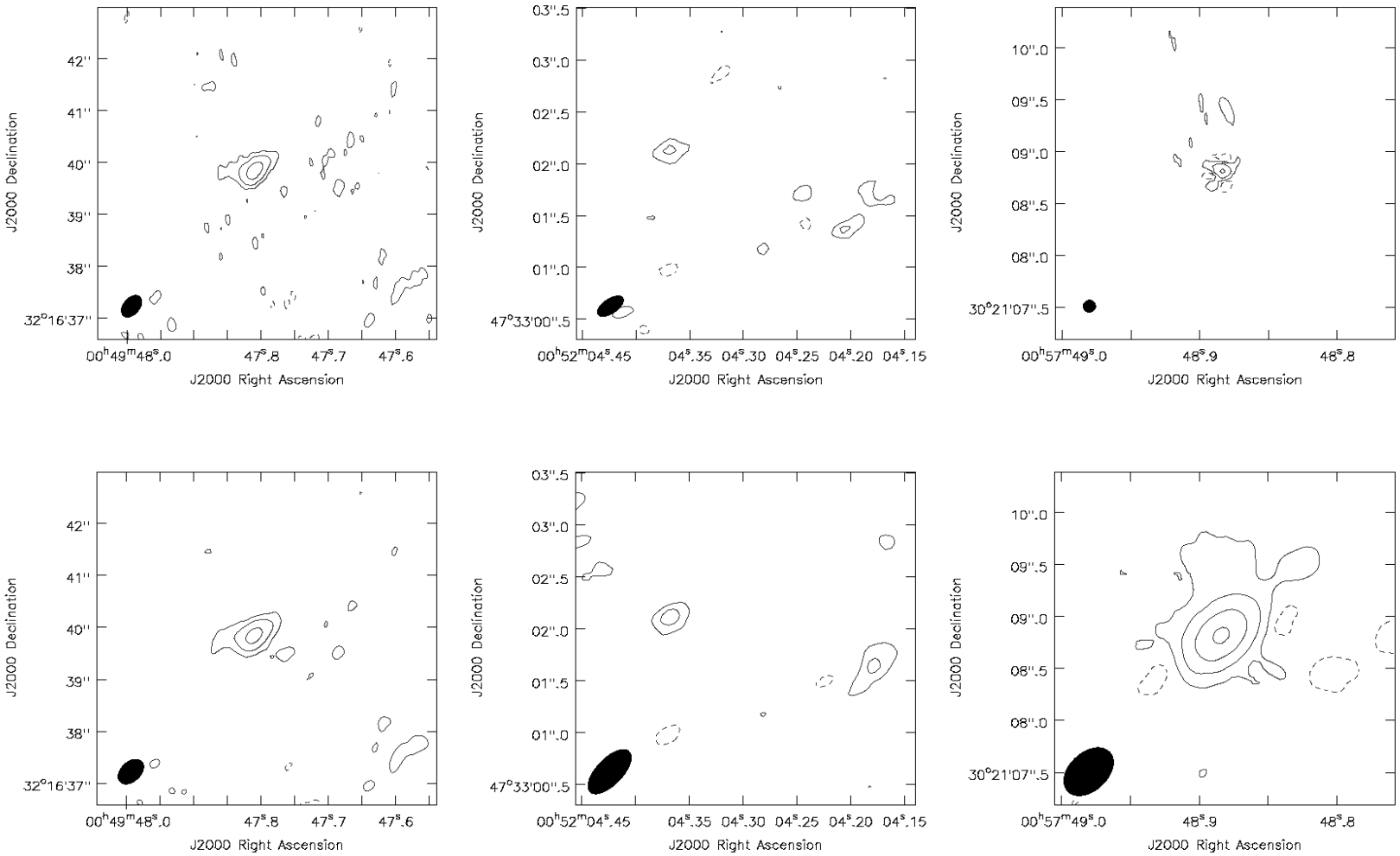

Figure B.1: e-MERLIN 1.5-GHz images of the identified LeMMINGs galaxies. This page: NGC 266 (left), NGC 278 (centre), NGC 315 (right). The *Top* image shows the full resolution image and the *Bottom* image shows the lower resolution image

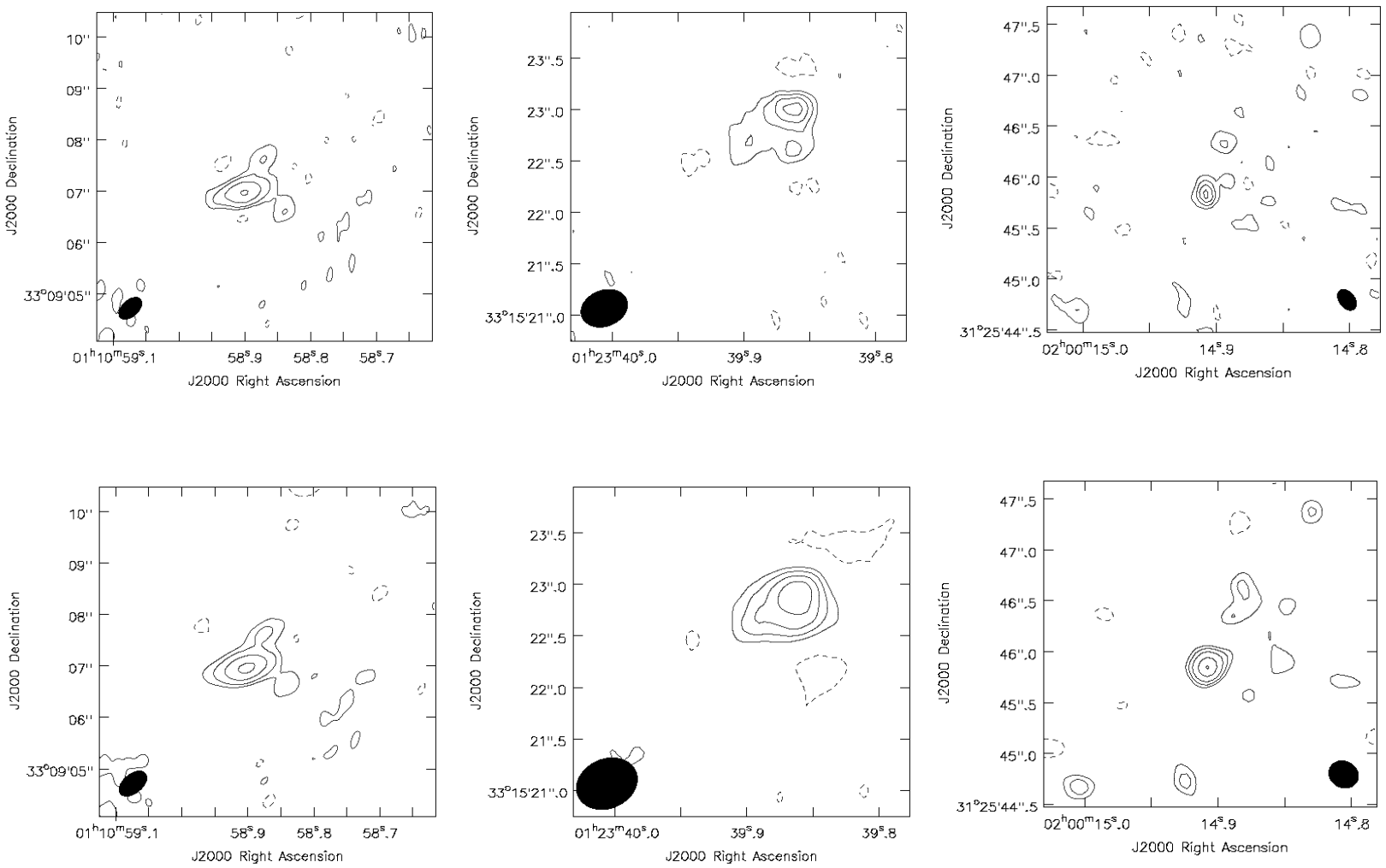

Figure B.1: e-MERLIN 1.5-GHz images of the identified LeMMINGs galaxies. This page: NGC 410 (left), NGC 507 (centre), NGC 777 (right). The *Top* image shows the full resolution image and the *Bottom* image shows the lower resolution image

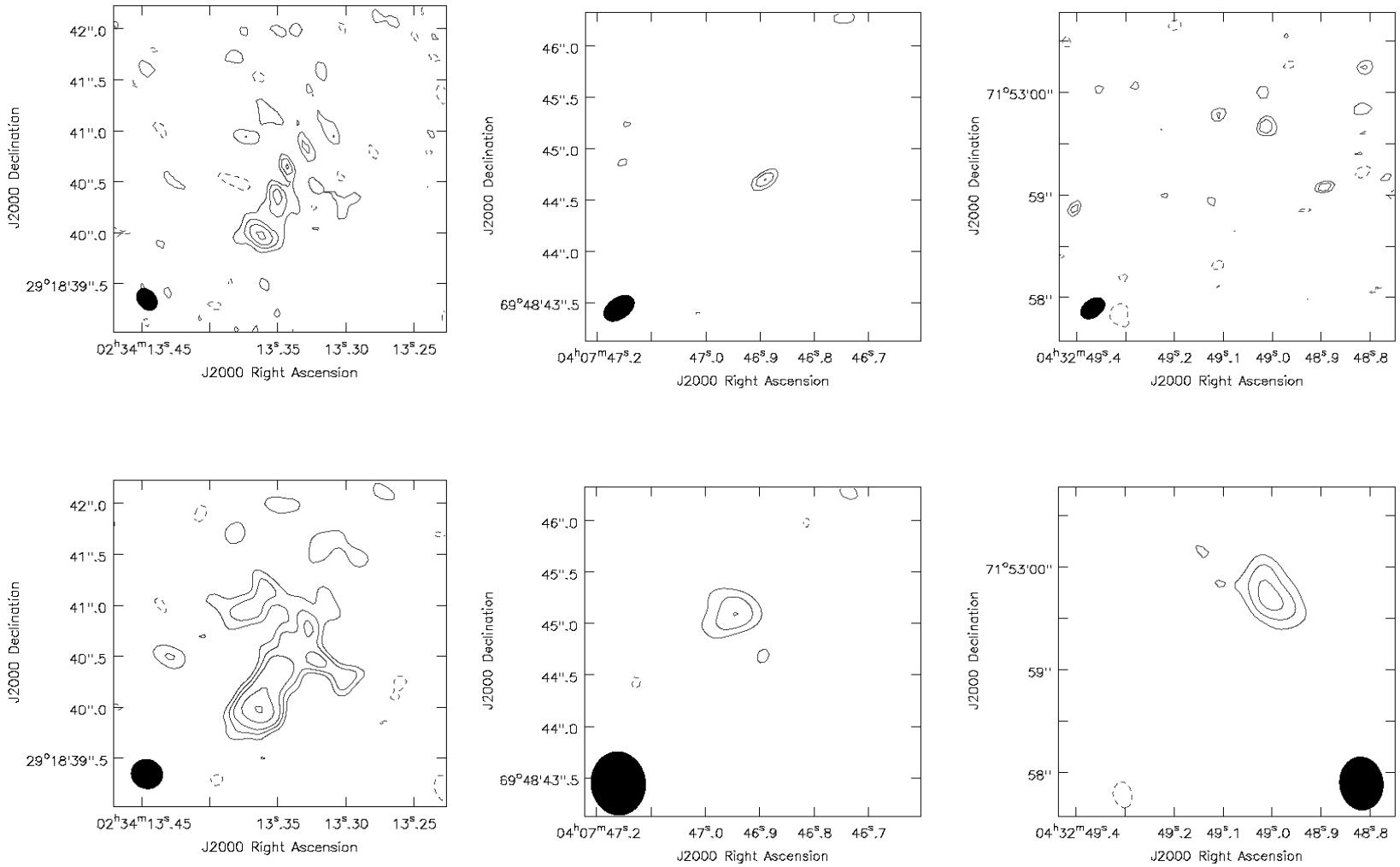

Figure B.1: e-MERLIN 1.5-GHz images of the identified LeMMINGs galaxies. This page: NGC 972 (left), IC 356 (centre), NGC 1560 (right). The *Top* image shows the full resolution image and the *Bottom* image shows the lower resolution image

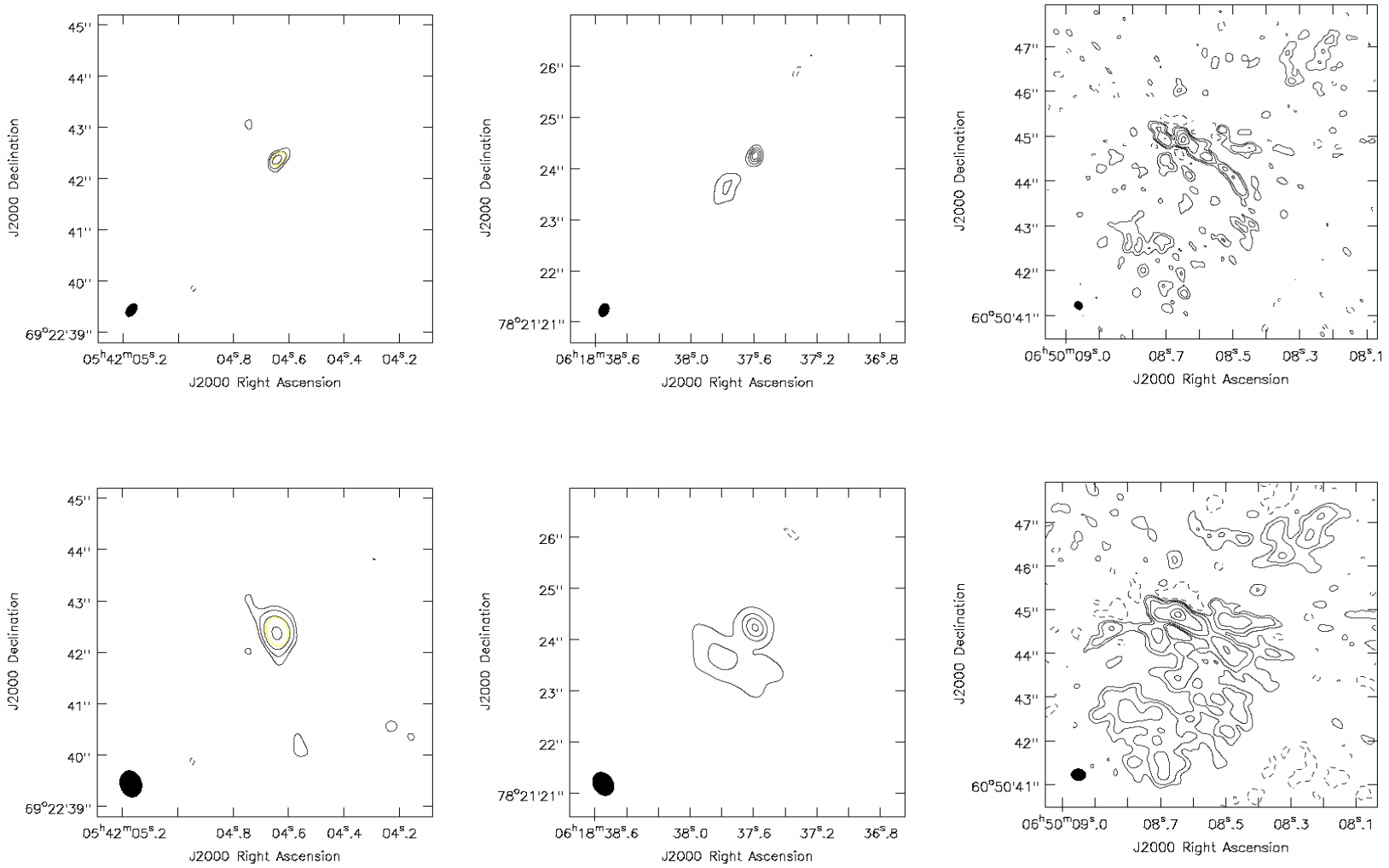

Figure B.1: e-MERLIN 1.5-GHz images of the identified LeMMINGs galaxies. This page: NGC 1961 (left), NGC 2146 (centre), NGC 2273 (right). The *Top* image shows the full resolution image and the *Bottom* image shows the lower resolution image

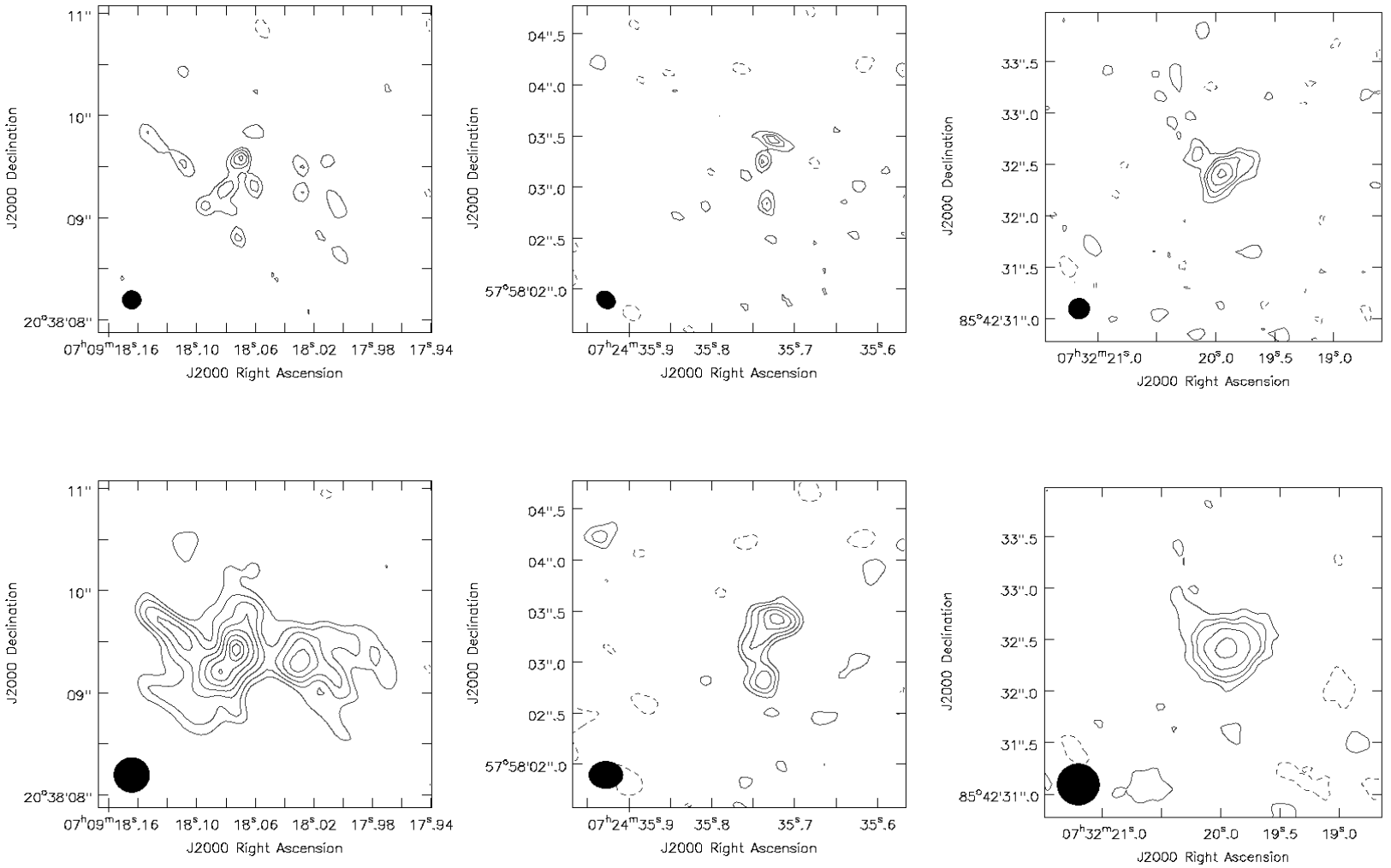

Figure B.1: e-MERLIN 1.5-GHz images of the identified LeMMINGs galaxies. This page: NGC 2342 (left), UGC 3828 (centre), NGC 2300 (right). The *Top* image shows the full resolution image and the *Bottom* image shows the lower resolution image

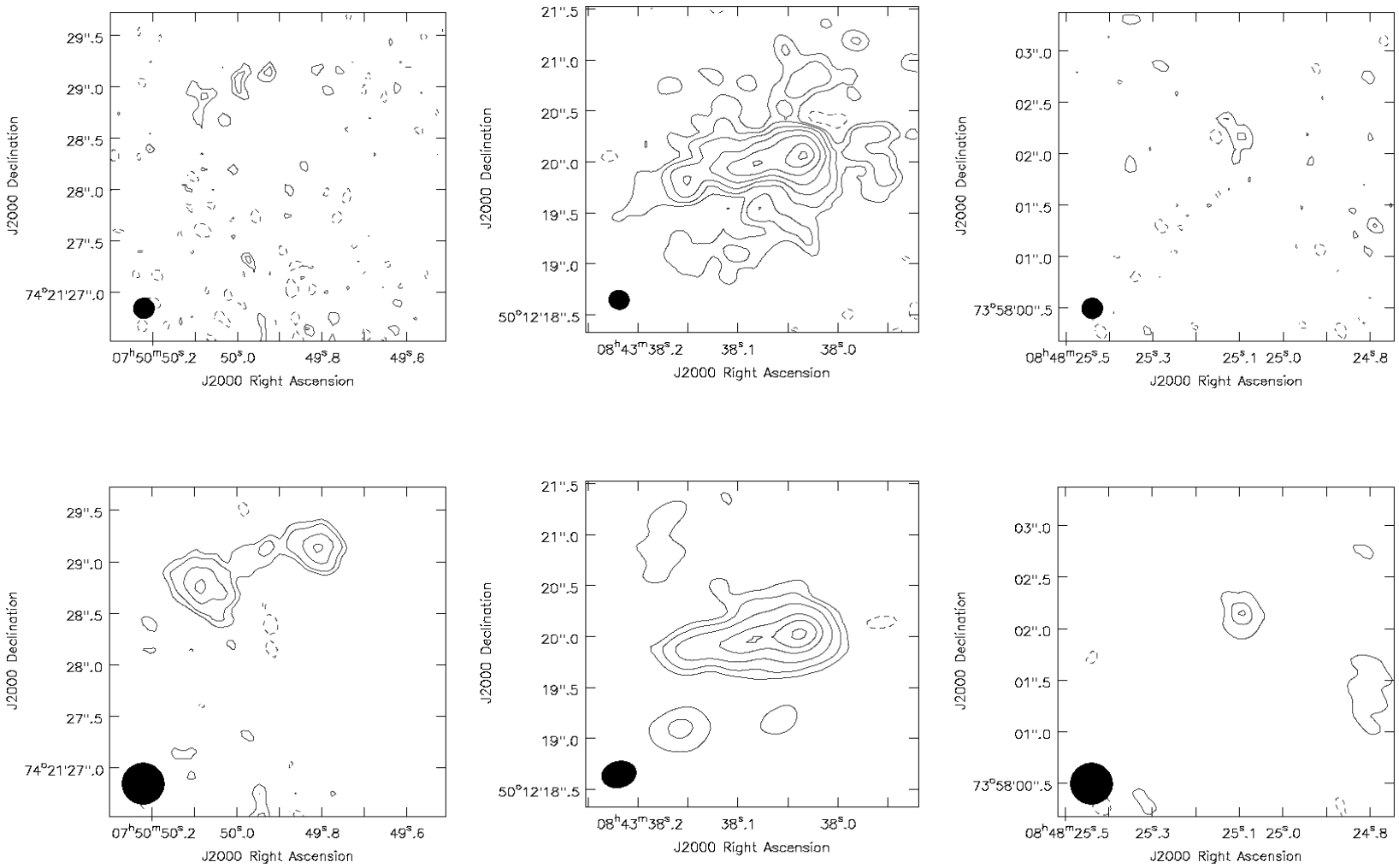

Figure B.1: e-MERLIN 1.5-GHz images of the identified LeMMINGs galaxies. This page: UGC 4028 (left), NGC 2639 (centre), NGC 2634 (right). The *Top* image shows the full resolution image and the *Bottom* image shows the lower resolution image

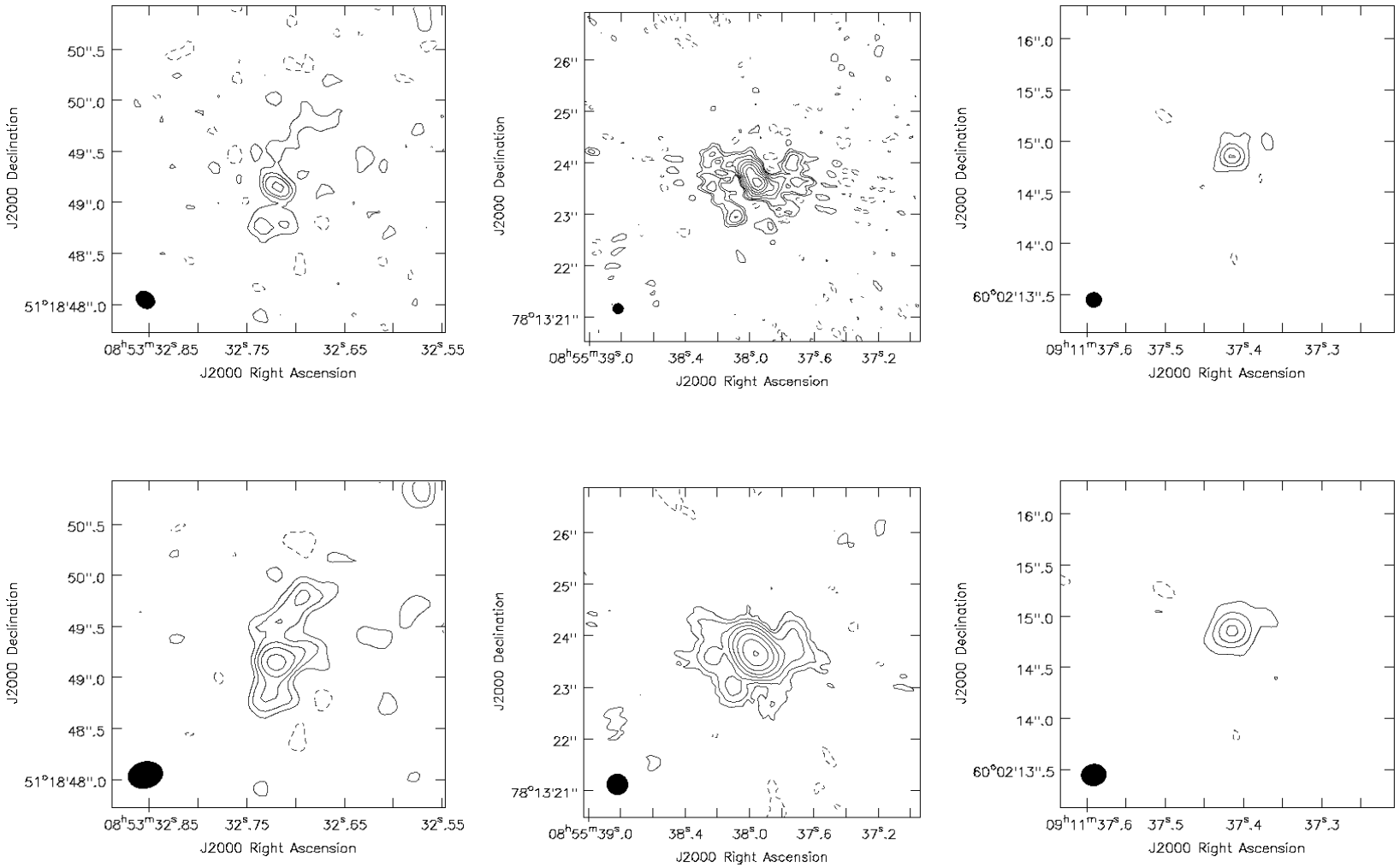

Figure B.1: e-MERLIN 1.5-GHz images of the identified LeMMINGs galaxies. This page: NGC 2681 (left), NGC 2655 (centre), NGC 2768 (right). The *Top* image shows the full resolution image and the *Bottom* image shows the lower resolution image

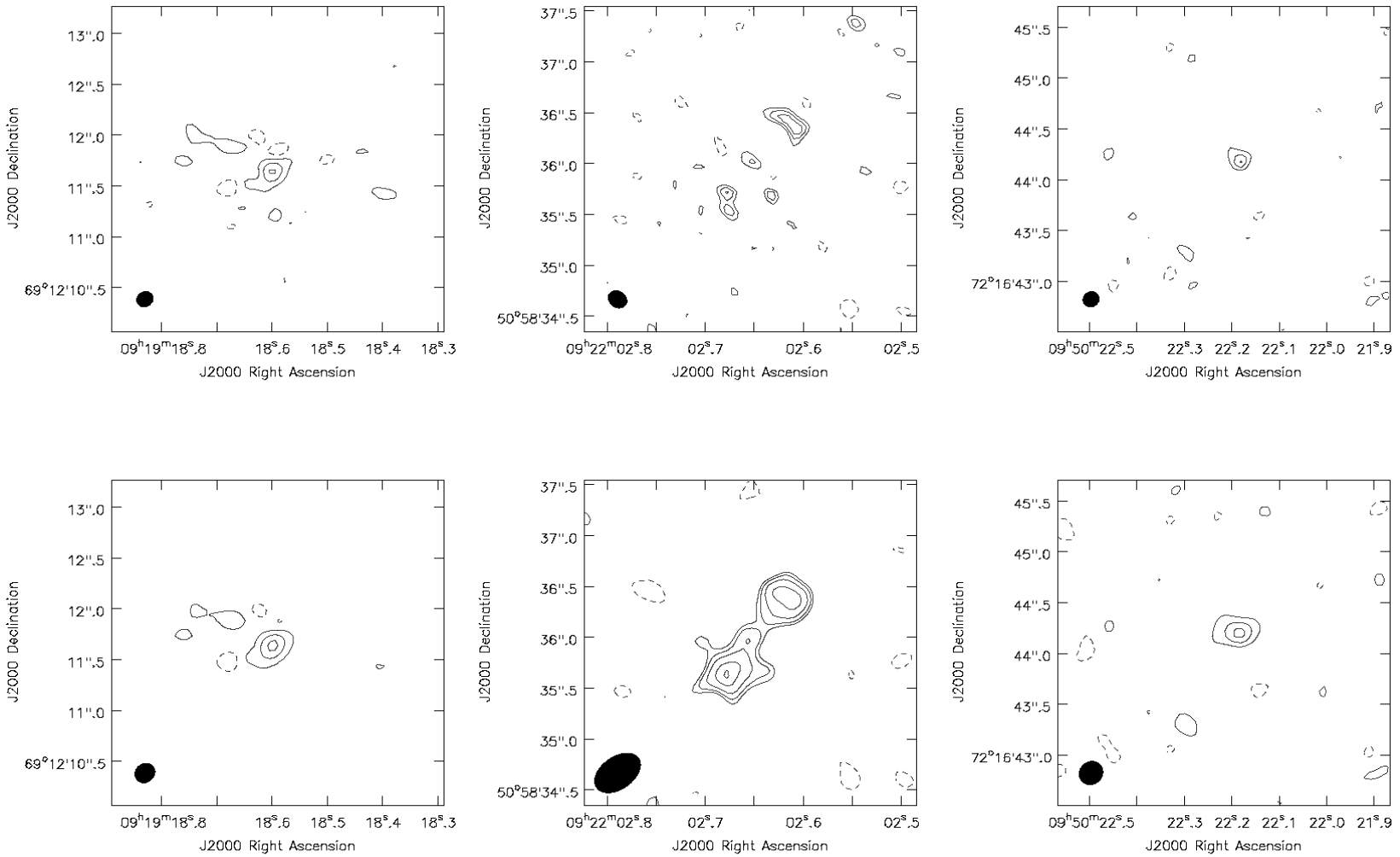

Figure B.1: e-MERLIN 1.5-GHz images of the identified LeMMINGs galaxies. This page: NGC 2787 (left), NGC 2841 (centre), NGC 2985 (right). The *Top* image shows the full resolution image and the *Bottom* image shows the lower resolution image

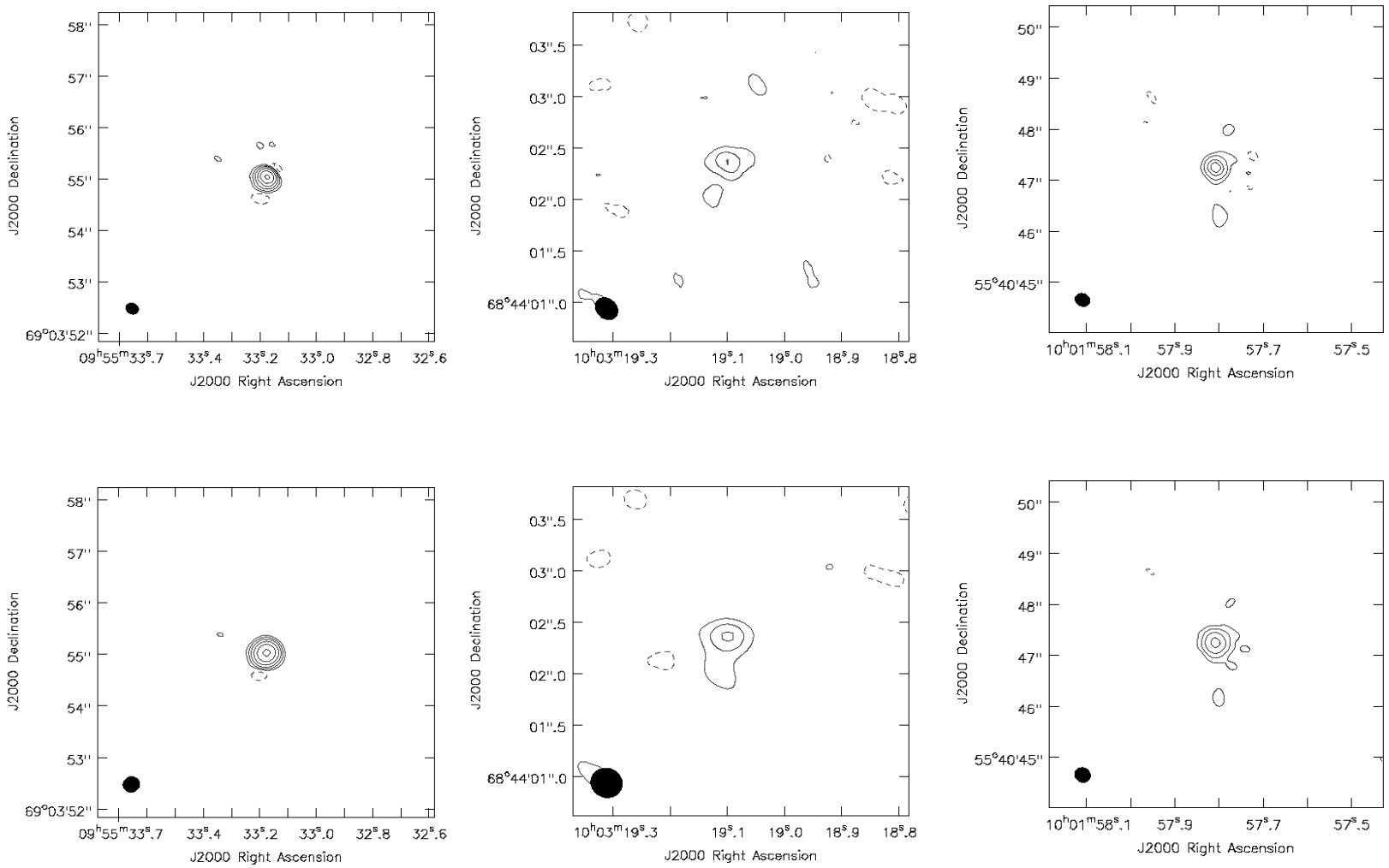

Figure B.1: e-MERLIN 1.5-GHz images of the identified LeMMINGs galaxies. This page: NGC 3031 (left), NGC 3077 (centre), NGC 3079 (right). The *Top* image shows the full resolution image and the *Bottom* image shows the lower resolution image

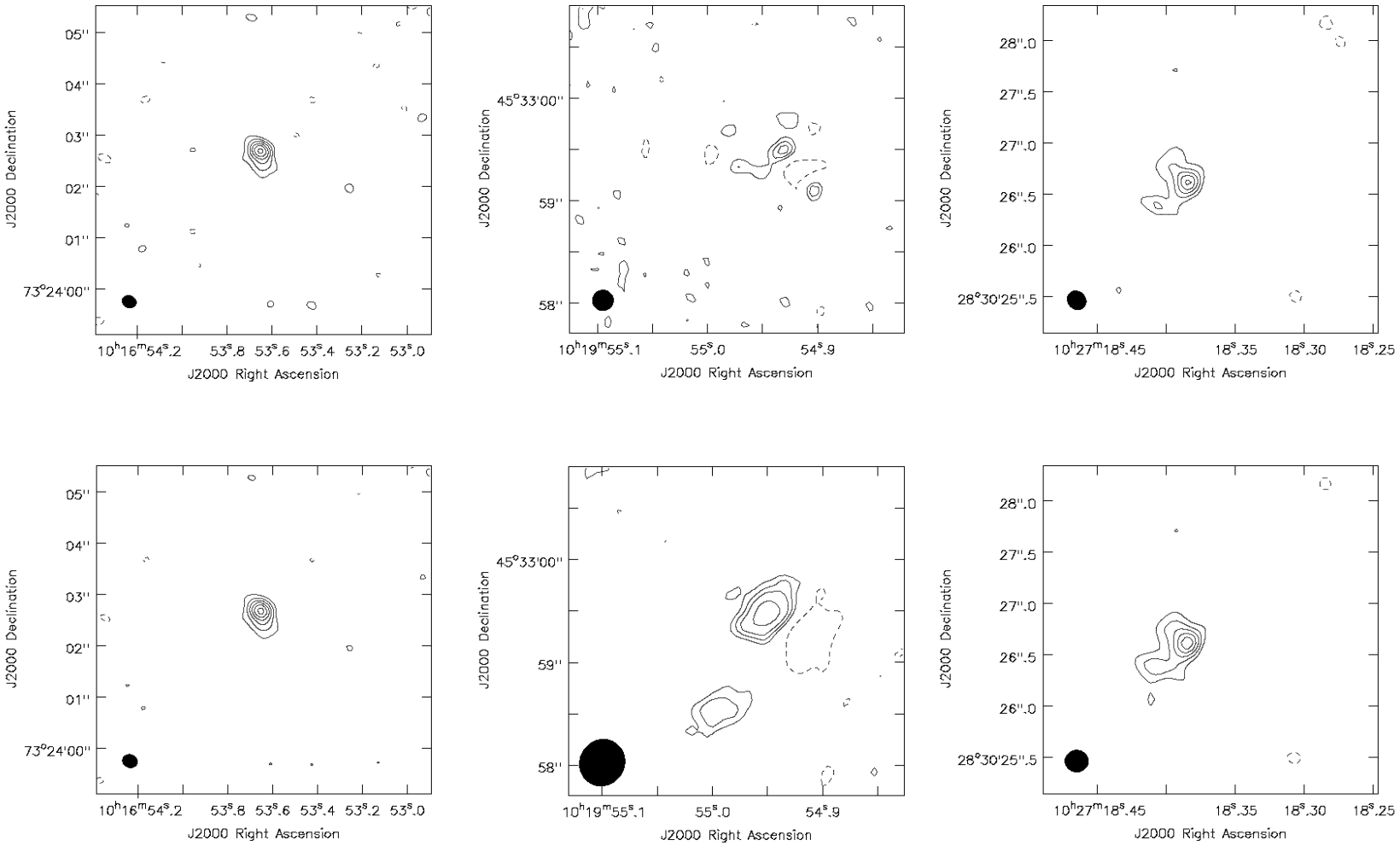

Figure B.1: e-MERLIN 1.5-GHz images of the identified LeMMINGs galaxies. This page: NGC 3147 (left), NGC 3198 (centre), NGC 3245 (right). The *Top* image shows the full resolution image and the *Bottom* image shows the lower resolution image

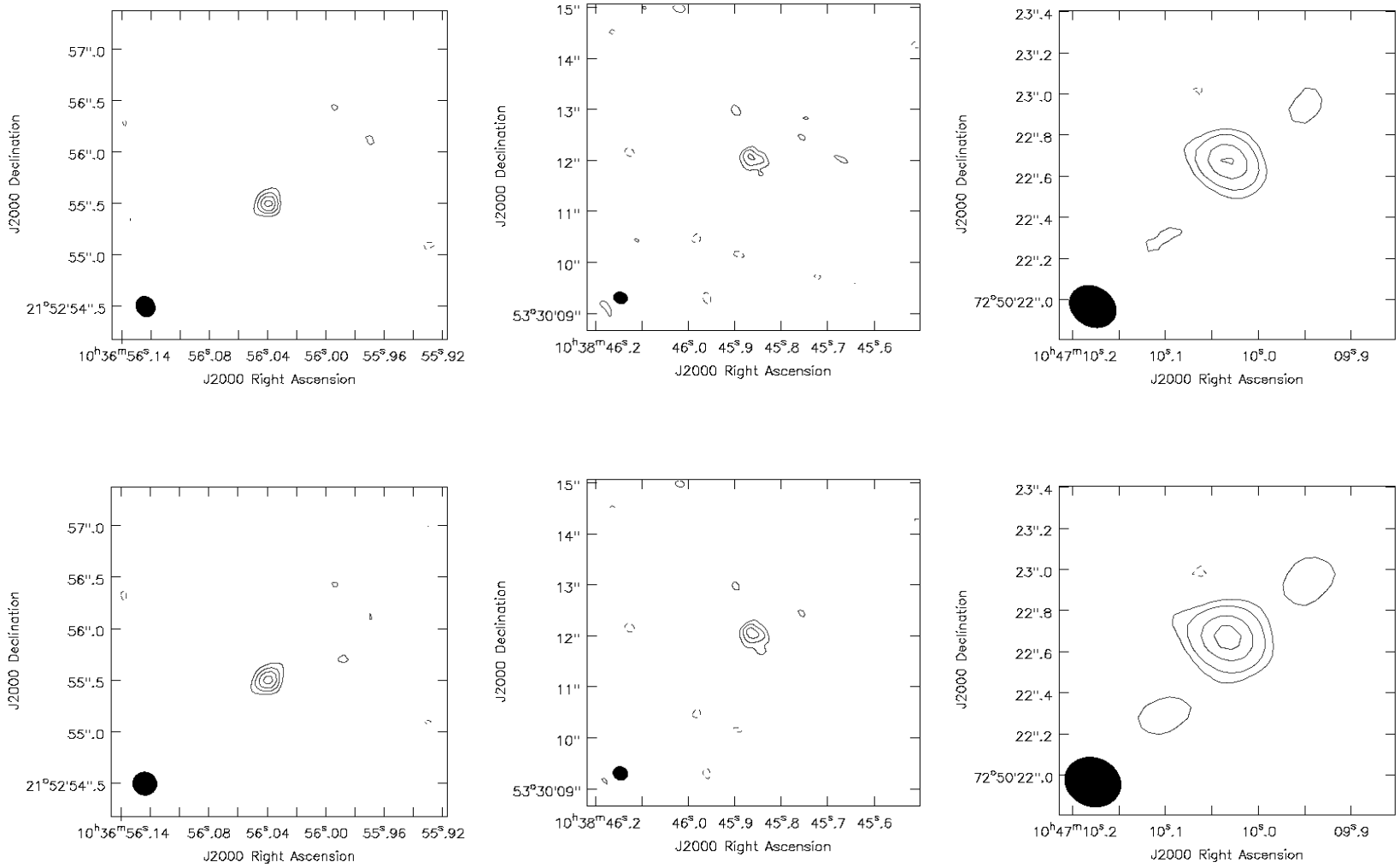

Figure B.1: e-MERLIN 1.5-GHz images of the identified LeMMINGs galaxies. This page: NGC 3301 (left), NGC 3310 (centre), NGC 3348 (right). The *Top* image shows the full resolution image and the *Bottom* image shows the lower resolution image

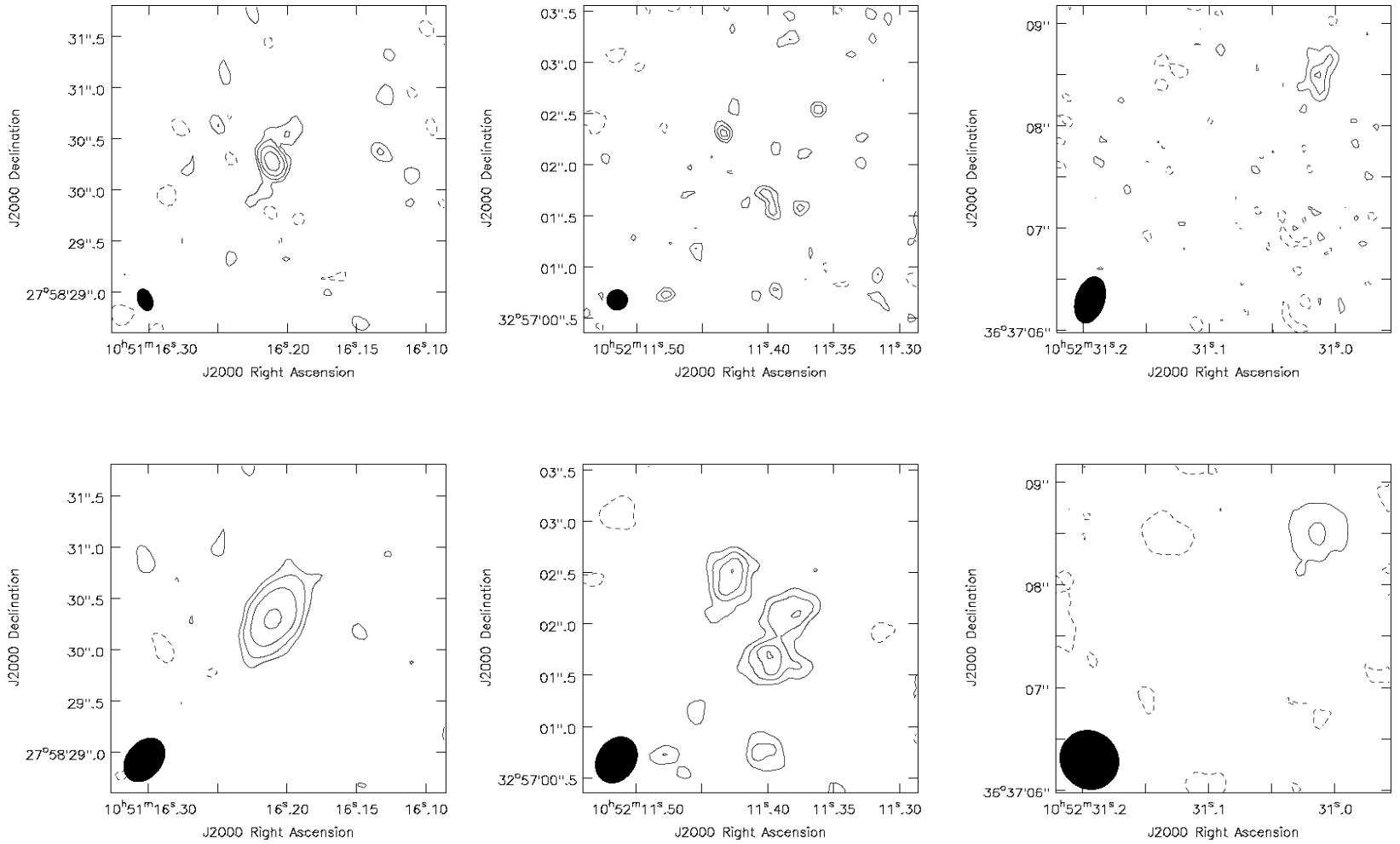

Figure B.1: e-MERLIN 1.5-GHz images of the identified LeMMINGs galaxies. This page: NGC 3414 (left), NGC 3430 (centre), NGC 3432 (right). The *Top* image shows the full resolution image and the *Bottom* image shows the lower resolution image

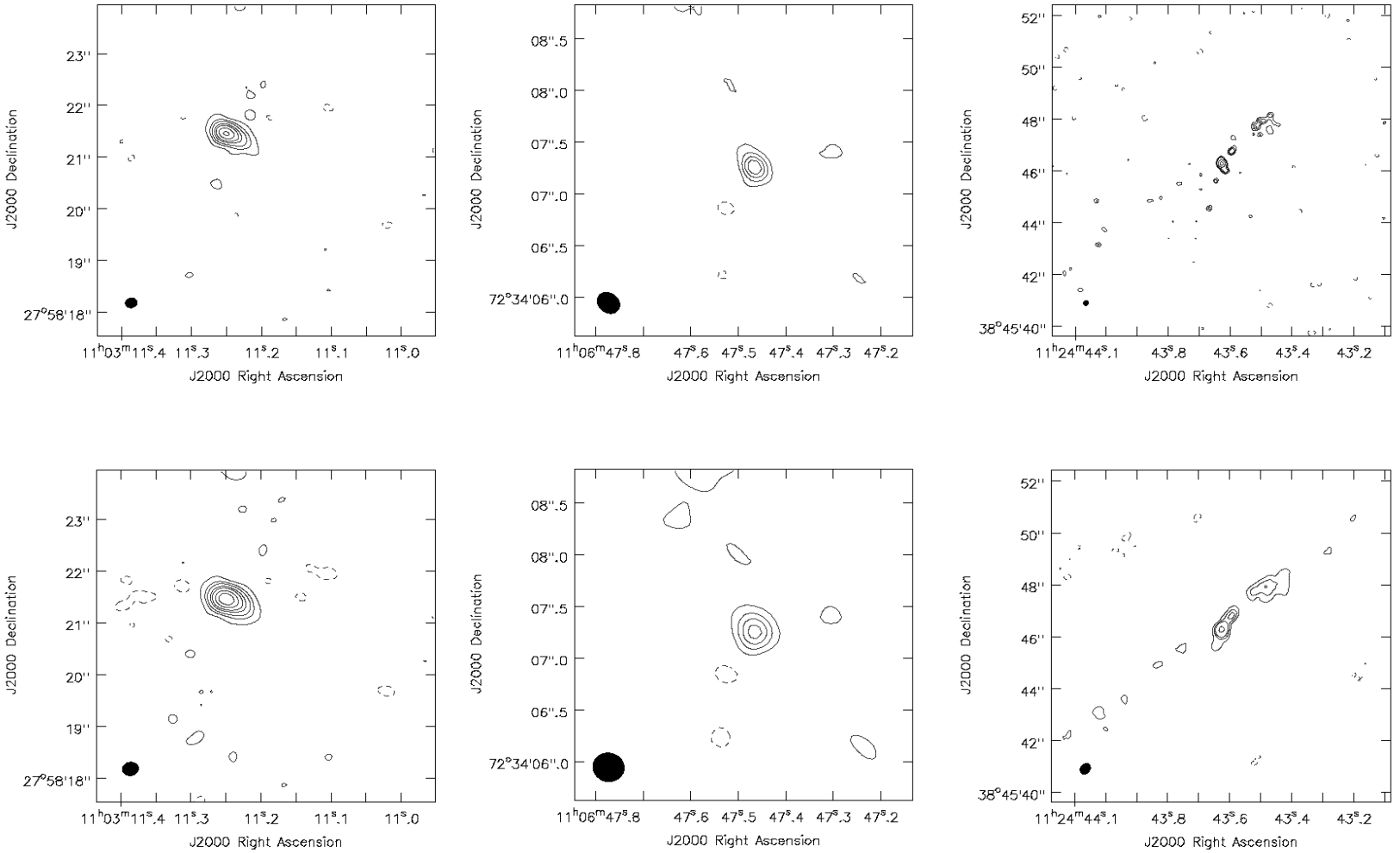

Figure B.1: e-MERLIN 1.5-GHz images of the identified LeMMINGs galaxies. This page: NGC 3504 (left), NGC 3516 (centre), NGC 3665 (right). The *Top* image shows the full resolution image and the *Bottom* image shows the lower resolution image

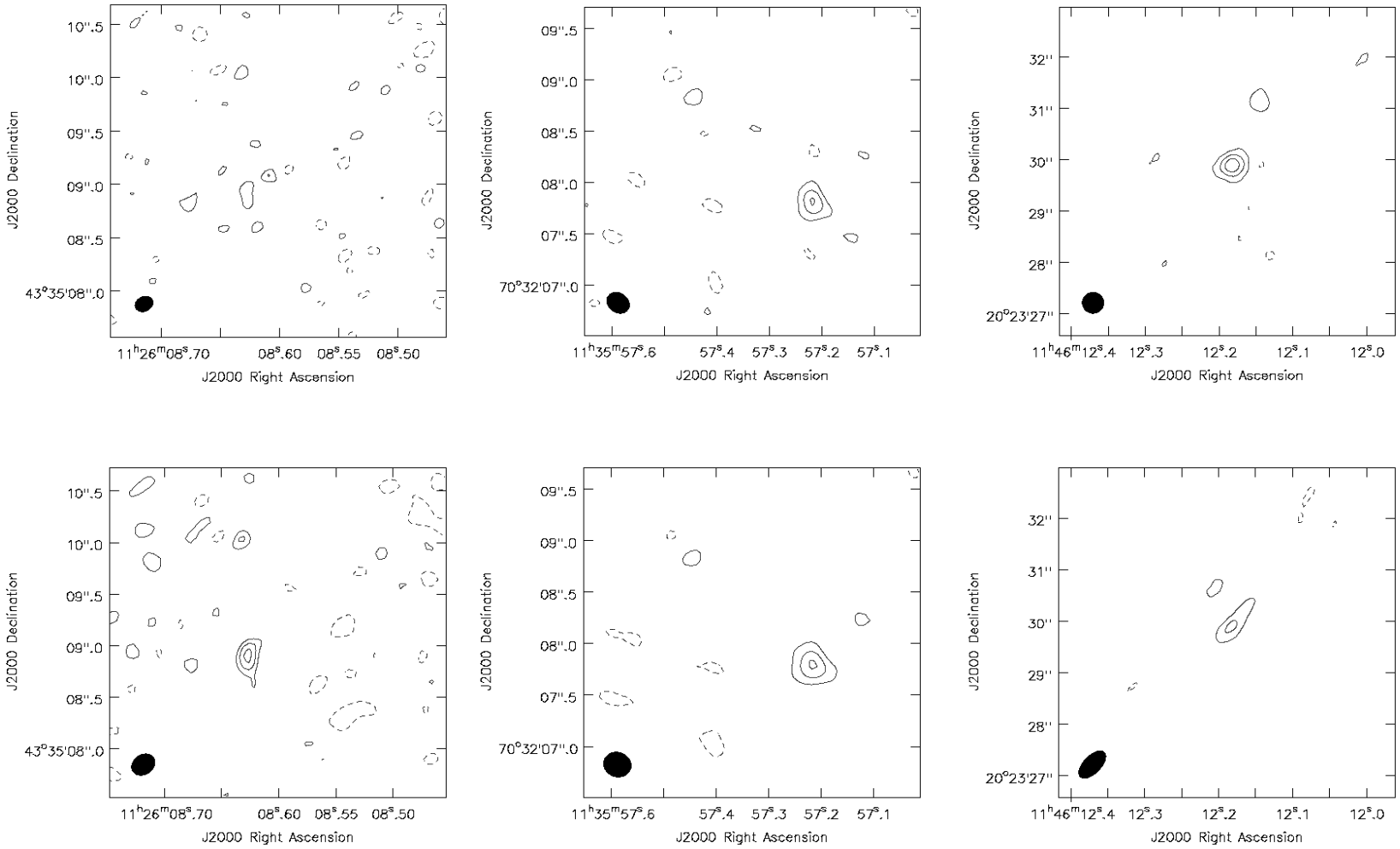

Figure B.1: e-MERLIN 1.5-GHz images of the identified LeMMINGs galaxies. This page: NGC 3675 (left), NGC 3735 (centre), NGC 3884 (right). The *Top* image shows the full resolution image and the *Bottom* image shows the lower resolution image

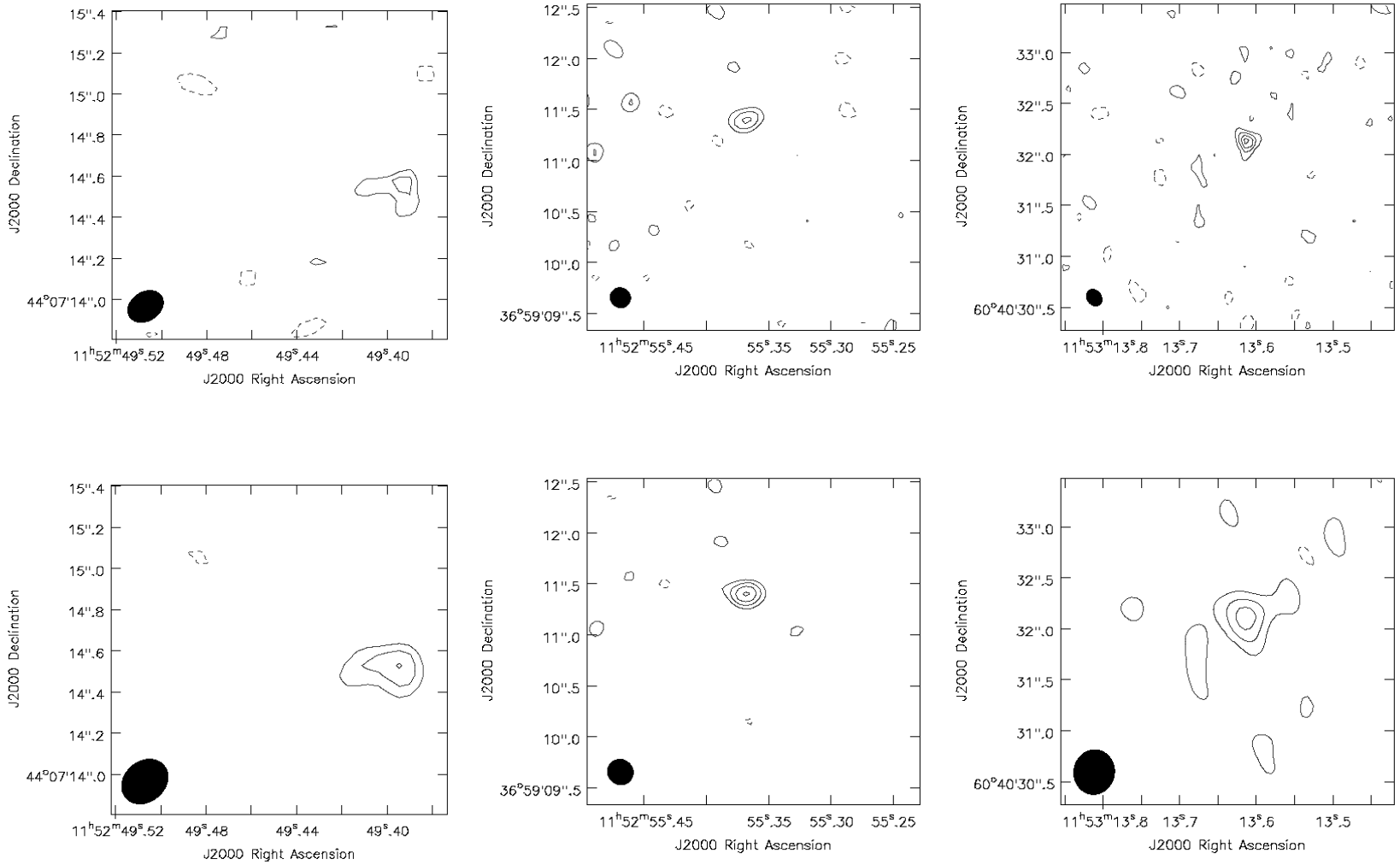

Figure B.1: e-MERLIN 1.5-GHz images of the identified LeMMINGs galaxies. This page: NGC 3938 (left), NGC 3941 (centre), NGC 3945 (right). The *Top* image shows the full resolution image and the *Bottom* image shows the lower resolution image

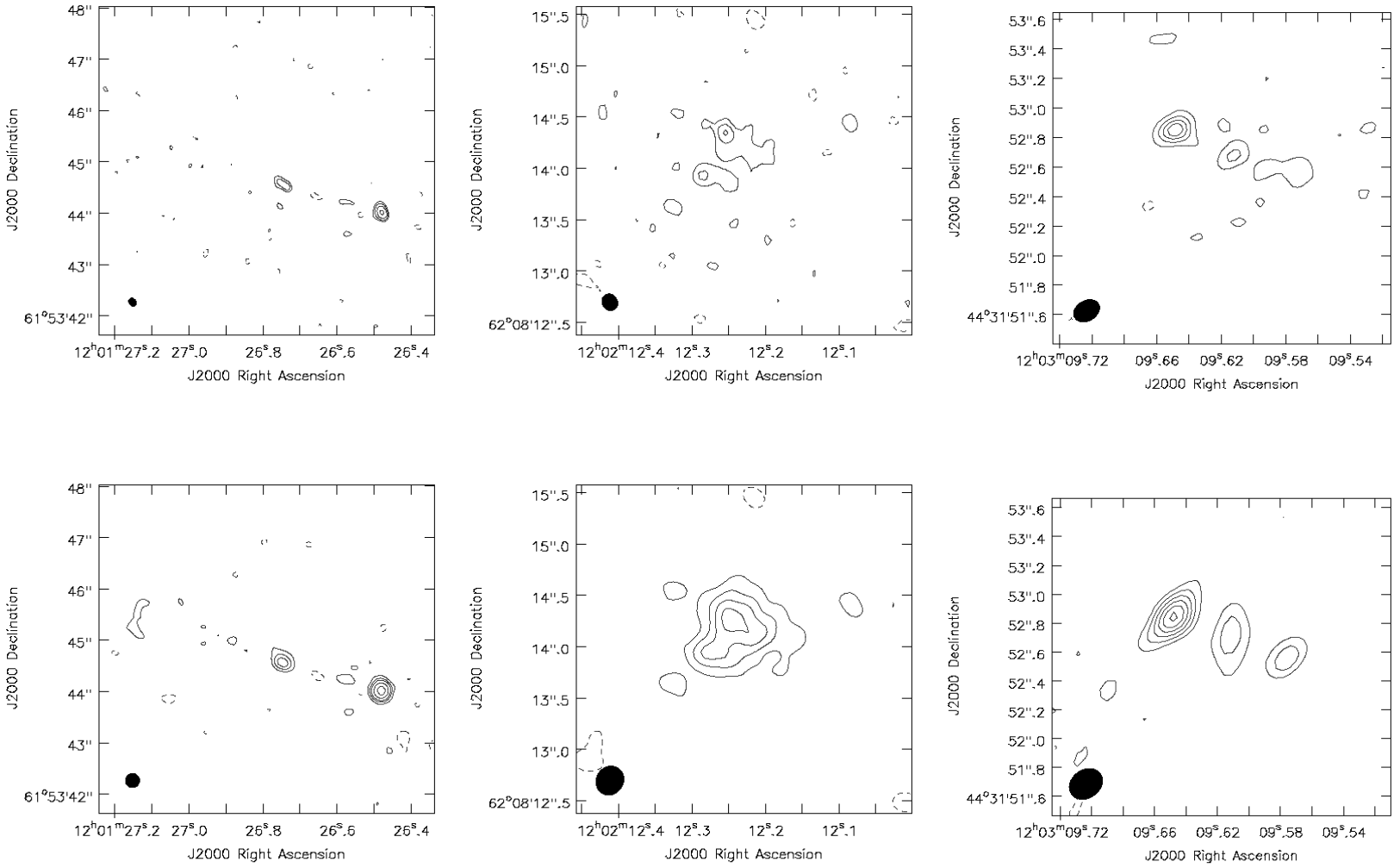

Figure B.1: e-MERLIN 1.5-GHz images of the identified LeMMINGs galaxies. This page: NGC 4036 (left), NGC 4041 (centre), NGC 4051 (right). The *Top* image shows the full resolution image and the *Bottom* image shows the lower resolution image

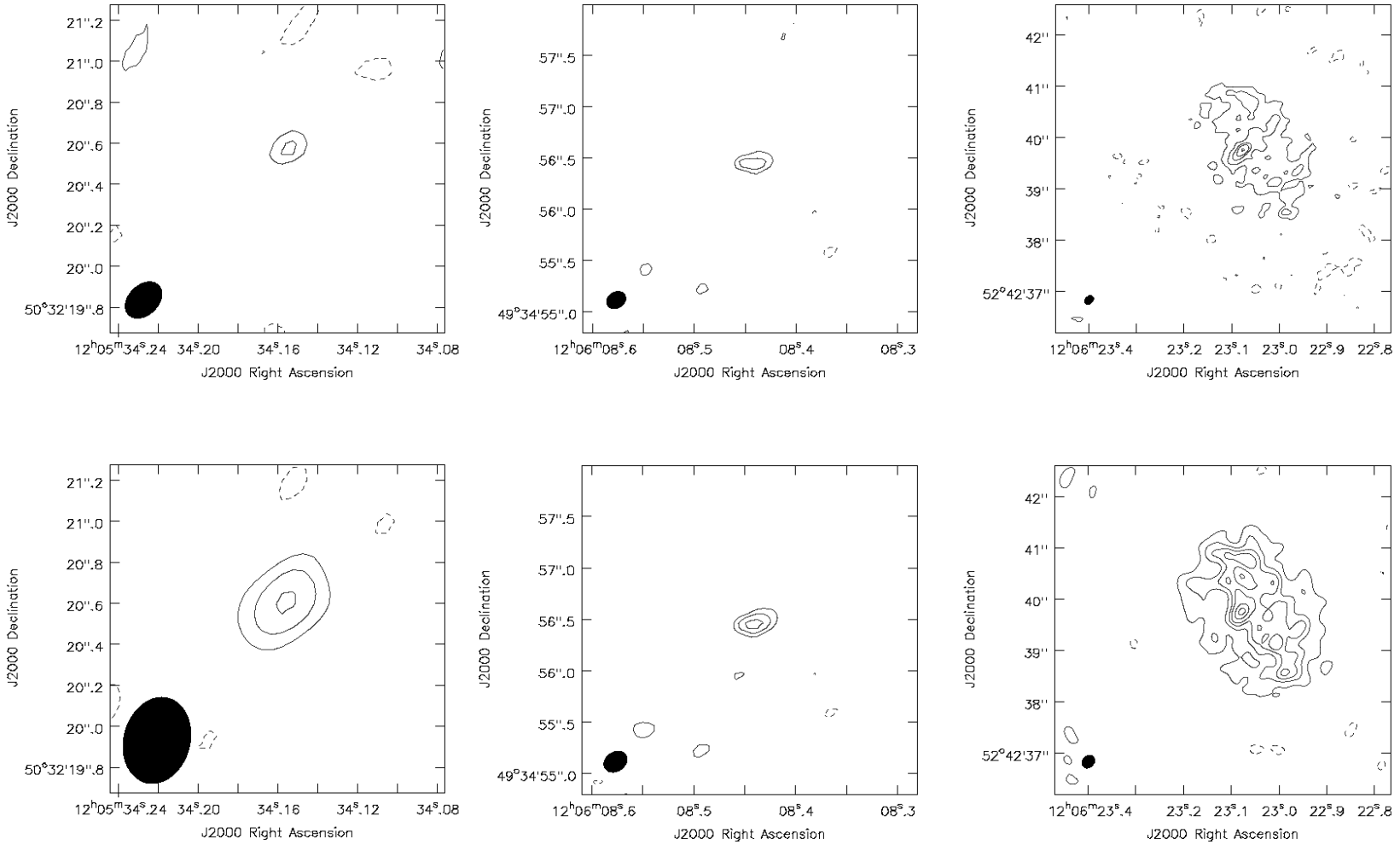

Figure B.1: e-MERLIN 1.5-GHz images of the identified LeMMINGs galaxies. This page: NGC 4088 (left), NGC 4100 (centre), NGC 4102 (right). The *Top* image shows the full resolution image and the *Bottom* image shows the lower resolution image

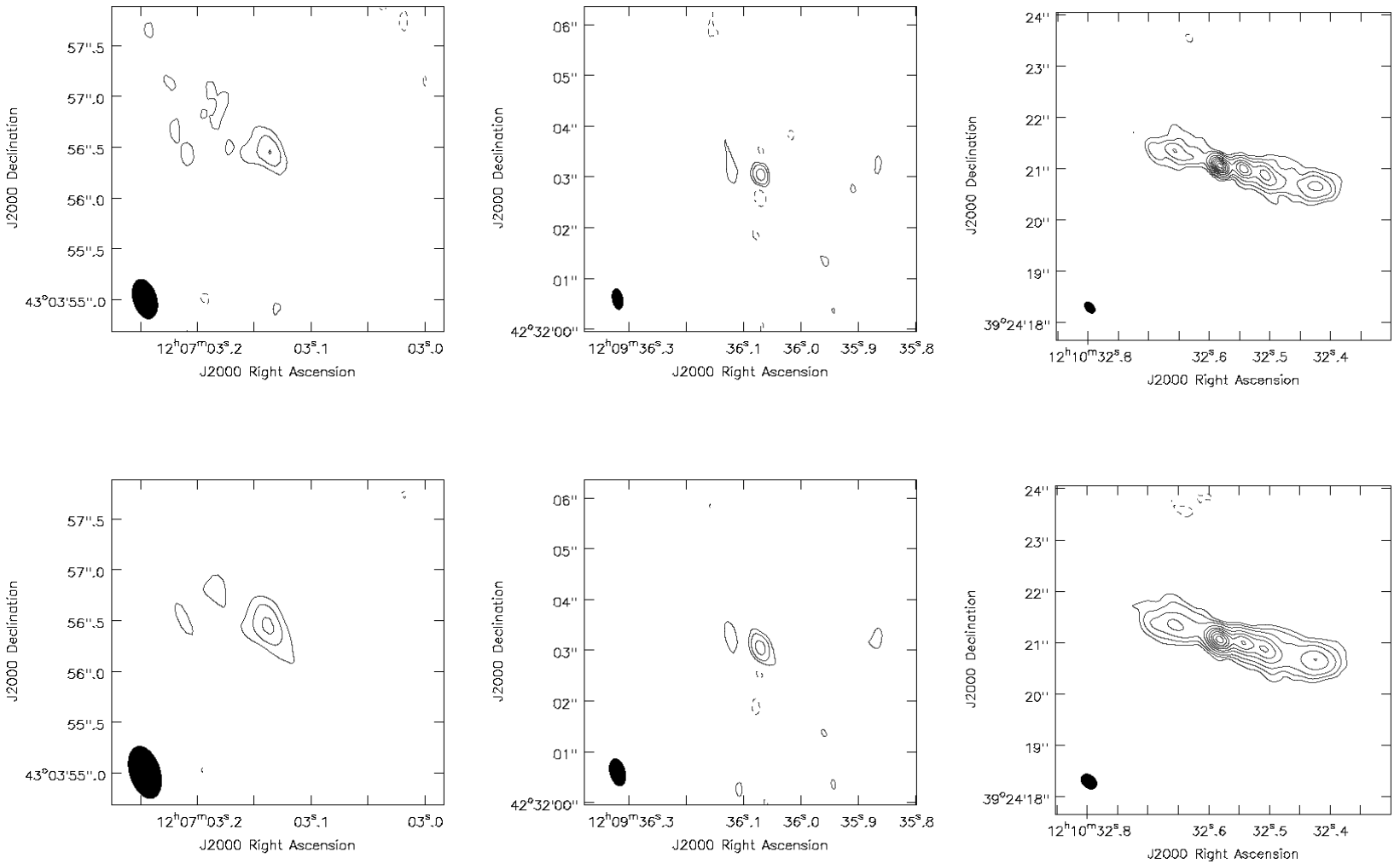

Figure B.1: e-MERLIN 1.5-GHz images of the identified LeMMINGs galaxies. This page: NGC 4111 (left), NGC 4143 (centre), NGC 4151 (right). The *Top* image shows the full resolution image and the *Bottom* image shows the lower resolution image

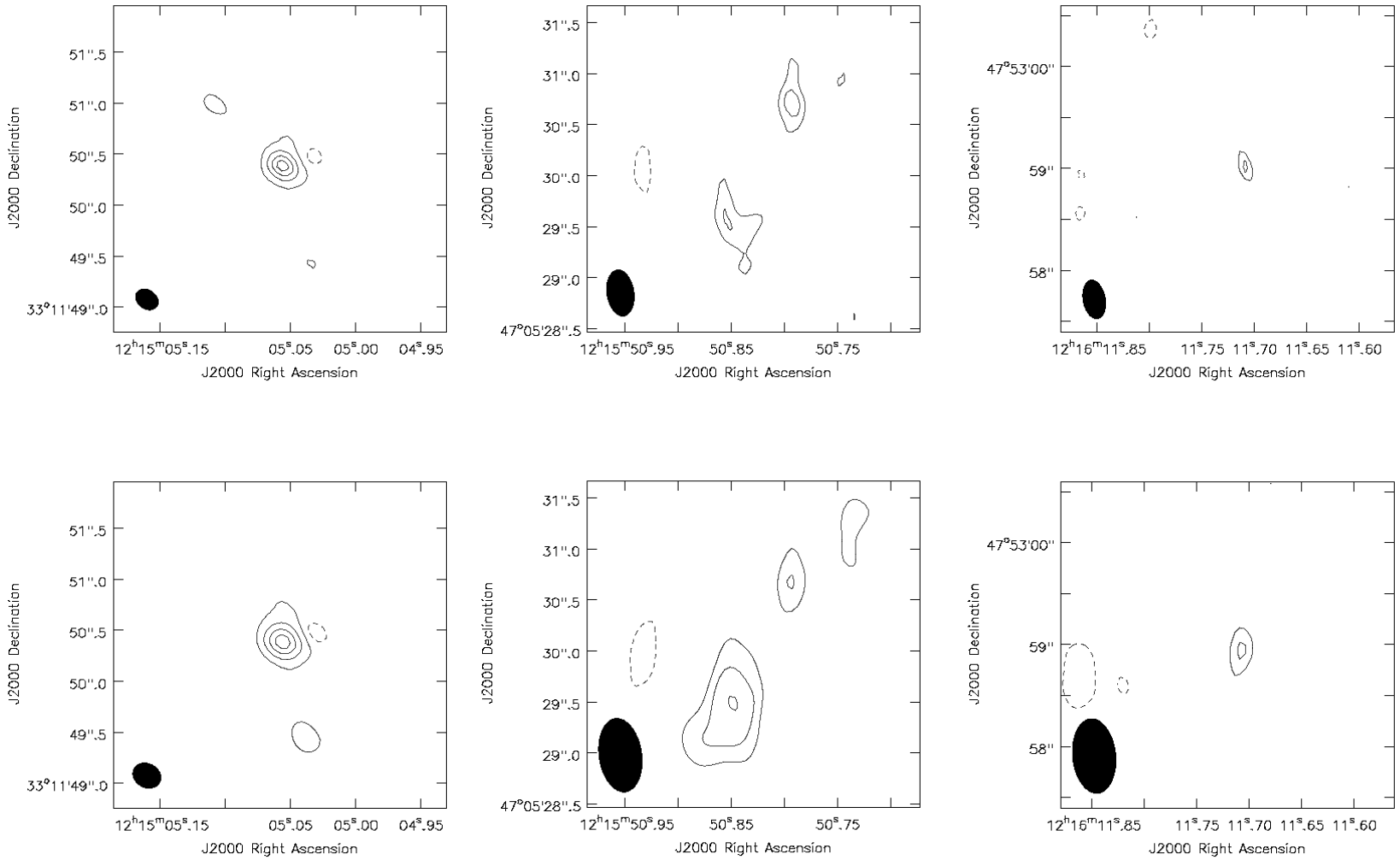

Figure B.1: e-MERLIN 1.5-GHz images of the identified LeMMINGs galaxies. This page: NGC 4203 (left), NGC 4217 (centre), NGC 4220 (right). The *Top* image shows the full resolution image and the *Bottom* image shows the lower resolution image

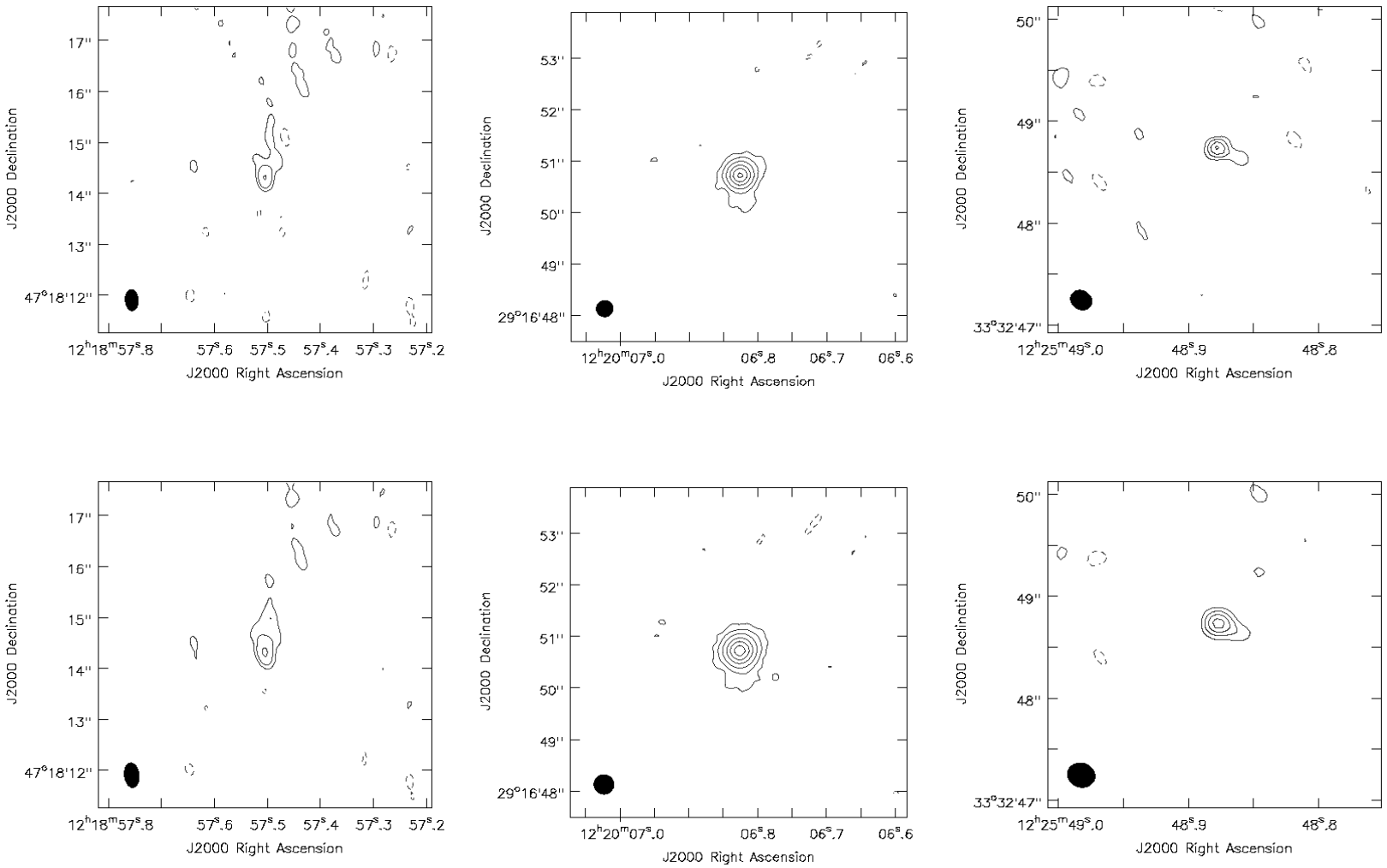

Figure B.1: e-MERLIN 1.5-GHz images of the identified LeMMINGs galaxies. This page: NGC 4258 (left), NGC 4278 (centre), NGC 4395 (right). The *Top* image shows the full resolution image and the *Bottom* image shows the lower resolution image

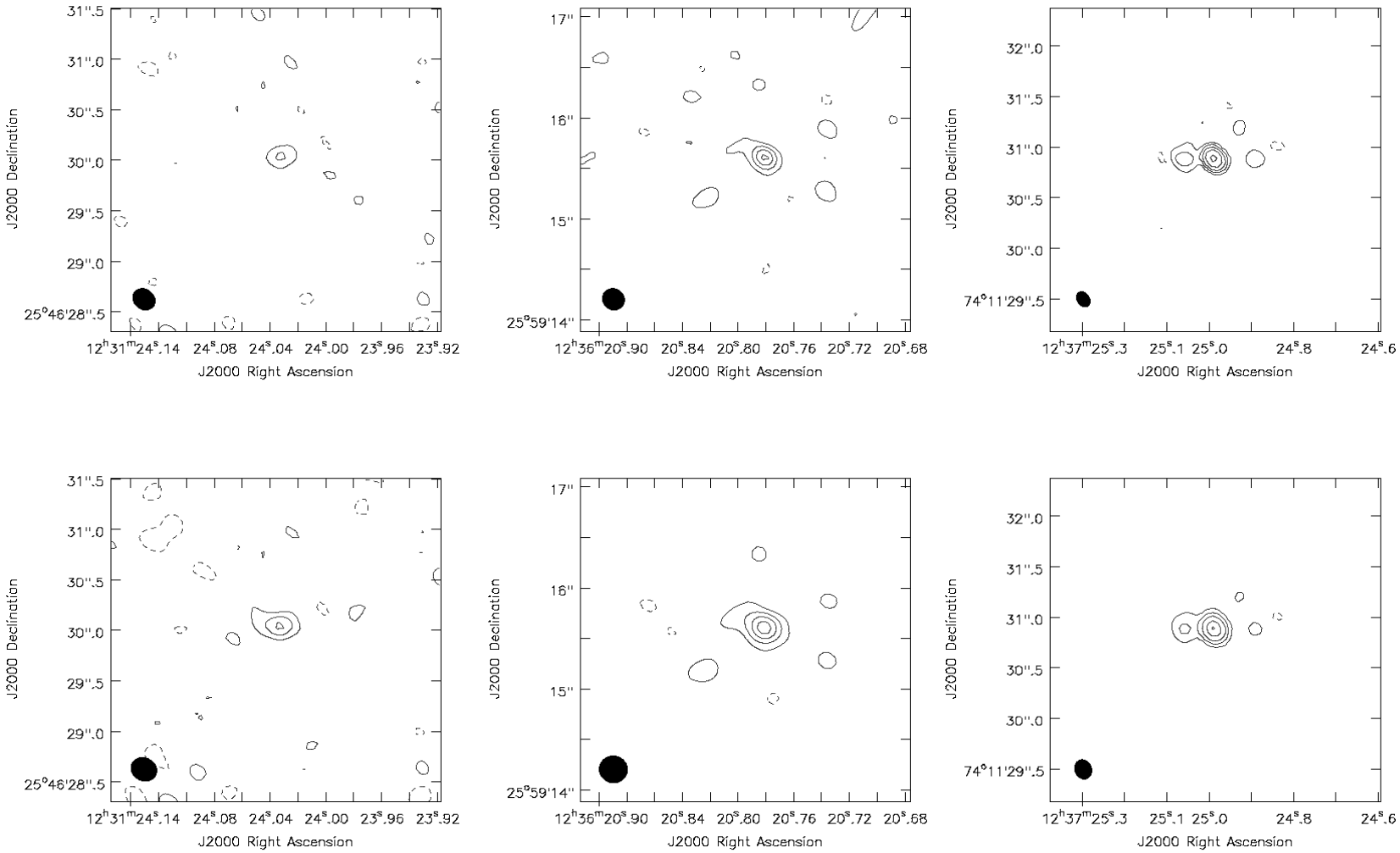

Figure B.1: e-MERLIN 1.5-GHz images of the identified LeMMINGs galaxies. This page: NGC 4494 (left), NGC 4565 (centre), NGC 4589 (right). The *Top* image shows the full resolution image and the *Bottom* image shows the lower resolution image

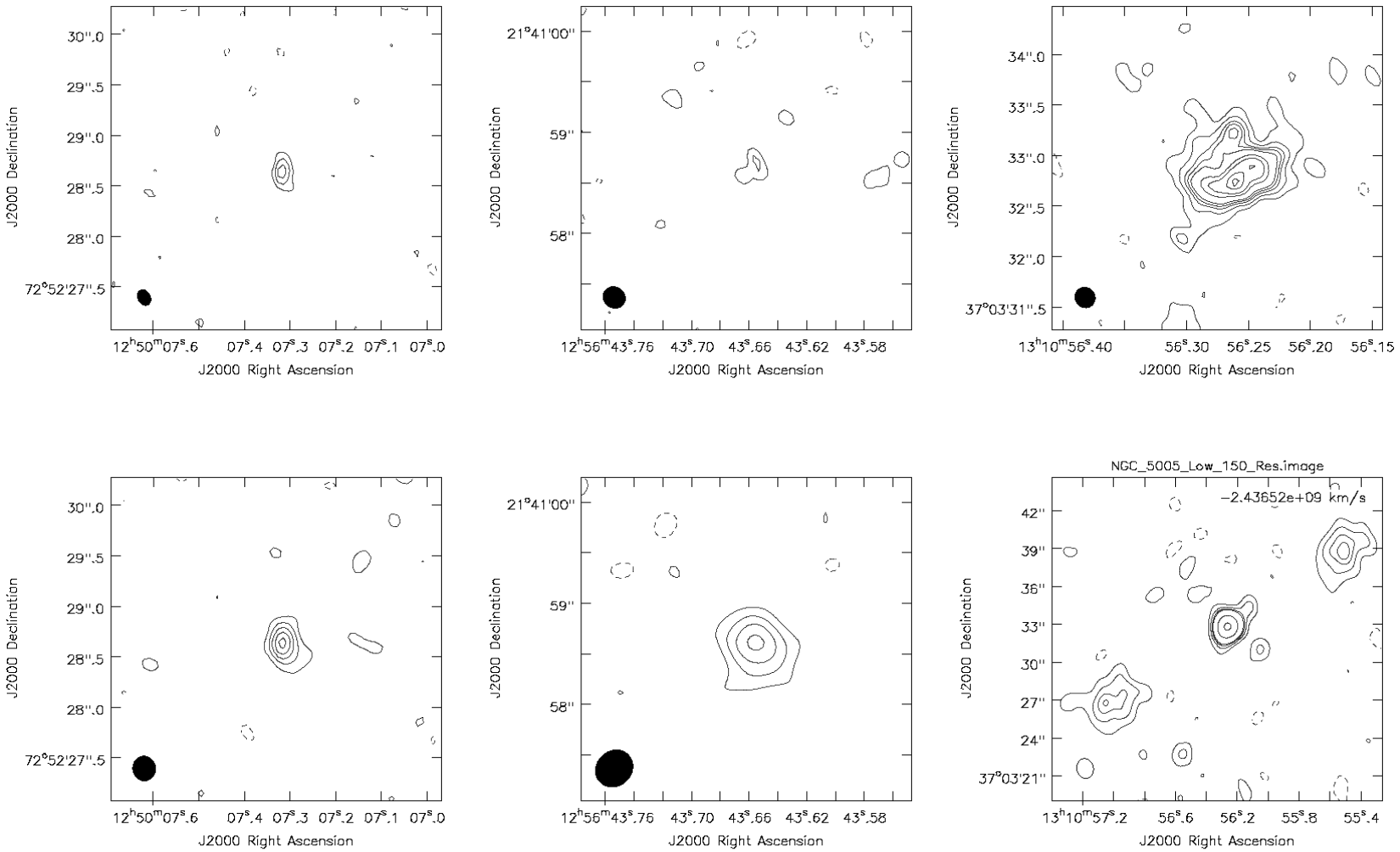

Figure B.1: e-MERLIN 1.5-GHz images of the identified LeMMINGs galaxies. This page: NGC 4750 (left), NGC 4826 (centre), NGC 5005 (right). The *Top* image shows the full resolution image and the *Bottom* image shows the lower resolution image

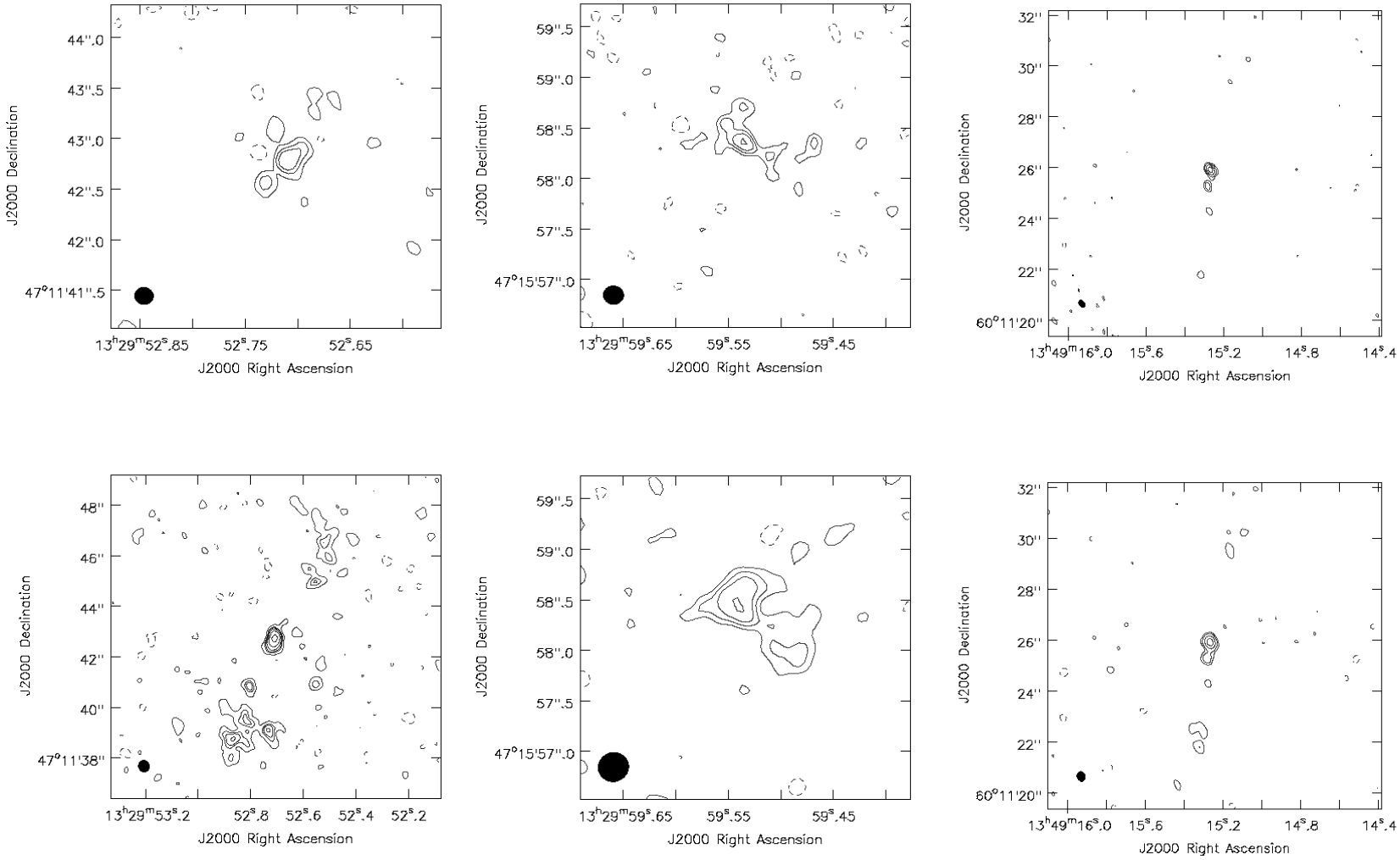

Figure B.1: e-MERLIN 1.5-GHz images of the identified LeMMINGs galaxies. This page: NGC 5194 (left), NGC 5195 (centre), NGC 5322 (right). The *Top* image shows the full resolution image and the *Bottom* image shows the lower resolution image

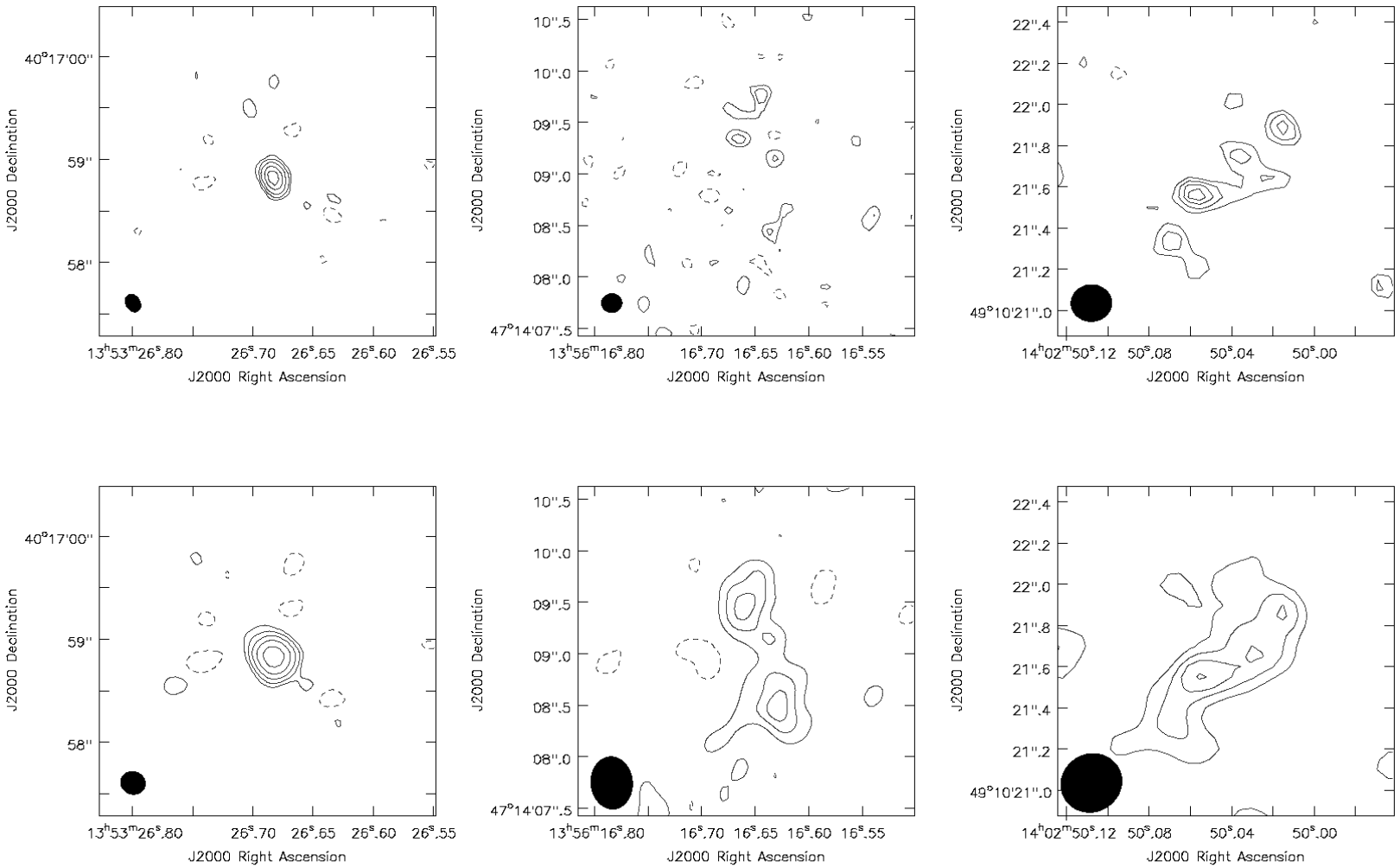

Figure B.1: e-MERLIN 1.5-GHz images of the identified LeMMINGs galaxies. This page: NGC 5353 (left), NGC 5377 (centre), NGC 5448 (right). The *Top* image shows the full resolution image and the *Bottom* image shows the lower resolution image

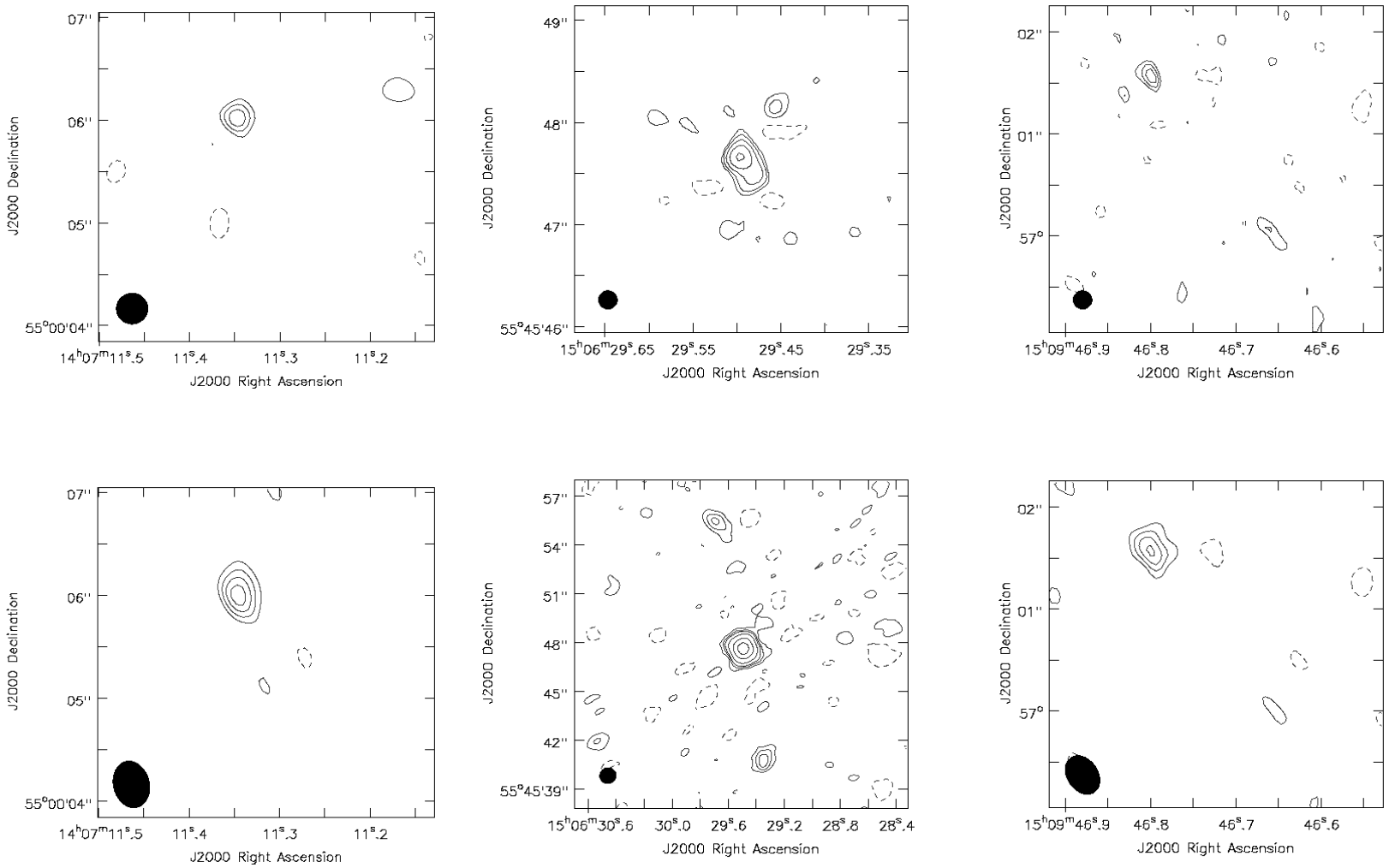

Figure B.1: e-MERLIN 1.5-GHz images of the identified LeMMINGs galaxies. This page: NGC 5485 (left), NGC 5866 (centre), NGC 5979 (right). The *Top* image shows the full resolution image and the *Bottom* image shows the lower resolution image

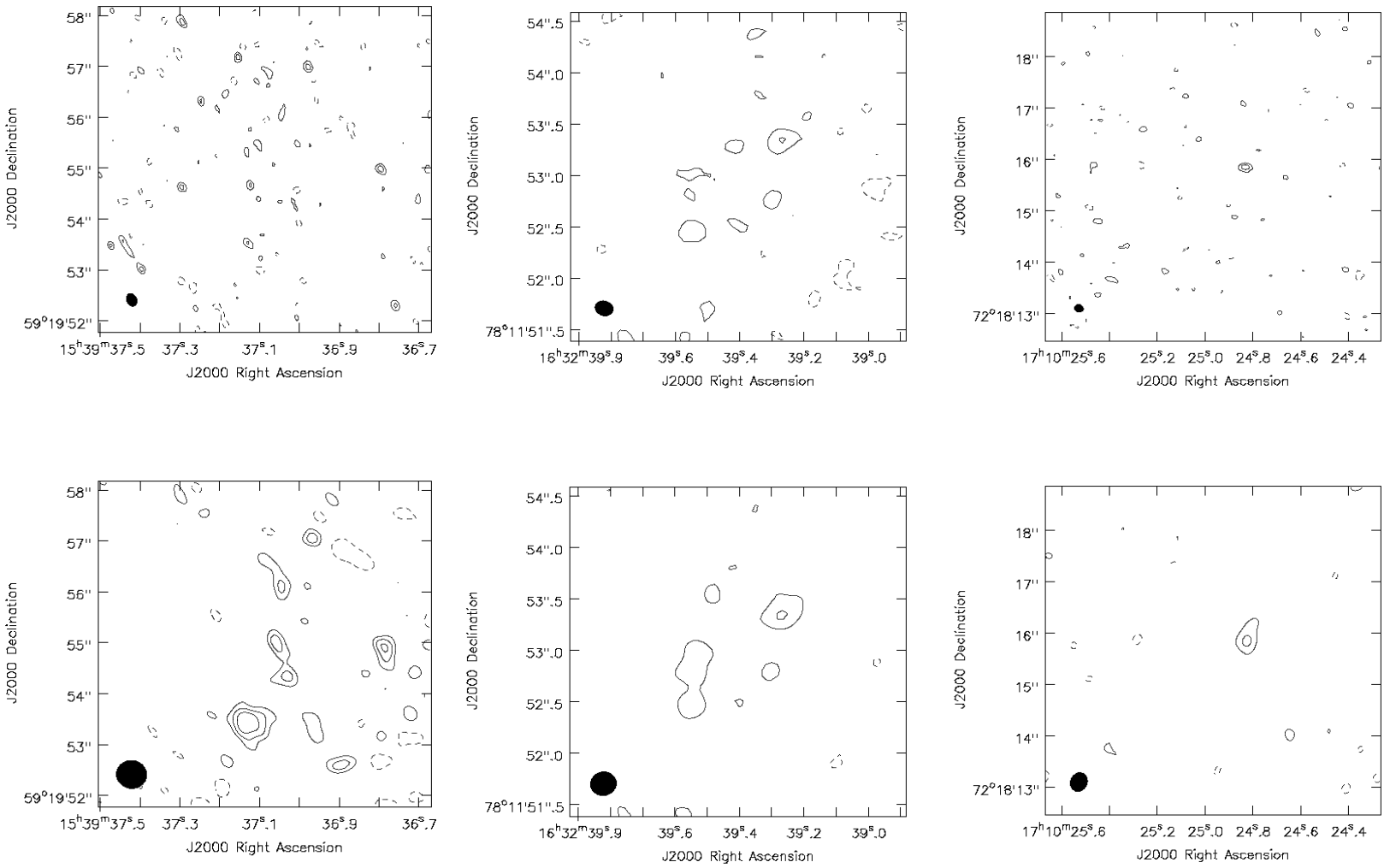

Figure B.1: e-MERLIN 1.5-GHz images of the identified LeMMINGs galaxies. This page: NGC 5985 (left), NGC 6217 (centre), NGC 6340 (right). The *Top* image shows the full resolution image and the *Bottom* image shows the lower resolution image

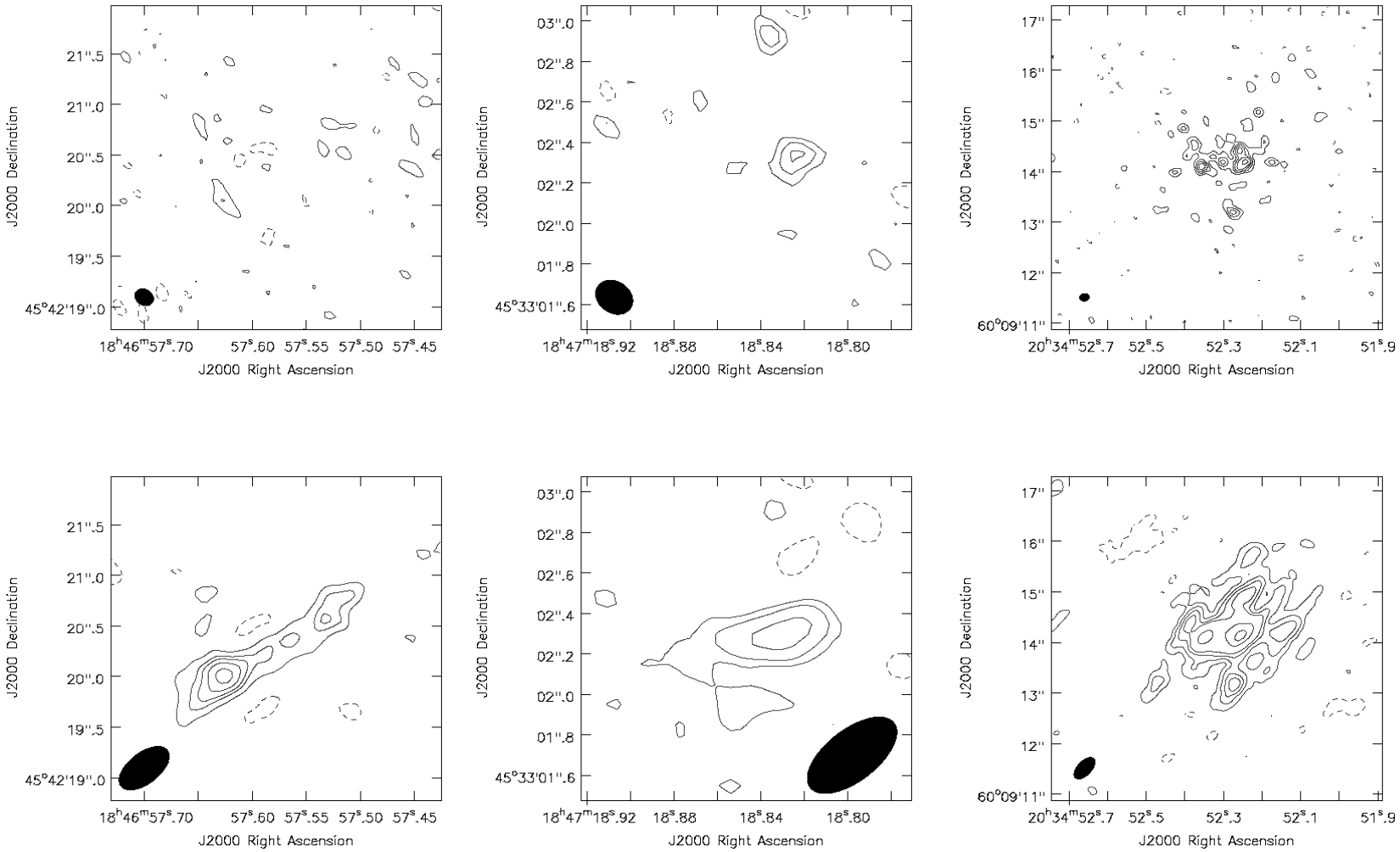

Figure B.1: e-MERLIN 1.5-GHz images of the identified LeMMINGs galaxies. This page: NGC 6702 (left), NGC 6703 (centre), NGC 6946 (right). The *Top* image shows the full resolution image and the *Bottom* image shows the lower resolution image

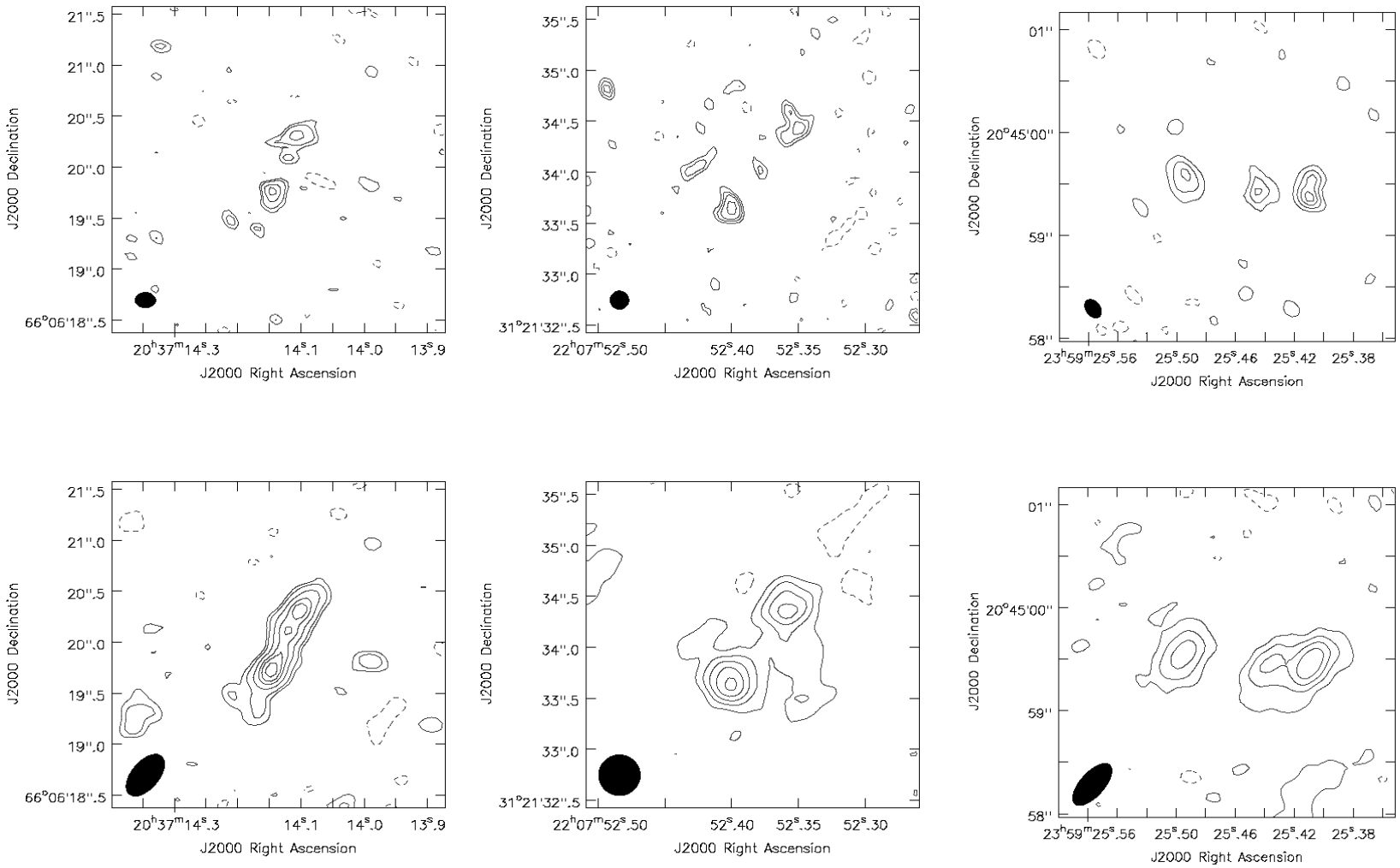

Figure B.1: e-MERLIN 1.5-GHz images of the identified LeMMINGs galaxies. This page: NGC 6951 (left), NGC 7217 (centre), NGC 7798 (right). The *Top* image shows the full resolution image and the *Bottom* image shows the lower resolution image

B.2 e-MERLIN LeMMINGs Shallow Survey 1.5 GHz Maps of unidentified sources

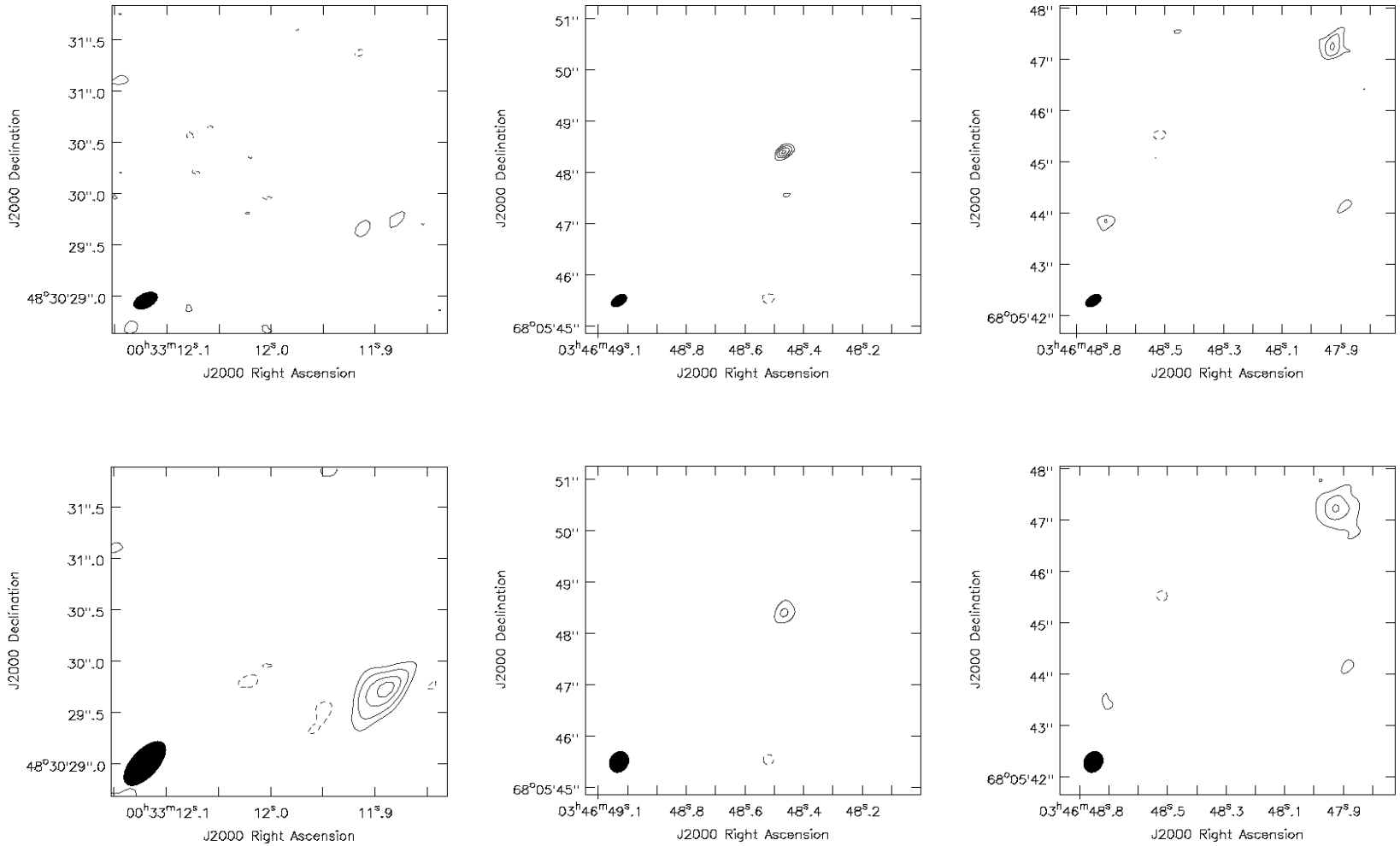

Figure B.2: e-MERLIN 1.5-GHz images of the unidentified LeMMINGs galaxies. This page: NGC 147 (left), IC 342 (centre and right). The *Top* image shows the full resolution image and the *Bottom* image shows the lower resolution image

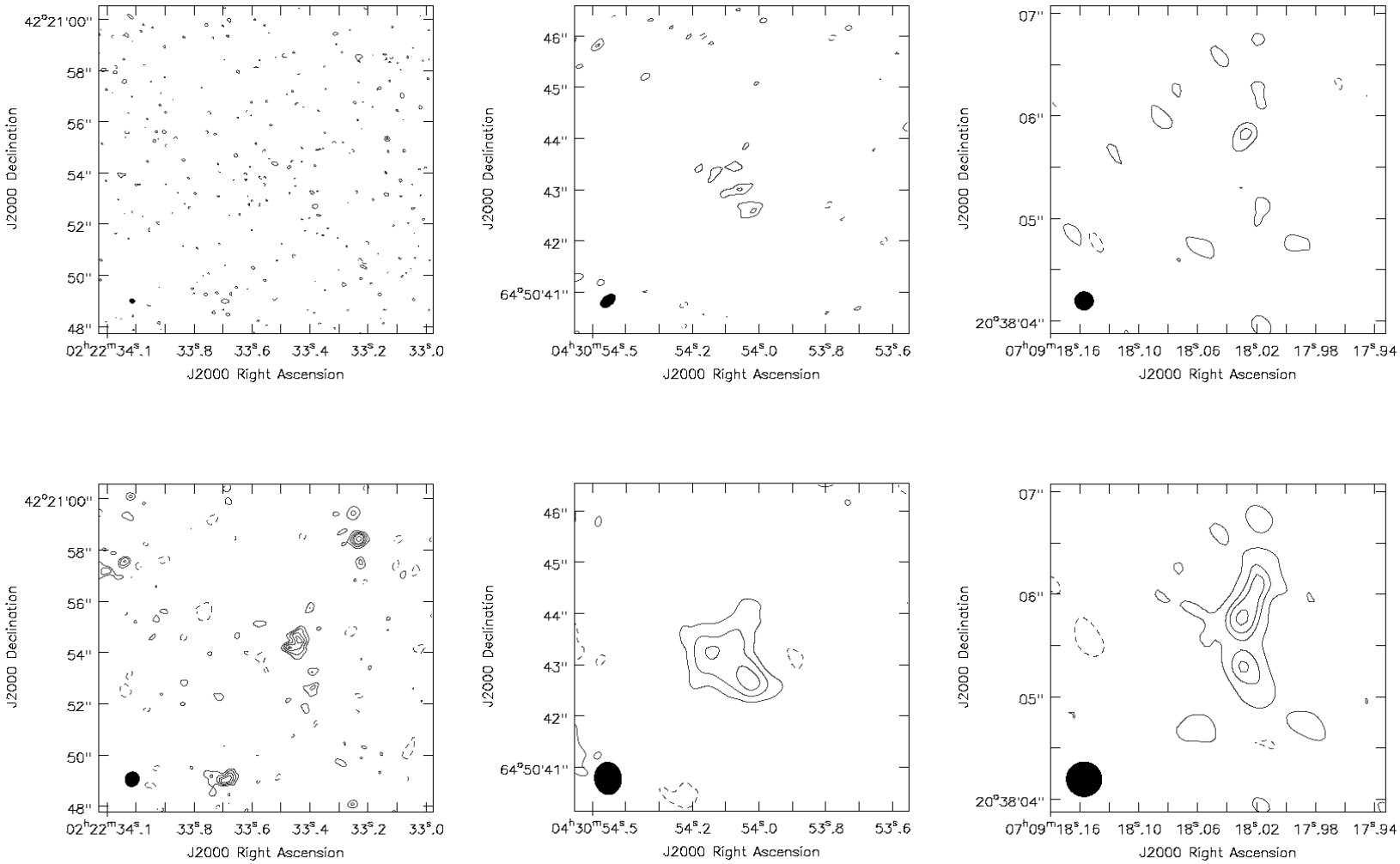

Figure B.2: e-MERLIN 1.5-GHz images of the unidentified LeMMINGs galaxies. This page: NGC 891 (left), NGC 1569 (centre), NGC 2342 (right). The *Top* image shows the full resolution image and the *Bottom* image shows the lower resolution image

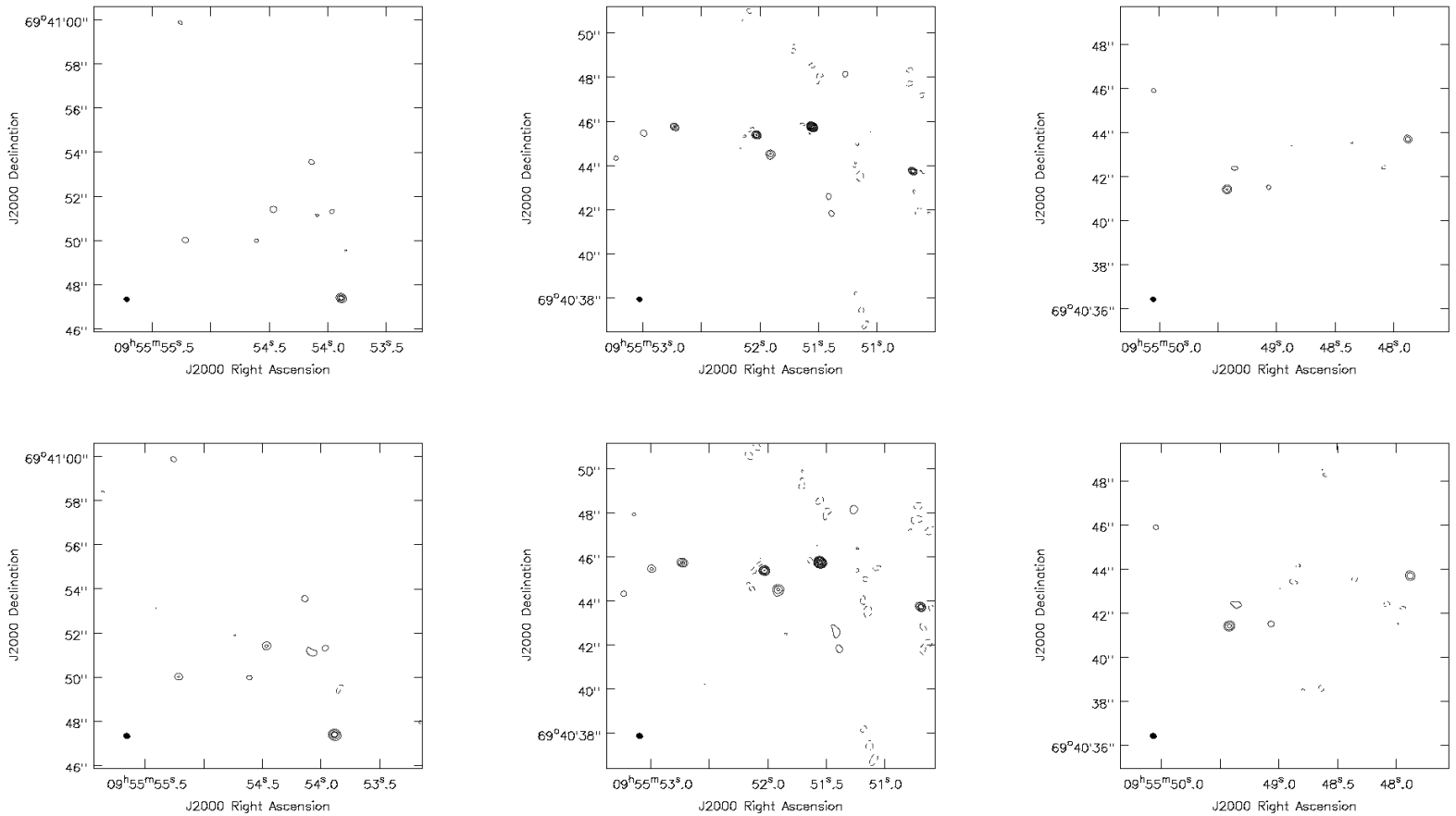

Figure B.2: e-MERLIN 1.5-GHz images of the unidentified LeMMINGs galaxies. This page: NGC 3034 East (left), NGC 3034 Central (centre), NGC 3034 West (right). The *Top* image shows the full resolution image and the *Bottom* image shows the lower resolution image

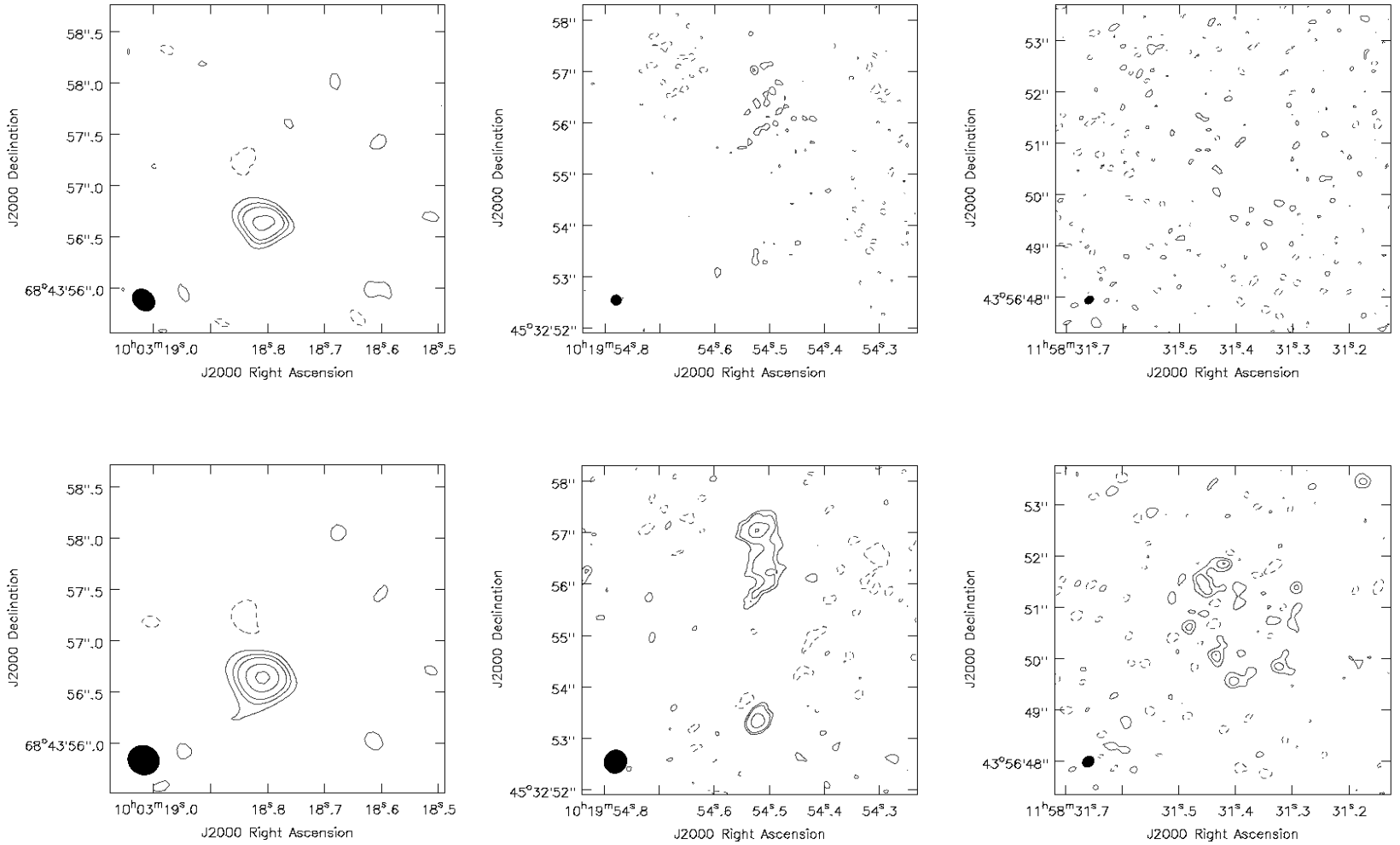

Figure B.2: e-MERLIN 1.5-GHz images of the unidentified LeMMINGs galaxies. This page: NGC 3077 (left), NGC 3198 (centre), NGC 4013 (right). The *Top* image shows the full resolution image and the *Bottom* image shows the lower resolution image

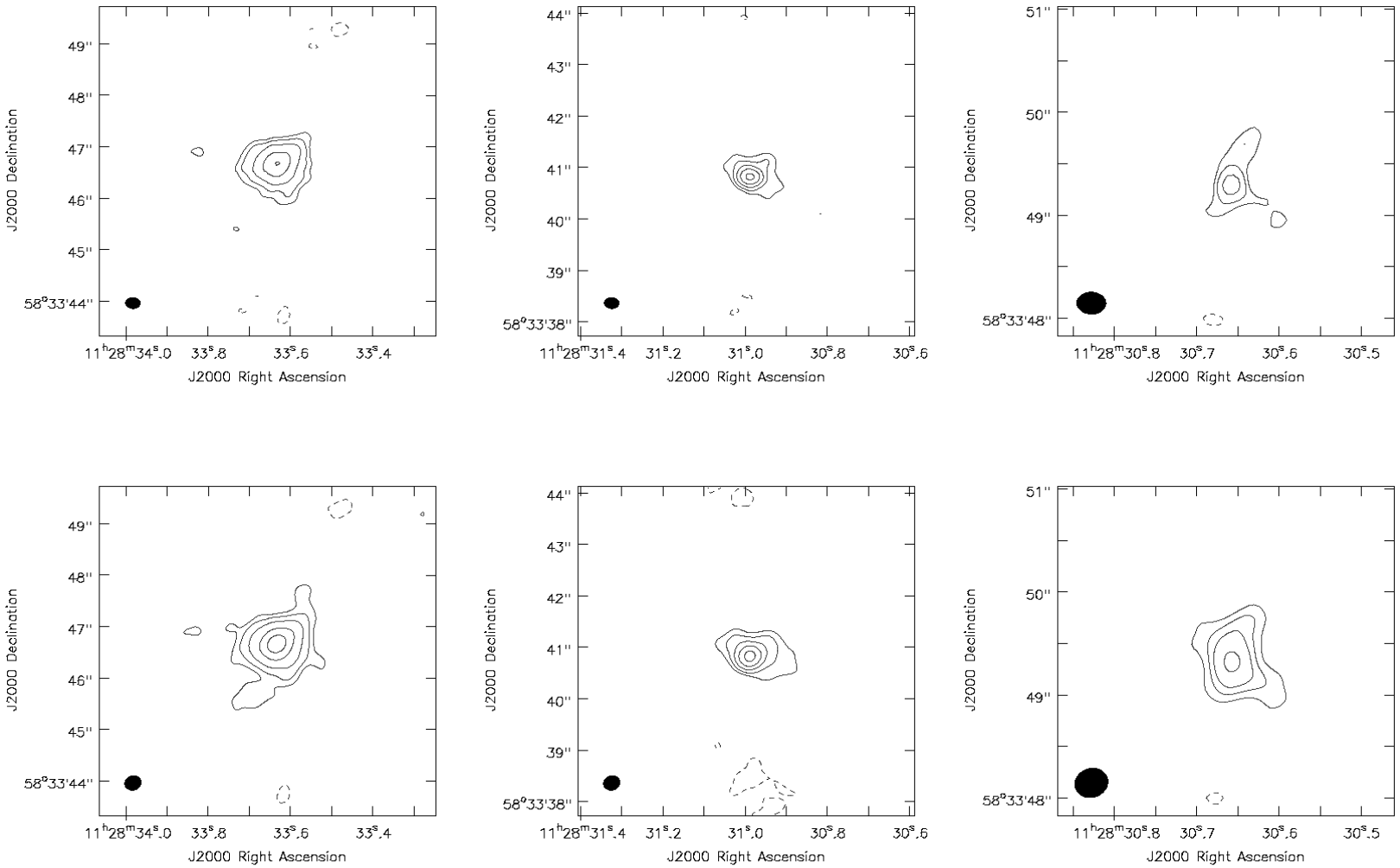

Figure B.2: e-MERLIN 1.5-GHz images of the unidentified LeMMINGs galaxies. This page: NGC 3690, all three sources going from left to right: the AGN in Arp 299a, the TDE in Arp 299b and the background source north of Arp 299b. The *Top* image shows the full resolution image and the *Bottom* image shows the lower resolution image

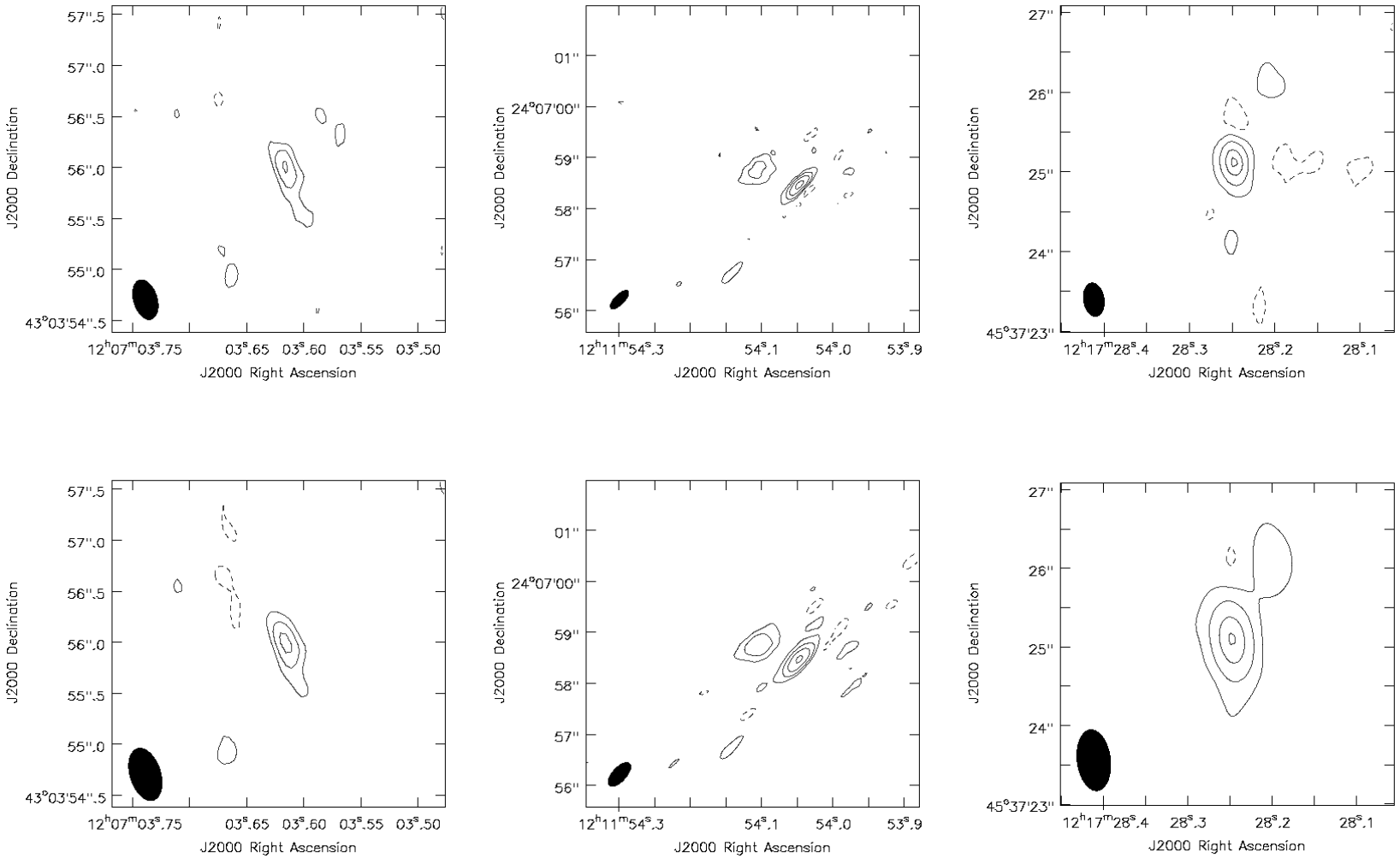

Figure B.2: e-MERLIN 1.5-GHz images of the unidentified LeMMINGs galaxies. This page: NGC 4111 (left), NGC 4162 (centre), NGC 4242 (right). The *Top* image shows the full resolution image and the *Bottom* image shows the lower resolution image

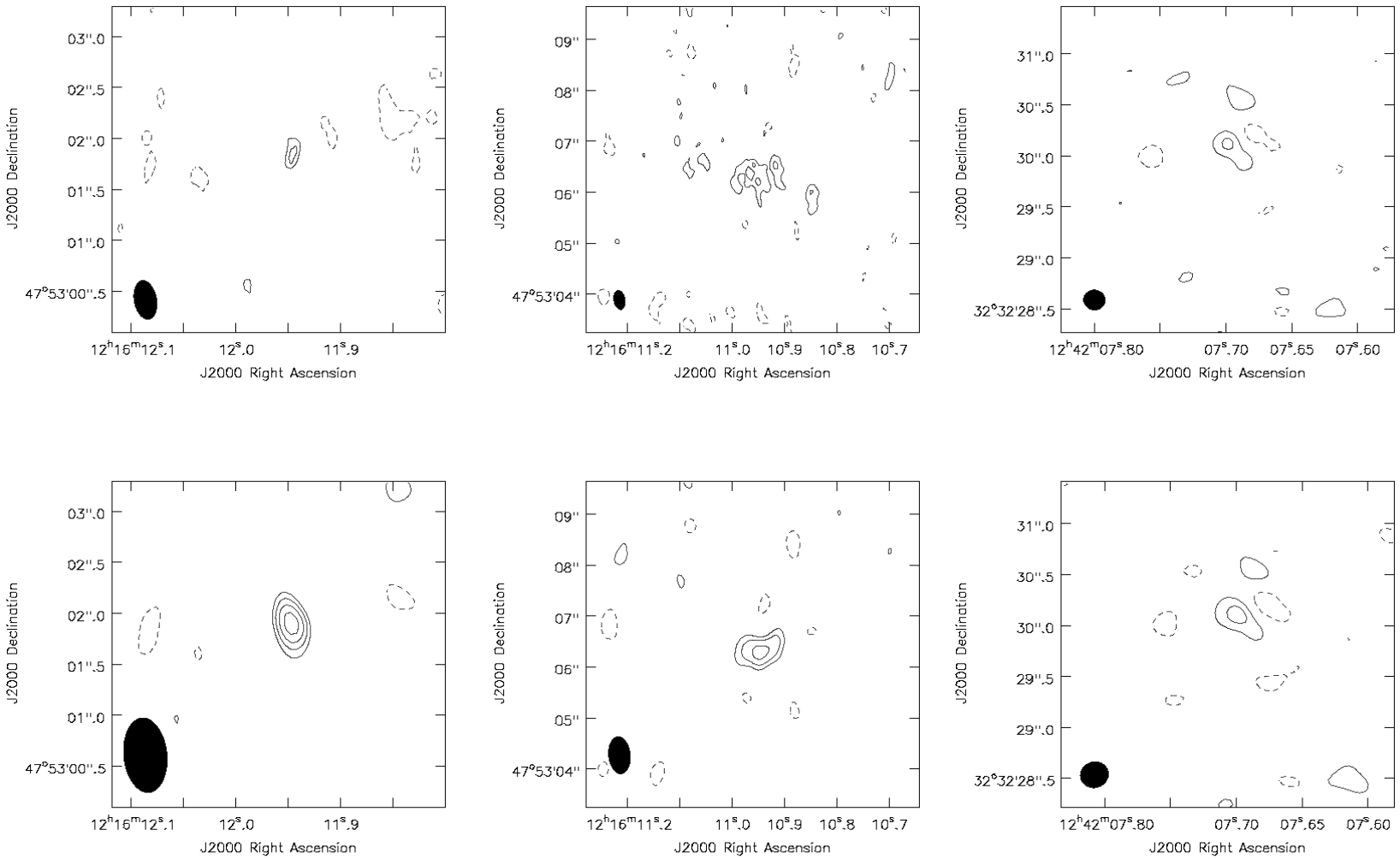

Figure B.2: e-MERLIN 1.5-GHz images of the unidentified LeMMINGs galaxies. This page: NGC 4220 (left and centre), NGC 4631 (right). The *Top* image shows the full resolution image and the *Bottom* image shows the lower resolution image

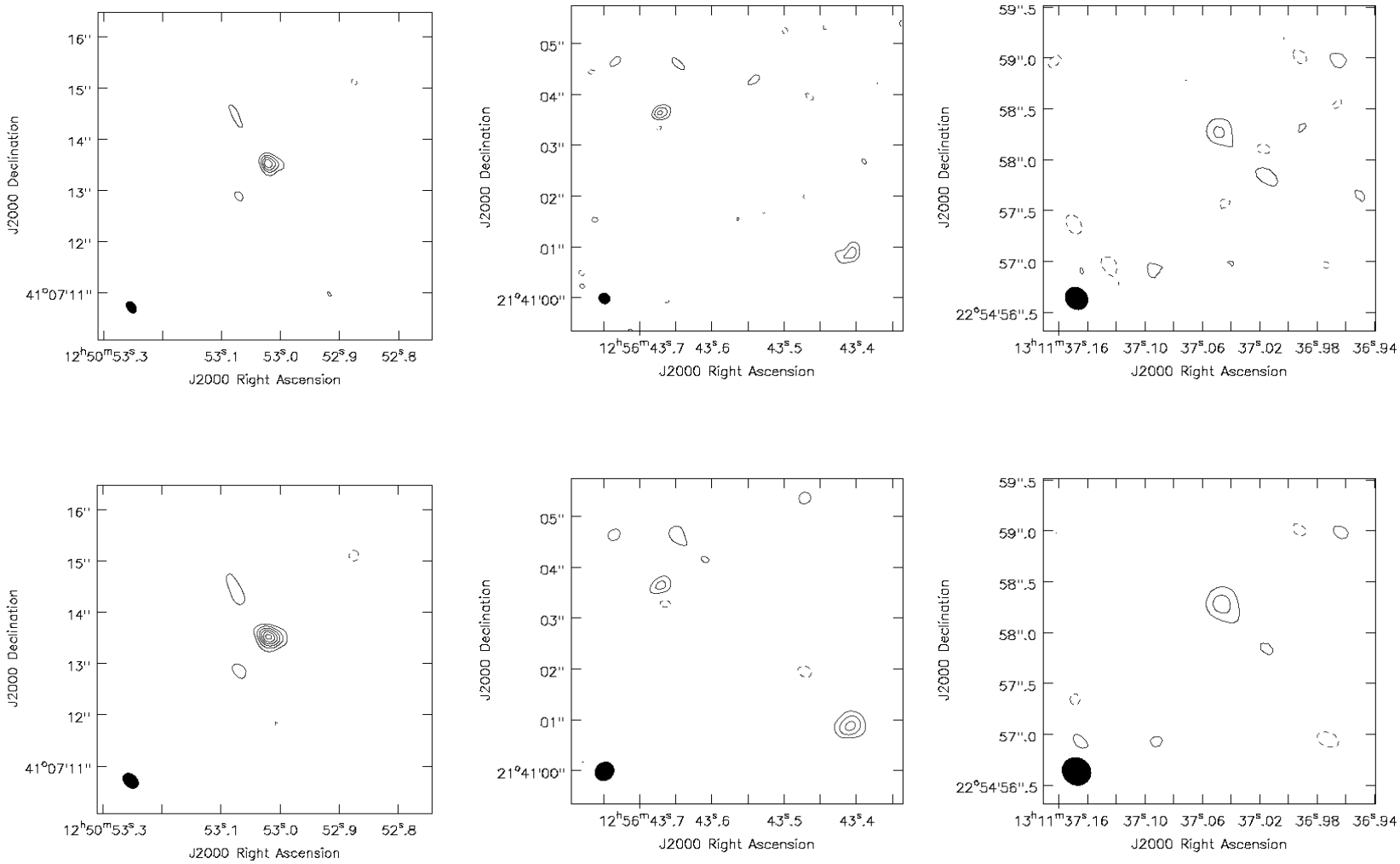

Figure B.2: e-MERLIN 1.5-GHz images of the unidentified LeMMINGs galaxies. This page: NGC 4736 (left), NGC 4826 (centre), NGC 5012 (right). The *Top* image shows the full resolution image and the *Bottom* image shows the lower resolution image

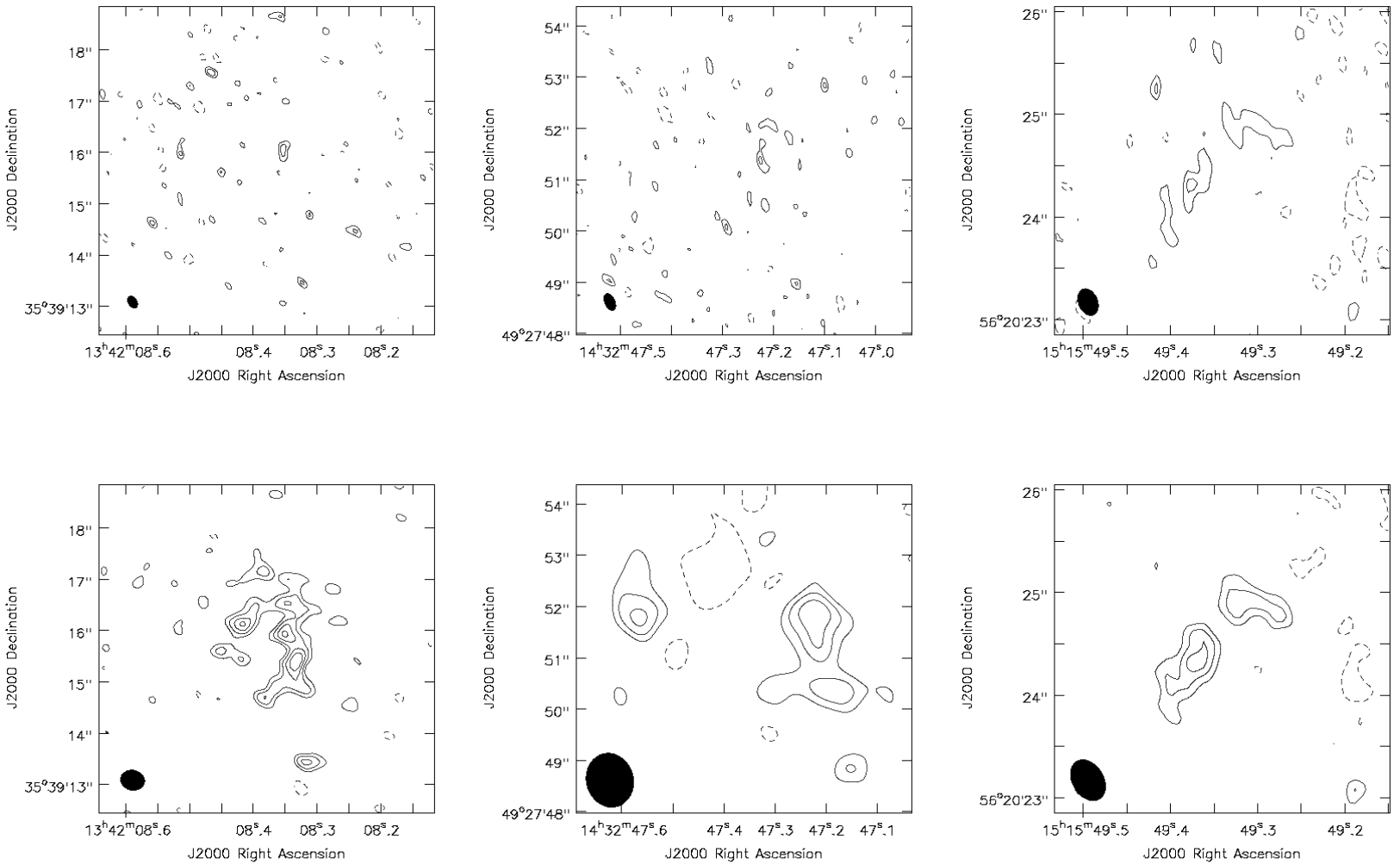

Figure B.2: e-MERLIN 1.5-GHz images of the unidentified LeMMINGs galaxies. This page: NGC 5273 (left), NGC 5676 (centre), NGC 5907 (right). The *Top* image shows the full resolution image and the *Bottom* image shows the lower resolution image

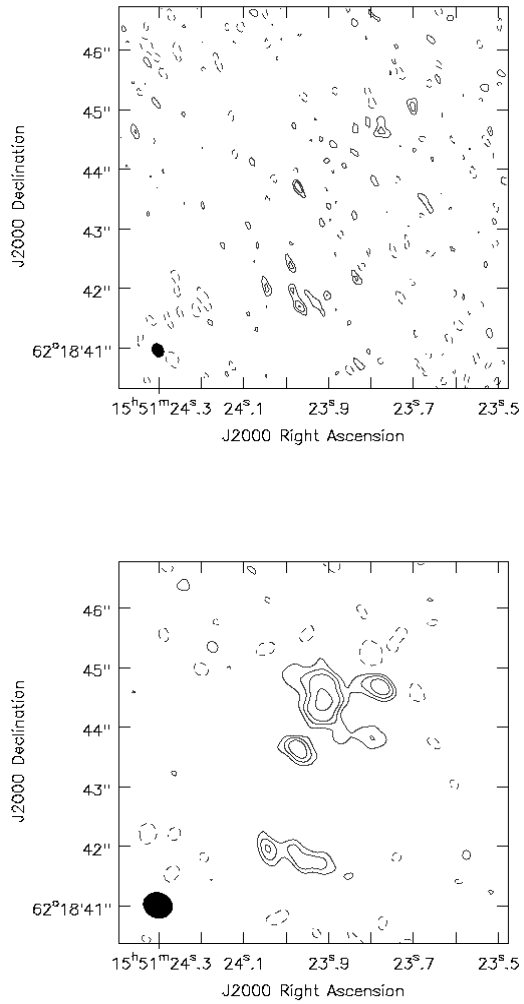

Figure B.2: e-MERLIN 1.5-GHz images of the unidentified LeMMINGs galaxies. This page: NGC 6015 (centre). The *Top* image shows the full resolution image and the *Bottom* image shows the lower resolution image

B.3 LeMMINGs Radio and Optical Properties

Table B.1: The radio and optical properties of the LeMMINGS 'shallow' sample.

Name	Data Quality	Data Format	Beam $'' \times ''$	PA deg.	rms mJy/beam	det.	morph.	σ km s^{-1}	log(M_{BH}) $M_\odot$	L_{core} erg s^{-1}	L_{tot} erg s^{-1}	$L_{[OIII]}$ erg s^{-1}	log(L_{bol}/L_{Edd})
(1)	(2)	(3)	(4)	(5)	(6)	(7)	(8)	(9)	(10)	(11)	(12)	(13)	(14)
NGC 7817	++	AIPS	0.21×0.13	33.4	82	U		66.7	6.21	<35.64	–	39.29	−1.51
IC 10	++	AIPS	0.21×0.11	88.2	89	U		35.5	5.11	<32.91	–	37.13	−2.57
NGC 147	++	AIPS	0.24×0.14	-63.2	73	I	A	22	4.28	32.39	32.92	[a]	–
NGC 185	++	AIPS	0.17×0.14	-84.3	82	U		19.9	4.10	<32.33	–	34.63	−4.06
NGC 205	++	AIPS	0.20×0.13	79.8	86	U		23.3	4.34*	<32.36	–	[a]	–
NGC 221	++	AIPS	0.36×0.15	-34.7	82	U		72.1	6.36*	<32.33	–	[a]	–
NGC 224	++	AIPS	0.19×0.14	-71.4	79	U		169.8	7.84	<32.32	–	[a]	–
NGC 266	+	AIPS	0.48×0.31	-40.0	95	I	A	229.6	8.37	36.94	37.02	39.43	−3.53
NGC 278	++	AIPS	0.29×0.14	-55.2	50	I	A	47.6	5.62	34.81	35.83	37.47	−2.74
NGC 315	+	AIPS	0.12×0.12	45.0	5500	I	A	303.7	8.92*	39.58	39.61	39.43	−4.02
NGC 404	+	AIPS	0.43×0.26	-46.8	61	U		40	5.65*	<33.28	–	37.16	−3.08
NGC 410	+	AIPS	0.52×0.32	-46.85	140	I	A	299.7	8.84	37.26	37.53	<39.32	<-4.11
NGC 507	+	AIPS	0.46×0.35	-67.8	180	I	A	307.7	8.88	36.86	37.07	–	–
NGC 598	+	AIPS	0.32×0.13	12.1	103	U		21	4.20	<32.43	–	<34.63[a]	<-4.16
IC 1727	+	AIPS	0.48×0.17	-8.8	98	U		136.8	7.47	<34.55	–	37.34	−4.72
NGC 672	+	AIPS	0.50×0.23	-16.3	118	U		<64.3	<6.15	<34.55	–	37.66	−3.08
NGC 697	+	AIPS	0.43×0.13	13.7	95	U		75	6.42	<35.95	–	37.86	−3.15
NGC 777	m	AIPS	0.23×0.15	7.6	77	I	A	324.1	8.97	36.77	36.98	38.38[b]	−5.18
NGC 783	-	Unobs	-	-	-	-	-	101.4	6.94	-	-	38.81	−2.69
NGC 784	+	AIPS	0.48×0.22	-29.3	131	U		35.5	5.11	<34.19	–	37.68[c]	−2.02
NGC 812	m	AIPS	0.21×0.16	-76.5	79	U		120.9	7.25	<36.70	–	38.68	−3.16
NGC 818	m	AIPS	0.21×0.17	54.9	72	U		151.3	7.64	<36.14	–	38.46	−3.77

Continued on Next Page

Table B.1 – Continued

Name	Data Quality	Data Format	Beam $'' \times ''$	PA deg.	rms mJy/beam	det.	morph.	σ km s^{-1}	log(M_{BH}) $M_\odot$	L_{core} erg s^{-1}	L_{tot} erg s^{-1}	$L_{[OIII]}$ erg s^{-1}	log(L_{bol}/L_{Edd})
(1)	(2)	(3)	(4)	(5)	(6)	(7)	(8)	(9)	(10)	(11)	(12)	(13)	(14)
NGC 841	m	AIPS	0.21×0.18	50.3	81	U		159.2	7.73	<36.19	–	38.74[d]	−3.58
NGC 890	m	AIPS	0.22×0.18	42.1	75	U		210.9	8.22	<36.06	–	–	–
NGC 891	m	AIPS	0.20×0.17	65.6	64	unI		73.1	6.37	<34.65	–	36.29[c,e]	−4.66
NGC 925	m	AIPS	0.22×0.18	42.7	75	U		71.9	6.34	<34.55	–	37.21	−3.72
NGC 959	m	AIPS	0.20×0.15	43.4	81	U		43.6	5.47	<34.65	–	37.40	−2.66
NGC 972	m	AIPS	0.24×0.17	37.2	69	I	B	102.8	6.97	35.31	36.06	38.64	−2.92
IC 239	-	Unobs	-	-	-	-	-	92.3	6.78	-	-	36.93	−4.41
NGC 1003	-	Unobs	-	-	-	-	-	-	-	-	-	37.23[f]	–
NGC 1023	-	Unobs	-	-	-	-	-	204.5	7.62*	-	-	–	–
NGC 1058	-	Unobs	-	-	-	-	-	31	4.88	-	-	35.95[f]	−3.49
NGC 1156	-	Unobs	-	-	-	-	-	35.9	5.13	-	-	39.15	−0.54
NGC 1161	-	Unobs	-	-	-	-	-	258.4	8.58	-	-	38.13	−5.01
NGC 1167	-	Unobs	-	-	-	-	-	216.9	8.27	-	-	40.17	−2.66
NGC 1169	-	Unobs	-	-	-	-	-	181.3	7.96	-	-	38.58	−3.93
NGC 1186	-	Unobs	-	-	-	-	-	119.8	7.24	-	-	38.95	−2.84
NGC 1275	-	Unobs	-	-	-	-	-	258.9	8.98*	-	-	41.61	−1.53
IC 342	+	CASA	0.33×0.20	-57.3	150	I	E	74.3	6.41*	34.42	34.46	35.99[e]	−4.97
IC 356	+	CASA	0.33×0.20	-54.5	113	I	A	156.6	7.70	35.59	35.46	37.57	−4.69
NGC 1569	+	CASA	0.33×0.20	-50.1	110	unI		44	5.49	<33.18	–	36.49[e]	−3.55
NGC 1560	+	CASA	0.26×0.17	-53.7	95	I	A	33.9	5.03	33.75	33.82	37.38	−2.21
NGC 1961	+	CASA	0.29×0.18	-35.8	126	I	A	241.3	8.29*	37.15	37.24	39.11	−3.90
NGC 2146	+	CASA	0.27×0.18	-23.7	134	I	B	126.8	7.33	36.34	36.39	38.36	−3.53

Continued on Next Page

Table B.1 – Continued

Name	Data Quality	Data Format	Beam $'' \times ''$	PA deg.	rms mJy/beam	det.	morph.	σ km s^{-1}	log(M_{BH}) $M_\odot$	L_{core} erg s^{-1}	L_{tot} erg s^{-1}	$L_{[OIII]}$ erg s^{-1}	log(L_{bol}/L_{Edd})
(1)	(2)	(3)	(4)	(5)	(6)	(7)	(8)	(9)	(10)	(11)	(12)	(13)	(14)
NGC 2273	++	AIPS	0.20×0.16	48.1	930	I	E	148.9	6.93*	36.64	37.98	40.43	−1.77
NGC 2342	++	AIPS	0.18×0.18	0.0	65	I	E	147.3	7.60	36.55	37.64	39.71	−2.48
UGC 3714	+	CASA	0.30×0.19	-17.9	89	U		104	6.99	<34.10	–	38.49	−3.06
NGC 2268	+	AIPS	0.20×0.20	0.0	91	U		143.3	7.55	<35.76	–	39.27	−2.87
UGC 3828	++	AIPS	0.19×0.16	50.3	71	I	C	73.9	6.39	36.07	36.63	38.84	−2.14
NGC 2336	+	CASA	0.27×0.20	-11.7	90	U		116.2	7.18	<35.75	–	38.20	−3.54
NGC 2276	+	AIPS	0.20×0.20	0.0	110	U		83.5	6.61	<35.90	–	38.17	−3.03
NGC 2366	+	CASA	0.32×0.19	-11.8	96	U		–	–	<33.64	–	–	–
IC 467	+	CASA	0.26×0.19	-15.7	90	U		64.2	6.15	<35.56	–	37.15	−3.55
NGC 2300	+	AIPS	0.20×0.20	0.0	60	I	A	261.1	8.60	36.23	36.41	–	–
NGC 2403	+	CASA	0.15×0.15	84.9	97	U		68.4	6.26	<33.96	–	35.91	−4.9
UGC 4028	+	AIPS	0.20×0.20	0.0	100	I	C	80.5	6.54	36.22	36.70	38.88	−2.25
NGC 2500	++	AIPS	0.20×0.16	48.6	93	U		47.1	5.61	<34.71	–	36.55[c]	−3.65
NGC 2543	++	AIPS	0.24×0.16	35.0	77	U		112.4	7.12	<35.65	–	38.55	−3.16
NGC 2537	++	AIPS	0.21×0.16	40.3	92	U		63	6.11	<34.60	–	38.72	−1.98
NGC 2541	++	AIPS	0.20×0.16	48.9	87	U		53	5.81	<34.72	–	36.80[f]	−3.60
NGC 2549	+	CASA	0.16×0.15	-85.9	95	U		142.6	7.16*	<35.26	–	–	–
NGC 2639	++	AIPS	0.20×0.19	68.0	130	I	C	179.3	7.94	37.61	38.50	39.60[g]	−2.93
NGC 2634	+	AIPS	0.20×0.20	0.0	82	I	A	181.1	7.96	35.81	35.87	–	–
NGC 2683	-	Unobs	-	-	-	-	-	130.2	7.38			37.06	−4.88
NGC 2681	++	AIPS	0.19×0.16	51.8	920	I	C	109.1	7.07	35.51	35.99	38.37[h]	−3.29
IC 520	+	AIPS	0.20×0.20	0.0	102	U		138.1	7.48	<36.08	–	39.03	−3.04

Continued on Next Page

Table B.1 – Continued

Name	Data Quality	Data Format	Beam $'' \times ''$	PA deg.	rms mJy/beam	det.	morph.	σ km s^{-1}	log(M_{BH}) $M_\odot$	L_{core} erg s^{-1}	L_{tot} erg s^{-1}	$L_{[OIII]}$ erg s^{-1}	log(L_{bol}/L_{Edd})
(1)	(2)	(3)	(4)	(5)	(6)	(7)	(8)	(9)	(10)	(11)	(12)	(13)	(14)
NGC 2685	-	Unobs	-	-	-	-	-	93.8	6.59*			38.41	−2.96
NGC 2655	+	AIPS	0.20×0.20	0.0	120	I	E	159.8	7.74	37.59	37.97	39.44	−2.89
NGC 2750	-	Unobs	-	-	-	-	-	52.4	5.79			39.20	−1.15
NGC 2742	+	CASA	0.15×0.15	-55.9	88	U		65.6	6.18	<35.37	–	37.73	−3.01
NGC 2715	+	AIPS	0.20×0.20	0.0	93	U		84.6	6.63	<35.32	–	37.79	−3.43
NGC 2770	-	Unobs	-	-	-	-	-	81	6.55			37.56	−3.55
NGC 2768	+	CASA	0.15×0.15	88.6	122	I	A	181.8	7.96	37.10	37.16	38.61	−3.91
NGC 2776	-	Unobs	-	-	-	-	-	47.7	5.63			38.32	−1.87
NGC 2748	+	AIPS	0.20×0.20	0.0	90	U		83	7.65*	<35.44	–	37.83	−4.41
NGC 2782	-	Unobs	-	-	-	-	-	183.1	7.98			39.99	−2.54
NGC 2787	+	CASA	0.16×0.15	-53.8	141	I	B	202	7.61*	36.28	36.37	38.37	−4.33
NGC 2832	-	Unobs	-	-	-	-	-	334	9.03			39.05	−4.53
NGC 2841	++	AIPS	0.19×0.16	52.7	74	I	C	222	8.31	34.84	35.47	38.19[c]	−4.63
NGC 2859	-	Unobs	-	-	-	-	-	188.2	8.02			38.57	−4.01
NGC 2903	-	Unobs	-	-	-	-	-	89	7.06*			37.35	−3.93
NGC 2950	+	CASA	0.15×0.14	53.5	100	U		163	7.77	<35.47	–	–	–
NGC 2964	-	Unobs	-	-	-	-	-	109.4	6.73*			38.71	−2.93
NGC 2977	+	CASA	0.16×0.15	-58.3	91	U		104.5	7.00	<35.91	–	38.20	−3.36
NGC 2976	++	CASA	0.24×0.19	48.5	74	U		36	5.14	<33.24	–	36.58	−3.11
NGC 3003	-	Unobs	-	-	-	-	-	44.1	5.49			38.90	−1.14
NGC 2985	+	CASA	0.16×0.15	-54.9	91	I	A	140.8	7.52	35.78	35.88	38.69	−3.38
NGC 3031	++	CASA	0.25×0.21	61.5	178	I	A	161.6	7.81*	35.50	35.53	37.72	−4.59

Continued on Next Page

Table B.1 – Continued

Name	Data Quality	Data Format	Beam $'' \times ''$	PA deg.	rms mJy/beam	det.	morph.	σ km s^{-1}	log(M_{BH}) $M_\odot$	L_{core} erg s^{-1}	L_{tot} erg s^{-1}	$L_{[OIII]}$ erg s^{-1}	log(L_{bol}/L_{Edd})
(1)	(2)	(3)	(4)	(5)	(6)	(7)	(8)	(9)	(10)	(11)	(12)	(13)	(14)
NGC 3027	+	CASA	0.16×0.15	-52.1	95	U		25.6	4.54	<35.29	–	37.69	−1.40
NGC 3034	++	CASA	0.24×0.20	60.1	131	unI		129.5	7.37	<34.28	–	38.33[e]	−3.60
NGC 3043	+	CASA	0.15×0.14	72.4	99	U		51.9	5.77	<35.91	–	38.08	−2.25
NGC 3073	+	CASA	0.29×0.25	66.6	91	U		35.6	5.12	<35.26	–	38.02	−1.66
NGC 3077	++	CASA	0.24×0.19	46.6	88	I	B	32.4	4.95	33.68	34.00	37.15	−2.36
NGC 3079	+	CASA	0.30×0.25	64.7	257	I	A	182.3	6.40*	37.28	37.49	37.67[f]	−3.28
NGC 3162	++	CASA	0.20×0.19	-64.6	58	U		89	6.72	<35.19	–	38.04	−3.23
NGC 3147	++	CASA	0.23×0.19	51.9	99	I	A	219.8	8.29	37.36	37.49	39.54	−3.32
NGC 3185	++	CASA	0.20×0.20	-60.5	58	U		79.3	6.51	35.15	–	39.44	−1.63
NGC 3190	++	CASA	0.20×0.20	-81.0	77	U		188.1	8.02	<35.32	–	38.71	−3.87
NGC 3184	++	AIPS	0.34×0.28	32.4	108	U		43.3	5.46	<34.64	–	37.31	−2.74
NGC 3193	++	CASA	0.21×0.20	-84.5	59	U		194.3	8.08	<35.23	–	38.42	−4.21
NGC 3198	++	AIPS	0.20×0.20	0.00	114	I	A	46.1	5.57	35.02	35.19	36.97	−3.19
NGC 3245	++	CASA	0.19×0.17	39.1	70	I	E	209.9	8.38*	35.71	36.14	38.70	−4.07
IC 2574	++	CASA	0.24×0.19	46.3	74	U		33.9	5.03	<33.67	–	35.55	−4.03
NGC 3254	++	CASA	0.19×0.17	42.4	62	U		117.8	7.21	<35.27	–	38.60	−3.16
NGC 3294	++	AIPS	0.37×0.29	-56.4	119	U		56.4	5.92	<35.66	–	38.33	−2.18
NGC 3301	++	CASA	0.21×0.18	26.8	74	I	A	132.3	7.41	35.67	35.86	38.30	−3.66
NGC 3310	+	CASA	0.27×0.23	69.4	101	I	A	84	6.70*	34.56	36.23	36.15[f]	−2.82
NGC 3319	++	AIPS	0.45×0.33	-49.0	98	U		87.4	6.68	<34.84	–	37.07[i]	−4.20
NGC 3344	++	CASA	0.20×0.17	32.1	64	U		73.6	6.38	<34.11	–	38.24	−2.70
NGC 3359	++	CASA	0.25×0.20	40.6	81	U		55.3	5.89	<35.21	–	37.36	−3.08

Continued on Next Page

Table B.1 – Continued

Name	Data Quality	Data Format	Beam $'' \times ''$	PA deg.	rms mJy/beam	det.	morph.	σ km s^{-1}	log(M_{BH}) $M_\odot$	L_{core} erg s^{-1}	L_{tot} erg s^{-1}	$L_{[OIII]}$ erg s^{-1}	log(L_{bol}/L_{Edd})
(1)	(2)	(3)	(4)	(5)	(6)	(7)	(8)	(9)	(10)	(11)	(12)	(13)	(14)
NGC 3348	++	CASA	0.23×0.19	56.7	78	I	C	236.4	8.42	36.58	36.59	–	–
NGC 3395	-	Unobs	-	-	-	-	-	96.5	6.86			37.93[f]	−3.48
NGC 3414	++	AIPS	0.22×0.14	20.60	60	I	C	236.8	8.40*	36.20	36.33	39.06[q]	−3.95
NGC 3430	++	AIPS	0.20×0.20	0.0	100	I	E	50.4	5.72	35.74	36.19	37.74	−2.57
NGC 3432	++	AIPS	0.47×0.28	-16.7	110	I	A	37	5.18	34.82	34.83	38.00	−1.77
NGC 3448	+	CASA	0.27×0.22	71.5	86	U		50.7	5.7	<35.44	–	39.48	−0.81
NGC 3486	++	CASA	0.19×0.17	41.0	62	U		65	6.17	<34.26	–	37.93	−2.79
NGC 3504	++	CASA	0.22×0.19	-77.4	57	I	A	119.3	7.23	37.30	37.64	39.88	−1.90
NGC 3516	++	CASA	0.23×0.19	50.9	97	I	A	181	7.96	36.84	36.93	40.80	−1.71
NGC 3556	+	CASA	0.26×0.23	73.1	78	U		79.4	6.52	<34.92	–	37.62	−3.46
NGC 3583	++	AIPS	0.17×0.13	-59.4	79	U		131.7	7.40	<35.69	–	38.26	−3.73
NGC 3600	++	AIPS	0.17×0.14	-55.8	77	U		49.8	5.70	<34.66	–	38.21	−2.08
NGC 3610	+	CASA	0.26×0.22	82.7	79	U		161.2	7.75	<35.56	–	–	–
NGC 3613	+	CASA	0.26×0.22	80.9	84	U		220.1	8.30	<35.69	–	–	–
NGC 3631	++	CASA	0.19×0.15	-45.2	67	U		43.9	5.48	<36.23	–	37.53	−2.51
NGC 3646	m	CASA	0.62×0.24	-39.2	55	U		153.1	7.66	<35.98	–	39.15	−3.07
NGC 3642	+	CASA	0.27×0.22	79.9	87	U		85	7.42*	<35.55	–	38.96	−2.23
NGC 3652	++	AIPS	0.20×0.20	0.0	89	U		56.4	5.92	<35.73	–	38.51	−2.00
NGC 3665	++	AIPS	0.20×0.20	0.0	61	I	B	236.8	8.76*	36.85	37.67	38.28	−4.73
NGC 3675	++	AIPS	0.17×0.14	-63.3	80	I	A	108	7.26*	34.96	35.17	37.79[e]	−3.85
NGC 3690	+	CASA	0.28×0.21	88.2	184	unI	A	143.9	7.56			39.98	−2.12
UGC 6484	+	CASA	0.26×0.23	78.4	82	U		61.1	6.06	<35.67	–	37.47	−3.19

Continued on Next Page

Table B.1 – Continued

Name	Data Quality	Data Format	Beam $'' \times ''$	PA deg.	rms mJy/beam	det.	morph.	σ km s^{-1}	log(M_{BH}) $M_\odot$	L_{core} erg s^{-1}	L_{tot} erg s^{-1}	$L_{[OIII]}$ erg s^{-1}	log(L_{bol}/L_{Edd})
(1)	(2)	(3)	(4)	(5)	(6)	(7)	(8)	(9)	(10)	(11)	(12)	(13)	(14)
NGC 3718	-	Unobs	-	-	-	-	-	158.1	7.72			36.52[f]	−5.75
NGC 3726	++	AIPS	0.18×0.13	-59.0	63	U		41.5	5.38	<34.99	–	37.80	−2.17
NGC 3729	-	Unobs	-	-	-	-	-	76.2	6.45			36.60[f]	−4.40
NGC 3738	-	Unobs	-	-	-	-	-	49.1	5.68			37.77	−2.46
NGC 3735	++	CASA	0.23×0.19	52.4	79	I	A	140.6	7.51	36.24	36.45	39.88	−2.19
NGC 3756	-	Unobs	-	-	-	-	-	47.6	5.62			37.04	−3.14
NGC 3780	-	Unobs	-	-	-	-	-	89.8	6.73			37.84	−3.45
NGC 3813	+	CASA	0.20×0.19	38.8	90	U		72.1	6.35	<35.53	–	37.59	−3.31
NGC 3838	-	Unobs	-	-	-	-	-	141.4	7.52			–	–
NGC 3877	++	AIPS	0.18×0.13	-54.7	66	U		86.1	6.66	<36.47	–	37.86	−3.39
NGC 3884	m	CASA	0.41×0.41	0.0	167	I	A	208.3	8.20	37.63	37.58	38.71	−2.56
NGC 3893	++	AIPS	0.18×0.13	-59.4	58	U		85.3	6.64	<34.96	–	37.44	−3.79
NGC 3900	m	CASA	0.50×0.17	-41.7	91	U		139.2	7.50	<35.63	–	38.35	−3.70
NGC 3898	-	Unobs	-	-	-	-	-	206.5	8.19			38.52	−4.03
NGC 3917	++	CASA	0.19×0.15	-44.1	70	U		38	5.23	<35.04	–	36.90	−2.89
NGC 3938	++	AIPS	0.19×0.14	-54.2	74	I	A	29.1	4.76	35.16	35.49	37.61[e,j]	−1.74
NGC 3941	+	CASA	0.20×0.19	41.1	90	I	A	133	7.42	35.46	35.70	38.52	−3.45
NGC 3945	++	CASA	0.17×0.14	33.5	75	I	D	191.5	6.94*	35.77	35.77	38.39	−4.24
NGC 3949	++	AIPS	0.18×0.13	-56.5	71	U		82	6.57	<35.05	–	37.44	−3.72
NGC 3953	++	CASA	0.19×0.15	-43.8	76	U		116	7.33*	<35.07	–	37.90	−3.84
NGC 3963	-	Unobs	-	-	-	-	-	40.9	5.36			38.09	−1.83
NGC 3982	-	Unobs	-	-	-	-	-	73	6.95*			39.83	−1.09

Continued on Next Page

Table B.1 – Continued

Name	Data Quality	Data Format	Beam $'' \times ''$	PA deg.	rms mJy/beam	det.	morph.	σ km s^{-1}	log(M_{BH}) $M_\odot$	L_{core} erg s^{-1}	L_{tot} erg s^{-1}	$L_{[OIII]}$ erg s^{-1}	log(L_{bol}/L_{Edd})
(1)	(2)	(3)	(4)	(5)	(6)	(7)	(8)	(9)	(10)	(11)	(12)	(13)	(14)
NGC 3992	++	CASA	0.19×0.15	-43.9	76	U		148.4	7.51*	<35.07	–	37.10[l]	−4.97
NGC 3998	-	Unobs	-	-	-	-	-	304.6	8.93*			39.56[p]	−3.92
NGC 4013	++	AIPS	0.19×0.14	-56.4	70	unI		86.5	6.67	<35.10	–	37.36[e,i]	−3.90
NGC 4026	++	CASA	0.20×0.15	-40.6	83	U		177.2	8.26*	<35.11	–	–	–
NGC 4036	++	CASA	0.17×0.14	34.7	74	I	C	215.1	7.89*	35.99	36.17	39.16	−3.65
NGC 4041	++	CASA	0.17×0.15	30.1	71	I	B	95	6.83	35.59	35.93	38.24	−3.15
NGC 4051	++	AIPS	0.18×0.14	-58.6	71	I	C	89	6.10*	35.29	36.92	40.17[e,k]	−1.14
NGC 4062	+	CASA	0.21×0.19	52.6	85	U		93.2	6.80	<34.63	–	36.51	−4.84
NGC 4088	++	CASA	0.20×0.14	-44.0	81	I	A	77	6.79*	35.22	35.41	37.48	−3.54
NGC 4096	++	CASA	0.20×0.16	-49.5	81	U		79.5	6.52	<34.53	–	36.15	−4.93
NGC 4100	++	CASA	0.20×0.16	-55.9	83	I	A	75.5	6.43	35.36	35.72	37.43	−3.03
NGC 4102	++	CASA	0.20×0.15	-42.9	91	I	E	174.3	7.89	35.91	36.65	38.63	−3.35
NGC 4111	+	CASA	0.40×0.23	16.1	102	I	A	147.9	7.60	35.34	35.87	38.65	−3.51
NGC 4125	++	CASA	0.17×0.13	34.5	73	U		226.7	8.35	<35.36	–	38.71	−4.19
NGC 4136	+	CASA	0.22×0.20	30.1	90	U		38.4	5.25	<34.66	–	37.39	−2.41
NGC 4138	+	CASA	0.43×0.24	17.5	125	U		120.9	7.25	<35.29	–	38.75	−3.06
NGC 4143	+	CASA	0.42×0.20	9.7	117	I	B	204.9	7.92*	36.14	36.03	38.81	−3.92
NGC 4144	+	CASA	0.39×0.20	-176.5	115	U		64.3	6.15	<34.02	–	36.26	−4.44
NGC 4145	++	CASA	0.26×0.17	39.3	66	U		–	–	<35.18	–	37.29	2.73
NGC 4151	++	CASA	0.26×0.16	38.8	201	I	C	97	7.81*	37.75	37.81	41.74	0.32
NGC 4150	+	CASA	0.22×0.20	34.3	82	U		87	5.94*	<34.62	–	35.83[f]	−4.67
NGC 4157	++	CASA	0.19×0.16	-51.2	76	U		90.1	6.74	<35.07	–	37.17[e]	−4.12

Continued on Next Page

Table B.1 – Continued

Name	Data Quality	Data Format	Beam $'' \times ''$	PA deg.	rms mJy/beam	det.	morph.	σ km s^{-1}	log(M_{BH}) $M_\odot$	L_{core} erg s^{-1}	L_{tot} erg s^{-1}	$L_{[OIII]}$ erg s^{-1}	log(L_{bol}/L_{Edd})
(1)	(2)	(3)	(4)	(5)	(6)	(7)	(8)	(9)	(10)	(11)	(12)	(13)	(14)
NGC 4162	m	CASA	0.57×0.18	-39.3	120	UnI		76.1	6.44	<35.98	–	38.44	−2.56
NGC 4169	+	CASA	0.22×0.20	37.1	88	U		183	7.97	<36.08	–	38.99	−3.55
NGC 4183	+	CASA	0.41×0.19	10.4	96	U		34.4	5.06	<35.17	–	37.90	−1.72
NGC 4203	+	CASA	0.22×0.18	54.7	142	I	A	167	7.82*	36.05	36.00	38.28[l]	−4.10
NGC 4214	+	CASA	0.22×0.19	49.9	80	U		51.6	5.76	<33.72	–	38.71	−1.61
NGC 4217	+	CASA	0.46×0.26	8.0	85	I	B	91.3	6.76	35.23	35.68	36.93	−4.39
NGC 4220	+	CASA	0.38×0.21	6.8	83	I	A	105.5	7.01	35.24	35.40	36.19[f]	−-5.38
NGC 4236	++	CASA	0.16×0.12	25.0	71	U		62.8	6.11	<33.27	–	36.24	−4.43
NGC 4244	+	CASA	0.20×0.20	33.7	86	U		36.8	5.17	<33.65	–	36.05	−3.68
NGC 4242	+	CASA	0.42×0.25	8.3	86	UnI		–	–	<34.42	–	35.82	1.26
NGC 4245	m	CASA	0.56×0.18	-38.9	87	U		82.7	7.19*	<34.64	–	37.36	−3.78
NGC 4251	m	CASA	0.57×0.18	-39.5	90	U		119.4	7.23	<34.66	–	–	–
NGC 4258	+	CASA	0.42×0.25	-176.3	87	I	A	148	7.58*	34.94	35.00	38.76	−3.40
NGC 4274	m	CASA	0.55×0.19	-39.3	83	U		96.6	6.86	<34.62	–	37.59	−3.83
NGC 4278	m	CASA	0.32×0.32	-38.8	110	I	A	261	7.96*	37.61	37.64	38.88	−4.27
NGC 4291	++	CASA	0.16×0.12	26.5	68	U		285.3	8.99*	<35.50	–	–	–
NGC 4314	m	CASA	0.52×0.20	-38.7	89	U		117	6.91*	<34.65	–	37.75	−4.00
NGC 4346	+	CASA	0.39×0.22	6.1	123	U		146.5	7.59	<35.28	–	37.83	−4.31
NGC 4369	-	Unobs	-	-	-	-	-	71.6	6.34			38.83	−2.06
NGC 4395	+	CASA	0.22×0.18	56.2	110	I	A	30	4.82	34.17	34.29	38.35	−1.03
NGC 4414	m	CASA	0.49×0.19	-39.8	94	U		117	7.19	<34.67	–	36.46[f]	−5.29
NGC 4449	++	CASA	0.24×0.17	35.8	79	U		17.8	3.91	<33.58	–	38.28	−0.18

Continued on Next Page

Table B.1 – Continued

Name	Data Quality	Data Format	Beam $'' \times ''$	PA deg.	rms mJy/beam	det.	morph.	σ km s^{-1}	log(M_{BH}) $M_\odot$	L_{core} erg s^{-1}	L_{tot} erg s^{-1}	$L_{[OIII]}$ erg s^{-1}	log(L_{bol}/L_{Edd})
(1)	(2)	(3)	(4)	(5)	(6)	(7)	(8)	(9)	(10)	(11)	(12)	(13)	(14)
NGC 4448	++	CASA	0.23×0.20	53.5	58	U		119.8	7.24	<34.47	–	37.34	−4.45
NGC 4460	++	CASA	0.25×0.17	34.6	65	U		39.8	5.31	<34.36	–	38.09	−1.78
NGC 4485	-	Unobs	-	-	-	-	-	52.2	5.78			36.95	−3.39
NGC 4490	++	CASA	0.25×0.16	32.8	66	U		45.1	5.5	<34.33	–	37.12[e]	−-2.96
NGC 4494	++	CASA	0.23×0.20	49.3	67	I	A	145	7.57	34.69	34.76	37.35	−4.77
NGC 4559	++	CASA	0.22×0.20	52.5	61	U		49.2	5.68	<34.49	–	37.01	−3.23
NGC 4565	++	CASA	0.22×0.20	44.4	68	I	A	136	7.46	35.20	35.20	38.22	−3.80
NGC 4589	++	CASA	0.16×0.12	30.9	85	I	C	224.3	8.33	37.45	37.46	38.78	−4.11
NGC 4605	++	CASA	0.17×0.13	46.3	69	U		26.1	4.57	<33.77	–	36.63	−2.50
NGC 4618	++	CASA	0.25×0.16	33.2	66	U		54.6	5.86	<34.28	–	37.97	−2.45
NGC 4648	++	CASA	0.16×0.12	29.8	70	U		224.5	8.33	<35.45	–	–	–
NGC 4631	++	CASA	0.21×0.20	77.9	77	UnI		71.9	6.34	<34.30	–	37.12	−3.78
NGC 4656	++	CASA	0.21×0.20	70.1	74	U		70.4	6.31	<34.32	–	37.93	−2.93
NGC 4750	++	CASA	0.16×0.12	27.2	61	I	A	136	7.46	35.84	36.13	38.76	−3.26
NGC 4725	++	CASA	0.21×0.20	70.9	73	U		140	7.51	<34.78	–	38.51	−3.55
NGC 4736	++	CASA	0.25×0.16	33.1	91	I	E	112	7	34.81	35.10	37.33[e]	−4.35
NGC 4800	++	CASA	0.24×0.16	33.9	66	U		111	7.02[*]	<34.21	–	37.62	−4.04
NGC 4793	++	CASA	0.21×0.19	73.5	74	U		26.6	4.61	<35.78	–	38.36	−0.81
NGC 4826	++	CASA	0.22×0.20	46.4	74	I	A	96	6.85	33.88	34.29	37.92[p]	−3.48
NGC 4914	++	AIPS	0.21×0.19	28.4	71	U		224.7	8.33	<36.17	–	–	–
NGC 5005	++	AIPS	0.21×0.19	27.0	93	I	D	172	8.27[*]	36.29	37.54	39.41	−3.05
NGC 5012	++	CASA	0.23×0.20	42.5	79	UnI		141.4	7.52	<35.84	–	38.58	−3.50

Continued on Next Page

Table B.1 – Continued

Name	Data Quality	Data Format	Beam $'' \times ''$	PA deg.	rms mJy/beam	det.	morph.	σ km s^{-1}	log(M_{BH}) $M_\odot$	L_{core} erg s^{-1}	L_{tot} erg s^{-1}	$L_{[OIII]}$ erg s^{-1}	log(L_{bol}/L_{Edd})
(1)	(2)	(3)	(4)	(5)	(6)	(7)	(8)	(9)	(10)	(11)	(12)	(13)	(14)
NGC 5033	-	Unobs	-	-	-	-	-	151	7.64			39.34	−2.85
NGC 5055	++	AIPS	0.20×0.19	68.1	84	U		117	8.92*	<34.37	–	37.44[l]	−6.07
NGC 5112	++	AIPS	0.20×0.19	34.4	104	U		<60.8	<6.05	<35.40	–	37.42	−3.22
NGC 5204	m	CASA	0.34×0.21	29.8	112	U		39.9	5.32	<34.14	–	36.58	−3.29
NGC 5194	++	AIPS	0.18×0.17	82.7	101	I	D	96	6.85	35.06	36.14	38.91	−2.53
NGC 5195	++	AIPS	0.20×0.18	82.8	80	I	C	124.8	7.31	34.90	35.59	37.84[e]	−4.06
NGC 5273	m	AIPS	0.25×0.17	32.4	57	unI		71	6.61*	<35.31	–	39.82	−1.38
NGC 5297	++	AIPS	0.20×0.19	85.9	102	U		61.3	6.07	<35.89	–	38.22[m]	−2.44
NGC 5308	m	CASA	0.31×0.21	34.2	116	U		249	8.51	<35.82	–	–	–
NGC 5322	m	CASA	0.31×0.22	33.0	117	I	C	232.2	8.39	36.96	36.98	38.20	−4.74
NGC 5353	m	AIPS	0.18×0.14	29.6	180	I	A	286.4	8.76	37.63	37.66	38.73	−4.62
NGC 5354	-	Unobs	-	-	-	-	-	217.4	8.28			38.61	−4.22
NGC 5371	m	AIPS	0.20×0.15	35.0	80	U		179.8	7.94	<35.79	–	39.03	−3.50
NGC 5377	++	AIPS	0.20×0.18	-86.5	91	I	C	169.7	7.84	35.71	36.35	38.81	−3.62
NGC 5383	m	AIPS	0.20×0.15	35.0	85	U		96.5	6.86	<35.82	–	38.07	−3.38
NGC 5395	m	AIPS	0.23×0.15	30.8	77	U		145.5	7.57	<35.96	–	38.66[i]	−3.50
NGC 5448	++	AIPS	0.19×0.18	-86.6	86	I	C	124.5	7.30	35.73	36.46	38.55	−3.34
NGC 5457	m	CASA	0.36×0.18	19.9	120	U		23.6	6.41*	<34.28	–	36.99	−1.96
NGC 5473	m	CASA	0.36×0.18	20.1	112	U		220.5	8.30	<35.82	–	–	–
NGC 5474	m	CASA	0.39×0.20	15.7	124	U		29	4.76	<34.38	–	37.35	−1.97
NGC 5485	m	CASA	0.30×0.30	27.1	178	I	A	207.5	8.19	36.34	36.27	38.31	−4.44
NGC 5523	m	AIPS	0.26×0.14	26.5	79	U		30.1	4.82	<35.29	–	37.25	−2.16

Continued on Next Page

Table B.1 – Continued

Name	Data Quality	Data Format	Beam $'' \times ''$	PA deg.	rms mJy/beam	det.	morph.	σ km s^{-1}	log(M_{BH}) $M_\odot$	L_{core} erg s^{-1}	L_{tot} erg s^{-1}	$L_{[OIII]}$ erg s^{-1}	log(L_{bol}/L_{Edd})
(1)	(2)	(3)	(4)	(5)	(6)	(7)	(8)	(9)	(10)	(11)	(12)	(13)	(14)
NGC 5548	-	Unobs	-	-	-	-	-	291	7.70*			41.60	−1.74
NGC 5557	m	AIPS	0.24×0.15	30.6	90	U		295.3	8.81	<35.94	–	–	–
NGC 5585	m	CASA	0.38×0.18	28.5	128	U		42	5.41	<34.53	–	37.68	−2.28
NGC 5631	m	CASA	0.38×0.18	31.0	135	U		168.1	7.83	<35.89	–	38.76	−3.62
NGC 5660	++	AIPS	0.29×0.17	13.4	77	U		60.7	6.05	<35.76	–	38.10	−2.54
NGC 5656	m	AIPS	0.23×0.15	29.6	86	U		116.7	7.19	<35.92	–	$37.99^{i,n}$	−3.79
NGC 5678	m	CASA	0.39×0.18	34.3	125	U		132.8	7.42	<35.93	–	38.27	−3.70
NGC 5676	++	AIPS	0.35×0.19	23.2	85	unI		116.7	7.19	<35.74	–	37.96	−3.82
NGC 5866	++	AIPS	0.18×0.18	0.0	97	I	D	169.1	7.84	36.50	36.76	37.50	−4.93
NGC 5879	++	AIPS	0.18×0.18	0.0	71	I	A	73.9	6.62*	35.27	35.39	37.89	−3.09
NGC 5905	++	AIPS	0.28×0.19	18.6	75	U		174.6	7.89	<35.90	–	39.03	−3.45
NGC 5907	++	AIPS	0.28×0.19	18.6	90	unI		120.2	7.24	<35.03	–	36.88	−4.94
NGC 5982	++	AIPS	0.26×0.19	20.2	78	U		239.4	8.44	<35.80	–	<38.55	<-4.48
NGC 5985	++	AIPS	0.26×0.19	22.1	57	I	D	157.6	7.71	35.76	36.30	38.76	−3.54
NGC 6015	++	AIPS	0.23×0.18	25.4	67	unI		43.5	5.47	<35.04	–	37.18	−2.88
NGC 6140	++	AIPS	0.23×0.18	23.2	75	U		49.4	5.69	<35.15	–	37.52	−2.76
NGC 6217	+	CASA	0.17×0.14	72.4	102	I	A	70.3	6.30	35.64	36.13	39.25	−1.61
NGC 6207	+	CASA	0.22×0.17	76.6	95	U		92.1	6.78	<35.19	–	38.30	−3.03
NGC 6236	+	CASA	0.18×0.15	65.9	85	U		46.1	5.57	<35.40	–	37.93	−2.19
NGC 6340	+	CASA	0.17×0.15	69.8	84	I	A	143.9	7.56	35.53	35.98	38.31	−3.80
NGC 6412	+	CASA	0.17×0.14	80.9	84	U		49.9	5.71	<35.40	–	37.59	−2.68
NGC 6503	+	CASA	0.18×0.14	71.4	100	U		46	6.30*	<34.30	–	–	–

Continued on Next Page

Table B.1 – Continued

Name	Data Quality	Data Format	Beam $'' \times ''$	PA deg.	rms mJy/beam	det.	morph.	σ km s^{-1}	log(M_{BH}) $M_\odot$	L_{core} erg s^{-1}	L_{tot} erg s^{-1}	$L_{[OIII]}$ erg s^{-1}	log(L_{bol}/L_{Edd})
(1)	(2)	(3)	(4)	(5)	(6)	(7)	(8)	(9)	(10)	(11)	(12)	(13)	(14)
NGC 6482	+	CASA	0.19×0.16	51.3	112	U		310.4	8.90	<36.22	–	–	–
NGC 6643	+	CASA	0.17×0.15	82.9	84	U		95.4	6.84	<35.47	–	37.52	−3.88
NGC 6654	+	CASA	0.17×0.15	81.0	87	U		172.2	7.87	<35.61	–	–	–
NGC 6689	+	CASA	0.18×0.14	80.2	89	U		26	4.57	<34.85	–	37.17	−1.95
NGC 6702	m	AIPS	0.19×0.16	56.7	74	I	C	173.6	7.88	36.19	36.85	–	–
NGC 6703	m	AIPS	0.19×0.15	53.6	66	I	A	179.9	7.95	35.78	35.91	38.46	−4.08
NGC 6946	m	AIPS	0.19×0.15	-84.1	57	I	E	55.8	5.90	34.43	35.73	37.03	−3.46
NGC 6951	m	AIPS	0.20×0.15	88.5	55	I	C	127.8	6.93*	35.42	36.02	38.69^o	−3.25
NGC 7080	-	Unobs	-	-	-	-	-	95.3	6.84			–	–
NGC 7217	m	AIPS	0.18×0.18	0.0	75	I	C	141.4	7.52	35.09	35.87	38.31	−3.80
NGC 7331	m	AIPS	0.15×0.15	0.0	81	U		137.2	8.02*	<34.95	–	38.30^p	−3.76
NGC 7332	m	AIPS	0.15×0.15	0.0	86	U		124.1	7.08*	<35.18	–	–	–
NGC 7457	m	AIPS	0.15×0.15	0.0	92	U		69.4	6.95*	<34.88	–	–	–
NGC 7640	m	AIPS	0.15×0.15	0.0	81	U		48.1	5.64	<34.51	–	36.84	−3.39
NGC 7741	++	AIPS	0.19×0.14	36.0	70	U		29.4	4.78	<34.7	–	37.91	−1.46
NGC 7798	++	AIPS	0.20×0.14	35.9	31	I	C	75.1	6.42	35.64	36.54	38.64	−2.37

Column description: (1) source name; (2) raw data and calibration quality: '++' = very good; '+' = good; 'm' = moderate; '-' = Unobserved/Not good enough data; (3) Data processed and calibrated in AIPS or CASA, or Unobserved (4) restoring beam size in arcsec in full resolution map; (5) PA angle (degree) in full resolution map; (6) rms in full resolution map in μJy beam^{-1}; (7) radio detection status of the source: 'I' = detected and core identified; 'U' = undetected; 'unI' = detected but core unidentified; (8) radio morphological class for detected sources: A = core/core–jet; B = one-sided jet; C = triple; D = doubled-lobed ; E = jet+complex; (9) stellar velocity dispersion

(km s^{-1}) from Ho et al. (2009); (10) logarithm of the SMBH mass ($M_{\odot}$) determined based on stellar velocity dispersions (Tremaine et al., 2002) and the galaxies marked with * have direct BH mass measurements from van den Bosch (2016); (11)-(12) radio core and total luminosities (erg s^{-1}); (13) [O III] luminosities from Ho et al. (1997a); (14) Eddington ratio, i.e. ratio between the bolometric and Eddington luminosity.
Notes: letters correspond to following publications: *a* Lira et al. (2007); *b* Annibali et al. (2010); *c* Gavazzi et al. (2013); *d* Cid Fernandes et al. (2005); *e* Goulding and Alexander (2009); *f* Moustakas and Kennicutt (2006); *g* Trippe et al. (2010); *h* Cappellari et al. (2001); *i* SDSS; *j* Dale et al. (2006); *k* Balmaverde and Capetti (2014); *l* Balmaverde and Capetti (2013); *m* Rampazzo et al. (1995); *n* Leech et al. (1989); *o* Pérez et al. (2000); *p* Keel (1983), Bower (1992); *q* Falco et al. (1999), Sarzi et al. (2006).

B.4 LeMMINGs Radio Data of Detected Galaxies

Table B.2: Properties of the detected sources.

		Full resolution								Low resolution				
name	comp	$\theta_M \times \theta_m$	PA_d	rms	α(J2000)	δ(J2000)	F_{peak}	F_{tot}	$u-v$	$\theta_M \times \theta_m$	PA_d	rms	F_{peak}	morph/size
		arcsec	deg	mJB			mJB	mJy	kλ	arcsec	deg	mJB	mJB	
NGC 266	core	0.16× <0.26	174.1	0.095	00 49 47.810	32 16 39.83	1.24±0.10	1.31	750	0.20×0.12	159.0	0.10	1.28±0.10	core-jet (A) 1.5″ →480pc
	Tot												1.5±0.1	
NGC 278		0.19× <0.34	109.0	0.050	00 52 04.203	47 33 01.38	0.26±0.06	0.29	750	0.48×0.05	157.3	0.054	2.1±0.05	core (A) + components
	core	0.17× <0.25	62.4	0.050	00 52 04.368	47 33 02.13	0.26±0.06	0.34	750	0.16× <0.30	146.6	0.054	0.24±0.05	
		0.04× <0.28	74.7	0.050	00 52 0.4527	47 33 02.899	0.18±0.06	0.20	750	0.17× <0.45	159.8	0.054	0.24±0.05	
	Tot												2.7±0.2	
NGC 315	core	0.01×0.08	67.3	5.5	00 57 48.883	30 21 08.82	490±30	503	750	0.10× <0.21	71.0	4.0	331±26	core-jet (A)
	Tot												520±50	
NGC 410	core	0.53×0.11	89.6	0.14	01 10 58.901	33 09 06.98	2.05±0.14	3.62	750	0.55×0.10	93.6	0.16	2.21±0.16	core-jet (A)
	Tot												3.8±0.2	
NGC 507	core	0.24× <0.41	68.4	0.18	01 23 39.863	33 15 23.00	0.93±0.18	1.02	750	0.42×0.24	16.7	0.26	1.01±0.26	core-jet (A)
	Tot												1.5±0.1	
NGC 777		0.17× <0.23	152.6	0.077	02 00 14.894	31 25 46.33	0.36±0.09	0.59	600	0.88× <0.22	163.8	0.081	0.32±0.12	core (A) + components
	core	0.17× <0.14	171.7	0.077	02 00 14.908	31 25 45.84	0.74±0.10	0.84	600	0.16× <0.25	108.9	0.081	0.84±0.12	
	Tot												1.2±0.2	
NGC 972	core	0.06× <0.06	164.2	0.069	02 34 13.34	29 18 40.65	0.25±0.08	0.38	750	0.42×0.26	157.6	0.069	0.26±0.09	one-sided jet (B) 1.7″ →185pc
		<0.24× <0.17	162.2	0.069	02 34 13.35	29 18 40.40	0.30±0.08	0.33	750	0.45×0.29	148.4	0.069	0.35±0.09	
		0.40×0.27	152.5	0.069	02 34 13.56	29 18 34.99	0.38±0.08	1.44	750	0.39×0.26	145.8	0.069	0.55±0.09	
	Tot												1.4±0.2	

Continued on Next Page

Table B.2 – Continued

		Full resolution								Low resolution				
name	comp	$\theta_M \times \theta_m$	PA$_d$	rms	α(J2000)	δ(J2000)	F$_{peak}$	F$_{tot}$	$u-v$	$\theta_M \times \theta_m$	PA$_d$	rms	F$_{peak}$	morph/size
		arcsec	deg	mJB			mJB	mJy	kλ	arcsec	deg	mJB	mJB	
IC 356	core	<0.33× <0.20	0.0	0.113	04 07 46.890	69 48 44.70	0.56±0.04	0.43	300	<0.62× <0.52	0.0	70	0.31±0.03	core (A)
	Tot												0.42±0.06	
NGC 1560	core	<0.20× <0.05	0.0	0.095	04 32 49.008	71 52 59.67	0.35±0.05	0.40	300	0.52× 0.09	47	0.098	0.53±0.04	core (A)
	Tot												0.81±0.08	
NGC 1961	core	0.14×0.08	-35.8	0.126	05 42 04.638	69 22 42.38	2.81±0.16	3.46	300	<0.30× <0.08	0.0	0.080	3.12±0.13	core (A)
	Tot												3.35±0.23	
NGC 2146	core	0.09×0.04	32	0.134	06 18 37.590	78 21 24.25	4.10±0.17	4.61	300	0.19×0.10	135	0.131	4.23±0.17	core + one-sided
		0.56×0.36	152	0.134	06 18 37.771	78 21 23.62	1.75±0.15	8.87	300	0.72×0.42	68.2	0.131	2.52±0.06	jet (B)
	Tot												13.68±0.9	1.0″ →65pc
NGC 2273		0.19×0.06	72.1	0.930	06 50 08.577	60 50 44.55	1.64±0.10	2.26	750			0.12	<3.25	twin jet +
	core	0.25×0.16	169.4	0.930	06 50 08.647	60 50 44.93	2.99±0.10	7.12	750	0.29×0.19	61.9	0.12	4.87±0.13	extended
		0.30×0.11	48.3	0.930	06 50 08.701	60 50 44.94	1.68±0.09	4.17	750			0.12	<4.82	emission (E)
	Tot												66.1±3.0	2.2″ →280pc
NGC 2342				0.065	07 09 18.029	20 38 09.26	<0.41		750	0.53×0.34	164.3	0.068	0.51±0.09	complex (E)
	core	0.17×0.08	151.6	0.065	07 09 18.069	20 38 09.59	0.41±0.08	0.54	750	0.53×0.28	172.4	0.068	<5.8	2.5″ →865pc
		0.26×0.03	133.5	0.065	07 09 18.080	20 38 09.28	0.30±0.08	0.52	750	0.63×0.34	135.2	0.068	0.59±0.09	
	Tot												5.0±0.2	
UGC 3828	lobeN	0.22× <0.12	73.2	0.071	07 24 35.726	57 58 03.47	0.32±0.10	0.51	750	0.32×0.19	93.3	0.078	0.49±0.11	double jet (C)
	lobeS	0.16× <0.29	1.4	0.071	07 24 35.733	57 58 02.83	0.29±0.10	0.35	750	0.23× <0.38	178.1	0.078	0.38±0.12	1″ →238pc
	core	0.13×0.23	156.69	0.071	07 24 35.7372	57 58 03.261	0.30±0.10	0.31	750			0.078	<4.8	
	Tot												1.09±0.10	
NGC 2300	core	0.18×0.06	138.2	0.060	07 32 19.945	85 42 32.41	0.99±0.08	1.25	750	0.22×0.09	116.3	0.065	1.21±0.08	core-jet (A) 0.75″ →103pc
	Tot												1.5±0.1	

Continued on Next Page

Table B.2 – Continued

		Full resolution								Low resolution				
name	comp	$\theta_M \times \theta_m$	PA$_d$	rms	α(J2000)	δ(J2000)	F$_{peak}$	F$_{tot}$	u–v	$\theta_M \times \theta_m$	PA$_d$	rms	F$_{peak}$	morph/size
		arcsec	deg	mJB			mJB	mJy	kλ	arcsec	deg	mJB	mJB	
UGC 4028	lobeW			0.10	07 50 49.810	74 21 29.15	<0.30		750	0.21×0.26	53.2	0.072	0.44±0.08	twin jets (C)
	core	>0.18× >14	155	0.10	07 50 49.931	74 21 29.13	0.33±0.10	0.33	750	0.12× <0.26	127.8	0.072	0.23±0.08	1.5″ →406pc
	lobeW			0.10	07 50 50.0749	74 21 28.77	<0.30		750	0.46×0.24	55.96	0.072	0.43±0.08	
	Tot												1.0±0.1	
NGC 2639		0.32×0.25	121.1	0.13	08 43 38.034	50 12 20.07	17.5±0.1	25.2	750	0.38×0.26	102.1	0.29	24.5±0.3	twin jets (C)
	core	0.42×0.08	108.4	0.13	08 43 38.080	50 12 19.99	12.6±0.1	17.8	750	0.42×0.18	105.0	0.29	17.6±0.3	1.5″ →340pc
		0.29×0.20	141.8	0.13	08 43 38.151	50 12 19.82	3.40±0.1	8.3	750			0.29	<11.4	
	Tot												98±10	
NGC 2634	core	0.25× <0.3	38.8	0.082	08 48 25.095	73 58 02.15	0.39±0.11	0.59	750	0.10× <0.4	31.4	0.081	0.41±0.12	core (A)
	Tot												0.45±0.1	
NGC 2681	jetN			0.92	08 53 32.693	51 18 49.78	<3.7		750	0.68×0.18	141.1	0.099	0.57±0.12	twin jets (C)
	core	0.17×0.07	56.7	0.92	08 53 32.718	51 18 49.15	1.03±0.10	1.49	750	0.20×0.16	175.2	0.099	1.22±0.12	1.5″ →70pc
		0.20×0.16	169.5	0.92	08 53 32.733	51 18 48.77	0.473±0.10	0.90	750	0.41×0.28	161.6	0.099	0.54±0.12	
	Tot												3.1±0.2	
NGC 2655	core	0.17×0.07	40.8	0.12	08 55 37.950	78 13 23.63	36.81±0.13	51.5	750	0.37×0.10	38.2	0.16	53.04±0.17	S-shaped jet + components (E)
		0.17×0.10	148.0	0.12	08 55 38.09	78 13 22.96	1.62±0.13	2.35	750	0.45×0.31	170.1	0.16	2.09±0.17	2″ →204pc
	Tot												88±2	
NGC 2768	core	0.06×0.05	144	0.133	09 11 37.414	60 02 14.86	12.63±0.39	14.26±0.74	500	0.12×0.05	152	0.160	13.13±0.34	core (A)
	Tot												15.16±0.64	
NGC 2787	core	0.13×0.05	147	0.163	09 19 18.599	69 12 11.64	6.11±0.41	8.14±0.88	750	<0.16× <0.04	0.0	0.133	6.64±0.26	
		<0.16× <0.15	0.0	0.163	09 19 18.703	69 12 11.95	1.19±0.22	4.50±1.10	750	<0.20× <0.18	0.0	0.133	1.24±0.25	one-side jet (B)
	Tot												10.30±0.87	1.2″ →60pc

Continued on Next Page

Table B.2 – Continued

		Full resolution								Low resolution				
name	comp	$\theta_M \times \theta_m$	PA$_d$	rms	α(J2000)	δ(J2000)	F$_{peak}$	F$_{tot}$	$u-v$	$\theta_M \times \theta_m$	PA$_d$	rms	F$_{peak}$	morph/size
		arcsec	deg	mJB			mJB	mJy	kλ	arcsec	deg	mJB	mJB	
NGC 2841	lobeN	0.45× <0.12	50.4	0.074	09 22 02.611	50 58 36.39	0.40±0.09	0.51	600	0.36× <0.40	46.9	0.081	0.51±0.11	twin jets (C)
	core	0.19× <0.12	52.7	0.074	09 22 02.652	50 58 36.03	0.27±0.09	0.31	600	0.36× <0.45	166.9	0.081	0.31±0.11	1.5″ →68pc
	lobeS	0.02× <0.19	52.7	0.074	09 22 02.676	50 58 35.65	0.31±0.09	0.63	600	0.23× <0.51	114.2	0.081	0.52±0.11	
	Tot												1.15±0.15	
NGC 2985	core	0.15×0.03	71	0.091	09 50 22.184	72 16 44.21	0.63±0.10	0.89±0.22	500	0.28×0.04	83.8	0.103	0.74±0.07	core (A)
	Tot												1.18±0.16	
NGC 3031	core	0.08×0.04	13	0.46	09 55 33.174	69 03 55.04	90.3±2.4	97.9	500	0.06×<0.04	21	0.35	93.6±1.0	core(A)
	Tot												95.8±1.8	
NGC 3077	core	0.28×0.17	96	0.088	10 03 19.097	68 44 02.37	0.60±0.05	1.27	500	0.28×0.19	128	0.090	0.70±0.06	
		0.25×0.16	156	0.088	10 03 19.122	68 44 02.04	0.29±0.03	0.57	500	0.40×0.10	18	0.090	0.39±0.03	one-sided jet (B)
	Tot												1.14±0.32	1.0″ →10pc
NGC 3079	core	0.25×0.17	165	0.630	10 01 57.806	55 40 47.26	25.2±1.1	41.1±2.7	750	0.27×0.24	171	0.537	26.3±46.6	
		0.60×0.26	15.2	0.630	10 01 57.798	55 40 46.32	4.91±0.42	16.7±1.8	750	0.56×0.23	4.5	0.537	3.72±0.25	core(A)
	Tot												74.60±2.97	
NGC 3147	core	0.21×0.06	16	0.099	10 16 53.651	+73 24 02.68	7.71±0.28	10.38±0.60	750	0.22×0.08	15	0.129	7.90±0.28	core(A)
	Tot												10.65±0.59	
NGC 3198	core	0.15× <0.08	125.9	0.114	10 19 54.931	45 32 59.50	0.50±0.12	0.52	750	0.45× <0.05	137.7	0.81	0.49±0.09	core+ component
				0.114	10 19 54.994	45 32 58.53	<0.33		750	0.47× <0.19	120.2	0.81	0.30±0.09	(A)
	Tot												0.74±0.15	
NGC 3245	core	0.25×0.22	39	0.070	10 27 18.386	+28 30 26.63	0.58±0.05	1.55±0.18	750	0.33×0.23	87	0.073	0.61±0.06	
		0.39×0.14	79	0.070	10 27 18.406	+28 30 26.40	0.30±0.02	0.91±0.06	750	0.41×0.23	91	0.073	0.37±0.02	complex (E)
	Tot												2.11±0.29	1.0″ →100pc

Continued on Next Page

Table B.2 – Continued

		Full resolution								Low resolution				
name	comp	$\theta_M \times \theta_m$	PA$_d$	rms	α(J2000)	δ(J2000)	F$_{peak}$	F$_{tot}$	$u-v$	$\theta_M \times \theta_m$	PA$_d$	rms	F$_{peak}$	morph/size
		arcsec	deg	mJB			mJB	mJy	kλ	arcsec	deg	mJB	mJB	
NGC 3301	core	0.20×0.05	139	0.074	10 36 56.039	21 52 55.51	0.52±0.06	0.80	750	<0.31× <0.08	0.0	0.083	0.52±0.06	core (A)
	Tot												0.75±0.13	
NGC 3310	core	0.47×0.45	138	0.110	10 38 45.857	53 30 12.01	0.59±0.08	2.62±0.43	750	0.50×0.44	16	0.102	0.65±0.08	core (A)
	Tot												2.53±0.38	
NGC 3348	core	<0.10× <0.04	0.0	0.078	10 47 10.032	+72 50 22.67	1.50±0.09	1.51±0.16	750	<0.09× <0.04	0.0	0.08	1.52±0.06	core + lobes (C)
		<0.30× <0.14	0.0	0.078	10 47 09.948	+72 50 22.94	0.32±0.10	0.37±0.19	750	<0.27× <0.24	0.0	0.08	0.34±0.05	
		<0.23× <0.19	0.0	0.078	10 47 10.102	+72 50 22.29	0.30±0.05	0.34±0.10	750	<0.27× <0.24	0.0	0.08	0.33±0.04	
	Tot												1.97±0.26	
NGC 3414	core	0.07× <0.12	162.4	0.060	10 51 16.211	27 58 30.28	1.56±0.10	1.67	750	0.32×0.07	159.7	0.11	1.89±0.13	twin jet (C) 1″ →95pc
	Tot												2.1±0.1	
NGC 3430				0.10	10 52 11.384	32 57 02.11	<0.30		750	0.29× >0.28	113.5	0.069	0.33±0.08	double-lobed/complex (E) 2.2″ →230pc
	core			0.10	10 52 11.403	32 57 01.63	<0.30		750	0.42× >0.29	102.6	0.069	0.43±0.08	
		0.17× <0.13	167.4	0.10	10 52 11.433	32 57 02.32	0.41±0.11	0.42	750	0.64 ×0.59	55.3	0.069	0.42±0.11	
	Tot												1.2±0.2	
NGC 3432	core	>0.38× >0.21	173.4	0.11	10 52 31.012	36 37 08.50	0.60±0.14	0.61	750	>0.53× >0.44	142.7	0.13	0.47±0.14	core (A)
	Tot												0.62±0.15	
NGC 3504	core	0.32×0.13	63	0.057	11 03 11.249	27 58 21.47	15.93±0.31	34.43±0.94	500	0.34×0.13	62.4	0.061	20.79±0.37	core(A)
	Tot												35.75±0.96	
NGC 3516	core	<0.18× <0.06		0.150	11 06 47.465	72 34 07.26	2.55±0.12	3.11±0.24	500	0.18×0.04	25	0.200	2.72±0.16	core + jet on one side (B)
	Tot												3.26±0.32	

Continued on Next Page

Table B.2 – Continued

		Full resolution								Low resolution				
name	comp	$\theta_M \times \theta_m$	PA$_d$	rms	α(J2000)	δ(J2000)	F$_{peak}$	F$_{tot}$	$u-v$	$\theta_M \times \theta_m$	PA$_d$	rms	F$_{peak}$	morph/size
		arcsec	deg	mJB			mJB	mJy	kλ	arcsec	deg	mJB	mJB	
NGC 3665	blobN			0.061	11 24 43.482	38 45 47.89	<5.3		500	1.78×0.82	107.8	0.45	2.27±0.45	extended
	jetN			0.061	11 24 43.592	38 45 46.80	0.71±0.08	1.13	500				<3.5	one-sided jet (B)
	core	0.10×0.01	20.5	0.061	11 24 43.626	38 45 46.31	3.78±0.08	4.25	500	0.44×0.32	167.4	0.45	4.71±0.44	4.2″ →580pc
	Tot												25±3	
NGC 3675	core			0.080	11 26 08.627	43 35 08.91	<0.53		750	0.31 × <0.15	174.5	0.077	0.31±0.08	core + comp (A)
	Tot												0.5±0.1	
NGC 3735	core	0.22×0.11	20	0.079	11 35 57.216	+70 32 07.81	0.57±0.06	0.93±0.15	750	0.29×0.15	47	0.109	0.59±0.06	core(A)
	Tot												1.05±0.15	
NGC 3884	core	<0.41× <0.41	0.0	0.167	11 46 12.181	20 23 29.90	2.81±0.10	2.50±0.17	750	0.51×0.08	144	0.226	2.63±0.23	core (A)
	Tot												3.44±0.52	
NGC 3938	core	<0.15× <0.07	144.6	0.074	11 52 49.393	44 07 14.57	0.28±0.07	0.33	750	0.41×0.08	90.4	0.083	0.32±0.08	core (A)
	Tot												0.6±0.1	
NGC 3941	core	0.25×0.08	94	0.090	11 52 55.368	36 59 11.41	0.45±0.06	0.79±0.17	500	<0.25× <0.24	0.0	0.085	0.54±0.06	core (A)
	Tot												0.66±0.11	
NGC 3945	core	<0.17× <0.14	23	0.075	11 53 13.612	60 40 32.131	0.65±0.08	0.65	300	<0.44× <0.39	24	0.083	0.63±0.08	lobed (D)
	Tot												0.8±0.1	2.5″ →270pc
NGC 4036	core	<0.17× <0.14	34.0	0.074	12 01 26.740	61 53 44.550	0.90±0.08	1.37	500	<0.26× <0.08	0.0	0.079	1.17×0.09	(C) Multi-
	blob W	0.14×0.05	14.8	0.074	12 01 26.478	61 53 44.019	2.41±0.1	3.36	500	0.12×0.03	8.8	0.079	3.06×0.09	components in a
	blob E			0.074	12 01 27.135	61 53 45.375	<0.30		500	0.52×0.22	1.8	0.079	0.60×0.10	line, 4″ →470pc
	Tot												8.01±0.18	
NGC 4041	core	0.23×0.12	18	0.071	12 02 12.253	62 08 14.325	0.42± 0.07	0.93	500	0.63×0.56	158	0.073	0.60×0.07	(B) One-sided jet
		0.20×0.14	85	0.071	12 02 12.279	62 08 13.938	0.31± 0.07	0.69	500	0.62×0.33	114	0.073	0.51×0.07	2″ →210pc
	Tot												3.0±0.2	

Continued on Next Page

Table B.2 – Continued

		Full resolution								Low resolution				
name	comp	$\theta_M \times \theta_m$	PA$_d$	rms	α(J2000)	δ(J2000)	F$_{peak}$	F$_{tot}$	$u-v$	$\theta_M \times \theta_m$	PA$_d$	rms	F$_{peak}$	morph/size
		arcsec	deg	mJB			mJB	mJy	kλ	arcsec	deg	mJB	mJB	
NGC 4051	lobeW	0.28×0.07	132.2	0.071	12 03 09.576	44 31 52.572	0.35±0.07	0.57	750	0.28×0.07	132.2	0.20	8.41±2.1	triple source (C)
	core	0.15×0.11	145.2	0.071	12 03 09.612	44 31 52.69	0.38±0.07	0.63	750	0.47×0.14	175.3	0.20	7.96±2.1	1″ →50pc
	lobeE	0.10×0.06	78.3	0.071	12 03 09.648	44 31 52.85	0.86±0.07	1.08	750	0.29×0.08	144.4	0.20	15.9±2.1	
	Tot												64.5±7.0	
NGC 4088	core	0.20×0.05	113	0.081	12 05 34.155	50 32 20.58	0.32±0.03	0.49±0.07	300	<0.43× <0.32	0.0	0.135	0.47±0.02	core(A)
	Tot												0.57±0.04	
NGC 4100	core	0.32×0.1	101.3	0.067	12 06 08.440	+49 34 56.46	0.44±0.05	1.02±0.16	750	0.32×0.07	111	0.104	0.53±0.07	core(A)
	Tot												0.93±0.18	
NGC 4102	core	0.51×0.32	139	0.091	12 06 23.077	+52 42 39.76	1.55±0.15	8.60±0.95	500	0.51×0.39	158	0.148	2.26±0.19	core + diffuse radio emission (E)
	Tot												68.11±0.56	
NGC 4111	core	0.82×0.39	73	0.102	12 07 03.145	43 03 56.48	0.37±0.07	1.85±0.40	500	0.72×0.45	48	0.110	0.41±0.05	core (A)
	Tot												1.30±0.22	
NGC 4143	core	<0.42× <0.20	0.0	0.117	12 09 36.070	42 32 03.05	2.63±0.13	2.09±0.20	500	<0.55× <0.30	0.0	0.117	2.32±0.14	one-sided jet (B)
		<0.42× <0.20	0.0	0.117	12 09 36.122	42 32 03.20	0.86±0.07	2.09±0.20	500	<0.89× <0.03	0.0	0.117	0.65±0.04	1.3″ →110pc
	Tot												2.57±0.47	
NGC 4151	C1	0.53×0.29	86.9	0.201	12 10 32.426	39 24 20.66	10.48±0.55	51.7	500	0.57×0.30	85.9	0.237	16.77±0.79	two-sided jet ,
	C2	0.37×0.21	50.7	0.201	12 10 32.507	39 24 30.88	20.08±0.73	57.4	500	0.47×0.22	56.0	0.237	29.59±0.14	multiple
	C3	0.22×0.12	73	0.201	12 10 32.542	39 24 21.01	32.5±1.3	55.0	500	0.53×0.12	79.2	0.237	41.12±0.63	components (C)
	core C4	0.10×0.05	75.3	0.201	12 10 32.582	39 24 21.07	75.99±0.58	86.2	500	0.14×0.06	76.2	0.237	81.57±0.34	4.5″ →450pc
	C5	0.37×0.20	63	0.201	12 10 32.654	39 24 21.35	8.67±0.57	24.2	500	0.49×0.25	74.2	0.237	12.11±0.42	
	Tot												302±12.5	
NGC 4203	core	<0.08× <0.04	0.0	0.117	12 15 05.055	33 11 50.39	7.36±0.17	7.65±0.30	500	<0.28× <0.23	0.0	0.123	7.56±0.20	core (A)
	Tot												7.51±0.35	

Continued on Next Page

Table B.2 – Continued

		Full resolution								Low resolution				
name	comp	$\theta_M \times \theta_m$	PA$_d$	rms	α(J2000)	δ(J2000)	F$_{peak}$	F$_{tot}$	$u-v$	$\theta_M \times \theta_m$	PA$_d$	rms	F$_{peak}$	morph/size
		arcsec	deg	mJB			mJB	mJy	kλ	arcsec	deg	mJB	mJB	
NGC 4217		<0.46× <0.26	0.0	0.085	12 15 50.792	47 05 30.75	0.33±0.05	0.80±0.20	300	<0.73× <0.41	0.0	0.110	0.36±0.04	one-sided jet (B)
		1.02×0.50	171	0.085	12 15 50.846	47 05 29.48	<0.26	1.33±0.26	300	1.23×0.29	154	0.110	0.48±0.07	3″ →250pc
	Tot												1.26±0.20	
NGC 4220	core	0.26×0.14	13	0.087	12 16 11.709	47 52 59.02	0.34±0.03	0.49±0.07	300	<0.73× <0.41	0.0	0.101	0.33±0.03	core (A)
	Tot												0.34±0.05	
NGC 4258	core	0.22×0.08	177	0.097	12 18 57.503	47 18 14.35	1.03±0.09	1.23±0.18	750	0.33×0.10	11	0.100	1.06±0.09	core (A)
	Tot												1.37±0.19	
NGC 4278	core	0.32×0.32	0.0	0.548	12 20 06.825	29 16 50.73	239.1±1.8	251±3.1	750	0.38×0.38	0.0	0.587	240.2±1.7	core (A)
	Tot												253.7±3.1	
NGC 4395	core	0.30×0.09	70	0.110	12 25 48.873	33 32 48.72	0.56±0.07	1.07±0.21	500	0.27×0.10	58	0.099	0.69±0.07	core (A)
	Tot												1.05±0.16	
NGC 4494	core	<0.28× <0.20	49	0.067	12 31 24.032	25 46 30.042	0.29±0.07	0.34	750	0.26×0.23	58	0.071	0.34±0.07	core (A)
	Tot												0.49±0.08	
NGC 4565	core	<0.19× <0.23	63	0.068	12 36 20.780	25 59 15.611	0.93±0.07	0.94	500	0.21×0.05	59	0.074	0.99±0.08	core (A)
	Tot												1.2±0.1	
NGC 4589	core	0.16×0.12	37.6	0.085	12 37 24.988	74 11 30.8908	17.51±0.09	18.0	750	<0.07× <0.04	0.0	0.200	17.35±0.06	triple source (C)
	jet-east	0.15×0.09	92.0	0.085	12 37 25 057	74 11 30 8915	2.80±0.20	4.9	750	<0.20× <0.16	0.0	0.200	1.80±0.12	1″ →145pc
	jet-ovest	<0.16× <0.12	30.9	0.085	12 37 24.890	74 11 30.890	1.82±0.13	1.93	750	0.12×0.09	117	0.200	3.39±0.15	
	Tot												24.51±1.59	
NGC 4750	core	0.23×0.05	179	0.061	12 50 07.315	72 52 28.643	0.57±0.06	1.11	500	0.26×0.07	7	0.063	0.80±0.06	core (A)
	Tot												1.2±0.1	

Continued on Next Page

Table B.2 – Continued

		Full resolution								Low resolution				
name	comp	$\theta_M \times \theta_m$	PA$_d$	rms	α(J2000)	δ(J2000)	F$_{peak}$	F$_{tot}$	u–v	$\theta_M \times \theta_m$	PA$_d$	rms	F$_{peak}$	morph/size
		arcsec	deg	mJB			mJB	mJy	kλ	arcsec	deg	mJB	mJB	
NGC 4826	core	0.35×0.15	170	0.074	12:56:43.655	21 40 58.582	0.25±0.07	0.64	300	0.51×0.34	33	0.080	0.67±0.08	core (A)
	Tot												1.54±0.14	
NGC 5005	lobeN			0.093	13 10 55.512	37 03 38.96	<0.24		200	2.41×2.32	153.7	0.34	2.8±0.3	double-lobed jets (D) 26″ →1.7kpc
		0.54×0.28	106.3	0.093	13 10 56.247	37 03 32.87	2.08±0.09	10.6	750			0.090	<8.4	
	core	0.34×0.23	138.3	0.093	13 10 56.260	37 03 32.74	2.37±0.09	7.49	200	0.88×0.41	128.7	0.34	15.2±0.3	
	lobeS			0.093	13 10 57.009	37 03 26.81	<0.29		200	2.20×2.10	123.1	0.34	2.5±0.3	
	Tot												42.3±3.0	
NGC 5194	lobeN			0.101	13 29 52.510	47 11 45.97	<0.34		500			0.078	4.7±0.2^{tot}	double-lobed (D) on 10″ →370pc
	core	0.18×0.09	145.3	0.091	13 29 52.708	47 11 42.80	1.08±0.09	1.74	500	0.50×0.10	170.3	0.078	1.7±0.1	
	lobeS			0.111	13 29 52.819	47 11 38.92	<0.35		500			0.078	5.8±0.2^{tot}	
	Tot												13.1±1.5	
NGC 5195	jetW			0.080	13 29 59.493	47 15 58.07	<0.24		750	0.93×0.59	35.9	0.11	0.33±0.1	twin jet (C) 1″ →37pc
	core	0.21×0.02	55.0	0.080	13 29 59.535	47 15 58.37	0.51±0.09	0.77	750			0.11	<6.3	
	jetE			0.080	13 29 59.539	47 15 58.50	<0.25		750	0.54×0.34	158.5	0.11	0.61±0.1	
	Tot												2.5±0.2	
NGC 5322		0.74×0.22	154	0.117	13 49 15.170	60 11 29.45	<0.302	1.51±0.33	500	0.64×0.28	5.6	0.134	0.52±0.05	two-sided jet, multiple components (C) 8.5″ →1280pc
	core	<0.14× <0.03	0.0	0.117	13 49 15.265	60 11 25.94	5.13±0.12	5.35±0.21	500	0.16×0.07	16	0.134	4.90±0.10	
		<0.31× <0.22	0.0	0.117	13 49 15.279	60 11 25.29	1.15±0.08	1.31±0.16	500	<0.34× <0.16	0.0	0.134	1.26±0.08	
		0.37×0.24	116	0.117	13 49 15.278	60 11 24.30	0.46±0.08	1.14±0.26	500	0.38×0.17	126	0.134	0.45± 0.05	
		0.30×0.24	102	0.117	13 49 15.321	60 11 21.81	0.50±0.06	1.06±0.18	500	0.57×0.33	30	0.134	0.62±0.07	
	Tot												18.1±0.18	

Continued on Next Page

Table B.2 – Continued

		Full resolution								Low resolution				
name	comp	$\theta_M \times \theta_m$	PA$_d$	rms	α(J2000)	δ(J2000)	F$_{peak}$	F$_{tot}$	$u-v$	$\theta_M \times \theta_m$	PA$_d$	rms	F$_{peak}$	morph/size
		arcsec	deg	mJB			mJB	mJy	kλ	arcsec	deg	mJB	mJB	
NGC 5353	core	0.12×0.04	8.4	0.18	13 53 26.682	40 16 58.83	16.5±0.2	21.0	500	0.12×0.07	21.1	0.14	17.6±0.2	core (A)
	Tot												17.9±0.1	
NGC 5377	jetS			0.091	13 56 16.627	47 14 08.52	<5.1		500	0.60×0.21	4.0	0.11	0.53±0.12	twin jets (C)
	core	0.11×0.04	168.2	0.091	13 56 16.631	47 14 09.16	0.30±0.09	0.36	500	0.19× <0.33	57.8	0.11	0.38±0.13	1.8″ →227pc
	jetN			0.091	13 56 16.658	47 14 09.49	<1.0		500	0.50×0.27	156.1	0.11	0.53±0.12	
	Tot												1.3±0.2	
NGC 5448		0.10× <0.21	28.0	0.086	14 02 50.015	49 10 21.89	0.35±0.10	0.50	750	0.19×0.14	21.9	0.082	0.37±0.11	twin jet (C)
	core	0.22×0.05	59.1	0.086	14 02 50.035	49 10 21.75	0.28±0.09	0.45	750	0.59×0.34	137.8	0.082	0.36±0.11	1″ →141pc
		0.18× <0.12	86.1	0.086	14 02 50.057	49 10 21.56	0.39±0.10	0.53	750	0.43× <0.21	98.6	0.082	0.45±0.11	
		0.19×0.10	53.5	0.086	14 02 50.069	49 10 21.34	0.30±0.10	0.40	750	0.69×0.24	172.6	0.082	0.32±0.10	
	Tot												1.5±0.2	
NGC 5485	core	0.30×0.30	0.0	0.178	14 07 11.346	55 00 06.03	1.14±0.13	0.978±0.11	500	0.46×0.34	13.2	0.178	1.11±0.08	core (A)
	Tot												1.02±0.13	
NGC 5866	lobeN			0.097	15 06 29.344	55 45 40.77	<0.32		200	1.01× <0.66	56.0	0.133	0.95±0.19	core+jet, two
	core	0.12×0.07	20.8	0.097	15 06 29.492	55 45 47.66	7.6±0.1	9.3	200	0.44× <0.22	12.3	0.133	10.2±0.2	lobes (D)
	lobeS			0.097	15 06 29.686	55 45 55.49	<0.37		200	1.11× <0.75	163.8	0.133	0.83±0.19	16″ →960pc
	Tot												13.6±0.5	
NGC 5879	core	0.19× <0.14	27.2	0.071	15 09 46.801	57 00 01.58	0.37±0.10	0.51	750	0.21×0.16	142.3	0.068	0.37±0.09	core (A)
	Tot												0.49±0.12	
NGC 5985	lobeN			0.057	15 39 37.031	59 19 55.95	<0.31		380	1.94× <0.21	22.9	0.066	0.22±0.09	double-lobed (D)
	core			0.057	15 39 37.062	59 19 55.09	<0.17		380	0.36×0.32	15.7	0.066	0.21±0.09	4″ →530pc
	lobeS			0.057	15 39 37.130	59 19 53.45	<0.32		380	0.45×0.25	40.8	0.066	0.30±0.09	
	Tot												0.73±0.15	

Continued on Next Page

Table B.2 – Continued

		Full resolution								Low resolution				
name	comp	$\theta_M \times \theta_m$	PA$_d$	rms	α(J2000)	δ(J2000)	F$_{peak}$	F$_{tot}$	u–v	$\theta_M \times \theta_m$	PA$_d$	rms	F$_{peak}$	morph/size
		arcsec	deg	mJB			mJB	mJy	kλ	arcsec	deg	mJB	mJB	
NGC 6217	core	0.26×0.15	121	0.102	16 32 39.267	78 11 53.35	0.45±0.04	1.21±0.12	500	0.27×0.17	117	0.102	0.56±0.04	core (A)
		0.30×0.24	121	0.102	16 32 39.546	78 11 52.46	0.33±0.02	1.29±0.11	500	0.35×0.0.28	1.4	0.102	0.36±0.01	
	Tot												3.82±0.18	
NGC 6340	core	0.21×0.08	89	0.086	17 10 24.827	72 18 15.85	0.39±0.06	0.72±0.17	300	0.54×0.12	163	0.120	0.66±0.06	core (A)
													1.22±0.17	
NGC 6702		0.08× <0.24	19.6	0.074	18 46 57.534	45 42 20.57	0.20±0.08	0.23	600	0.20× <0.57	133.1	0.066	0.27±0.09	twin jet (C)
	core			0.074	18 46 57.564	45 42 20.36	<0.22		600	0.36×0.10	96.6	0.066	0.22±0.09	2″ →656pc
		0.27×0.10	28.5	0.074	18 46 57.626	45 42 20.04	0.30±0.08	0.34	600	0.29×0.56	137.5	0.066	0.42±0.09	
	Tot												1.0±0.1	
NGC 6703	core	0.18×0.04	128.8	0.066	18 47 18.823	45 33 02.34	0.26±0.08	0.42	750	0.30× <0.24	72.7	0.063	0.32±0.08	core+jet (A)
	Tot												0.35±0.09	
NGC 6946		0.04× <0.16	66.4	0.057	20 34 52.172	60 09 14.20	0.37±0.07	0.37	700	0.77×0.39	114.1	0.067	0.48±0.07	jet+complex (E)
		0.38×0.16	133.8	0.057	20 34 52.242	60 09 14.20	0.83±0.08	1.61	700	0.55×0.28	123.1	0.067	1.59±0.08	2.3″ →42pc
		0.24×0.10	0.33	0.057	20 34 52.255	60 09 14.42	0.61±0.07	1.31	700			0.067	<2.57	
		0.21×0.03	56.0	0.057	20 34 52.273	60 09 13.20	0.48±0.07	0.72	700	0.34× <0.50	124.5	0.067	0.63±0.08	
	core	0.09×0.04	12.5	0.057	20 34 52.299	60 09 14.20	0.49±0.07	0.57	700			0.067	<0.35	
		0.17×0.10	12.7	0.057	20 34 52.320	60 09 14.10	0.67±0.07	1.11	700	0.60×0.32	116.0	0.067	1.28±0.08	
	Tot												10.0±0.3	
NGC 6951		0.23×0.11	97.6	0.055	20 37 14.106	66 06 20.31	0.40±0.08	0.66	750	0.05× <0.21	142.6	0.065	0.63±0.09	twin jet (C)
	core	0.06× <0.23	83.3	0.055	20 37 14.118	66 06 20.10	0.25±0.08	0.24	750	0.16× <0.26	136.2	0.065	0.56±0.09	1.6″ →175pc
		0.14×0.06	172.9	0.055	20 37 14.144	66 06 19.76	0.51±0.08	0.73	750	0.09× <0.26	130.6	0.065	0.73±0.09	
	Tot												1.0±0.1	

Continued on Next Page

Table B.2 – Continued

		Full resolution								Low resolution				
name	comp	$\theta_M \times \theta_m$	PA_d	rms	α(J2000)	δ(J2000)	F_{peak}	F_{tot}	$u-v$	$\theta_M \times \theta_m$	PA_d	rms	F_{peak}	morph/size
		arcsec	deg	mJB			mJB	mJy	kλ	arcsec	deg	mJB	mJB	
NGC 7217		0.24×0.11	138.2	0.075	22 07 52.350	31 21 34.44	0.37±0.09	0.72	700	0.19× <0.17	99.0	0.063	0.67±0.08	twin lobes (C)
	core	0.14× <0.11	27.5	0.075	22 07 52.378	31 21 34.03	0.27±0.09	0.28	700			0.063	<1.00	1.5″ →120pc
		0.19×0.12	4.2	0.075	22 07 52.400	31 21 33.64	0.55±0.09	0.79	700	0.21× <0.21	8.9	0.063	0.79±0.08	
	Tot												1.6±0.2	
NGC 7798		0.14×0.12	22.1	0.031	23 59 25.410	20 44 59.38	0.33±0.04	0.53	750	0.29×0.21	2.0	0.058	0.51±0.07	triple source (C)
	core	0.22×0.06	162.2	0.031	23 59 25.444	20 44 59.43	0.23±0.04	0.43	750			0.058	<0.34	1.4″ →240pc
		0.35×0.20	28.1	0.031	23 59 25.494	20 44 59.57	0.23±0.04	0.82	750	0.33×0.27	173.7	0.058	0.36±0.07	
	Tot												1.8±0.1	

Column description: (1) galaxy name; (2) radio component: core, jet, lobe, blob or unidentified component if not labeled (N or S stand for North or South); (3) deconvolved FWHM dimensions (major × minor axes, $\theta_M \times \theta_m$) of the fitted component, determined from an ellitpical Gaussian fit from the full-resolution radio map; (4) PA of the deconvolved component, PA_d from the full-resolution radio map (degree); (5) rms of the radio map close to the specific component from the full-resolution radio map (mJB, mJy beam^{-1}); (6)-(7) radio position in epoch J2000; (8) peak flux density in mJy beam^{-1}, F_{peak} from the full-resolution radio map: this represents the radio core flux density; (9) integrated flux density, F_{tot} in mJy, from the full-resolution radio map; (10) uv-taper scale of the low-resolution radio map in kλ; (11) deconvolved FWHM dimensions (major × minor axes, $\theta_M \times \theta_m$) of the fitted component, determined from an ellitpical Gaussian fit from the low-resolution radio map; (12) PA of the deconvolved component, PA_d, from the low-resolution radio map (degree); (13) rms of the radio map close to the specific component from the low-resolution radio map (mJy beam^{-1}); (14) peak flux density in mJy beam^{-1}, F_{peak} from the low-resolution radio map. For NGC 5194 we give the total integrated flux densities of the radio lobes instead of the peak flux densities. At the bottom of each target the total flux density of the radio source associated with the galaxy is given in mJy, measured from the low-resolution map; (15) radio morphology (A, B, C, D, E) and size in arcsec and pc (see Section 5.3.2).

B.5 LeMMINGs Radio Data of Detected Galaxies with no core radio emission

Table B.3: Properties of the unidentified sources.

		Full resolution								Low resolution				
name	comp	$\theta_M \times \theta_m$	PA_d	rms	α(J2000)	δ(J2000)	F_{peak}	F_{tot}	$u-v$	$\theta_M \times \theta_m$	PA_d	rms	F_{peak}	morph/size
		arcsec	deg	mJB			mJB	mJy	kλ	arcsec	deg	mJB	mJB	
NGC 147	core	0.13× <0.198	28.40	0.073	00 33 11.894	48 30 29.69	<0.28	0.95	750	0.39×0.07	142.8	0.070	0.5±0.09	component near
	Tot												0.95±0.10	nucleus ∼3″
IC 342		<0.2× <0.8	0.0	0.150	03 46 48.464	68 05 48.41	1.62±0.09	1.78	500	<0.62× <0.52	0.0	0.208	1.35±0.10	multi-components
		0.54×0.41	168	0.150	03 46 47.926	68 05 47.28	1.18±0.08	5.18	500	0.81×0.56	29	0.208	1.52±0.16	near nucleus ∼3″
		0.43×0.30	107	0.150	03 46 48.701	68 05 43.83	0.84±0.08	2.50	500	0.59×0.30	3.8	0.208	0.66±0.04	
		<0.33× <0.20	0.0	0.150	03 46 47.884	68 05 44.14	0.92±0.08	1.11	500	<0.43× <0.35	0.0	0.208	0.81±0.04	
	Tot												11.58±0.9	
NGC 891		0.23×0.10	10.6	0.063	02 22 33.230	42 20 58.56	0.27±0.07	0.40	400	0.22×0.45	74.6	0.060	0.40±0.08	multi-components
				0.063	02 22 33.441	42 20 54.70	<0.25		400	0.50×0.30	12.9	0.060	0.30±0.08	
				0.063	02 22 33.451	42 20 54.27	<0.20		400	1.0× <0.50	120.0	0.060	0.30±0.08	
		0.24×0.17	65.6	0.063	02 22 33.705	42 20 48.80	0.25±0.08	0.50	400	0.76×0.41	139.854	0.060	0.34±0.08	
	Tot												1.5±0.2	
NGC 1569		0.46×0.30	90	0.110	04 30 54.026	64 50 42.62	0.40±0.03	1.29±0.14	300	0.80×0.30	56.2	0.140	0.95±0.04	source ∼30″ from
		<0.33× <0.20	103.2	0.110	04 30 54.054	64 50.43.01	0.38±0.03	1.46±0.15	300	<0.63× <0.52	0.0	0.140	<0.42	core
		0.92×0.29	138.0	0.110	04 30 54.131	64 50 43.39	<0.33	1.51±0.32	300	0.89×0.78	57	0.140	0.82±0.04	
	Tot												3.70±0.40	
NGC 2342		0.47×<0.13	11.2	0.065	07 09 18.018	20 38 06.25	0.22±0.08	0.36	750	0.64×<0.22	163.2	0.068	0.46±0.09	twin-jets?
(field)				0.065	07 09 18.027	20 38 05.29	<0.40		750	0.44×0.16	32.1	0.068	0.42±0.09	2″ →692pc, 4″
	core?	0.13×0.11	136.8	0.065	07 09 18.027	20 38 05.83	0.39±0.08	0.48	750	0.34×0.11	163.5	0.068	0.55±0.09	offset
	Tot												1.7±0.2	
NGC 3077		0.28×0.19	46.6	0.088	10 03 18.808	68 43 56.65	1.32±0.08	2.92	500	0.24×0.17	85	0.090	1.81±0.10	ULX
													1.82±0.28	

Continued on Next Page

Table B.3 – Continued

		Full resolution								Low resolution				
name	comp	$\theta_M \times \theta_m$	PA$_d$	rms	α(J2000)	δ(J2000)	F$_{peak}$	F$_{tot}$	u–v	$\theta_M \times \theta_m$	PA$_d$	rms	F$_{peak}$	morph/size
		arcsec	deg	mJB			mJB	mJy	kλ	arcsec	deg	mJB	mJB	
NGC 3034	SNR	<0.23× <0.04	0.0	0.131	09 55 55.405	+69 40 53.15	1.95±0.24	2.47±0.49	750	<0.28× <0.25	0.0	0.420	2.19±0.19	multi-
	SNR	0.44×0.20	40	0.131	09 55 55.259	+69 40 59.91	2.23±0.15	6.12±0.55	750	0.56×0.25	35	0.420	2.23±0.24	components,
	SNR	0.27×0.16	80	0.131	09 55 55.214	+69 40 50.03	3.38±0.27	7.08±0.80	750	0.27×0.21	64	0.420	3.89±0.27	largely SF, SNe
	SNR	<0.14× <0.08	0.0	0.131	09 55 54.609	+69 40 49.99	3.03±0.25	3.26±0.47	750	<0.28× <0.25	0.0	0.420	3.17±0.26	remnants, XRBs
	SNR	0.24×0.19	132	0.131	09 55 54.460	+69 40 51.43	3.88±0.17	7.56±0.47	750	0.25×0.20	133	0.420	4.52±0.21	and ULXs, see
	Rad Sou	0.51×0.37	168	0.131	09 55 54.097	+69 40 46.45	1.47±0.15	5.73±0.73	750	0.42×0.36	177	0.420	1.92±0.19	Muxlow et al.
	SNR	0.13×0.08	150	0.131	09 55 54.133	+69 40 53.58	3.67±0.16	4.56±0.33	750	0.12×0.04	152	0.420	4.01±0.18	(2010)
	SNR	0.44×0.24	127	0.131	09 55 53.967	+69 40 51.31	2.06±0.31	8.2±1.5	750	0.51×0.30	128	0.420	2.49±0.34	
	SNR	0.14×0.13	97	0.131	09 55 53.880	+69 40 47.40	14.38±0.49	20.0±1.1	750	0.17×0.15	90	0.420	15.28±0.48	
	SNR	<0.36× <0.07	0.0	0.131	09 55 53.628	+69 40 47.31	1.58±0.30	2.57±0.76	750	<0.37× <0.04	0.0	0.420	1.91±0.27	
	SNR	0.26×0.18	85	0.131	09 55 53.145	+69 40 47.96	1.98±0.09	4.09±0.27	750	0.31×0.18	87	0.420	2.23±0.12	
	SNR	0.19×0.14	176	0.131	09 55 53.229	+69 40 44.36	2.93±0.17	4.39±0.38	750	0.19×0.12	9	0.420	3.20±0.24	
	SNR	0.16×0.15	2	0.131	09 55 52.991	+69 40 45.49	4.26±0.17	6.36±0.38	750	0.15×0.13	14	0.420	4.82±0.23	
	SNG	0.11×0.03	57	0.131	09 55 52.727	+69 40 45.77	10.63±0.25	11.87±0.47	750	0.12×0.02	57	0.420	10.83±0.26	
	Rad Sou	<0.24× <0.20	0.0	0.131	09 55 52.028	+69 40 45.41	22.89±0.60	20.50±0.97	750	<0.28× <0.25	0.0	0.420	22.88±0.64	
	SNR	0.22×0.17	156	0.131	09 55 51.908	+69 40 44.54	7.87±0.51	14.2±1.3	750	0.26×0.19	156	0.420	8.69±0.48	
	SN 2008iz	0.22×0.17	156	0.131	09 55 51.551	+69 40 45.78	59.00±0.44	56.22±0.74	750	<0.28× <0.25	0.0	0.420	58.61±0.47	
	SNR	0.83×0.34	18	0.131	09 55 51.416	+69 40 42.66	2.22±0.19	17.4±1.7	750	0.74×0.34	20	0.420	2.95±0.20	
	SNR	0.41×0.13	22	0.131	09 55 51.386	+69 40 41.86	2.99±0.28	7.03±0.92	750	0.66×0.14	22	0.420	2.94±0.39	
	SNR	0.44×0.31	174	0.131	09 55 51.261	+69 40 48.17	2.59±0.22	8.94±0.97	750	0.53×0.25	172	0.420	2.95±0.32	
		0.41×0.26	57	0.131	09 55 51.230	+69 40 46.42	1.83±0.27	3.79±0.80	750	0.43×0.26	64	0.420	1.81±0.34	
	X-ray Sou	<0.24× <0.20	0.0	0.131	09 55 50.688	+69 40 43.75	16.22±0.36	15.33±0.60	750	<0.28× <0.25	0.0	0.420	16.07±0.41	
	SNR	<0.24× <0.20	0.0	0.131	09 55 50.049	+69 40 45.92	3.50±0.24	3.18±0.39	750	<0.28× <0.25	0.0	0.420	3.67±0.29	
	SNR	0.20×0.12	137	0.131	09 55 49.421	+69 40 41.43	8.93±0.15	13.87±0.36	750	10.20×0.13	139	0.420	10.20±0.13	
	SNR	0.54×0.34	68	0.131	09 55 49.363	+69 40 42.42	2.27±0.22	11.2±1.3	750	0.54×0.43	62	0.420	2.81±0.32	
	SNR	0.31×0.20	81	0.131	09 55 49.061	+69 40 41.52	2.51±0.21	5.61±0.65	750	0.36×0.20	80	0.420	2.84±0.21	
	SNR	0.20×0.15	4	0.131	09 55 47.873	+69 40 43.72	6.14±0.15	10.12±0.36	750	0.20×0.15	4	0.420	6.94±0.18	

Continued on Next Page

Table B.3 – Continued

		Full resolution								Low resolution				
name	comp	$\theta_M \times \theta_m$	PA$_d$	rms	α(J2000)	δ(J2000)	F$_{peak}$	F$_{tot}$	u–v	$\theta_M \times \theta_m$	PA$_d$	rms	F$_{peak}$	morph/size
		arcsec	deg	mJB			mJB	mJy	kλ	arcsec	deg	mJB	mJB	
	Tot												F TOT	
NGC 3198		>0.19× >0.08	166.6	0.114	10 19 54.519	45 32 57.07	0.35±0.12	0.40	750	0.37× >0.25	105.7	0.81	0.61±0.09	
(field)				0.114	10 19 54.520	45 32 53.35	<0.34		750	>0.29× >0.32	171.3	0.81	0.62±0.09	elongated jet? 4.5″ →202pc, 6″ offset
	Tot												2.1±0.2	
NGC 3690	X-ray Sou	0.75×0.45	168	0.233	11 28 30.657	58 33 49.28	1.11±0.13	7.80±1.10	500	0.72×0.48	13	0.299	1.70±0.17	
	Arp299b	0.25×0.21	59	0.233	11 28 30.987	58 33 40.83	13.98±0.46	26.10±1.20	500	0.31×0.27	79	0.299	14.60±0.48	multi-source including TDE
	Arp299a	0.53×0.42	128.5	0.233	11 28 33.631	58 33 46.68	22.75±0.52	108.8±3.0	500	0.53×0.43	127	0.299	31.23±0.61	
	Tot												±	
NGC 4013				0.070	11 58 31.321	43 56 49.86	< 0.24		500	0.20×0.02	58.4	0.064	0.23±0.06	
				0.070	11 58 31.402	43 56 49.57	<0.24		500	0.18×0.07	64.0	0.064	0.25±0.06	
				0.070	11 58 31.422	43 56 51.85	<0.24		500	0.20× <0.15	75.9	0.064	0.28±0.06	star-foring ring?
				0.070	11 58 31.433	43 56 50.05	<0.24		500	0.18× <0.24	25.2	0.064	0.27±0.06	1.5″ →90pc
				0.070	11 58 31.455	43 56 50.46	<0.24		500	0.47×0.15	29.0	0.064	0.27±0.06	
				0.070	11 58 31.481	43 56 50.63	<0.21		500	0.08× <0.22	118.7	0.064	0.24±0.06	
	Tot												3.8±0.3	
NGC 4111		0.63×0.16	19.6	0.102	12 07 03.614	43 03 55.99	0.48±0.05	1.08±0.15	500	<0.68× <0.08	0.0	0.110	0.50±0.04	component near nucleus ∼6″
													0.7±0.1	
NGC 4162		0.36×0.27	104	0.175	12 11 54.104	+24 06 58.76	2.40±0.24	5.35±0.76	500	<0.58× <0.27	0.0	0.210	3.11±0.27	
		<0.47× <0.19	0.0	0.175	12 11 54.046	+24 06 58.47	7.75±0.28	6.70±0.54	500	<0.58× <0.27	0.0	0.210	6.96±0.20	≳30″ offset from nucleus
	Tot												10.0±0.99	
NGC 4220		1.0×0.70	73	0.087	12 16 10.955	47 53 06.30	0.30±0.05	2.96±0.5	300	<0.73×0.41	0.0	0.101	0.51±0.05	off nuclear sources
		0.39×0.0.12	73	0.087	12 16 11.947	47 53 01.89	0.32±0.05	0.53±0.12	300	<0.73×0.41	0.0	0.101	0.42±0.03	
	Tot												±	

Continued on Next Page

Table B.3 – Continued

		Full resolution								Low resolution				
name	comp	$\theta_M \times \theta_m$	PA$_d$	rms	α(J2000)	δ(J2000)	F$_{peak}$	F$_{tot}$	u–v	$\theta_M \times \theta_m$	PA$_d$	rms	F$_{peak}$	morph/size
		arcsec	deg	mJB			mJB	mJy	kλ	arcsec	deg	mJB	mJB	
NGC 4242		<0.42× <0.25	0.0	0.085	12 17 28.247	45 37 25.11	11.25±0.23	11.06±0.41	300	<0.26×0.06	0.0	0.095	10.70±0.27	double lobed
		0.30×0.24	1.5	0.087	12 17 28.20	47 37 26.13	1.31±0.15	2.24±0.39	300	<0.82×0.25	0.0	0.095	1.77±0.24	source, ≳25″
	Tot												12.02±2.18	from core
NGC 4631		0.20×0.21	78	0.077	12 42 07.697	32 32 30.077	0.34±0.08	0.79	500	0.25×0.27	-67.7	0.076	0.40×0.08	compact source,
	Tot												0.62±0.18	≳3″ offset from nucleus
NGC 4736		<0.25× <0.16	33.1	0.091	12 50 53.070	41 07 12.88	0.69±0.06	0.56	500	<0.21× <0.04	0.0	0.101	0.68±0.04	one-sided jet?
	core	0.22×0.16	103	0.091	12 50 53.079	41 07 15.42	1.95±0.11	3.76	500	0.23×0.13	99	0.101	2.60±0.11	
		0.59×0.10	21.6	0.091	12 50 53.076	41 07 14.48	0.59±0.06	1.58	500	<0.34× <0.24	0.0	0.101	0.79±0.06	
	Tot												4.77±0.53	
NGC 4826		0.40×0.16	125	0.074	12 56 43.408	21 41 00.883	0.51±0.07	1.39	300	0.25×0.12	91	0.080	0.74×0.08	multi-component,
		<0.26× <0.19	110	0.074	12:56:43.670	21.41.03.661	0.73±0.07	0.77	300	<0.34× <0.39	122	0.080	0.60×0.10	≳5″ offset from
	Tot												1.29±0.12	nucleus
NGC 5012		0.13×0.07	45	0.079	13 11 37.048	22 54 58.277	0.41±0.08	0.44	500	<0.30× <0.24	31	0.068	0.41×0.07	core, ≳3″ offset
	Tot												0.45±0.10	from nucleus
NGC 5273				0.057	13 42 08.312	35 39 13.45	<0.19		500	0.35× < 0.28	92.5	0.049	0.25±0.05	
				0.057	13 42 08.333	35 39 15.40	<0.22		500	0.92× <0.32	167.5	0.049	0.31±0.05	
				0.057	13 42 08.350	35 39 16.76	<0.23		500	0.87×0.22	159.3	0.049	0.28±0.05	star-forming ring?
		0.26× <0.20	150.50	0.057	13 42 08.354	35 39 15.92	0.24±0.06	0.33	500	0.92×0.12	155.1	0.049	0.30±0.05	3″ →230pc
				0.057	13 42 08.415	35 39 16.35	<0.25		500	1.30×0.22	140.3	0.049	0.32±0.05	
	Tot												2.6±0.2	
NGC 5676				0.085	14 32 47.221	49 27 51.79	<0.28		200	0.38× <1.0	14.5	0.091	0.38±0.09	multi-
				0.085	14 32 47.565	49 27 51.83	<0.26		200	0.46×0.2	30.7	0.091	0.31±0.09	components,
	Tot												0.7±0.2	27.7″ offset

Continued on Next Page

Table B.3 – Continued

		Full resolution								Low resolution				
name	comp	$\theta_M \times \theta_m$	PA_d	rms	α(J2000)	δ(J2000)	F_{peak}	F_{tot}	u–v	$\theta_M \times \theta_m$	PA_d	rms	F_{peak}	morph/size
		arcsec	deg	mJB			mJB	mJy	kλ	arcsec	deg	mJB	mJB	
NGC 5907		0.19× <0.13	22.2	0.097	15 15 49.124	56 20 26.42	0.44±0.10	0.72	750	0.16× <0.19	31.9	0.090	0.41±0.09	multi-
		1.90×0.33	29.5	0.097	15 15 49.300	56 20 25.01	0.30±0.10	0.53	750	1.90×0.15	69.9	0.090	0.33±0.09	components,
		1.63×0.22	157.6	0.097	15 15 49.372	56 20 24.33	0.34±0.10	0.52	750	0.63× <0.35	145.8	0.090	0.42±0.09	55.7″ offset
	Tot												2.1±0.2	
NGC 6015				0.082	15 51 23.775	62 18 44.72	<0.32		500	0.07×0.18	57.6	0.079	0.38±0.10	multi-
				0.082	15 51 23.911	62 18 44.45	<0.35		500	1.03×0.36	4.5	0.079	0.50±0.09	components,
				0.082	15 51 23.974	62 18 43.70	<0.34		500	<0.33× <0.42	78.7	0.079	0.39±0.09	11.6″ offset
				0.082	15 51 24.037	62 18 42.17	<0.39		500	1.14× <0.25	57.5	0.079	0.27±0.09	
				0.082	15 51 24.039	62 18 41.945	<0.38		500	0.38×0.04	21.1	0.079	0.32±0.09	
	Tot												2.6±0.2	

Column description: (1) galaxy name; (2) radio component: core, jet, or lobe or unidentified component if not labeled (N or S stand for North or South); (3) deconvolved FWHM dimensions (major × minor axes, $\theta_M \times \theta_m$) of the fitted component, determined from an elliptical Gaussian fit from the full-resolution radio map; (4) PA of the deconvolved component, PA_d from the full-resolution radio map (degree); (5) rms of the radio map close to the specific component from the full-resolution radio map (mJB, mJy beam^{-1}); (6)-(7) radio position in epoch J2000; (8) peak flux density in mJy beam^{-1}, F_{peak} from the full-resolution radio map; (9) integrated flux density, F_{rmtot} in mJy, from the full-resolution radio map; (10) uv-taper scale of the low-resolution radio map in kλ; (11) deconvolved FWHM dimensions (major × minor axes, $\theta_M \times \theta_m$) of the fitted component, determined from an ellitpical Gaussian fit from the low-resolution radio map; (12) PA of the deconvolved component, PA_d from the low-resolution radio map (degree); (13) rms of the radio map close to the specific component from the low-resolution radio map (mJy beam^{-1}); (14) peak flux density in mJy beam^{-1}, F_{peak} from the low-resolution radio map. At the bottom of each target the total flux density of the radio source associated with the galaxy is given in mJy, measured from the low-resolution map; (15) radio morphology, size in arcsec and pc and offset from the optical centre, if present.

B.6 LeMMINGs Contour Levels

Table B.4: Radio contour levels

name	FR			LR			
	Beam	PA	levels	kλ	beam	PA	levels
NGC 147	0.24×0.14	−63.2	0.18×(−1,1)	750	0.537×0.25	−41.6	0.2×(−1,1,1.5,2,2.3)
NGC 266	0.48×0.31	−40.0	0.21×(−1,1,2,4)	750	0.57×0.37	−46.0	0.25×(−1,1,2,4)
NGC 278	0.29×0.14	−55.2	0.11×(−1,1,2)	750	0.54×0.25	−42.9	0.13×(−1,1,1.5)
NGC 315	0.12×0.12	45.0	25.0×(−1,1,5,15)	750	0.55×0.36	−45.7	10.0×(−1,1,5,15,30)
NGC 410	0.52×0.32	−46.85	0.28×(−1,1,2,4,7)	750	0.62×0.37	−49.9	0.28×(−1,1,2,4,7)
NGC 507	0.46×0.35	−67.8	0.34×(−1,1,1.5,2,2.5)	750	0.60×0.48	−64.6	0.34×(−1,1,1.5,2,2.5)
NGC 777	0.23×0.15	7.6	0.165×(−1,1,2,3,4)	600	0.29×0.26	58.7	0.21×(−1,1,1.42,2,3,3.9)
NGC 891	0.20×0.17	65.6	0.15×(−1,1,2)	400	0.59×0.53	−22.9	0.12×(−1,1,1.5,2,2.4,3)
NGC 972	0.24×0.17	37.2	0.13×(−1,1,1.5,2,2.7)	750	0.31×0.29	66.8	0.13×(−1,1,1.5,2,3,4.2)
IC 342	0.33×0.20	-57.3	0.6×(−1,1,1.5,2,2.5)	500	0.43×0.35	−29.5	0.6×(−1,1,2,3,4)
IC 356	0.33×0.20	-54.5	0.29×(−-1,1,1.4,1.8)	300	0.62×0.52	5.3	0.2×(−-1,1,1.3,1.6)
NGC 1560	0.26×0.17	-53.7	0.22×(−1,1,1.2)	300	0.52×0.41	-174.3	0.23×(−1,1,1.5,2,2.5)
NGC 1569	0.33×0.20	-50.1	0.26×(−1,1,1.5)	300	0.63×0.52	5.0	0.26×(−1,1,2,3)
NGC 1961	0.29×0.18	-35.8	0.5×(−1,1,2,4)	300	0.53×0.41	17.6	0.3×(−1,1,2,4,9)
NGC 2146	0.27×0.18	-23.7	0.8×(−1,1,2,3,4)	300	0.48×0.38	31.6	0.58×(−-1,1,3,5,7)
NGC 2273	0.20×0.16	48.1	0.20×(−1,1,2,4,8,13)	750	0.33×0.27	85.1	0.20×(−1,1,2,4,8,16,22)
NGC 2342	0.18×0.18	0.0	0.15×(−1,1,1.5,2,2.5)	750	0.34×0.34	0.0	0.15×(−1,1,1.5,2,2.5,3,3.5,3.9,4.15)
NGC 2342*	0.18×0.18	0.0	0.15×(−1,1,2)	750	0.34×0.34	0.0	0.17×(−1,1,1.9,2.4,3)
UGC 3828	0.19×0.16	50.3	0.15×(−1,1,1.5,1.85)	750	0.33×0.26	89.3	0.15×(−1,1,1.5,2,2.5,3)
NGC 2300	0.20×0.20	0.0	0.11×(−1,1,2,3,5,8)	750	0.40×0.40	0.0	0.13×(−1,1,2,3,5,8)
UGC 4028	0.20×0.20	0.0	0.17×(−1,1,1.5)	750	0.40×0.40	0.0	0.13×(−1,1,1.5,2.5,3.2)

Continued on Next Page

Table B.4 – Continued

name	FR			LR			
	Beam	PA	levels	kλ	beam	PA	levels
NGC 2639	0.20×0.19	68.0	0.40×(−1,1,2,4,8, 16,29,40)	750	0.34×0.26	−75.3	1.5×(−1,1,2,4, 8,11.2,15)
NGC 2634	0.20×0.20	0.0	0.18×(−1,1,2)	750	0.40×0.40	0.0	0.16×(−1,1,2,2.5)
NGC 2681	0.19×0.16	51.8	0.17×(−1,1,2,3,5)	750	0.34×0.26	−76.4	0.20×(−1,1,1.7,2.5,3.5,5)
NGC 2655	0.20×0.20	0.0	0.20×(−1,1,2,4,8, 16,32,64,128)	750	0.40×0.40	0.0	0.40×(−1,1,2,4,8, 16,32,64,128)
NGC 2768	0.15×0.15	88.6	0.7×(−1,1,4,9,16)	50	0.24×0.21	−81	0.7×(−1,1,4,9,16)
NGC 2787	0.16×0.15	-53.8	0.7×(−1,1,4,8)	750	0.20×0.18	−47.8	0.7×(−1,1,4,8)
NGC 2841	0.19×0.16	52.7	0.16×(−1,1,1.5,2)	600	0.50×0.32	−53.6	0.17×(−1,1,1.3,1.77,2.5,3)
NGC 2985	0.16×0.15	-54.9	0.23×(−1,1,2,3)	500	0.24×0.22	−44.5	0.23×(−1,1,2,3)
NGC 3031	0.25×0.21	61.5	0.002×(−1,1,2.5,5, 10,20,40)	500	0.32×0.30	110.1	0.002×(−1,1,2.5,5, 10,20,40)
NGC 3034	0.24×0.20	60.1	0.002×(−0.5,1,2,4,5, 10,15,20,25,30)	750	0.28×0.25	73.7	0.002×(−0.5,1,2,4,5, 10,15,20,25,30)
NGC 3077	0.24×0.19	46.6	0.21×(−1,1,2,3)	500	0.30×0.28	62.3	0.23×(−1,1,2,3)
NGC 3077*	0.24×0.19	46.6	0.21×(−1,1,2,3,5,7)	500	0.30×0.28	62.3	0.23×(−1,1,2,3,5,7)
NGC 3079	0.30×0.25	64.7	3.4×(−0.6,1,2,4,6)	750	0.31×0.28	59.1	2.9×(−0.6,1,2,4,8)
NGC 3147	0.23×0.19	51.9	0.35×(−1,1,3,6,10,15,21)	750	0.29×0.25	65.8	0.35×(−1,1,3,6,10,15,21)
NGC 3198	0.20×0.20	0.00	0.21×(−1,1,1.5,2)	750	0.46×0.43	−25.4	0.15×(−1,1,1.5,2,2.7)
NGC 3198*	0.20×0.20	0.00	0.3×(−1,1,1.5)	750	0.46×0.43	−25.4	0.15×(−1,1,1.5,3,4)
NGC 3245	0.19×0.17	39.1	0.2×(−1,1,1.5,2,2.5,3)	750	0.22×0.21	86.6	0.2×(−1,1,1.5,2,2.5,3)
NGC 3301	0.21×0.18	26.8	0.2×(−1,1,1.5,2,2.5)	750	0.23×0.22	60.5	0.2×(−1,1,1.5,2,2.5)
NGC 3310	0.27×0.23	69.4	0.3×(−1,1,1.5,2)	750	0.29×0.26	58.1	0.3×(−1,1,1.5,2)

Continued on Next Page

Table B.4 – Continued

name	FR			LR			
	Beam	PA	levels	kλ	beam	PA	levels
NGC 3348	0.23×0.19	56.7	0.23×(−1,1,2,4,6)	750	0.27×0.24	67.0	0.21×(−1,1,2,4,6)
NGC 3414	0.22×0.14	20.60	0.11×(−1,1,2,4,8)	750	0.47×0.34	−37.6	0.21×(−1,1,2,4,8)
NGC 3430	0.20×0.20	0.0	0.17×(−1,1,1.5,2)	750	0.48×0.37	−30.9	0.16×(−1,1,1.5,2,2.5)
NGC 3432	0.47×0.28	−16.7	0.21×(−1,1,2,3)	750	0.59×0.55	35.1	0.21×(−1,1,2)
NGC 3504	0.22×0.19	-77.4	0.2×(−1,1,5,10,20, 30,75)	500	0.31×0.26	−81.7	0.2×(−1,1,5,10,20, 30,75)
NGC 3516	0.23×0.19	50.9	0.5×(−0.8,1,2,3,4)	500	0.30×0.28	78.7	0.6×(−0.8,1,2,3,4)
NGC 3665	0.20×0.20	0.00	0.23×(−1,1,1.5, 2,5,12)	750	0.45×0.36	−34.6	0.90×(−0.80,1,1.5,2,4)
				500	0.57×0.50	−18.0	1.0×(−0.80,1,1.5,2,4)
NGC 3675	0.17×0.14	−63.3	0.16×(−1,1,1.5)	750	0.24×0.19	−54.0	0.14×(−1,1,1.5,2)
NGC 3690	0.28×0.21	88.2	0.8×(−0.8,1,2,4,8,16)	500	0.32×0.28	−68.7	0.8×(−0.8,1,2,4,8,16)
NGC 3690	0.28×0.21	88.2	0.8×(−0.8,1,2,5,15,30)	500	0.32×0.28	−68.7	0.8×(−1,1,2,5,15,30)
NGC 3690	0.28×0.21	88.2	0.6×(−0.8,1.2,1.5,2)	500	0.32×0.28	−68.7	0.6×(−1,1,1.5,2,3)
NGC 3735	0.23×0.19	-59.0	0.19×(−1,1,2,3)	750	0.27×0.24	68	0.2×(−1,1,2,3)
NGC 3884	0.41×0.41	0.0	0.4×(−1,1,3,5)	750	0.66×0.33	−43.1	1.2×(−0.8,1,2)
NGC 3938	0.19×0.14	−54.2	0.15×(−1,1,1.5)	750	0.24×0.19	−47.0	0.15×(−1,1,1.5,2)
NGC 3941	0.20×0.19	41.1	0.2×(−1,1,1.5,2)	500	0.25×0.24	37.7	0.2×(−1,1,1.5,2,2.5)
NGC 3945	0.17×0.14	33.5	0.14×(−1,1,2,3,4)	300	0.44×0.39	−8.2	0.18×(−1,1,2,3)
NGC 4013	0.19×0.14	−56.4	0.14×(−1,1)	500	0.24× 0.20	−51.0	0.09×(−1,1,2,3)
NGC 4036	0.17×0.14	34.7	0.25×(−0.8,1,2,4,8)	500	0.28×0.27	−26	0.3×(−0.8,1,2,3,5,8)
NGC 4041	0.17×0.15	30.1	0.14×(−1,1,2,3)	500	0.29×0.26	−27.2	0.14×(−1,1,2,3,4)
NGC 4051	0.18×0.14	−58.6	0.19×(−1,1,1.5,2, 2.5,3,3.5,4,5)	750	0.24×0.19	−53.13	0.44×(−0.8,1,1.5,2,2.5, 3,3.5)

Continued on Next Page

Table B.4 – Continued

name	FR			LR			
	Beam	PA	levels	kλ	beam	PA	levels
NGC 4088	0.20×0.14	−44.0	0.2×(−1,1,1.5)	300	0.43×0.32	−14.1	0.22×(−1,1,1.5,2)
NGC 4100	0.20×0.16	-55.9	0.22×(−1,1,1.5)	750	0.24×0.19	−55.1	0.22×(−1,1,1.5,2)
NGC 4102	0.20×0.15	-42.9	0.31×(−1,1,2,3,4,6)	500	0.27×0.22	−39.1	0.30×(−1,1,2,3,4,6,8)
NGC 4111	0.40×0.23	16.1	0.27×(−1,1,1.4,1.8)	500	0.53×0.29	16.6	0.26×(−1,1,1.4,1.8)
NGC 4111*	0.40×0.23	16.1	0.27×(−0.8,1,1.4,1.8)	500	0.53×0.29	16.6	0.26×(−0.8,1,1.4,1.8)
NGC 4143	0.42×0.20	9.7	0.44×(−1,1,2,4)	500	0.55×0.30	−PA	0.44×(−1,1,2,4)
NGC 4151	0.26×0.16	38.8	1×(−0.5,1,2,4,9,16, 25,36,49,64)	500	0.34×0.25	47.3	1.1×(−0.5,1,2,4,9,16, 25,36,49,64)
NGC 4162	0.47×0.19	-43.8	0.7×(−1,1,2.5,5,9)	500	0.58×0.27	−41.4	0.7×(−1,1,2.5,5,9)
NGC 4203	0.22×0.18	54.7	0.4×(−1,1,5,10,15)	500	0.28×0.23	59.5	0.4×(−1,1,5,10,15)
NGC 4217	0.46×0.26	8.0	0.2×(−1,1,1.4)	300	0.73×0.41	7.9	0.26×(−1,1,1.4,1.8)
NGC 4220	0.38×0.21	9.8	0.28×(−0.8,1,1.2)	300	0.73×0.41	−174.5	0.26×(−0.8,1,1.2)
NGC 4220*1	0.38×0.21	9.8	0.25×(−0.8,1,1.2)	300	0.73×0.41	−174.5	0.25×(−0.8,1,1.2,1.4,1.6)
NGC 4220*2	0.38×0.21	9.8	0.22×(−0.8,1,1.5)	300	0.73×0.41	−174.5	0.25×(−0.8,1,1.4,1.8)
NGC 4242	0.42×0.25	8.3	0.08×(−0.8,1,4,9,13)	300	0.78×0.41	6.7	0.08×(−0.8,1,4,9,13)
NGC 4258	0.42×0.25	-176.3	0.25×(−1,1,2,4)	750	0.49×0.28	−173.9	0.25×(−1,1,2,4)
NGC 4278	0.32×0.32	0.0	2.5×(−1,1,5,15,35, 60,90)	750	0.38×0.38	0.0	2.2×(−1,1,5,15,35, 60,90)
NGC 4395	0.22×0.18	56.2	0.25×(−1,1,1.5,2,2.5)	500	0.27×0.24	70.2	0.26×(−1,1,1.5,2,2.5)
NGC 4494	0.23×0.20	49.3	0.13×(−1,1,2)	750	0.26×0.23	57.6	0.11×(−1,1,2,3)
NGC 4565	0.22×0.20	44.4	0.25×(−1,1,2,3,4)	500	0.28×0.27	69.1	0.22×(−0.8,1,2,3,4)
NGC 4589	0.16×0.12	30.9	0.07×(−0.8,1,2.5,5,10,20)	750	0.20×0.16	20.9	0.11×(−0.8,1,2.5,5,10,15)
NGC 4631	0.21×0.20	77.9	0.16×(−1,1,2)	500	0.27×0.25	−67.7	0.16×(−1,1,2)

Continued on Next Page

Table B.4 – Continued

name	FR			LR			
	Beam	PA	levels	kλ	beam	PA	levels
NGC 4750	0.16×0.12	27.2	0.15×(−1,1,2,3)	500	0.25×0.22	−5.9	0.15×(−1,1,2,3,4,5)
NGC 4736	0.25×0.16	33.1	0.4×(−1,1,2,3,4,5)	500	0.34×0.24	45.2	0.4×(−1,1,2,3,4,5,6)
NGC 4826	0.22×0.20	46.4	0.14×(−1,1,1.5)	300	0.39×0.34	−42.0	0.16×(−1,1,2,3,4)
NGC 4826*	0.22×0.20	46.4	0.19×(−1,1,2,3)	300	0.39×0.34	−42.0	0.21×(−1,1,2,3)
NGC 5005	0.21×0.19	27.0	0.19×(−1,1,2,3,3.7, 4.5,7,8.5,10.75,12)	750	0.34×0.30	25.8	0.23×(−1,1,2,7,16)
				150	1.57×1.28	11.9	0.70×(−1,1,2,3,3.7,10,20)
NGC 5012	0.23×0.20	42.5	0.17×(−1,1,2)	750	0.29×0.26	48.5	0.15×(−1,1,2)
NGC 5194	0.18×0.17	82.7	0.21×(−1,1,2,3)	750	0.30×0.27	−53.6	0.18×(−1,1,2,3,6)
				500	0.47×0.42	14.7	0.18×(−1,1,2,2.5,3.3,5,8)
NGC 5195	0.20×0.18	82.8	0.17×(−1,1,1.5,2,2.8)	750	0.30×0.29	−59.9	0.21×(−1,1,1.5,2,2.8)
NGC 5273	0.25×0.17	32.4	0.11×(−1,1,1.5)	500	0.46×0.39	76.2	0.11×(−1,1,1.5,2,2.4)
NGC 5322	0.31×0.22	33.0	0.35×(−1,1,2,5,10)	500	0.40×0.31	17.7	0.35×(−1,1,2,5,10)
NGC 5353	0.18×0.14	29.6	0.90×(−1,1,2,4,8,13)	500	0.24×0.22	66.3	0.70×(−1,1,2,4,8,16)
NGC 5377	0.20×0.18	−86.5	0.18×(−1,1,1.5)	750	0.51×0.39	4.3	0.19×(−1,1,1.85,2.5)
NGC 5448	0.19×0.18	−86.6	0.19×(−1,1,1.3, 1.6,1.85)	750	0.30×0.28	−51.8	0.19×(−1,1,1.5,1.88,2.3)
NGC 5485	0.30×0.30	0.0	0.44×(−1,1,1.5,2)	500	0.46×0.34	13.2	0.38×(−1,1,1.5,2,2.5)
NGC 5676	0.35×0.19	23.2	0.19×(−1,1,1.5)	200	1.06×0.89	13.2	0.15×(−1,1,1.5,2)
NGC 5866	0.18×0.18	0.0	0.40×(−1,1,2,4,8,16)	200	1.00×0.96	−50.8	0.25×(−1,1,2,3,6,15,30)
NGC 5879	0.18×0.18	0.0	0.15×(−1,1,1.5,2,)	750	0.41×0.30	32.0	0.15×(−1,1,1.5,2,2.5)
NGC 5907	0.28×0.19	18.6	0.20×(−1,1,1.5)	750	0.42×0.30	29.8	0.19×(−1,1,1.5,2)
NGC 5985	0.26×0.19	22.1	0.13×(−1,1,1.5)	380	0.58×0.55	78.3	0.11×(−1,1,1.5,2)
				200	1.13×0.96	−81.03	0.11×(−1,1,1.5,2,2.5)

Continued on Next Page

Table B.4 – Continued

name	FR			LR			
	Beam	PA	levels	kλ	beam	PA	levels
NGC 6015	0.23×0.18	25.4	0.15×(−1,1,1.5,2)	500	0.48×0.42	67.5	0.15×(−1,1,1.5,2,3)
NGC 6217	0.17×0.14	72.4	0.22×(−1,1,2)	500	0.25×0.23	115	0.26×(−1,1,2)
NGC 6340	0.17×0.15	69.8	0.2×(−1,1,1.5)	300	0.37×0.32	−21.6	0.3×(−1,1,2)
NGC 6702	0.19×0.16	56.7	0.14(−1,1,2)	600	0.57×0.30	−51.2	0.12×(−1,1,1.7,2.1,2.6,3.2)
NGC 6703	0.19×0.15	53.6	0.12×(−1,1,1.5,2)	750	0.52×0.25	−51.51	0.10×(−1,1,1.5,2.5)
NGC 6946	0.19×0.15	−84.1	0.13×(−1,1,2,3,4,5.5)	700	0.52×0.27	−42.73	0.13×(−1,1,2,3,4,8,11)
NGC 6951	0.20×0.15	88.5	0.13×(1,1,1.5,2.5,3.5)	750	0.48×0.26	−39.3	0.13×(−1,1,1.5,2.5,3.5,4.2,5)
NGC 7217	0.18×0.18	0.0	1.5×(−1,1,1.5,2, 3,4,5)	700	0.40×0.4	0.0	1.5×(−1,1,2,3,4,5)
NGC 7798	0.20×0.14	35.9	0.07×(−1,1,2,3,4)	750	0.50×0.23	−41.0	0.1×(−1,1,2,3,4)

Column description: (1) source name; (2) FWHM of the elliptical Gaussian restoring beam in arcsec of the full-resolution maps; (3) PA of the restoring beam (degree) of the full-resolution maps; (4) radio contour levels (mJy beam^{-1}) of the full-resolution maps (Fig. **??** and **??**); (5) uvtaper scale parameter in kλ of the low-resolution radio maps; (6) FWHM of the elliptical Gaussian restoring beam in arcsec of the low-resolution maps; (7) PA of the restoring beam (degree) of the low-resolution maps; (8) radio contour levels (mJy beam^{-1}) of the low-resolution maps (Fig. **??** and **??**). $*$ identifies the secondary radio source detected in the field, probably a background AGN.

Appendix C

LeMMINGs BPT Diagram Classifications

C.1 LeMMINGs BPT Diagrams

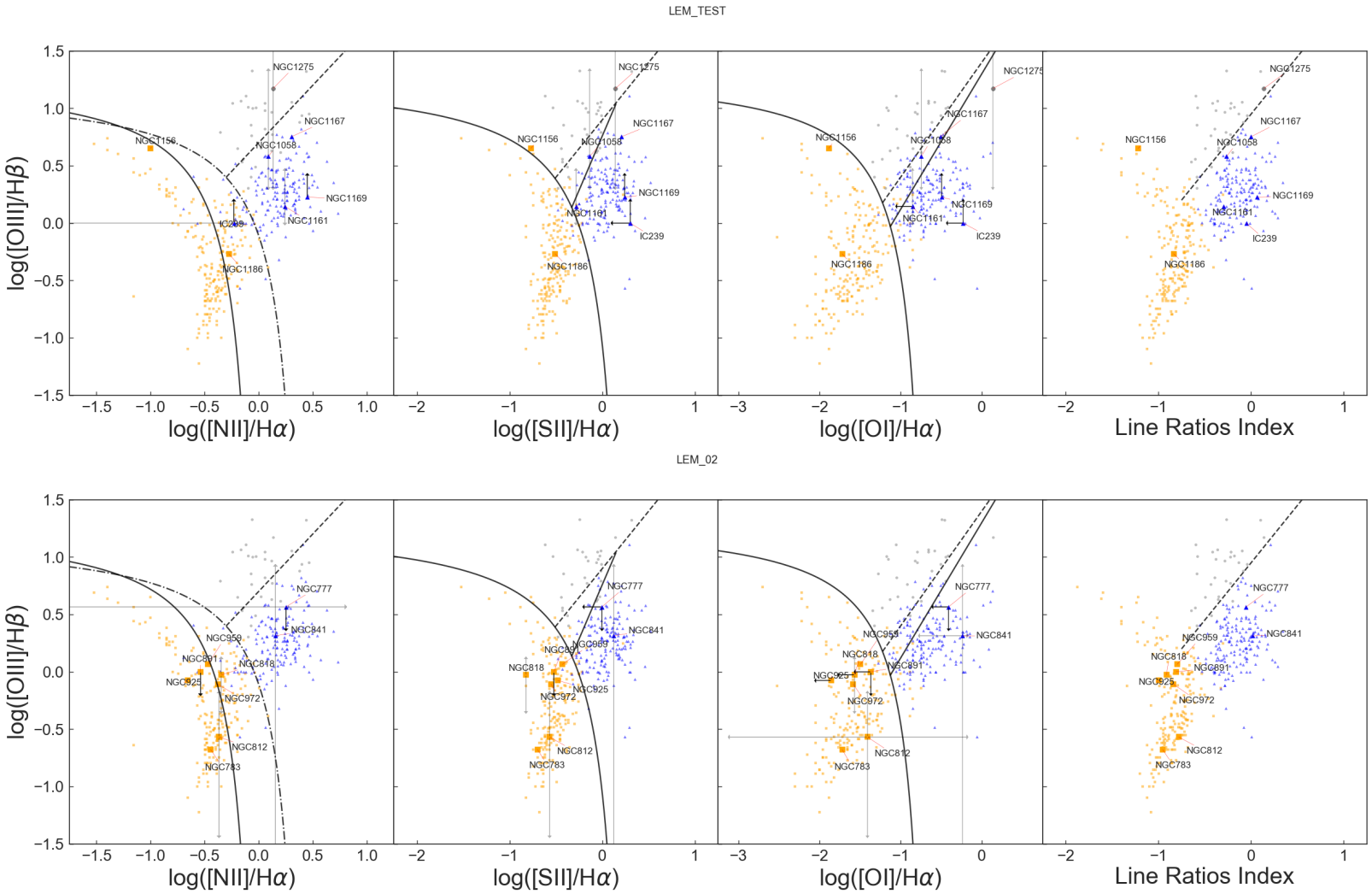

Figure C.1: BPT emission line diagnostic diagrams for the LeMMINGs data blocks LEMTEST (top) and LEM02 (bottom). Going from left to right, the panels show the log[O III]/Hβ ratio against (panel 1) log[N II]/Hα, (2) log[S II]/Hα, (3) log[O I]/Hα and (4) Line Ratios Index. The black lines are the Kewley et al. (2001) diagnostic lines, the dot-dashed line in the first panel shows the Kewley et al. (2006) maximum starburst line and the dashed lines show the Buttiglione et al. (2010) classification between LINERs and Seyferts. The BPT diagram for the whole Palomar sample, re-classified in Section 2 is shown in the background, with HII galaxies in orange, LINERs in blue and Seyferts in grey. This colour scheme is used for the 10 objects in each of the blocks above, including errors given as black arrows for upper/lower limts, and grey arrows for measurement uncertainties from the Ho et al. (1997a) emission line ratio data. Absorption Line Galaxies are not shown for either block, due to their lack of measured emission line ratios. For LEMTEST, this accounts for the galaxies NGC 1003 and NGC 1023 not being present, and for LEM02, explains the lack of data for NGC 890.

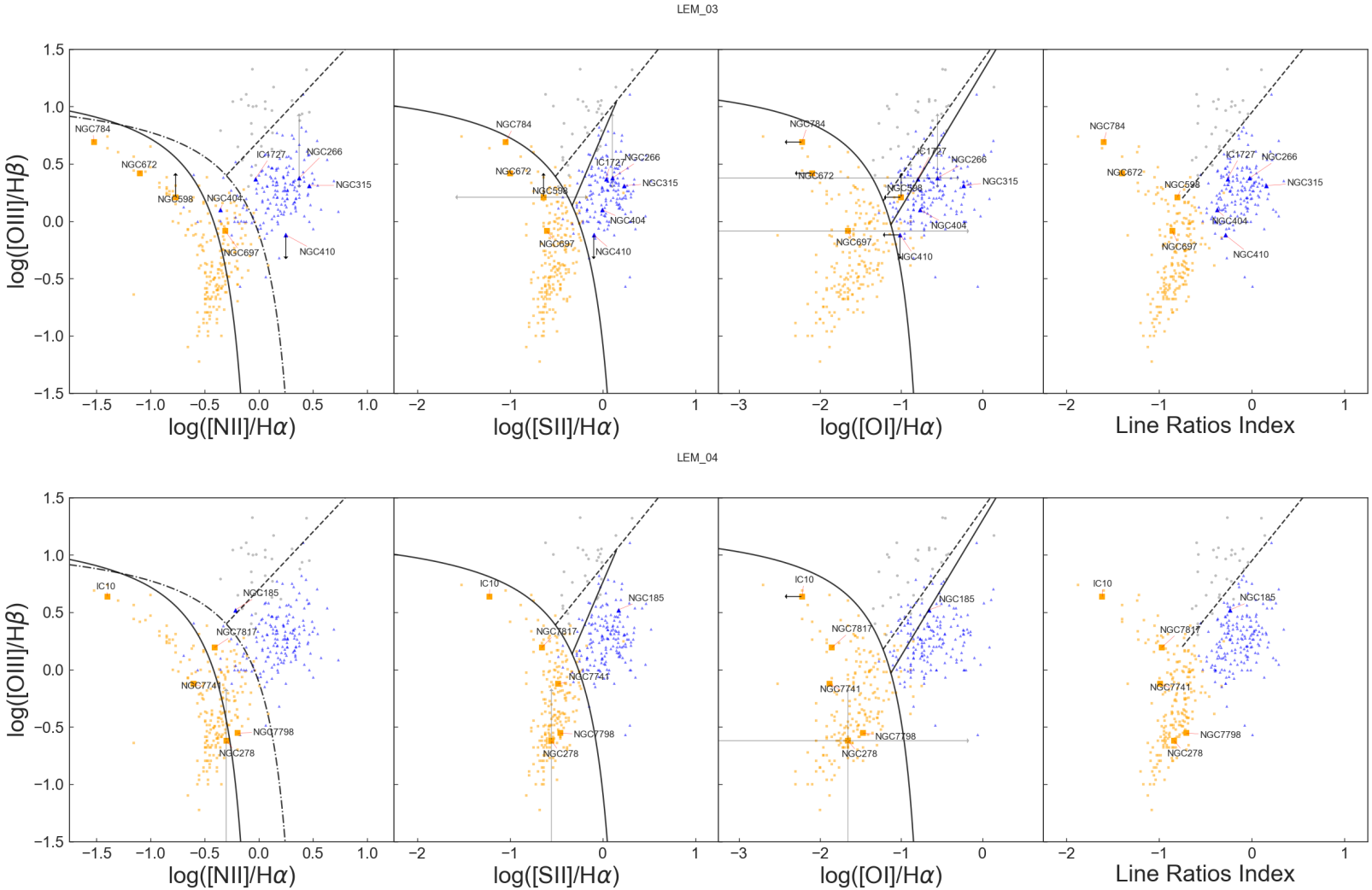

Figure C.1: BPT emission line diagnostic diagrams for the LeMMINGs data blocks LEM03 (top) and LEM04 (bottom). Going from left to right, the panels show the log[O III]/Hβ ratio against (panel 1) log[N II]/Hα, (2) log[S II]/Hα, (3) log[O I]/Hα and (4) Line Ratios Index. The black lines are the Kewley et al. (2001) diagnostic lines, the dot-dashed line in the first panel shows the Kewley et al. (2006) maximum starburst line and the dashed lines show the Buttiglione et al. (2010) classification between LINERs and Seyferts. The BPT diagram for the whole Palomar sample, re-classified in Section 2 is shown in the background, with HII galaxies in orange, LINERs in blue and Seyferts in grey. This colour scheme is used for the 10 objects in each of the blocks above, including errors given as black arrows for upper/lower limts, and grey arrows for measurement uncertainties from the Ho et al. (1997a) emission line ratio data. Absorption Line Galaxies are not shown for either block, due to their lack of measured emission line ratios. For LEM03, this accounts for the galaxy NGC 507 not being present, and for LEM04, explains the lack of data for NGC 147, NGC 205, NGC 221 and NGC 224.

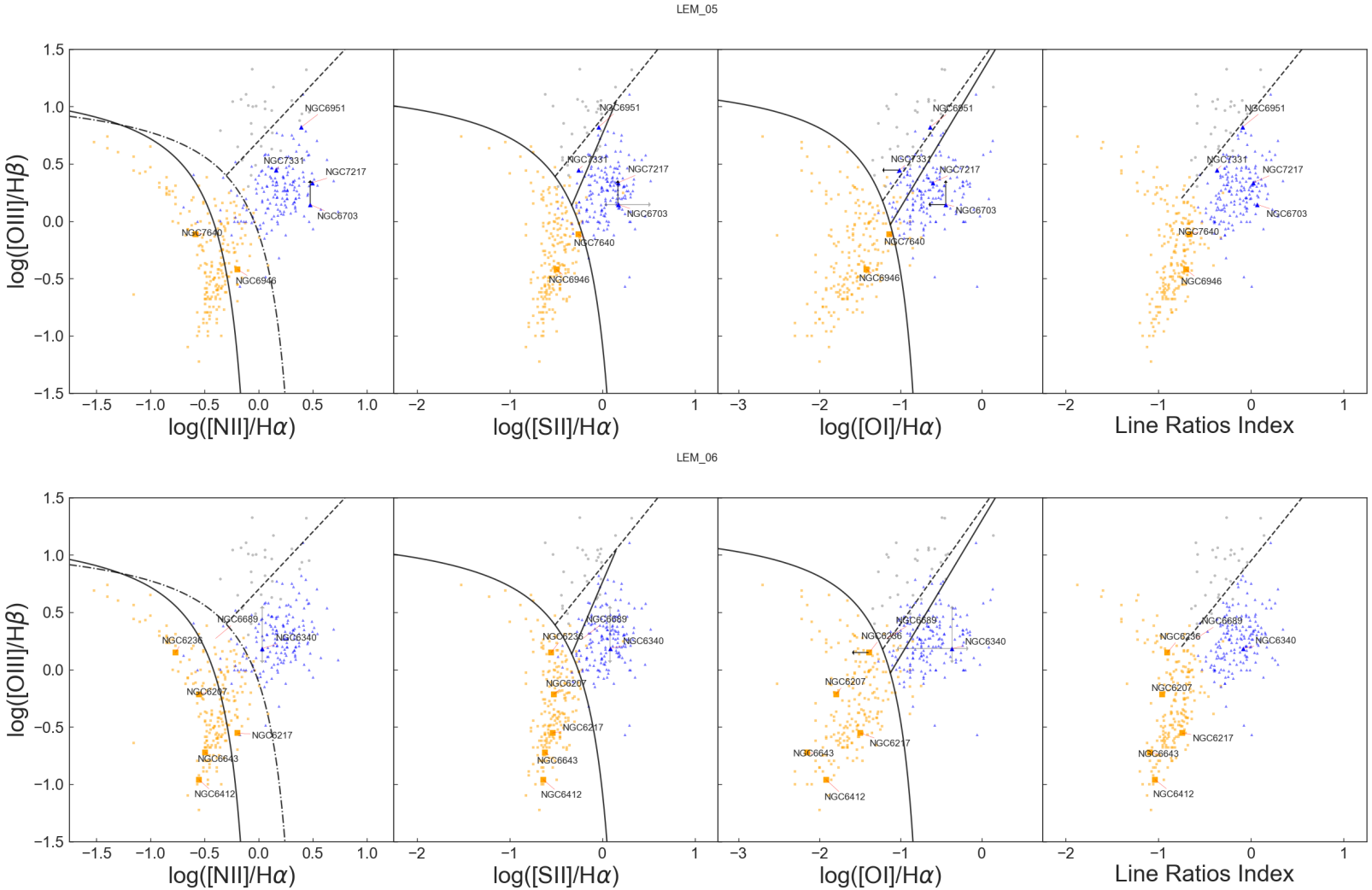

Figure C.1: BPT emission line diagnostic diagrams for the LeMMINGs data blocks LEM05 (top) and LEM06 (bottom). Going from left to right, the panels show the log[O III]/Hβ ratio against (panel 1) log[N II]/Hα, (2) log[S II]/Hα, (3) log[O I]/Hα and (4) Line Ratios Index. The black lines are the Kewley et al. (2001) diagnostic lines, the dot-dashed line in the first panel shows the Kewley et al. (2006) maximum starburst line and the dashed lines show the Buttiglione et al. (2010) classification between LINERs and Seyferts. The BPT diagram for the whole Palomar sample, re-classified in Section 2 is shown in the background, with HII galaxies in orange, LINERs in blue and Seyferts in grey. This colour scheme is used for the 10 objects in each of the blocks above, including errors given as black arrows for upper/lower limts, and grey arrows for measurement uncertainties from the Ho et al. (1997a) emission line ratio data. Absorption Line Galaxies are not shown for either block, due to their lack of measured emission line ratios. For LEM05, this accounts for the galaxies NGC 6702, NGC 7332, NGC 7457 and NGC 7080 not being present, and for LEM06, explains the lack of data for NGC 6482, NGC 6503, NGC 6654 and NGC 6689.

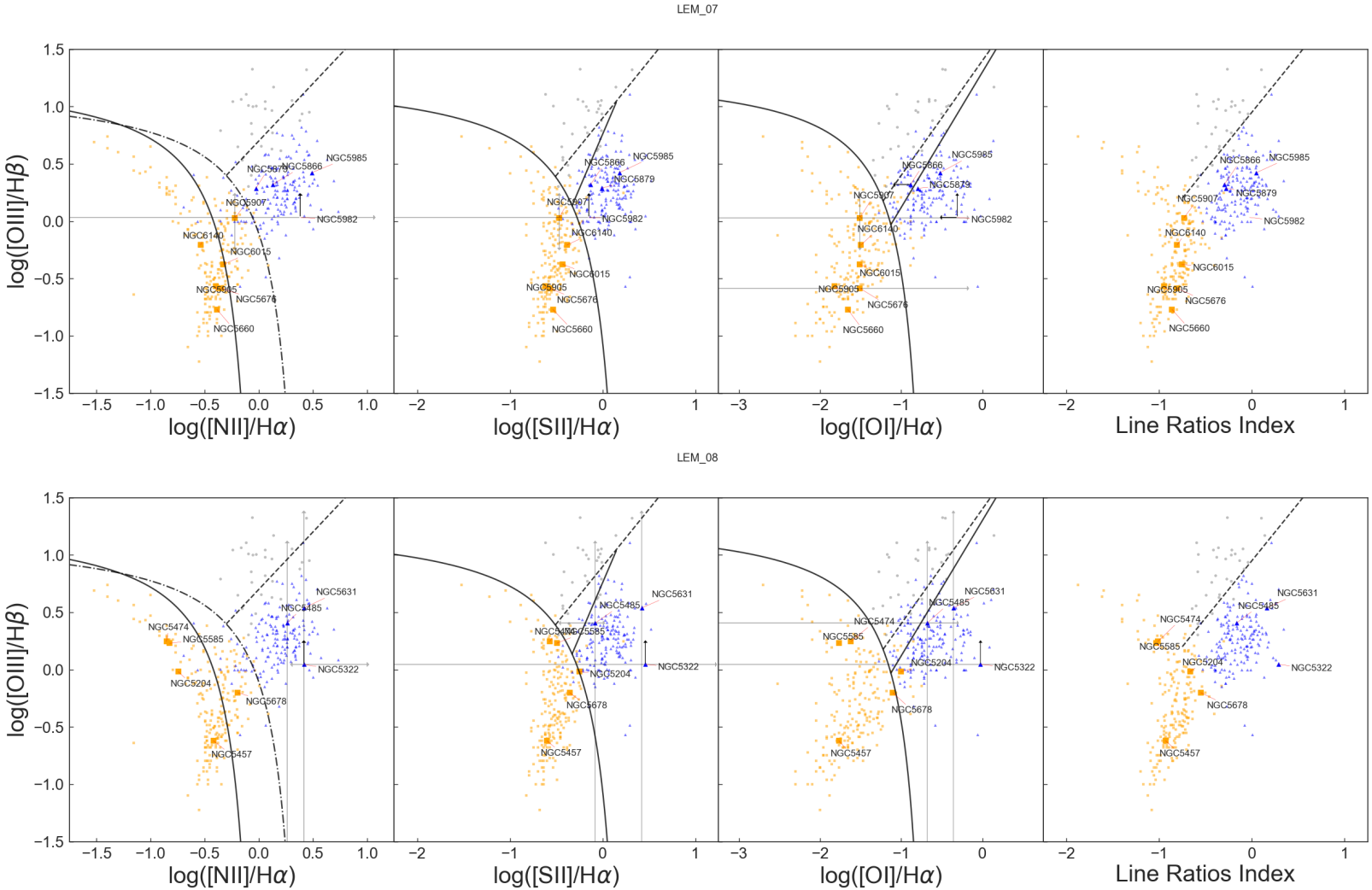

Figure C.1: BPT emission line diagnostic diagrams for the LeMMINGs data blocks LEM07 (top) and LEM08 (bottom). Going from left to right, the panels show the log[O III]/Hβ ratio against (panel 1) log[N II]/Hα, (2) log[S II]/Hα, (3) log[O I]/Hα and (4) Line Ratios Index. The black lines are the Kewley et al. (2001) diagnostic lines, the dot-dashed line in the first panel shows the Kewley et al. (2006) maximum starburst line and the dashed lines show the Buttiglione et al. (2010) classification between LINERs and Seyferts. The BPT diagram for the whole Palomar sample, re-classified in Section 2 is shown in the background, with HII galaxies in orange, LINERs in blue and Seyferts in grey. This colour scheme is used for the 10 objects in each of the blocks above, including errors given as black arrows for upper/lower limts, and grey arrows for measurement uncertainties from the Ho et al. (1997a) emission line ratio data. Absorption Line Galaxies are not shown for either block, due to their lack of measured emission line ratios. For LEM07, this accounts for the galaxy NGC 5982 *[Actually based off other data]* not being present, and for LEM08, explains the lack of data for NGC 5308 and NGC 5473.

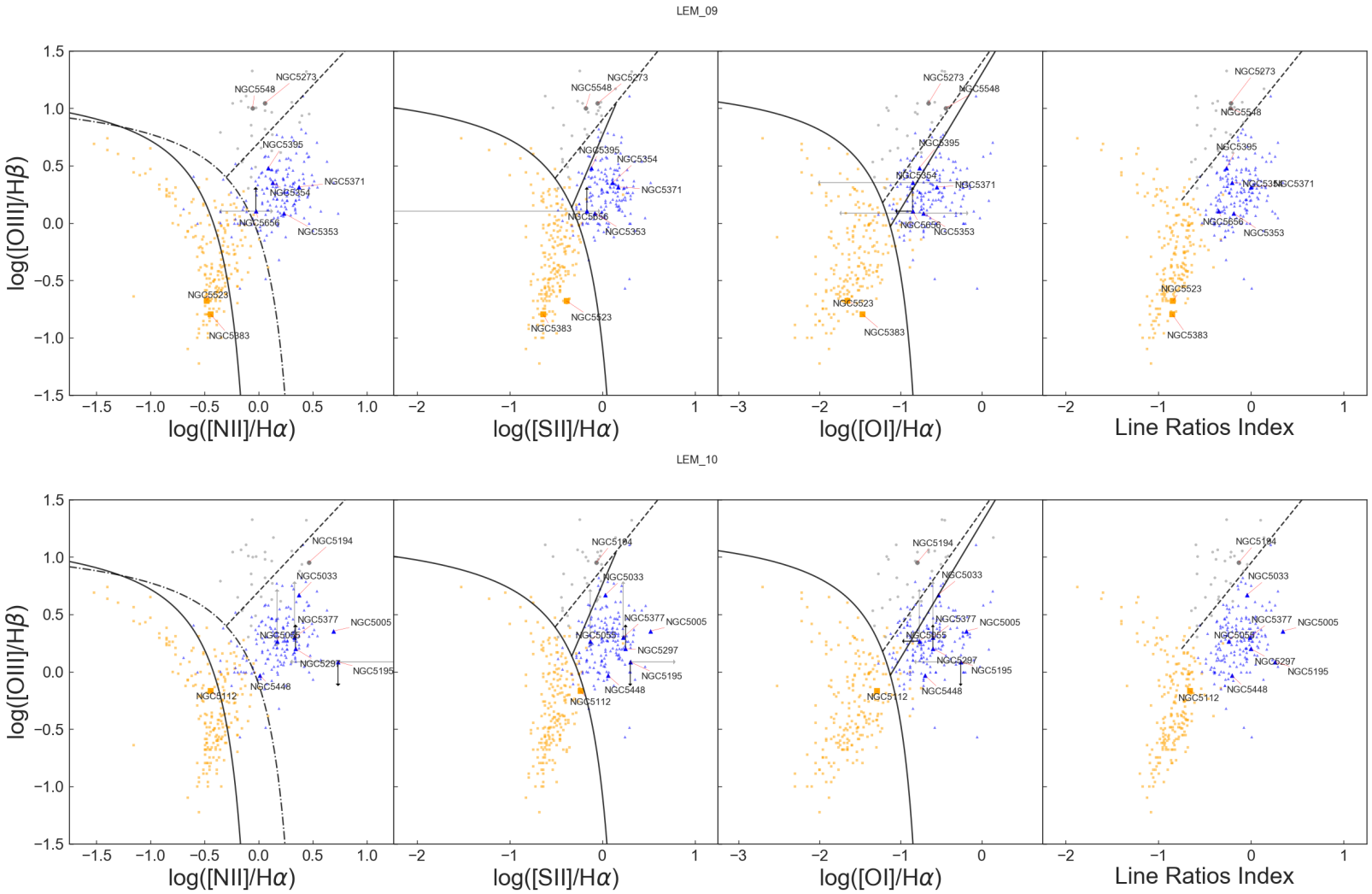

Figure C.1: BPT emission line diagnostic diagrams for the LeMMINGs data blocks LEM09 (top) and LEM10 (bottom). Going from left to right, the panels show the log[O III]/Hβ ratio against (panel 1) log[N II]/Hα, (2) log[S II]/Hα, (3) log[O I]/Hα and (4) Line Ratios Index. The black lines are the Kewley et al. (2001) diagnostic lines, the dot-dashed line in the first panel shows the Kewley et al. (2006) maximum starburst line and the dashed lines show the Buttiglione et al. (2010) classification between LINERs and Seyferts. The BPT diagram for the whole Palomar sample, re-classified in Section 2 is shown in the background, with HII galaxies in orange, LINERs in blue and Seyferts in grey. This colour scheme is used for the 10 objects in each of the blocks above, including errors given as black arrows for upper/lower limts, and grey arrows for measurement uncertainties from the Ho et al. (1997a) emission line ratio data. Absorption Line Galaxies are not shown for either block, due to their lack of measured emission line ratios. For LEM09, this accounts for the galaxy NGC 5557 not being present, and for LEM10, explains the lack of data for NGC 4914.

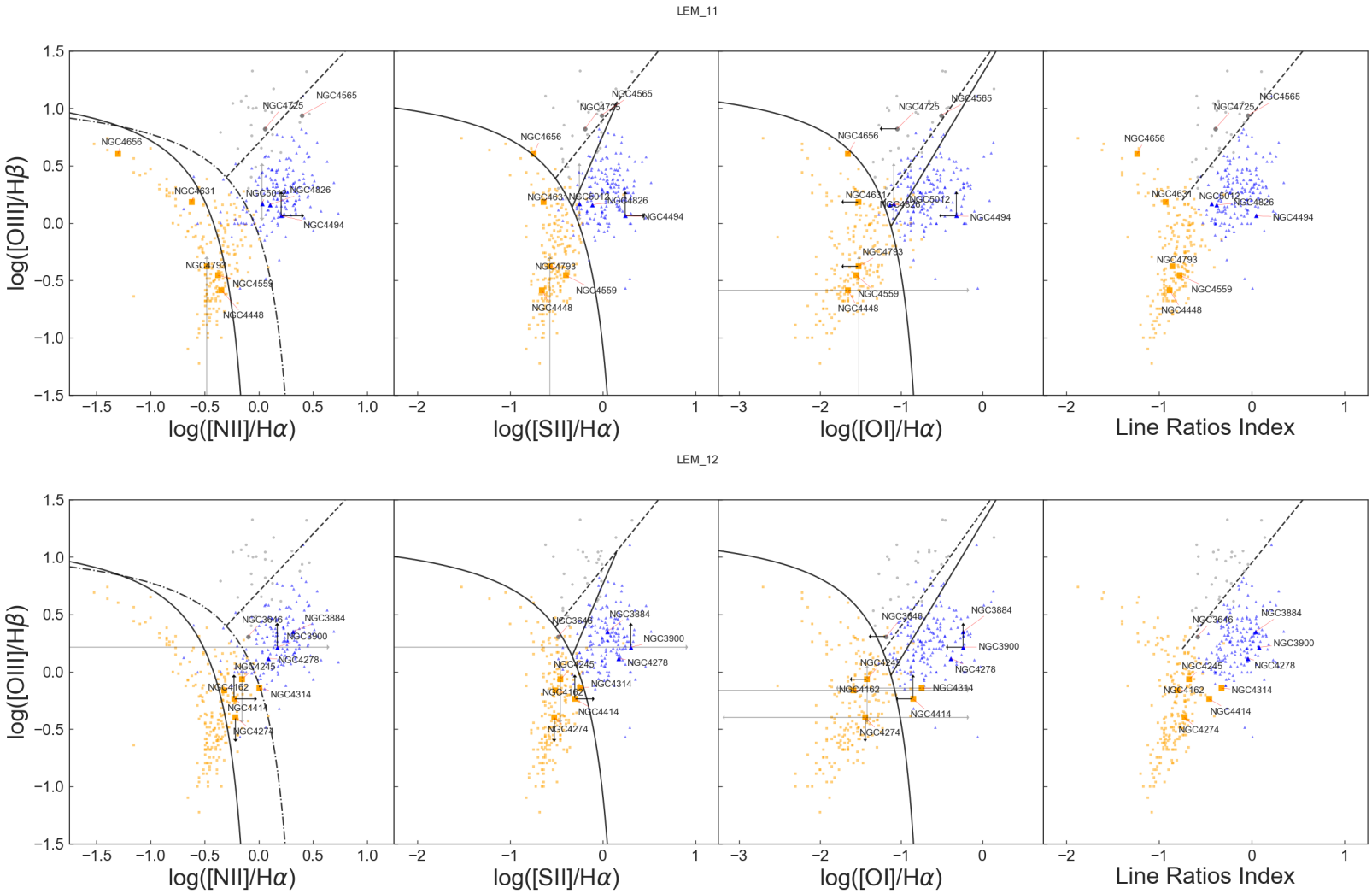

Figure C.1: BPT emission line diagnostic diagrams for the LeMMINGs data blocks LEM11 (top) and LEM12 (bottom). Going from left to right, the panels show the log[O III]/Hβ ratio against (panel 1) log[N II]/Hα, (2) log[S II]/Hα, (3) log[O I]/Hα and (4) Line Ratios Index. The black lines are the Kewley et al. (2001) diagnostic lines, the dot-dashed line in the first panel shows the Kewley et al. (2006) maximum starburst line and the dashed lines show the Buttiglione et al. (2010) classification between LINERs and Seyferts. The BPT diagram for the whole Palomar sample, re-classified in Section 2 is shown in the background, with HII galaxies in orange, LINERs in blue and Seyferts in grey. This colour scheme is used for the 10 objects in each of the blocks above, including errors given as black arrows for upper/lower limts, and grey arrows for measurement uncertainties from the Ho et al. (1997a) emission line ratio data. Absorption Line Galaxies are not shown for either block, due to their lack of measured emission line ratios. For LEM12, this accounts for the lack of data for galaxy NGC 4251.

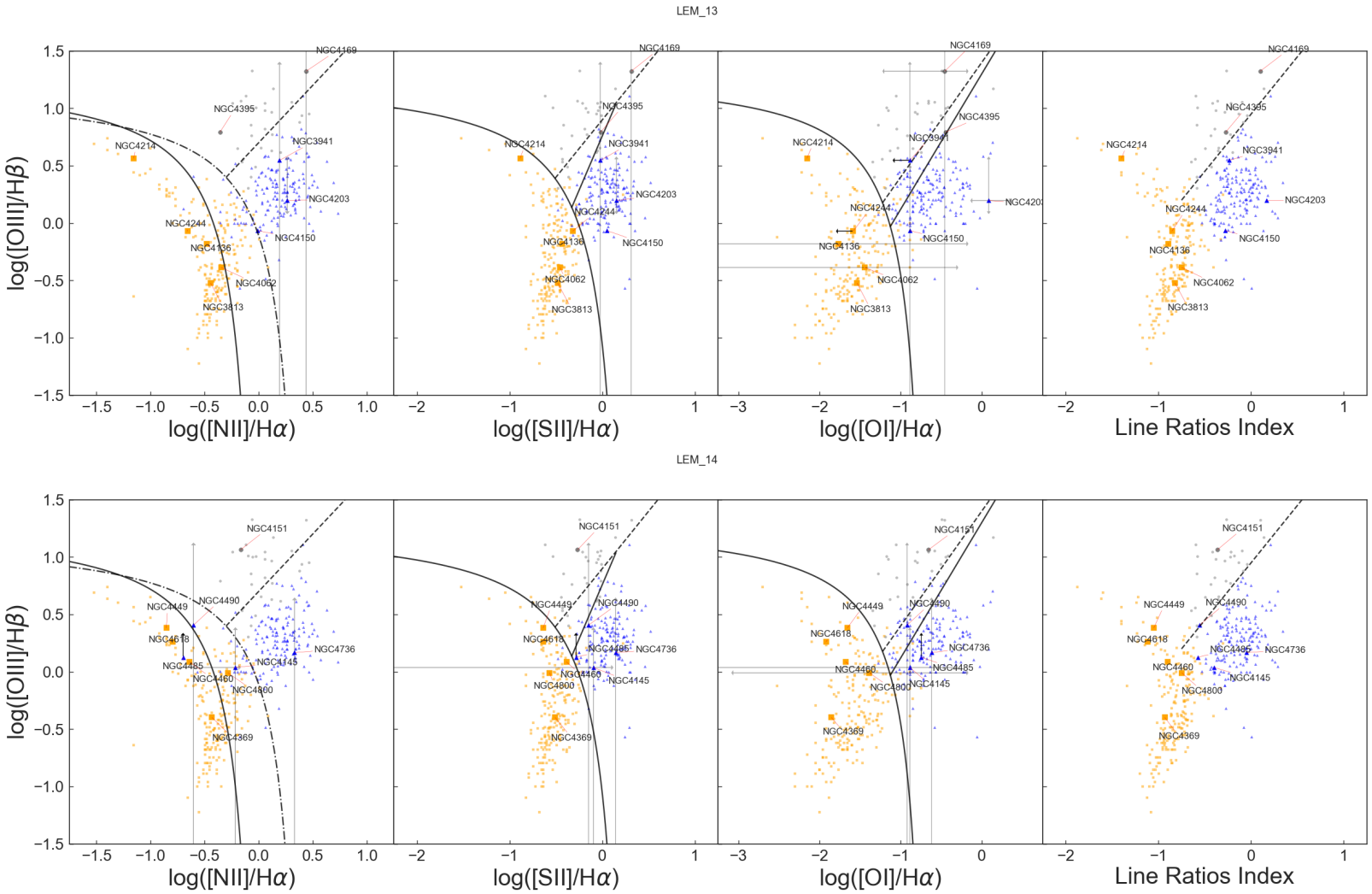

Figure C.1: BPT emission line diagnostic diagrams for the LeMMINGs data blocks LEM13 (top) and LEM14 (bottom). Going from left to right, the panels show the log[O III]/Hβ ratio against (panel 1) log[N II]/Hα, (2) log[S II]/Hα, (3) log[O I]/Hα and (4) Line Ratios Index. The black lines are the Kewley et al. (2001) diagnostic lines, the dot-dashed line in the first panel shows the Kewley et al. (2006) maximum starburst line and the dashed lines show the Buttiglione et al. (2010) classification between LINERs and Seyferts. The BPT diagram for the whole Palomar sample, re-classified in Section 2 is shown in the background, with HII galaxies in orange, LINERs in blue and Seyferts in grey. This colour scheme is used for the 10 objects in each of the blocks above, including errors given as black arrows for upper/lower limts, and grey arrows for measurement uncertainties from the Ho et al. (1997a) emission line ratio data. Absorption Line Galaxies are not shown for either block, due to their lack of measured emission line ratios, however, this affects neither of these blocks.

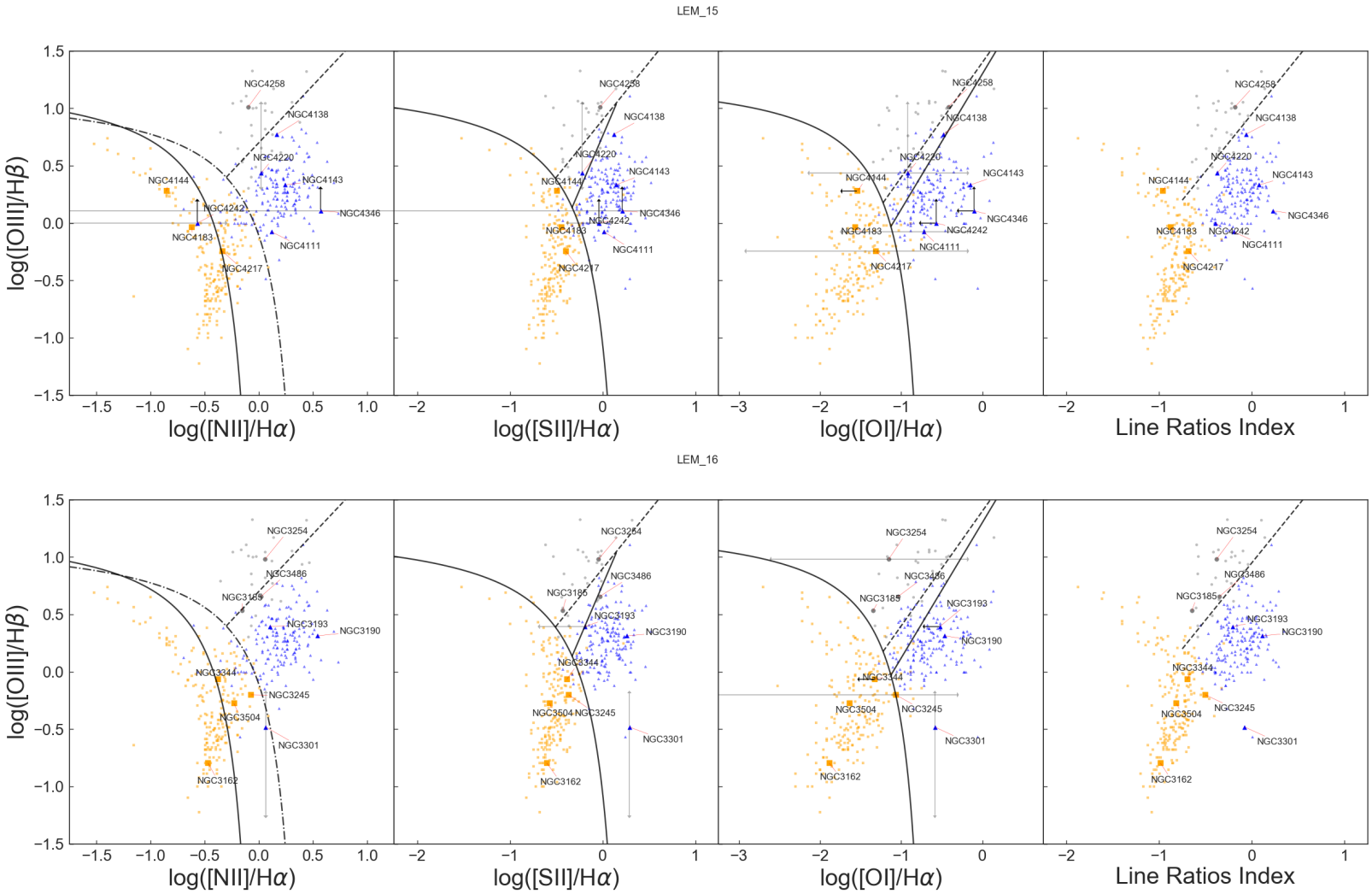

Figure C.1: BPT emission line diagnostic diagrams for the LeMMINGs data blocks LEM15 (top) and LEM16 (bottom). Going from left to right, the panels show the log[O III]/Hβ ratio against (panel 1) log[N II]/Hα, (2) log[S II]/Hα, (3) log[O I]/Hα and (4) Line Ratios Index. The black lines are the Kewley et al. (2001) diagnostic lines, the dot-dashed line in the first panel shows the Kewley et al. (2006) maximum starburst line and the dashed lines show the Buttiglione et al. (2010) classification between LINERs and Seyferts. The BPT diagram for the whole Palomar sample, re-classified in Section 2 is shown in the background, with HII galaxies in orange, LINERs in blue and Seyferts in grey. This colour scheme is used for the 10 objects in each of the blocks above, including errors given as black arrows for upper/lower limts, and grey arrows for measurement uncertainties from the Ho et al. (1997a) emission line ratio data. Absorption Line Galaxies are not shown for either block, due to their lack of measured emission line ratios, however, this affects neither of these blocks.

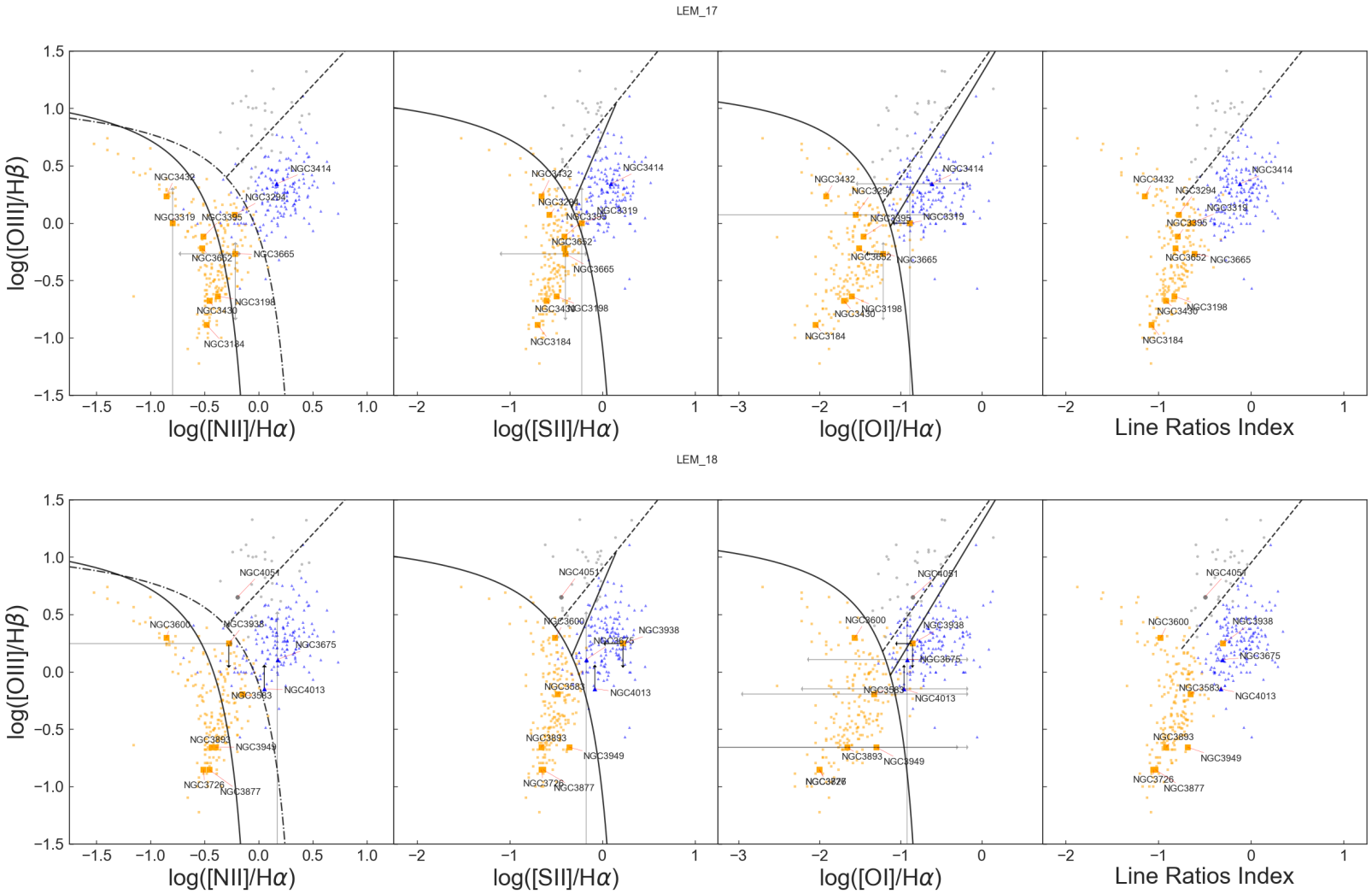

Figure C.1: BPT emission line diagnostic diagrams for the LeMMINGs data blocks LEM17 (top) and LEM18 (bottom). Going from left to right, the panels show the log[O III]/Hβ ratio against (panel 1) log[N II]/Hα, (2) log[S II]/Hα, (3) log[O I]/Hα and (4) Line Ratios Index. The black lines are the Kewley et al. (2001) diagnostic lines, the dot-dashed line in the first panel shows the Kewley et al. (2006) maximum starburst line and the dashed lines show the Buttiglione et al. (2010) classification between LINERs and Seyferts. The BPT diagram for the whole Palomar sample, re-classified in Section 2 is shown in the background, with HII galaxies in orange, LINERs in blue and Seyferts in grey. This colour scheme is used for the 10 objects in each of the blocks above, including errors given as black arrows for upper/lower limts, and grey arrows for measurement uncertainties from the Ho et al. (1997a) emission line ratio data. Absorption Line Galaxies are not shown for either block, due to their lack of measured emission line ratios, however, this affects neither of these blocks.

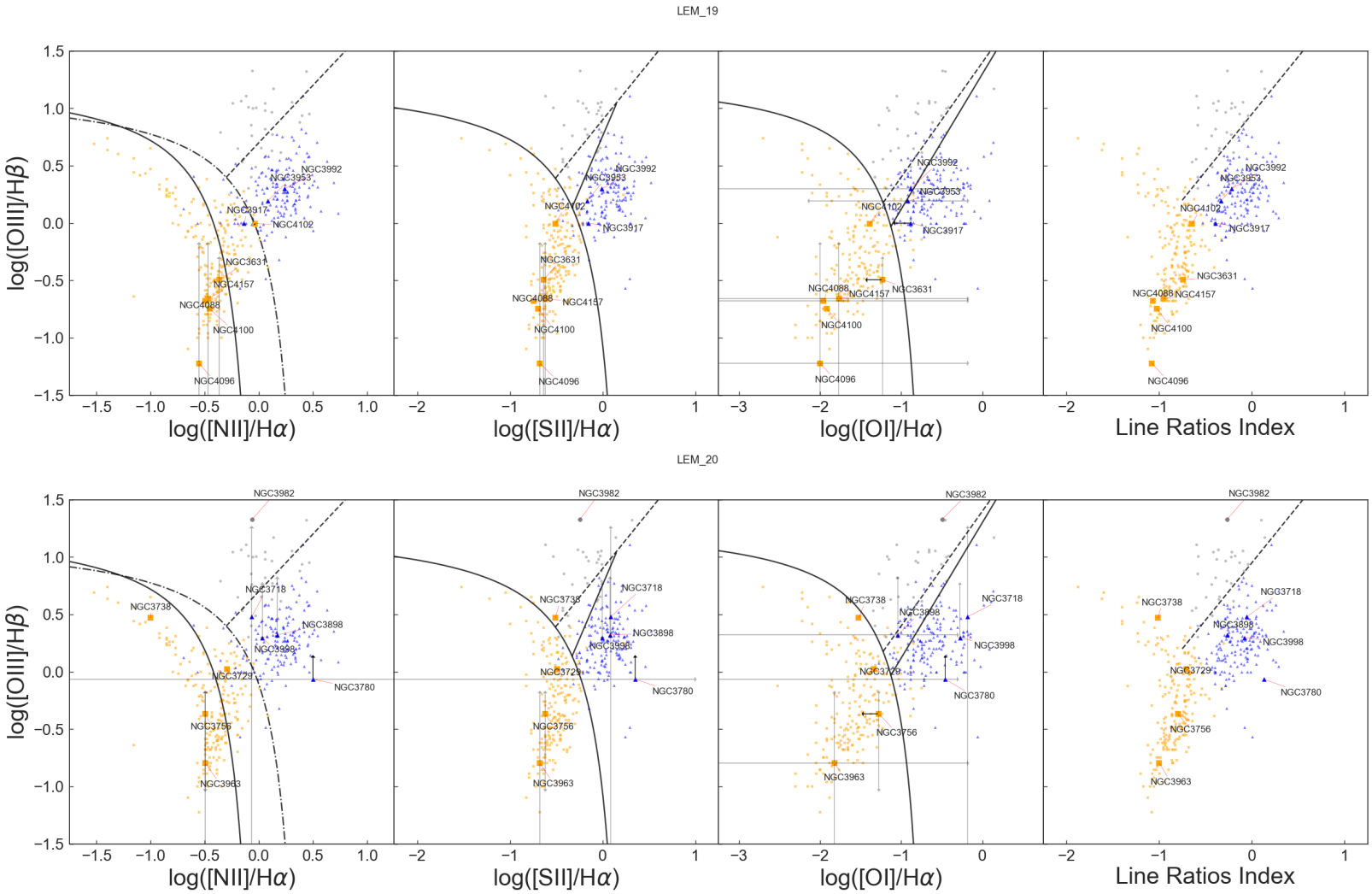

Figure C.1: BPT emission line diagnostic diagrams for the LeMMINGs data blocks LEM19 (top) and LEM20 (bottom). Going from left to right, the panels show the log[O III]/Hβ ratio against (panel 1) log[N II]/Hα, (2) log[S II]/Hα, (3) log[O I]/Hα and (4) Line Ratios Index. The black lines are the Kewley et al. (2001) diagnostic lines, the dot-dashed line in the first panel shows the Kewley et al. (2006) maximum starburst line and the dashed lines show the Buttiglione et al. (2010) classification between LINERs and Seyferts. The BPT diagram for the whole Palomar sample, re-classified in Section 2 is shown in the background, with HII galaxies in orange, LINERs in blue and Seyferts in grey. This colour scheme is used for the 10 objects in each of the blocks above, including errors given as black arrows for upper/lower limts, and grey arrows for measurement uncertainties from the Ho et al. (1997a) emission line ratio data. Absorption Line Galaxies are not shown for either block, due to their lack of measured emission line ratios. For LEM19, this accounts for the galaxy NGC 4026 not being present, and for LEM20, explains the lack of data for NGC 3838.

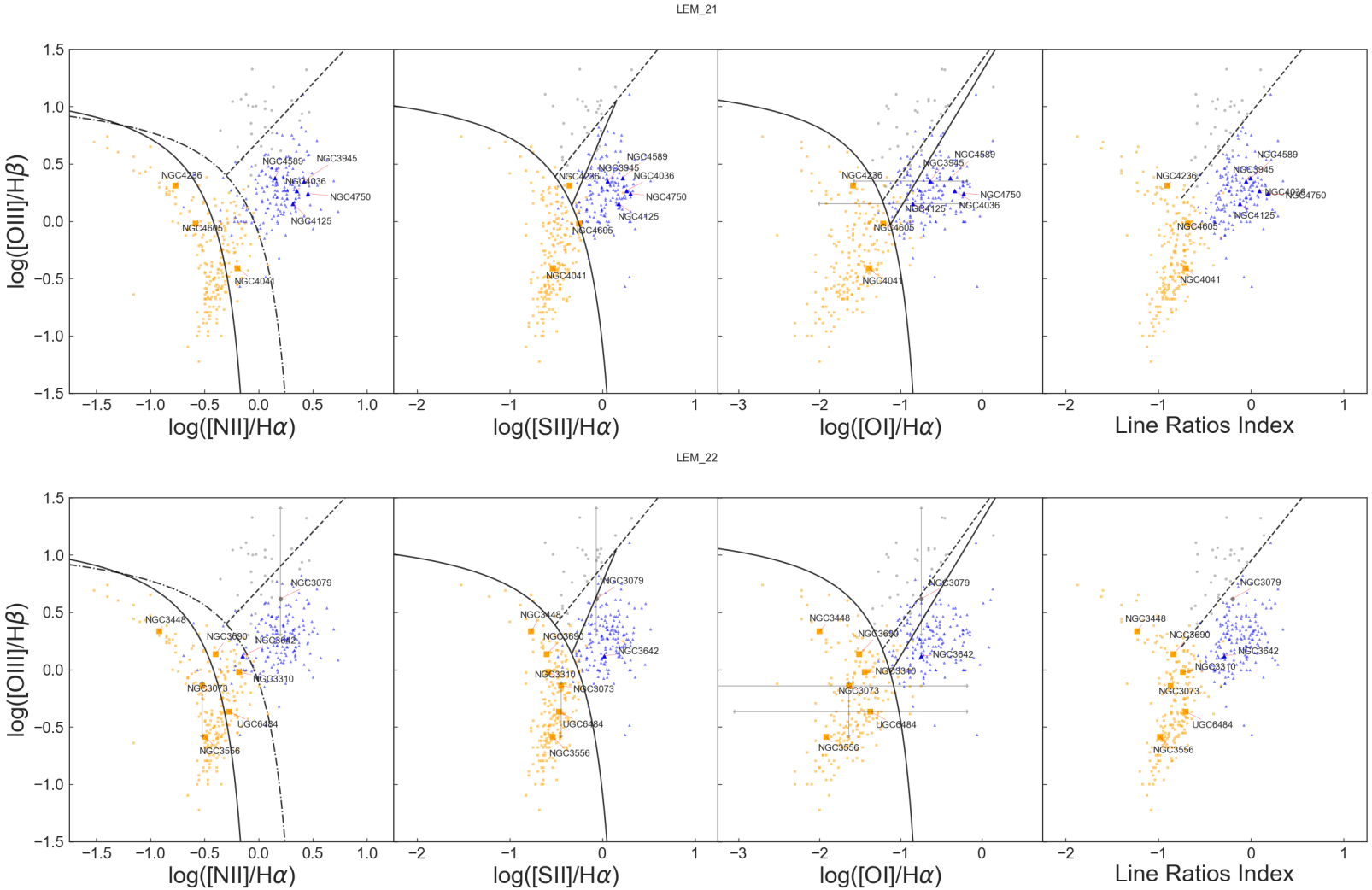

Figure C.1: BPT emission line diagnostic diagrams for the LeMMINGs data blocks LEM21(top) and LEM22 (bottom). Going from left to right, the panels show the log[O III]/Hβ ratio against (panel 1) log[N II]/Hα, (2) log[S II]/Hα, (3) log[O I]/Hα and (4) Line Ratios Index. The black lines are the Kewley et al. (2001) diagnostic lines, the dot-dashed line in the first panel shows the Kewley et al. (2006) maximum starburst line and the dashed lines show the Buttiglione et al. (2010) classification between LINERs and Seyferts. The BPT diagram for the whole Palomar sample, re-classified in Section 2 is shown in the background, with HII galaxies in orange, LINERs in blue and Seyferts in grey. This colour scheme is used for the 10 objects in each of the blocks above, including errors given as black arrows for upper/lower limts, and grey arrows for measurement uncertainties from the Ho et al. (1997a) emission line ratio data. Absorption Line Galaxies are not shown for either block, due to their lack of measured emission line ratios. For LEM21, this accounts for the galaxies NGC 4291 and NGC 4648 not being present, and for LEM22, explains the lack of data for NGC 3610 and NGC 3613.

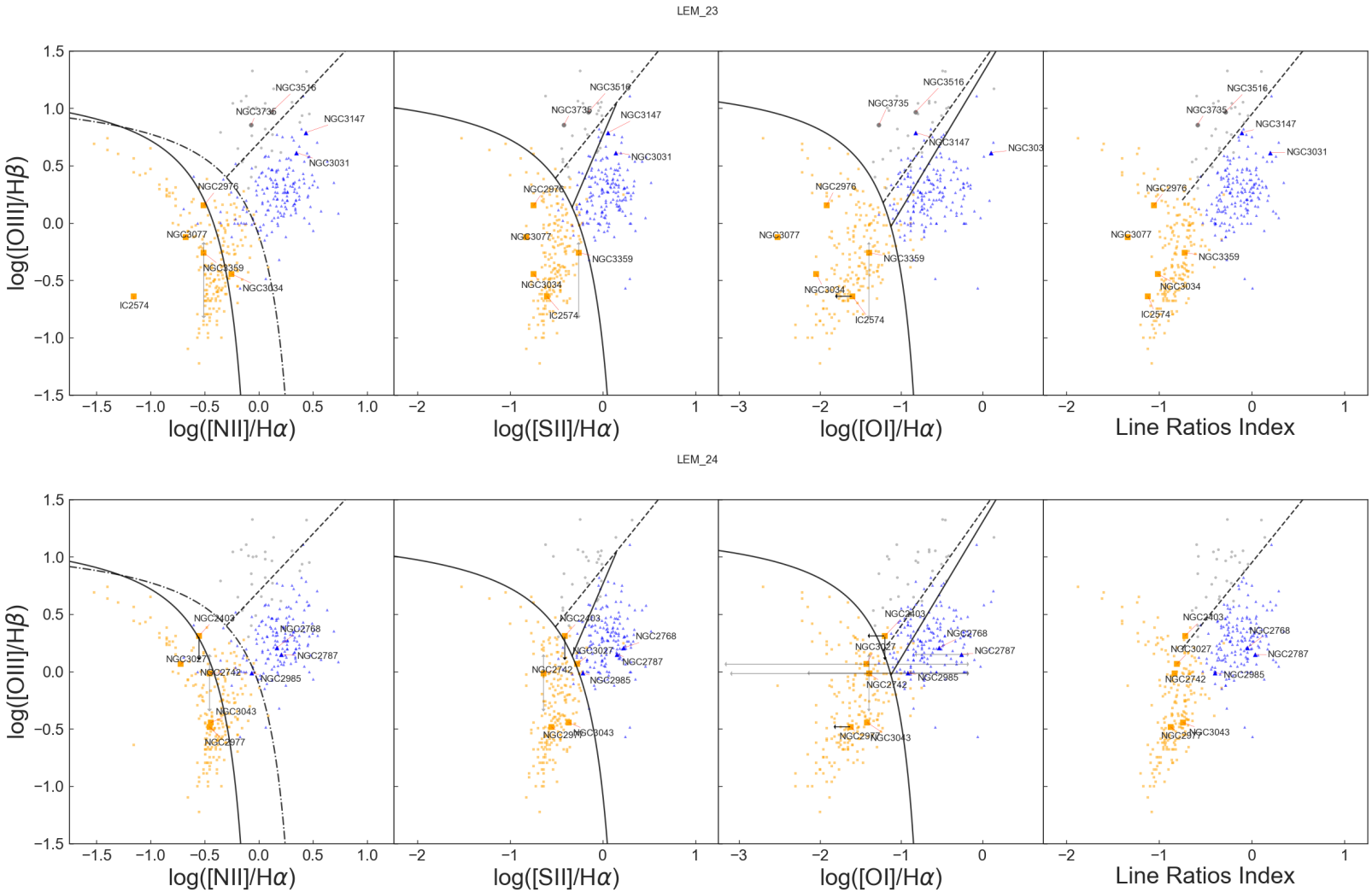

Figure C.1: BPT emission line diagnostic diagrams for the LeMMINGs data blocks LEM23 (top) and LEM24 (bottom). Going from left to right, the panels show the log[O III]/Hβ ratio against (panel 1) log[N II]/Hα, (2) log[S II]/Hα, (3) log[O I]/Hα and (4) Line Ratios Index. The black lines are the Kewley et al. (2001) diagnostic lines, the dot-dashed line in the first panel shows the Kewley et al. (2006) maximum starburst line and the dashed lines show the Buttiglione et al. (2010) classification between LINERs and Seyferts. The BPT diagram for the whole Palomar sample, re-classified in Section 2 is shown in the background, with HII galaxies in orange, LINERs in blue and Seyferts in grey. This colour scheme is used for the 10 objects in each of the blocks above, including errors given as black arrows for upper/lower limts, and grey arrows for measurement uncertainties from the Ho et al. (1997a) emission line ratio data. Absorption Line Galaxies are not shown for either block, due to their lack of measured emission line ratios. For LEM23, this accounts for the galaxy NGC 3348 not being present, and for LEM24, explains the lack of data for NGC 2549 and NGC 2950.

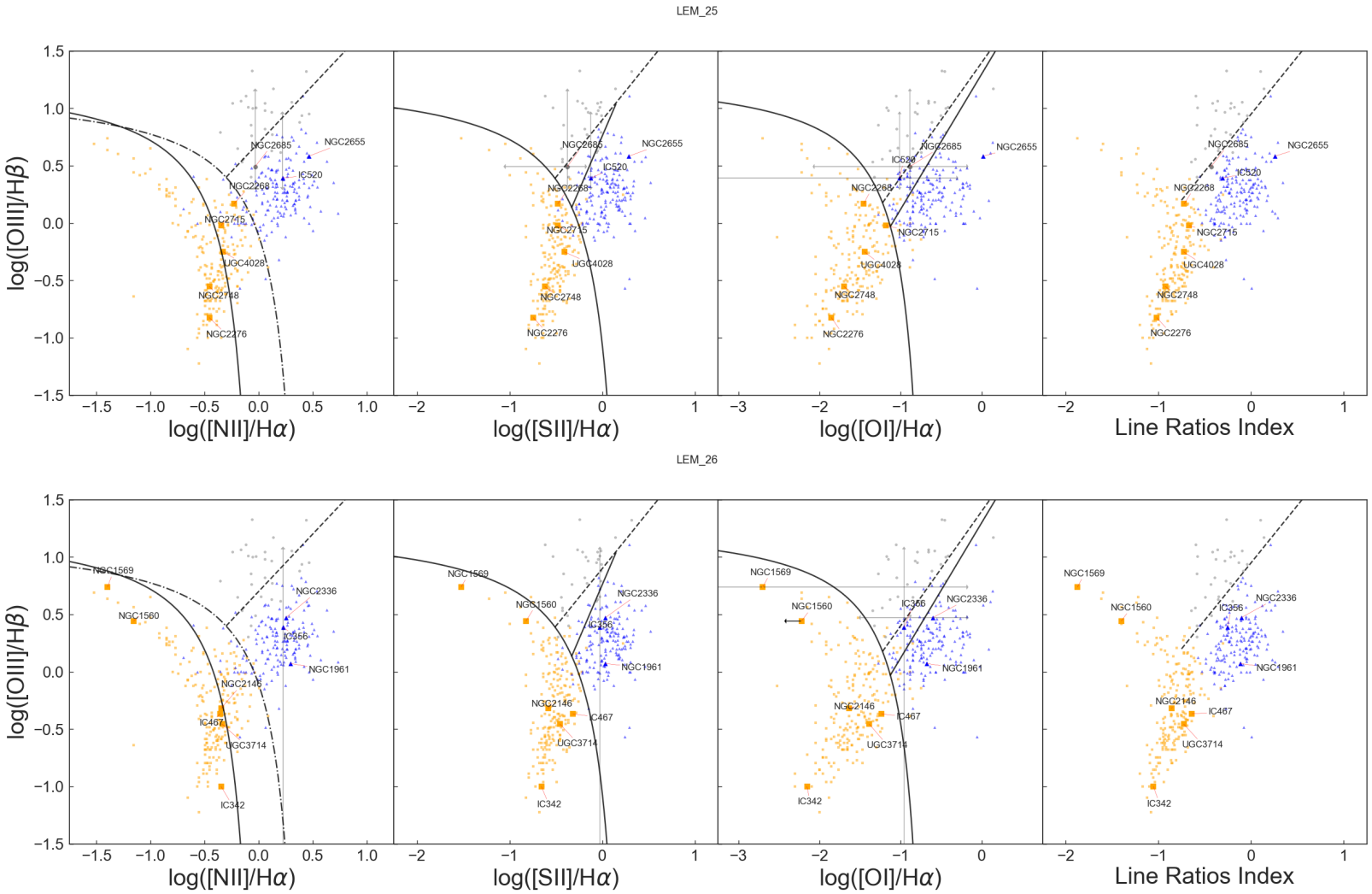

Figure C.1: BPT emission line diagnostic diagrams for the LeMMINGs data blocks LEM25 (top) and LEM26 (bottom). Going from left to right, the panels show the log[O III]/Hβ ratio against (panel 1) log[N II]/Hα, (2) log[S II]/Hα, (3) log[O I]/Hα and (4) Line Ratios Index. The black lines are the Kewley et al. (2001) diagnostic lines, the dot-dashed line in the first panel shows the Kewley et al. (2006) maximum starburst line and the dashed lines show the Buttiglione et al. (2010) classification between LINERs and Seyferts. The BPT diagram for the whole Palomar sample, re-classified in Section 2 is shown in the background, with HII galaxies in orange, LINERs in blue and Seyferts in grey. This colour scheme is used for the 10 objects in each of the blocks above, including errors given as black arrows for upper/lower limts, and grey arrows for measurement uncertainties from the Ho et al. (1997a) emission line ratio data. Absorption Line Galaxies are not shown for either block, due to their lack of measured emission line ratios. For LEM25, this accounts for the galaxies NGC 2300 and NGC 2634 not being present, and for LEM26, explains the lack of data for NGC 2366.

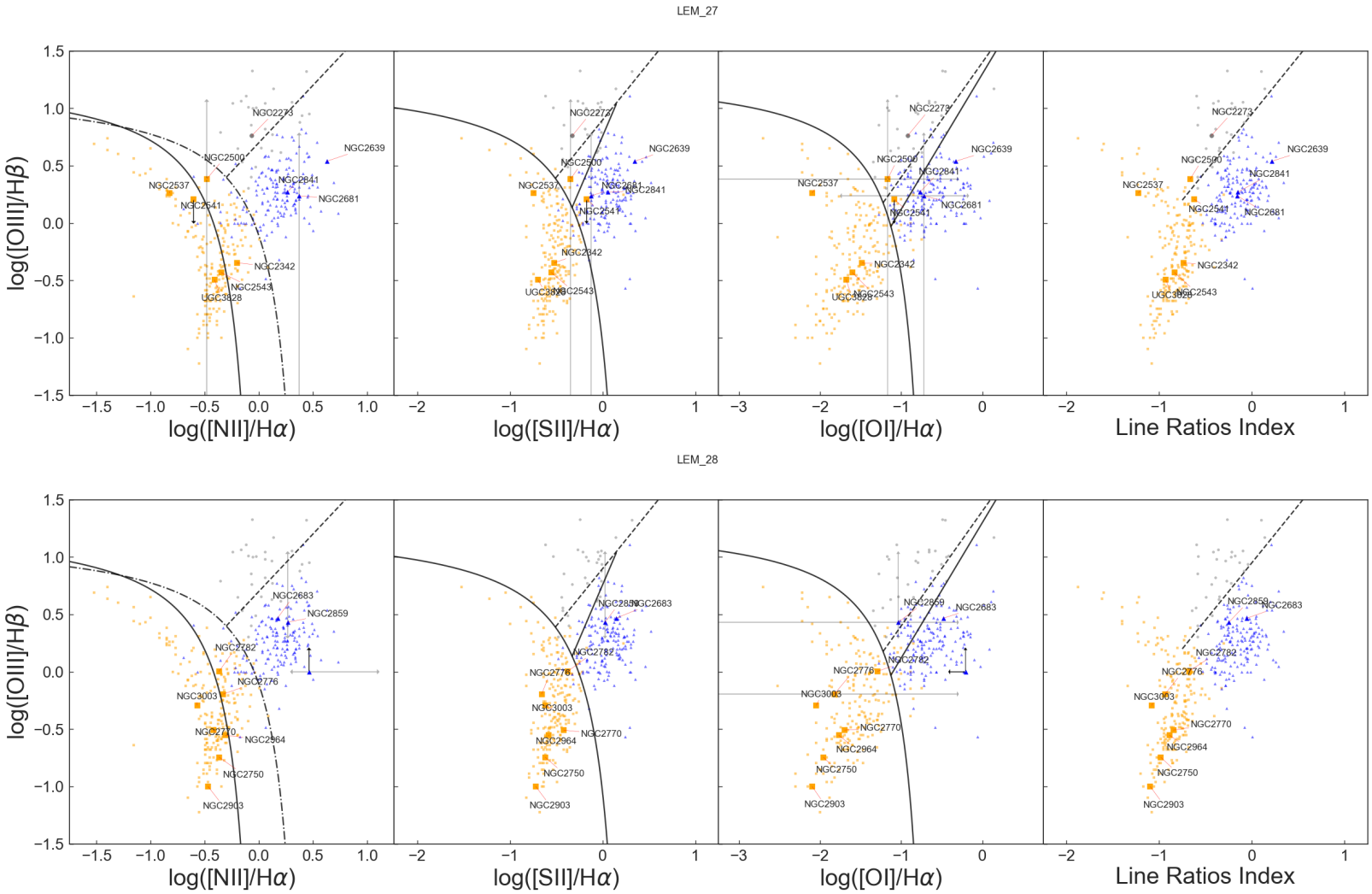

Figure C.1: BPT emission line diagnostic diagrams for the LeMMINGs data blocks LEM27 (top) and LEM28 (bottom). Going from left to right, the panels show the log[O III]/Hβ ratio against (panel 1) log[N II]/Hα, (2) log[S II]/Hα, (3) log[O I]/Hα and (4) Line Ratios Index. The black lines are the Kewley et al. (2001) diagnostic lines, the dot-dashed line in the first panel shows the Kewley et al. (2006) maximum starburst line and the dashed lines show the Buttiglione et al. (2010) classification between LINERs and Seyferts. The BPT diagram for the whole Palomar sample, re-classified in Section 2 is shown in the background, with HII galaxies in orange, LINERs in blue and Seyferts in grey. This colour scheme is used for the 10 objects in each of the blocks above, including errors given as black arrows for upper/lower limts, and grey arrows for measurement uncertainties from the Ho et al. (1997a) emission line ratio data. Absorption Line Galaxies are not shown for either block, due to their lack of measured emission line ratios, however, this affects neither of these blocks.

Appendix D

X-Ray Spectra of LeMMINGs Shallow Survey

D.1 X−Ray Images and spectra of the LeMMINGs Shallow sample

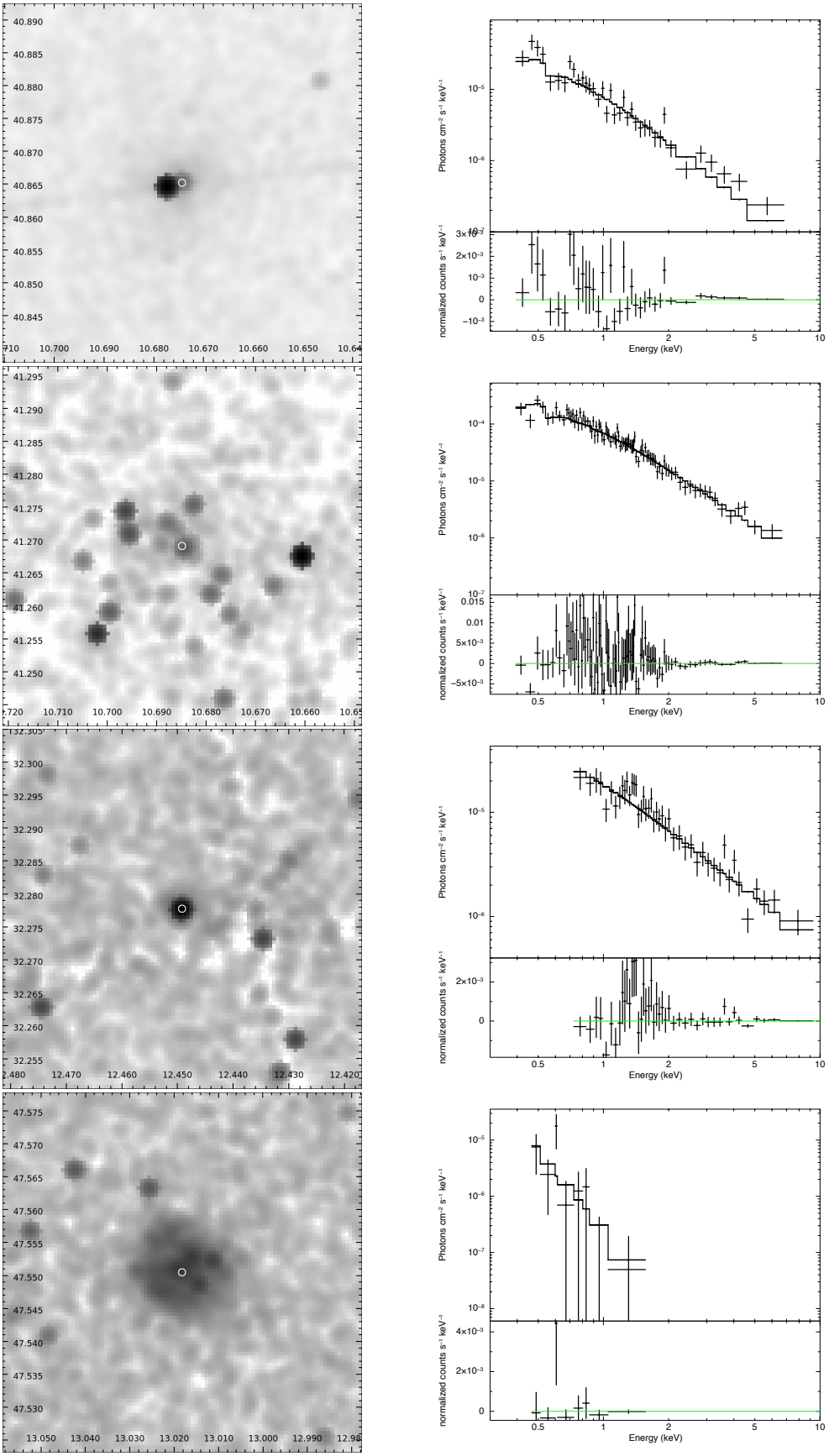

Figure D.1: Images and spectra of NGC 221 (top), NGC 224 (top-middle), NGC 266 (bottom-middle), NGC 278 (bottom)

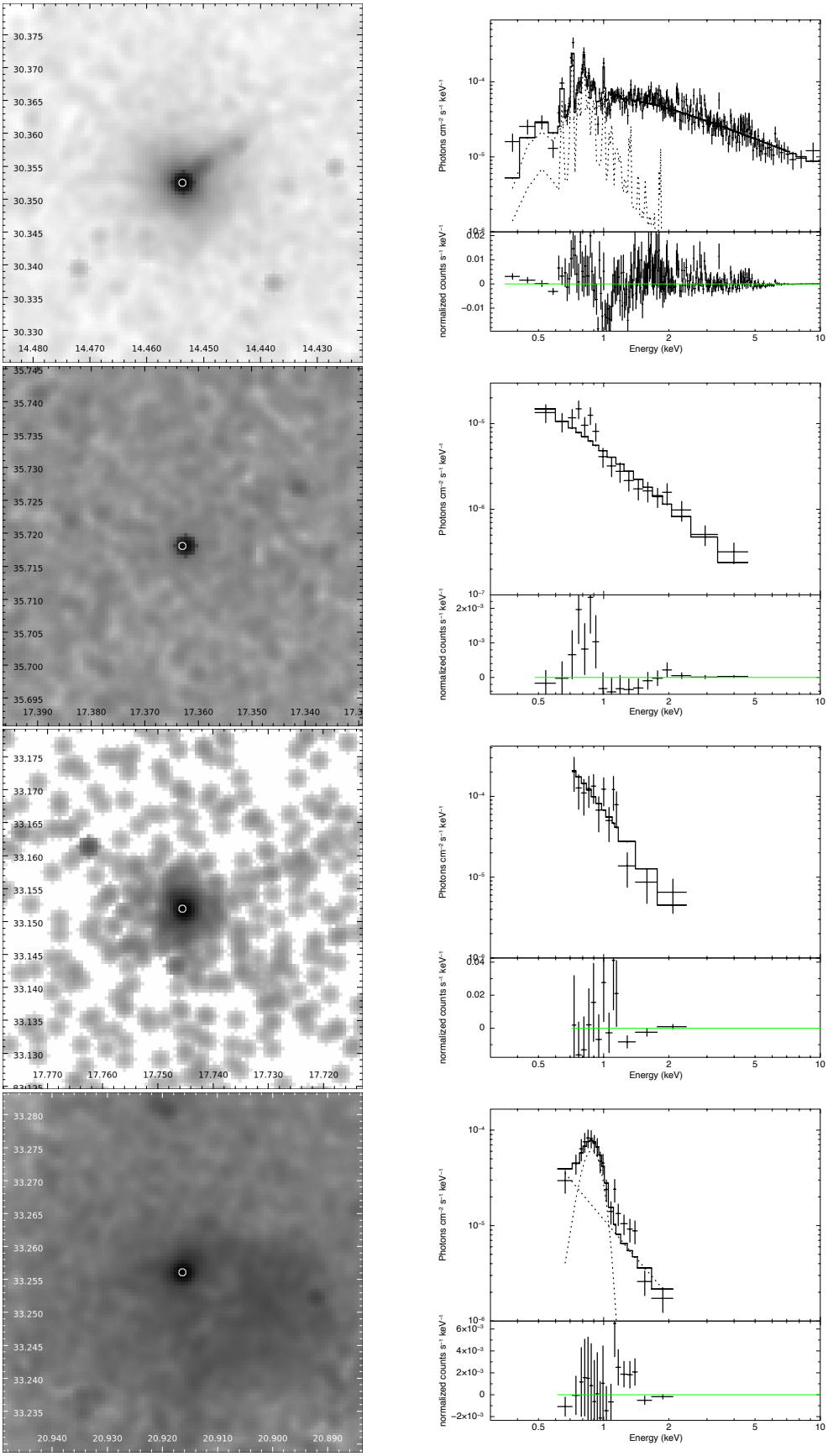

Figure D.1: Images and spectra of NGC 315 (top), NGC 404 (top-middle), NGC 410 (bottom-middle), NGC 507 (bottom)

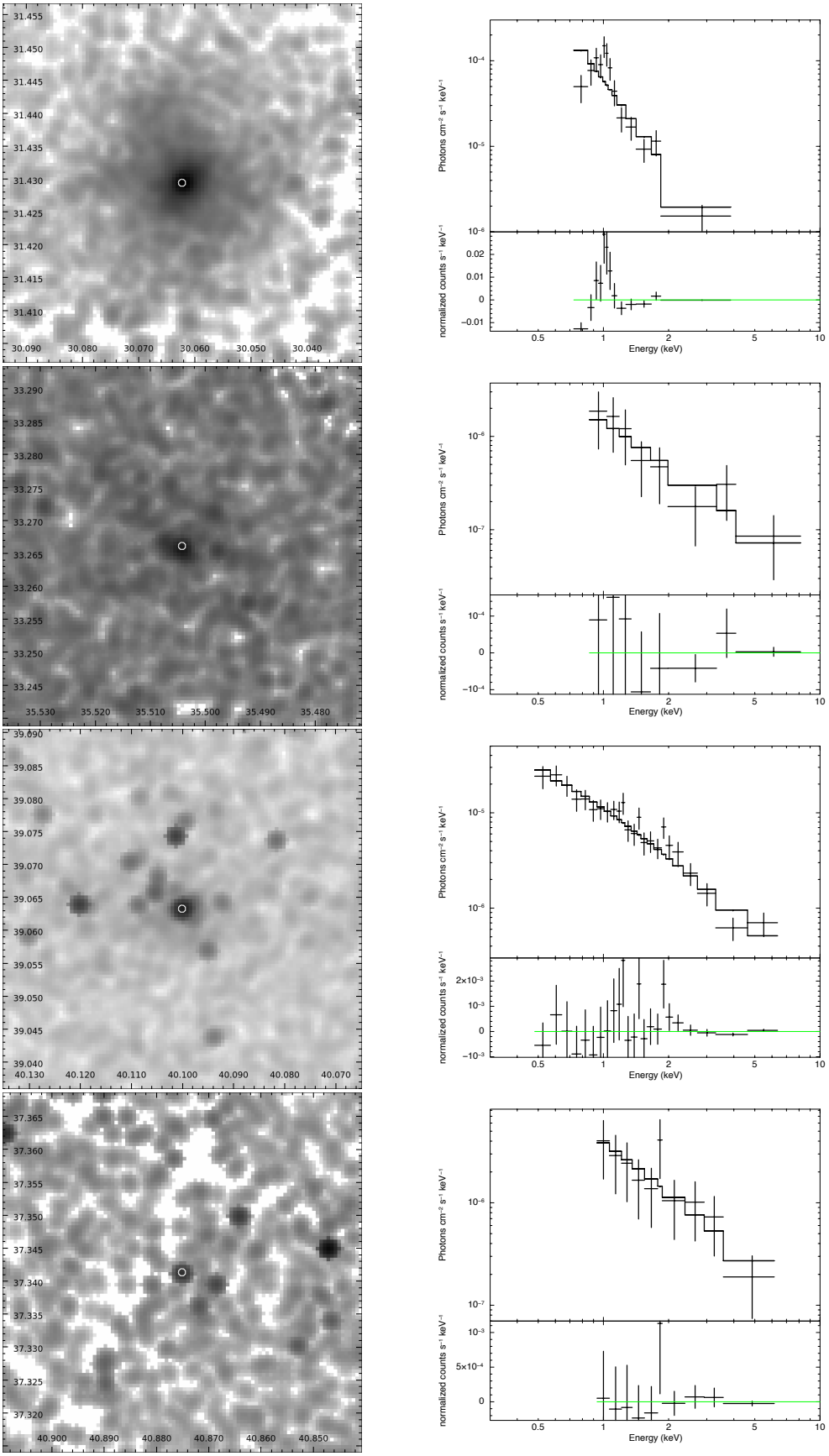

Figure D.1: Images and spectra of NGC 777 (top), NGC 890 (top-middle), NGC 1023 (bottom-middle), NGC 1058 (bottom)

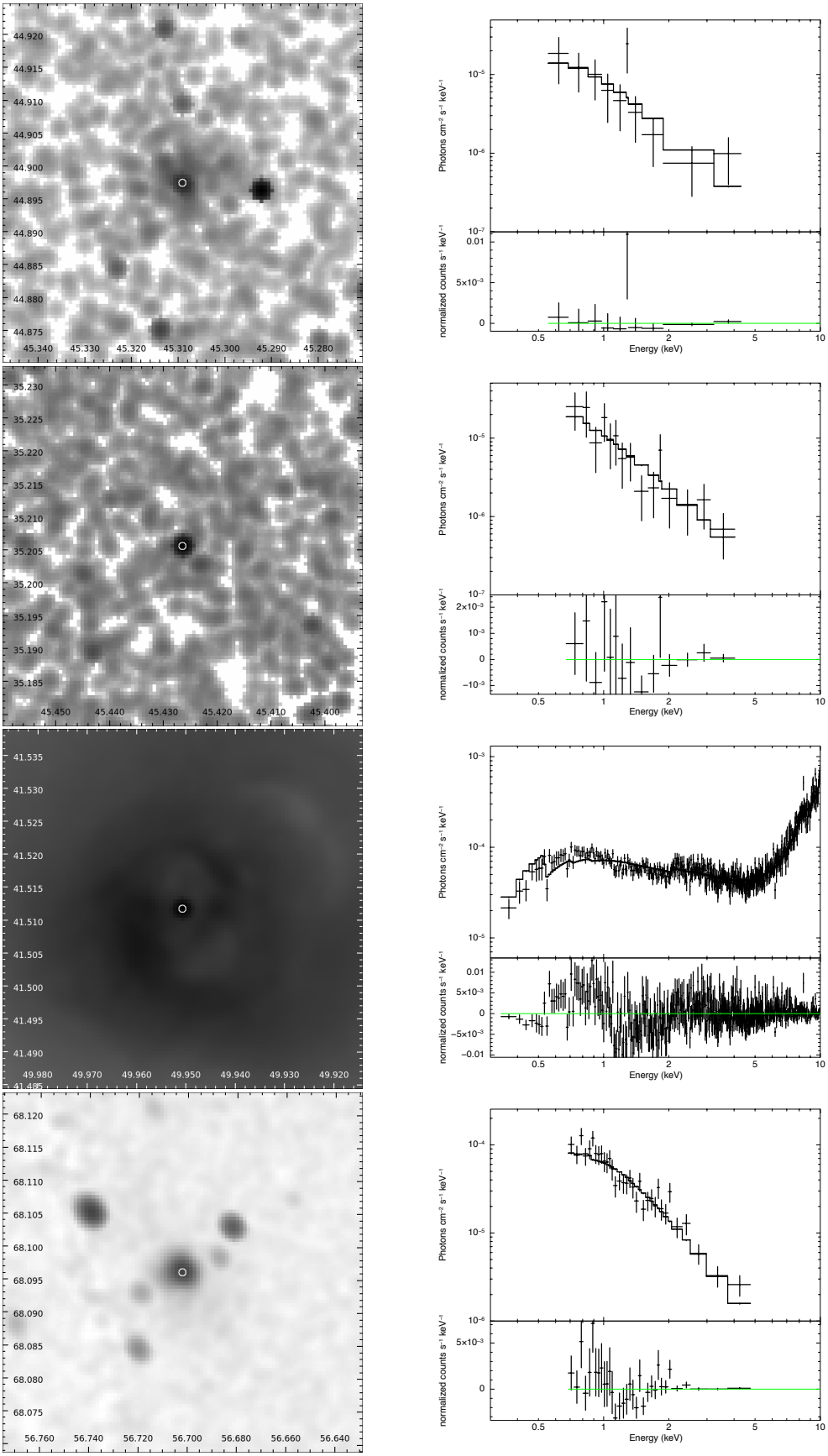

Figure D.1: Images and spectra of NGC 1161 (top), NGC 1167 (top-middle), NGC 1275 (bottom-middle), IC 342 (bottom)

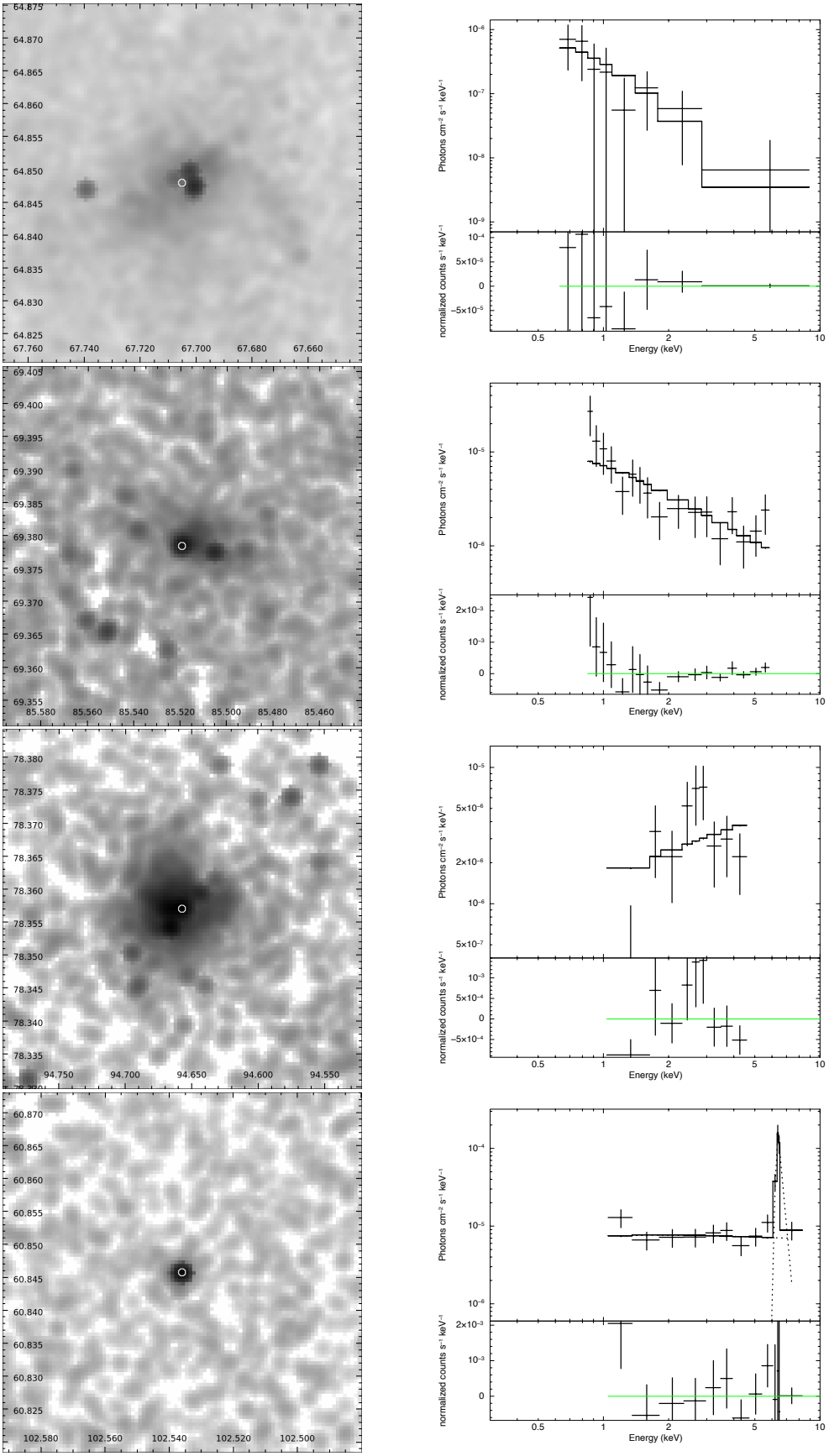

Figure D.1: Images and spectra of NGC 1569 (top), NGC 1961 (top-middle), NGC 2146 (bottom-middle), NGC 2273 (bottom)

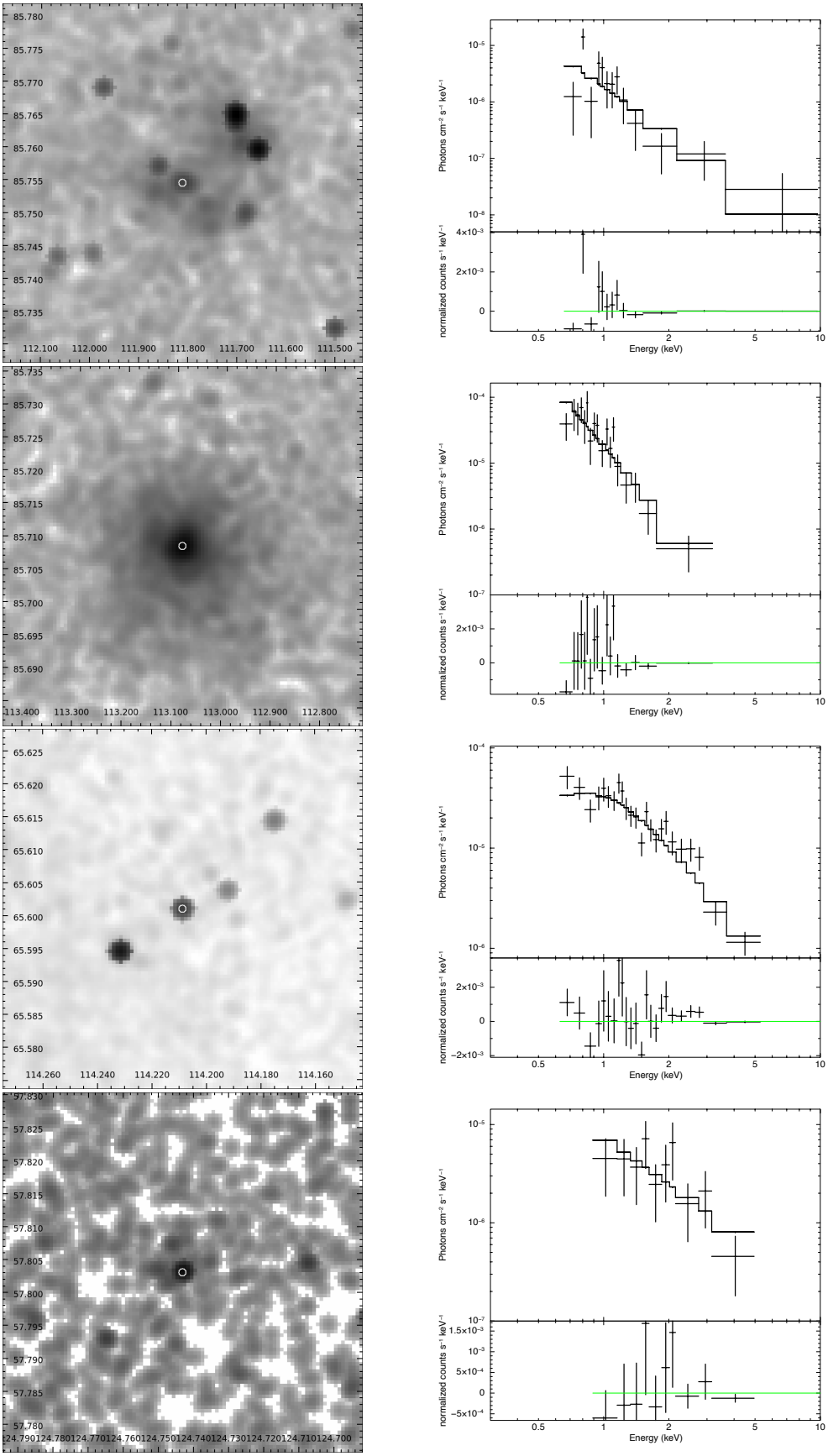

Figure D.1: Images and spectra of NGC 2276 (top), NGC 2300 (top-middle), NGC 2403 (bottom-middle), NGC 2549 (bottom)

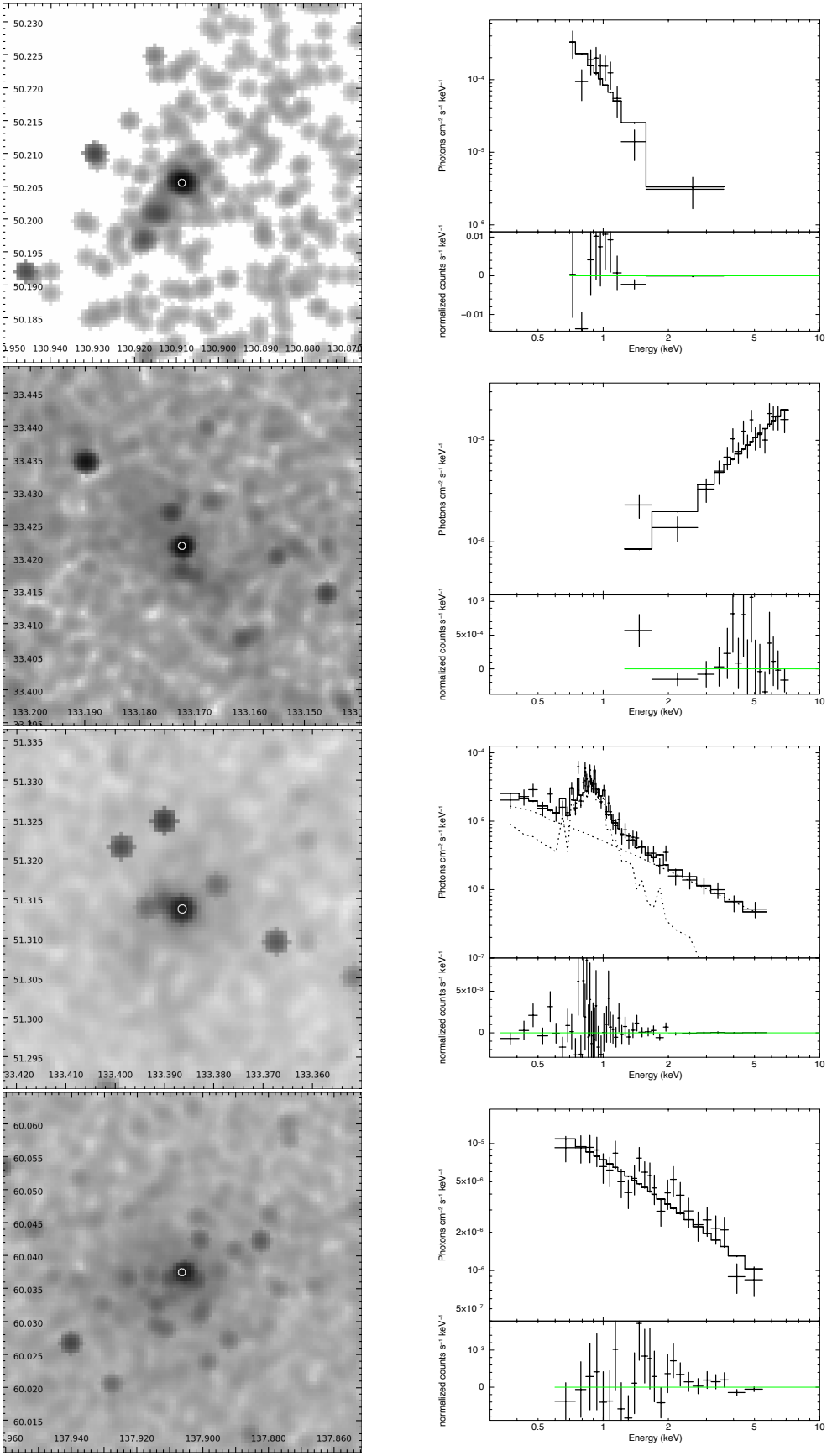

Figure D.1: Images and spectra of NGC 2639 (top), NGC 2683 (top-middle), NGC 2681 (bottom-middle), NGC 2768 (bottom)

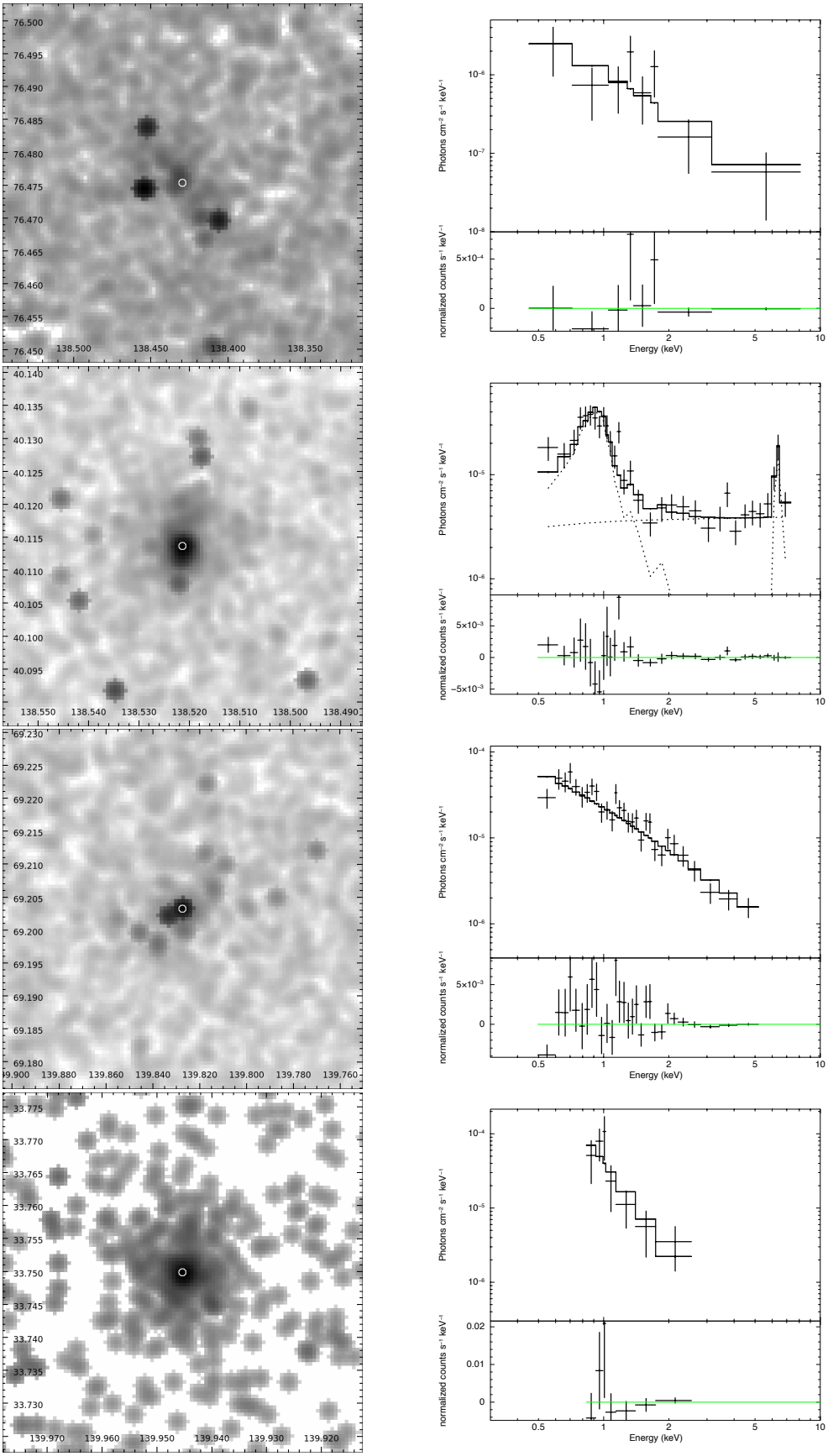

Figure D.1: Images and spectra of NGC 2748 (top), NGC 2782 (top-middle), NGC 2787 (bottom-middle), NGC 2832 (bottom)

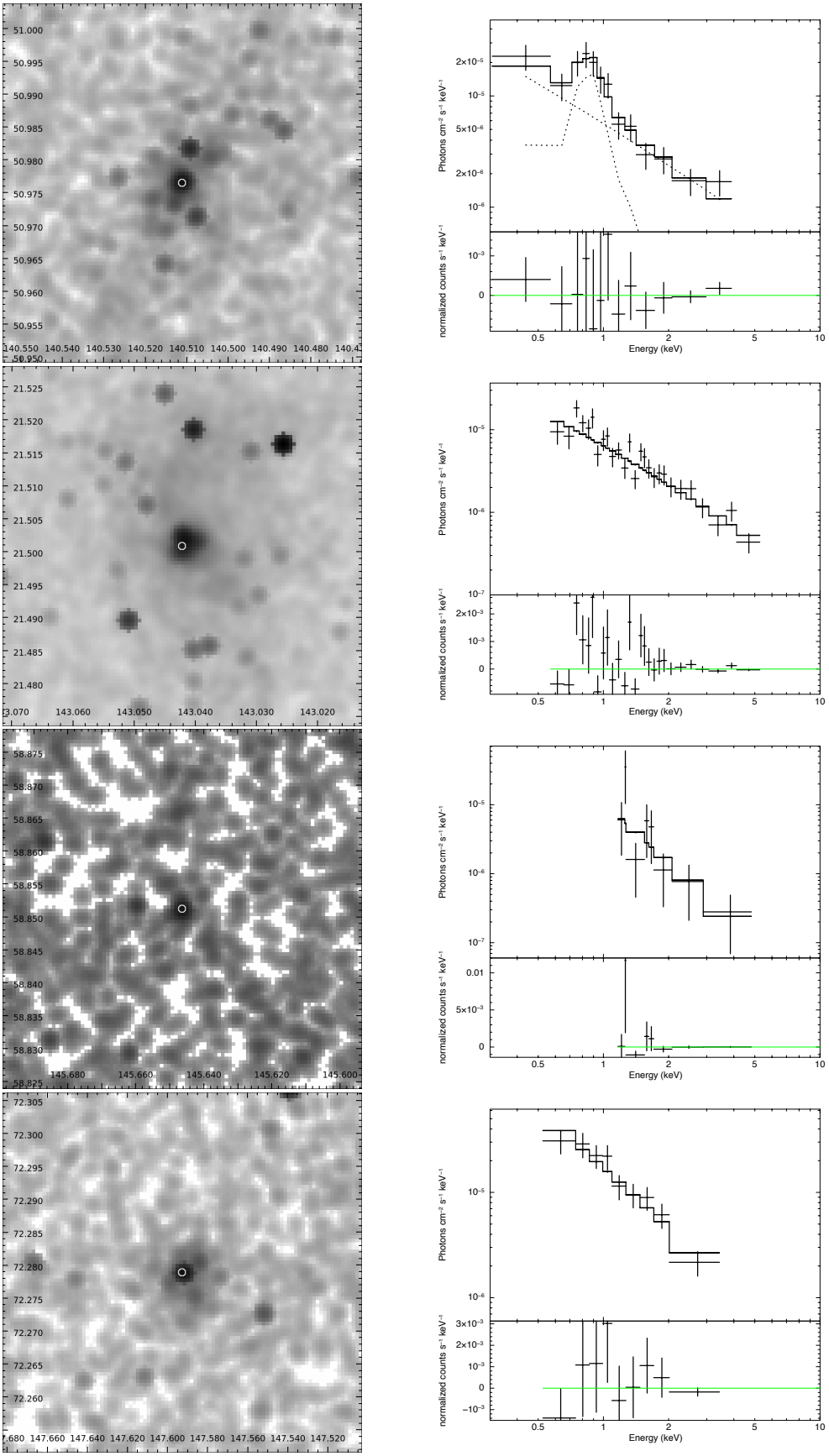

Figure D.1: Images and spectra of NGC 2841 (top), NGC 2903 (top-middle), NGC 2950 (bottom-middle), NGC 2985 (bottom)

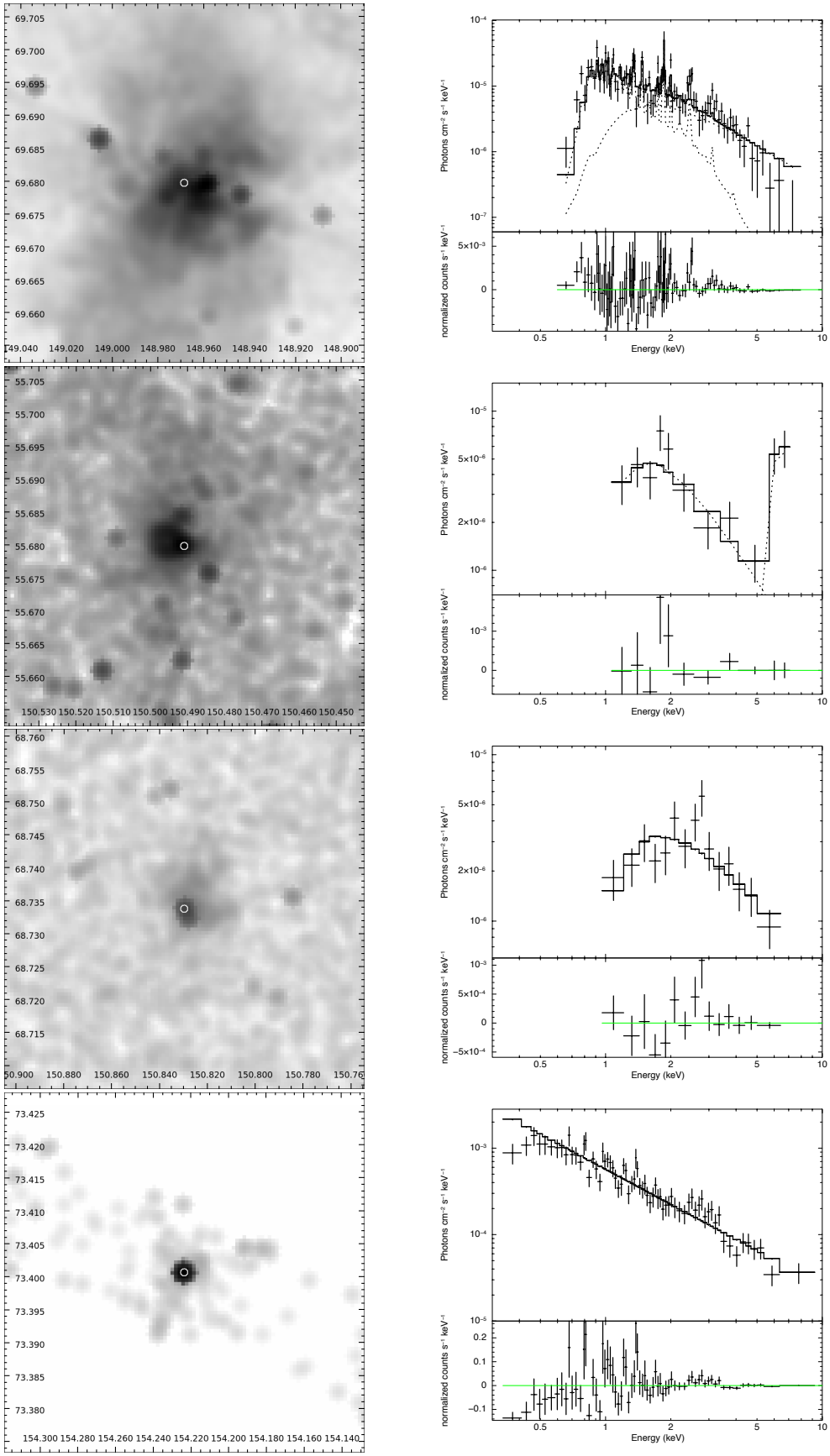

Figure D.1: Images and spectra of NGC 3034 (top), NGC 3079 (top-middle), NGC 3077 (bottom-middle), NGC 3147 (bottom)

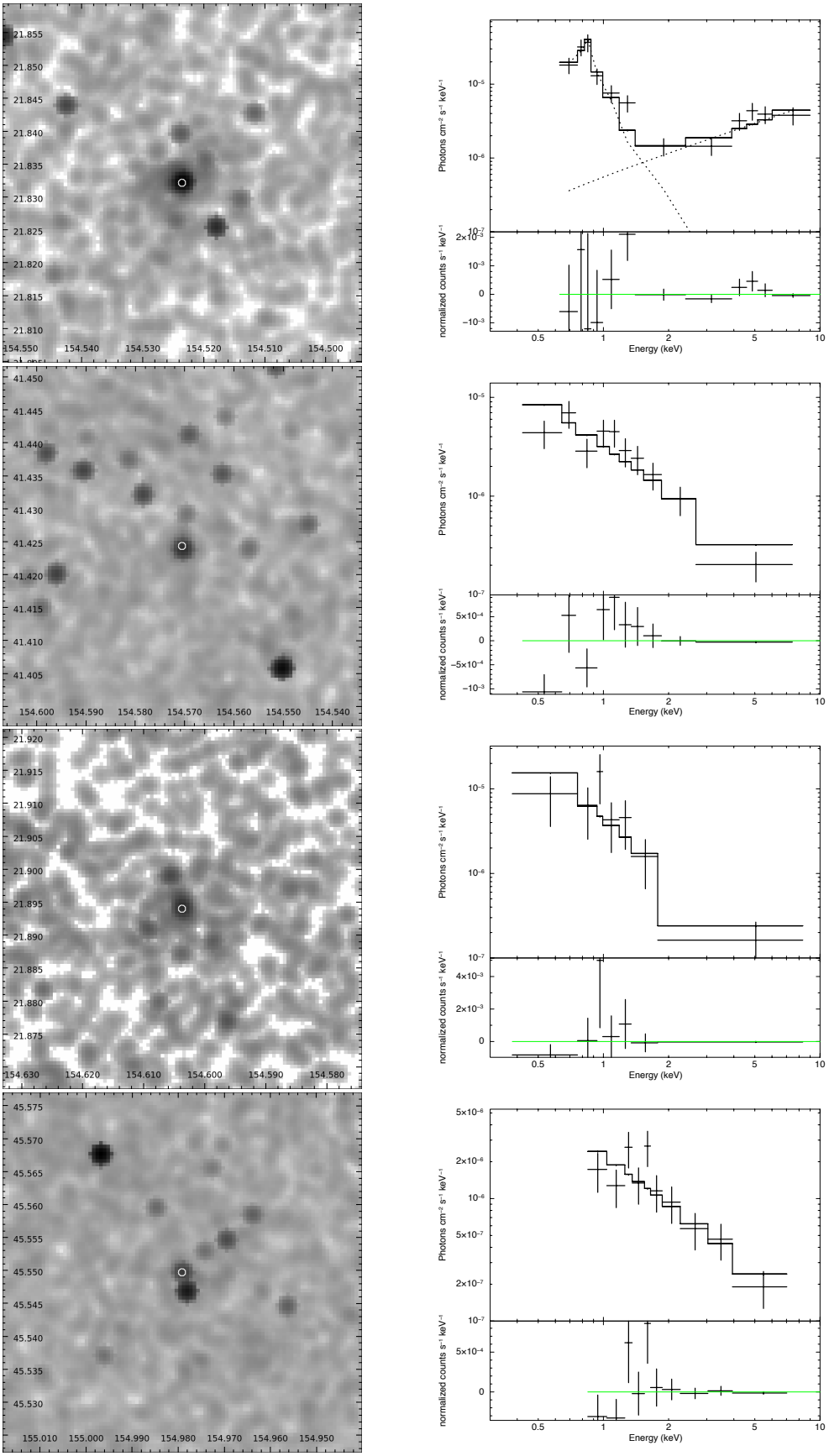

Figure D.1: Images and spectra of NGC 3190 (top), NGC 3184 (top-middle), NGC 3193 (bottom-middle), NGC 3198 (bottom)

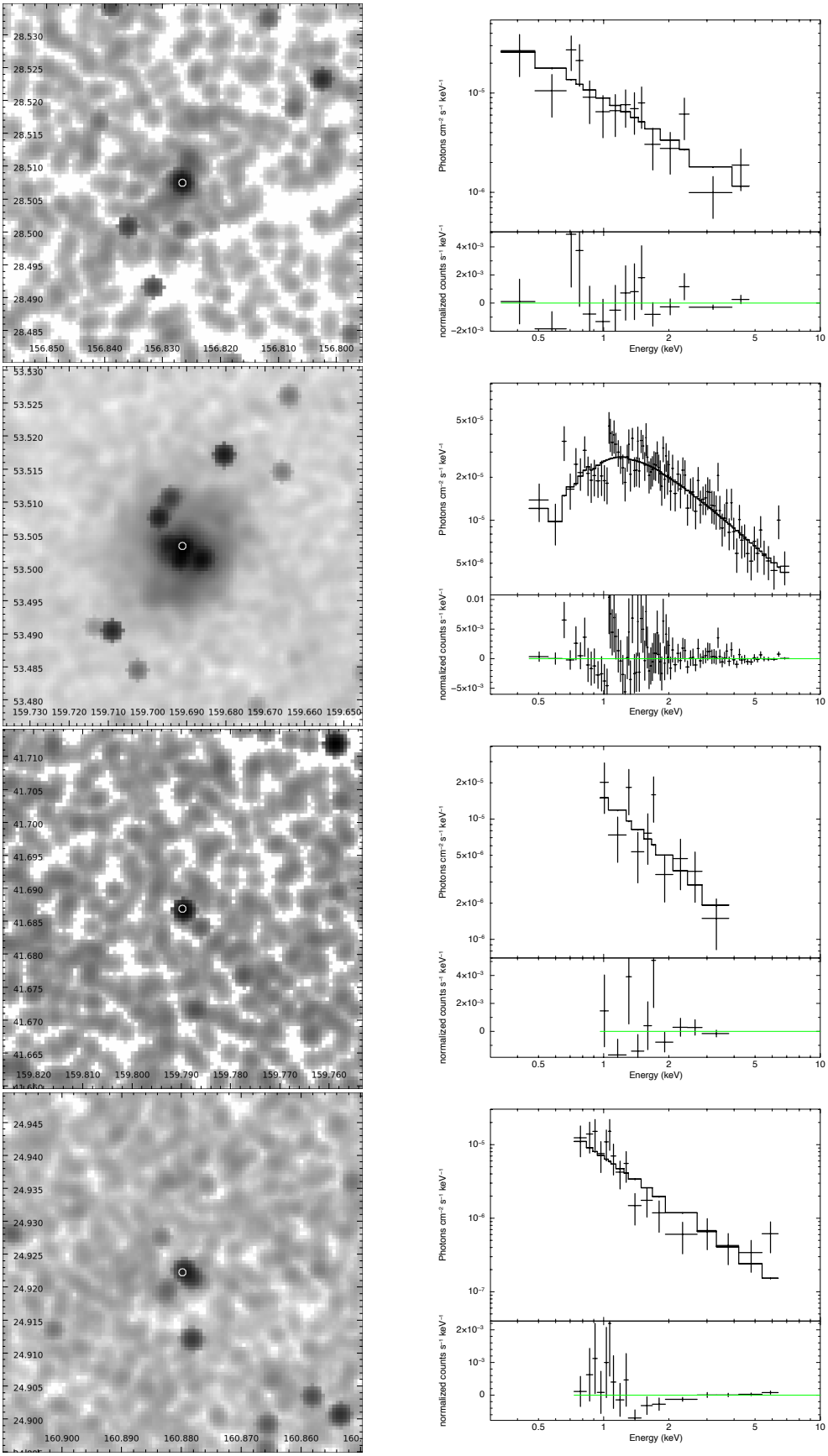

Figure D.1: Images and spectra of NGC 3245 (top), NGC 3310 (top-middle), NGC 3319 (bottom-middle), NGC 3344 (bottom)

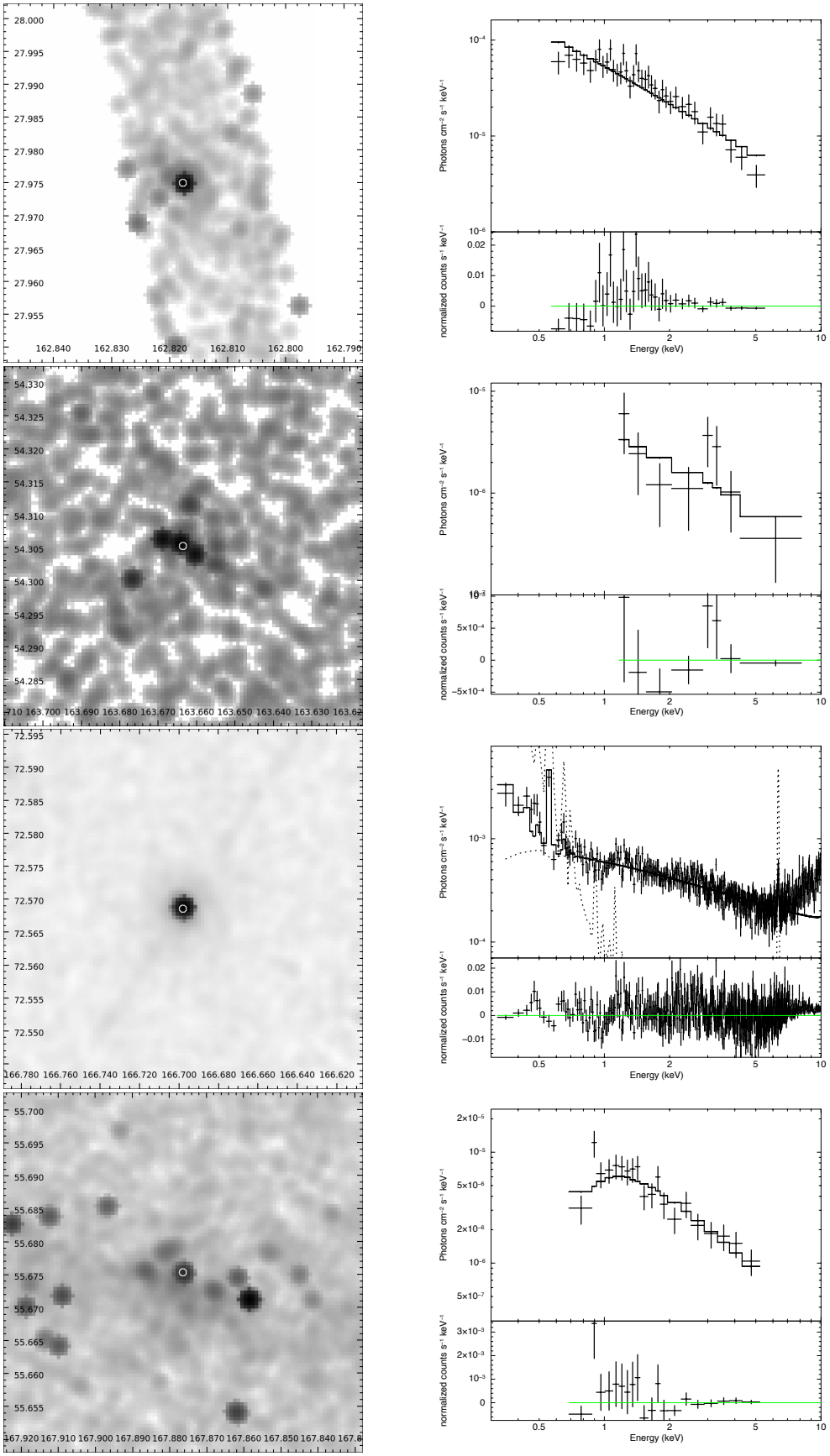

Figure D.1: Images and spectra of NGC 3414 (top), NGC 3448 (top-middle), NGC 3516 (bottom-middle), NGC 3556 (bottom)

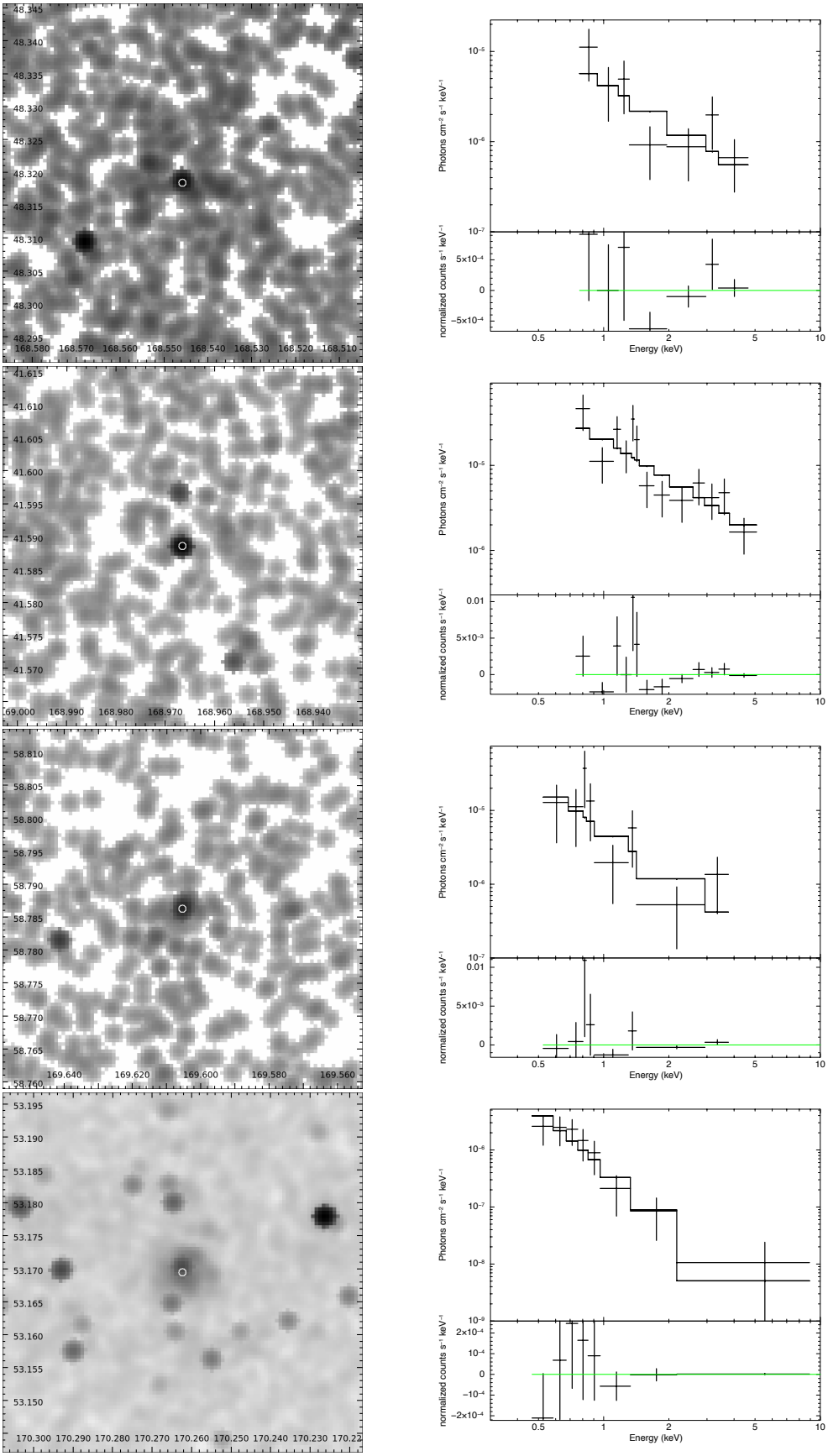

Figure D.1: Images and spectra of NGC 3583 (top), NGC 3600 (top-middle), NGC 3610 (bottom-middle), NGC 3631 (bottom)

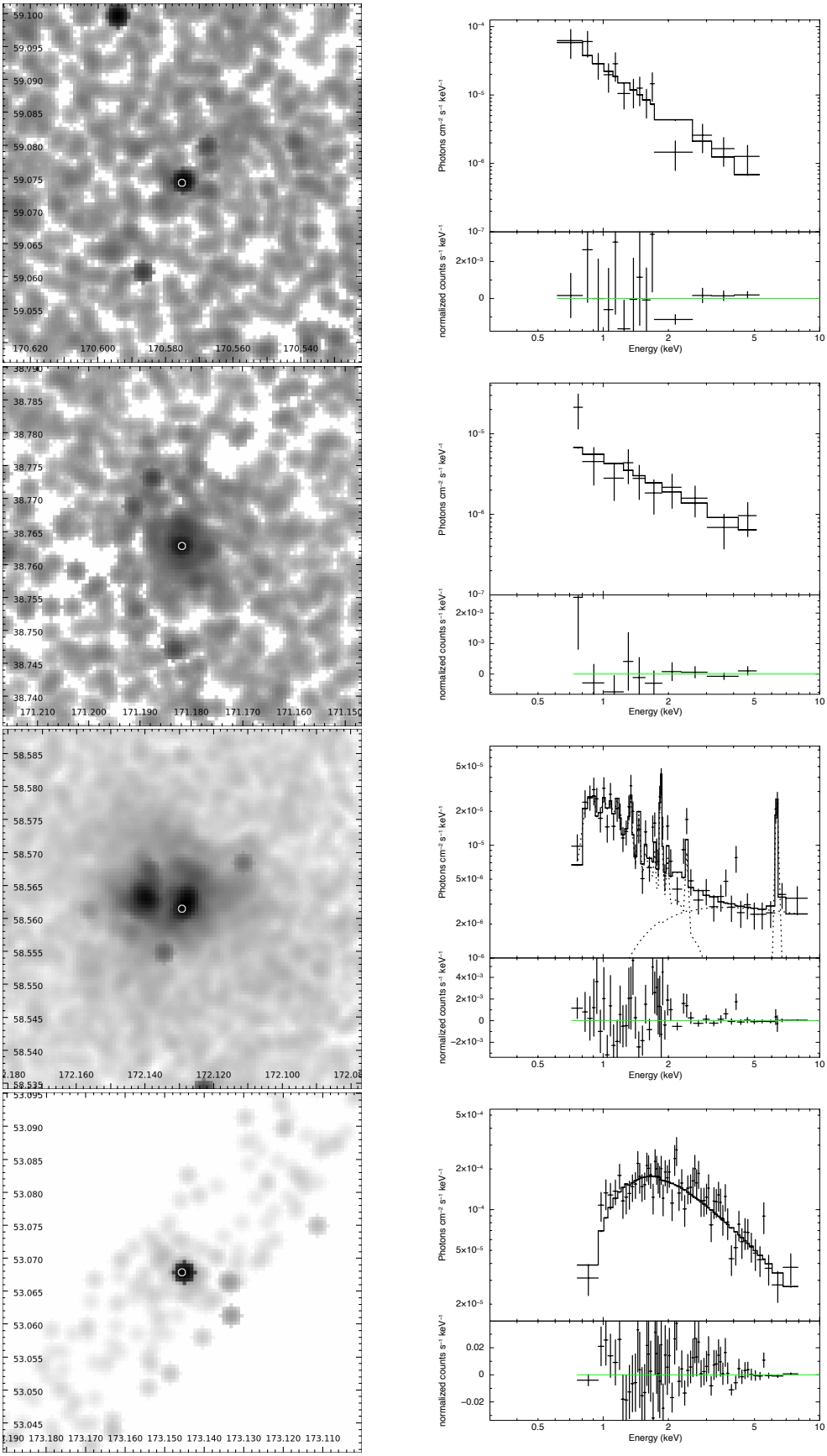

Figure D.1: Images and spectra of NGC 3642 (top), NGC 3665 (top-middle), NGC 3690 (bottom-middle), NGC 3718 (bottom)

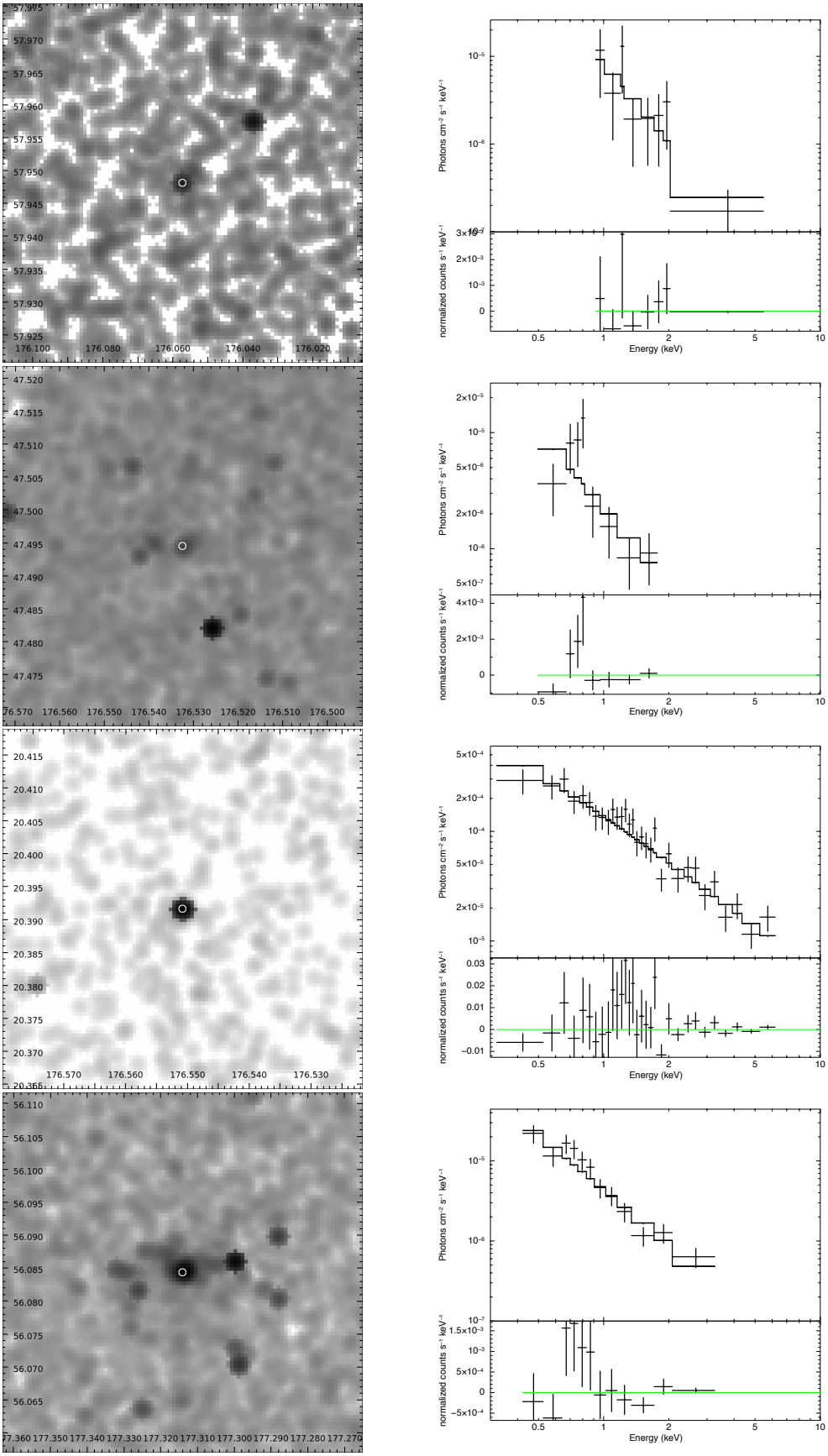

Figure D.1: Images and spectra of NGC 3838 (top), NGC 3877 (top-middle), NGC 3884 (bottom-middle), NGC 3898 (bottom)

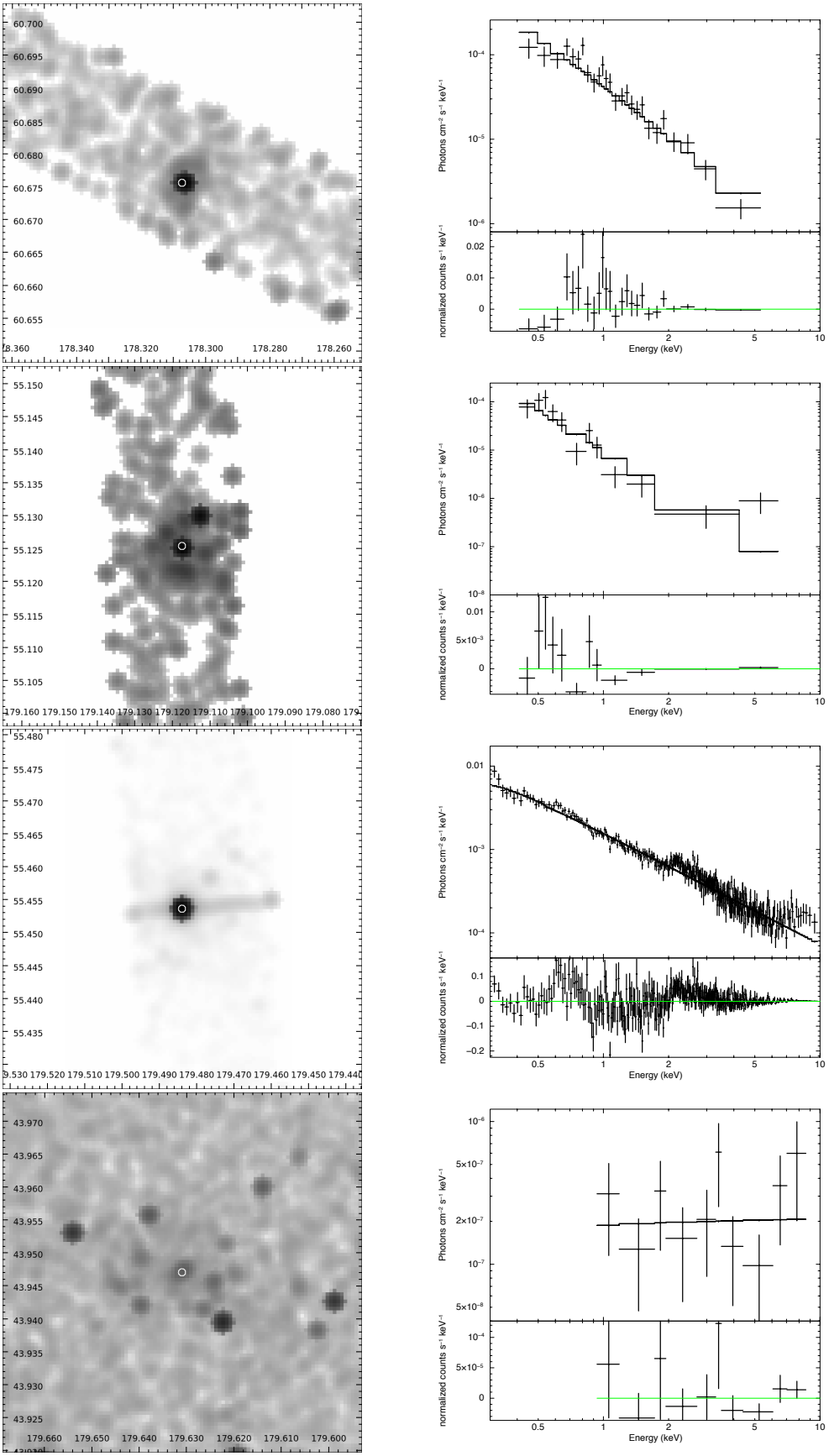

Figure D.1: Images and spectra of NGC 3945 (top), NGC 3982 (top-middle), NGC 3998 (bottom-middle), NGC 4013 (bottom)

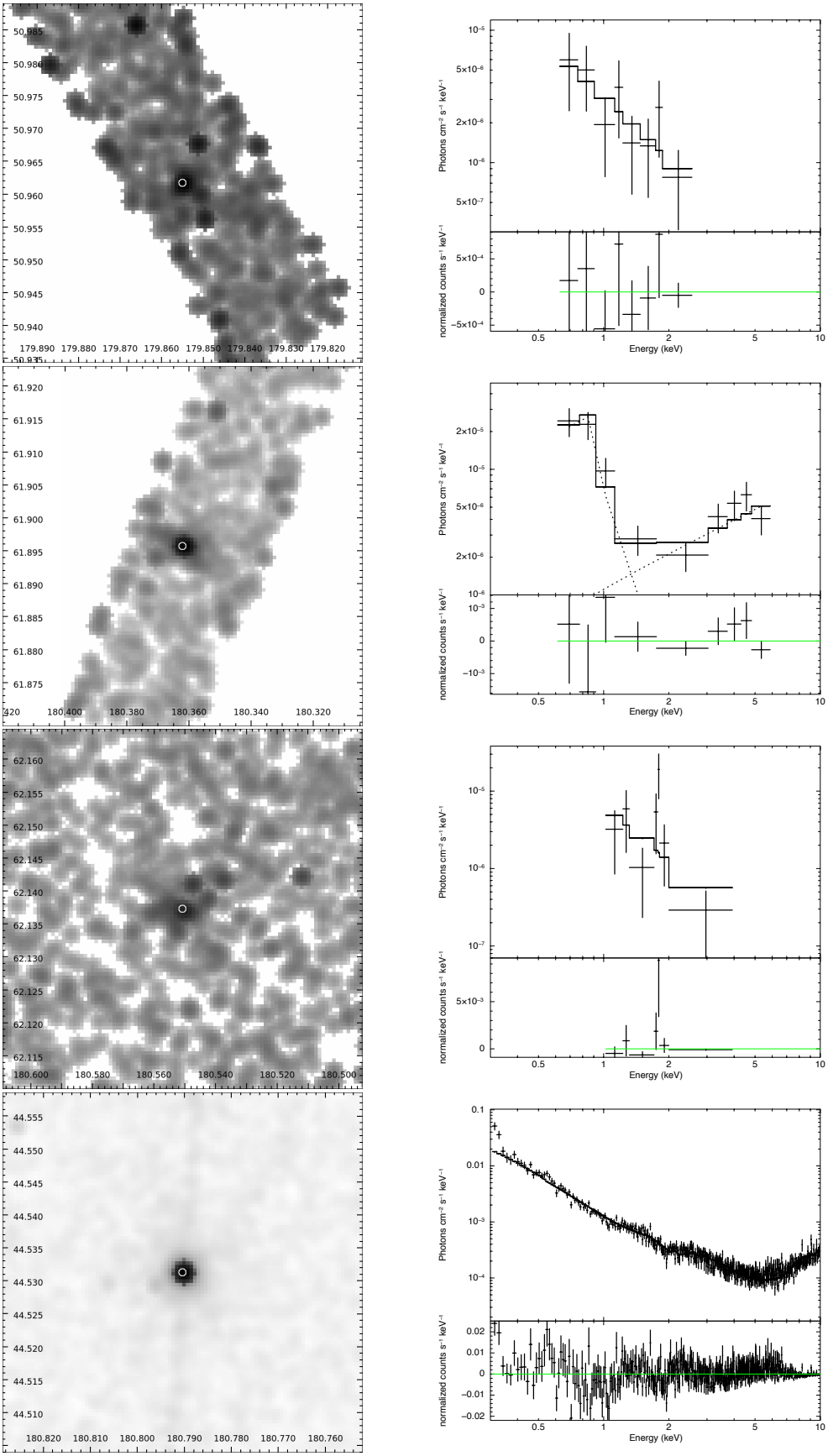

Figure D.1: Images and spectra of NGC 4026 (top), NGC 4036 (top-middle), NGC 4041 (bottom-middle), NGC 4051 (bottom)

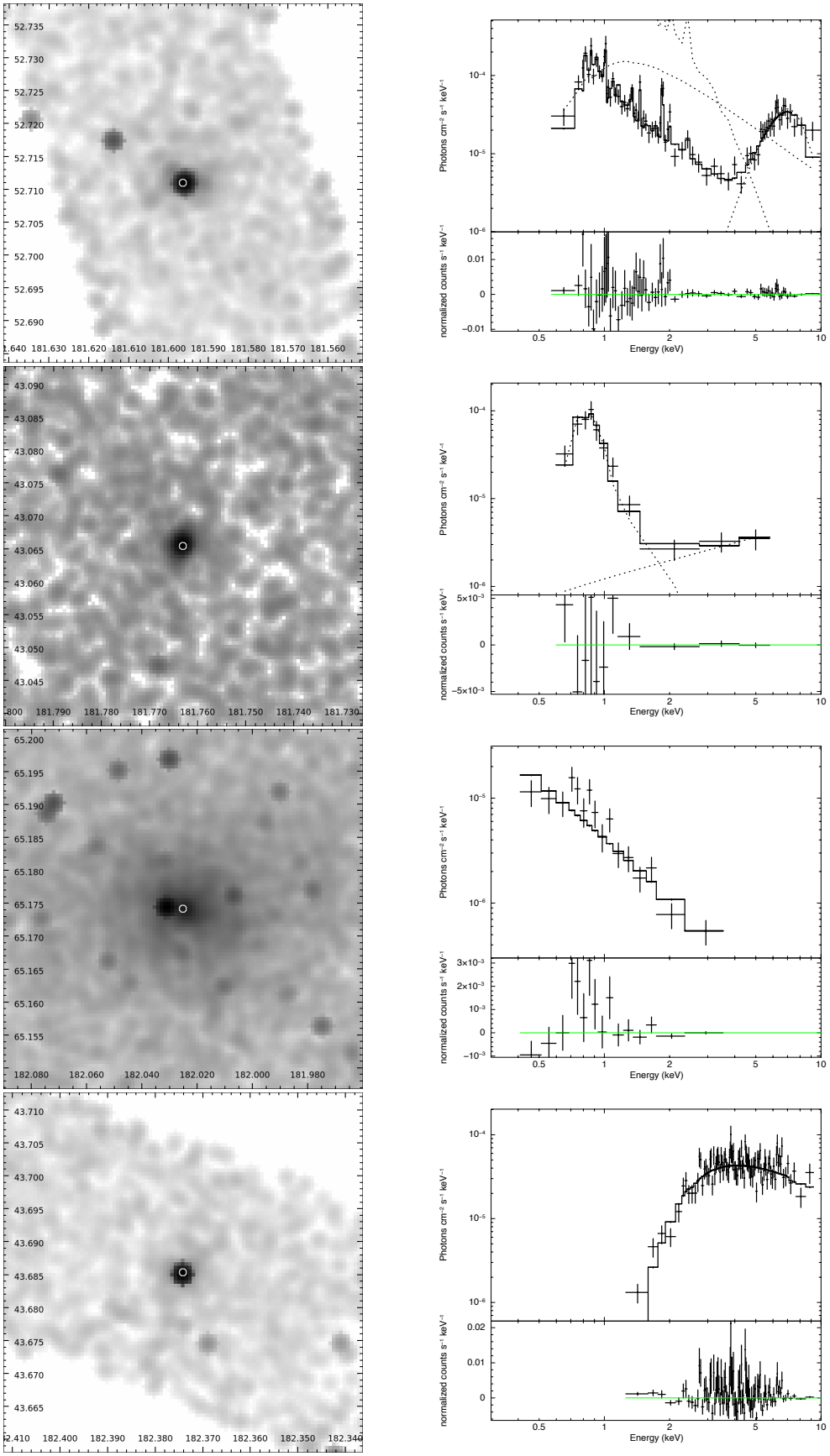

Figure D.1: Images and spectra of NGC 4102 (top), NGC 4111 (top-middle), NGC 4125 (bottom-middle), NGC 4138 (bottom)

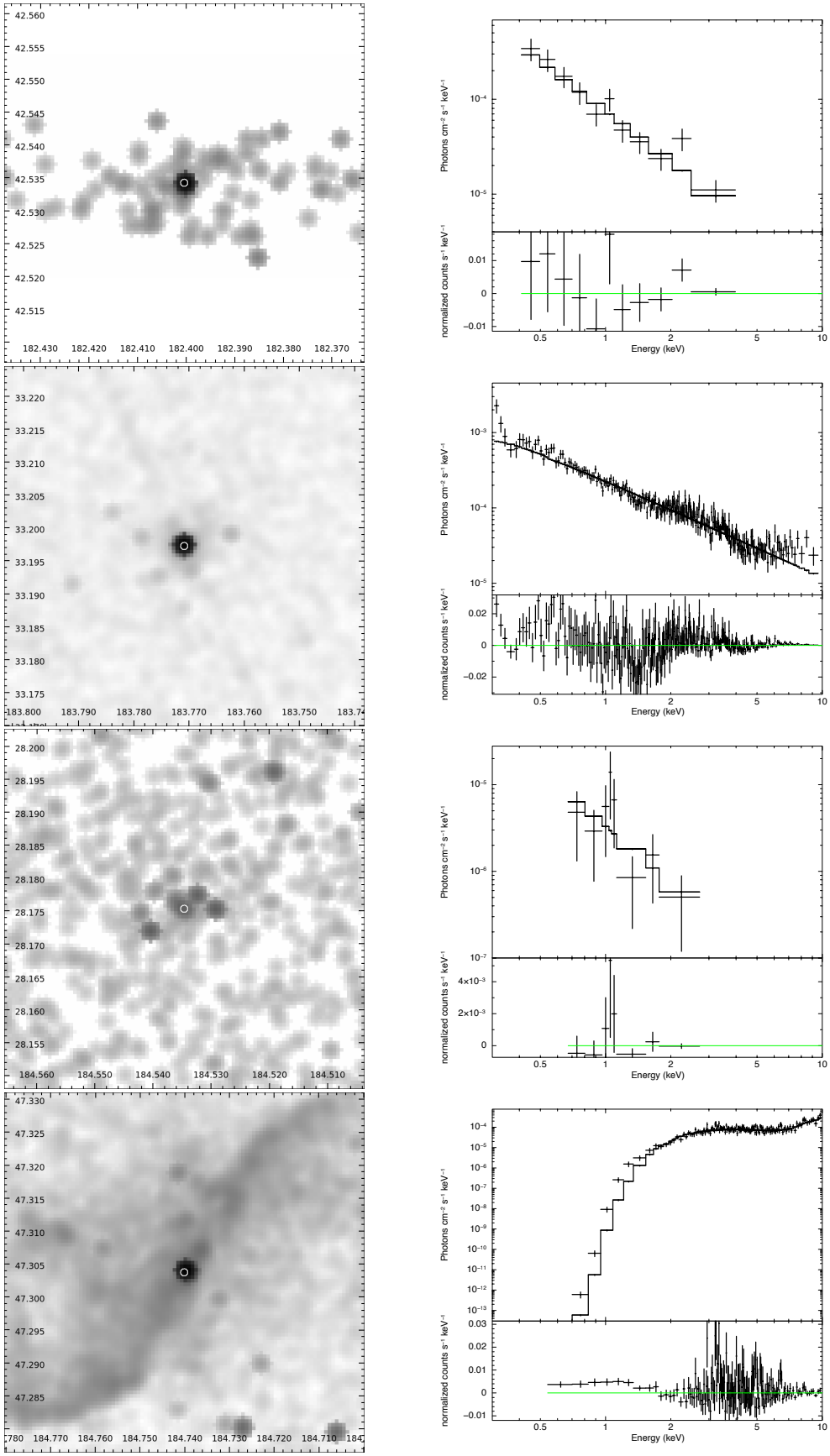

Figure D.1: Images and spectra of NGC 4143 (top), NGC 4203 (top-middle), NGC 4251 (bottom-middle), NGC 4258 (bottom)

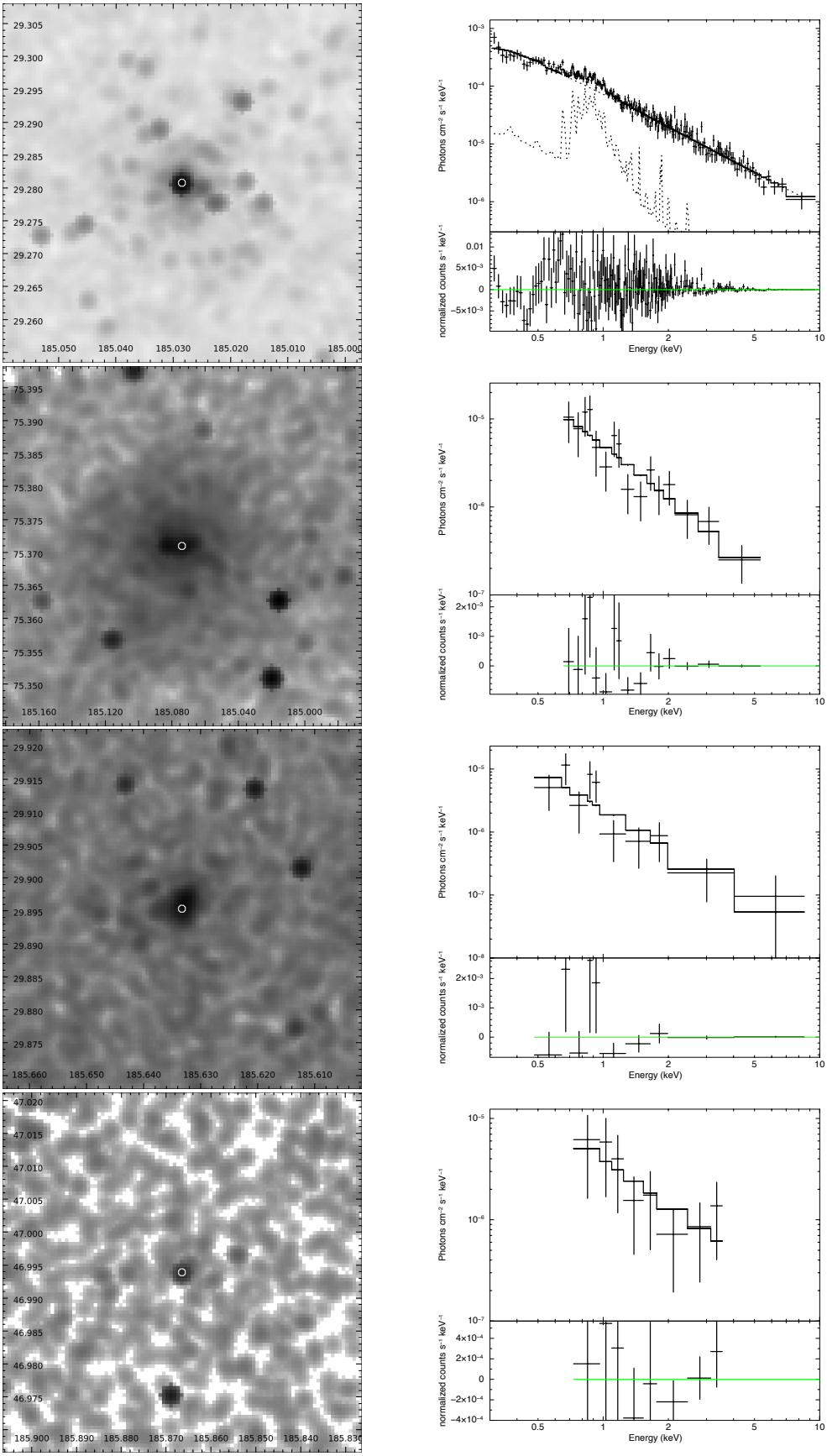

Figure D.1: Images and spectra of NGC 4278 (top), NGC 4291 (top-middle), NGC 4314 (bottom-middle), NGC 4346 (bottom)

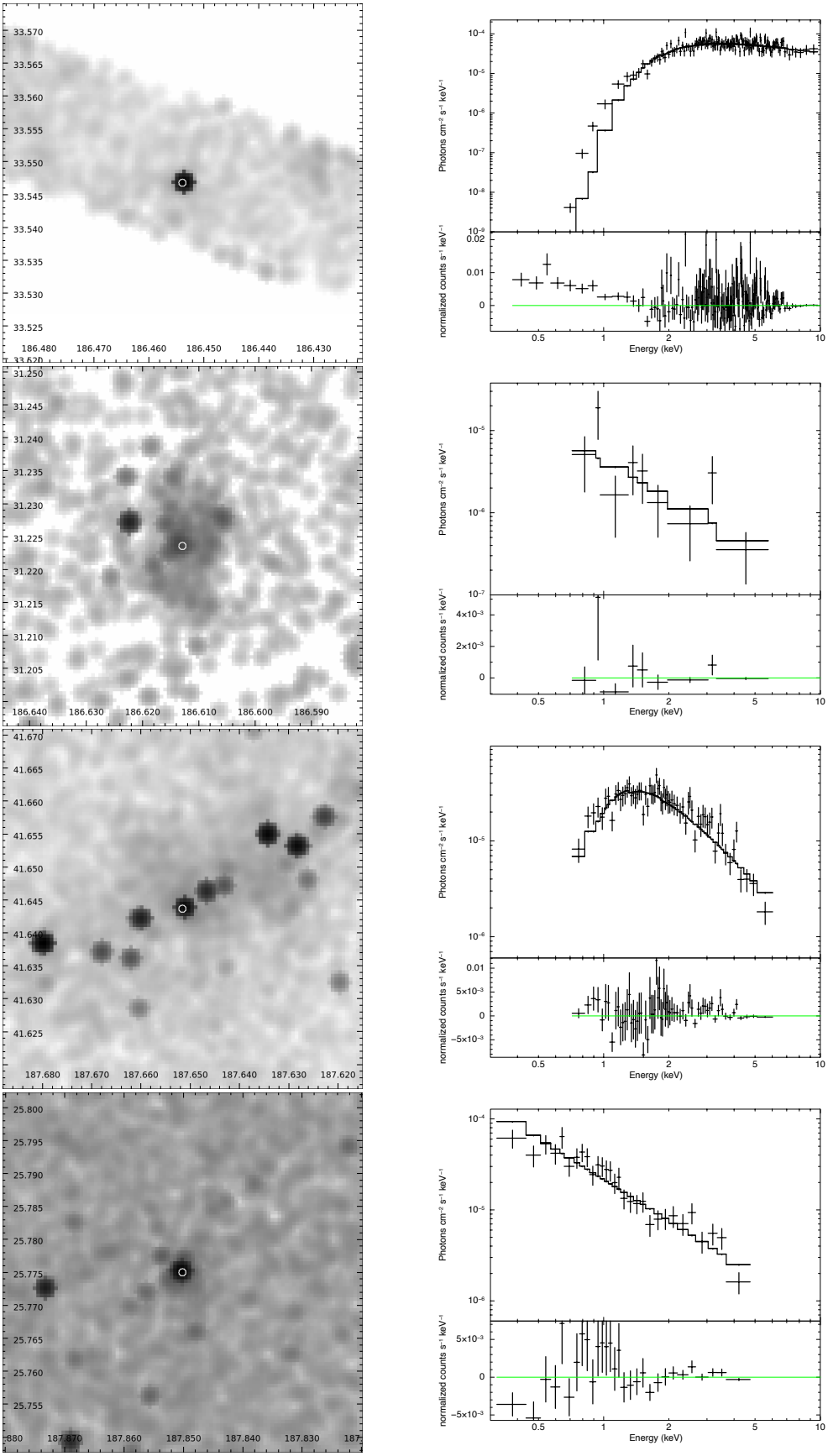

Figure D.1: Images and spectra of NGC 4395 (top), NGC 4414 (top-middle), NGC 4490 (bottom-middle), NGC 4494 (bottom)

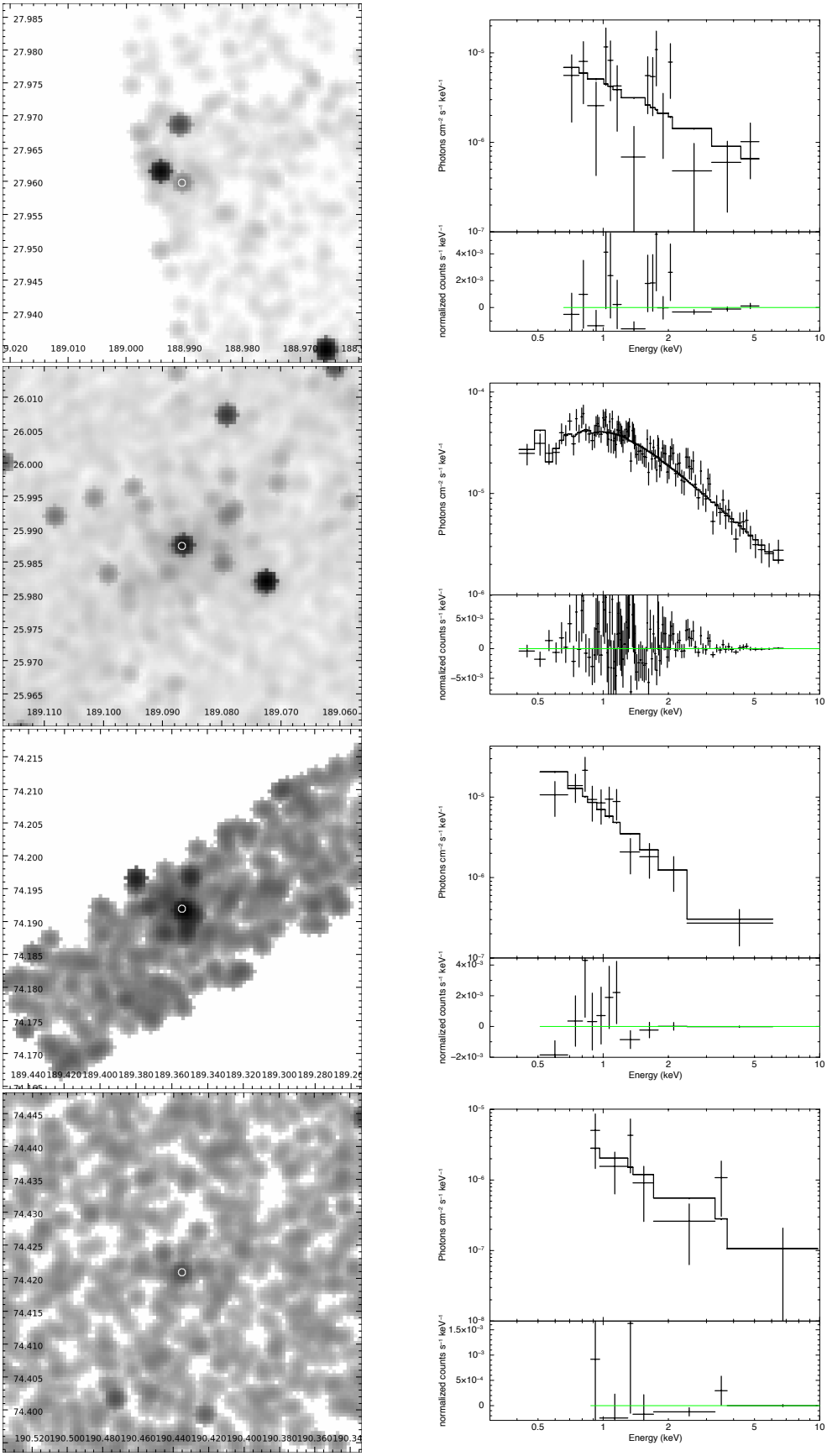

Figure D.1: Images and spectra of NGC 4559 (top), NGC 4565 (top-middle), NGC 4589 (bottom-middle), NGC 4648 (bottom)

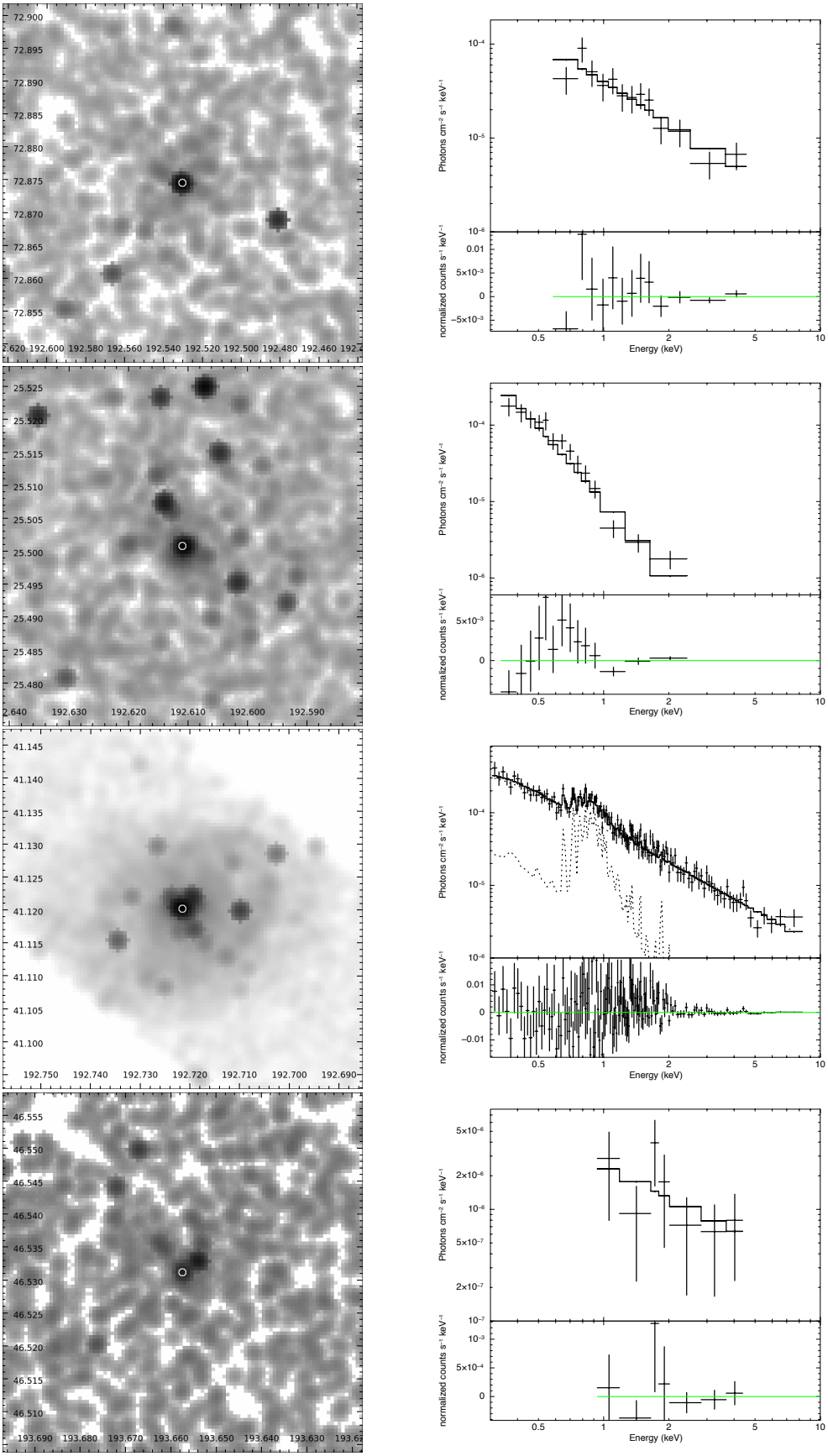

Figure D.1: Images and spectra of NGC 4750 (top), NGC 4725 (top-middle), NGC 4736 (bottom-middle), NGC 4800 (bottom)

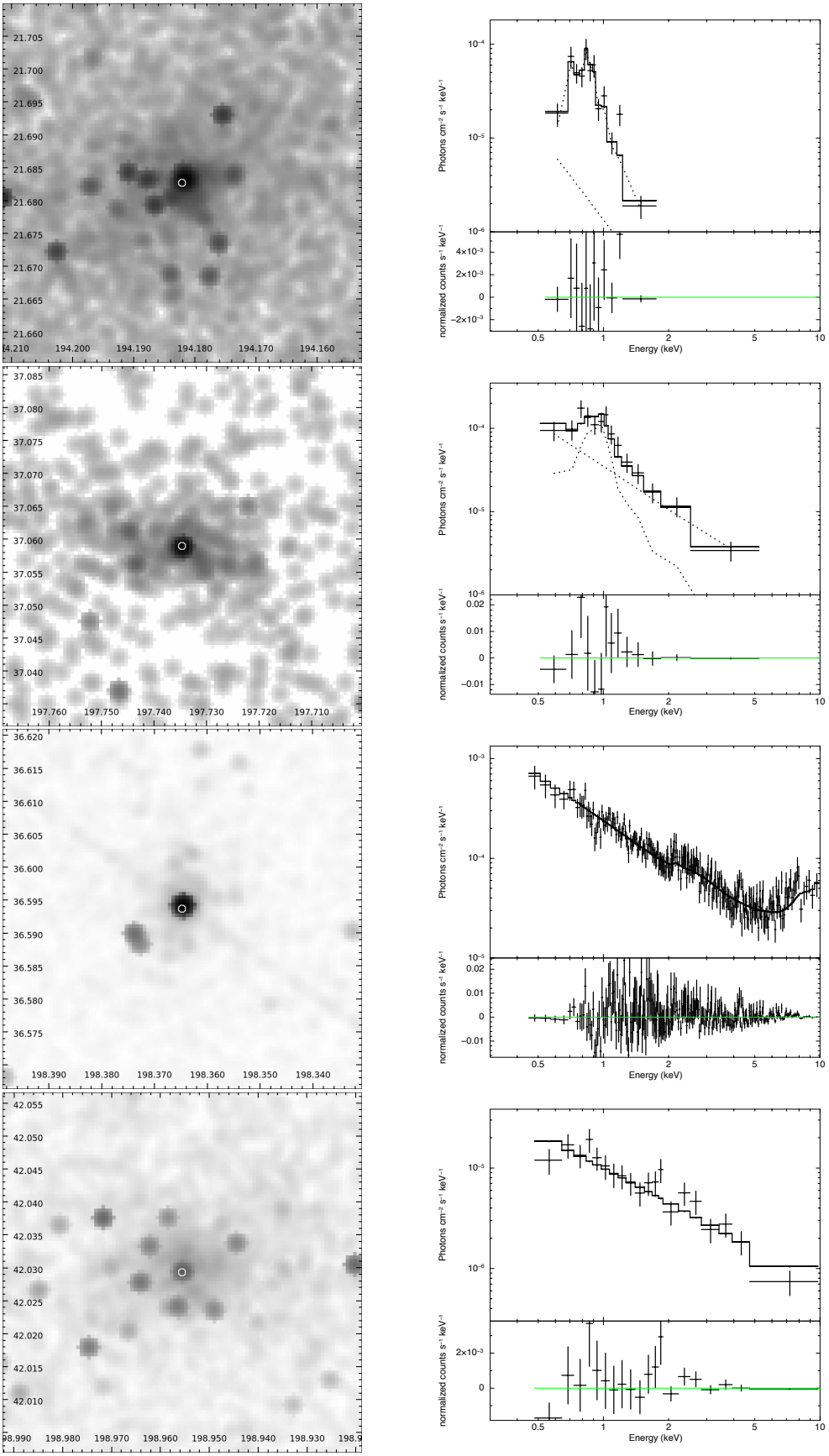

Figure D.1: Images and spectra of NGC 4826 (top), NGC 5005 (top-middle), NGC 5033 (bottom-middle), NGC 5055 (bottom)

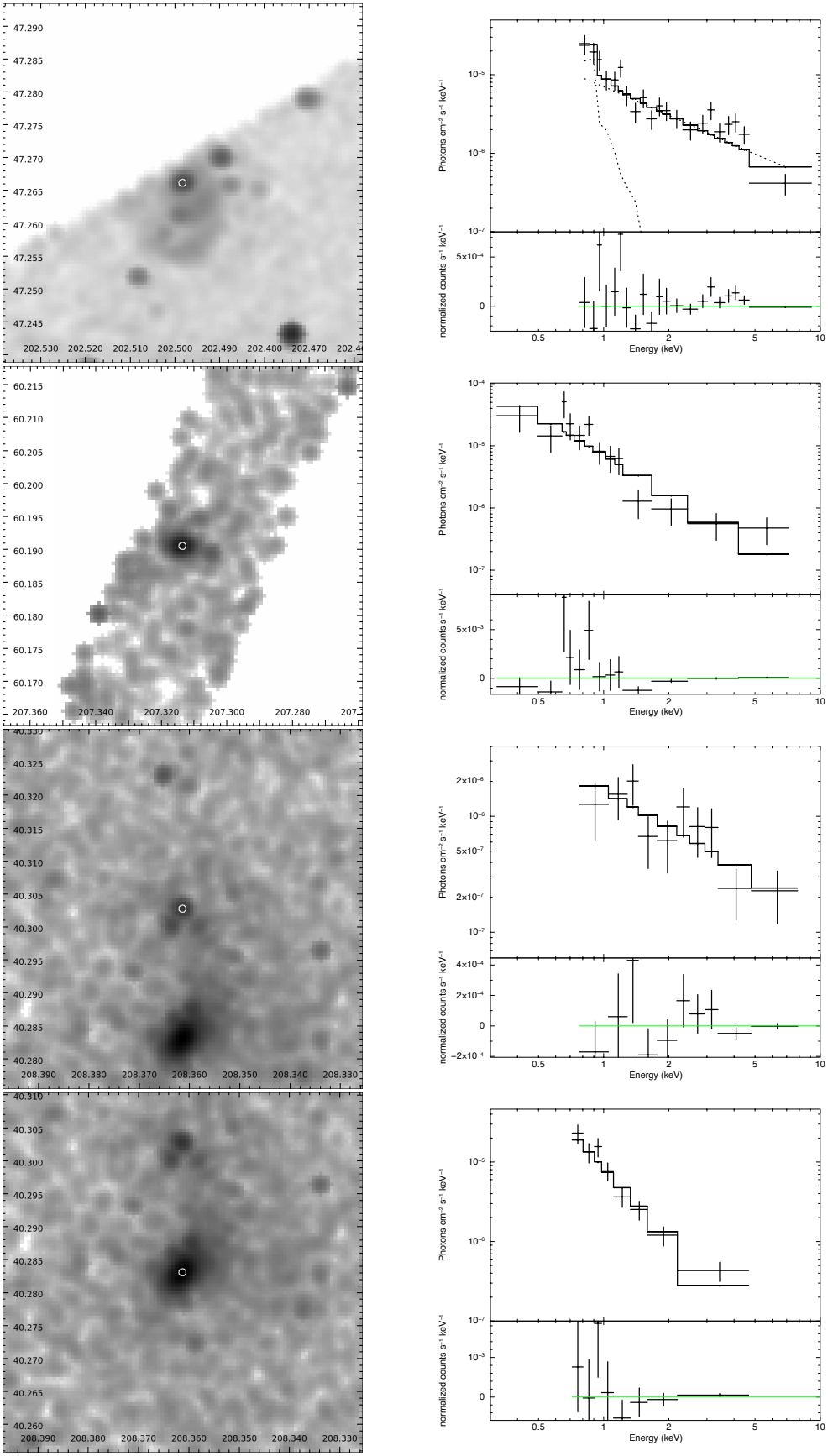

Figure D.1: Images and spectra of NGC 5195 (top), NGC 5322 (top-middle), NGC 5354 (bottom-middle), NGC 5353 (bottom)

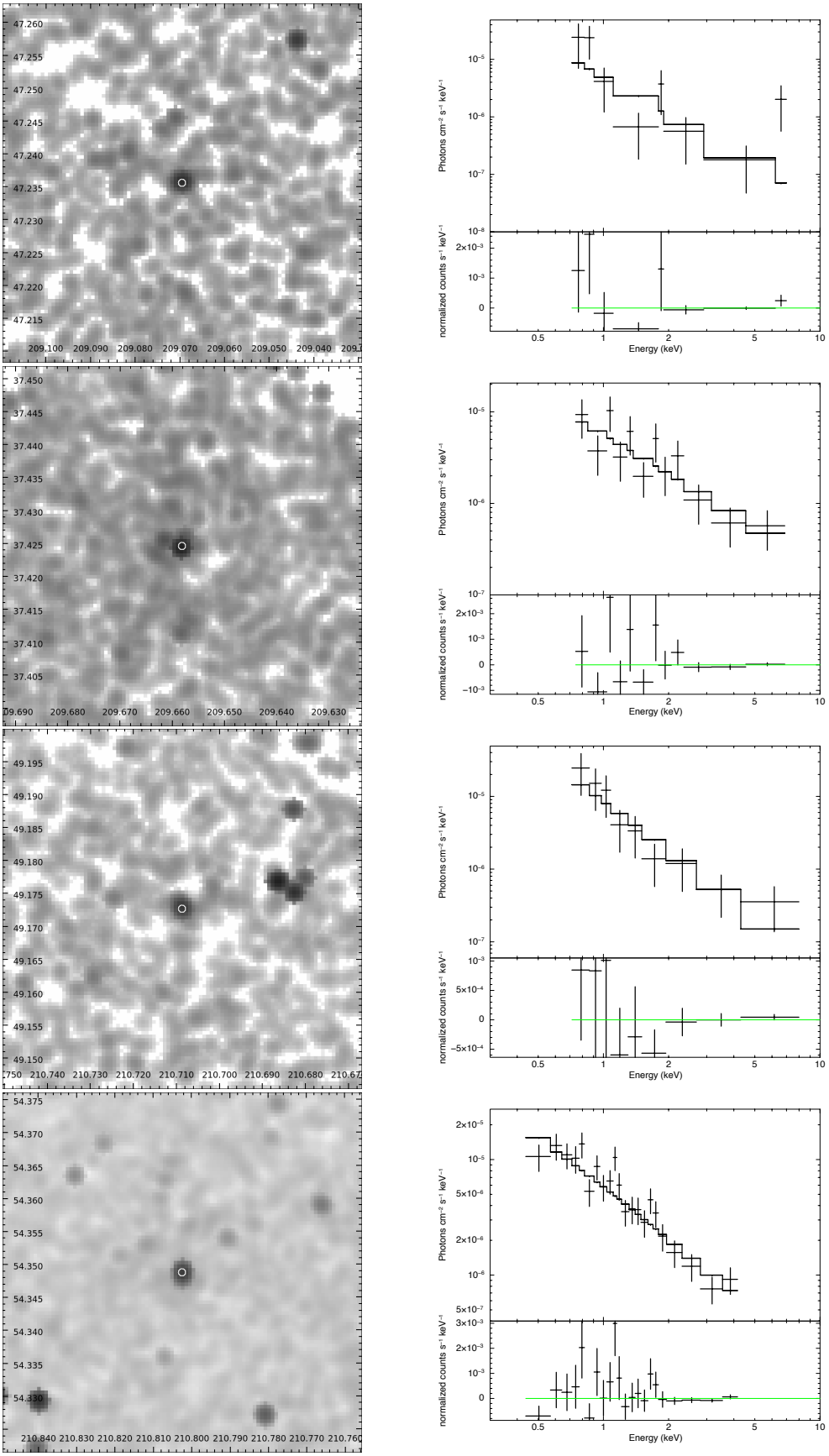

Figure D.1: Images and spectra of NGC 5377 (top), NGC 5395 (top-middle), NGC 5448 (bottom-middle), NGC 5457 (bottom)

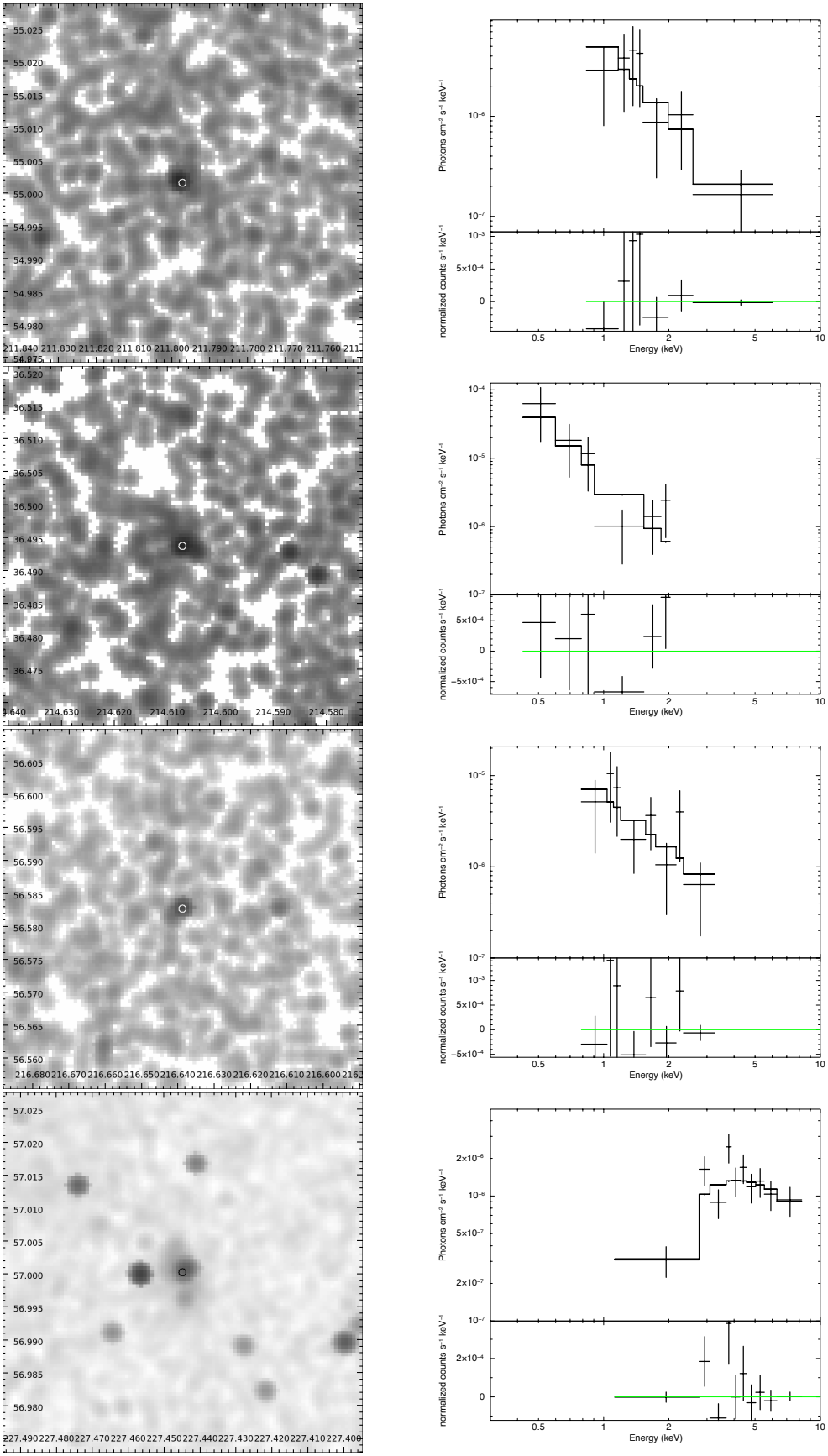

Figure D.1: Images and spectra of NGC 5485 (top), NGC 5557 (top-middle), NGC 5631 (bottom-middle), NGC 5879 (bottom)

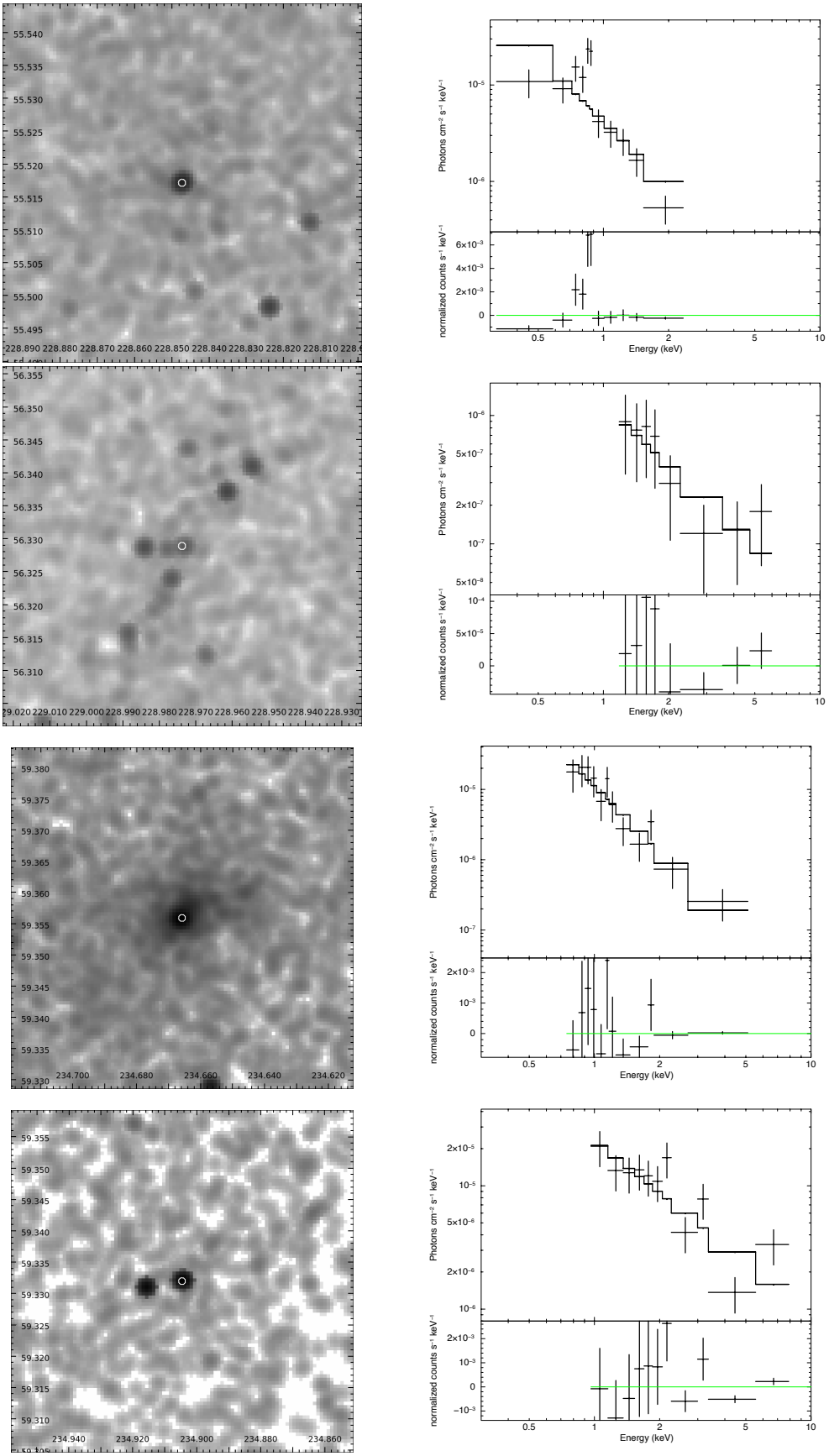

Figure D.1: Images and spectra of NGC 5905 (top), NGC 5907 (top-middle), NGC 5982 (bottom-middle), NGC 5985 (bottom)

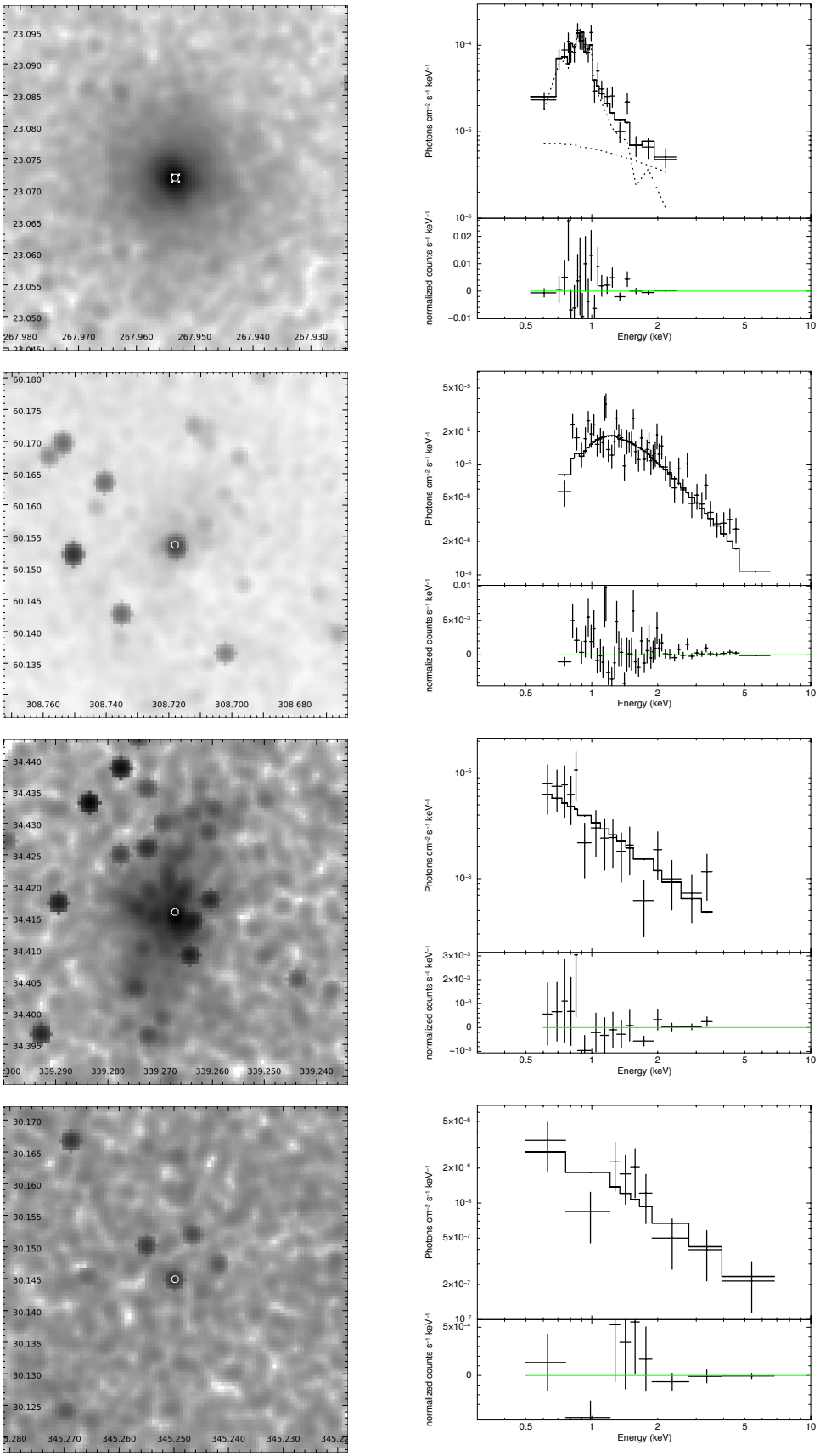

Figure D.1: Images and spectra of NGC 6482 (top), NGC 6946 (top-middle), NGC 7331 (bottom-middle), NGC 7457 (bottom)

D.2 Chandra X−ray Data

Name	Obsid	Exp (ks)	Det?	Flux 0.3−10	Lum 0.3−10	Lum 0.3−2	Lum 2−10	Un.Abs. Flux 0.3−10	Un.Abs. Lum 0.3−10	HR
(1)	(2)	(3)	(4)	(5)	(6)	(7)	(8)	(9)	(10)	(11)
NGC 7817	–	–	U	–	–	–	–	–	–	–
IC 10	8458	44	<	7.21E−16	35.16	–	–	−15.01	35.30	–
NGC 147	–	–	U	–	–	–	–	–	–	–
NGC 185	–	–	U	–	–	–	–	–	–	–
NGC 205	4691	10	<	2.84E−15	35.22	–	–	−14.41	35.36	–
NGC 221	5690	116	D	3.16E−14	36.27±0.04	$36.04^{+0.03}_{-0.04}$	$35.88^{+0.09}_{-0.10}$	−13.31	36.46	0.70
NGC 224	14196	53.8	D	2.93E−13	$37.23^{+0.13}_{-0.11}$	$36.98^{+0.10}_{-0.11}$	36.89±0.25	−12.33	37.44	0.82
NGC 266	16013	86	D	1.42E−13	40.82±0.03	40.33±0.04	40.65±0.05	−12.81	40.86	2.10
NGC 278	2055	38.7	D	2.37E−15	$37.60^{+0.22}_{-0.32}$	$37.60^{+0.22}_{-0.32}$	$35.18^{+0.22}_{-0.32}$	−13.89	38.34	0.004
NGC 315	4156	56	D	4.83E−14	$40.40^{+1.43}_{1.41}$	40.97±0.01	41.75±0.01	−11.81	41.91	6.023
NGC 404	12239	100	D	2.22E−14	$37.18^{+0.04}_{-0.05}$	$36.95^{+0.04}_{-0.05}$	$36.81^{+0.04}_{-0.05}$	−13.56	37.27	0.723
NGC 410	5897	2.6	D	3.65E−13	$41.34^{+0.08}_{-0.09}$	$41.32^{+0.08}_{-0.09}$	$39.98^{+0.08}_{-0.09}$	−12.17	41.60	0.045
NGC 507	2882	44	D	2.00E−14	$40.01^{+0.07}_{-0.08}$	$40.01^{+0.07}_{-0.08}$	$39.76^{+0.07}_{-0.08}$	−13.10	40.62	0.555
NGC 598	786	47	D	–	–	–	–	–	–	–
IC 1727	1634	1.7	<	9.49E−15	37.88	–	–	−13.89	38.02	–
NGC 672	7090	2.2	<	1.48E−14	38.00	–	–	−13.69	38.13	–
NGC 697	15046	15	<	9.65E−14	40.30	–	–	−12.88	40.44	–
NGC 777	5001	10	D	2.97E−13	41.12±0.06	41.17±0.06	39.96±0.06	−12.31	41.42	0.06
NGC 783	–	–	U	–	–	–	–	–	–	–
NGC 784	–	–	U	–	–	–	–	–	–	–
NGC 812	–	–	U	–	–	–	–	–	–	–
NGC 818	–	–	U	–	–	–	–	–	–	–
NGC 841	–	–	U	–	–	–	–	–	–	–

Continued on Next Page

Table D.1 : *cont.*

Name	Obsid	Exp (ks)	Det?	Flux 0.3−10	Lum 0.3−10	Lum 0.3−2	Lum 2−10	Un.Abs. Flux 0.3−10	Un.Abs. Lum 0.3−10	HR
(1)	(2)	(3)	(4)	(5)	(6)	(7)	(8)	(9)	(10)	(11)
NGC 890	19325	35	D	9.44E−15	$39.51^{+0.14}_{-0.16}$	$39.08^{+0.14}_{-0.16}$	$39.31^{+0.14}_{-0.16}$	−13.97	39.56	1.69
NGC 891	4613	120	<	3.53E−15	37.59	–	–	−14.32	37.73	–
NGC 925	7104	2.3	D*	4.66E−14	$38.69^{+0.20}_{-0.23}$	–	–	−13.20	38.83	–
NGC 959	7111	2.2	<	9.08E−15	38.04	–	–	−13.91	38.18	–
NGC 972	–	–	U	–	–	–	–	–	–	–
IC 239	7131	4.6	<	4.23E−15	38.15	–	–	−14.24	38.29	–
NGC 1003	7116	2.7	<	8.75E−15	38.08	–	–	−13.92	38.22	–
NGC 1023	8198	50.4	D	6.62E−14	38.94±0.05	$38.57^{+0.04}_{-0.05}$	$38.70^{+0.08}_{-0.09}$	−13.12	39.00	1.36
NGC 1058	9579	19	D	2.51E−14	$38.40^{+0.13}_{-0.14}$	$37.98^{+0.13}_{-0.14}$	$38.18^{+0.13}_{-0.14}$	−13.55	38.45	1.575
NGC 1156	7088	2	<	1.01E−14	37.694683	–	–	−13.86	37.83	–
NGC 1161	12958	7.5	D	3.09E−14	$39.40^{+0.18}_{-0.15}$	$39.17^{+0.16}_{-0.16}$	$39.00^{+0.37}_{-0.40}$	−13.24	39.67	0.685
NGC 1167	19313	13	D	4.29E−14	40.34±0.10	$40.14^{+0.17}_{-0.17}$	39.91±0.29	−13.17	40.53	0.593
NGC 1169	–	–	U	–	–	–	–	–	–	–
NGC 1186	–	–	U	–	–	–	–	–	–	–
NGC 1275	4952	166	D	1.30E−11	42.88±0.01	41.06±0.01	42.88±0.01	−10.57	43.20	65.723
IC 342	7069	58.5	D	1.99E−13	38.33±0.04	38.13±0.04	37.90±0.10	−12.14	38.89	0.597
IC 356	–	–	U	–	–	–	–	–	–	–
NGC 1569	782	98	D	8.96E−16	$35.44^{+0.21}_{-0.33}$	$35.297569^{+0.21}_{-0.33}$	$34.88^{+0.21}_{-0.33}$	−14.52	35.96	0.383
NGC 1560	–	–	U	–	–	–	–	–	–	–
NGC 1961	10531	33.3	D	8.68E−14	$40.47^{+0.13}_{-0.12}$	39.78±0.12	$40.37^{+0.07}_{-0.08}$	−13.03	40.50	3.857
NGC 2146	3135	10.2	D	3.77E−13	$40.12^{+0.12}_{-0.13}$	$38.30^{+0.12}_{-0.13}$	$40.12^{+0.12}_{-0.13}$	−12.42	40.13	66.262
NGC 2273	19377	10	D	9.35E−13	40.96±0.05	39.34±0.05	40.94±0.05	−12.03	40.96	40.205
NGC 2342	–	–	U	–	–	–	–	–	–	–

Continued on Next Page

Table D.1 : *cont.*

Name	Obsid	Exp (ks)	Det?	Flux 0.3−10	Lum 0.3−10	Lum 0.3−2	Lum 2−10	Un.Abs. Flux 0.3−10	Un.Abs. Lum 0.3−10	HR
(1)	(2)	(3)	(4)	(5)	(6)	(7)	(8)	(9)	(10)	(11)
UGC 3714	–	–	U	–	–	–	–	–	–	–
NGC 2268	–	–	U	–	–	–	–	–	–	–
UGC 3828	19364	10	D*	7.65E−15	$39.30^{+0.27}_{-0.37}$	–	–	−13.98	39.44	–
NGC 2336	–	–	U	–	–	–	–	–	–	–
NGC 2276	4968	46.1	D	7.23E−15	39.07±0.12	$38.99^{+0.12}_{-0.13}$	$38.31^{+0.13}_{-0.12}$	−13.96	39.25	0.21
NGC 2366	–	–	U	–	–	–	–	–	–	–
IC 467	–	–	U	–	–	–	–	–	–	–
NGC 2300	4968	46.1	D	1.16E−13	$40.13^{+0.18}_{-0.16}$	$40.11^{+0.19}_{-0.18}$	$38.53^{+0.29}_{-0.30}$	−12.64	40.42	0.026
NGC 2403	4630	50.6	D	1.34E−13	$38.45^{+0.04}_{-0.04}$	$38.15^{+0.04}_{-0.04}$	$38.15^{+0.04}_{-0.04}$	−12.43	38.89	1.01
UGC 4028	–	–	U	–	–	–	–	–	–	–
NGC 2500	7112	2.6	<	3.60E−14	38.64	–	–	−13.31	38.78	–
NGC 2543	–	–	U	–	–	–	–	–	–	–
NGC 2537	19359	10	D*	1.92E−14	$38.27^{+0.27}_{-0.36}$	–	–	−13.58	38.40	–
NGC 2541	1635/19354	10	<	8.37E−15	38.05	–	–	−13.94	38.19	–
NGC 2549	19339	10	D	5.26E−14	$39.35^{+0.20}_{-0.16}$	$38.88^{+0.24}_{-0.23}$	$39.16^{+0.30}_{-0.31}$	−13.28	39.35	1.901
NGC 2639	5682	5	D	6.78E−13	$41.17^{+0.27}_{-0.22}$	$41.16^{+0.27}_{-0.24}$	$39.54^{+0.36}_{-0.39}$	−12.17	41.17	0.024
NGC 2634	13005	5	<	3.70E−14	39.61	–	–	−13.30	39.74	–
NGC 2683	11311	39	D	1.69E−12	$39.82^{+0.08}_{-0.10}$	$36.99^{+0.13}_{-0.16}$	$39.82^{+0.08}_{-0.09}$	−11.77	39.82	671.114
NGC 2681	2060	81.9	D	6.14E−14	39.11±0.05	$38.82^{+0.02}_{-0.03}$	$38.81^{+0.09}_{-0.10}$	−13.19	39.14	0.978
IC 520	–	–	U	–	–	–	–	–	–	–
NGC 2685	–	–	U	–	–	–	–	–	–	–
NGC 2655	–	–	U	–	–	–	–	–	–	–
NGC 2750	–	–	U	–	–	–	–	–	–	–

Continued on Next Page

Table D.1 : *cont.*

Name	Obsid	Exp (ks)	Det?	Flux 0.3−10	Lum 0.3−10	Lum 0.3−2	Lum 2−10	Un.Abs. Flux 0.3−10	Un.Abs. Lum 0.3−10	HR
(1)	(2)	(3)	(4)	(5)	(6)	(7)	(8)	(9)	(10)	(11)
NGC 2742	19353	10	<	1.03E−14	38.78	–	–	−13.85	38.92	–
NGC 2715	–	–	U	–	–	–	–	–	–	–
NGC 2770	9104	18.1	<	2.07E−15	38.34	–	–	−14.55	38.47	–
NGC 2768	9528	65.5	D	8.31E−14	39.75±0.04	39.11±0.04	39.63±0.04	−13.06	39.77	3.348
NGC 2776	19384	10	<	2.77E−15	38.70	–	–	−14.42	38.83	–
NGC 2748	11776	30	D	7.53E−15	38.71±0.01	38.29±0.01	38.50±0.01	−14.11	38.72	1.641
NGC 2782	3014	30	D	3.98E−13	40.82±0.03	39.78±0.03	40.78±0.03	−12.40	40.82	9.996
NGC 2787	4689	31	D	1.43E−13	39.46±0.03	39.06±0.03	39.24±0.03	−12.80	39.51	1.501
NGC 2832	5904	3	D	3.31E−13	$41.52^{+0.14}_{-0.16}$	$41.51^{+0.14}_{-0.16}$	$39.89^{+0.14}_{-0.16}$	−12.40	41.60	0.024
NGC 2841	6096	28.6	D	6.89E−14	$39.07^{+0.05}_{-0.06}$	$38.61^{+0.05}_{-0.06}$	$38.89^{+0.05}_{-0.06}$	−13.15	39.08	1.948
NGC 2859	–	–	U	–	–	–	–	–	–	–
NGC 2903	11260	95	D	4.63E−14	38.34±0.04	37.90±0.04	38.15±0.04	−13.31	38.37	1.747
NGC 2950	19338	10	D	4.84E−14	$39.50^{+0.17}_{-0.19}$	$39.42^{+0.17}_{-0.19}$	$38.70^{+0.17}_{-0.19}$	−13.32	39.50	0.192
NGC 2964	–	–	U	–	–	–	–	–	–	–
NGC 2977	–	–	U	–	–	–	–	–	–	–
NGC 2976	9542	10	<	1.09E−14	36.76	–	–	−13.82	36.90	–
NGC 3003	–	–	U	–	–	–	–	–	–	–
NGC 2985	11669	14	D	9.62E−14	$39.76^{+0.06}_{-0.07}$	$39.45^{+0.06}_{-0.07}$	$39.47^{+0.06}_{-0.07}$	−12.99	39.79	1.027
NGC 3031	12301	79	D	–	–	–	–	–	–	–
NGC 3027	–	–	U	–	–	–	–	–	–	–
NGC 3034	10542	120	D	1.18E−13	$38.58^{+0.02}_{-0.03}$	$38.06^{+0.02}_{-0.03}$	$38.43^{+0.02}_{-0.03}$	−12.29	39.22	2.33
NGC 3043	19365	10	<	2.97E−15	38.74	–	–	−14.39	38.87	–
NGC 3073	2038	27	<	1.85E−14	38.92	–	–	−13.60	39.05	–

Continued on Next Page

Table D.1 : *cont.*

Name	Obsid	Exp (ks)	Det?	Flux 0.3−10	Lum 0.3−10	Lum 0.3−2	Lum 2−10	Un.Abs. Flux 0.3−10	Un.Abs. Lum 0.3−10	HR
(1)	(2)	(3)	(4)	(5)	(6)	(7)	(8)	(9)	(10)	(11)
NGC 3079	2038	27	D	1.44E−13	$39.86^{+0.05}_{-0.06}$	$38.72^{+0.05}_{-0.06}$	$39.82^{+0.05}_{-0.06}$	−12.62	40.08	12.71
NGC 3077	2076	54	D	8.56E−14	37.65±0.05	36.54±0.05	37.62±0.05	−13.06	37.66	11.96
NGC 3162	–	–	U	–	–	–	–	–	–	–
NGC 3147	1615	2.4	D	5.47E−12	42.04±0.02	41.44±0.02	41.91±0.02	−11.25	42.05	2.964
NGC 3185	2760	20	D*	4.80E−14	$39.42^{+0.19}_{-0.35}$	–	–	−13.18	39.55	–
NGC 3190	2760	20	D	3.31E−13	$40.30^{+0.05}_{-0.06}$	$39.03^{+0.05}_{-0.06}$	$40.27^{+0.05}_{-0.06}$	−12.48	40.30	17.564
NGC 3184	804	42.6	D	2.59E−14	38.37±0.07	37.88±0.07	38.20±0.07	−13.58	38.38	2.106
NGC 3193	11360	7	D	2.15E−14	$39.14^{+0.15}_{-0.17}$	$38.92^{+0.15}_{-0.17}$	$38.74^{+0.15}_{-0.17}$	−13.63	39.18	0.658
NGC 3198	9551	62	D	2.25E−14	$38.50^{+0.07}_{-0.08}$	$37.92^{+0.07}_{-0.08}$	$38.36^{+0.07}_{-0.08}$	−13.64	38.50	2.743
NGC 3245	2926	9.7	D	8.14E−14	39.68±0.08	39.14±0.08	39.53±0.08	−13.08	39.69	2.491
IC 2574	792	10	<	2.57E−15	36.55	–	–	−14.45	36.689	–
NGC 3254	–	–	U	–	–	–	–	–	–	–
NGC 3294	–	–	U	–	–	–	–	–	–	–
NGC 3301	–	–	U	–	–	–	–	–	–	–
NGC 3310	2939	48	D	4.78E−13	40.30±0.02	39.47±0.02	40.23±0.02	−12.24	40.38	5.77
NGC 3319	19350	10	D	9.97E−14	$39.20^{+0.09}_{-0.10}$	$38.82^{+0.09}_{-0.10}$	$38.96^{+0.09}_{-0.10}$	−12.98	39.21	1.39
NGC 3344	15387	48	D	3.36E−14	38.18±0.08	37.94±0.08	37.80±0.08	−13.43	38.22	0.74
NGC 3359	16347	50	<	1.72E−15	37.88 –	–	–	–	–	–
NGC 3348	–	–	U	–	–	–	–	–	–	–
NGC 3395	2042	20	<	5.50E−15	38.69 –	–	–	–	–	–
NGC 3414	6779	15	D	5.37E−13	40.60±0.03	40.02±0.03	40.47±0.03	−12.26	40.61	2.805
NGC 3430	16821	10	D*	5.78E−15	$38.69^{+0.30}_{-0.43}$	–	–	−14.10	38.83	–
NGC 3432	7091	2	<	1.01E−14	37.87	–	–	−13.86	38.00	–

Continued on Next Page

Table D.1 : *cont.*

Name	Obsid	Exp (ks)	Det?	Flux 0.3−10	Lum 0.3−10	Lum 0.3−2	Lum 2−10	Un.Abs. Flux 0.3−10	Un.Abs. Lum 0.3−10	HR
(1)	(2)	(3)	(4)	(5)	(6)	(7)	(8)	(9)	(10)	(11)
NGC 3448	19360	10	D	5.65E−14	$39.61^{+0.14}_{-0.16}$	$38.91^{+0.14}_{-0.16}$	$39.51^{+0.14}_{-0.16}$	−13.251	39.61	4.011
NGC 3486	393	1.8	<	1.77E−14	38.06	–	–	−13.62	38.20	–
NGC 3504	–	–	U	–	–	–	–	–	–	–
NGC 3516	2080	75	D	1.89E−11	42.53±0.01	41.55±0.01	42.49±0.01	−10.71	42.54	8.545
NGC 3556	2025	60	D	6.74E−14	39.20±0.04	38.54±0.04	39.10±0.04	−13.00	39.38	3.599
NGC 3583	19381	10	D	3.60E−14	$39.70^{+0.15}_{-0.17}$	$39.20^{+0.15}_{-0.17}$	$39.53^{+0.15}_{-0.17}$	−13.43	39.71	2.123
NGC 3600	19356/7114	10	D	1.56E−13	$39.31^{+0.08}_{-0.09}$	$38.85^{+0.08}_{-0.09}$	$39.13^{+0.08}_{-0.09}$	−12.80	39.32	1.929
NGC 3610	7141	5	D	2.77E−14	$39.45^{+0.17}_{-0.19}$	$39.22^{+0.17}_{-0.19}$	$39.07^{+0.17}_{-0.19}$	−13.55	39.46	0.714
NGC 3613	–	–	U	–	–	–	–	–	–	–
NGC 3631	3951	90	D	2.61E−15	$38.16^{+0.15}_{-0.16}$	$38.13^{+0.15}_{-0.16}$	$37.08^{+0.15}_{-0.16}$	−14.54	38.21	0.091
NGC 3646	–	–	U	–	–	–	–	–	–	–
NGC 3642	19379	10	D	1.20E−13	$40.04^{+0.08}_{-0.09}$	$39.87^{+0.08}_{-0.09}$	$39.54^{+0.08}_{-0.09}$	−12.91	40.05	0.470
NGC 3652	–	–	U	–	–	–	–	–	–	–
NGC 3665	3222	18	D	4.93E−14	$39.79^{+0.10}_{-0.11}$	$39.21^{+0.10}_{-0.11}$	$39.66^{+0.10}_{-0.11}$	−13.30	39.80	2.797
NGC 3675	19368/396	10	D*	9.30E−15	$38.26^{+0.27}_{-0.37}$	–	–	−13.90	38.40	–
NGC 3690	15077	52.5	D	2.98E−13	40.77±0.03	39.90±0.03	40.70±0.03	−12.32	40.97	6.400
UGC 6484	19343	10	<	5.81E−15	38.86	–	–	−14.10	39.00	–
NGC 3718	3993	5.4	D	3.43E−12	41.07±0.02	40.14±0.02	41.02±0.02	−11.92	40.62	7.607
NGC 3726	19346	10	<	4.70E−15	38.21	–	–	−14.19	38.35	–
NGC 3729	10356	8	D*	4.68E−14	$39.21^{+0.28}_{-0.36}$	–	–	−13.19	39.35	–
NGC 3738	19357	10	<	3.23E−15	36.85	–	–	−14.35	36.99	–
NGC 3735	–	–	U	–	–	–	–	–	–	–
NGC 3756	19355	10	<	4.46E−15	38.47	–	–	−14.21	38.606	–

Continued on Next Page

Table D.1 : *cont.*

Name	Obsid	Exp (ks)	Det?	Flux 0.3−10	Lum 0.3−10	Lum 0.3−2	Lum 2−10	Un.Abs. Flux 0.3−10	Un.Abs. Lum 0.3−10	HR
(1)	(2)	(3)	(4)	(5)	(6)	(7)	(8)	(9)	(10)	(11)
NGC 3780	19373	10	<	4.45E−15	38.87	–	–	−14.22	39.004	–
NGC 3813	–	–	U	–	–	–	–	–	–	–
NGC 3838	19342	10	D	4.09E−14	$39.47^{+0.17}_{-0.20}$	$39.41^{+0.17}_{-0.20}$	$38.57^{+0.17}_{-0.20}$	−13.35	39.51	0.143
NGC 3877	1972	30	D	1.04E−14	$38.56^{+0.11}_{-0.12}$	$38.37^{+0.11}_{-0.12}$	$38.10^{+0.11}_{-0.12}$	−13.93	38.61	0.541
NGC 3884	12999	5	D	1.21E−12	42.08±0.03	41.56±0.03	41.93±0.03	−11.90	42.10	2.35
NGC 3893	21091	10	<	1.07E−14	38.57	–	–	−13.83	38.71	–
NGC 3900	–	–	U	–	–	–	–	–	–	–
NGC 3898	4740	58	D	2.11E−14	$39.08^{+0.05}_{-0.06}$	$38.91^{+0.05}_{-0.056}$	$38.61^{+0.05}_{-0.06}$	−13.66	39.10	0.501
NGC 3917	19380	10	<	6.41E−15	38.35	–	–	−14.06	38.482	–
NGC 3938	18456	46	D*	8.80E−16	$37.48^{+0.43}_{-1.79}$	–	–	−14.92	37.618	–
NGC 3941	–	–	U	–	–	–	–	–	–	–
NGC 3945	6780	15	D	2.22E−13	$40.13^{+0.03}_{-0.04}$	$39.86^{+0.03}_{-0.04}$	$39.80^{+0.03}_{-0.04}$	−12.62	40.16	0.872
NGC 3949	16990	3.4	D*	8.80E−16	$37.48^{+0.43}_{-1.79}$	–	–	−14.92	37.618	–
NGC 3953	19367	11	D*	7.50E−15	$38.41^{+0.28}_{-0.38}$	–	–	−13.99	38.552	–
NGC 3963	19362	9	<	5.07E−15	39.04	–	–	−14.16	39.18	–
NGC 3982	4845	10	D	4.45E−14	39.19±0.09	39.12±0.09	38.37±0.09	−13.32	39.22	0.181
NGC 3992	19366	10	<	1.19E−14	38.61	–	–	−13.79	38.751	–
NGC 3998	6781	15	D	1.58E−11	41.94±0.01	41.37±0.01	41.81±0.01	−10.80	41.95	2.779
NGC 4013	4739	80	D	1.64E−14	$38.75^{+0.14}_{-0.15}$	$37.31^{+0.14}_{-0.15}$	$38.74^{+0.14}_{-0.15}$	−13.79	38.75	26.617
NGC 4026	6782	15	D	2.30E−14	$38.90^{+0.14}_{-0.16}$	$38.46^{+0.14}_{-0.15}$	$38.71^{+0.14}_{-0.16}$	−13.62	38.92	1.771
NGC 4036	6783	15	D	5.07E−13	$40.56^{+0.06}_{-0.07}$	$39.13^{+0.06}_{-0.07}$	$40.55^{+0.06}_{-0.07}$	−12.29	40.57	26.024
NGC 4041	19383	10	D	2.95E−14	$39.26^{+0.03}_{-0.41}$	$39.09^{+0.35}_{-0.04}$	$38.77^{+0.18}_{-0.21}$	−13.49	39.30	0.479
NGC 4051	859	81	D	1.91E−11	41.82±0.01	41.20±0.01	41.70±0.01	−10.74	41.80	3.209

Continued on Next Page

Table D.1 : *cont.*

Name	Obsid	Exp (ks)	Det?	Flux 0.3−10	Lum 0.3−10	Lum 0.3−2	Lum 2−10	Un.Abs. Flux 0.3−10	Un.Abs. Lum 0.3−10	HR
(1)	(2)	(3)	(4)	(5)	(6)	(7)	(8)	(9)	(10)	(11)
NGC 4062	7106	2	<	8.96E−15	38.00	–	–	−13.91	38.14	–
NGC 4088	14442	20	D*	4.63E−15	$38.20^{+0.22}_{-0.29}$	–	–	−14.20	38.34	–
NGC 4096	19345/7103	10	<	5.59E−15	37.71	–	–	−14.12	37.85	–
NGC 4100	19347	10	<	8.10E−15	38.45	–	–	−13.95	38.58	–
NGC 4102	17117	30	D	4.99E−14	$39.24^{+1.45}_{1.44}$	39.68±0.02	40.65±0.02	−11.69	40.85	9.359
NGC 4111	1578	15	D	3.95E−13	$40.14^{+0.05}_{-0.06}$	$39.25^{+0.05}_{-0.06}$	$40.07^{+0.05}_{-0.06}$	−12.40	40.14	6.663
NGC 4125	2071	65	D	2.35E−14	39.22±0.05	38.91±0.05	38.92±0.05	−13.60	39.24	1.040
NGC 4136	2921	20	D*	4.90E−15	$37.74^{+0.20}_{-0.24}$	–	–	−13.98	38.07	–
NGC 4138	17118	29	D	2.35E−12	40.91±0.02	38.30±0.02	40.91±0.02	−11.37	41.16	405.481
NGC 4143	1617	3	D	4.73E−13	$40.21^{+0.05}_{-0.06}$	$39.86^{+0.05}_{-0.06}$	$39.96^{+0.05}_{-0.06}$	−12.31	40.23	1.246
NGC 4144	16991	1	<	2.28E−14	37.66	–	–	−13.50	37.80	–
NGC 4145	–	–	U	–	–	–	–	–	–	–
NGC 4151	9217	125	D	–	–	–	–	–	–	–
NGC 4157	11310	60	<	2.33E−15	37.91	–	–	−14.50	38.04	–
NGC 4162	–	–	U	–	–	–	–	–	–	–
NGC 4169	–	–	U	–	–	–	–	–	–	–
NGC 4183	16992	4	<	9.55E−15	38.518903	–	–	−13.88	38.66	–
NGC 4203	10535	42	D	2.44E−12	40.44±0.01	39.83±0.01	40.32±0.01	−11.61	40.44	3.064
NGC 4214	5197	29	<	1.06E−15	36.19	–	–	−14.84	36.33	–
NGC 4217	4738	74	D*	1.90E−15	$37.82^{+0.18}_{-0.23}$	–	–	−14.59	37.954	–
NGC 4220	19378	10	D*	1.91E−14	$38.82^{+0.17}_{-0.20}$	–	–	−13.58	38.956	–
NGC 4236	9543	11	<	4.17E−15	36.38	–	–	−14.24	36.52	–
NGC 4244	942	50	<	7.08E−16	35.91	–	–	−15.01	36.05	–

Continued on Next Page

Table D.1 : *cont.*

Name	Obsid	Exp (ks)	Det?	Flux 0.3−10	Lum 0.3−10	Lum 0.3−2	Lum 2−10	Un.Abs. Flux 0.3−10	Un.Abs. Lum 0.3−10	HR
(1)	(2)	(3)	(4)	(5)	(6)	(7)	(8)	(9)	(10)	(11)
NGC 4242	19351	10	<	3.03E−15	37.31	–	–	−14.38	37.45	–
NGC 4245	7107	91	<	8.85E−15	37.99	–	–	−13.92	38.13	–
NGC 4251	4695	10	D	1.59E−14	$38.25^{+0.17}_{-0.20}$	$38.05^{+0.17}_{-0.20}$	$37.82^{+0.60}_{-0.23}$	−13.76	38.29	0.592
NGC 4258	1618	21	D	1.01E−11	40.75±0.01	37.94±0.01	40.75±0.01	−11.06	40.69	42.59
NGC 4274	7108	2	<	1.64E−14	38.27	–	–	−13.65	38.40	–
NGC 4278	7081	112	D	4.39E−13	39.69±0.01	39.42±0.01	39.37±0.01	−12.33	39.72	0.895
NGC 4291	11778	30	D	2.63E−14	$39.44^{0.08}_{-0.09}$	$39.16^{0.08}_{-0.09}$	$39.11^{0.08}_{-0.09}$	−13.54	39.48	0.894
NGC 4314	2062	16	D	1.16E−14	$38.12^{0.13}_{-0.15}$	$37.88^{+0.13}_{-0.15}$	$37.74^{+0.13}_{-0.15}$	−13.90	38.15	0.727
NGC 4346	19374	10	D	3.13E−14	$39.03^{0.17}_{-0.19}$	$38.56^{+0.17}_{-0.19}$	$38.85^{+0.17}_{-0.19}$	−13.50	39.04	1.958
NGC 4369	–	–	U	–	–	–	–	–	–	–
NGC 4395	5302	31	D	3.36E−12	39.72±0.01	37.79±0.01	39.71±0.01	−11.37	39.82	82.664
NGC 4414	14796	10	D	3.49E−14	$38.59^{+0.14}_{-0.16}$	$38.11^{+0.14}_{-0.16}$	$38.42^{+0.14}_{-0.16}$	−13.45	38.61	2.060
NGC 4449	10875	60	<	5.49E−15	36.77	–	–	−14.122	36.91	–
NGC 4448	7110	2	<	2.90E−14	38.51	–	–	−13.40	38.65	–
NGC 4460	19363	10	<	7.51E−15	37.77	–	–	−13.99	37.91	–
NGC 4485	4726	40	<	1.50E−15	37.19	–	–	−14.69	37.33	–
NGC 4490	4726	40	D	3.13E−13	39.36±0.02	38.74±0.02	39.24±0.02	−12.02	39.84	3.122
NGC 4494	2079	25	D	1.76E−13	39.30±0.03	38.80±0.03	39.13±0.03	−12.74	39.31	2.152
NGC 4559	2026	10	D	5.11E−14	$38.76^{+0.01}_{-0.26}$	$38.14^{+0.12}_{-0.14}$	$38.64^{+0.12}_{-0.14}$	−13.28	38.77	3.138
NGC 4565	3950	60	D	3.17E−13	39.55±0.02	39.02±0.02	39.40±0.02	−12.33	39.73	2.424
NGC 4589	6785	15	D	3.13E−14	$39.53^{+0.09}_{-0.10}$	$39.34^{+0.09}_{-0.10}$	$39.07^{+0.09}_{-0.10}$	−13.46	39.57	0.533
NGC 4605	19344	10	D*	6.58E−15	$37.10^{+0.30}_{-0.43}$	–	–	−14.04	37.24	–
NGC 4618	7147	9.4	<	4.08E−15	37.42	–	–	−14.25	37.55	–

Continued on Next Page

Table D.1 : *cont.*

Name	Obsid	Exp (ks)	Det?	Flux 0.3−10	Lum 0.3−10	Lum 0.3−2	Lum 2−10	Un.Abs. Flux 0.3−10	Un.Abs. Lum 0.3−10	HR
(1)	(2)	(3)	(4)	(5)	(6)	(7)	(8)	(9)	(10)	(11)
NGC 4648	11362	11	D	1.62E−14	$39.17^{+0.18}_{-0.21}$	$38.78^{+0.18}_{-0.21}$	$38.94^{+0.18}_{-0.21}$	−13.76	39.19	1.440
NGC 4631	797	60	<	9.31E−16	36.72	–	–	−14.90	36.86	–
NGC 4656	–	–	U	–	–	–	–	–	–	–
NGC 4750	4020	5	D	3.35E−13	40.44±0.06	39.93±0.06	40.27±0.06	−12.46	40.45	2.169
NGC 4725	2976	26	D	5.39E−14	38.99±0.05	38.96±0.05	37.91±0.05	−13.23	39.03	0.090
NGC 4736	808	50	D	4.91E−13	39.04±0.01	38.66±0.01	38.80±0.01	−12.30	39.05	1.380
NGC 4800	19385	10	D	3.94E−14	$39.04^{+0.18}_{-0.21}$	$38.25^{+0.18}_{-0.21}$	$38.96^{+0.18}_{-0.21}$	−13.40	39.04	5.069
NGC 4793	–	–	U	–	–	–	–	–	–	–
NGC 4826	9545	26.3	D	3.74E−14	$37.88^{+-1.36}_{-1.47}$	$37.86^{+0.05}_{-0.06}$	$36.47^{+1.46}_{1.35}$	−13.36	37.94	0.0405
NGC 4914	18037	6.4	D*	8.25E−15	$39.58^{+0.31}_{-0.43}$	–	–	−13.95	39.72	–
NGC 5005	4021	5	D	3.05E−13	40.22±0.05	39.96±0.05	39.87±0.05	−12.50	40.23	0.797
NGC 5012	–	–	U	–	–	–	–	–	–	–
NGC 5033	16354	50	D	3.96E−12	41.22±0.01	40.44±0.01	41.14±0.01	−11.54	41.08	5.032
NGC 5055	2197	28	D	1.24E−13	$38.89^{+0.04}_{-0.057}$	$38.22^{+0.04}_{-0.05}$	$38.78^{+0.04}_{-0.05}$	−12.90	38.89	3.667
NGC 5112	–	–	U	–	–	–	–	–	–	–
NGC 5204	3933	49	<	5.54E−16	36.18	–	–	−15.12	36.32	–
NGC 5194	13814	192	D	–	–	–	–	–	–	–
NGC 5195	13814	192	D	1.65E−13	$39.23^{+0.04}_{-0.05}$	$39.03^{+0.04}_{-0.05}$	$38.80^{+0.04}_{-0.05}$	−12.73	39.281340	0.581
NGC 5273	415	1.8	D	–	–	–	–	–	–	–
NGC 5297	19370	10	<	7.10E−15	39.08	–	–	−14.01	39.221	–
NGC 5308	19341	10	D*	1.51E−14	$39.28^{+0.20}_{-0.25}$	–	–	−13.68	39.415	–
NGC 5322	6787	15	D	3.56E−14	$39.63^{+0.08}_{-0.09}$	$39.40^{+0.08}_{-0.09}$	$39.24^{+0.08}_{-0.09}$	−13.80	39.28	0.685
NGC 5354	14903	41	D	2.37E−14	$39.49^{+0.10}_{-0.11}$	$38.76^{+0.10}_{-0.11}$	$39.40^{+0.10}_{-0.11}$	−13.62	39.49	4.351

Continued on Next Page

Table D.1 : *cont.*

Name	Obsid	Exp (ks)	Det?	Flux 0.3−10	Lum 0.3−10	Lum 0.3−2	Lum 2−10	Un.Abs. Flux 0.3−10	Un.Abs. Lum 0.3−10	HR
(1)	(2)	(3)	(4)	(5)	(6)	(7)	(8)	(9)	(10)	(11)
NGC 5353	14903	41	D	4.12E−14	$39.85^{+0.06}_{-0.07}$	$39.79^{+0.06}_{-0.08}$	$38.97^{+0.06}_{-0.07}$	−13.35	39.88	0.154
NGC 5371	13006	5.5	D*	2.32E−14	$39.60^{+0.18}_{-0.22}$	–	–	−13.498	39.735	–
NGC 5377	19372	10	D	2.38E−14	$39.44^{+0.17}_{-0.20}$	$39.23^{+0.17}_{-0.20}$	$39.01^{+0.17}_{-0.20}$	−13.59	39.47	0.594
NGC 5383	19358/13007	10	D*	6.40E−15	$39.04^{+0.40}_{-0.69}$	–	–	−14.057	39.175	–
NGC 5395	10395	16	D	5.02E−14	$40.12^{+0.09}_{-0.10}$	$39.60^{+0.09}_{-0.10}$	$39.96^{+0.09}_{-0.10}$	−13.29	40.12	2.291
NGC 5448	19371	10	D	4.06E−14	$39.719^{+0.13}_{-0.15}$	$39.52^{+0.13}_{-0.15}$	$39.27^{+0.13}_{-0.15}$	−13.36	39.75	0.560
NGC 5457	4736	78	D	4.60E−14	38.21±0.04	37.73±0.04	38.03±0.04	−13.32	38.22	1.962
NGC 5473	–	–	U	–	–	–	–	–	–	–
NGC 5474	9546	30	<	1.36E−14	37.77	–	–	−13.73	37.904	–
NGC 5485	19375	10	D	2.30E−14	$39.47^{+0.18}_{-0.21}$	$39.29^{+0.18}_{-0.21}$	$39.01^{+0.18}_{-0.21}$	−13.61	39.50	0.533
NGC 5523	–	–	U	–	–	–	–	–	–	–
NGC 5548	3046	154	D	–	–	–	–	–	–	–
NGC 5557	19324	9	D	2.42E−14	$39.72^{+0.20}_{-0.23}$	$39.67^{+0.20}_{-0.23}$	$38.74^{+0.20}_{-0.23}$	−13.58	39.76	0.116
NGC 5585	7150/19348	10	<	5.96E−15	37.54	–	–	−14.09	37.68	–
NGC 5631	19376	10	D	3.35E−14	$39.63^{+0.16}_{-0.18}$	$39.33^{+0.16}_{-0.18}$	$39.33^{+0.16}_{-0.18}$	−13.46	39.65	0.995
NGC 5660	19361	10	<	3.99E−14	39.82	–	–	−13.26	39.96	–
NGC 5656	–	–	U	–	–	–	–	–	–	–
NGC 5678	19382/4022	10	<	2.10E−14	39.50	–	–	−13.54	39.64	–
NGC 5676	19352	10	<	5.70E−15	38.91	–	–	−14.11	39.05	–
NGC 5866	2879	34	D*	8.00E−15	$38.35^{+0.13}_{-0.14}$	–	–	−13.96	38.49	–
NGC 5879	2241	90	D	7.18E−14	$39.38^{+0.06}_{-0.07}$	$36.75^{+0.06}_{-0.07}$	$39.38^{+0.06}_{-0.07}$	−12.88	39.65	425.999
NGC 5905	7728	45	D	2.03E−14	$39.68^{+0.06}_{-0.07}$	$39.49^{+0.06}_{-0.07}$	$39.22^{+0.06}_{-0.07}$	−13.67	39.71	0.535
NGC 5907	20830	52	D	9.18E−15	$38.39^{+0.15}_{-0.17}$	$37.94^{+0.15}_{-0.17}$	$38.20^{+0.15}_{-0.17}$	−14.03	38.40	1.799

Continued on Next Page

Table D.1 : *cont.*

Name	Obsid	Exp (ks)	Det?	Flux 0.3−10	Lum 0.3−10	Lum 0.3−2	Lum 2−10	Un.Abs. Flux 0.3−10	Un.Abs. Lum 0.3−10	HR
(1)	(2)	(3)	(4)	(5)	(6)	(7)	(8)	(9)	(10)	(11)
NGC 5982	20069	23	D	5.52E−14	$40.00^{+0.09}_{-0.10}$	$39.95^{+0.09}_{-0.10}$	$39.03^{+0.09}_{-0.10}$	−13.20	40.06	0.120
NGC 5985	19369	10	D	2.10E−13	$40.59^{+0.07}_{-0.07}$	40.05±0.07	40.44±0.07	−12.67	40.60	2.449
NGC 6015	19349	10	D*	1.23E−14	$38.65^{+0.21}_{-0.27}$	–	–	−13.77	38.789	–
NGC 6140	–	–	U	–	–	–	–	–	–	–
NGC 6217	–	–	U	–	–	–	–	–	–	–
NGC 6207	–	–	U	–	–	–	–	–	–	–
NGC 6236	–	–	U	–	–	–	–	–	–	–
NGC 6340	–	–	U	–	–	–	–	–	–	–
NGC 6412	–	–	U	–	–	–	–	–	–	–
NGC 6503	872	13.4	D*	5.43E−15	$37.38^{+0.23}_{-0.32}$	–	–	−14.13	37.520	–
NGC 6482	3218	19.6	D	1.79E−13	40.77±0.04	40.41±0.04	40.52±0.04	−12.69	40.83	1.269
NGC 6643	10118	10	D*	4.85E−15	$38.58^{+0.31}_{-0.52}$	–	–	−14.18	38.713	–
NGC 6654	–	–	U	–	–	–	–	–	–	–
NGC 6689	7123	3.5	<	6.36E−15	38.05	–	–	−14.06	38.190	–
NGC 6702	–	–	U	–	–	–	–	–	–	–
NGC 6703	–	–	U	–	–	–	–	–	–	–
NGC 6946	1043	59	D	1.33E−13	$38.68^{+0.02}_{-0.03}$	$38.17^{+0.02}_{-0.03}$	$38.52^{+0.02}_{-0.03}$	−12.43	39.13	2.213
NGC 6951	–	–	U	–	–	–	–	–	–	–
NGC 7080	–	–	U	–	–	–	–	–	–	–
NGC 7217	–	–	U	–	–	–	–	–	–	–
NGC 7331	2198	30	D	2.41E−14	$38.77^{+0.08}_{-0.09}$	$38.34^{+0.08}_{-0.09}$	$38.57^{+0.08}_{-0.09}$	−13.56	38.83	1.688
NGC 7332	–	–	U	–	–	–	–	–	–	–
NGC 7457	11786	29	D	2.01E−14	$38.56^{+0.10}_{-0.11}$	$37.92^{+0.102}_{-0.11}$	$38.45^{+0.10}_{-0.11}$	−13.68	38.58	3.40

Continued on Next Page

Table D.1 : *cont.*

Name	Obsid	Exp (ks)	Det?	Flux 0.3−10	Lum 0.3−10	Lum 0.3−2	Lum 2−10	Un.Abs. Flux 0.3−10	Un.Abs. Lum 0.3−10	HR
(1)	(2)	(3)	(4)	(5)	(6)	(7)	(8)	(9)	(10)	(11)
NGC 7640	7101	2	<	1.67E−14	38.17	–	–	−13.64	38.31	–
NGC 7741	7124	3.6	<	8.80E−15	38.20	–	–	−13.92	38.34	–
NGC 7798	–	–	U	–	–	–	–	–	–	–

Table D.1: Column Description: (1) Galaxy Name; (2) *Chandra* Observation ID, if two observations were used for fitting/imaging, these are both given; (3) Exposure in kiloseconds, if two observations have been used, then their combined exposure is given; (4) Indication of the detection status of the source: 'D' indicates a detection with spectral information, 'D*' indicates a detection without spectral information, 'U' indicates and unobserved source, '<' indicates no detection of the source hence an upper limit is given on the flux values; (5) Flux in the 0.3-10.0 keV band, in erg s^{-1} obtained from fitting spectra or from the automated pipeline. If undetected the upper limit is given; (6) Luminosity in the 0.3-10.0 keV band, in erg s^{-1}. If undetected the upper limit is given; (7) Luminosity in the 0.3-2.0 keV band, in erg s^{-1}. If undetected the upper limit is given; (8) Luminosity in the 2.0-10.0 keV band, in erg s^{-1}. If undetected the upper limit is given; (9) Unabsorbed Flux in the 0.3-10.0 keV band, in erg s^{-1} obtained from fitting spectra or from the automated pipeline. If undetected the upper limit is given; (10) Unabsorbed Luminosity in the 0.3-10.0 keV band, in erg s^{-1}. If undetected the upper limit is given; (11) Hardness Ratio, denoted by the flux in the hard band divide by the soft band

D.3 Chandra X−ray Spectral Information

Name	Mod.	Sta.	Gal. Abs.	Ex. Abs.	Γ	Γ norm	APEC kT	APEC norm	Gau.	Gau. norm	Gau.	Chi dof	Not.
(1)	(2)	(3)	(4)	(5)	(6)	(7)	(8)	(9)	(10)	(11)	(12)	(13)	(14)
NGC 221	α	Chi	0.10900	-	2.48±0.16	-4.99±0.03	-	-	-	-	-	1.485	-
NGC 224	α	Chi	0.12700	-	2.56±0.08	-4.02±0.02	-	-	-	-	-	0.9054	-
NGC 266	α	Chi	0.05700	-	$1.63^{0.11}_{-0.10}$	-4.67±0.04	-	-	-	-	-	1.134	-
NGC 278	α	Cstat	0.12100	-	5.86±uc	-	-	-	-	-	-	7.14/6	-
NGC 315	δ	Chi	0.05830	$0.25^{0.10}_{-0.05}$	$1.13^{0.11}_{-0.07}$	$-3.95^{0.06}_{-0.04}$	$0.46^{0.09}_{-0.13}$	$0.09^{0.41}_{-0.20}$	-	-	-	1.3456	-
NGC 404	α	Chi	0.05130	-	$2.27^{0.23}_{-0.23}$	$-5.26^{0.04}_{-0.05}$	-	-	-	-	-	1.285	-
NGC 410	α	Cstat	0.05450	-	$3.94^{0.76}_{-0.72}$	$-4.08^{0.09}_{-0.09}$	-	-	-	-	-	13.06/11	-
NGC 507	η	Chi	0.05250	-	$2.70^{0.50}_{-1.20}$	$-4.92^{0.11}_{-0.33}$	-	-	$0.88^{0.03}_{-0.05}$	$0.09^{0.08}_{-0.03}$	$-4.77^{0.22}_{-0.14}$	1.463	-
NGC 777	α	Cstat	0.04790	-	$3.72^{0.46}_{-0.44}$	$-4.15^{0.07}_{-0.07}$	-	-	-	-	-	38.27/11	-
NGC 890	α	Cstat	0.06010	-	$1.78^{0.78}_{-0.70}$	$-5.77^{0.24}_{-0.27}$	-	-	-	-	-	2.77/6	-
NGC 1023	α	Chi	0.05500	-	$1.90^{0.14}_{-0.14}$	$-4.89^{0.034}_{-0.04}$	-	-	-	-	-	0.8827	-
NGC 1058	α	Cstat	0.05440	-	$1.80^{0.67}_{-0.62}$	$-5.35^{0.20}_{-0.23}$	-	-	-	-	-	3.64/8	-
NGC 1161	α	Cstat	0.15100	-	$2.61^{0.75}_{-0.70}$	$-4.92^{0.14}_{-0.16}$	-	-	-	-	-	8.45/8	-
NGC 1167	α	Cstat	0.09770	-	$2.56^{0.62}_{-0.60}$	$-4.84^{0.13}_{-0.15}$	-	-	-	-	-	8.68/13	-
NGC 1275	α	Chi	0.13600	-	$0.97^{0.03}_{-0.03}$	$-2.77^{0.02}_{-0.02}$	-	-	-	-	-	1.2003	-
IC 342	α	Chi	0.29900	-	$3.09^{0.22}_{-0.21}$	$-3.87^{0.04}_{-0.04}$	-	-	-	-	-	1.242	-
NGC 1569	α	Cstat	0.22000	-	$3.22^{3.04}_{-1.47}$	$-6.27^{0.22}_{-0.33}$	-	-	-	-	-	1.87/6	-
NGC 1961	α	Cstat	0.08110	-	$1.29^{0.35}_{-0.35}$	$-5.05^{0.13}_{-0.14}$	-	-	-	-	-	17.34/15	-
NGC 2146	α	Cstat	0.07080	-	$-0.58^{0.67}_{-0.77}$	$-5.78^{0.31}_{-0.41}$	-	-	-	-	-	12.82/7	-
NGC 2273	ϵ	Chi	0.06730	-	$0.10^{0.35}_{-0.37}$	$-5.07^{0.16}_{-0.20}$	-	-	$6.40^{0.04}_{-0.04}$	$0.09^{0.06}_{-0.05}$	$-4.44^{0.11}_{-0.14}$	0.888	-
NGC 2276	α	Cstat	0.05690	-	$3.05^{0.72}_{-0.81}$	$-5.66^{0.12}_{-0.14}$	-	-	-	-	-	25.04/11	-
NGC 2300	α	Cstat	0.05610	-	$4.27^{0.61}_{-0.58}$	$-4.67^{0.08}_{-0.08}$	-	-	-	-	-	19.28/16	-
NGC 2403	β	Chi	0.04360	$0.28^{0.15}_{-0.13}$	$2.72^{0.40}_{-0.35}$	$-4.12^{0.16}_{-0.15}$	-	-	-	-	-	1.487	-

Continued on Next Page

Table D.2 : *cont.*

Name	Mod.	Sta.	Gal. Abs.	Ex. Abs.	Γ	Γ norm	APEC kT	APEC norm	Gau.	Gau. norm	Gau.	Chi dof	Not.
(1)	(2)	(3)	(4)	(5)	(6)	(7)	(8)	(9)	(10)	(11)	(12)	(13)	(14)
NGC 2549	α	Cstat	0.04550	-	$1.66^{0.70}_{-0.67}$	$-5.09^{0.21}_{-0.24}$	-	-	-	-	-	6.80/8	-
NGC 2639	α	Cstat	0.02990	-	$4.16^{0.80}_{-0.74}$	$-3.99^{0.09}_{-0.10}$	-	-	-	-	-	13.50/8	-
NGC 2683	α	Chi	0.02510	-	$-2.03^{0.29}_{-0.32}$	$-6.40^{0.19}_{-0.22}$	-	-	-	-	-	1.218	-
NGC 2681	γ	Chi	0.02470	-	$1.52^{0.16}_{-0.18}$	$-5.26^{0.06}_{-0.08}$	$0.85^{0.07}_{-0.05}$	$0.07^{0.05}_{-0.06}$	-	-	-	0.8491	-
NGC 2768	α	Chi	0.04130	-	$1.30^{0.14}_{-0.14}$	$-5.08^{0.05}_{-0.05}$	-	-	-	-	-	0.943	-
NGC 2748	α	Cstat	0.01550	-	$1.67^{0.66}_{-0.60}$	$-5.96^{0.17}_{-0.20}$	-	-	-	-	-	6.37/6	-
NGC 2782	η	Chi	0.01460	-	$-0.03^{0.41}_{-0.39}$	$-5.44^{0.19}_{-0.22}$	$0.99^{0.06}_{-0.08}$	$0.06^{0.08}_{-0.10}$	$6.36^{0.10}_{-0.16}$	$0.15^{0.34}_{-0.15}$	$-5.22^{0.21}_{-0.30}$	1.144	-
NGC 2787	α	Chi	0.04620	-	$1.81^{0.13}_{-0.12}$	$-4.60^{0.03}_{-0.04}$	-	-	-	-	-	1.31	-
NGC 2832	α	Cstat	0.01380	-	$4.06^{1.59}_{-1.43}$	$-4.33^{0.18}_{-0.21}$	-	-	-	-	-	4.79/5	-
NGC 2841	γ	Chi	0.01330	-	$1.30^{0.39}_{-0.54}$	$-5.23^{0.11}_{-0.19}$	$0.81^{0.22}_{-0.20}$	$0.22^{0.16}_{-0.24}$	-	-	-	0.471	-
NGC 2903	α	Chi	0.02890	-	$1.67^{0.16}_{-0.15}$	$-5.16^{0.04}_{-0.05}$	-	-	-	-	-	1.365	-
NGC 2950	α	Cstat	0.01590	-	$2.91^{1.48}_{-1.22}$	$-4.96^{0.36}_{-0.38}$	-	-	-	-	-	8.42/6	-
NGC 2985	α	Chi	0.02200	-	$1.97^{0.30}_{-0.29}$	$-4.74^{0.06}_{-0.07}$	-	-	-	-	-	0.656	-
NGC 3034	δ	Chi	0.05040	$1.01^{0.16}_{-0.18}$	$1.95^{0.29}_{-0.37}$	$-4.54^{0.18}_{-0.27}$	$0.80^{0.10}_{-0.11}$	$0.10^{0.16}_{-0.25}$	-	-	-	1.1908	-
NGC 3079	ζ	Chi	0.00885	$1.07^{1.13}_{-0.79}$	$2.21^{1.55}_{-1.01}$	$-4.51^{0.74}_{-0.54}$	-	-	$6.40^{0.24}_{-0.21}$	$0.43^{0.31}_{-0.29}$	$-5.09^{0.18}_{-0.23}$	1.14	-
NGC 3077	β	Chi	0.05050	$0.97^{0.66}_{-0.49}$	$1.39^{0.54}_{-0.48}$	$-4.89^{0.33}_{-0.30}$	-	-	-	-	-	1.077	-
NGC 3147	α	Chi	0.02850	-	$1.35^{0.07}_{-0.06}$	$-3.24^{0.02}_{-0.02}$	-	-	-	-	-	1.228	-
NGC 3190	γ	Chi	0.01960	-	$-1.01^{0.47}_{-0.51}$	$-6.24^{0.28}_{-0.36}$	$0.67^{0.12}_{-0.01}$	$0.12^{0.08}_{-0.09}$	-	-	-	1.37	-
NGC 3184	α	Cstat	0.01100	-	$1.51^{0.25}_{-0.25}$	$-5.50^{0.07}_{-0.08}$	-	-	-	-	-	14.20/8	-
NGC 3193	α	Cstat	0.02110	-	$2.20^{0.69}_{-0.66}$	$-5.33^{0.15}_{-0.18}$	-	-	-	-	-	5.33/5	-
NGC 3198	α	Cstat	0.00875	-	$1.34^{0.33}_{-0.32}$	$-5.64^{0.11}_{-0.12}$	-	-	-	-	-	10.27/8	-
NGC 3245	α	Cstat	0.02020	-	$1.43^{0.31}_{-0.31}$	$-5.03^{0.08}_{-0.09}$	-	-	-	-	-	14.05/13	-
NGC 3310	β	Chi	0.01350	$0.31^{0.06}_{-0.06}$	$1.35^{0.13}_{-0.13}$	$-4.23^{0.07}_{-0.06}$	-	-	-	-	-	0.9013	-

Continued on Next Page

Table D.2 : *cont.*

Name	Mod.	Sta.	Gal. Abs.	Ex. Abs.	Γ	Γ norm	APEC kT	APEC norm	Gau.	Gau. norm	Gau.	Chi dof	Not.
(1)	(2)	(3)	(4)	(5)	(6)	(7)	(8)	(9)	(10)	(11)	(12)	(13)	(14)
NGC 3319	α	Cstat	0.01540	-	$1.77^{0.65}_{-0.62}$	$-4.80^{0.17}_{-0.18}$	-	-	-	-	-	11.02/8	-
NGC 3344	α	Cstat	0.02460	-	$2.18^{0.38}_{-0.37}$	$-5.14^{0.10}_{-0.11}$	-	-	-	-	-	24.37/15	-
NGC 3414	α	Chi	0.01590	-	$1.35^{0.10}_{-0.10}$	$-4.25^{0.03}_{-0.04}$	-	-	-	-	-	1.161	-
NGC 3448	α	Cstat	0.00805	-	$1.11^{0.73}_{-0.71}$	$-5.37^{0.31}_{-0.35}$	-	-	-	-	-	8.31/6	-
NGC 3516	η	Chi	0.03450	-	$0.61^{0.03}_{-0.03}$	$-1.88^{0.02}_{-0.02}$	$0.10^{0.04}_{-0.02}$	$0.04^{0.44}_{-0.53}$	$6.34^{0.03}_{-0.03}$	$0.03^{0.04}_{-0.03}$	$-3.36^{0.12}_{-0.15}$	1.6535	-
NGC 3556	β	Chi	0.00778	$0.38^{0.16}_{-0.15}$	$1.80^{0.44}_{-0.39}$	$-4.80^{0.18}_{-0.17}$	-	-	-	-	-	1.088	-
NGC 3583	α	Cstat	0.01450	-	$1.51^{0.84}_{-0.81}$	$-5.35^{0.24}_{-0.28}$	-	-	-	-	-	6.82/5	-
NGC 3600	α	Cstat	0.01510	-	$1.57^{0.43}_{-0.42}$	$-4.69^{0.13}_{-0.14}$	-	-	-	-	-	16.59/11	-
NGC 3610	α	Cstat	0.00642	-	$2.13^{0.96}_{-0.90}$	$-5.26^{0.18}_{-0.21}$	-	-	-	-	-	9.91/6	-
NGC 3631	α	Cstat	0.01100	-	$3.31^{0.94}_{-0.95}$	$-6.30^{0.17}_{-0.19}$	-	-	-	-	-	2.95/6	-
NGC 3642	α	Cstat	0.00700	-	$2.36^{0.44}_{-0.42}$	$-4.59^{0.11}_{-0.12}$	-	-	-	-	-	15.70/12	-
NGC 3665	α	Cstat	0.02000	-	$1.36^{0.48}_{-0.47}$	$-5.28^{0.15}_{-0.17}$	-	-	-	-	-	7.32/8	-
NGC 3690	θ	Chi	0.00901	$1.08^{0.11}_{-0.12}$	$0.27^{0.57}_{-0.31}$	$-5.36^{0.36}_{-0.41}$	$0.71^{0.10}_{-0.12}$	$0.10^{0.14}_{-0.13}$	$6.34^{0.04}_{-0.04}$	$0.07^{0.05}_{-0.07}$	$-5.31^{0.14}_{-0.22}$	1.197	-
NGC 3718	β	Chi	0.01060	$0.88^{0.15}_{-0.13}$	$1.67^{0.19}_{-0.18}$	$-3.12^{0.10}_{-0.10}$	-	-	-	-	-	1.026	-
NGC 3838	α	Cstat	0.00890	-	$3.04^{1.29}_{-1.09}$	$-5.07^{0.26}_{-0.30}$	-	-	-	-	-	4.99/6	-
NGC 3877	α	Cstat	0.02480	-	$2.35^{0.80}_{-0.79}$	$-5.62^{0.11}_{-0.13}$	-	-	-	-	-	13.78/6	-
NGC 3884	α	Chi	0.01210	-	$1.47^{0.12}_{-0.11}$	$-3.83^{0.04}_{-0.04}$	-	-	-	-	-	0.9872	-
NGC 3898	α	Chi	0.00861	-	$2.33^{0.28}_{-0.28}$	$-5.35^{0.05}_{-0.06}$	-	-	-	-	-	1.212	-
NGC 3945	α	Chi	0.02200	-	$2.06^{0.13}_{-0.12}$	$-4.35^{0.03}_{-0.04}$	-	-	-	-	-	1.3	-
NGC 3982	α	Cstat	0.00951	-	$2.91^{0.53}_{-0.45}$	$-5.02^{0.09}_{-0.10}$	-	-	-	-	-	29.72/10	-
NGC 3998	α	Chi	0.01010	-	$1.34^{0.02}_{-0.02}$	$-2.80^{0.01}_{-0.01}$	-	-	-	-	-	1.3907	-
NGC 4013	α	Cstat	0.01260	-	$-0.03^{0.63}_{-0.65}$	$-6.72^{0.30}_{-0.37}$	-	-	-	-	-	8.92/8	-
NGC 4026	α	Cstat	0.02060	-	$1.64^{0.97}_{-0.97}$	$-5.48^{0.16}_{-0.19}$	-	-	-	-	-	3.09/6	-

Continued on Next Page

Table D.2 : *cont.*

Name	Mod.	Sta.	Gal. Abs.	Ex. Abs.	Γ	Γ norm	APEC kT	APEC norm	Gau.	Gau. norm	Gau.	Chi dof	Not.
(1)	(2)	(3)	(4)	(5)	(6)	(7)	(8)	(9)	(10)	(11)	(12)	(13)	(14)
NGC 4036	γ	Chi	0.01890	-	$-0.88^{0.49}_{-0.55}$	$-5.94^{0.27}_{-0.34}$	$0.60^{0.24}_{-0.26}$	$0.24^{0.11}_{-0.14}$	-	-	-	1.32	-
NGC 4041	α	Cstat	0.01790	-	$2.41^{1.45}_{-1.29}$	$-5.17^{0.33}_{-0.38}$	-	-	-	-	-	14.43/5	-
NGC 4051	α	Chi	0.01150	-	$2.53^{0.03}_{-0.03}$	$-1.64^{0.02}_{-0.02}$	-	-	-	-	-	1.1884	-
NGC 4102	θ	Chi	0.01680	$0.55^{0.14}_{-0.20}$	$1.98^{0.67}_{-1.24}$	$-4.33^{0.2}_{-0.64}$	$0.76^{0.09}_{-0.04}$	$0.09^{0.22}_{-0.37}$	$7.01^{0.33}_{-0.27}$	$1.25^{0.24}_{-0.18}$	$-3.98^{0.08}_{-0.09}$	0.9334	-
NGC 4111	γ	Chi	0.01210	-	$-0.66^{0.79}_{-1.02}$	$-5.90^{0.42}_{-0.65}$	$0.77^{0.08}_{-0.0}$	$0.08^{0.07}_{-0.08}$	-	-	-	0.764	-
NGC 4125	α	Chi	0.01740	-	$1.943^{0.20}_{-0.20}$	$-5.36^{0.05}_{-0.05}$	-	-	-	-	-	1.551	-
NGC 4138	β	Chi	0.01250	$6.40^{1.11}_{-0.98}$	$1.18^{0.31}_{-0.29}$	$-3.46^{0.23}_{-0.22}$	-	-	-	-	-	1.4606	-
NGC 4143	α	Chi	0.01290	-	$1.82^{0.29}_{-0.27}$	$-4.11^{0.05}_{-0.06}$	-	-	-	-	-	1.02	-
NGC 4203	α	Chi	0.01110	-	$1.28^{0.03}_{-0.03}$	$-3.63^{0.01}_{-0.01}$	-	-	-	-	-	1.2237	-
NGC 4251	α	Cstat	0.01910	-	$2.28^{1.33}_{-1.23}$	$-5.46^{0.19}_{-0.23}$	-	-	-	-	-	6.72/6	-
NGC 4258	β	Chi	0.01600	$5.70^{0.96}_{-0.86}$	$1.24^{0.35}_{-0.33}$	$-2.96^{0.24}_{-0.23}$	-	-	-	-	-	1.4311	-
NGC 4278	γ	Chi	0.02070	-	$1.97^{0.04}_{-0.04}$	$-4.11^{0.01}_{-0.01}$	$0.80^{0.06}_{-0.07}$	$0.06^{0.06}_{-0.08}$	-	-	-	0.99575	-
NGC 4291	α	Cstat	0.02870	-	$2.07^{0.41}_{-0.40}$	$-5.26^{0.10}_{-0.11}$	-	-	-	-	-	11.91/14	-
NGC 4314	α	Cstat	0.02090	-	$2.16^{0.77}_{-0.57}$	$-5.61^{0.13}_{-0.15}$	-	-	-	-	-	9.27/8	-
NGC 4346	α	Cstat	0.01200	-	$1.56^{1.11}_{-1.11}$	$-5.39^{0.27}_{-0.33}$	-	-	-	-	-	2.74/6	-
NGC 4395	β	Chi	0.01850	$2.55^{0.39}_{-0.36}$	$0.72^{0.18}_{-0.17}$	$-3.74^{0.12}_{-0.12}$	-	-	-	-	-	1.7909	-
NGC 4414	α	Cstat	0.01600	-	$1.53^{0.68}_{-0.65}$	$-5.35^{0.20}_{-0.23}$	-	-	-	-	-	10.96/7	-
NGC 4490	β	Chi	0.01810	$0.86^{0.14}_{-0.12}$	$2.45^{0.20}_{-0.19}$	$-3.71^{0.10}_{-0.10}$	-	-	-	-	-	1.318	-
NGC 4494	α	Chi	0.01420	-	$1.50^{0.11}_{-0.11}$	$-4.66^{0.03}_{-0.04}$	-	-	-	-	-	1.278	-
NGC 4559	α	Cstat	0.01430	-	$1.28^{0.56}_{-0.53}$	$-5.31^{0.16}_{-0.19}$	-	-	-	-	-	20.38/13	-
NGC 4565	β	Chi	0.01170	$0.26^{0.04}_{-0.03}$	$1.93^{0.12}_{-0.12}$	$-4.09^{0.05}_{-0.05}$	-	-	-	-	-	0.993	-
NGC 4589	α	Cstat	0.02010	-	$2.344^{0.46}_{-0.43}$	$-5.15^{0.10}_{-0.10}$	-	-	-	-	-	9.61/9	-
NGC 4648	α	Cstat	0.02010	-	$1.77^{1.11}_{-0.89}$	$-5.58^{0.27}_{-0.32}$	-	-	-	-	-	6.17/5	-

Continued on Next Page

Table D.2 : *cont.*

Name	Mod.	Sta.	Gal. Abs.	Ex. Abs.	Γ	Γ norm	APEC kT	APEC norm	Gau.	Gau. norm	Gau.	Chi dof	Not.
(1)	(2)	(3)	(4)	(5)	(6)	(7)	(8)	(9)	(10)	(11)	(12)	(13)	(14)
NGC 4750	α	Cstat	0.01700	-	$1.51^{0.28}_{-0.28}$	$-4.38^{0.07}_{-0.08}$	-	-	-	-	-	10.09/11	-
NGC 4725	α	Chi	0.00840	-	$3.29^{0.25}_{-0.24}$	$-4.99^{0.06}_{-0.07}$	-	-	-	-	-	1.661	-
NGC 4736	γ	Chi	0.01240	-	$1.63^{0.05}_{-0.05}$	$-4.21^{0.02}_{-0.02}$	$0.80^{0.06}_{-0.06}$	$0.06^{0.06}_{-0.07}$	-	-	-	0.91995	-
NGC 4800	α	Cstat	0.01460	-	$0.99^{1.07}_{-1.07}$	$-5.60^{0.35}_{-0.43}$	-	-	-	-	-	3.73/5	-
NGC 4826	γ	Chi	0.02850	-	$3.27^{-3.30}_{-3.30}$	$-5.84^{0.47}_{-2.88}$	$0.66^{0.10}_{-0.08}$	$0.10^{0.08}_{-0.11}$	-	-	-	- 1.19	-
NGC 5005	γ	Chi	0.01110	-	$1.78^{0.32}_{-0.37}$	$-4.44^{0.12}_{-0.17}$	$1.02^{0.30}_{-0.14}$	$0.30^{0.14}_{-0.20}$	-	-	-	0.776	-
NGC 5033	α	Chi	0.01060	-	$1.57^{0.04}_{-0.06}$	$-3.43^{0.02}_{-0.02}$	-	-	-	-	-	1.0765	-
NGC 5055	α	Chi	0.01290	-	$1.18^{0.14}_{-0.13}$	$-4.99^{0.05}_{-0.05}$	-	-	-	-	-	1.057	-
NGC 5195	γ	Chi	0.01790	-	$1.26^{0.24}_{-0.22}$	$-5.13^{0.10}_{-0.11}$	$0.15^{0.82}_{-0.10}$	$0.82^{4.03}_{-1.18}$	-	-	-	1.798	-
NGC 5322	α	Cstat	0.01640	-	$2.18^{0.35}_{-0.34}$	$-5.13^{0.08}_{-0.09}$	-	-	-	-	-	22.26/11	-
NGC 5354	α	Cstat	0.00952	-	$1.07^{0.42}_{-0.41}$	$-5.77^{0.16}_{-0.18}$	-	-	-	-	-	7.43/8	-
NGC 5353	α	Chi	0.00954	-	$3.00^{0.59}_{-0.51}$	$-5.05^{0.08}_{-0.10}$	-	-	-	-	-	0.94	-
NGC 5377	α	Cstat	0.01680	-	$2.26^{1.34}_{-0.95}$	$-5.29^{0.26}_{-0.29}$	-	-	-	-	-	18.97/6	-
NGC 5395	α	Cstat	0.00983	-	$1.45^{0.40}_{-0.38}$	$-5.23^{0.13}_{-0.14}$	-	-	-	-	-	11.06/10	-
NGC 5448	α	Cstat	0.01640	-	$2.31^{0.76}_{-0.68}$	$-5.05^{0.19}_{-0.21}$	-	-	-	-	-	4.92/7	-
NGC 5457	α	Chi	0.01800	-	$1.57^{0.16}_{-0.16}$	$-5.22^{0.04}_{-0.05}$	-	-	-	-	-	1.203	-
NGC 5485	α	Cstat	0.01350	-	$2.32^{1.13}_{-0.98}$	$-5.30^{0.28}_{-0.33}$	-	-	-	-	-	3.1/5	-
NGC 5557	α	Cstat	0.00985	-	$3.17^{1.37}_{-1.47}$	$-5.30^{0.20}_{-0.23}$	-	-	-	-	-	6.64/4	-
NGC 5631	α	Cstat	0.01370	-	$1.96^{1.17}_{-1.14}$	$-5.21^{0.25}_{-0.30}$	-	-	-	-	-	5.34/6	-
NGC 5879	β	Chi	0.01580	$6.54^{4.91}_{-3.14}$	$1.20^{1.15}_{-0.95}$	$-4.95^{0.87}_{-}$	-	-	-	-	-	1.21	-
NGC 5905	α	Cstat	0.01210	-	$2.30^{0.33}_{-0.34}$	$-5.35^{0.06}_{-0.07}$	-	-	-	-	-	51.75/9	-
NGC 5907	α	Cstat	0.01210	-	$1.61^{0.93}_{-0.84}$	$-5.90^{0.32}_{-0.35}$	-	-	-	-	-	3.13/6	-
NGC 5982	α	Cstat	0.01520	-	$3.17^{0.62}_{-0.56}$	$-4.92^{0.11}_{-0.13}$	-	-	-	-	-	8.57/10	-

Continued on Next Page

Table D.2 : *cont.*

Name	Mod.	Sta.	Gal. Abs.	Ex. Abs.	Γ	Γ norm	APEC kT	APEC norm	Gau.	Gau. norm	Gau.	Chi dof	Not.
(1)	(2)	(3)	(4)	(5)	(6)	(7)	(8)	(9)	(10)	(11)	(12)	(13)	(14)
NGC 5985	α	Cstat	0.01550	-	$1.43^{0.32}_{-0.31}$	$-4.62^{0.12}_{-0.13}$	-	-	-	-	-	21.45/9	-
NGC 6482	γ	Chi	0.07740	-	$1.02^{0.95}_{-2.42}$	$-5.10^{0.25}_{-0.78}$	$0.86^{0.07}_{-0.06}$	$0.07^{0.08}_{-0.08}$	-	-	-	1.168	-
NGC 6946	β	Chi	0.18400	$0.43^{0.10}_{-0.09}$	$2.48^{0.21}_{-0.20}$	$-4.11^{0.09}_{-0.09}$	-	-	-	-	-	1.547	-
NGC 7331	α	Cstat	0.06150	-	$1.78^{0.48}_{-0.47}$	$-5.37^{0.10}_{-0.11}$	-	-	-	-	-	13.26/14	-
NGC 7457	α	Cstat	0.04600	-	$1.30^{0.43}_{-0.42}$	$-5.69^{0.14}_{-0.15}$	-	-	-	-	-	8.14/7	-

Table D.2: Column Description: (1) Galaxy Name; (2) Model used if detected, else 'Undet': Undetected. The used models are as follows: 'α' Absorbed Power-Law (PHABS × ZPOWERLAW); 'β' Absorbed Power-Law with additional absorber (PHABS × ZPHABS × ZPOWERLAW); 'γ' Absorbed Power-Law with additional thermal emission (PHABS × [ZPOWERLAW + APEC]); 'δ' Absorbed Power-Law with additional absorber and thermal emission (PHABS × ZPHABS × [ZPOWERLAW + APEC]); 'ϵ' Absorbed Power-Law and Gaussian (PHABS × [ZPOWERLAW + GAUSS]); 'ζ' Absorbed Power-Law with additional absorber and Gaussian (PHABS × ZPHABS × [ZPOWERLAW + GAUSS]); 'η' Absorbed Power-Law and thermal emission and Gaussian (PHABS × [ZPOWERLAW + APEC + GAUSS]); 'θ' Absorbed Power-Law and thermal emission and Gaussian (PHABS × ZPHABS × [ZPOWERLAW + APEC + GAUSS]); (3) Statistical method used to extract the spectrum: 'Chi' indicates a spectrum with enough counts for ^{2} fitting to take place; 'Cstat' indicates a spectrum with not enough counts and so Cash statistics were used. (4) Galactic Absorption, measured from (Kalberla et al., 2005) using the HEASARC web interface at https://heasarc.gsfc.nasa.gov/cgi−bin/Tools/w3nh/w3nh.pl, measured in cm^{-2}. (5) Additional absorber, measured in cm^{-2}, if required in the model. (6) Photon index. (7) Photon index normalisation, measured in logarithm. (8) APEC temperature, measured in keV, if required in the model. (9) APEC normalisation, measured in logarithm, if required in the model. (10) Gaussian centroid position, measured in keV, if required in the model. (11) Gaussian sigma (width), measured in keV, if required in the model. (12) Gaussian normalisation, measured in logarithm, if required in the model. (13) The reduced ^{2} if fit with ^{2} statistics, else the number of bins divided by the degrees of freedom for Cash statistics. (14) Notes on the objects: 'pile-up' indicated an additional pile-up component was required in the model fitting.

Appendix E

Fundamental Plane Appendix

E.1 Fundamental Plane of Black Hole Activity Fits and Regressions

E.2 Optical Fundamental Plane of Black Hole Activity Fits and Regressions

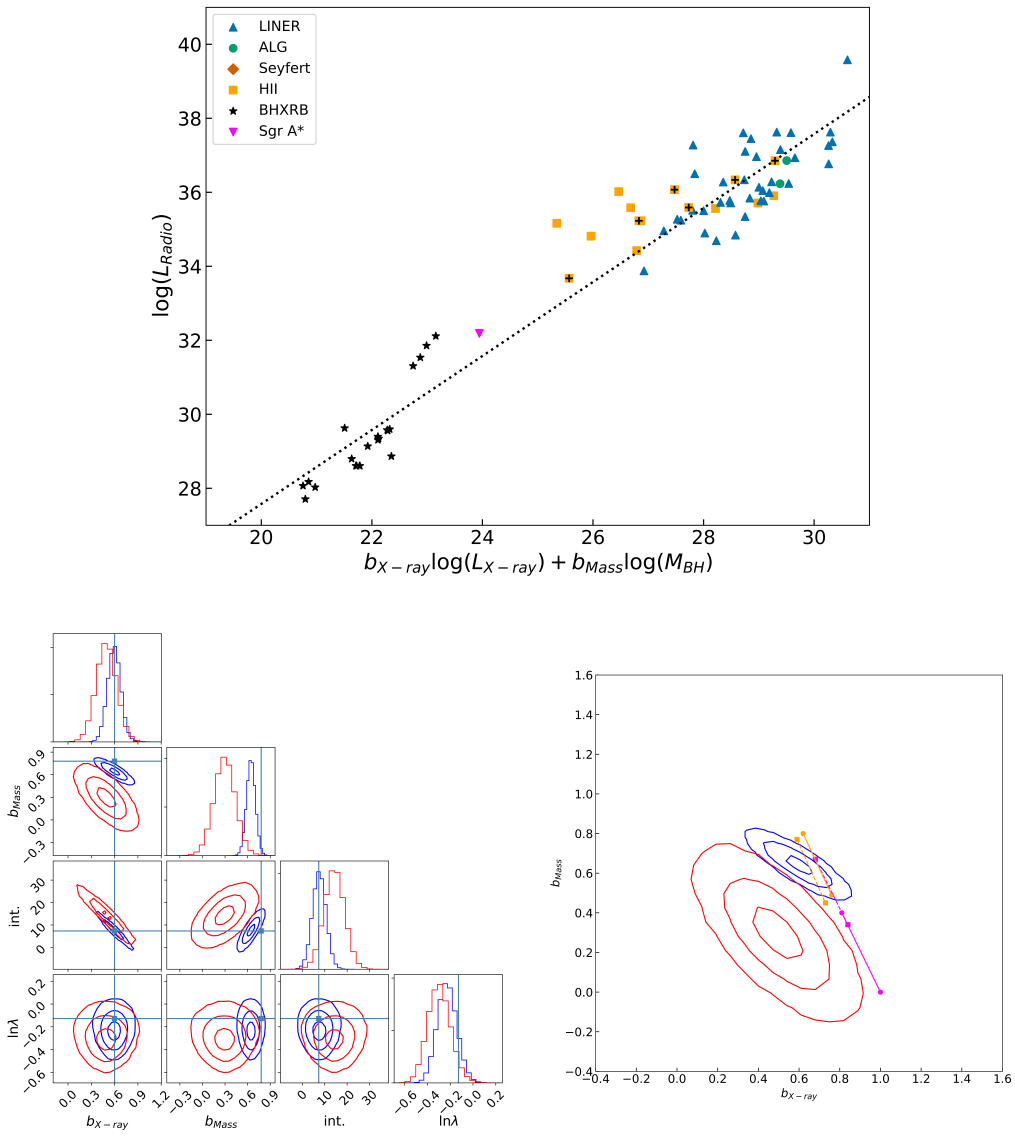

Figure E.1: *Top panel:* The FPBHA for the 'ADAF + BHXRB' sample, with the luminosities in erg s^{-1} and BH masses in $M_\odot$. The different classes are coded (colour and symbol) according to the legend. The jetted HII galaxies show an additional plus symbol. *Bottom panel, left:* The posterior probability distribution of the marginalised slopes for the 'ADAF' (red) and 'ADAF + BHXRB' (blue) samples, as detailed in Section 7.4 and Table 7.2. The contours show the 1, 2 and 3 σ levels of the 2d Gaussians for the slopes b_{X-ray} and b_{Mass}. The orange lines correspond to the 'ADAF' model and the magenta lines correspond to the 'jet' model. The radio spectral index increases from 0.0 to 0.5 as you go down and to the right along the lines, with each end corresponding to these values respectively. The filled lines correspond to a particle distribution of p = 2, and the dashed lines correspond to p = 3. *Bottom panel, right:* The corner plot of the marginalised posterior probability distribution for the entire parameter space, including b_{X-ray}, b_{Mass}, intercept and intrinsic scatter, for both the 'ADAF' (red) and 'ADAF + BHXRB' (blue) samples, as detailed in Section 7.4 and Table 7.2. The green lines correspond to the values of those parameters as published in M03.

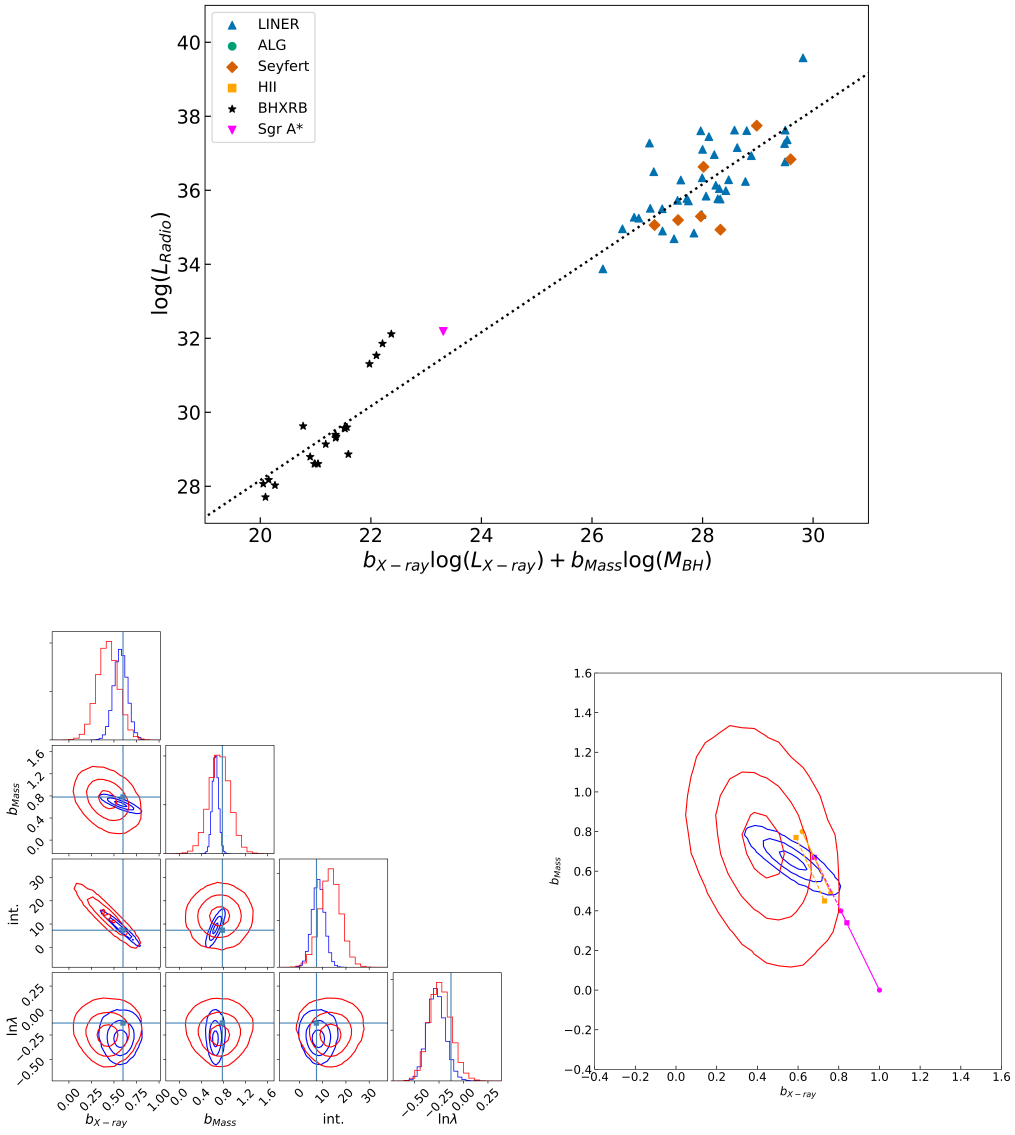

Figure E.1: *Top panel:* The FPBHA for the 'AGN + BHXRB' sample, with the luminosities in erg s^{-1} and BH masses in $M_{\odot}$. The different classes are coded (colour and symbol) according to the legend. The jetted HII galaxies show an additional plus symbol. *Bottom panel, left:* The posterior probability distribution of the marginalised slopes for the 'AGN' (red) and 'AGN + BHXRB' (blue) samples, as detailed in Section 7.4 and Table 7.2. The contours show the 1, 2 and 3 σ levels of the 2d Gaussians for the slopes b_{X-ray} and b_{Mass}. The orange lines correspond to the 'ADAF' model and the magenta lines correspond to the 'jet' model. The radio spectral index increases from 0.0 to 0.5 as you go down and to the right along the lines, with each end corresponding to these values respectively. The filled lines correspond to a particle distribution of p = 2, and the dashed lines correspond to p = 3. *Bottom panel, right:* The corner plot of the marginalised posterior probability distribution for the entire parameter space, including b_{X-ray}, b_{Mass}, intercept and intrinsic scatter, for both the 'AGN' (red) and 'AGN + BHXRB' (blue) samples, as detailed in Section 7.4 and Table 7.2. The green lines correspond to the values of those parameters as published in M03.

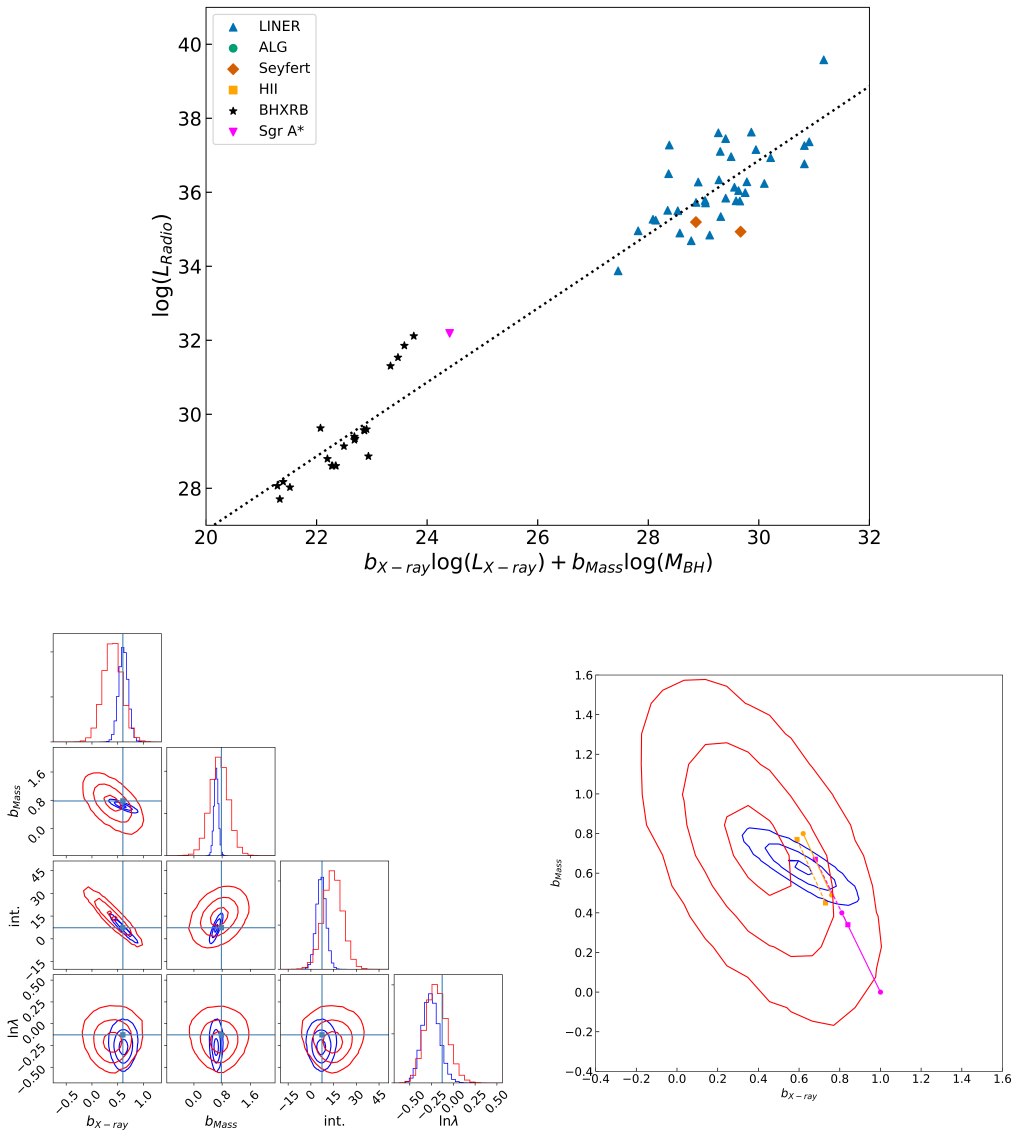

Figure E.1: *Top panel:* The FPBHA for the 'AGN Low Accretion Rate + BHXRB' sample, with the luminosities in erg s^{-1} and BH masses in $M_\odot$. The different classes are coded (colour and symbol) according to the legend. The jetted HII galaxies show an additional plus symbol. *Bottom panel, left:* The posterior probability distribution of the marginalised slopes for the 'AGN Low Accretion Rate' (red) and 'AGN Low Accretion Rate + BHXRB' (blue) samples, as detailed in Section 7.4 and Table 7.2. The contours show the 1, 2 and 3 σ levels of the 2d Gaussians for the slopes b_{X-ray} and b_{Mass}. The orange lines correspond to the 'ADAF' model and the magenta lines correspond to the 'jet' model. The radio spectral index increases from 0.0 to 0.5 as you go down and to the right along the lines, with each end corresponding to these values respectively. The filled lines correspond to a particle distribution of p = 2, and the dashed lines correspond to p = 3. *Bottom panel, right:* The corner plot of the marginalised posterior probability distribution for the entire parameter space, including b_{X-ray}, b_{Mass}, intercept and intrinsic scatter, for both the 'AGN Low Accretion Rate' (red) and 'AGN Low Accretion Rate + BHXRB' (blue) samples, as detailed in Section 7.4 and Table 7.2. The green lines correspond to the values of those parameters as published in M03.

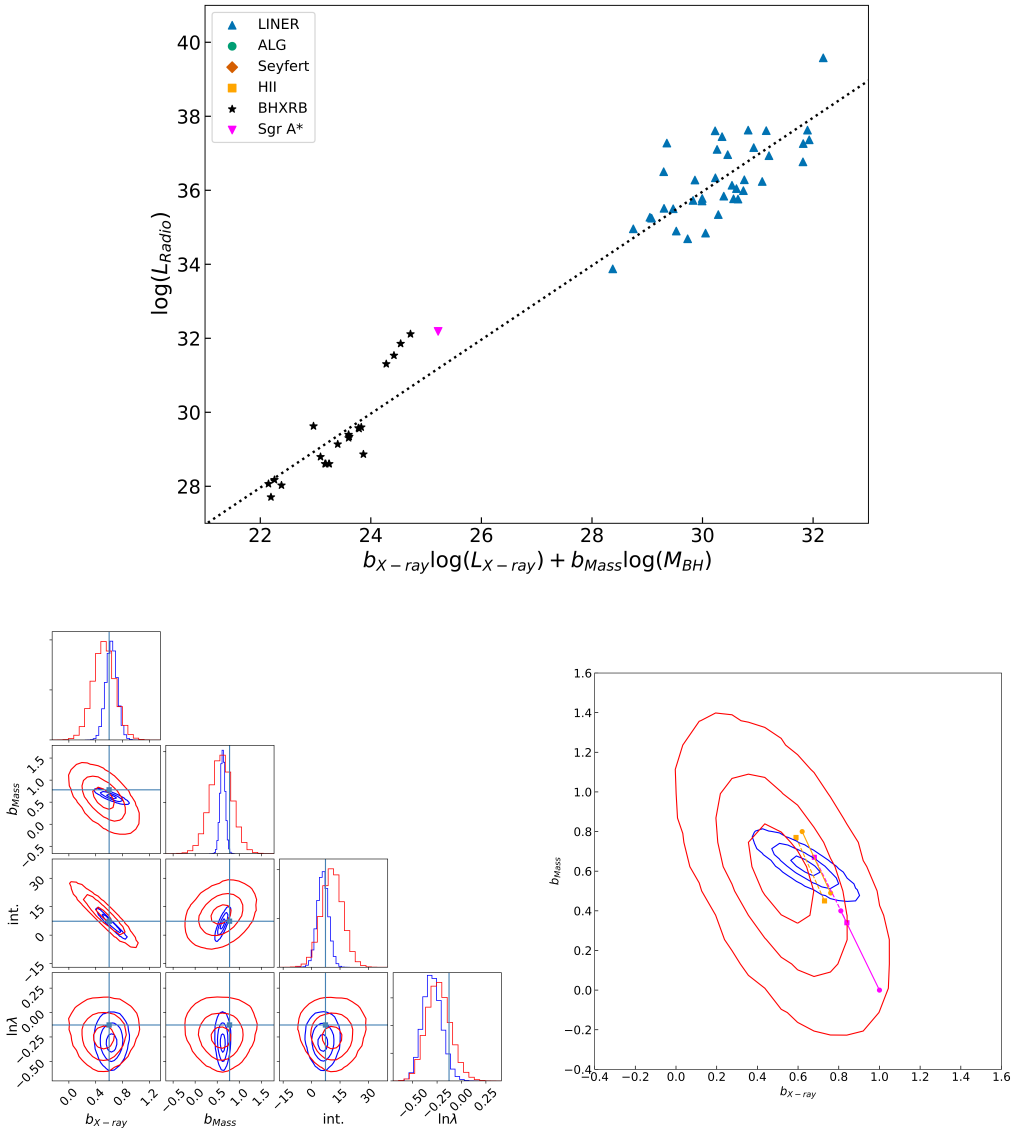

Figure E.1: *Top panel:* The FPBHA for the 'LINER + BHXRB' sample, with the luminosities in erg s^{-1} and BH masses in $M_{\odot}$. The different classes are coded (colour and symbol) according to the legend. The jetted HII galaxies show an additional plus symbol. *Bottom panel, left:* The posterior probability distribution of the marginalised slopes for the 'LINER' (red) and 'LINER + BHXRB' (blue) samples, as detailed in Section 7.4 and Table 7.2. The contours show the 1, 2 and 3 σ levels of the 2d Gaussians for the slopes b_{X-ray} and b_{Mass}. The orange lines correspond to the 'ADAF' model and the magenta lines correspond to the 'jet' model. The radio spectral index increases from 0.0 to 0.5 as you go down and to the right along the lines, with each end corresponding to these values respectively. The filled lines correspond to a particle distribution of p = 2, and the dashed lines correspond to p = 3. *Bottom panel, right:* The corner plot of the marginalised posterior probability distribution for the entire parameter space, including b_{X-ray}, b_{Mass}, intercept and intrinsic scatter, for both the 'LINER' (red) and 'LINER + BHXRB' (blue) samples, as detailed in Section 7.4 and Table 7.2. The green lines correspond to the values of those parameters as published in M03.

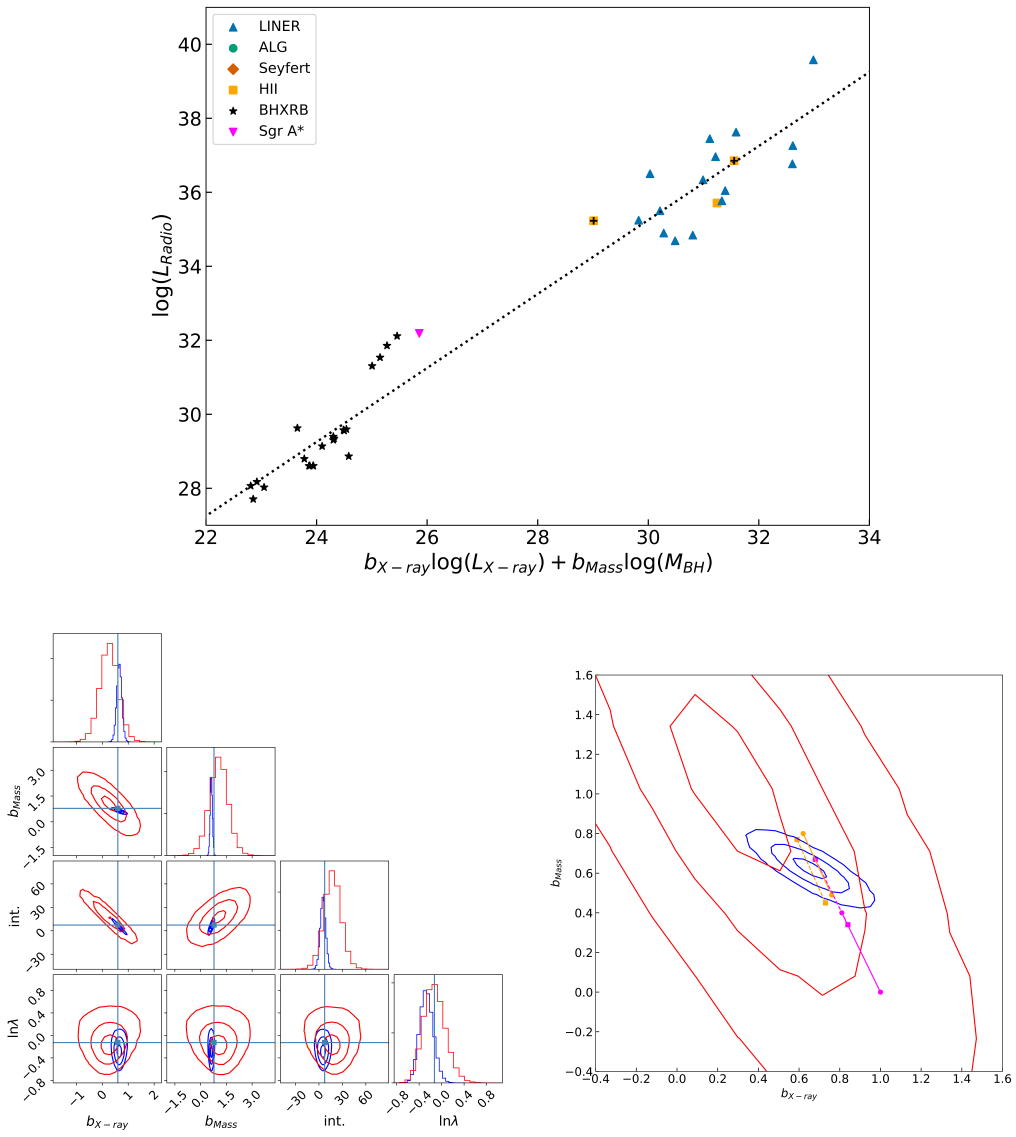

Figure E.1: *Top panel:* The FPBHA for the 'Low Accretion Rate + BHXRB' sample, with the luminosities in erg s^{-1} and BH masses in $M_\odot$. The different classes are coded (colour and symbol) according to the legend. The jetted HII galaxies show an additional plus symbol. *Bottom panel, left:* The posterior probability distribution of the marginalised slopes for the 'Low Accretion Rate' (red) and 'Low Accretion Rate + BHXRB' (blue) samples, as detailed in Section 7.4 and Table 7.2. The contours show the 1, 2 and 3 σ levels of the 2d Gaussians for the slopes b_{X-ray} and b_{Mass}. The orange lines correspond to the 'ADAF' model and the magenta lines correspond to the 'jet' model. The radio spectral index increases from 0.0 to 0.5 as you go down and to the right along the lines, with each end corresponding to these values respectively. The filled lines correspond to a particle distribution of p = 2, and the dashed lines correspond to p = 3. *Bottom panel, right:* The corner plot of the marginalised posterior probability distribution for the entire parameter space, including b_{X-ray}, b_{Mass}, intercept and intrinsic scatter, for both the 'Low Accretion Rate' (red) and 'Low Accretion Rate + BHXRB' (blue) samples, as detailed in Section 7.4 and Table 7.2. The green lines correspond to the values of those parameters as published in M03.

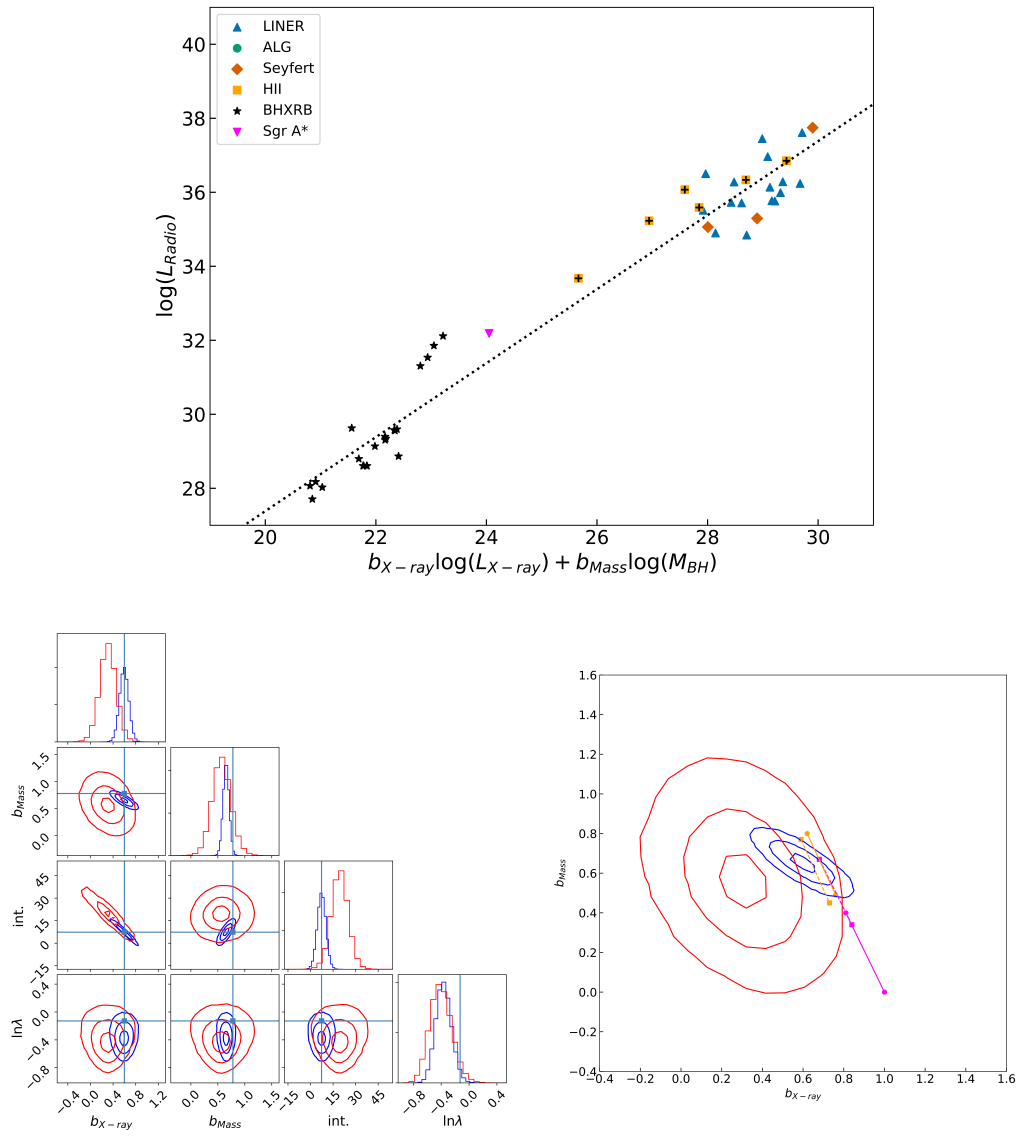

Figure E.1: *Top panel:* The FPBHA for the 'Jetted + BHXRB' sample, with the luminosities in erg s^{-1} and BH masses in $M_{\odot}$. The different classes are coded (colour and symbol) according to the legend. The jetted HII galaxies show an additional plus symbol. *Bottom panel, left:* The posterior probability distribution of the marginalised slopes for the 'Jetted' (red) and 'Jetted + BHXRB' (blue) samples, as detailed in Section 7.4 and Table 7.2. The contours show the 1, 2 and 3 σ levels of the 2d Gaussians for the slopes b_{X-ray} and b_{Mass}. The orange lines correspond to the 'ADAF' model and the magenta lines correspond to the 'jet' model. The radio spectral index increases from 0.0 to 0.5 as you go down and to the right along the lines, with each end corresponding to these values respectively. The filled lines correspond to a particle distribution of p = 2, and the dashed lines correspond to p = 3. *Bottom panel, right:* The corner plot of the marginalised posterior probability distribution for the entire parameter space, including b_{X-ray}, b_{Mass}, intercept and intrinsic scatter, for both the 'Jetted' (red) and 'Jetted + BHXRB' (blue) samples, as detailed in Section 7.4 and Table 7.2. The green lines correspond to the values of those parameters as published in M03.

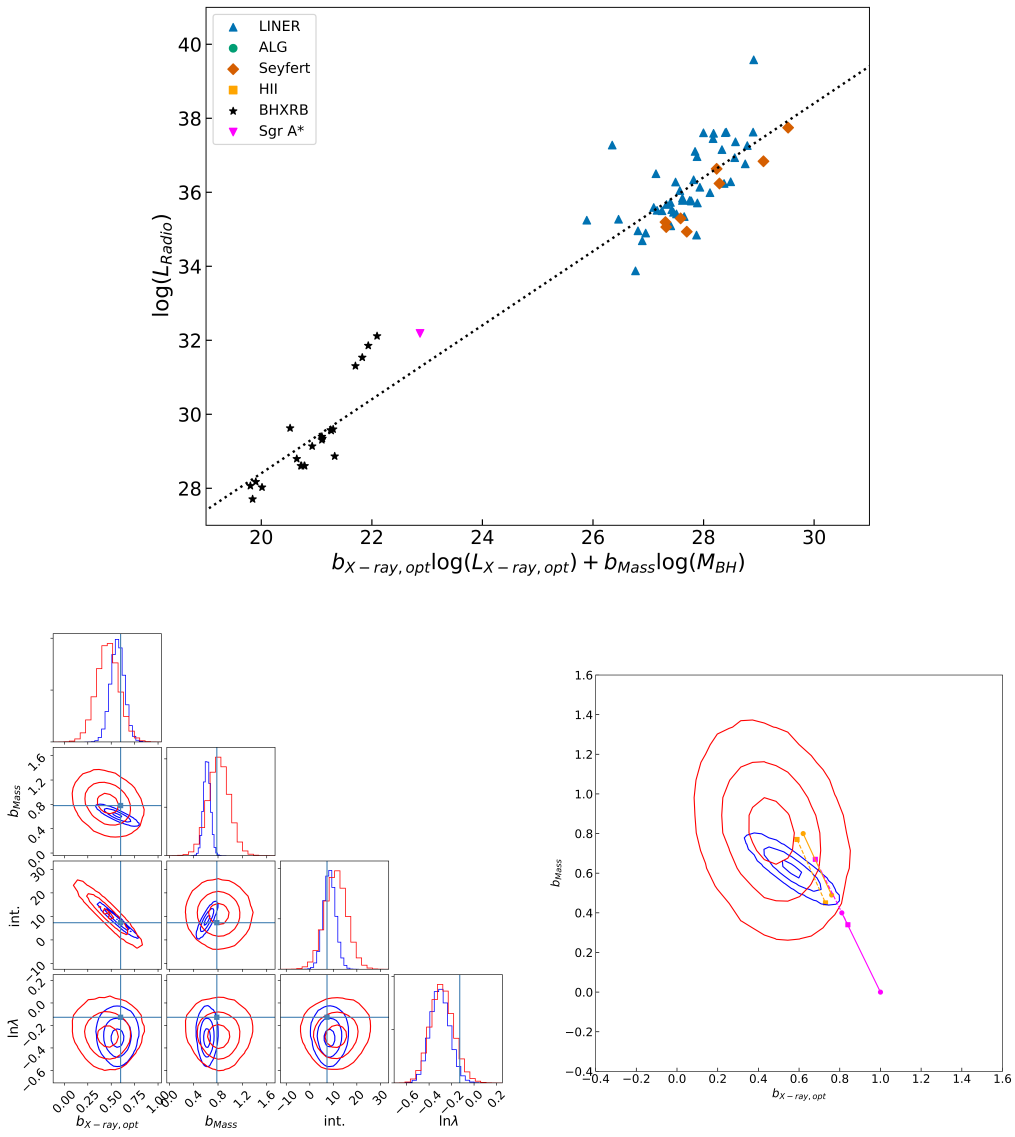

Figure E.2: *Top panel:* The Optical FPBHA for the 'AGN + BHXRB' sample, with the luminosities in erg s^{-1} and BH masses in $M_{\odot}$. The different classes are coded (colour and symbol) according to the legend. The jetted HII galaxies show an additional plus symbol. *Bottom panel, left:* The posterior probability distribution of the marginalised slopes for the 'AGN' (red) and 'AGN + BHXRB' (blue) samples, as detailed in Section 7.4 and Table 7.2. The contours show the 1, 2 and 3 σ levels of the 2d Gaussians for the slopes b_{X-ray} and b_{Mass}. The orange lines correspond to the 'ADAF' model and the magenta lines correspond to the 'jet' model. The radio spectral index increases from 0.0 to 0.5 as you go down and to the right along the lines, with each end corresponding to these values respectively. The filled lines correspond to a particle distribution of p = 2, and the dashed lines correspond to p = 3. *Bottom panel, right:* The corner plot of the marginalised posterior probability distribution for the entire parameter space, including b_{X-ray}, b_{Mass}, intercept and intrinsic scatter, for both the 'AGN' (red) and 'AGN + BHXRB' (blue) samples, as detailed in Section 7.4 and Table 7.2. The green lines correspond to the values of those parameters as published in M03.

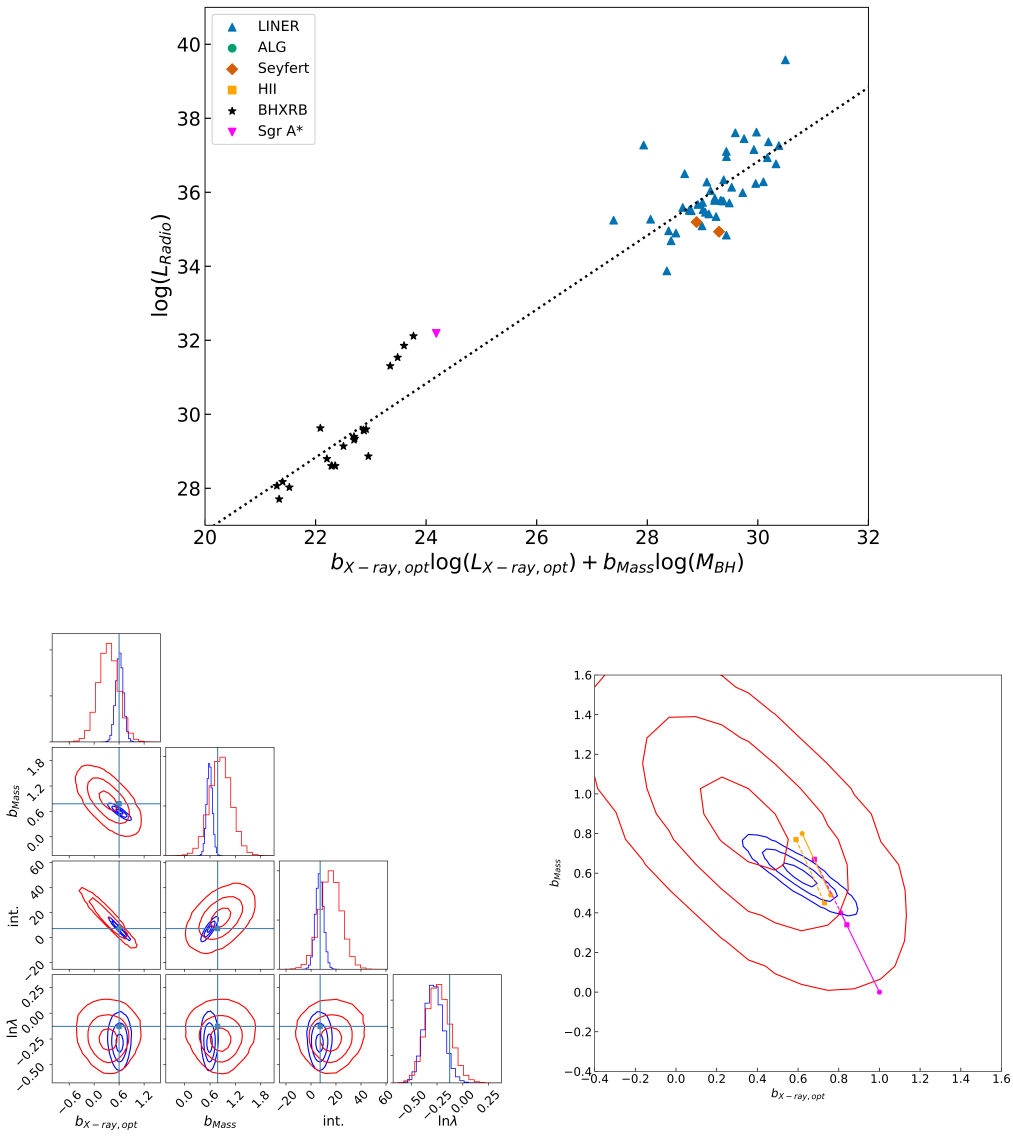

Figure E.2: *Top panel:* The Optical FPBHA for the 'AGN Low Accretion Rate + BHXRB' sample, with the luminosities in erg s^{-1} and BH masses in $M_{\odot}$. The different classes are coded (colour and symbol) according to the legend. The jetted HII galaxies show an additional plus symbol. *Bottom panel, left:* The posterior probability distribution of the marginalised slopes for the 'AGN Low Accretion Rate' (red) and 'AGN Low Accretion Rate + BHXRB' (blue) samples, as detailed in Section 7.4 and Table 7.2. The contours show the 1, 2 and 3 σ levels of the 2d Gaussians for the slopes b_{X-ray} and b_{Mass}. The orange lines correspond to the 'ADAF' model and the magenta lines correspond to the 'jet' model. The radio spectral index increases from 0.0 to 0.5 as you go down and to the right along the lines, with each end corresponding to these values respectively. The filled lines correspond to a particle distribution of p = 2, and the dashed lines correspond to p = 3. *Bottom panel, right:* The corner plot of the marginalised posterior probability distribution for the entire parameter space, including b_{X-ray}, b_{Mass}, intercept and intrinsic scatter, for both the 'AGN Low Accretion Rate' (red) and 'AGN Low Accretion Rate + BHXRB' (blue) samples, as detailed in Section 7.4 and Table 7.2. The green lines correspond to the values of those parameters as published in M03.

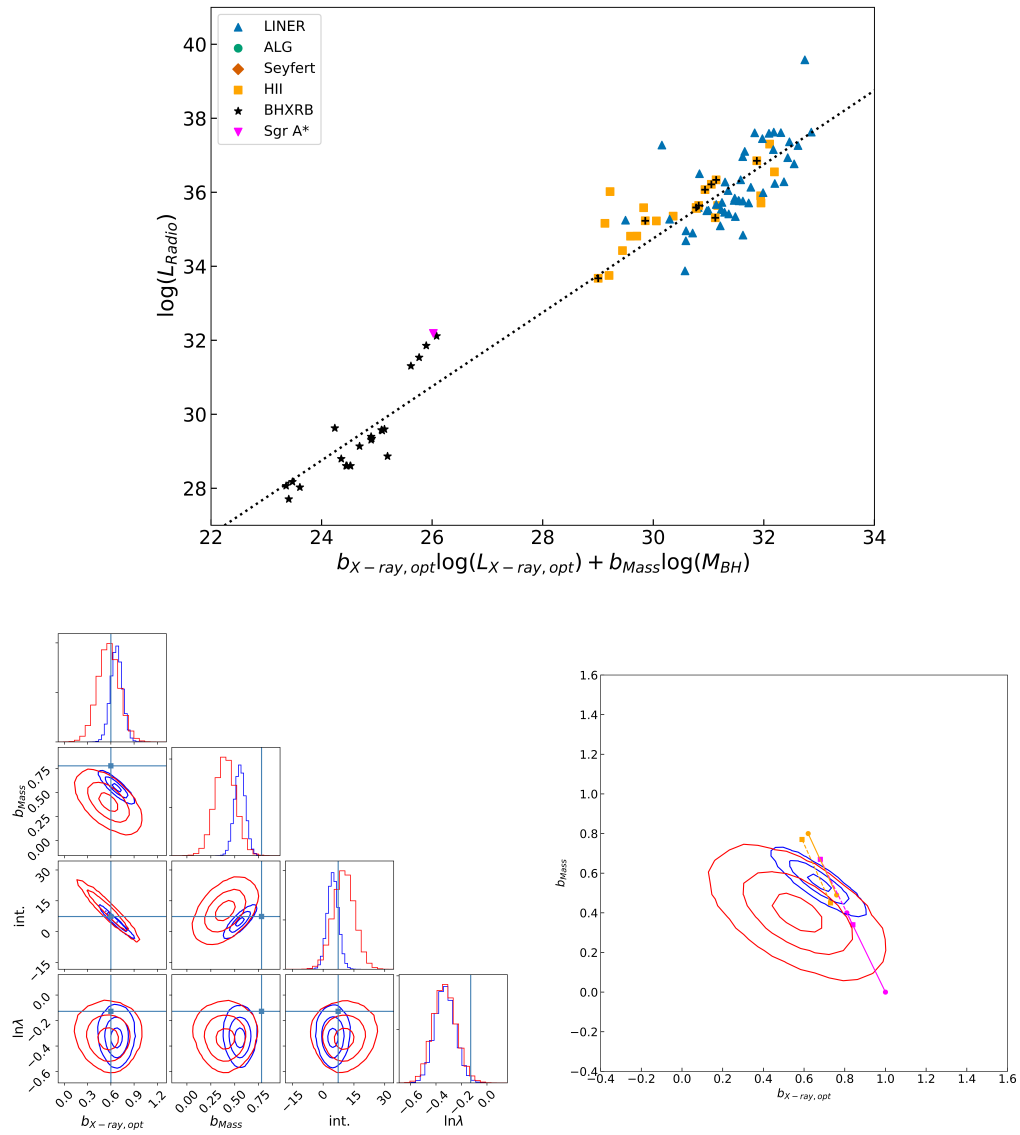

Figure E.2: *Top panel:* The FPBHA for the 'ADAF + BHXRB' sample, with the luminosities in erg s^{-1} and BH masses in $M_\odot$. The different classes are coded (colour and symbol) according to the legend. The jetted HII galaxies show an additional plus symbol. *Bottom panel, left:* The posterior probability distribution of the marginalised slopes for the 'ADAF' (red) and 'ADAF + BHXRB' (blue) samples, as detailed in Section 7.4 and Table 7.2. The contours show the 1, 2 and 3 σ levels of the 2d Gaussians for the slopes b_{X-ray} and b_{Mass}. The orange lines correspond to the 'ADAF' model and the magenta lines correspond to the 'jet' model. The radio spectral index increases from 0.0 to 0.5 as you go down and to the right along the lines, with each end corresponding to these values respectively. The filled lines correspond to a particle distribution of p = 2, and the dashed lines correspond to p = 3. *Bottom panel, right:* The corner plot of the marginalised posterior probability distribution for the entire parameter space, including b_{X-ray}, b_{Mass}, intercept and intrinsic scatter, for both the 'ADAF' (red) and 'ADAF + BHXRB' (blue) samples, as detailed in Section 7.4 and Table 7.2. The green lines correspond to the values of those parameters as published in M03.

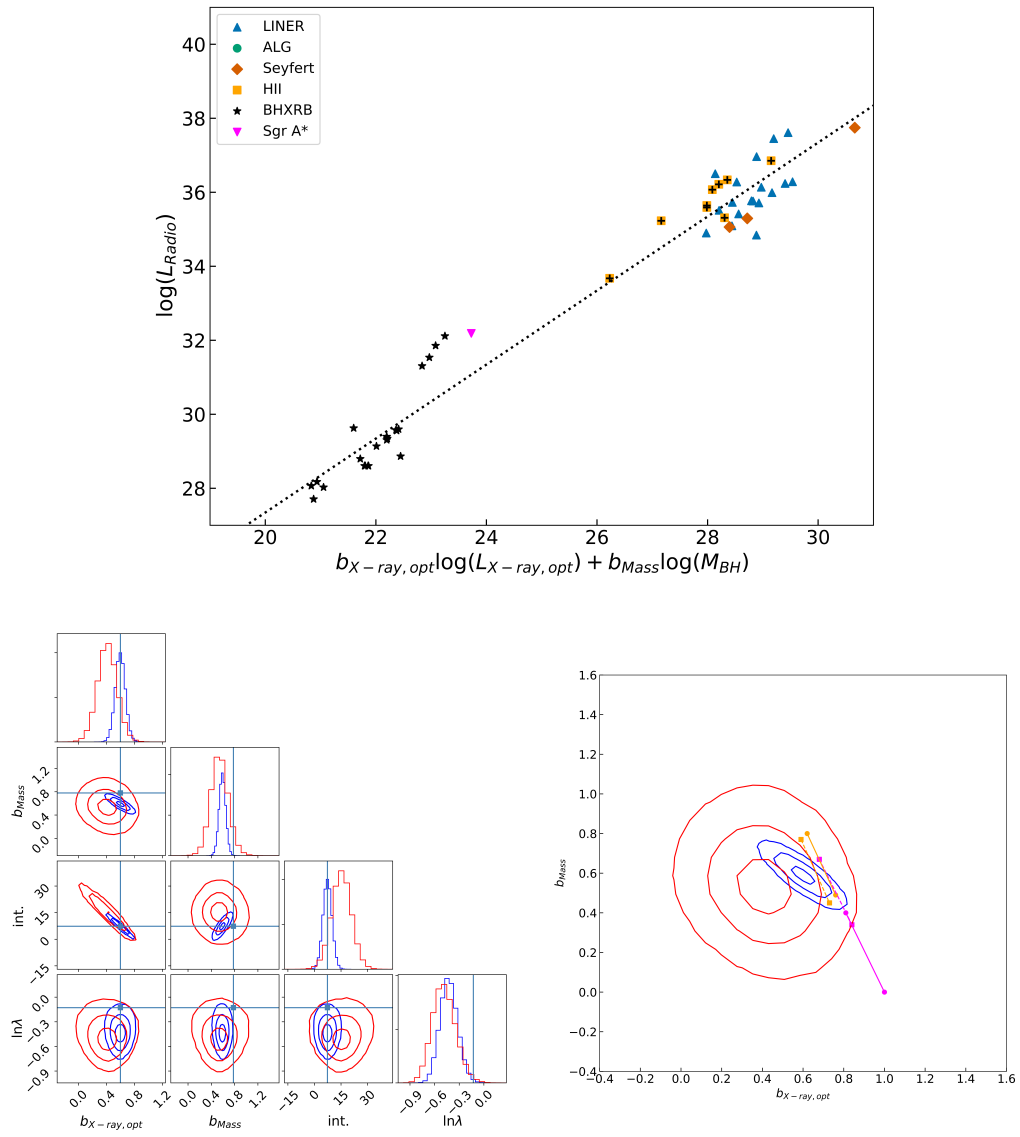

Figure E.2: *Top panel:* The FPBHA for the 'Jetted + BHXRB' sample, with the luminosities in erg s^{-1} and BH masses in $M_{\odot}$. The different classes are coded (colour and symbol) according to the legend. The jetted HII galaxies show an additional plus symbol. *Bottom panel, left:* The posterior probability distribution of the marginalised slopes for the 'Jetted' (red) and 'Jetted + BHXRB' (blue) samples, as detailed in Section 7.4 and Table 7.2. The contours show the 1, 2 and 3 σ levels of the 2d Gaussians for the slopes b_{X-ray} and b_{Mass}. The orange lines correspond to the 'ADAF' model and the magenta lines correspond to the 'jet' model. The radio spectral index increases from 0.0 to 0.5 as you go down and to the right along the lines, with each end corresponding to these values respectively. The filled lines correspond to a particle distribution of p = 2, and the dashed lines correspond to p = 3. *Bottom panel, right:* The corner plot of the marginalised posterior probability distribution for the entire parameter space, including b_{X-ray}, b_{Mass}, intercept and intrinsic scatter, for both the 'Jetted' (red) and 'Jetted + BHXRB' (blue) samples, as detailed in Section 7.4 and Table 7.2. The green lines correspond to the values of those parameters as published in M03.

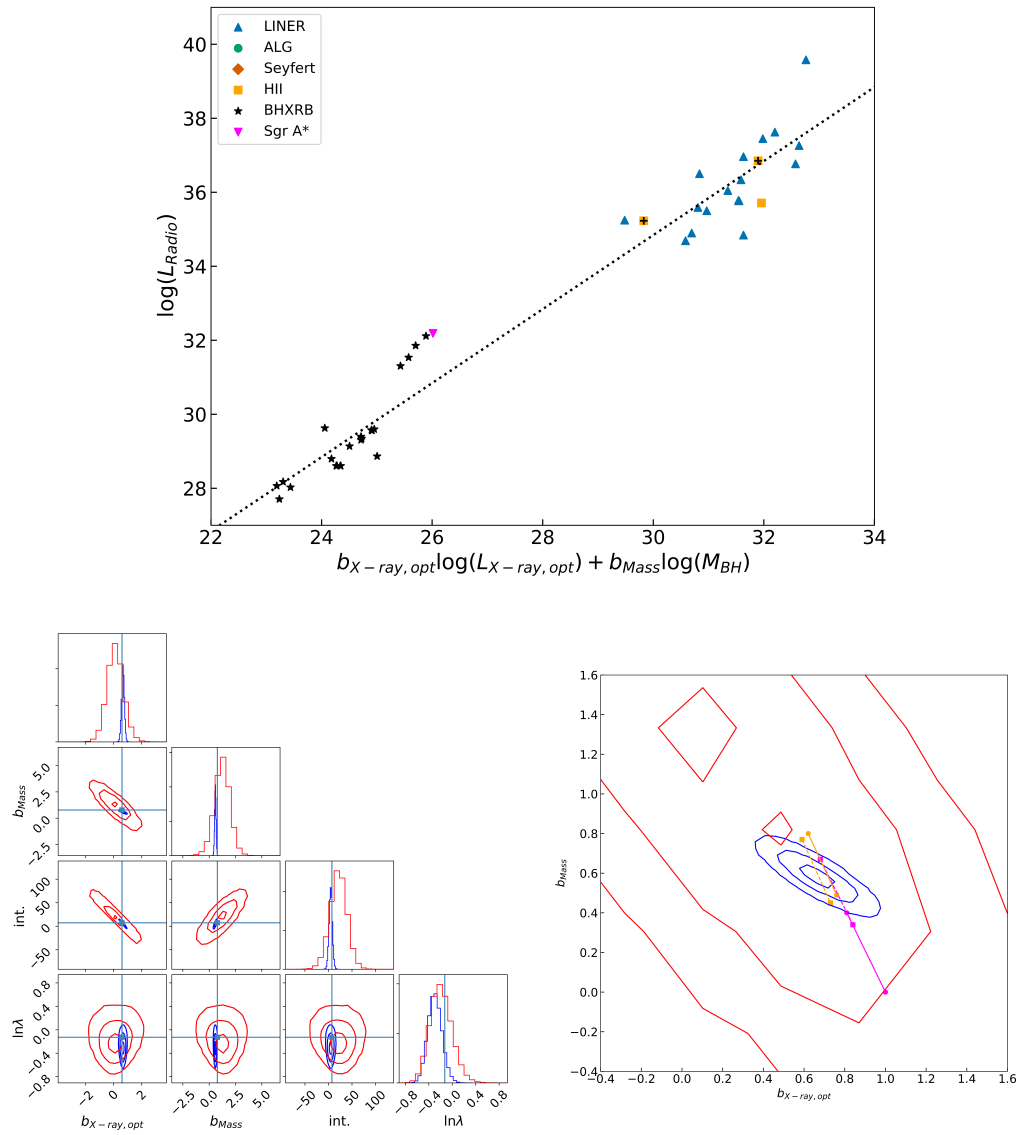

Figure E.2: *Top panel:* The FPBHA for the 'Low Accretion Rate + BHXRB' sample, with the luminosities in erg s^{-1} and BH masses in $M_\odot$. The different classes are coded (colour and symbol) according to the legend. The jetted HII galaxies show an additional plus symbol. *Bottom panel, left:* The posterior probability distribution of the marginalised slopes for the 'Low Accretion Rate' (red) and 'Low Accretion Rate + BHXRB' (blue) samples, as detailed in Section 7.4 and Table 7.2. The contours show the 1, 2 and 3 σ levels of the 2d Gaussians for the slopes b_{X-ray} and b_{Mass}. The orange lines correspond to the 'ADAF' model and the magenta lines correspond to the 'jet' model. The radio spectral index increases from 0.0 to 0.5 as you go down and to the right along the lines, with each end corresponding to these values respectively. The filled lines correspond to a particle distribution of p = 2, and the dashed lines correspond to p = 3. *Bottom panel, right:* The corner plot of the marginalised posterior probability distribution for the entire parameter space, including b_{X-ray}, b_{Mass}, intercept and intrinsic scatter, for both the 'Low Accretion Rate' (red) and 'Low Accretion Rate + BHXRB' (blue) samples, as detailed in Section 7.4 and Table 7.2. The green lines correspond to the values of those parameters as published in M03.

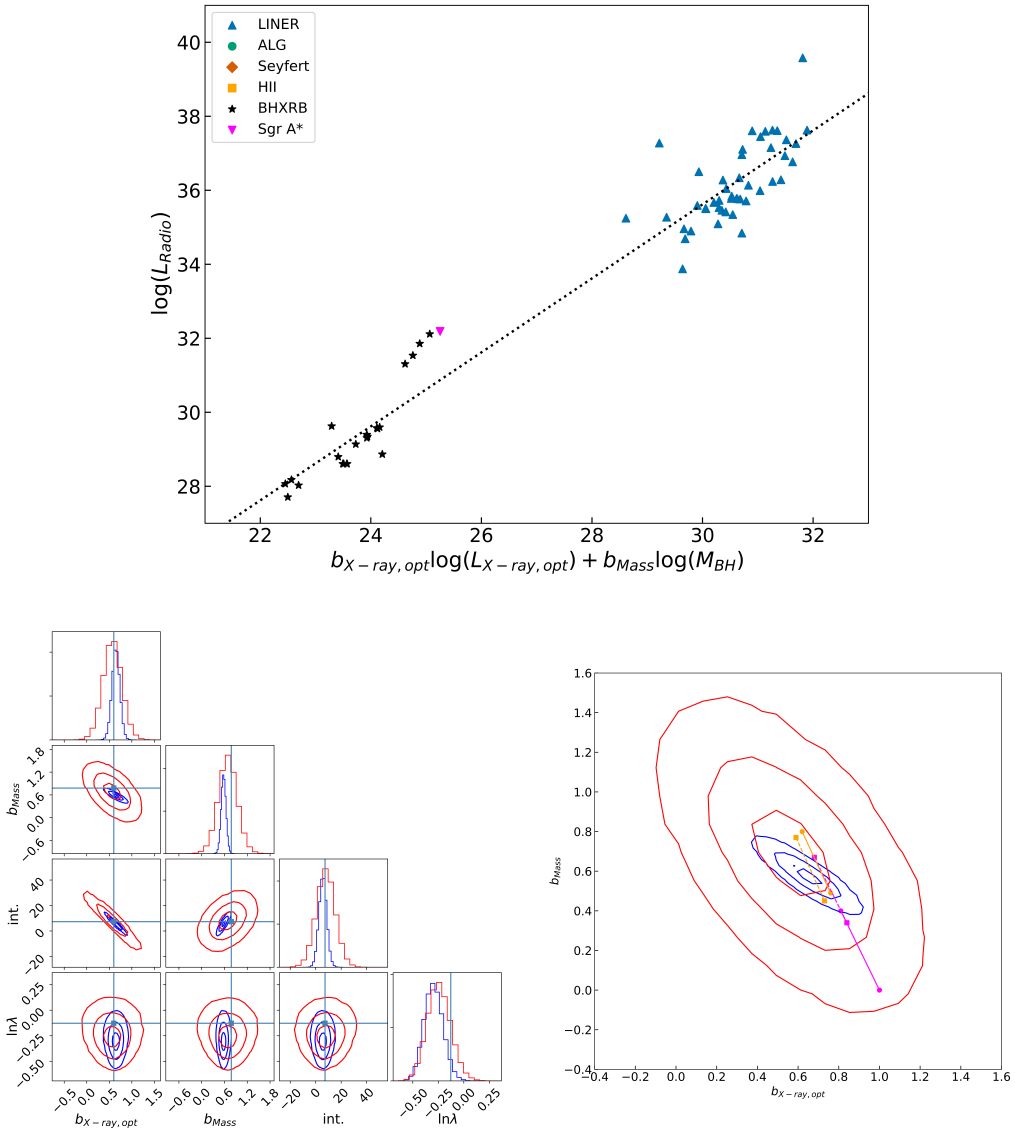

Figure E.2: *Top panel:* The Optical FPBHA for the 'LINER + BHXRB' sample, with the luminosities in erg s^{-1} and BH masses in $M_{\odot}$. The different classes are coded (colour and symbol) according to the legend. The jetted HII galaxies show an additional plus symbol. *Bottom panel, left:* The posterior probability distribution of the marginalised slopes for the 'LINER' (red) and 'LINER + BHXRB' (blue) samples, as detailed in Section 7.4 and Table 7.2. The contours show the 1, 2 and 3 σ levels of the 2d Gaussians for the slopes b_{X-ray} and b_{Mass}. The orange lines correspond to the 'ADAF' model and the magenta lines correspond to the 'jet' model. The radio spectral index increases from 0.0 to 0.5 as you go down and to the right along the lines, with each end corresponding to these values respectively. The filled lines correspond to a particle distribution of p = 2, and the dashed lines correspond to p = 3. *Bop panel, right:* The corner plot of the marginalised posterior probability distribution for the entire parameter space, including b_{X-ray}, b_{Mass}, intercept and intrinsic scatter, for both the 'LINER' (red) and 'LINER + BHXRB' (blue) samples, as detailed in Section 7.4 and Table 7.2. The green lines correspond to the values of those parameters as published in M03.

Bibliography

Akylas, A. and Georgantopoulos, I. (2009). XMM-Newton observations of Seyfert galaxies from the Palomar spectroscopic survey: the X-ray absorption distribution. *A&A*, 500:999–1012.

Allen, M. G., Groves, B. A., Dopita, M. A., Sutherland, R. S., and Kewley, L. J. (2008). The MAPPINGS III Library of Fast Radiative Shock Models. *ApJS*, 178:20–55.

Anderson, J. M. and Ulvestad, J. S. (2005). The Size of the Radio-Emitting Region in Low-Luminosity Active Galactic Nuclei. *ApJ*, 627:674–700.

Anderson, J. M., Ulvestad, J. S., and Ho, L. C. (2004). Low-Luminosity Active Galactic Nuclei at the Highest Resolution: Jets or Accretion Flows? *ApJ*, 603:42–50.

Annibali, F., Bressan, A., Rampazzo, R., Zeilinger, W. W., Vega, O., and Panuzzo, P. (2010). Nearby early-type galaxies with ionized gas. IV. Origin and powering mechanism of the ionized gas. *A&A*, 519:A40.

Antonucci, R. (1993). Unified models for active galactic nuclei and quasars. *ARA&A*, 31:473–521.

Antonucci, R. R. J. and Miller, J. S. (1985). Spectropolarimetry and the nature of NGC 1068. 297:621–632.

Appl, S. and Camenzind, M. (1992). The stability of current-carrying jets. *A&A*, 256:354–370.

Argo, M. (2015). The e-MERLIN Data Reduction Pipeline. *ArXiv e-prints*.

Argo, M. K., van Bemmel, I. M., Connolly, S. D., and Beswick, R. J. (2015). A new period of activity in the core of NGC 660. *MNRAS*, 452:1081–1088.

Arnaud, K. A. (1996). XSPEC: The First Ten Years. In Jacoby, G. H. and Barnes, J., editors, *Astronomical Data Analysis Software and Systems V*, volume 101 of *Astronomical Society of the Pacific Conference Series*, page 17.

Asmus, D., Gandhi, P., Hönig, S. F., Smette, A., and Duschl, W. J. (2015). The subarcsecond mid-infrared view of local active galactic nuclei - II. The mid-infrared-X-ray correlation. *MNRAS*, 454:766–803.

Asmus, D., Hönig, S. F., and Gandhi, P. (2016). The Subarcsecond Mid-infrared View of Local Active Galactic Nuclei. III. Polar Dust Emission. *ApJ*, 822:109.

Axon, D. J., Marconi, A., Capetti, A., Macchetto, F. D., Schreier, E., and Robinson, A. (1998). Jet-Driven Motions in the Narrow-Line Region of NGC 1068. *ApJ*, 496:L75–L78.

Baade, W. and Minkowski, R. (1954). On the Identification of Radio Sources. *ApJ*, 119:215.

Baganoff, F. K., Maeda, Y., Morris, M., Bautz, M. W., Brandt, W. N., Cui, W., Doty, J. P., Feigelson, E. D., Garmire, G. P., Pravdo, S. H., Ricker, G. R., and Townsley, L. K. (2003). Chandra X-Ray Spectroscopic Imaging of Sagittarius A* and the Central Parsec of the Galaxy. *ApJ*, 591:891–915.

Bagchi, J., Gopal-Krishna, Krause, M., and Joshi, S. (2007). A Giant Radio Jet Ejected by an Ultramassive Black Hole in a Single-lobed Radio Galaxy. *ApJ*, 670:L85–L88.

Baldi, R. D. and Capetti, A. (2009). Radio and spectroscopic properties of miniature radio galaxies: revealing the bulk of the radio-loud AGN population. *A&A*, 508:603–614.

Baldi, R. D. and Capetti, A. (2010). Spectro-photometric properties of the bulk of the radio-loud AGN population. *A&A*, 519:A48.

Baldi, R. D., Capetti, A., Buttiglione, S., Chiaberge, M., and Celotti, A. (2013a). An optical spectroscopic survey of the 3CR sample of radio galaxies with z 0.3. V. Implications for the unified model for FR IIs. *A&A*, 560:A81.

Baldi, R. D., Capetti, A., Chiaberge, M., and Celotti, A. (2014). The radio-loud AGN population at z sim 1 in the COSMOS field. I. selection and spectral energy distributions. *A&A*, 567:A76.

Baldi, R. D., Capetti, A., and Giovannini, G. (2015). Pilot study of the radio-emitting AGN population: the emerging new class of FR 0 radio-galaxies. *A&A*, 576:A38.

Baldi, R. D., Capetti, A., and Massaro, F. (2018a). FR0CAT: a FIRST catalog of FR 0 radio galaxies. *A&A*, 609:A1.

Baldi, R. D., Chiaberge, M., Capetti, A., Rodriguez-Zaurin, J., Deustua, S., and Sparks, W. B. (2013b). Spectral Energy Distributions of Low-luminosity Radio Galaxies at z ˜1-3: A High-z View of the Host/AGN Connection. *ApJ*, 762:30.

Baldi, R. D., Chiaberge, M., Capetti, A., Sparks, W., Macchetto, F. D., O'Dea, C. P., Axon, D. J., Baum, S. A., and Quillen, A. C. (2010). The 1.6 μm Near-infrared Nuclei of 3C Radio Galaxies: Jets, Thermal Emission, or Scattered Light? *ApJ*, 725:2426–2443.

Baldi, R. D., Williams, D. R. A., McHardy, I. M., Beswick, R. J., Argo, M. K., Dullo, B. T., Knapen, J. H., Brinks, E., Muxlow, T. W. B., Aalto, S., Alberdi, A., Bendo, G. J., Corbel, S., Evans, R., Fenech, D. M., Green, D. A., Klöckner, H.-R., Körding, E., Kharb, P., Maccarone, T. J., Martí-Vidal, I., Mundell, C. G., Panessa, F., Peck, A. B., Pérez-Torres,

M. A., Saikia, D. J., Saikia, P., Shankar, F., Spencer, R. E., Stevens, I. R., Uttley, P., and Westcott, J. (2018b). LeMMINGs - I. The eMERLIN legacy survey of nearby galaxies. 1.5-GHz parsec-scale radio structures and cores. *MNRAS*, 476:3478–3522.

Baldwin, J. A., Phillips, M. M., and Terlevich, R. (1981). Classification parameters for the emission-line spectra of extragalactic objects. 93:5–19.

Balick, B. and Heckman, T. M. (1982). Extranuclear clues to the origin and evolution of activity in galaxies. *ARA&A*, 20:431–468.

Balmaverde, B. and Capetti, A. (2006a). The host galaxy/AGN connection in nearby early-type galaxies. Is there a miniature radio-galaxy in every "core" galaxy? *A&A*, 447:97–112.

Balmaverde, B. and Capetti, A. (2006b). The host galaxy/AGN connection in nearby early-type galaxies. Is there a miniature radio-galaxy in every "core" galaxy? 447:97–112.

Balmaverde, B. and Capetti, A. (2013). Multi-band constraints on the nature of emission line galaxies. *A&A*, 549:A144.

Balmaverde, B. and Capetti, A. (2014). The HST view of the broad line region in low luminosity AGN. *A&A*, 563:A119.

Balmaverde, B., Capetti, A., and Grandi, P. (2006). The Chandra view of the 3C/FR I sample of low luminosity radio-galaxies. *A&A*, 451:35–44.

Barausse, E., Shankar, F., Bernardi, M., Dubois, Y., and Sheth, R. K. (2017). Selection bias in dynamically measured supermassive black hole samples: scaling relations and correlations between residuals in semi-analytic galaxy formation models. *MNRAS*, 468:4782–4791.

Barvainis, R., Lonsdale, C., and Antonucci, R. (1996). Radio Spectra of Radio Quiet Quasars. *AJ*, 111:1431.

Baum, S. A., O'Dea, C. P., Dallacassa, D., de Bruyn, A. G., and Pedlar, A. (1993). Kiloparsec-Scale Radio Emission in Seyfert Galaxies: Evidence for Starburst-driven Superwinds? *ApJ*, 419:553.

Baum, S. A., O'Dea, C. P., Giovannini, G., Cotton, W. B., Koff, S. d., Feretti, L., Golombek, D., Lara, L., Macchetto, F. D., Miley, G. K., Sparks, W. B., Venturi, T., and Komissarov, S. S. (1997). HST and Merlin Observations of 3C 264–A Laboratory for Jet Physics and Unified Schemes. *ApJ*, 483:178–193.

Beasley, A. J., Gordon, D., Peck, A. B., Petrov, L., MacMillan, D. S., Fomalont, E. B., and Ma, C. (2002). The VLBA Calibrator Survey-VCS1. *ApJS*, 141:13–21.

Becker, R. H., White, R. L., and Helfand, D. J. (1995). The FIRST Survey: Faint Images of the Radio Sky at Twenty Centimeters. *ApJ*, 450:559–+.

Begelman, M. C. (2012). Radiatively inefficient accretion: breezes, winds and hyperaccretion. *MNRAS*, 420:2912–2923.

Begelman, M. C., Blandford, R. D., and Rees, M. J. (1984). Theory of extragalactic radio sources. *Reviews of Modern Physics*, 56:255–351.

Behar, E., Baldi, R. D., Laor, A., Horesh, A., Stevens, J., and Tzioumis, T. (2015). Discovery of millimetre-wave excess emission in radio-quiet active galactic nuclei. *MNRAS*, 451:517–526.

Belfiore, F., Maiolino, R., Maraston, C., Emsellem, E., Bershady, M. A., Masters, K. L., Yan, R., Bizyaev, D., Boquien, M., Brownstein, J. R., Bundy, K., Drory, N., Heckman, T. M., Law, D. R., Roman-Lopes, A., Pan, K., Stanghellini, L., Thomas, D., Weijmans, A.-M., and Westfall, K. B. (2016). SDSS IV MaNGA - spatially resolved diagnostic diagrams: a proof that many galaxies are LIERs. *MNRAS*, 461:3111–3134.

Belles, P.-E., Beswick, R., Argo, M., Jackson, N., Muxlow, T., and Richards, A. (2015). *e-MERLIN CookBook - version 3.0, 2015 February*. JBCA.

Best, P. N. and Heckman, T. M. (2012). On the fundamental dichotomy in the local radio-AGN population: accretion, evolution and host galaxy properties. *MNRAS*, 421:1569–1582.

Best, P. N., Kauffmann, G., Heckman, T. M., Brinchmann, J., Charlot, S., Ivezić, Ž., and White, S. D. M. (2005a). The host galaxies of radio-loud active galactic nuclei: mass dependences, gas cooling and active galactic nuclei feedback. *MNRAS*, 362:25–40.

Best, P. N., Kauffmann, G., Heckman, T. M., and Ivezić, Ž. (2005b). A sample of radio-loud active galactic nuclei in the Sloan Digital Sky Survey. 362:9–24.

Beswick, R., Argo, M. K., Evans, R., McHardy, I., Williams, D. R. A., and Westcott, J. (2014). LeMMINGs e-MERLIN survey of nearby galaxies. In *Proceedings of the 12th European VLBI Network Symposium and Users Meeting (EVN 2014). 7-10 October 2014. Cagliari, Italy.*, page 10.

Bicknell, G. V., de Ruiter, H. R., Fanti, R., Morganti, R., and Parma, P. (1990). Physical properties of jets in low-luminosity radio sources. *ApJ*, 354:98–115.

Bicknell, G. V., Dopita, M. A., and O'Dea, C. P. O. (1997). Unification of the Radio and Optical Properties of Gigahertz Peak Spectrum and Compact Steep-Spectrum Radio Sources. *ApJ*, 485:112–124.

Bicknell, G. V., Dopita, M. A., Tsvetanov, Z. I., and Sutherland, R. S. (1998). Are Seyfert Narrow-Line Regions Powered by Radio Jets? *ApJ*, 495:680–690.

Biretta, J. A., Stern, C. P., and Harris, D. E. (1991). The radio to X-ray spectrum of the M87 jet and nucleus. *AJ*, 101:1632–1646.

Bisogni, S., Marconi, A., and Risaliti, G. (2017). Orientation effects on spectral emission features of quasars. *MNRAS*, 464:385–397.

Blandford, R. D. and Payne, D. G. (1982). Hydromagnetic flows from accretion discs and the production of radio jets. *MNRAS*, 199:883–903.

Blandford, R. D. and Znajek, R. L. (1977). Electromagnetic extraction of energy from Kerr black holes. *MNRAS*, 179:433–456.

Blumenthal, G. R., Keel, W. C., and Miller, J. S. (1982). X-ray, optical, and radio properties of quasars. 257:499–508.

Boksenberg, A., Catchpole, R. M., Macchetto, F., Albrecht, R., Barbieri, C., Blades, J. C., Crane, P., Deharveng, J. M., Disney, M. J., Jakobsen, P., Kampermann, T. M., King, I. R., Mackay, C. D., Paresce, F., Weigelt, G., Baxter, D., Greenfield, P., Jedrzejewski, R., Nota, A., and Sparks, W. B. (1995). Faint Object Camera imaging and spectroscopy of NGC 4151. *ApJ*, 440:151–165.

Bonchi, A., La Franca, F., Melini, G., Bongiorno, A., and Fiore, F. (2013). On the radio luminosity distribution of active galactic nuclei and the black hole fundamental plane. 429:1970–1980.

Bondi, H. (1952). On spherically symmetrical accretion. *MNRAS*, 112:195.

Bondi, M., Parma, P., de Ruiter, H., Fanti, R., Laing, R. A., and Fomalont, E. B. (2000). The radio jets in B2 0755+379. *MNRAS*, 314:11–22.

Bonzini, M., Padovani, P., Mainieri, V., Kellermann, K. I., Miller, N., Rosati, P., Tozzi, P., and Vattakunnel, S. (2013). The sub-mJy radio sky in the Extended Chandra Deep Field-South: source population. *MNRAS*, 436:3759–3771.

Booler, R. V., Pedlar, A., and Davies, R. D. (1982). High-resolution 1666-MHz observations of the nucleus of NGC 4151. 199:229–237.

Bower, G. A. (1992). *A search for dead QSO's among nearby luminous galaxies*. PhD thesis, Michigan Univ., Ann Arbor.

Briggs, E. L. (1995). Development and Application of Methods for Performing Large Scale Electronic Structure Calculations. *Ph.D. Thesis*.

Brown, R. H. and Hazard, C. (1961). The radio emission from normal galaxies, II. *MNRAS*, 122:479.

Brunthaler, A., Martí-Vidal, I., Menten, K. M., Reid, M. J., Henkel, C., Bower, G. C., Falcke, H., Feng, H., Kaaret, P., Butler, N. R., Morgan, A. N., and Weiß, A. (2010a).

VLBI observations of SN 2008iz. I. Expansion velocity and limits on anisotropic expansion. *A&A*, 516:A27.

Brunthaler, A., Marti-Vidal, I., Menten, K. M., Reid, M. J., Henkel, C., Bower, G. C., Falcke, H. D. E., Beswick, R. J., Muxlow, T. W. B., and Fenech, D. (2010b). The expansion of SN2008iz in M82. In *10th European VLBI Network Symposium and EVN Users Meeting: VLBI and the New Generation of Radio Arrays*, page 55.

Bruzual, G. and Charlot, S. (2011). GALAXEV: Evolutionary Stellar Population Synthesis Models. Astrophysics Source Code Library.

Busch, G., Zuther, J., Valencia-S., M., Moser, L., Fischer, S., Eckart, A., Scharwächter, J., Gadotti, D. A., and Wisotzki, L. (2014). A low-luminosity type-1 QSO sample. I. Overluminous host spheroidals or undermassive black holes. *A&A*, 561:A140.

Buta, R. J., Sheth, K., Athanassoula, E., Bosma, A., Knapen, J. H., Laurikainen, E., Salo, H., Elmegreen, D., Ho, L. C., Zaritsky, D., Courtois, H., Hinz, J. L., Muñoz-Mateos, J.-C., Kim, T., Regan, M. W., Gadotti, D. A., Gil de Paz, A., Laine, J., Menéndez-Delmestre, K., Comerón, S., Erroz Ferrer, S., Seibert, M., Mizusawa, T., Holwerda, B., and Madore, B. F. (2015). A Classical Morphological Analysis of Galaxies in the Spitzer Survey of Stellar Structure in Galaxies (S4G). 217:32.

Buttiglione, S., Capetti, A., Celotti, A., Axon, D. J., Chiaberge, M., Macchetto, F. D., and Sparks, W. B. (2009). An optical spectroscopic survey of the 3CR sample of radio galaxies with z 0.3. I. Presentation of the data. *A&A*, 495:1033–1060.

Buttiglione, S., Capetti, A., Celotti, A., Axon, D. J., Chiaberge, M., Macchetto, F. D., and Sparks, W. B. (2010). An optical spectroscopic survey of the 3CR sample of radio galaxies with z 0.3 . II. Spectroscopic classes and accretion modes in radio-loud AGN. *A&A*, 509:A6.

Cabrera-Lavers, A. and Garzón, F. (2004). An Optical Study of a Sample of Spiral Galaxies. *AJ*, 127:1386–1404.

Calzetti, D., Armus, L., Bohlin, R. C., Kinney, A. L., Koornneef, J., and Storchi-Bergmann, T. (2000). The Dust Content and Opacity of Actively Star-forming Galaxies. *ApJ*, 533:682–695.

Capetti, A., Axon, D. J., Macchetto, F. D., Marconi, A., and Winge, C. (1999). The Origin of the Narrow-Line Region of Markarian 3: An Overpressured Jet Cocoon. *ApJ*, 516:187–194.

Capetti, A. and Baldi, R. D. (2011). Emission lines in early-type galaxies: active nuclei or stars? *A&A*, 529:A126.

Capetti, A. and Balmaverde, B. (2006). The host galaxy/AGN connection in nearby early-type galaxies. A new view of the origin of the radio-quiet/radio-loud dichotomy? *A&A*, 453:27 –37.

Capetti, A., Kharb, P., Axon, D. J., Merritt, D., and Baldi, R. D. (2009). A Very Large Array Radio Survey of Early-Type Galaxies in the Virgo Cluster. *AJ*, 138:1990–1997.

Cappellari, M., Bertola, F., Burstein, D., Buson, L. M., Greggio, L., and Renzini, A. (2001). The Cuspy Liner Nucleus of the S0/a Galaxy NGC 2681. *ApJ*, 551:197–205.

Carral, P., Turner, J. L., and Ho, P. T. P. (1990). 15 GHz compact structure in galactic nuclei. 362:434–442.

Casares, J., Jonker, P. G., and Israelian, G. (2017). *X-Ray Binaries*, page 1499.

Cash, W. (1979). Parameter estimation in astronomy through application of the likelihood ratio. *ApJ*, 228:939–947.

Chartas, G., Worrall, D. M., Birkinshaw, M., Cresitello-Dittmar, M., Cui, W., Ghosh, K. K., Harris, D. E., Hooper, E. J., Jauncey, D. L., Kim, D.-W., Lovell, J., Mathur, S., Schwartz, D. A., Tingay, S. J., Virani, S. N., and Wilkes, B. J. (2000). The Chandra X-Ray Observatory Resolves the X-Ray Morphology and Spectra of a Jet in PKS 0637-752. *ApJ*, 542:655–666.

Chiaberge, M., Capetti, A., and Celotti, A. (1999). The HST view of FR I radio galaxies: evidence for non-thermal nuclear sources. *A&A*, 349:77–87.

Chiaberge, M. and Marconi, A. (2011). On the origin of radio loudness in active galactic nuclei and its relationship with the properties of the central supermassive black hole. *MNRAS*, 416:917–926.

Cid Fernandes, R., González Delgado, R. M., Storchi-Bergmann, T., Martins, L. P., and Schmitt, H. (2005). The stellar populations of low-luminosity active galactic nuclei - III. Spatially resolved spectral properties. *MNRAS*, 356:270–294.

Cid Fernandes, R., Schlickmann, M., Stasinska, G., Asari, N. V., Gomes, J. M., Schoenell, W., Mateus, A., and Sodré, Jr., L. (2009). The Starburst-AGN Disconnection: LINERs as Retired Galaxies. In Wang, W., Yang, Z., Luo, Z., and Chen, Z., editors, *The Starburst-AGN Connection*, volume 408 of *Astronomical Society of the Pacific Conference Series*, page 122.

Cirasuolo, M., Magliocchetti, M., Celotti, A., and Danese, L. (2003). The radio-loud/radio-quiet dichotomy: news from the 2dF QSO Redshift Survey. *MNRAS*, 341:993–1004.

Colbert, E. J. M., Baum, S. A., Gallimore, J. F., O'Dea, C. P., and Christensen, J. A. (1996a). Large-Scale Outflows in Edge-on Seyfert Galaxies. II. Kiloparsec-Scale Radio Continuum Emission. *ApJ*, 467:551.

Colbert, E. J. M., Baum, S. A., Gallimore, J. F., O'Dea, C. P., and Christensen, J. A. (1996b). Large-Scale Outflows in Edge-on Seyfert Galaxies. II. Kiloparsec-Scale Radio Continuum Emission. *ApJ*, 467:551.

Comerón, S., Knapen, J. H., Beckman, J. E., Laurikainen, E., Salo, H., Martínez-Valpuesta, I., and Buta, R. J. (2010). AINUR: Atlas of Images of NUclear Rings. *MNRAS*, 402:2462–2490.

Condon, J. J. (1987). A 1.49 GHz atlas of spiral galaxies with B(T) = +12 or less and delta = -45 deg or greater. 65:485–541.

Condon, J. J. (1992). Radio emission from normal galaxies. 30:575–611.

Condon, J. J., Condon, M. A., Gisler, G., and Puschell, J. J. (1982). Strong radio sources in bright spiral galaxies. II - Rapid star formation and galaxy-galaxy interactions. *ApJ*, 252:102–124.

Condon, J. J., Huang, Z.-P., Yin, Q. F., and Thuan, T. X. (1991). Compact starbursts in ultraluminous infrared galaxies. *ApJ*, 378:65–76.

Condon, J. J. and Ransom, S. M. (2016). *Essential Radio Astronomy*.

Congiu, E., Berton, M., Giroletti, M., Antonucci, R., Caccianiga, A., Kharb, P., Lister, M. L., Foschini, L., Ciroi, S., Cracco, V., Frezzato, M., Järvelä, E., La Mura, G., Richards, J. L., and Rafanelli, P. (2017). Kiloparsec-scale emission in the narrow-line Seyfert 1 galaxy Mrk 783. *A&A*, 603:A32.

Connolly, S. D., McHardy, I. M., Skipper, C. J., and Emmanoulopoulos, D. (2016). Long-term X-ray spectral variability in AGN from the Palomar sample observed by Swift. *MNRAS*, 459:3963–3985.

Conway, J. E., Myers, S. T., Pearson, T. J., Readhead, A. C. S., Unwin, S. C., and Xu, W. (1994). Evidence for two classes of parsec-scale radio double source in active galactic nuclei. *ApJ*, 425:568–581.

Corbel, S., Coriat, M., Brocksopp, C., Tzioumis, A. K., Fender, R. P., Tomsick, J. A., Buxton, M. M., and Bailyn, C. D. (2013). The 'universal' radio/X-ray flux correlation: the case study of the black hole GX 339-4. 428:2500–2515.

Corbel, S., Nowak, M. A., Fender, R. P., Tzioumis, A. K., and Markoff, S. (2003). Radio/X-ray correlation in the low/hard state of GX 339-4. *aap*, 400:1007–1012.

Corral-Santana, J. M., Casares, J., Muñoz-Darias, T., Bauer, F. E., Martínez-Pais, I. G., and Russell, D. M. (2016). BlackCAT: A catalogue of stellar-mass black holes in X-ray transients. *A&A*, 587:A61.

Czerny, B., Siemiginowska, A., Janiuk, A., Nikiel-Wroczyński, B., and Stawarz, Ł. (2009). Accretion Disk Model of Short-Timescale Intermittent Activity in Young Radio Sources. *ApJ*, 698:840–851.

Dale, D. A., Smith, J. D. T., Armus, L., Buckalew, B. A., Helou, G., Kennicutt, Jr., R. C., Moustakas, J., Roussel, H., Sheth, K., Bendo, G. J., Calzetti, D., Draine, B. T.,

Engelbracht, C. W., Gordon, K. D., Hollenbach, D. J., Jarrett, T. H., Kewley, L. J., Leitherer, C., Li, A., Malhotra, S., Murphy, E. J., and Walter, F. (2006). Mid-Infrared Spectral Diagnostics of Nuclear and Extranuclear Regions in Nearby Galaxies. *ApJ*, 646:161–173.

de Gasperin, F., Merloni, A., Sell, P., Best, P., Heinz, S., and Kauffmann, G. (2011). Testing black hole jet scaling relations in low-luminosity active galactic nuclei. *MNRAS*, 415:2910–2919.

de Vaucouleurs, G., de Vaucouleurs, A., Corwin, Jr., H. G., Buta, R. J., Paturel, G., and Fouqué, P. (1991). *Third Reference Catalogue of Bright Galaxies. Volume I: Explanations and references. Volume II: Data for galaxies between 0^h and 12^h. Volume III: Data for galaxies between 12^h and 24^h.*

de Vaucouleurs, G., de Vaucouleurs, A., and Corwin, J. R. (1976). Second reference catalogue of bright galaxies. In *Second reference catalogue of bright galaxies, Vol. 1976, p. Austin: University of Texas Press.*, volume 1976.

Decarli, R., Gavazzi, G., Arosio, I., Cortese, L., Boselli, A., Bonfanti, C., and Colpi, M. (2007). The census of nuclear activity of late-type galaxies in the Virgo cluster. *MNRAS*, 381:136–150.

Di Matteo, T., Colberg, J., Springel, V., Hernquist, L., and Sijacki, D. (2008). Direct Cosmological Simulations of the Growth of Black Holes and Galaxies. *ApJ*, 676:33–53.

Di Matteo, T., Springel, V., and Hernquist, L. (2005). Energy input from quasars regulates the growth and activity of black holes and their host galaxies. *Nature*, 433:604–607.

Dicken, D., Tadhunter, C., Morganti, R., Axon, D., Robinson, A., Magagnoli, M., Kharb, P., Ramos Almeida, C., Mingo, B., Hardcastle, M., Nesvadba, N. P. H., Singh, V., Kouwenhoven, M. B. N., Rose, M., Spoon, H., Inskip, K. J., and Holt, J. (2014). Spitzer Mid-IR Spectroscopy of Powerful 2Jy and 3CRR Radio Galaxies. II. AGN Power Indicators and Unification. *ApJ*, 788:98.

Done, C., Gierliński, M., Sobolewska, M., and Schurch, N. (2007). The Origin of the Soft Excess in AGN. In Ho, L. C. and Wang, J.-W., editors, *The Central Engine of Active Galactic Nuclei*, volume 373 of *Astronomical Society of the Pacific Conference Series*, page 121.

Donea, A.-C. and Biermann, P. L. (1996). The symbiotic system in quasars: black hole, accretion disk and jet. *A&A*, 316:43–52.

Donea, A.-C. and Biermann, P. L. (2002). The Structure of Accretion Flow at the Base of Jets in AGN. *PASA*, 19:125–128.

Dopita, M. A. and Sutherland, R. S. (1996). Spectral Signatures of Fast Shocks. I. Low-Density Model Grid. *ApJS*, 102:161.

Dullo, B. T., Knapen, J. H., Williams, D. R. A., Beswick, R. J., Bendo, G., Baldi, R. D., Argo, M., McHardy, I. M., Muxlow, T., and Westcott, J. (2018a). The nuclear activity and central structure of the elliptical galaxy NGC 5322. *MNRAS*, 475:4670–4682.

Dullo, B. T., Knapen, J. H., Williams, D. R. A., Beswick, R. J., Bendo, G., Baldi, R. D., Argo, M., McHardy, I. M., Muxlow, T., and Westcott, J. (2018b). The nuclear activity and central structure of the elliptical galaxy NGC 5322. *MNRAS*.

Dullo, B. T., Martínez-Lombilla, C., and Knapen, J. H. (2016). Complex central structures suggest complex evolutionary paths for barred S0 galaxies. *MNRAS*, 462:3800–3811.

Ekers, R. D. and Ekers, J. A. (1973). A Survey of Elliptical Galaxies at 6 CM. *A&A*, 24:247.

Elmouttie, E., Haynes, R. F., Jones, K. L., Ehle, M., Beck, R., and Wielebinski, R. (1995). The polarized radio lobes of the Circinus galaxy. *MNRAS*, 275:L53–L59.

Elmouttie, M., Haynes, R. F., Jones, K. L., Sadler, E. M., and Ehle, M. (1998). Radio continuum evidence for nuclear outflow in the Circinus galaxy. *MNRAS*, 297:1202–1218.

Elvis, M., Wilkes, B. J., McDowell, J. C., Green, R. F., Bechtold, J., Willner, S. P., Oey, M. S., Polomski, E., and Cutri, R. (1994). Atlas of quasar energy distributions. *ApJS*, 95:1–68.

Esin, A. A., McClintock, J. E., and Narayan, R. (1997). Advection-Dominated Accretion and the Spectral States of Black Hole X-Ray Binaries: Application to Nova Muscae 1991. *ApJ*, 489:865–889.

Evans, I. N., Tsvetanov, Z., Kriss, G. A., Ford, H. C., Caganoff, S., and Koratkar, A. P. (1993). Hubble Space Telescope Imaging of the Narrow-Line Region of NGC 4151. *ApJ*, 417:82.

Falcke, H. and Biermann, P. L. (1995). The jet-disk symbiosis. I. Radio to X-ray emission models for quasars. *A&A*, 293:665–682.

Falcke, H., Körding, E., and Markoff, S. (2004). A scheme to unify low-power accreting black holes. Jet-dominated accretion flows and the radio/X-ray correlation. *A&A*, 414:895–903.

Falcke, H., Nagar, N. M., Wilson, A. S., and Ulvestad, J. S. (2000). Radio Sources in Low-Luminosity Active Galactic Nuclei. II. Very Long Baseline Interferometry Detections of Compact Radio Cores and Jets in a Sample of LINERs. *ApJ*, 542:197–200.

Falco, E. E., Kurtz, M. J., Geller, M. J., Huchra, J. P., Peters, J., Berlind, P., Mink, D. J., Tokarz, S. P., and Elwell, B. (1999). The Updated Zwicky Catalog (UZC). *PASP*, 111:438–452.

Falocco, S., Larsson, J., and Nandi, S. (2017). A (likely) X-ray jet from NGC6217 observed by XMM-Newton. *ArXiv e-prints*.

Fanaroff, B. L. and Riley, J. M. (1974). The morphology of extragalactic radio sources of high and low luminosity. *MNRAS*, 167:31P–36P.

Fasano, G. and Vio, R. (1988). Fitting a Straight Line with Errors on both Coordinates. *Bulletin d'Information du Centre de Donnees Stellaires*, 35:191.

Fath, E. A. (1913). No. 67. The spectra of spiral nebulae and globular star clusters. *Contributions from the Mount Wilson Observatory / Carnegie Institution of Washington*, 67:1–6.

Fender, R. P. (2001). Powerful jets from black hole X-ray binaries in low/hard X-ray states. *MNRAS*, 322:31–42.

Fender, R. P., Belloni, T. M., and Gallo, E. (2004). Towards a unified model for black hole X-ray binary jets. *MNRAS*, 355:1105–1118.

Fenech, D. M., Muxlow, T. W. B., Beswick, R. J., Pedlar, A., and Argo, M. K. (2008). Deep MERLIN 5GHz radio imaging of supernova remnants in the M82 starburst. *MNRAS*, 391:1384–1402.

Ferland, G. J. and Netzer, H. (1983). Are there any shock-heated galaxies. *ApJ*, 264:105–113.

Ferrarese, L. and Merritt, D. (2000). A Fundamental Relation between Supermassive Black Holes and Their Host Galaxies. *ApJL*, 539:L9–L12.

Field, G. B. and Rogers, R. D. (1993). Radiation from magnetized accretion disks in active galactic nuclei. *ApJ*, 403:94–109.

Filho, M. E., Barthel, P. D., and Ho, L. C. (2000). The Nature of Composite LINER/H II Galaxies as Revealed from High-Resolution VLA Observations. *ApJS*, 129:93–110.

Filho, M. E., Barthel, P. D., and Ho, L. C. (2002). The Radio Properties of Composite LINER/H II Galaxies. *ApJS*, 142:223–238.

Filho, M. E., Barthel, P. D., and Ho, L. C. (2006). A radio census of nuclear activity in nearby galaxies. *A&A*, 451:71–83.

Filho, M. E., Fraternali, F., Markoff, S., Nagar, N. M., Barthel, P. D., Ho, L. C., and Yuan, F. (2004). Further clues to the nature of composite LINER/H II galaxies. *A&A*, 418:429–443.

Filippenko, A. V. and Sargent, W. L. W. (1985). A search for 'dwarf' Seyfert 1 nuclei. I - The initial data and results. 57:503–522.

Fiore, F., Pellegrini, S., Matt, G., Antonelli, L. A., Comastri, A., della Ceca, R., Giallongo, E., Mathur, S., Molendi, S., Siemiginowska, A., Trinchieri, G., and Wilkes, B. (2001). The BeppoSAX View of the X-Ray Active Nucleus of NGC 4258. *ApJ*, 556:150–157.

Foreman-Mackey, D., Hogg, D. W., Lang, D., and Goodman, J. (2013). emcee: The MCMC Hammer. *PASP*, 125:306.

Fraix-Burnet, D., Despringre, V., and Baudry, A. (1997). EVN-MERLIN observations of 3C66B. *Vistas in Astronomy*, 41:237–240.

Francis, P. J., Hewett, P. C., Foltz, C. B., Chaffee, F. H., Weymann, R. J., and Morris, S. L. (1991). A high signal-to-noise ratio composite quasar spectrum. *ApJ*, 373:465–470.

Gallimore, J. F., Axon, D. J., O'Dea, C. P., Baum, S. A., and Pedlar, A. (2006). A Survey of Kiloparsec-Scale Radio Outflows in Radio-Quiet Active Galactic Nuclei. *AJ*, 132:546–569.

Gallimore, J. F., Baum, S. A., and O'Dea, C. P. (2004). The Parsec-Scale Radio Structure of NGC 1068 and the Nature of the Nuclear Radio Source. *ApJ*, 613:794–810.

Gallimore, J. F., Baum, S. A., O'Dea, C. P., and Pedlar, A. (1996). The Subarcsecond Radio Structure in NGC 1068. I. Observations and Results. *ApJ*, 458:136.

Gallo, E., Fender, R. P., and Pooley, G. G. (2003). A universal radio-X-ray correlation in low/hard state black hole binaries. *MNRAS*, 344:60–72.

Gallo, E., Treu, T., Jacob, J., Woo, J.-H., Marshall, P. J., and Antonucci, R. (2008). AMUSE-Virgo. I. Supermassive Black Holes in Low-Mass Spheroids. *ApJ*, 680:154–168.

Gallo, E., Treu, T., Marshall, P. J., Woo, J.-H., Leipski, C., and Antonucci, R. (2010). AMUSE-Virgo. II. Down-sizing in Black Hole Accretion. *ApJ*, 714:25–36.

Garofalo, D. (2013). Retrograde versus Prograde Models of Accreting Black Holes. *Advances in Astronomy*, 2013:213105.

Garofalo, D., Evans, D. A., and Sambruna, R. M. (2010). The evolution of radio-loud active galactic nuclei as a function of black hole spin. *MNRAS*, 406:975–986.

Gavazzi, G., Consolandi, G., Dotti, M., Fossati, M., Savorgnan, G., Gualandi, R., and Bruni, I. (2013). Red-channel (6000-8000 Å) nuclear spectra of 376 local galaxies. *A&A*, 558:A68.

Gebhardt, K., Bender, R., Bower, G., Dressler, A., Faber, S. M., Filippenko, A. V., Green, R., Grillmair, C., Ho, L. C., Kormendy, J., Lauer, T. R., Magorrian, J., Pinkney, J., Richstone, D., and Tremaine, S. (2000). A Relationship between Nuclear Black Hole Mass and Galaxy Velocity Dispersion. 539:L13–L16.

Gendre, M. A., Best, P. N., Wall, J. V., and Ker, L. M. (2013). The relation between morphology, accretion modes and environmental factors in local radio AGN. *MNRAS*, 430:3086–3101.

Ghisellini, G., Haardt, F., and Matt, G. (2004). Aborted jets and the X-ray emission of radio-quiet AGNs. *A&A*, 413:535–545.

Gilfanov, M., Grimm, H.-J., and Sunyaev, R. (2004). HMXB, ULX and star formation. *Nuclear Physics B Proceedings Supplements*, 132:369–375.

Giovannini, G., Cotton, W. D., Feretti, L., Lara, L., and Venturi, T. (1998). VLBI Observations of a Complete Sample of Radio Galaxies. VIII. Proper Motion in 3C 338. *ApJ*, 493:632–640.

Giovannini, G., Taylor, G. B., Feretti, L., Cotton, W. D., Lara, L., and Venturi, T. (2005). The Bologna Complete Sample of Nearby Radio Sources. *ApJ*, 618:635–648.

Giroletti, M. and Panessa, F. (2009). The Faintest Seyfert Radio Cores Revealed by VLBI. *ApJ*, 706:L260–L264.

González-Martín, O., Masegosa, J., Márquez, I., and Guainazzi, M. (2009). Fitting Liner Nuclei within the Active Galactic Nucleus Family: A Matter of Obscuration? *ApJ*, 704:1570–1585.

González-Martín, O. and Vaughan, S. (2012). X-ray variability of 104 active galactic nuclei. XMM-Newton power-spectrum density profiles. *A&A*, 544:A80.

Gonzalez-Serrano, J. I., Perez-Fournon, I., Junor, W., and Spencer, R. (1989). Radio to optical spectral index variations along the M87 jet. *Ap&SS*, 157:183–186.

Goulding, A. D. and Alexander, D. M. (2009). Towards a complete census of AGN in nearby Galaxies: a large population of optically unidentified AGN. *MNRAS*, 398:1165–1193.

Graham, A. W. and Scott, N. (2013). The M $_{BH}$-L $_{spheroid}$ Relation at High and Low Masses, the Quadratic Growth of Black Holes, and Intermediate-mass Black Hole Candidates. *ApJ*, 764:151.

Gültekin, K., Cackett, E. M., Miller, J. M., Di Matteo, T., Markoff, S., and Richstone, D. O. (2009). The Fundamental Plane of Accretion onto Black Holes with Dynamical Masses. 706:404–416.

Gursky, H., Kellogg, E. M., Leong, C., Tananbaum, H., and Giacconi, R. (1971). Detection of X-Rays from the Seyfert Galaxies NGC 1275 and NGC 4151 by the UHURU Satellite. 165:L43.

Gusev, A. S., Pilyugin, L. S., Sakhibov, F., Dodonov, S. N., Ezhkova, O. V., and Khramtsova, M. S. (2012). Oxygen and nitrogen abundances of H II regions in six spiral galaxies. *MNRAS*, 424:1930–1940.

Gusev, A. S., Sakhibov, F., Piskunov, A. E., Kharchenko, N. V., Bruevich, V. V., Ezhkova, O. V., Guslyakova, S. A., Lang, V., Shimanovskaya, E. V., and Efremov, Y. N. (2016). A spectral and photometric study of 102 star-forming regions in seven spiral galaxies. *MNRAS*, 457:3334–3355.

Halpern, J. P. and Steiner, J. E. (1983). Low-ionization active galactic nuclei - X-ray or shock heated? *ApJ*, 269:L37–L41.

Hardcastle, M. J., Croston, J. H., and Kraft, R. P. (2007). A Chandra Study of Particle Acceleration in the Multiple Hot Spots of Nearby Radio Galaxies. *ApJ*, 669:893–904.

Hardcastle, M. J., Evans, D. A., and Croston, J. H. (2009). The active nuclei of z 1.0 3CRR radio sources. *MNRAS*, 396:1929–1952.

Hardcastle, M. J. and Worrall, D. M. (2000). Radio, optical and X-ray nuclei in nearby 3CRR radio galaxies. *MNRAS*, 314:359–363.

Hardcastle, M. J., Worrall, D. M., Kraft, R. P., Forman, W. R., Jones, C., and Murray, S. S. (2003). Radio and X-Ray Observations of the Jet in Centaurus A. 593:169–183.

Harris, D. E. and Krawczynski, H. (2006). X-Ray Emission from Extragalactic Jets. *ARA&A*, 44:463–506.

Harris, D. E., Lee, N. P., Schwartz, D. A., Siemiginowska, A., Massaro, F., Birkinshaw, M., Worrall, D. M., Cheung, C. C., Gelbord, J. M., Jorstad, S. G., Marscher, A. P., Landt, H., Marshall, H., Perlman, E. S., Stawarz, L., Uchiyama, Y., and Urry, C. M. (2017). A Multi-band Study of the Remarkable Jet in Quasar 4C+19.44. *ApJ*, 846:119.

Harrison, B., Pedlar, A., Unger, S. W., Burgess, P., Graham, D. A., and Preuss, E. (1986). The parsec-scale structure of the radio nucleus of NGC 4151. 218:775–784.

Heckman, T. M. (1980). An optical and radio survey of the nuclei of bright galaxies - Activity in normal galactic nuclei. *A&A*, 87:152–164.

Heckman, T. M., Kauffmann, G., Brinchmann, J., Charlot, S., Tremonti, C., and White, S. D. M. (2004). Present-Day Growth of Black Holes and Bulges: The Sloan Digital Sky Survey Perspective. *ApJ*, 613:109–118.

Heckman, T. M., Lehnert, M. D., and Armus, L. (1993). Galactic Superwinds. In Shull, J. M. and Thronson, H. A., editors, *The Environment and Evolution of Galaxies*, volume 188 of *Astrophysics and Space Science Library*, page 455.

Heckman, T. M., Ptak, A., Hornschemeier, A., and Kauffmann, G. (2005). The Relationship of Hard X-Ray and Optical Line Emission in Low-Redshift Active Galactic Nuclei. *ApJ*, 634:161–168.

Heesen, V., Beck, R., Krause, M., and Dettmar, R.-J. (2009). Cosmic rays and the magnetic field in the nearby starburst galaxy NGC 253. I. The distribution and transport of cosmic rays. *A&A*, 494:563–577.

Heinz, S. and Sunyaev, R. A. (2003). The non-linear dependence of flux on black hole mass and accretion rate in core-dominated jets. *MNRAS*, 343:L59–L64.

Hernández-García, L., González-Martín, O., Masegosa, J., and Márquez, I. (2014). X-ray spectral variability of LINERs selected from the Palomar sample. *A&A*, 569:A26.

Herrero-Illana, R., Pérez-Torres, M. Á., Randriamanakoto, Z., Alberdi, A., Efstathiou, A., Väisänen, P., Kankare, E., Kool, E., Mattila, S., Ramphul, R., and Ryder, S. (2017). Star formation and AGN activity in a sample of local luminous infrared galaxies through multiwavelength characterization. *MNRAS*, 471:1634–1651.

Ho, L. C. (1999a). LINERs as low-luminosity active galactic nuclei. *Advances in Space Research*, 23:813–822.

Ho, L. C. (1999b). The Spectral Energy Distributions of Low-Luminosity Active Galactic Nuclei. *ApJ*, 516:672–682.

Ho, L. C. (2002). On the Relationship between Radio Emission and Black Hole Mass in Galactic Nuclei. *ApJ*, 564:120–132.

Ho, L. C. (2008). Nuclear Activity in Nearby Galaxies. 46:475–539.

Ho, L. C., Filippenko, A. V., and Sargent, W. L. (1995). A search for 'dwarf' Seyfert nuclei. 2: an optical spectral atlas of the nuclei of nearby galaxies. 98:477–593.

Ho, L. C., Filippenko, A. V., and Sargent, W. L. W. (1993). A Reevaluation of the Excitation Mechanism of LINERs. *ApJ*, 417:63.

Ho, L. C., Filippenko, A. V., and Sargent, W. L. W. (1997a). A Search for "Dwarf" Seyfert Nuclei. III. Spectroscopic Parameters and Properties of the Host Galaxies. 112:315–390.

Ho, L. C., Filippenko, A. V., and Sargent, W. L. W. (1997b). A Search for "Dwarf" Seyfert Nuclei. V. Demographics of Nuclear Activity in Nearby Galaxies. 487:568–578.

Ho, L. C., Filippenko, A. V., and Sargent, W. L. W. (1997c). The Influence of Bars on Nuclear Activity. 487:591–602.

Ho, L. C., Filippenko, A. V., and Sargent, W. L. W. (2003). A Search for "Dwarf" Seyfert Nuclei. VI. Properties of Emission-Line Nuclei in Nearby Galaxies. 583:159–177.

Ho, L. C., Filippenko, A. V., Sargent, W. L. W., and Peng, C. Y. (1997d). A Search for "Dwarf" Seyfert Nuclei. IV. Nuclei with Broad Hα Emission. 112:391–414.

Ho, L. C., Filippenko, A. V., Sargent, W. L. W., and Peng, C. Y. (1997e). A Search for "Dwarf" Seyfert Nuclei. IV. Nuclei with Broad Hα Emission. *ApJS*, 112:391–414.

Ho, L. C., Greene, J. E., Filippenko, A. V., and Sargent, W. L. W. (2009). A Search for "Dwarf" Seyfert Nuclei. VII. A Catalog of Central Stellar Velocity Dispersions of Nearby Galaxies. 183:1–16.

Ho, L. C. and Peng, C. Y. (2001). Nuclear Luminosities and Radio Loudness of Seyfert Nuclei. *ApJ*, 555:650–662.

Ho, L. C. and Ulvestad, J. S. (2001a). Radio Continuum Survey of an Optically Selected Sample of Nearby Seyfert Galaxies. *ApJS*, 133:77–118.

Ho, L. C. and Ulvestad, J. S. (2001b). Radio Continuum Survey of an Optically Selected Sample of Nearby Seyfert Galaxies. 133:77–118.

Hocuk, S. and Barthel, P. D. (2010). The asymmetric radio structure and record jet of giant quasar 4C 34.47. *A&A*, 523:A9.

Högbom, J. A. (1974). Aperture Synthesis with a Non-Regular Distribution of Interferometer Baselines. *A&AS*, 15:417.

Hogg, D. W., Bovy, J., and Lang, D. (2010). Data analysis recipes: Fitting a model to data. *ArXiv e-prints*.

Hönig, S. F., Kishimoto, M., Tristram, K. R. W., Prieto, M. A., Gandhi, P., Asmus, D., Antonucci, R., Burtscher, L., Duschl, W. J., and Weigelt, G. (2013). Dust in the Polar Region as a Major Contributor to the Infrared Emission of Active Galactic Nuclei. *ApJ*, 771:87.

Hönig, S. F., Watson, D., Kishimoto, M., and Hjorth, J. (2014). A dust-parallax distance of 19 megaparsecs to the supermassive black hole in NGC 4151. 515:528–530.

Hota, A. and Saikia, D. J. (2006). Radio bubbles in the composite AGN-starburst galaxy NGC6764. *MNRAS*, 371:945–956.

Hummel, E., Pedlar, A., Davies, R. D., and van der Hulst, J. M. (1985). A radio continuum survey of SBC spiral galaxies at 1.465 GHz. 60:293–313.

Hutchings, J. B., Crenshaw, D. M., Danks, A. C., Gull, T. R., Kraemer, S. B., Nelson, C. H., Weistrop, D., Kaiser, M. E., and Joseph, C. L. (1999). High-Velocity Line Emission in the Narrow-Line Region of NGC 4151. *AJ*, 118:2101–2107.

Hutchings, J. B., Crenshaw, D. M., Kaiser, M. E., Kraemer, S. B., Weistrop, D., Baum, S., Bowers, C. W., Feinberg, L. D., Green, R. F., Gull, T. R., Hartig, G. F., Hill, G., and Lindler, D. J. (1998). Gas Cloud Kinematics near the Nucleus of NGC 4151. *ApJ*, 492:L115–L119.

Ichimaru, S. (1977). Bimodal behavior of accretion disks - Theory and application to Cygnus X-1 transitions. *ApJ*, 214:840–855.

Irwin, J. A. and Saikia, D. J. (2003). Giant Metrewave Radio Telescope observations of NGC 3079. *MNRAS*, 346:977–986.

Irwin, J. A., Schmidt, P., Damas-Segovia, A., Beck, R., English, J., Heald, G., Henriksen, R. N., Krause, M., Li, J.-T., Rand, R. J., Wang, Q. D., Wiegert, T., Kamieneski, P., Paré, D., and Sullivan, K. (2017). CHANG-ES - VIII. Uncovering hidden AGN activity in radio polarization. *MNRAS*, 464:1333–1346.

Ishibashi, W. and Courvoisier, T. J.-L. (2010). X-ray power law spectra in active galactic nuclei. 512:A58.

James, P. A., Shane, N. S., Beckman, J. E., Cardwell, A., Collins, C. A., Etherton, J., de Jong, R. S., Fathi, K., Knapen, J. H., Peletier, R. F., Percival, S. M., Pollacco, D. L., Seigar, M. S., Stedman, S., and Steele, I. A. (2004). The Hα galaxy survey. I. The galaxy sample, Hα narrow-band observations and star formation parameters for 334 galaxies. *A&A*, 414:23–43.

Jenkner, H., Lasker, B. M., Sturch, C. R., McLean, B. J., Shara, M. M., and Russel, J. L. (1990). The Guide Star Catalog. III - Production, database organization, and population statistics. *AJ*, 99:2082–2154.

Jester, S., Röser, H.-J., Meisenheimer, K., and Perley, R. (2005). The radio-ultraviolet spectral energy distribution of the jet in 3C 273. 431:477–502.

Johnston, K. J., Elvis, M., Kjer, D., and Shen, B. S. P. (1982). Radio jets in NGC 4151. 262:61–65.

Jones, S. (2012). Radio/X-ray variability and structure investigation of Seyfert galaxy NGC 4051. *Ph.D. Thesis*.

Jones, S., McHardy, I., and Maccarone, T. J. (2017). A comprehensive long-term study of the radio and X-ray variability of NGC 4051 Paper II. *MNRAS*, 465:1336–1347.

Jones, S., McHardy, I., Moss, D., Seymour, N., Breedt, E., Uttley, P., Körding, E., and Tudose, V. (2011). Radio and X-ray variability in the Seyfert galaxy NGC 4051. *MNRAS*, 412:2641–2652.

Kaiser, M. E., Bradley, II, L. D., Hutchings, J. B., Crenshaw, D. M., Gull, T. R., Kraemer, S. B., Nelson, C. H., Ruiz, J., and Weistrop, D. (2000). The Resolved Narrow-Line Region in NGC 4151. *ApJ*, 528:260–275.

Kalberla, P. M. W., Burton, W. B., Hartmann, D., Arnal, E. M., Bajaja, E., Morras, R., and Pöppel, W. G. L. (2005). The Leiden/Argentine/Bonn (LAB) Survey of Galactic HI. Final data release of the combined LDS and IAR surveys with improved stray-radiation corrections. *A&A*, 440:775–782.

Kandalyan, R. A. and Al-Naimiy, H. M. K. (2002). Broad-Band Radio to X-Ray Properties of Seyfert Galaxies. *Astrophysics*, 45:277–287.

Kaspi, S., Smith, P. S., Netzer, H., Maoz, D., Jannuzi, B. T., and Giveon, U. (2000). Reverberation Measurements for 17 Quasars and the Size-Mass-Luminosity Relations in Active Galactic Nuclei. *ApJ*, 533:631–649.

Kauffmann, G., Heckman, T. M., and Best, P. N. (2008). Radio jets in galaxies with actively accreting black holes: new insights from the SDSS. *MNRAS*, 384:953–971.

Keel, W. C. (1983). Spectroscopic evidence for activity in the nuclei of normal spiral galaxies. *ApJ*, 269:466–486.

Kellermann, K. I., Sramek, R., Schmidt, M., Shaffer, D. B., and Green, R. (1989). VLA observations of objects in the Palomar Bright Quasar Survey. 98:1195–1207.

Kelly, B. C. (2007). Some Aspects of Measurement Error in Linear Regression of Astronomical Data. *ApJ*, 665:1489–1506.

Kennicutt, R. (1983). The origin of the nonthermal radio emission in normal disk galaxies. *A&A*, 120:219–222.

Kennicutt, Jr., R. C. (1998). Star Formation in Galaxies Along the Hubble Sequence. *ARA&A*, 36:189–232.

Kettenis, M., van Langevelde, H. J., Reynolds, C., and Cotton, B. (2006). ParselTongue: AIPS Talking Python. In Gabriel, C., Arviset, C., Ponz, D., and Enrique, S., editors, *Astronomical Data Analysis Software and Systems XV*, volume 351 of *Astronomical Society of the Pacific Conference Series*, page 497.

Kewley, L. J., Dopita, M. A., Sutherland, R. S., Heisler, C. A., and Trevena, J. (2001). Theoretical Modeling of Starburst Galaxies. 556:121–140.

Kewley, L. J., Groves, B., Kauffmann, G., and Heckman, T. (2006). The host galaxies and classification of active galactic nuclei. 372:961–976.

Khachikian, E. Y. and Weedman, D. W. (1974). An atlas of Seyfert galaxies. 192:581–589.

Kharb, P., Capetti, A., Axon, D. J., Chiaberge, M., Grandi, P., Robinson, A., Giovannini, G., Balmaverde, B., Macchetto, D., and Montez, R. (2012). Examining the Radio-loud/Radio-quiet Dichotomy with New Chandra and VLA Observations of 13 UGC Galaxies. *AJ*, 143:78.

Kharb, P., Hota, A., Croston, J. H., Hardcastle, M. J., O'Dea, C. P., Kraft, R. P., Axon, D. J., and Robinson, A. (2010). Parsec-scale Imaging of the Radio-bubble Seyfert Galaxy NGC 6764. *ApJ*, 723:580–586.

Kharb, P., Lal, D. V., and Merritt, D. (2017). A candidate sub-parsec binary black hole in the Seyfert galaxy NGC 7674. *Nature Astronomy*, 1:727–733.

Kharb, P., O'Dea, C. P., Baum, S. A., Colbert, E. J. M., and Xu, C. (2006). A Radio Study of the Seyfert Galaxy Markarian 6: Implications for Seyfert Life Cycles. *ApJ*, 652:177–188.

Kharb, P., O'Dea, C. P., Baum, S. A., Hardcastle, M. J., Dicken, D., Croston, J. H., Mingo, B., and Noel-Storr, J. (2014). Very Large Baseline Array observations of Mrk 6: probing the jet-lobe connection. *MNRAS*, 440:2976–2987.

Kimani, N., Sendlinger, K., Brunthaler, A., Menten, K. M., Martí-Vidal, I., Henkel, C., Falcke, H., Muxlow, T. W. B., Beswick, R. J., and Bower, G. C. (2016). Radio evolution of supernova SN 2008iz in M 82. *A&A*, 593:A18.

King, A. L., Miller, J. M., Cackett, E. M., Fabian, A. C., Markoff, S., Nowak, M. A., Rupen, M., Gültekin, K., and Reynolds, M. T. (2011). A Distinctive Disk-Jet Coupling in the Seyfert-1 Active Galactic Nucleus NGC 4051. *ApJ*, 729:19.

King, A. R. (2004). Ultraluminous X-ray sources and star formation. *MNRAS*, 347:L18–L20.

Kinney, A. L., Schmitt, H. R., Clarke, C. J., Pringle, J. E., Ulvestad, J. S., and Antonucci, R. R. J. (2000). Jet Directions in Seyfert Galaxies. *ApJ*, 537:152–177.

Knapen, J. H. and James, P. A. (2009). The Hα Galaxy Survey. VIII. Close Companions and Interactions, and the Definition of Starbursts. *ApJ*, 698:1437–1455.

Knapen, J. H., Stedman, S., Bramich, D. M., Folkes, S. L., and Bradley, T. R. (2004). Structure and star formation in disk galaxies. II. Optical imaging. *A&A*, 426:1135–1141.

Koratkar, A. and Blaes, O. (1999). The Ultraviolet and Optical Continuum Emission in Active Galactic Nuclei: The Status of Accretion Disks. *PASP*, 111:1–30.

Koratkar, A. P. and Gaskell, C. M. (1991). Radius-luminosity and mass-luminosity relationships for active galactic nuclei. *ApJ*, 370:L61–L64.

Körding, E., Falcke, H., and Corbel, S. (2006). Refining the fundamental plane of accreting black holes. 456:439–450.

Körding, E. G., Jester, S., and Fender, R. (2008). Measuring the accretion rate and kinetic luminosity functions of supermassive black holes. *MNRAS*, 383:277–288.

Kormendy, J. and Ho, L. C. (2013). Coevolution (Or Not) of Supermassive Black Holes and Host Galaxies. *ARA&A*, 51:511–653.

Kraan-Korteweg, R. C. (1986). A catalog of 2810 nearby galaxies - The effect of the Virgocentric flow model on their observed velocities. *A&AS*, 66:255–279.

Kraemer, S. B., Schmitt, H. R., and Crenshaw, D. M. (2008). Probing the Ionization Structure of the Narrow-Line Region in the Seyfert 1 Galaxy NGC 4151. *ApJ*, 679:1128–1143.

Kraft, R. P., Forman, W. R., Jones, C., Murray, S. S., Hardcastle, M. J., and Worrall, D. M. (2002). Chandra Observations of the X-Ray Jet in Centaurus A. 569:54–71.

Krichbaum, T. P., Graham, D. A., Witzel, A., Greve, A., Wink, J. E., Grewing, M., Colomer, F., de Vicente, P., Gomez-Gonzalez, J., Baudry, A., and Zensus, J. A. (1998). VLBI observations of the galactic center source SGR A* at 86 GHz and 215 GHz. *A&A*, 335:L106–L110.

Kukula, M. J., Ghosh, T., Pedlar, A., and Schilizzi, R. T. (1999). Parsec-Scale Radio Structures in the Nuclei of Four Seyfert Galaxies. *ApJ*, 518:117–128.

Kukula, M. J., Ghosh, T., Pedlar, A., Schilizzi, R. T., Miley, G. K., de Bruyn, A. G., and Saikia, D. J. (1993). High-Resolution Radio Observations of MARKARIAN:3. *MNRAS*, 264:893.

Kukula, M. J., Pedlar, A., Baum, S. A., and O'Dea, C. P. (1995). High-resolution radio observations of the CfA Seyfert Sample -I. The observations. *MNRAS*, 276:1262–1280.

Laor, A. (2000). On Black Hole Masses and Radio Loudness in Active Galactic Nuclei. *ApJ*, 543:L111–L114.

Laor, A. (2003). Some Comments related to AGN Radio Loudness. *ArXiv Astrophysics e-prints*.

Laor, A. and Behar, E. (2008). On the origin of radio emission in radio-quiet quasars. *MNRAS*, 390:847–862.

Lasota, J.-P., Abramowicz, M. A., Chen, X., Krolik, J., Narayan, R., and Yi, I. (1996). Is the Accretion Flow in NGC 4258 Advection Dominated? *ApJ*, 462:142–+.

Lavalley, M., Isobe, T., and Feigelson, E. (1992). ASURV: Astronomy Survival Analysis Package. In Worrall, D. M., Biemesderfer, C., and Barnes, J., editors, *Astronomical Data Analysis Software and Systems I*, volume 25 of *Astronomical Society of the Pacific Conference Series*, page 245.

Leech, K. J., Penston, M. V., Terlevich, R., Lawrence, A., Rowan-Robinson, M., and Crawford, J. (1989). High-luminosity IRAS galaxies. II - Optical spectroscopy, modelling of starburst regions and comparison with structure. *MNRAS*, 240:349–372.

Lira, P., Johnson, R. A., Lawrence, A., and Cid Fernandes, R. (2007). Multiwavelength study of the nuclei of a volume-limited sample of galaxies - II. Optical, infrared and radio observations. *MNRAS*, 382:1552–1590.

Liu, J. (2011). Chandra ACIS Survey of X-ray Point Sources in 383 Nearby Galaxies. I. The Source Catalog. *ApJS*, 192:10.

Livio, M., Ogilvie, G. I., and Pringle, J. E. (1999). Extracting Energy from Black Holes: The Relative Importance of the Blandford-Znajek Mechanism. *ApJ*, 512:100–104.

Lovell, B. (1968). *The story of Jodrell Bank*.

Maccarone, T. J., Gallo, E., and Fender, R. (2003). The connection between radio-quiet active galactic nuclei and the high/soft state of X-ray binaries. *MNRAS*, 345:L19–L24.

Magorrian, J., Tremaine, S., Richstone, D., Bender, R., Bower, G., Dressler, A., Faber, S. M., Gebhardt, K., Green, R., Grillmair, C., Kormendy, J., and Lauer, T. (1998). The Demography of Massive Dark Objects in Galaxy Centers. 115:2285–2305.

Malmquist, K. G. (1922). On some relations in stellar statistics. *Meddelanden fran Lunds Astronomiska Observatorium Serie I*, 100:1–52.

Maoz, D. (2007). Low-Luminosity Active Galactic Nuclei: Are They UV-Faint and Radio Loud? *astro-ph/0702292*.

Marin, F. (2016). Are there reliable methods to estimate the nuclear orientation of Seyfert galaxies? *MNRAS*, 460:3679–3705.

Markoff, S., Nowak, M. A., and Wilms, J. (2005). Going with the Flow: Can the Base of Jets Subsume the Role of Compact Accretion Disk Coronae? *ApJ*, 635:1203–1216.

Marscher, A. P. and Gear, W. K. (1985). Models for high-frequency radio outbursts in extragalactic sources, with application to the early 1983 millimeter-to-infrared flare of 3C 273. *ApJ*, 298:114–127.

Marshall, H. L., Miller, B. P., Davis, D. S., Perlman, E. S., Wise, M., Canizares, C. R., and Harris, D. E. (2002). A High-Resolution X-Ray Image of the Jet in M87. *ApJ*, 564:683–687.

Martini, P., Regan, M. W., Mulchaey, J. S., and Pogge, R. W. (2003). Circumnuclear Dust in Nearby Active and Inactive Galaxies. I. Data. *ApJS*, 146:353–406.

Massaglia, S., Bodo, G., Rossi, P., Capetti, S., and Mignone, A. (2016). Making Faranoff-Riley I radio sources. I. Numerical hydrodynamic 3D simulations of low-power jets. *A&A*, 596:A12.

Mattila, S., Greimel, R., Gerardy, C., Meikle, W. P. S., Monard, L. A. G., Boles, T., Pugh, H., Graham, J., and Li, W. (2005). Supernovae 2005Q, 2005R, 2005S, 2005T, 2005U. *IAU Circ.*, 8473.

Mattila, S., Pérez-Torres, M., Efstathiou, A., Mimica, P., Fraser, M., Kankare, E., Alberdi, A., Aloy, M. Á., Heikkilä, T., Jonker, P. G., Lundqvist, P., Martí-Vidal, I., Meikle, W. P. S., Romero-Cañizales, C., Smartt, S. J., Tsygankov, S., Varenius, E., Alonso-Herrero, A., Bondi, M., Fransson, C., Herrero-Illana, R., Kangas, T., Kotak, R., Ramírez-Olivencia, N., Väisänen, P., Beswick, R. J., Clements, D. L., Greimel, R., Harmanen, J., Kotilainen, J., Nandra, K., Reynolds, T., Ryder, S., Walton, N. A., Wiik, K., and Östlin, G. (2018). A dust-enshrouded tidal disruption event with a resolved radio jet in a galaxy merger. *ArXiv e-prints*.

Mauch, T. and Sadler, E. M. (2007). Radio sources in the 6dFGS: local luminosity functions at 1.4GHz for star-forming galaxies and radio-loud AGN. *MNRAS*, 375:931–950.

McKinney, J. C., Tchekhovskoy, A., and Blandford, R. D. (2012). General relativistic magnetohydrodynamic simulations of magnetically choked accretion flows around black holes. *MNRAS*, 423:3083–3117.

McMullin, J. P., Waters, B., Schiebel, D., Young, W., and Golap, K. (2007). CASA Architecture and Applications. In Shaw, R. A., Hill, F., and Bell, D. J., editors, *Astronomical Data Analysis Software and Systems XVI*, volume 376 of *Astronomical Society of the Pacific Conference Series*, page 127.

Meier, D. L. (2001). The Association of Jet Production with Geometrically Thick Accretion Flows and Black Hole Rotation. *ApJ*, 548:L9–L12.

Merloni, A. and Heinz, S. (2007). Measuring the kinetic power of active galactic nuclei in the radio mode. *MNRAS*, 381:589–601.

Merloni, A., Heinz, S., and di Matteo, T. (2003). A Fundamental Plane of black hole activity. 345:1057–1076.

Merloni, A., Körding, E., Heinz, S., Markoff, S., Di Matteo, T., and Falcke, H. (2006). Why the fundamental plane of black hole activity is not simply a distance driven artifact. 11:567–576.

Miller, N. A., Hornschemeier, A. E., Mobasher, B., Bridges, T. J., Hudson, M. J., Marzke, R. O., and Smith, R. J. (2009). The Radio Luminosity Function and Galaxy Evolution in the Coma Cluster. *AJ*, 137:4450–4467.

Mingo, B., Watson, M. G., Rosen, S. R., Hardcastle, M. J., Ruiz, A., Blain, A., Carrera, F. J., Mateos, S., Pineau, F.-X., and Stewart, G. C. (2016). The MIXR sample: AGN activity versus star formation across the cross-correlation of WISE, 3XMM, and FIRST/NVSS. *MNRAS*, 462:2631–2667.

Moldón, J., Ribó, M., and Paredes, J. M. (2012). Periodic morphological changes in the radio structure of the gamma-ray binary LS 5039. *A&A*, 548:A103.

Morganti, R. (2017). Archaeology of active galaxies across the electromagnetic spectrum. *Nature Astronomy*, 1:596–605.

Morganti, R., Fanti, C., Fanti, R., Parma, P., and de Ruiter, H. R. (1987). VLA observations of low luminosity radio galaxies. V - A detailed radio study of five jets. *A&A*, 183:203–216.

Morganti, R., Tsvetanov, Z. I., Gallimore, J., and Allen, M. G. (1999). Radio continuum morphology of southern Seyfert galaxies. *A&AS*, 137:457–471.

Mościbrodzka, M., Falcke, H., and Noble, S. (2016). Scale-invariant radio jets and varying black hole spin. *A&A*, 596:A13.

Moustakas, J. and Kennicutt, Jr., R. C. (2006). An Integrated Spectrophotometric Survey of Nearby Star-forming Galaxies. *ApJS*, 164:81–98.

Mundell, C. G., Ferruit, P., Nagar, N., and Wilson, A. S. (2009). Radio Variability in Seyfert Nuclei. *ApJ*, 703:802–815.

Mundell, C. G., Pedlar, A., Baum, S. A., O'Dea, C. P., Gallimore, J. F., and Brinks, E. (1995). MERLIN observations of neutral hydrogen absorption in the Seyfert nucleus of NGC 4151. *MNRAS*, 272:355–362.

Mundell, C. G., Wrobel, J. M., Pedlar, A., and Gallimore, J. F. (2003). The Nuclear Regions of the Seyfert Galaxy NGC 4151: Parsec-Scale H I Absorption and a Remarkable Radio Jet. 583:192–204.

Murphy, E. J., Dong, D., Momjian, E., Linden, S., Kennicutt, Jr., R. C., Meier, D. S., Schinnerer, E., and Turner, J. L. (2017). The Star Formation in Radio Survey: Jansky Very Large Array 33 GHz Observations of Nearby Galaxy Nuclei and Extranuclear Star-Forming Regions. *ArXiv e-prints*.

Mushotzky, R. F., Done, C., and Pounds, K. A. (1993). X-ray spectra and time variability of active galactic nuclei. *ARA&A*, 31:717–761.

Muxlow, T. W. B., Beswick, R. J., Garrington, S. T., Pedlar, A., Fenech, D. M., Argo, M. K., van Eymeren, J., Ward, M., Zezas, A., and Brunthaler, A. (2010). Discovery of an unusual new radio source in the star-forming galaxy M82: faint supernova, supermassive black hole or an extragalactic microquasar? *MNRAS*, 404:L109–L113.

Muxlow, T. W. B., Pedlar, A., Beswick, R. J., Argo, M. K., O'Brien, T. J., Fenech, D., and Trotman, W. (2005). Is 41.95+575 in M82 actually an SNR? . 76:586.

Muxlow, T. W. B., Pedlar, A., Wilkinson, P. N., Axon, D. J., Sanders, E. M., and de Bruyn, A. G. (1994). The Structure of Young Supernova Remnants in M82. *MNRAS*, 266:455.

Nagar, N. M., Falcke, H., and Wilson, A. S. (2005). Radio sources in low-luminosity active galactic nuclei. IV. Radio luminosity function, importance of jet power, and radio properties of the complete Palomar sample. *A&A*, 435:521–543.

Nagar, N. M., Falcke, H., Wilson, A. S., and Ho, L. C. (2000). Radio Sources in Low-Luminosity Active Galactic Nuclei. I. VLA Detections of Compact, Flat-Spectrum Cores. *ApJ*, 542:186–196.

Nagar, N. M., Falcke, H., Wilson, A. S., and Ulvestad, J. S. (2002). Radio sources in low-luminosity active galactic nuclei. III. "AGNs" in a distance-limited sample of "LLAGNs". 392:53–82.

Nagar, N. M., Wilson, A. S., and Falcke, H. (2001). Evidence for Jet Domination of the Nuclear Radio Emission in Low-Luminosity Active Galactic Nuclei. *ApJ*, 559:L87–L90.

Nandra, K. and Pounds, K. A. (1994). GINGA Observations of the X-Ray Spectra of Seyfert Galaxies. 268:405.

Narayan, R., Kato, S., and Honma, F. (1997). Global Structure and Dynamics of Advection-dominated Accretion Flows around Black Holes. 476:49–60.

Narayan, R., Mahadevan, R., and Quataert, E. (1998). Advection-dominated accretion around black holes. In Abramowicz, M. A., Björnsson, G., and Pringle, J. E., editors, *Theory of Black Hole Accretion Disks*, pages 148–182.

Narayan, R. and McClintock, J. E. (2008). Advection-dominated accretion and the black hole event horizon. , 51:733–751.

Narayan, R. and Yi, I. (1994). Advection-dominated accretion: A self-similar solution. *ApJ*, 428:L13–L16.

Narayan, R. and Yi, I. (1995). Advection-dominated accretion: Self-similarity and bipolar outflows. *ApJ*, 444:231–243.

Nelson, C. H., Weistrop, D., Hutchings, J. B., Crenshaw, D. M., Gull, T. R., Kaiser, M. E., Kraemer, S. B., and Lindler, D. (2000). Space Telescope Imaging Spectrograph Long-Slit Spectroscopy of the Narrow-Line Region of NGC 4151. I. Kinematics and Emission-Line Ratios. *ApJ*, 531:257–277.

Nemmen, R. S., Bower, R. G., Babul, A., and Storchi-Bergmann, T. (2007). Models for jet power in elliptical galaxies: a case for rapidly spinning black holes. *MNRAS*, 377:1652–1662.

Nemmen, R. S., Storchi-Bergmann, T., and Eracleous, M. (2014). Spectral models for low-luminosity active galactic nuclei in LINERs: the role of advection-dominated accretion and jets. *MNRAS*, 438:2804–2827.

Nicholson, K. L., Mittaz, J. P. D., and Mason, K. O. (1997). Variability of faint ROSAT field sources. *MNRAS*, 285:831–838.

Nyland, K., Davis, T. A., Nguyen, D. D., Seth, A., Wrobel, J. M., Kamble, A., Lacy, M., Alatalo, K., Karovska, M., Maksym, W. P., Mukherjee, D., and Young, L. M. (2017). A Multi-wavelength Study of the Turbulent Central Engine of the Low-mass AGN Hosted by NGC 404. *ApJ*, 845:50.

Nyland, K., Young, L. M., Wrobel, J. M., Sarzi, M., Morganti, R., Alatalo, K., Blitz, L., Bournaud, F., Bureau, M., Cappellari, M., Crocker, A. F., Davies, R. L., Davis, T. A., de Zeeuw, P. T., Duc, P.-A., Emsellem, E., Khochfar, S., Krajnović, D., Kuntschner, H., McDermid, R. M., Naab, T., Oosterloo, T., Scott, N., Serra, P., and Weijmans, A.-M. (2016). The ATLAS^{3D} Project - XXXI. Nuclear radio emission in nearby early-type galaxies. *MNRAS*, 458:2221–2268.

Offringa, A. R., van de Gronde, J. J., and Roerdink, J. B. T. M. (2012). A morphological algorithm for improving radio-frequency interference detection. *A&A*, 539.

Ogle, P. M., Marshall, H. L., Lee, J. C., and Canizares, C. R. (2000). Chandra Observations of the X-Ray Narrow-Line Region in NGC 4151. 545:L81–L84.

Orienti, M. (2016). Radio properties of Compact Steep Spectrum and GHz-Peaked Spectrum radio sources. *Astronomische Nachrichten*, 337:9.

Osterbrock, D. E. and Pogge, R. W. (1985). The spectra of narrow-line Seyfert 1 galaxies. *ApJ*, 297:166–176.

Pacholczyk, A. G. and Scott, J. S. (1976). In situ particle acceleration and physical conditions in radio tail galaxies. *ApJ*, 203:313–315.

Padovani, P. (2016). The faint radio sky: radio astronomy becomes mainstream. *A&A Rev.*, 24:13.

Padovani, P., Perlman, E. S., Landt, H., Giommi, P., and Perri, M. (2003). What Types of Jets Does Nature Make? A New Population of Radio Quasars. *ApJ*, 588:128–142.

Page, K. L., Reeves, J. N., O'Brien, P. T., and Turner, M. J. L. (2005). XMM-Newton spectroscopy of high-redshift quasars. 364:195–207.

Pakull, M. W., Soria, R., and Motch, C. (2010). A 300-parsec-long jet-inflated bubble around a powerful microquasar in the galaxy NGC 7793. *Nature*, 466:209–212.

Panessa, F., Barcons, X., Bassani, L., Cappi, M., Carrera, F. J., Ho, L. C., and Pellegrini, S. (2007). The X-ray and Radio Connection in Low-luminosity Active Nuclei. *astro-ph/0701546*.

Panessa, F., Bassani, L., Cappi, M., Dadina, M., Barcons, X., Carrera, F. J., Ho, L. C., and Iwasawa, K. (2006). On the X-ray, optical emission line and black hole mass properties of local Seyfert galaxies. *A&A*, 455:173–185.

Panessa, F. and Giroletti, M. (2013). Sub-parsec radio cores in nearby Seyfert galaxies. *MNRAS*, 432:1138–1143.

Parma, P., de Ruiter, H. R., Fanti, C., and Fanti, R. (1986). VLA observations of low luminosity radio galaxies. I - Sources with angular size smaller than two arcminutes. *A&AS*, 64:135–171.

Parma, P., Fanti, C., Fanti, R., Morganti, R., and de Ruiter, H. R. (1987). VLA observations of low-luminosity radio galaxies. VI - Discussion of radio jets. *A&A*, 181:244–264.

Peck, L. W. and Fenech, D. M. (2013). SERPent: Automated reduction and RFI-mitigation software for e-MERLIN. *Astronomy and Computing*, 2:54–66.

Pedlar, A., Kukula, M. J., Longley, D. P. T., Muxlow, T. W. B., Axon, D. J., Baum, S., O'Dea, C., and Unger, S. W. (1993). The Radio Nucleus of NGC4151 at 5-GHZ and 8-GHZ. *MNRAS*, 263:471.

Pedlar, A., Unger, S. W., and Dyson, J. E. (1985). Radio Seyferts and the forbidden-line region. *MNRAS*, 214:463–473.

Pellegrini, S. (2005). Nuclear Accretion in Galaxies of the Local Universe: Clues from Chandra Observations. *ApJ*, 624:155–161.

Perez, E., Gonzalez-Delgado, R., Tadhunter, C., and Tsvetanov, Z. (1989). The complex narrow-line region in NGC 4151. *MNRAS*, 241:31P–36P.

Pérez, E., Márquez, I., Marrero, I., Durret, F., González Delgado, R. M., Masegosa, J., Maza, J., and Moles, M. (2000). Circumnuclear structure and kinematics in the active galaxy NGC 6951. *A&A*, 353:893–909.

Pérez-Torres, M. A., Alberdi, A., Marcaide, J. M., Guirado, J. C., Lara, L., Mantovani, F., Ros, E., and Weiler, K. W. (2002). A distorted radio shell in the young supernova SN 1986J. *MNRAS*, 335:L23–L28.

Peterson, B. M. (1997). Book Review: An introduction to active galactic nuclei / Cambridge U Press, 1997. *The Observatory*, 117:314.

Piconcelli, E., Jimenez-Bailón, E., Guainazzi, M., Schartel, N., Rodríguez-Pascual, P. M., and Santos-Lleó, M. (2005). The XMM-Newton view of PG quasars. I. X-ray continuum and absorption. 432:15–30.

Pietsch, W. and Arp, H. (2001). A possible X-ray jet from the starburst galaxy NGC 6217. 376:393–401.

Plotkin, R. M., Markoff, S., Kelly, B. C., Körding, E., and Anderson, S. F. (2012). Using the Fundamental Plane of black hole activity to distinguish X-ray processes from weakly accreting black holes. 419:267–286.

Press, W. H., Teukolsky, S. A., Vetterling, W. T., and Flannery, B. P. (2002). *Numerical recipes in C++ : the art of scientific computing*.

Ptak, A. (2001). Low-luminosity AGN and normal galaxies. *X-ray Astronomy: Stellar Endpoints, AGN, and the Diffuse X-ray Background*, 599:326–335.

Ptak, A., Terashima, Y., Ho, L. C., and Quataert, E. (2004). Testing Radiatively Inefficient Accretion Flow Theory: An XMM-Newton Observation of NGC 3998. *ApJ*, 606:173–184.

Quataert, E., Di Matteo, T., Narayan, R., and Ho, L. C. (1999). Possible Evidence for Truncated Thin Disks in the Low-Luminosity Active Galactic Nuclei M81 and NGC 4579. *ApJ*, 525:L89–L92.

Ramírez-Olivencia, N., Varenius, E., Pérez-Torres, M., Alberdi, A., Pérez, E., Alonso-Herrero, A., Deller, A., Herrero-Illana, R., Moldón, J., Barcos-Muñoz, L., and Martí-Vidal, I. (2018). Sub-arcsecond imaging of Arp 299-A at 150 MHz with LOFAR: Evidence for a starburst-driven outflow. *A&A*, 610:L18.

Ramos Almeida, C. and Ricci, C. (2017). Nuclear obscuration in active galactic nuclei. *Nature Astronomy*, 1:679–689.

Rampadarath, H., Soria, R., Urquhart, R., Argo, M. K., Brightman, M., Lacey, C. K., Schlegel, E. M., Beswick, R. J., Baldi, R. D., Muxlow, T. W. B., McHardy, I. M., Williams, D. R. A., and Dumas, G. (2018). Jets, Arcs and Shocks: NGC 5195 at radio wavelengths. *MNRAS*.

Rampazzo, R., Reduzzi, L., Sulentic, J. W., and Madejsky, R. (1995). Gaseous and stellar components in mixed pairs of galaxies. I. The data. *A&AS*, 110:131.

Ranalli, P., Comastri, A., Vignali, C., Carrera, F. J., Cappelluti, N., Gilli, R., Puccetti, S., Brandt, W. N., Brunner, H., Brusa, M., Georgantopoulos, I., Iwasawa, K., and Mainieri, V. (2013). The XMM deep survey in the CDF-S. III. Point source catalogue and number counts in the hard X-rays. *A&A*, 555:A42.

Rau, U. and Cornwell, T. J. (2011). A multi-scale multi-frequency deconvolution algorithm for synthesis imaging in radio interferometry. *A&A*, 532:A71.

Rees, M. J. (1984). Black Hole Models for Active Galactic Nuclei. *ARA&A*, 22:471–506.

Reeves, J. N. and Turner, M. J. L. (2000). X-ray spectra of a large sample of quasars with ASCA. 316:234–248.

Reynolds, C. S. (1997). An X-ray spectral study of 24 type 1 active galactic nuclei. *MNRAS*, 286:513–537.

Richards, E. E., van Zee, L., Barnes, K. L., Staudaher, S., Dale, D. A., Braun, T. T., Wavle, D. C., Calzetti, D., Dalcanton, J. J., Bullock, J. S., and Chandar, R. (2015). Baryonic distributions in the dark matter halo of NGC 5005. *MNRAS*, 449:3981–3996.

Richards, G. T., Myers, A. D., Gray, A. G., Riegel, R. N., Nichol, R. C., Brunner, R. J., Szalay, A. S., Schneider, D. P., and Anderson, S. F. (2009). Efficient Photometric Selection of Quasars from the Sloan Digital Sky Survey. II. ˜1,000,000 Quasars from Data Release 6. *ApJS*, 180:67–83.

Risaliti, G., Salvati, M., and Marconi, A. (2011). [O III] equivalent width and orientation effects in quasars. *MNRAS*, 411:2223–2229.

Roberts, T. P. and Warwick, R. S. (2000). A ROSAT High Resolution Imager survey of bright nearby galaxies. *MNRAS*, 315:98–114.

Robinson, A., Vila-Vilaro, B., Axon, D. J., Perez, E., Wagner, S. J., Baum, S. A., Boisson, C., Durret, F., Gonzalez-Delgado, R., Moles, M., Masegosa, J., O'Brien, P. T., O'Dea, C., del Olmo, A., Pedlar, A., Penston, M. V., Perea, J., Perez-Fournon, I., Rodriguez-Espinosa, J. M., Tadhunter, C., Terlevich, R. J., Unger, S. W., and Ward, M. J. (1994). The extended narrow line region of NGC 4151. *A&A*, 291:351–391.

Robitaille, T. P., Rossa, J., Bomans, D. J., and van der Marel, R. P. (2007). The morphology of minor axis gaseous outflows in edge-on Seyfert galaxies. *A&A*, 464:541–552.

Sadler, E. M. (1984). Radio and optical observations of a complete sample of E and SO galaxies. III. A radio continuum survey at 2.7 and 5.0 GHz. *AJ*, 89.

Sadler, E. M., Jenkins, C. R., and Kotanyi, C. G. (1989). Low-luminosity radio sources in early-type galaxies. *MNRAS*, 240:591–635.

Sadler, E. M., Slee, O. B., Reynolds, J. E., and Roy, A. L. (1995). Parsec-scale radio cores in spiral galaxies. *MNRAS*, 276:1373–1381.

Saikia, P., K örding, E., and Dibi, S. (2018). 1.4 GHz on the Fundamental Plane of Black Hole Activity. *ArXiv e-prints*.

Saikia, P., Körding, E., and Falcke, H. (2015). The Fundamental Plane of black hole activity in the optical band. 450:2317–2326.

Salak, D., Tomiyasu, Y., Nakai, N., and Miyamoto, Y. (2016). Multi-line Imaging of the Starburst Galaxy NGC 1808 with ALMA. *ArXiv e-prints*.

Sambruna, R. M., Urry, C. M., Tavecchio, F., Maraschi, L., Scarpa, R., Chartas, G., and Muxlow, T. (2001). Chandra Observations of the X-Ray Jet of 3C 273. *ApJ*, 549:L161–L165.

Sánchez-Gallego, J. R., Knapen, J. H., Wilson, C. D., Barmby, P., Azimlu, M., and Courteau, S. (2012). The JCMT Nearby Galaxies Legacy Survey - VII. Hα imaging and massive star formation properties. *MNRAS*, 422:3208–3sub.

Sandage, A. and Tammann, G. A. (1981). Revised Shapley-Ames Catalog of Bright Galaxies. In *Carnegie Inst. of Washington, Publ. 635; Vol. 0; Page 0*, volume 0.

Sarzi, M., Falcón-Barroso, J., Davies, R. L., Bacon, R., Bureau, M., Cappellari, M., de Zeeuw, P. T., Emsellem, E., Fathi, K., Krajnović, D., Kuntschner, H., McDermid, R. M., and Peletier, R. F. (2006). The SAURON project - V. Integral-field emission-line kinematics of 48 elliptical and lenticular galaxies. *MNRAS*, 366:1151–1200.

Sarzi, M., Shields, J. C., Schawinski, K., Jeong, H., Shapiro, K., Bacon, R., Bureau, M., Cappellari, M., Davies, R. L., de Zeeuw, P. T., Emsellem, E., Falcón-Barroso, J., Krajnović, D., Kuntschner, H., McDermid, R. M., Peletier, R. F., van den Bosch, R. C. E., van de Ven, G., and Yi, S. K. (2010). The SAURON project - XVI. On the sources of ionization for the gas in elliptical and lenticular galaxies. *MNRAS*, 402:2187–2210.

Sądowski, A., Narayan, R., Penna, R., and Zhu, Y. (2013). Energy, momentum and mass outflows and feedback from thick accretion discs around rotating black holes. *MNRAS*, 436:3856–3874.

Scheuer, P. A. G. and Williams, P. J. S. (1968). Radio Spectra. *ARA&A*, 6:321.

Schmidt, M. (1963). 3C 273 : A Star-Like Object with Large Red-Shift. *Nature*, 197:1040.

Schmidt, M. (1968). Space Distribution and Luminosity Functions of Quasi-Stellar Radio Sources. *ApJ*, 151:393.

Schwartz, D. A., Marshall, H. L., Lovell, J. E. J., Piner, B. G., Tingay, S. J., Birkinshaw, M., Chartas, G., Elvis, M., Feigelson, E. D., Ghosh, K. K., Harris, D. E., Hirabayashi, H., Hooper, E. J., Jauncey, D. L., Lanzetta, K. M., Mathur, S., Preston, R. A., Tucker, W. H., Virani, S., Wilkes, B., and Worrall, D. M. (2000). Chandra Discovery of a 100 kiloparsec X-Ray Jet in PKS 0637-752. *ApJ*, 540:69–72.

Seyfert, C. K. (1941). Nuclear Emission in Spiral Nebulae. 53:231–231.

Seymour, N., McHardy, I. M., and Gunn, K. F. (2004). Radio observations of the 13^hXMM-Newton/ROSAT Deep X-ray Survey Area. *MNRAS*, 352:131–141.

Shabala, S. S. (2018). The role of environment in the observed Fundamental Plane of radio active galactic nuclei. *MNRAS*, 478:5074–5080.

Shakura, N. I. and Sunyaev, R. A. (1973). Black holes in binary systems. Observational appearance. 24:337–355.

Shankar, F., Bernardi, M., Sheth, R. K., Ferrarese, L., Graham, A. W., Savorgnan, G., Allevato, V., Marconi, A., Läsker, R., and Lapi, A. (2016). Selection bias in dynamically measured supermassive black hole samples: its consequences and the quest for the most fundamental relation. *MNRAS*, 460:3119–3142.

Shankar, F., Weinberg, D. H., and Miralda-Escudé, J. (2009). Self-Consistent Models of the AGN and Black Hole Populations: Duty Cycles, Accretion Rates, and the Mean Radiative Efficiency. 690:20–41.

Shapiro, S. L., Lightman, A. P., and Eardley, D. M. (1976). A two-temperature accretion disk model for Cygnus X-1 - Structure and spectrum. *ApJ*, 204:187–199.

Sheth, K., Regan, M., Hinz, J. L., Gil de Paz, A., Menéndez-Delmestre, K., Muñoz-Mateos, J.-C., Seibert, M., Kim, T., Laurikainen, E., Salo, H., Gadotti, D. A., Laine, J., Mizusawa, T., Armus, L., Athanassoula, E., Bosma, A., Buta, R. J., Capak, P., Jarrett, T. H., Elmegreen, D. M., Elmegreen, B. G., Knapen, J. H., Koda, J., Helou, G., Ho, L. C., Madore, B. F., Masters, K. L., Mobasher, B., Ogle, P., Peng, C. Y., Schinnerer, E., Surace, J. A., Zaritsky, D., Comerón, S., de Swardt, B., Meidt, S. E., Kasliwal, M., and Aravena, M. (2010). The Spitzer Survey of Stellar Structure in Galaxies (). *PASP*, 122:1397.

Shu, X. W., Yaqoob, T., and Wang, J. X. (2010). The Cores of the Fe Kα Lines in Active Galactic Nuclei: An Extended Chandra High Energy Grating Sample. *The Astrophysical Journal Supplement Series*, 187:581–606.

Sikora, M., Stawarz, Ł., and Lasota, J.-P. (2007). Radio Loudness of Active Galactic Nuclei: Observational Facts and Theoretical Implications. *ApJ*, 658:815–828.

Sikora, M., Stawarz, Ł., and Lasota, J.-P. (2008). Radio-loudness of active galaxies and the black hole evolution. , 51:891–897.

Singh, R., van de Ven, G., Jahnke, K., Lyubenova, M., Falcón-Barroso, J., Alves, J., Cid Fernandes, R., Galbany, L., García-Benito, R., Husemann, B., Kennicutt, R. C., Marino, R. A., Márquez, I., Masegosa, J., Mast, D., Pasquali, A., Sánchez, S. F., Walcher, J., Wild, V., Wisotzki, L., and Ziegler, B. (2013). The nature of LINER galaxies:. Ubiquitous hot old stars and rare accreting black holes. *A&A*, 558:A43.

Slee, O. B., Sadler, E. M., Reynolds, J. E., and Ekers, R. D. (1994). Parsecscale Radio Cores in Early Type Galaxies. *MNRAS*, 269:928.

Slipher, V. M. (1917). The spectrum and velocity of the nebula N.G.C. 1068 (M 77). *Lowell Observatory Bulletin*, 3:59–62.

Stirling, A. M., Spencer, R. E., de la Force, C. J., Garrett, M. A., Fender, R. P., and Ogley, R. N. (2001). A relativistic jet from Cygnus X-1 in the low/hard X-ray state. 327:1273–1278.

Stoughton, C., Lupton, R. H., Bernardi, M., Blanton, M. R., Burles, S., Castander, F. J., Connolly, A. J., Eisenstein, D. J., Frieman, J. A., Hennessy, G. S., Hindsley, R. B., Ivezić, Ž., Kent, S., Kunszt, P. Z., Lee, B. C., Meiksin, A., Munn, J. A., Newberg, H. J., Nichol, R. C., Nicinski, T., Pier, J. R., Richards, G. T., Richmond, M. W., Schlegel, D. J., Smith, J. A., Strauss, M. A., SubbaRao, M., Szalay, A. S., Thakar, A. R., Tucker, D. L., Vanden Berk, D. E., Yanny, B., Adelman, J. K., Anderson, Jr., J. E., Anderson, S. F., Annis, J., Bahcall, N. A., Bakken, J. A., Bartelmann, M., Bastian, S., Bauer, A., Berman, E., Böhringer, H., Boroski, W. N., Bracker, S., Briegel, C., Briggs, J. W., Brinkmann, J., Brunner, R., Carey, L., Carr, M. A., Chen, B., Christian, D., Colestock, P. L., Crocker, J. H., Csabai, I., Czarapata, P. C., Dalcanton, J., Davidsen, A. F., Davis, J. E., Dehnen, W., Dodelson, S., Doi, M., Dombeck, T., Donahue, M., Ellman, N., Elms, B. R., Evans, M. L., Eyer, L., Fan, X., Federwitz, G. R., Friedman, S., Fukugita, M., Gal, R., Gillespie, B., Glazebrook, K., Gray, J., Grebel, E. K., Greenawalt, B., Greene, G., Gunn, J. E., de Haas, E., Haiman, Z., Haldeman, M., Hall, P. B., Hamabe, M., Hansen, B., Harris, F. H., Harris, H., Harvanek, M., Hawley, S. L., Hayes, J. J. E., Heckman, T. M., Helmi, A., Henden, A., Hogan, C. J., Hogg, D. W., Holmgren, D. J., Holtzman, J., Huang, C., Hull, C., Ichikawa, S., Ichikawa, T., Johnston, D. E., Kauffmann, G., Kim, R. S. J., Kimball, T., Kinney, E., Klaene, M., Kleinman, S. J., Klypin, A., Knapp, G. R., Korienek, J., Krolik, J., Kron, R. G., Krzesiński, J., Lamb, D. Q., Leger, R. F., Limmongkol, S., Lindenmeyer, C., Long, D. C., Loomis, C., Loveday, J., MacKinnon, B., Mannery, E. J., Mantsch, P. M., Margon, B., McGehee, P., McKay, T. A., McLean, B., Menou, K., Merelli, A., Mo, H. J., Monet, D. G., Nakamura, O., Narayanan, V. K., Nash, T., Neilsen, Jr., E. H., Newman, P. R., Nitta, A., Odenkirchen, M., Okada, N., Okamura, S., Ostriker, J. P., Owen, R., Pauls, A. G., Peoples, J., Peterson, R. S., Petravick, D., Pope, A., Pordes, R., Postman, M., Prosapio, A., Quinn, T. R., Rechenmacher, R., Rivetta, C. H., Rix, H.,

Rockosi, C. M., Rosner, R., Ruthmansdorfer, K., Sandford, D., Schneider, D. P., Scranton, R., Sekiguchi, M., Sergey, G., Sheth, R., Shimasaku, K., Smee, S., Snedden, S. A., Stebbins, A., Stubbs, C., Szapudi, I., Szkody, P., Szokoly, G. P., Tabachnik, S., Tsvetanov, Z., Uomoto, A., Vogeley, M. S., Voges, W., Waddell, P., Walterbos, R., Wang, S., Watanabe, M., Weinberg, D. H., White, R. L., White, S. D. M., Wilhite, B., Wolfe, D., Yasuda, N., York, D. G., Zehavi, I., and Zheng, W. (2002). Sloan Digital Sky Survey: Early Data Release. *AJ*, 123:485–548.

Swartz, D. A., Tennant, A. F., and Soria, R. (2009). Ultraluminous X-Ray Source Correlations with Star-Forming Regions. *ApJ*, 703:159–168.

Taniguchi, Y., Shioya, Y., and Murayama, T. (2000). Poststarburst Models of LINERS. *AJ*, 120:1265–1272.

Tchekhovskoy, A. and McKinney, J. C. (2012). Prograde and retrograde black holes: whose jet is more powerful? *MNRAS*, 423:L55–L59.

Tchekhovskoy, A., Narayan, R., and McKinney, J. C. (2011). Efficient generation of jets from magnetically arrested accretion on a rapidly spinning black hole. *MNRAS*, 418:L79–L83.

Terashima, Y. and Wilson, A. S. (2003). Chandra Snapshot Observations of Low-Luminosity Active Galactic Nuclei with a Compact Radio Source. 583:145–158.

Terlevich, R. and Melnick, J. (1985). Warmers - The missing link between Starburst and Seyfert galaxies. *MNRAS*, 213:841–856.

Tody, D. (1986). The IRAF Data Reduction and Analysis System. In Crawford, D. L., editor, *Instrumentation in astronomy VI*, volume 627 of *Proc. SPIE*, page 733.

Tody, D. (1993). IRAF in the Nineties. In Hanisch, R. J., Brissenden, R. J. V., and Barnes, J., editors, *Astronomical Data Analysis Software and Systems II*, volume 52 of *Astronomical Society of the Pacific Conference Series*, page 173.

Torresi, E., Grandi, P., Capetti, A., Baldi, R. D., and Giovannini, G. (2018). X-ray study of a sample of FR0 radio galaxies: unveiling the nature of the central engine. *MNRAS*.

Tremaine, S., Gebhardt, K., Bender, R., Bower, G., Dressler, A., Faber, S. M., Filippenko, A. V., Green, R., Grillmair, C., Ho, L. C., Kormendy, J., Lauer, T. R., Magorrian, J., Pinkney, J., and Richstone, D. (2002). The Slope of the Black Hole Mass versus Velocity Dispersion Correlation. *ApJ*, 574:740–753.

Trippe, M. L., Crenshaw, D. M., Deo, R. P., Dietrich, M., Kraemer, S. B., Rafter, S. E., and Turner, T. J. (2010). A Multi-wavelength Study of the Nature of Type 1.8/1.9 Seyfert Galaxies. *ApJ*, 725:1749–1767.

Trippe, S. (2014). Does the Jet Production Efficiency of Radio Galaxies Control Their Optical AGN Types? *Journal of Korean Astronomical Society*, 47:159–161.

Ulvestad, J. S. (2003). VLBI Imaging of Seyfert Galaxies. In Zensus, J. A., Cohen, M. H., and Ros, E., editors, *Radio Astronomy at the Fringe*, volume 300 of *Astronomical Society of the Pacific Conference Series*, page 97.

Ulvestad, J. S. and Ho, L. C. (2001a). Statistical Properties of Radio Emission from the Palomar Seyfert Galaxies. *ApJ*, 558:561–577.

Ulvestad, J. S. and Ho, L. C. (2001b). The Origin of Radio Emission in Low-Luminosity Active Galactic Nuclei: Jets, Accretion Flows, or Both? *ApJ*, 562:L133–L136.

Ulvestad, J. S. and Ho, L. C. (2002). A Search for Active Galactic Nuclei in Sc Galaxies with H II Spectra. *ApJ*, 581:925–931.

Ulvestad, J. S., Roy, A. L., Colbert, E. J. M., and Wilson, A. S. (1998). A Subparsec Radio Jet or Disk in NGC 4151. 496:196–202.

Ulvestad, J. S. and Wilson, A. S. (1984). Radio structures of Seyfert galaxies. VI - VLA observations of a nearby sample. *ApJ*, 285:439–452.

Ulvestad, J. S. and Wilson, A. S. (1989). Radio structures of Seyfert galaxies. VII - Extension of a distance-limited sample. *ApJ*, 343:659–671.

Ulvestad, J. S., Wilson, A. S., and Sramek, R. A. (1981). Radio structures of Seyfert galaxies. II. *ApJ*, 247:419–442.

Ulvestad, J. S., Wong, D. S., Taylor, G. B., Gallimore, J. F., and Mundell, C. G. (2005). VLBA Identification of the Milliarcsecond Active Nucleus in the Seyfert Galaxy NGC 4151. *AJ*, 130:936–944.

Unger, S. W., Booler, R. V., and Pedlar, A. (1984). A kiloparsec radio jet in the nucleus of the S0 galaxy NGC 1218 (3C78). *MNRAS*, 207:679–684.

Urry, C. M. and Padovani, P. (1995). Unified Schemes for Radio-Loud Active Galactic Nuclei. 107:803.

van den Bosch, R. C. E. (2016). Unification of the fundamental plane and Super Massive Black Hole Masses. *ApJ*, 831:134.

van Driel, W. and Buta, R. J. (1991). A study of the ringed galaxies NGC2273, 4826, and 6217. I - H I line observations. *A&A*, 245:7–26.

van Oers, P., Markoff, S., Rahoui, F., Maitra, D., Nowak, M., Wilms, J., Castro-Tirado, A. J., Rodriguez, J., Dhawan, V., and Harlaftis, E. (2010). Is the plateau state in GRS 1915+105 equivalent to canonical hard states? *MNRAS*, 409:763–776.

van Velzen, S., Anderson, G. E., Stone, N. C., Fraser, M., Wevers, T., Metzger, B. D., Jonker, P. G., van der Horst, A. J., Staley, T. D., Mendez, A. J., Miller-Jones, J. C. A., Hodgkin, S. T., Campbell, H. C., and Fender, R. P. (2016). A radio jet from the optical and x-ray bright stellar tidal disruption flare ASASSN-14li. *Science*, 351:62–65.

VanderPlas, J. (2014). Frequentism and Bayesianism: A Python-driven Primer. *ArXiv e-prints*.

Varenius, E., Conway, J. E., Martí-Vidal, I., Aalto, S., Beswick, R., Costagliola, F., and Klöckner, H.-R. (2014). The radio core structure of the luminous infrared galaxy NGC 4418. A young clustered starburst revealed? *A&A*, 566:A15.

Veilleux, S. and Osterbrock, D. E. (1987). Spectral classification of emission-line galaxies. 63:295–310.

Véron-Cetty, M.-P. and Véron, P. (2006). A catalogue of quasars and active nuclei: 12th edition. 455:773–777.

Vila, M. B., Pedlar, A., Davies, R. D., Hummel, E., and Axon, D. J. (1990a). Compact radio components in SBC galaxies. *MNRAS*, 242:379–394.

Vila, M. B., Pedlar, A., Davies, R. D., Hummel, E., and Axon, D. J. (1990b). Compact radio components in SBC galaxies. *MNRAS*, 242:379–394.

Vila-Vilaro, B., Robinson, A., Perez, E., Axon, D. J., Baum, S. A., Gonzalez-Delgado, R. M., Pedlar, A., Perez-Fournon, I., Perry, J. J., and Tadhunter, C. N. (1995). Circum-nuclear gas flows in NGC 4151. *A&A*, 302:58.

Volonteri, M., Sikora, M., Lasota, J.-P., and Merloni, A. (2013). The Evolution of Active Galactic Nuclei and their Spins. *ApJ*, 775:94.

Walter, F., Brinks, E., de Blok, W. J. G., Bigiel, F., Kennicutt, Jr., R. C., Thornley, M. D., and Leroy, A. (2008). THINGS: The H I Nearby Galaxy Survey. *AJ*, 136:2563–2647.

Wang, J., Fabbiano, G., Elvis, M., Risaliti, G., Karovska, M., Zezas, A., Mundell, C. G., Dumas, G., and Schinnerer, E. (2011a). A Deep Chandra ACIS Study of NGC 4151. III. The Line Emission and Spectral Analysis of the Ionization Cone. 742:23.

Wang, J., Fabbiano, G., Elvis, M., Risaliti, G., Mundell, C. G., Karovska, M., and Zezas, A. (2011b). A Deep Chandra ACIS Study of NGC 4151. II. The Innermost Emission Line Region and Strong Evidence for Radio Jet-NLR Cloud Collision. *ApJ*, 736:62.

Wang, J., Fabbiano, G., Risaliti, G., Elvis, M., Mundell, C. G., Dumas, G., Schinnerer, E., and Zezas, A. (2010). Extended X-ray Emission in the H I Cavity of NGC 4151: Galaxy-scale Active Galactic Nucleus Feedback? 719:L208–L212.

Wang, R., Wu, X.-B., and Kong, M.-Z. (2006). The Black Hole Fundamental Plane from a Uniform Sample of Radio and X-Ray-emitting Broad-Line AGNs. 645:890–899.

Weaver, R., McCray, R., Castor, J., Shapiro, P., and Moore, R. (1977). Interstellar bubbles. II - Structure and evolution. *ApJ*, 218:377–395.

Wells, D. C. (1985). *Data Analysis in Astronomy*. Springer US, Boston, MA.

Westcott, J., Brinks, E., Beswick, R. J., Heesen, V., Argo, M. K., Baldi, R. D., Fenech, D. M., McHardy, I. M., Smith, D. J. B., and Williams, D. R. A. (2017). A High-Resolution Radio Continuum Study Of The Dwarf Irregular Galaxy IC 10. *MNRAS*.

White, R. L., Becker, R. H., Gregg, M. D., Laurent-Muehleisen, S. A., Brotherton, M. S., Impey, C. D., Petry, C. E., Foltz, C. B., Chaffee, F. H., Richards, G. T., Oegerle, W. R., Helfand, D. J., McMahon, R. G., and Cabanela, J. E. (2000). The FIRST Bright Quasar Survey. II. 60 Nights and 1200 Spectra Later. *ApJS*, 126:133–207.

Williams, D. R. A., McHardy, I. M., Baldi, R. D., Beswick, R. J., Argo, M. K., Dullo, B. T., Knapen, J. H., Brinks, E., Fenech, D. M., Mundell, C. G., Muxlow, T. W. B., Panessa, F., Rampadarath, H., and Westcott, J. (2017). Radio jets in NGC 4151: where eMERLIN meets HST. 472:3842–3853.

Wilson, A. S. and Ulvestad, J. S. (1982). Radio structures of Seyfert galaxies. IV - Jets in NGC 1068 and NGC 4151. 263:576–594.

Wilson, A. S. and Ulvestad, J. S. (1983). Radio jets and high velocity gas in the Seyfert Galaxy NGC 1068. *ApJ*, 275:8–14.

Wilson, A. S. and Yang, Y. (2002). Chandra X-Ray Imaging and Spectroscopy of the M87 Jet and Nucleus. *ApJ*, 568:133–140.

Winge, C., Axon, D. J., Macchetto, F. D., and Capetti, A. (1997). The Narrow-Line Region of NGC 4151: A Turbulent Cauldron. *ApJ*, 487:L121–L124.

Winge, C., Axon, D. J., Macchetto, F. D., Capetti, A., and Marconi, A. (1999). Hubble Space Telescope Faint Object Camera Spectroscopy of the Narrow-Line Region of NGC 4151. I. Gas Kinematics. *ApJ*, 519:134–152.

Worrall, D. M. (2009). The X-ray jets of active galaxies. *A&A Rev.*, 17:1–46.

Worrall, D. M. and Birkinshaw, M. (2006). Multiwavelength Evidence of the Physical Processes in Radio Jets. In Alloin, D., editor, *Physics of Active Galactic Nuclei at all Scales*, volume 693 of *Lecture Notes in Physics, Berlin Springer Verlag*, page 39.

Wright, E. L., Eisenhardt, P. R. M., Mainzer, A. K., Ressler, M. E., Cutri, R. M., Jarrett, T., Kirkpatrick, J. D., Padgett, D., McMillan, R. S., Skrutskie, M., Stanford, S. A., Cohen, M., Walker, R. G., Mather, J. C., Leisawitz, D., Gautier, III, T. N., McLean, I., Benford, D., Lonsdale, C. J., Blain, A., Mendez, B., Irace, W. R., Duval, V., Liu, F., Royer, D., Heinrichsen, I., Howard, J., Shannon, M., Kendall, M., Walsh, A. L., Larsen, M., Cardon, J. G., Schick, S., Schwalm, M., Abid, M., Fabinsky, B., Naes, L., and Tsai, C.-W. (2010). The Wide-field Infrared Survey Explorer (WISE): Mission Description and Initial On-orbit Performance. *AJ*, 140:1868–1881.

Wrobel, J. M. (1991). Radio-continuum sources in nearby and bright E/S0 galaxies - Sample selection and well-studied cases. *AJ*, 101:127–147.

Wrobel, J. M. (2000). Photometric Variability and Astrometric Stability of the Radio Continuum Nucleus in the Seyfert Galaxy NGC 5548. *ApJ*, 531:716–726.

Wrobel, J. M. and Heeschen, D. S. (1991). Radio-continuum sources in nearby and bright E/S0 galaxies - Active nuclei versus star formation. *AJ*, 101:148–169.

Wrobel, J. M. and Ho, L. C. (2006). Radio Emission on Subparsec Scales from the Intermediate-Mass Black Hole in NGC 4395. *ApJ*, 646:L95–L98.

Xie, F.-G. and Yuan, F. (2017). Fundamental Plane of Black Hole Activity in the Quiescent Regime. *ApJ*, 836:104.

Younes, G., Porquet, D., Sabra, B., and Reeves, J. N. (2011). Study of LINER sources with broad Hα emission. X-ray properties and comparison to luminous AGN and X-ray binaries. *A&A*, 530:A149.

Yuan, F., Bu, D., and Wu, M. (2012). Numerical Simulation of Hot Accretion Flows. II. Nature, Origin, and Properties of Outflows and their Possible Observational Applications. *ApJ*, 761:130.

Yuan, F. and Cui, W. (2005). Radio-X-Ray Correlation and the "Quiescent State" of Black Hole Sources. 629:408–413.

Yuan, F., Markoff, S., Falcke, H., and Biermann, P. L. (2002). NGC 4258: A jet-dominated low-luminosity AGN? *A&A*, 391:139–148.

Yuan, F. and Narayan, R. (2014). Hot Accretion Flows Around Black Holes. 52:529–588.

Yuan, F., Yu, Z., and Ho, L. C. (2009). Revisiting the "Fundamental Plane" of Black Hole Activity at Extremely Low Luminosities. 703:1034–1043.

Zdziarski, A. A., Poutanen, J., and Johnson, W. N. (2000). Observations of Seyfert Galaxies by OSSE and Parameters of Their X-Ray/Gamma-Ray Sources. *ApJ*, 542:703–709.

Zhang, W. M., Soria, R., Zhang, S. N., Swartz, D. A., and Liu, J. F. (2009). A Census of X-ray Nuclear Activity in Nearby Galaxies. *ApJ*, 699:281–297.